METALS. SUPERCONDUCTORS

Initial stages in the decay of the amorphous phase in the bulk metallic glass Zr–Cu–Ti

G. E. Abrosimova,*) A. S. Aronin, A. F. Gurov, and Yu. V. Kir'yanov

Institute of Solid State Physics, Russian Academy of Sciences, 142432 Chernogolovka, Moscow District, Russia

V. V. Molokanov

Institute of Metallurgy, Russian Academy of Sciences, 117911 Moscow, Russia
(Submitted October 20, 1998)
Fiz. Tverd. Tela (St. Petersburg) **41**, 1129–1133 (July 1999)

Using methods of x-ray diffraction analysis, differential scanning calorimetry, dilatometry, and transmission electron microscopy, we have investigated the initial stages of decay of the amorphous phase in a bulk metallic glass based on zirconium. We found that crystallization of the bulk metallic glass proceeds in several stages, where in the first stage the bulk conversion effect is equal to more than 1.6%, or about 80% of the total bulk crystallization effect. We showed that the first stage of decay of the amorphous phase in the bulk metallic glass $Zr_{29}Ti_{11}Cu_{60}$ leads to the formation of a nanocrystalline structure with a grain size of 1–5 nm. We have analyzed the change in the shape of the diffraction maximum during the formation of the very fine nanocrystalline structure. © *1999 American Institute of Physics.*
[S1063-7834(99)00107-0]

The new upsurge of interest in amorphous materials is connected with the creation of new bulk amorphous alloys or bulk metallic glasses. The possibility of forming bulk metal glasses by quenching a melt is based on the fact that it has become possible to find new compositions which have a high viscosity in the liquid state and can produce the amorphous state at a comparatively moderate rate of cooling of the melt. The glass transition temperature of these materials is usually below the crystallization temperature. As a consequence, there is an extended temperature interval, wherein the alloy is found in the state of a supercooled liquid.[1–3] As a rule, these materials based on zirconium have a complex chemical makeup and only rarely contain less than three components. Bulk metallic glasses have good mechanical properties, characterized by a high stored energy of elastic deformation, such that the magnitude of the elastic deformation can exceed 3% (Ref. 4). In the temperature interval above the glass transition point, some bulk glasses, e.g., $Zr_{65}Al_{10}Ni_{10}Cu_{15}$, are superplastic,[5] the bulk glass $Zr_{57}Ti_5Al_{10}Cu_{20}Ni_8$ in the partially crystallized state possesses high flow and hardness limits (1800 and 1950 MPa, respectively),[6] and its hardness increases in the initial stages of crystallization.[7,8]

Bulk metallic glasses were developed and prepared independently by three research groups in Japan,[1] the USA,[3] and Russia.[9] The present paper is devoted to a study of thermal stabilization and of the initial stages of decay in the amorphous phase in the bulk metallic glass $Zr_{29}Ti_{11}Cu_{60}$, containing only three components.

1. EXPERIMENTAL TECHNIQUE

To prepare the alloys, we used pure metals ($>$99.8% purity). Ingots, 25 g in weight, were remelted four times in an arc furnace in an argon atmosphere. The metallic glass $Zr_{29}Ti_{11}Cu_{60}$ was obtained in the form of a rod of diameter 3 mm by pouring into a copper crucible in a helium atmosphere.

The structure and thermal stability of the metallic glass were investigated by differential scanning calorimetry, dilatometry, x-ray diffraction, and transmission electron microscopy. The calorimetric measurements used a Perkin–Elmer DSC-7 differential scanning calorimeter at a heating rate of 20 K/min. For the dilatometric measurements we used a Perkin-Elmer TMA-7 dilatometer; the heating rate in the dilatometric measurements was 10 K/min. The dilatometric and calorimetric measurements were performed in an argon atmosphere.

The structures of the initial and annealed samples were examined by x-ray diffraction, and by transmission and high-resolution electron microscopy on the same samples. The x-ray measurements were performed on a Siemens D-500 diffractometer with a Cu $K\alpha$ source. For the electron-microscope studies we used JEOL-100 CX and JEOL 4000 EX ($U = 400$ kV) instruments, with the electron microscope foils prepared by ion thinning.

The grain size in the crystallized samples was determined from electron-microscope data. In the analysis of the diffraction patterns we used special programs for separating the overlapping diffraction maxima and determining the half-widths of the diffraction peaks.
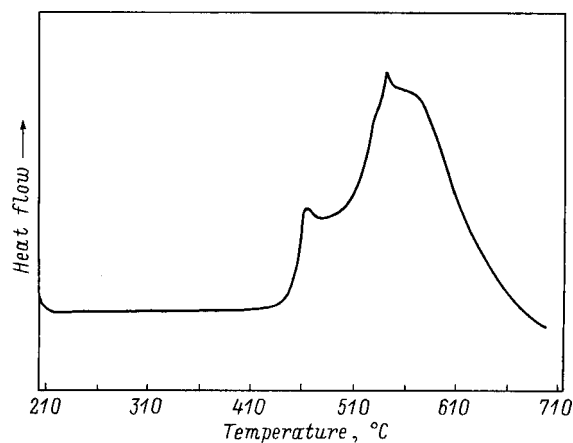
FIG. 1. Thermogram of the bulk metallic glass $Zr_{29}Ti_{11}Cu_{60}$.

2. EXPERIMENTAL RESULTS AND DISCUSSION

After preparation the samples were amorphous. Only diffuse reflections characteristic of the amorphous phase were present in the x-ray diffraction patterns and electron diffraction patterns. No signs of crystalline phases were detected in the electron-microscope images.

Figure 1 shows the calorimetric curve of a sample, taken at a heating rate of 20 K/min. A wide exothermic maximum is present in the thermogram, extending over the temperature interval 400–700 °C. This wide peak consists of at least three overlapping maxima. The temperatures of the maxima of the first two subpeaks are 491 and 545 °C, respectively. After heating in the calorimeter, the samples became coated with an oxide layer. Figure 2 displays an x-ray diffraction pattern of a sample heated in the calorimeter to 508 °C (ending point of the first DSC subpeak) and then cooled rapidly to room temperature. The x-ray diffraction pattern contains primarily reflections corresponding to the oxide ZrO_2. Besides reflections from the oxides, weak reflections from copper crystals

are also observed. After mechanically removing the surface layers, only diffuse reflections [Fig. 2(b)] remain in the x-ray diffraction patterns and at first glance the diffraction patterns show only signs of an amorphous structure.

After heating to 530 °C (the middle of the left branch of the second DSC subpeak) the samples contain a series of crystalline phases. Polishing the surface of the sample does not lead to a substantial change in the diffraction pattern: reflections from the oxide layer disappear, but reflections corresponding to the remaining crystalline phases are preserved. Thus, the impression is created that the first subpeak in the calorimetric curve is due to oxidation of the surface while maintaining the amorphous phase in the bulk of the sample, and crystallization corresponds to the higher-temperature subpeaks in the DSC curve.

In order to test this assumption, we carried out additional experiments.

1) The weight of the samples for the calorimetric measurements was substantially increased. In the first series of experiments we investigated samples of thickness 0.2 mm (the diameter of the samples was 3 mm). In the additional series of experiments the sample thickness was 1.5 mm. Thus, the surface area was increased by almost twofold while the weight of the sample was increased by a factor of 7.5. In this case, the contribution of oxidation to the total thermal conversion effect should have been markedly smaller since it is associated with surface oxidation. However, no significant change in the area of the first subpeak occurred. Consequently, it can be surmised that the first subpeak is associated with more than just surface oxidation.

2) We performed dilatometric measurements in the same temperature interval. The dilatometric curve, recorded at a heating rate of 10 K/min, is shown in Fig. 3. As can be seen from the figure, crystallization of the amorphous sample takes place in two stages. The bulk effect, corresponding to the first stage of conversion, is significantly greater than the
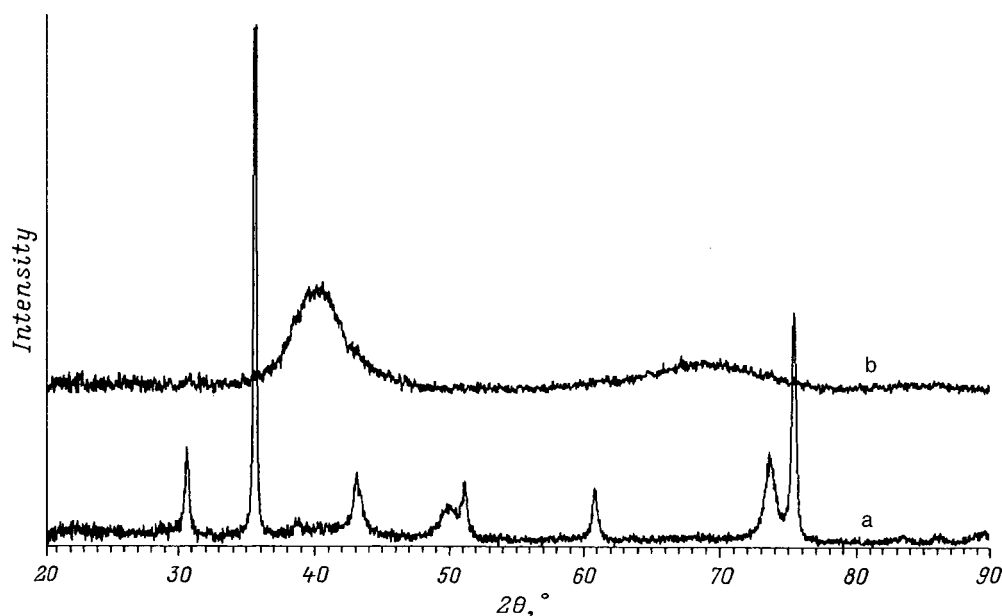

FIG. 2. X-ray diffraction pattern of a sample heated in the calorimeter to 508 °C before (a) and after (b) polishing of its surface.
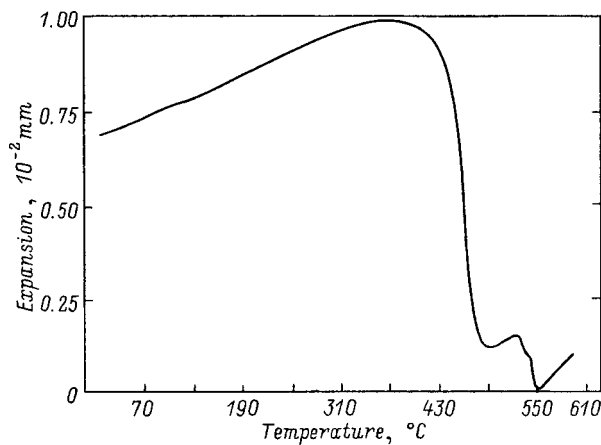
FIG. 3. Dilatometric curve for heating rate 10 K/min.

bulk effect in the second stage. Moreover, the second stage obviously includes within itself more than one process, as follows from the complex shape of the second maximum. Note that the first stage of conversion in the dilatometric curve corresponds to the first stage of conversion in the calorimetric curve, and the observed difference in temperatures is due to the different heating rate associated with peculiarities of the design of the dilatometer. The total bulk crystallization effect is around 2%, which is quite typical for crystallization of metallic glasses.[10] The bulk conversion effect in the first stage is around 80% of the total bulk crystallization effect. Such a large value of the bulk effect in the first stage does not agree with the conclusion drawn earlier that, after the first stage of conversion the structure remains amorphous. The magnitude of the bulk effect at this stage (more than 1.6%) is too large for structural-relaxation processes of the amorphous phase which occur during heating. Therefore it is natural to conclude that the alloy crystallizes during the conversion stage corresponding to the first DSC subpeak. Oxidation takes place in parallel and does not have a substantial effect on the shape of the DSC curves.

To investigate changes in the structure corresponding to the first stage of conversion, we performed x-ray diffraction measurements after polishing the samples, i.e., removing the
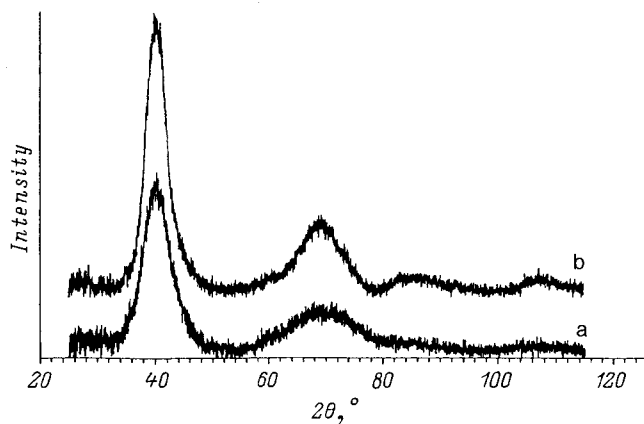

FIG. 4. Diffraction patterns of the starting sample (a) and after heating to 508 °C with subsequent polishing of its surface (b).

surface oxide layer. Figure 4 presents an x-ray diffraction pattern of the initial sample (*a*) and the sample heated in the calorimeter to 508 °C (b) (i.e., to a temperature above the end-point of the first DSC subpeak). Both patterns contain only diffuse maxima; however, the patterns differ markedly. We analyzed the diffraction patterns with the help of special computer programs which allow one to correct for the background, smooth data, separate overlapping maxima, and determine the half-widths of the maxima. We described the shape of the diffuse maximum with the help of the Gaussian

$$h \exp(-bx^2),$$

where the experimental curve and the calculated curve were fitted using both parameters: h and b. Note that the first maximum of curve a, corresponding to the initial amorphous phase, is described by a single Gaussian with a high degree of accuracy, and the half-width of the maximum is 4.3 in units of 2Θ (Cu $K\alpha$ radiation), which is quite typical for metallic glasses [Fig. 5(a)].

The diffraction pattern of sample (*b*), heated to the temperature marking the end-point of the first DSC subpeak, differs from patterns characteristic of metallic glasses. A typical diffraction pattern for the metallic amorphous phase consists of a set of diffuse maxima, the first of which is the most intense and differs sharply in intensity from all of the following maxima; the second maximum is characterized by the presence of a pronounced shoulder on the side of larger diffraction angles; subsequent maxima have abruptly decreasing intensities. During the structural relaxation preceding crystallization of metallic glasses, the height of the peaks of the interference function increases by $2-3\%$ (Ref. 11). T. Egami, investigating structural relaxation in metallic glasses, noted that structural relaxation is not the initial stage of crystallization, it leads to an increase in the stability of the amorphous state. Confirmation of this is provided by the fact that the changes in the second peak of the interference function during structural relaxation and crystallization are opposite.[12] The diffraction pattern we observed after heating the sample does not correspond to the case of structural relaxation of the amorphous phase. The normalized intensity of the first maximum in curve b is 10% greater than in curve a, the half-width of this maximum is 3.6 (in units of 2Θ) in comparison with 4.3 in the previous case, and the number and magnitude of the oscillations are considerably greater. The curve also changed considerably in the region of the second maximum: instead of a wide second maximum with a shoulder on the side of larger diffraction angles there appear two pronounced maxima, whose positions do not coincide with those of the shoulders of the maximum of the initial amorphous phase. And finally, there is one more important difference: the first maximum in the diffraction pattern of sample (*b*) cannot be described by a single Gaussian, but it is described quite well by a sum of two Gaussians [Fig. 5(b)], one of which corresponds to the amorphous phase. It may be conjectured that the second Gaussian with smaller half-width corresponds to the nascent nanocrystalline structure. The fraction of the nanocrystalline component of the structure is
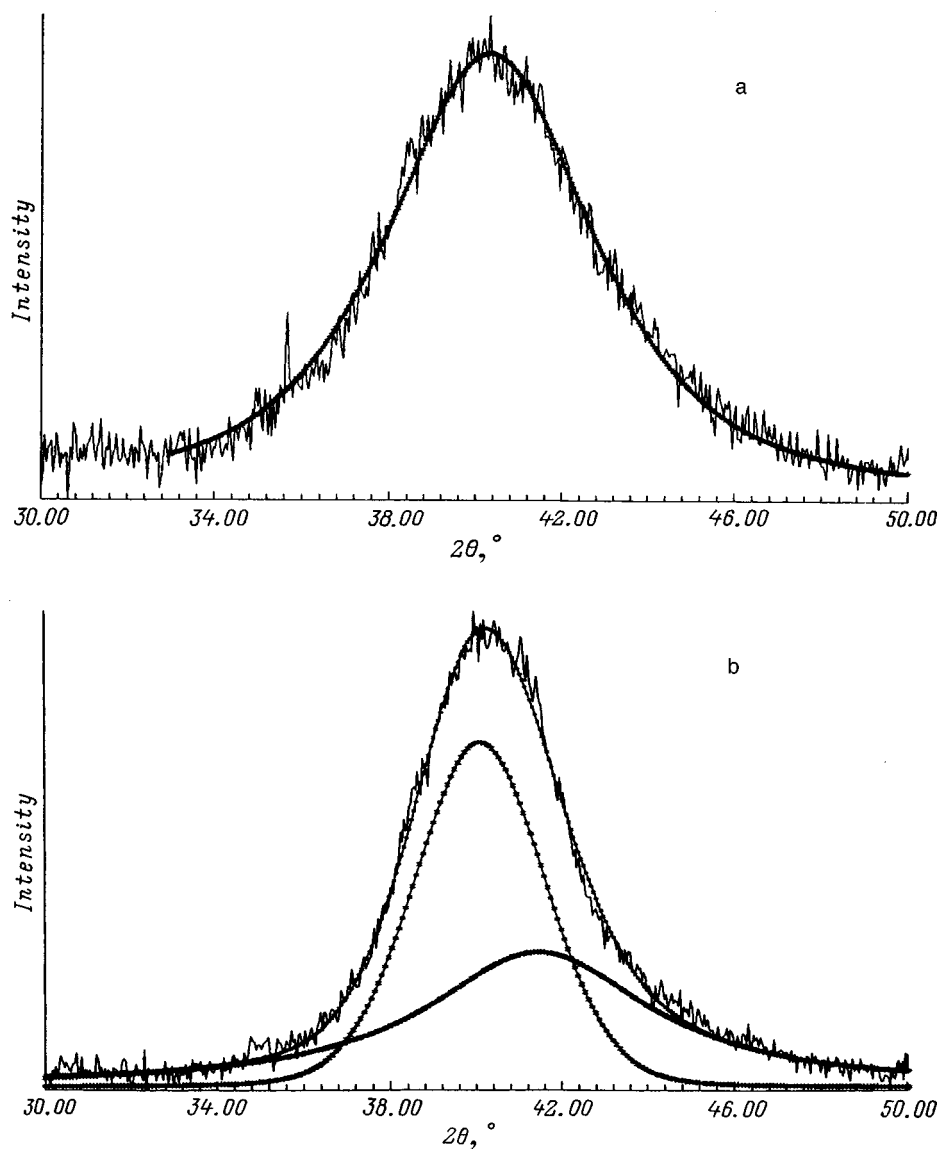
FIG. 5. Fitting of the first diffusion maximum of the starting sample (a) and after heating to 508 °C (b) (total curve is plotted along with its two Gaussian components).

greater than that of the amorphous phase, in agreement with the dilatometric measurements. Note that the difference in area of the diffuse maxima is not so large as could be expected from an analysis of the dilatometric data. However, it is necessary to bear in mind that in nanocrystalline materials with such grain size the fraction of grain boundaries is extraordinarily large and the disordered structure of boundaries undoubtedly contributes to diffuse scattering. The experimental data we have obtained do not permit us to draw any conclusions about possible changes in the chemical composition of the amorphous matrix during the formation in it of nanocrystals, nor does it allow us to draw any conclusions about the lattice parameter of the nanocrystals (it can be determined only with a large error) or the degree of chemical homogeneity or the chemical composition of the nanocrystals. In principle, the diffuse maximum observed in Fig. 5(b) can also be broken down into a sum of two Gaussians. The breakdown that we obtained corresponds to the case where the half-width of the maximum corresponding to the amor-

phous phase remains unchanged after heating, as is quite natural.

To test the conjectures advanced on the basis of the x-ray data, we investigated the structure of the samples using high-resolution transmission electron microscopy. According to the electron-microscope data, the starting sample is completely amorphous and only a hazy contrast is observed in the high-resolution electron-microscope images. In contrast, we found that sample (b), after being heated to 508 °C (the temperature corresponding to the end-point of the first sub-peak in the DSC plot and in x-ray diffraction pattern (*b*) in Fig. 4 which contains only diffuse maxima, has a very fine nanocrystalline structure. Figure 6 shows a high-resolution image of such a structure containing extraordinarily fine grains. For visual ease, we have circled images of a few nanocrystals in it. The size of the nanocrystals in this structure varies is $1-5$ nm.

Thus, the first stage of conversion during heating of samples of the metallic glass $Zr_{29}Ti_{11}Cu_{60}$, leading to a bulk
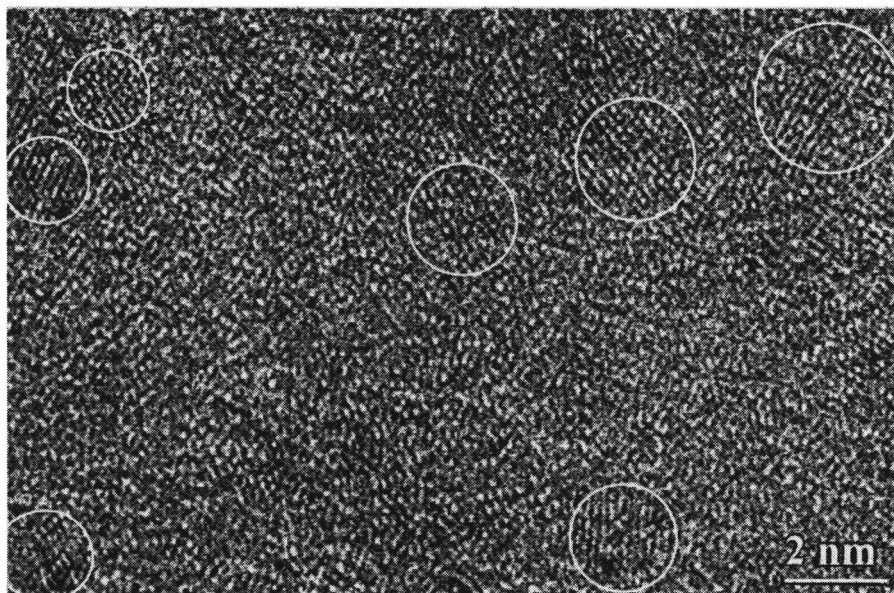
FIG. 6. High-resolution electron-microscope image of the structure of the sample after heating in the calorimeter to 508 °C.

effect greater than 1.6% leads to the formation of a nanocrystalline structure with a grain size of $1-5$ nm.

*)E-mail: gabros@issp.ac.ru

[1] A. Inoue, T. Zhang, N. Nishiyama, K. Ohba, and T. Masumoto, Mater. Trans., JIM **34**, 1234 (1993).

[2] A. Inoue, T. Shibata, and T. Zhang, Mater. Trans., JIM **36**, 1420 (1995).

[3] A. Peker and W. L. Johnson, Appl. Phys. Lett. **63**, 2342 (1993).

[4] L. Q. Xing, D. M. Herlach, M. Cornet, C. Bertrand, J.-P. Dallas, M.-H. Trichet, and J.-P. Chevalier, Mater. Sci. Eng., A **226−228**, 874 (1997).

[5] Y. Kawamura, T. Shibata, A. Inoue, and T. Masumoto, Scr. Mater. **37**, 431 (1997).

[6] L. Q. Xing, C. Bertrand, J.-P. Dallas, and M. Cornet, Mater. Lett. **34**, 90 (1998).

[7] S. Spriano, C. Antonione, R. Doglione, L. Battezzati, S. Cardoso, J. C. Soares, and M. F. da Silva, Philos. Mag. B **76**, 529 (1997).

[8] P. S. Frankwicz, S. Ram, and H.-J. Fecht, Appl. Phys. Lett. **68**, 2825 (1996).

[9] V. V. Molokanov, M. I. Petrzhik, T. N. Mikhailova, and Yu. K. Kovneristyi, J. Non-Cryst. Solids **205-207**, 508 (1996).

[10] I. V. Zolotukhin, *Physical Properties of Amorphous Metallic Materials* [in Russian] (Metallurgiya, Moscow, 1986), 176 pp.

[11] X. Waseda and T. Masumoto, Sci. Rep. Res. Inst. Tohoku Univ. A **27**, 21 (1978).

[12] T. Egami, J. Appl. Phys. **50**, 1564 (1979).

Translated by Paul F. Schippnick

Effect of nonstoichiometry and ordering on the period of the basis structure of cubic titanium carbide

L. V. Zueva and A. I. Gusev*⁾

Institute of Solid-State Chemistry, Ural Branch of the Russian Academy of Sciences, 620219 Ekaterinburg, Russia
(Submitted November 18, 1998)
Fiz. Tverd. Tela (St. Petersburg) **41**, 1134–1141 (July 1999)

We have examined the influence of nonstoichiometry and order–disorder phase transformations on the basis period (of type $B1$) of the structure of titanium carbide TiC_y ($0.5 < y < 1.0$). We found that ordering of titanium carbide TiC_y with formation of superstructures of the type Ti Ti_2C and Ti_3C_2 leads to growth of the period of the basis crystal lattice in comparison with the disordered carbide. Taking the change in the lattice period into account, we discuss the question of the directions of the static displacements of atoms near a vacancy. © *1999 American Institute of Physics.* [S1063-7834(99)00207-5]

Disordered titanium carbide TiC_y ($TiC_y\square_{1-y}$) with basis cubic structure of type $B1$ belongs to a group of strongly nonstoichiometric compounds and possesses a very wide range of homogeneity—from $TiC_{0.48}$ to $TiC_{1.00}$ (Refs. 1–3), within the limits of which the carbon atoms C and structural vacancies $\square$ form a substitutional solution in the nonmetallic sublattice. Depending on the composition, conditions of synthesis, and heat treatment, titanium carbide TiC_y can exist in either a disordered or ordered state.

Studies of order–disorder transitions in the related carbides VC_y,[4] NbC_y,[5,6] and TaC_y have revealed[6] that the period a_{B1} of the basis lattice of these carbides in the ordered state is larger than the period of disordered carbides with the same carbon content. Analogous systematic studies of the influence of ordering on the lattice period of titanium carbide have not been carried out. There are only disconnected indications of the variation of the period a_{B1} in TiC_y: in Refs. 7 and 8 the growth of a_{B1} after ordering anneals of $TiC_{0.53}$, $TiC_{0.58}$, $TiC_{0.63}$, and $TiC_{0.67}$; the authors of Ref. 9 reported on growth of the period of TiC_y ($0.6 \leq y < 0.9$) after annealing at 1000 and 900 K for 15 h after annealing at each temperature; the same effect was observed in $TiC_{0.49}$ and $TiC_{0.55}$ annealed at 773 K (Ref. 10).

The goal of the present work is to find out how nonstoichiometry and ordering affect the period of the basis structure of nonstoichiometric titanium carbide TiC_y.

1. SAMPLES AND EXPERIMENTAL TECHNIQUE

Samples of nonstoichiometric titanium carbide TiC_y ($0.50 \leq y \leq 1.00$) with differing carbon content were synthesized by three methods: 1 — solid-phase sintering of $TiC_{0.94}$ powders, gaseous soot, and metallic titanium at 2000 K for 6 h in a vacuum of 0.0013 Pa (1×10^{-5} Torr) with intermediate grinding of the products after 3 h of sintering; 2 — solid-phase sintering of powders of metallic titanium and gaseous soot at 1800 K for 8 h in a vacuum of 0.0013 Pa (1×10^{-5} Torr) with intermediate grinding of the products after 4 h of sintering; 3 — hot pressing of powder mixtures

of $TiC_{0.98}$ and metallic titanium in an atmosphere of high-purity argon (conditions of synthesis given in Table I). The synthesized samples were also annealed in vacuum quartz ampoules for 4 h at 1200 K with subsequent quenching of the ampoules with the samples in water to obtain the disordered state; the cooling rate during quenching was ~ 250 K min^{-1}.

The composition of the samples (Table I) and impurity content were determined by chemical and spectral analysis: the impurity nitrogen content was ~ 0.1 wt%; the oxygen impurity content in the samples prepared by hot pressing was $0.05 - 0.14$ wt.%, and in the samples prepared by solid-phase sintering it was 0.35 wt.% on average; the content of metallic impurities did not exceed 0.02 wt.%. X-ray analysis of the quenched samples was performed on a DRON-2 autodiffractometer with Cu $K\alpha_{1,2}$ emission using a comparison reference standard (powdered single-crystal silicon with cubic lattice period 0.543086 nm). The diffraction experiment showed that all of the quenched samples are homogeneous [splitting of x-ray reflection doublets was observed even for the $(311)_{B1}$ line] and contain only the disordered phase TiC_y with $B1$ structure. To determine the lattice period a_{B1}, we used the split doublets Cu $K\alpha_1$ and Cu $K\alpha_2$ of the structure reflections $(331)_{B1}$, $(420)_{B1}$, and $(422)_{B1}$. The error in the determination of a_{B1} did not exceed ± 0.0001 nm. The variation of the lattice period as a function of the composition of the disordered carbide TiC_y (Table I) is in good agreement with the most accurate data.[11]

To reach the ordered state, the titanium-carbide samples synthesized by solid-phase sintering were annealed for 455 h in the following regime: $1070 \text{ K} \times 23 \text{ h} + 1020 \text{ K} \times 90 \text{ h} + 970 \text{ K} \times 100 \text{ h} + 920 \text{ K} \times 65 \text{ h} + 870 \text{ K} \times 167 \text{ h}$; the temperature was then lowered to 300 K at a rate of 1 K·min^{-1}. Samples of the carbides $TiC_{0.52}$, $TiC_{0.54}$, $TiC_{0.58}$, $TiC_{0.62}$, $TiC_{0.68}$, $TiC_{0.83}$, and $TiC_{0.85}$, prepared by hot pressing, were annealed for 340 h in the regime $1070 \text{ K} \times 20 \text{ h} + 1020 \text{ K} \times 20 \text{ h} + 970 \text{ K} \times 24 \text{ h} + 920 \text{ K} \times 48 \text{ h} + 870 \text{ K} \times 72 \text{ h} + 820 \text{ K} \times 98 \text{ h} + 770 \text{ K} \times 48 \text{ h}$; the transition from one annealing temperature to the other, and also cooling from 770 to 300 K,

TABLE I. Composition, conditions of synthesis, and lattice period a_{B1} of samples of disordered titanium carbide TiC_y.

Composition TiC_y	Method of synthesis*	Composition, wt.%					Lattice period a_{B1}, nm	Conditions of synthesis		
		Ti	C_{bond}	C_{free}	O	N		temperature T, K	time t, h	pressing pressure p, MPa
$TiC_{0.50}$	1	88.42	11.18	None	0.24	0.15	0.43017	2000	6.0	–
$TiC_{0.50}$	2	88.45	11.20	–''–	0.17	0.08	0.43040	1800	8.0	–
$TiC_{0.52}$	3	88.29	11.51	–''–	0.05	0.06	0.43057	1773	0.5	20
$TiC_{0.54}$	3	87.87	11.96	–''–	0.08	0.06	0.43068	1773	0.5	25
$TiC_{0.55}$	1	87.32	12.08	–''–	0.20	0.07	0.43072	2000	6.0	–
$TiC_{0.58}$	3	87.13	12.71	–''–	0.11	0.07	0.43105	1773	0.5	25
$TiC_{0.59}$	1	86.62	12.90	–''–	0.21	0.08	0.43114	2000	6.0	–
$TiC_{0.60}$	2	86.68	13.13	–''–	0.15	0.07	0.43120	1800	8.0	–
$TiC_{0.62}$	3	86.31	13.43	–''–	0.08	0.07	0.43152	1923	0.5	23
$TiC_{0.63}$	1	86.05	13.58	–''–	0.30	0.06	0.43160	2000	6.0	–
$TiC_{0.67}$	2	85.52	14.30	–''–	0.14	0.08	0.43190	1800	8.0	–
$TiC_{0.68}$	1	84.45	14.37	–''–	0.76	0.07	0.43174	2000	6.0	–
$TiC_{0.68}$	3	85.26	14.63	–''–	0.10	0.07	0.43198	2173	0.5	30
$TiC_{0.69}$	1	84.38	14.70	–''–	0.30	0.08	0.43183	2000	6.0	–
$TiC_{0.70}$	2	85.24	14.84	–''–	0.06	0.05	0.43210	1800	8.0	–
$TiC_{0.80}$	2	82.83	16.67	–''–	0.21	0.09	0.43250	1800	8.0	–
$TiC_{0.81}$	1	82.14	16.75	–''–	0.18	0.08	0.43248	2000	6.0	–
$TiC_{0.83}$	1	82.02	17.03	–''–	0.38	0.07	0.43260	2000	6.0	–
$TiC_{0.83}$	3	82.45	17.24	–''–	0.14	0.07	0.43254	2173	0.5	30
$TiC_{0.85}$	3	82.18	17.51	–''–	0.12	0.07	0.43260	2173	0.5	30
$TiC_{0.90}$	1	80.79	18.30	–''–	0.45	0.08	0.43256	2000	6.0	–
$TiC_{0.90}$	2	80.92	18.32	–''–	0.23	0.06	0.43270	1800	8.0	–
$TiC_{0.925}$	1	80.41	18.65	0.25	0.51	0.07	0.43269	2000	6.0	–
$TiC_{0.94}$	1	79.68	18.84	⩽0.01	0.31	0.07	0.43259	2000	6.0	–
$TiC_{0.97}$	1	79.47	19.35	⩽0.01	0.22	0.08	0.43265	2000	6.0	–
$TiC_{0.98}$	3	80.02	19.69	None	0.08	0.07	0.43258	2473	0.5	35
$TiC_{0.99}$	2	79.60	19.72	0.18	0.17	0.09	0.43280	1800	8.0	–
$TiC_{1.00}$	2	79.07	19.79	0.28	0.18	0.12	0.43270	1800	8.0	–

*1 and 2—solid-phase vacuum sintering; 3—hot pressing.

were performed at a rate of $1\,K\cdot min^{-1}$. Annealing $TiC_{0.50}$ samples resulted in metallic titanium (α Ti) being liberated along the grain boundaries. Liberation of α Ti as a result of annealing of other carbides TiC_y ($y \geqslant 0.52$) was not observed.

The phase composition and crystal structure of the TiC_y samples after annealing were examined by x-ray analysis using Cu $K\alpha_{1,2}$ radiation scanning with a step $\Delta 2\theta = 0.02°$ in the angle interval $14° \leqslant 2\theta \leqslant 130°$; when recording the x-ray diffraction patterns we used an exposure time of 5 s at each point.

Annealing led to the appearance of superstructure reflections in the x-ray diffraction patterns of samples of $TiC_{0.50}$, $TiC_{0.52}$, $TiC_{0.54}$, $TiC_{0.55}$, $TiC_{0.58}$, $TiC_{0.59}$, $TiC_{0.62}$, $TiC_{0.63}$, $TiC_{0.67}$, and $TiC_{0.68}$. The same set of superstructure reflections corresponding to the cubic (space group $Fd3m$) of the ordered phase Ti_2C was observed in the x-ray diffraction patterns of annealed samples of $TiC_{0.50}$, $TiC_{0.52}$, $TiC_{0.54}$, and $TiC_{0.55}$. A distinguishing feature of the diffraction patterns of the annealed samples of $TiC_{0.58}$ and $TiC_{0.59}$ is trigonal splitting of the structure lines $(220)_{B1}$, $(311)_{B1}$, $(331)_{B1}$, $(420)_{B1}$, and $(422)_{B1}$, indicating the formation of a trigonal (space group $R\bar{3}m$) superstructure Ti_2C. In the x-ray diffraction patterns of the annealed carbides $TiC_{0.62}$ and $TiC_{0.63}$ along with reflections from the trigonal ordered phase Ti_2C we observed superstructure reflections from the rhom-

bic (space group $C222_1$) ordered phase Ti_3C_2. Annealing of the carbides $TiC_{0.67}$ and $TiC_{0.68}$ led to the appearance of superstructure reflections corresponding to the rhombic phase Ti_3C_2.

Thus, it follows from the structural data that during ordering of TiC_y in the ranges $TiC_{0.49} - TiC_{0.59}$ and $TiC_{0.63} - TiC_{0.68}$ ordered phases of the type Ti_2C and Ti_3C_2 are formed. A detailed analysis of the diffraction data and a description of the structure of the ordered phases of titanium carbide are given in a preceding paper (Ref. 12).

2. EXPERIMENTAL RESULTS AND DISCUSSION

The variation of the period of the basis crystal lattice as a function of composition of the disordered and ordered carbides TiC_y is plotted in Fig. 1. The dependence of the lattice period a_{B1} on the composition of the disordered carbide TiC_y was fitted by a second-degree polynomial $a_{B1}(y,0) = a_0 + a_1 y + a_2 y^2$ with $a_0 = 0.421595$ nm, $a_1 = 0.023699$ nm, and $a_2 = -0.012655$ nm.

As the composition varies from $TiC_{1.00}$ to $TiC_{0.92}$, the lattice period increases weakly and passes through a maximum at $TiC_{0.91-0.93}$. Further decrease of the carbon content in the disordered carbide TiC_y, i.e., growth in the concentration of structural vacancies, leads to a rapid decrease of the lattice period a_{B1}. The presence in the $a_{B1}(y)$ curve of an
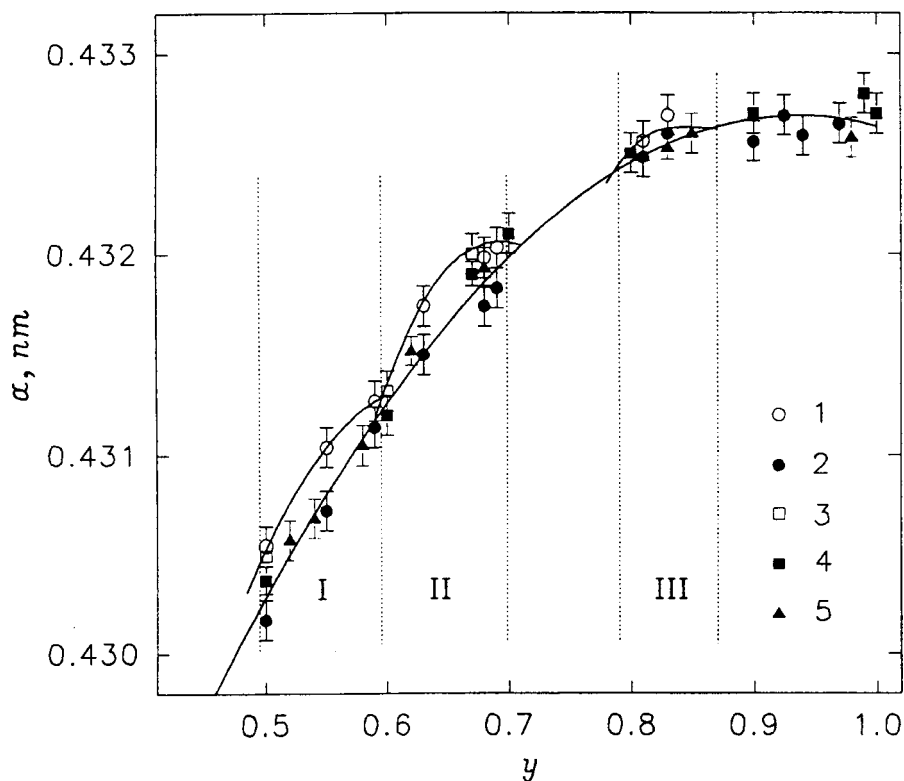
FIG. 1. Dependence of the period a_{B1} of the basis crystal lattice on the composition of the titanium carbide sample, TiC_y, in the quenched, disordered (*2, 4, 5*) and annealed, ordered (*1, 3*) states: *1, 2* — samples prepared by sintering Ti together with $TiC_{0.94}$; *3, 4* — samples prepared by sintering a mixture of Ti and C; *5* — samples prepared by hot pressing of Ti together with $TiC_{0.98}$; I, II, III — existence regions of ordered phases of Ti_2C, Ti_3C_2, and Ti_6C_5, respectively.

almost horizontal segment in the region $TiC_{0.90} - TiC_{1.00}$ (Fig. 1) indicates that, for a low concentration of structural vacancies, the perturbed regions created by them in the crystal lattice have a small radius and do not overlap. The absence of such a segment in the $a_{B1}(y)$ curve of NbC_y and TaC_y (Refs. 5 and 6) indicates that the perturbations created by the vacancies in these compounds are more long-range in nature than in titanium carbide TiC_y.

In carbides having the $B1$ structure each metal atom is in an octahedral environment of six sites of the nonmetallic sublattice, and each site of the nonmetallic sublattice is surrounded by six metal atoms. The presence of one or several structural vacancies in the immediate environment of a metal atom leads to its static displacement due to the asymmetry of the combined action of its nearest neighbors. Let us consider in what direction the metal atoms can be displaced so as to produce the experimentally observed decrease in the lattice period of TiC_y when the concentration of structural vacancies is increased.

If the metal atoms are displaced toward a vacancy, then growth of the concentration of vacant interstices $\Box M_6$ having a smaller linear dimension than the filled octahedral interstices CM_6 will be accompanied by a decrease in the lattice period a_{B1}. The period will decrease if the static displacements of the metal atom decrease monotonically and tend asymptotically to zero as the distance to a vacancy is increased and even in the case when the perturbations created by the vacancy extend out only to the first coordination sphere.

If the metal atoms nearest the vacancy are displaced away from it, then to decrease the lattice period the metal atoms forming the second coordination sphere should be dis-

placed in the opposite direction, i.e., toward a vacancy. Thus, the perturbation field created by a vacancy should extend out at least to the second coordination sphere of the metal atoms. In this case, the decay of perturbations with increasing distance undergoes Friedel oscillations. Judging from the estimates,[1,13–16] in nonstoichiometric cubic carbides MC_y the effective perturbation radius exceeds the period of the unit cell and the perturbation extends out past the second coordination sphere (e.g., in niobium carbide the correlations extend out to the eighth coordination sphere, Ref. 13).

Thus, in the most general case, a decrease in the lattice period of the disordered carbide with growth in the concentration of vacancies can occur when metal atoms of the first coordination sphere are displaced away from vacancies as well as toward them. The available experimental results on TiC_y show that titanium atoms in the first coordination sphere are shifted away from the vacancy.

The mean static atomic displacements $\langle u \rangle$ were determined in earlier studies by elastic diffuse neutron scattering on $TiC_{0.64}$ and $TiC_{0.76}$ single crystals.[16–18] The measurements were performed at 1173 K, which is quite clearly above the order–disorder transition temperature T_{trans}, that is, in disordered carbides. The values obtained for the short-range order parameter α and the static atomic displacements $\langle u \rangle$ for four coordination spheres centered about a vacancy are listed in Table II. Positive value of the displacements corresponds to movement of the atom away from the vacancy. As can be seen from Table II, for disordered carbides the main atomic displacement is a shift of the titanium atoms in the first coordination sphere away from the vacancy by roughly 0.005 nm.

A diagram of how the lattice period decreases, with in-

TABLE II. Short-range order parameter α, mean static atomic displacements $\langle u \rangle^*$ (in units of $a_{B1} \times 10^{-4}/2$) and displacements relative to an isolated vacancy u in titanium carbide.

Coordination sphere (hkl)		TiC$_{0.64}$ (a_{B1}=0.4322 nm at 300 K)				TiC$_{0.76}$ (a_{B1}=0.4330 mn at 300 K)			
		α Ref. 16	$\langle u \rangle^*$ Ref. 16	$\langle u \rangle$, nm (at 300 K)	u, nm (at 300 K)	α Ref. 16	$\langle u \rangle^*$ Ref. 16	$\langle u \rangle$, nm (at 300 K)	u, nm (at 300 K)
100 (I)	$\square$ — Ti	0	253	0.00547	0.00662	0	232	0.00502	0.00589
110 (II)	$\square$ — C	−0.058	−45	−0.00097		−0.047	−38	−0.00082	
111 (III)	$\square$ — Ti	0	−48	−0.00104		0	−40	−0.00087	
200 (IV)	$\square$ — C	−0.291	42	0.00091		−0.122	−13	−0.00028	

Note. The center of the coordination spheres is a vacancy.

dications of the directions of the atomic displacements during the formation of a vacancy, is shown in Fig. 2. It is constructed for the $(110)_{B1}$ plane of a nonstoichiometric carbide MC_y with $B1$ structure. The diagram takes into account propagation of the displacement field about the vacancy $\square$ out to several coordination spheres and the oscillating decay of the displacements with distance from the vacancy. Applying the data of Ref. 17, Fig. 3 plots the magnitude and direction of the static displacements of the titanium and carbon atoms $\langle u_{\square-\text{Ti}}^{hkl} \rangle$ and $\langle u_{\square-\text{C}}^{hkl} \rangle$ in the first 12 coordination spheres of a vacancy in the disordered carbide TiC$_{0.64}$. As can be seen from Fig. 3, the displacements of the Ti and C atoms oscillate, falling off in absolute value with distance r

from the vacancy, where the perturbations created by the vacancy propagate out to a distance equal to almost two periods of the unit cell.

The displacements $\langle u \rangle$, found from diffuse scattering, are averaged over all atomic configurations existing in TiC$_{0.64}$ and TiC$_{0.76}$ with a high concentration of structural vacancies. To first order, the displacement fields created by the vacancies are additive; therefore, the displacements $\langle u_{\square-\text{Ti}}^{100} \rangle$ of the titanium atoms of the first coordination sphere can be represented in the form

$$\langle u_{\square-\text{Ti}}^{100} \rangle = P_{\square-\text{C}}^{200} u_{\square-\text{Ti}}^{100} + P_{\square-\square}^{200} u_{\square-\text{Ti}}^{100(2)}, \tag{1}$$
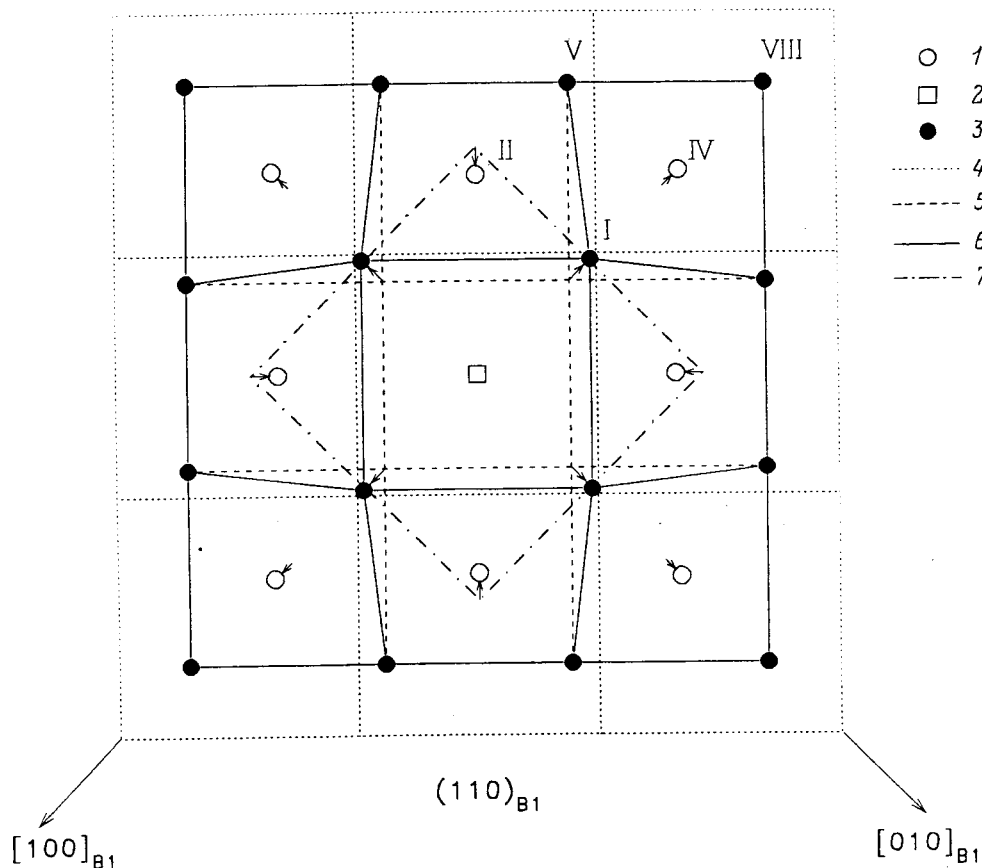

FIG. 2. Diagram of decrease in the lattice period of nonstoichiometric carbides MC_y (TiC$_y$) with structure $B1$ during formation of a $\square$ vacancy and static atomic displacements around the vacancy in the $(110)_{B1}$ plane: *1* — implantation atoms (C); *2* — vacancy; *3* — metal atoms (Ti); *4* — ideal defect-free lattice; *5* — lattice with vacancy (without atomic displacements taken into account); *6* — actual lattice with atomic displacements taken into account); *7* — contour of unit cell; I, II, IV, V, VIII — ordinal number of coordination spheres (relative to the vacancy); directions of displacements shown by arrows.
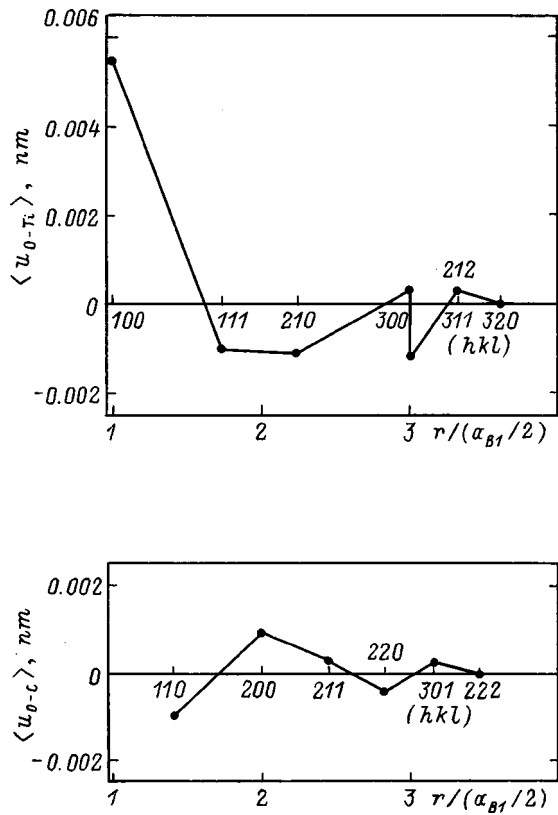
FIG. 3. Oscillation of the static displacements of the titanium and carbon atoms $\langle u_{\square - \text{Ti}} \rangle$ and $\langle u_{\square - \text{C}} \rangle$ relative to the vacancy with increasing radius r of the coordination sphere (hkl) in disordered titanium carbide $\text{TiC}_{0.64}$ (a positive value of the displacement corresponds to movement of the atom away from the vacancy, and a negative value corresponds to movement of the atom toward the vacancy); constructed with the help of experimental data from Ref. 17.

where $P^{200}_{\square - \text{C}} = y(1 - \alpha_{200})$ and $P^{200}_{\square - \square} = 1 - y(1 - \alpha_{200})$ are the probabilities of existence of the pairs $\square - \text{C}$ and $\square - \square$; $u^{100}_{\square - \text{Ti}}$ is the displacement of the titanium atoms relative to an isolated vacancy, i.e., in a chain of the sort $\square - \text{Ti} - \text{C}$; $u^{100(2)}_{\square - \text{Ti}} \equiv 0$, the displacement of the titanium atoms in a chain of the kind $\square - \text{Ti} - \square$, is identically equal to zero because of the symmetrical position of the Ti atom. Taking the above into account, the displacement of the titanium atoms relative to an isolated vacancy, $u^{100}_{\square - \text{Ti}}$, can be found using the formula

$$u^{100}_{\square - \text{Ti}} = \langle u^{100}_{\square - \text{Ti}} \rangle / [y(1 - \alpha_{200})]. \tag{2}$$

The calculated values of $u^{100}_{\square - \text{Ti}}$ (Table II) are equal to $0.006 - 0.007$ nm (the values of the displacements $u^{100}_{\square - \text{Ti}}$ given in Refs. 16 and 17 are incorrect since the values of α_{110} were used in the calculations by error instead of values of α_{200}). This is quite close to the data in the literature: the displacement of the Ti atoms from an isolated vacancy is 0.0044 nm in $\text{TiC}_{0.90}$ (Ref. 14), 0.0097 nm in $\text{TiC}_{0.94}$ (Ref. 19), and 0.0080 nm in $\text{TiC}_{0.97}$ (Ref. 20).

Studies of the structure of annealed samples of TiC_y show that in the composition intervals $\text{TiC}_{0.50} - \text{TiC}_{0.59}$ and $\text{TiC}_{0.63} - \text{TiC}_{0.68}$ the ordered phases Ti_2C and Ti_3C_2 form, and the composition interval $\text{TiC}_{0.59} - \text{TiC}_{0.63}$ corresponds to the two-phase region $\text{Ti}_2\text{C} + \text{Ti}_3\text{C}_2$. In addition, according to

theoretical calculations,[21] in the composition interval $\text{TiC}_{0.79} - \text{TiC}_{0.87}$ the formation of the ordered phase Ti_6C_5 is possible. Ordering is accompanied by growth of the period of the basis crystalline lattice a_{B1} of titanium carbide. In the dependence $a_{B1}(y)$ of the ordered carbide TiC_y it is possible to distinguish three segments corresponding to the possible ordered phases Ti_2C, Ti_3C_2, and Ti_6C_5 (Fig. 1). The most noticeable increase in the lattice period is observed for formation of the ordered phases Ti_3C_2 and, to a lesser degree, Ti_2C. In the composition range $\text{TiC}_{0.79} - \text{TiC}_{0.87}$, where formation of the phase Ti_6C_5 is possible, the increase in the period exceeds the measurement error by only an insignificant amount.

Ordering of titanium carbide is observed at high concentrations of structural vacancies $0.5 \geq (1 - y) > 0.2$. In the disordered carbide, at such concentrations of vacancies, the perturbed regions created by them overlap, and as a result the perturbations propagate throughout the entire crystal, leading to a rapid drop of the period a_{B1}. As a result of ordering, the vacancies and carbon atoms are redistributed over the sites of the nonmetallic sublattice in such a way that the relative number of vacancies that are nearest neighbors in the ordered carbide is less than in the disordered carbide of the same composition. The degree of overlap of perturbed regions is thereby lowered and the period a_{B1} of the basis crystalline lattice of the ordered carbide is greater than for the disordered carbide of the same composition.

A phenomenological model for quantitative analysis of variation of the lattice period a_{B1} during formation of the ordered phase $M_6\text{C}_5$ in the carbides NbC_y and TaC_y was suggested earlier by Lipatnikov *et al.*[6] Let us consider its application to the ordered phase $M_{2t}\text{C}_{2t-1}$ ($t = 1, 1.5, 2, 3,$ and 4), which can form in nonstoichiometric carbides.

In nonstoichiometric carbides with $B1$ basis structure, each metal atom is found in the immediate vicinity of six sites of the nonmetallic sublattice, which can be occupied by carbon atoms or be vacant. This makes it possible to represent a crystal with $B1$ structure as a set of clusters in the shape of a Dirichlet–Voronyĭ polyhedron, i.e., a distorted Wigner–Seitz cell (in the $B1$ structure, the Wigner–Seitz cell is a rhombododecahedron). Each cluster includes a metal atom located at its center, and six sites of the nonmetallic sublattice (Fig. 4). Such clusters in the form of Dirichlet–Voronyĭ polyhedra fill the entire crystal and occupy all sites of the crystal lattice.

To first approximation, we assume that the volume of a cluster V_m depends only on the number of vacancies m in it and does not depend on their mutual arrangement. In this case, the volume V of a crystal containing N metallic lattice sites has the form

$$V = N \sum_{m=0}^{6} \lambda_m P_m(y, \eta) V_m, \tag{3}$$

where $P_m(y, \eta)$ is the probability of formation of a cluster with m vacancies; η is the long-range order parameter; $\lambda_m = C_6^m$ is the multiplicity of an m-configuration of the cluster. On the other hand, the volume of disordered titanium carbide can be represented in terms of the period of the basis struc-
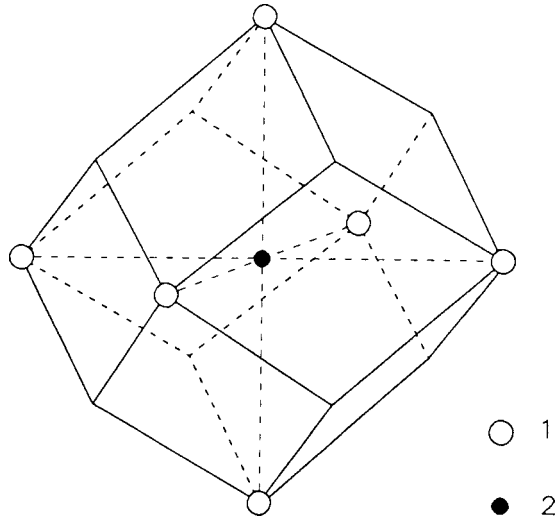
FIG. 4. Cluster figure (without distortions taken into account) used in the description of nonstoichiometric metal carbides MC_y with $B1$ basis structure: 1 — nonmetallic sublattice site; 2 — metal atom M.

ture $a_{B1}(y) = a_0 + a_1 y + a_2 y^2$ as $V = (N/4) a_{B1}^3(y)$. Taking this into account, Eq. (3) for the disordered carbide takes the form

$$\sum_{m=0}^{6} \lambda_m P_m(y,0) V_m = \frac{(a_0 + a_1 y + a_2 y^2)^3}{4}, \qquad (4)$$

where $P_m(y,0) = (1-y)^m y^{(6-m)}$ is the probability of formation in a disordered carbide of a cluster containing m vacancies. Solving Eq. (4), we find the volume of the cluster

$$V_m = \frac{1}{4} \sum_{k=m}^{6} A_{6-k} \frac{k!(6-m)!}{6!(k-m)!}, \qquad (5)$$

where A_{6-k} is the coefficient of y^k on the right-hand side of Eq. (4).

The contribution of each cluster to the total volume of the crystal is proportional to its probability P_m. For equilibrium conditions the probability $P_m(y,\eta)$ of the existence of

a cluster with m vacancies in an ordered phase of the type $M_{2t}C_{2t-1}$ with any degree of long-range order can be represented in the form[1,2,22]

$$P_{m,t}(y,\eta) = \frac{1}{\Phi} \sum_f \frac{g_f}{C_6^{\nu(t,f)}} \sum_{\nu=0}^{\nu(t,f)} C_{6-m}^{\nu(t,f)-\nu} C_m^{\nu}$$

$$\times n_1^{[\nu(t,f)-\nu]} n_2^{[6-m-\nu(t,f)+\nu]}$$

$$\times (1-n_1)^{\nu} (1-n_2)^{(m-\nu)}, \qquad (6)$$

where $n_1 = y - (2t-1)\eta/2t$ and $n_2 = y + \eta/2t$ are the probabilities of finding a carbon atom at a site of the vacancy and carbon sublattices during formation of a superstructure of the type $M_{2t}C_{2t-1}$; g_f is the multiplicity of nonequivalent positions of the metal atoms located at the center of each cluster ($\Sigma_f g_f = \Phi$); $\nu(t,f)$ is the number of sites of the vacancy sublattice belonging to a cluster with multiplicity g_f in the superstructure $M_{2t}C_{2t-1}$.

Using Eqs. (3), (5), and (6), it is possible to find the volume of the crystal and the period of the basis lattice a_{B1} of a nonstoichiometric carbide with any degree of order. We calculated the period a_{B1} of ordered titanium carbide in two ways.

In the first approach, we assumed that the maximum degree of long-range order η_{max} was reached in the crystal. According to Refs. 1 and 2, the dependence of η_{max} on the composition of the carbide MC_y during formation of an ordered phase of the type $M_{2t}C_{2t-1}$ has the form

$$\eta_{max}(y) = \begin{cases} 2t(1-y), & \text{if } y \geq (2t-1)/2t, \\ 2ty/(2t-1), & \text{if } y < (2t-1)/2t. \end{cases} \qquad (7)$$

In the second approach, we assumed that the long-range order parameter in ordered titanium carbide has the same value as it has at the order–disorder transition temperature T_{trans}, i.e., $\eta = \eta_{trans}$.

Calculation of the change in the lattice period $\Delta a_{B1} = a_{B1}(y,\eta) - a_{B1}(y,0)$ in the approximations $\eta = \eta_{max}$ and $\eta = \eta_{trans}$ (Table III) shows that the experimental values of

TABLE III. Variation of the period $\Delta a_{B1} = a_{B1}(y,\eta) - a_{B1}(y,0)$ of the basis (of type $B1$) of the crystal lattice during ordering of nonstoichiometric titanium carbide TiC_y.

			$\Delta a_{B1} = a_{B1}(y,\eta) - a_{B1}(y,0)$, nm						
			Calculation						
			$\eta = \eta_{equilib}$			$\eta = \eta_{trans}$		$\eta j = \eta_{max}$	
Carbide TiC_y	Phase transition	Experiment	η	T, K	Δa_{B1}	η	Δa_{B1}	η	Δ
$TiC_{0.50}$	$TiC_y \rightarrow Ti_2C$	0.00010	0.640	940	0.000100	—	—	1.000	0.000622
$TiC_{0.50}$	$TiC_y \rightarrow Ti_2C$	0.00035	0.735	760	0.000350	—	—	1.000	0.000622
$TiC_{0.55}$	$TiC_y \rightarrow Ti_2C$	0.00032	0.710	730	0.000320	—	—	0.900	0.000506
$TiC_{0.59}$	$TiC_y \rightarrow Ti_2C$	0.00013	0.510	1020	0.000229	—	—	0.820	0.000421
$TiC_{0.60}$	$TiC_y \rightarrow Ti_3C_2$	0.00010	0.340	800	0.000100	0.190	0.000018	0.900	0.000401
$TiC_{0.63}$	$TiC_y \rightarrow Ti_3C_2$	0.00014	0.400	760	0.000140	0.233	0.000030	0.945	0.000501
$TiC_{0.67}$	$TiC_y \rightarrow Ti_3C_2$	0.00010	0.365	760	0.000100	0.281	0.000043	0.990	0.000551
$TiC_{0.68}$	$TiC_y \rightarrow Ti_3C_2$	0.00024	0.560	600	0.000240	0.289	0.000046	0.960	0.000519
$TiC_{0.69}$	$TiC_y \rightarrow Ti_3C_2$	0.00020	0.515	610	0.000200	0.296	0.000049	0.930	0.000487
$TiC_{0.81}$	$TiC_y \rightarrow Ti_6C_5$	0.00008	<0.60	<600	0.000080	0.632	0.000140	0.972	0.000332
$TiC_{0.83}$	$TiC_y \rightarrow Ti_6C_5$	0.00020	0.750	610	0.000200	0.635	0.000142	0.996	0.000349

Δa_{B1} correspond to an intermediate value of the long-range order parameter $\eta_{trans} < \eta < \eta_{max}$. Table III lists calculated values of $\eta = \eta_{equilibr}$ at which the experimentally observed change in the lattice period Δa_{B1} is reached and the temperature T at which this value of the long-range parameter is the equilibrium value. The values of η_{trans} and $\eta_{equilibr}$ were calculated using the method of a functional of the order parameters.[2,21,22]

The changes Δa_{B1} in the period of TiC$_y$ during ordering, found in the present work, are similar to the values measured by the authors of Ref. 9: 0.00052 nm for TiC$_{0.60}$, 0.00028 nm for TiC$_{0.70}$, and 0.00012 nm for TiC$_{0.80}$. According to Ref. 8, after an extended ordering anneal of TiC$_{0.53}$ and TiC$_{0.58}$ the change in the lattice period, Δa_{B1}, was 0.00168 and 0.00112 nm. However, during annealing of these carbides metallic titanium was released in the amounts of 11.3 and 3.3 at.%, and the actual composition of the samples was TiC$_{0.58}$ and TiC$_{0.60}$. Taking this into account, the change in the lattice period, Δa_{B1}, due to ordering of TiC$_{0.58}$, TiC$_{0.60}$, TiC$_{0.63}$, and TiC$_{0.67}$ is equal to 0.00088, 0.00082, 0.00032, and 0.00008 nm (Ref. 8).

The changes in the lattice period of TiC$_y$ during ordering are comparable in magnitude to the changes in the lattice period in those parts of the homogeneity region of TiC$_y$ where ordered phases are formed. For example, as the composition of the disordered carbide varies from TiC$_{0.50}$ to TiC$_{0.59}$ the period a_{B1} increases by 0.00089 nm while as a result of the formation of the ordered phase Ti$_2$C the maximum increase of the period is equal to 0.00035 nm; in the region TiC$_{0.63}$−TiC$_{0.68}$, where a superstructure of the type Ti$_3$C$_2$ is formed, the period of the disordered carbide varies by 0.00036 nm whereas during ordering the lattice period changes by $\Delta a_{B1} = 0.\bar{0}0024$ nm. Thus, the effects of nonstoichiometry and ordering on the period of the basis lattice of TiC$_y$ are comparable in magnitude.

The changes in the period of the basis lattice taking place as a result of ordering in nonstoichiometric titanium carbide TiC$_y$ indicate that the phase transformations TiC$_y \leftrightarrow$ Ti$_2$C and TiC$_y \leftrightarrow$ Ti$_3$C$_2$ are most likely first-order. This coincides with the conclusions of Ref. 12 to the effect that the order–disorder phase transformations taking place in TiC$_y$ are first-order.

*)E-mail: gusev@chem.ural.ru

---

[1] A. I. Gusev and A. A. Rempel', *Structural Phase Transitions in Nonstoichiometric Compounds* [in Russian] (Nauka, Moscow, 1988).

[2] A. I. Gusev, *Physical Chemistry of Nonstoichiometric Refractory Compounds* [in Russian] (Nauka, Moscow, 1991).

[3] A. I. Gusev, Phys. Status Solidi B **163**, 17 (1991).

[4] T. Athanassiadis, N. Lorenzelli, and C. H. de Novion, Ann. Chim. (Paris) **12**, 129 (1987).

[5] A. I. Gusev and A. A. Rempel', Fiz. Tverd. Tela (Leningrad) **26**, 3622 (1984) [Sov. Phys. Solid State **26**, 2178 (1984)].

[6] V. N. Lipatnikov, A. A. Rempel', and A. I. Gusev, Izv. Akad. Nauk SSSR, Neorg. Mater. **26**, 2522 (1990).

[7] V. Moisy-Maurice, Structure atomique des carbures non-stoechiometriques de métaux de transition. Rapport CEA-R-5127. Commissariat à l'Energie Atomique. Gif-sur-Yvette, France (1981).

[8] V. Moisy-Maurice, N. Lorenzelli, C. H. de Novion, and P. Convert, Acta Metall. **30**, 1769 (1982).

[9] V. N. Lipatnikov, A. A. Rempel, and A. I. Gusev, Int. J. Refract. Metals and Hard Mater. **15**, Nos. 1–3, 61 (1997).

[10] A. N. Emel'yanov, Teplofiz. Vys. Temp. **28**, 269 (1990).

[11] L. Ramqvist, Jernkont. Annaler **152**, 517 (1968).

[12] V. N. Lipatnikov, A. Kottar, L. V. Zueva, and A. I. Gusev, Fiz. Tverd. Tela (St. Petersburg) **40**, 1332 (1998) [Phys. Solid State **40**, 1211 (1998)].

[13] V. Moisy-Maurice, C. H. de Novion, A. N. Christensen, and W. Just, Solid State Commun. **39**, 661 (1981).

[14] R. Kaufmann and O. Meyer, Solid State Commun. **51**, 539 (1984).

[15] A. I. Gusev and A. A. Rempel, Phys. Status Solidi B **154**, 453 (1989).

[16] C. H. de Novion, B. Beuneu, T. Priem, N. Lorenzelli, and A. Finel, in *The Physics and Chemistry of Carbides, Nitrides and Borides*, edited by R. Freer (Kluwer Acad. Publ., Netherlands, 1990), pp. 329–355.

[17] T. Priem, Etude de l'ordre a courte distance dans les carbures et nitrures non-stoechiométriques de métaux de transition par diffusion diffuse de neutrons. Rapport CEA-R-5499. Commissariat à l'Energie Atomique. Gif-sur-Yvette (France) (1989). 162 p.

[18] T. Priem, B. Beuneu, C. H. de Novion, J. Chevrier, F. Livet, A. Finel, and S. Lefebvre, Physica B **156−157**, 47 (1989).

[19] A. Dunand, H. D. Flack, and K. Yvon, Phys. Rev. B **31**, 2299 (1985).

[20] V. Moisy-Maurice and C. H. de Novion, J. Phys. (France) **49**, 1737 (1988).

[21] A. I. Gusev and A. A. Rempel, Phys. Status Solidi A **163**, 273 (1997).

[22] A. I. Gusev, Philos. Mag. B **60**, *3*, 307 (1989).

Translated by Paul F. Schippnick

NMR study of the intermetallic Laves alloys LuFe$_2$ and LuFe$_{1.96}$Al$_{0.04}$

V. S. Pokatilov

Moscow Institute of Radio Engineering and Automation, 117454 Moscow, Russia
(Submitted November 28, 1998)
Fiz. Tverd. Tela (St. Petersburg) **41**, 1142–1144 (July 1999)

NMR spectra of ^{57}Fe and ^{27}Al in LuFe$_2$ and LuFe$_{0.96}$Al$_{0.04}$ alloys were measured by the spin echo method at 4.2 K. The main contributions to the hyperfine fields on ^{57}Fe nuclei are estimated, along with the magnetic moments on the Fe and Lu atoms in LuFe$_2$. © *1999 American Institute of Physics.* [S1063-7834(99)00307-X]

During roughly the last ten years, the intermetallic Laves compounds AFe$_2$ ($A = Y$, Sc, Zr, Hf, etc.) have attracted a great deal of interest from the research community. Previously it was presumed that only the iron atom possesses a magnetic moment in these compounds. However, calculations of the electronic structures of many of these compounds have shown that the A atoms should also have a magnetic moment, with the magnetic moments of these atoms antiparallel to the moments of the iron atoms.[1–4] In polarized neutron scattering studies in the alloys YFe$_2$ (Ref. 5) and ZrFe$_2$ (Ref. 6), and also in NMR studies of YFe$_2$ (Ref. 7), ZrFe$_2$ (Ref. 8), and ScFe$_2$ (Ref. 9) it was found that the A atoms (Cs, Y, Zr) possess a negative magnetic moment relative to the moment of the iron atoms. A study of the dependence of the frequency of the maximum of the NMR spectrum f_0 on ^{89}Y nuclei in YFe$_2$ and ^{91}Zr nuclei in ZrFe$_2$ (Ref. 10) on the external pressure P has shown that f_0 grows with increasing P. These data point to the existence of a positive ''local'' contribution to the experimental hyperfine fields (HFF) on the ^{89}Y and ^{91}Zr nuclei and, consequently, negative magnetic moments on the Y and Zr atoms.

Calculations of the electronic structures of the alloy LuFe$_2$ (Ref. 4) predict a negative magnetic moment on the Lu atoms $\mu(\text{Lu}) = -0.41 \mu_b$. In a neutron scattering study of LuFe$_2$ (Ref. 11) the authors estimated only the magnetic moment on the iron atoms. Recently, a study of the dependence of the NMR frequency f_0 of ^{175}Lu nuclei on the external pressure P in LuFe$_2$ (Ref. 12) showed that the quantity $\partial f_0 / \partial P$ is positive and, consequently, the lutetium atoms should have a negative magnetic moment. Experimental estimates of the magnetic moments on the lutetium atoms are also lacking.

The present paper presents results of an NMR study of Laves alloys with cubic structure based on LuFe$_2$, containing an aluminum impurity, whose purpose was to measure the hyperfine fields on the ^{57}Fe and ^{27}Al nuclei, and also estimates of the magnetic moments on the iron and lutetium atoms.

1. EXPERIMENTAL DATA

Samples of the alloys LuFe$_2$ and LuFe$_{1.96}$Al$_{0.04}$ were prepared from metals of high purity in an arc furnace in an atmosphere of high-purity argon. In the melting process,

losses to metal evaporation were taken into account. Ingots of LuFe$_2$ and LuFe$_{1.96}$Al$_{0.04}$ obtained in this way were annealed for 50 h at 900 °C in an argon atmosphere. X-ray measurements on powder samples obtained from these ingots showed that the alloys had cubic structure and were single-phase. NMR spectra were recorded by the spin-echo method at 4.2 K. The NMR spectra were normalized to the square of the measurement frequency.

As is well known,[13] to obtain the necessary resolution and accurate measurements of the narrow NMR spectra in ferromagnets requires that one use radio pulses (to excite the echo) of comparatively long duration τ and small amplitude B_0. The NMR spectrum of ^{57}Fe in LuFe$_2$ was measured with the help of two identical radio pulses with $\tau \gtrsim 10\,\mu$s (i.e., the frequency range of echo excitation was $\Delta f \leqslant 0.1$ MHz) and $B_0 \leqslant 0.3 B_m$ (where B_m is the amplitude of the radio pulses corresponding to the strongest echo signal at the maximum of the NMR spectrum). For LuFe$_{1.96}$Al$_{0.04}$ the duration of the radio pulses was $\tau \gtrsim 5\,\mu$s. Besides the requirement of small angles (α) of rotation of the nuclear magnetization ($\alpha \sim \tau B_0$) in the measurement of the NMR spectra, it is also necessary to keep the quantity $B_0 f$ fixed for the entire range of measurement frequencies f. According to Ref. 14, provided these experimental conditions are observed, the measured NMR spectrum, normalized to the square of the frequency (f^2), corresponds to the true distribution of the resonant frequencies (or hyperfine fields) for the investigated ferromagnet.

Figure 1 shows NMR spectra of LuFe$_2$ and LuFe$_{1.96}$Al$_{0.04}$. The NMR spectrum of ^{57}Fe in LuFe$_2$ has an asymmetric line with maximum at 28.6 MHz. Usually, the NMR spectrum of ^{57}Fe in cubic Laves phases (MgCu$_2$) based on Fe consists of two lines (in the ratio 1:3) due to the two magnetically nonequivalent states of the Fe atoms, where the direction of the easy axis coincides with the $\langle 111 \rangle$ direction. For the case where the easy axis coincides with the $\langle 100 \rangle$ direction, the NMR spectrum of ^{57}Fe consists of a single line, and for the $\langle 110 \rangle$ direction, of two lines of identical intensity. From Fig. 1(a) it can be seen that in the frequency region around 28.0 MHz there is an additional contribution to the spectrum. Geometric separation of the lines shows that the ratio of areas of the lines with maxima at 28.0 and 28.6 MHz is equal roughly to 1:2. In the unannealed
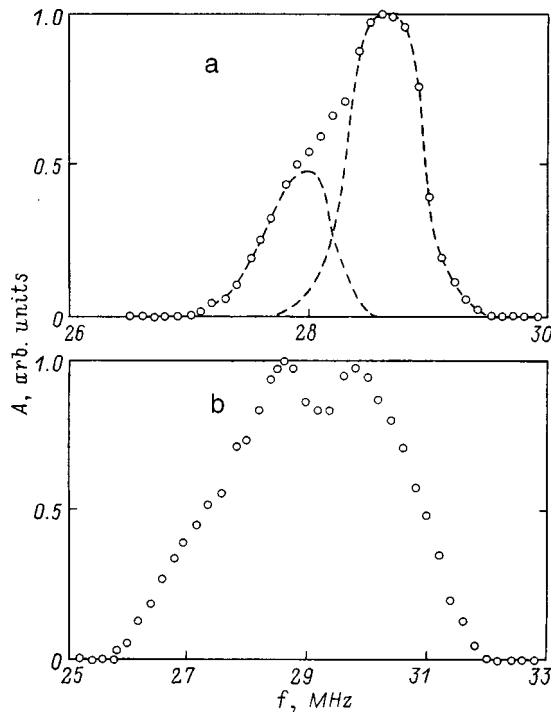
FIG. 1.

alloy this ratio is equal to $1:2.4$. The easy axis in LuFe$_2$ probably coincides with the $\langle 111 \rangle$ direction at 4.2 K. The NMR spectrum of LuFe$_{1.96}$Al$_{0.04}$ is found in the frequency range $20-30$ MHz and contains two resolved peaks, one of which belongs to the NMR spectrum of ^{57}Fe (at 28.6 MHz), and the other, to the NMR spectrum of ^{27}Al with maximum at 29.8 MHz.

2. DISCUSSION OF EXPERIMENTAL RESULTS

The hyperfine field on nuclei of magnetic atoms (e.g., ^{57}Fe) in ferromagnetic metallic alloys is usually represented as a sum of two main contributions, local and induced

$$H(\text{Fe}) = H_{loc}(\text{Fe}) + H_{tr}(\text{Fe}), \qquad (1)$$

where $H_{loc}(\text{Fe})$ is the contribution to the hyperfine field from the polarization of the inner and outer s electrons by the intrinsic magnetic moment of the iron atom $\mu(\text{Fe})$, and $H_{tr}(\text{Fe})$ is the contribution to the hyperfine field due to polarization of the outer s electrons by the magnetic moments of the neighboring atoms. Since $H_{loc}(\text{Fe})$ is proportional to $\mu(\text{Fe})$ (Ref. 15), it is usually assumed that $H_{loc}(\text{Fe}) = P(\text{Fe})\mu(\text{Fe})$, where $P(\text{Fe})$ is the polarization constant; for iron $P(\text{Fe}) = -9.05\tau/\mu_b$ (Ref. 15).

We determine $H(\text{Fe})$ from the experiment. To determine $\mu(\text{Fe})$ from the hyperfine-field data, it is necessary to estimate the contribution $H_{loc}(\text{Fe})$ [or $H_{tr}(\text{Fe})$] to $H(\text{Fe})$. At present, estimating the main contributions from the experimental data is one of the main problems in the method of hyperfine interactions. The most reliable experimental method for estimating the main contributions to the hyperfine field of the magnetic $3d$ atom is based on a measurement of the hyperfine field on nonmagnetic impurity atoms at the beginning and end of the $3d$ series.[16]

The quantity $H_{tr}(\text{Fe})$ in the Fe matrix was estimated in Ref. 17. An estimate based on shifts of the hyperfine field of ^{57}Fe, $\Delta H(\text{Fe})$, in diluted Fe-alloys and also in Fe$_3$Si compounds gave the value $H_{tr}(\text{Fe}) \approx -14.5$ T.

Reference 7 considered another method for estimating the induced contributions in Fe-based alloys. The authors proposed to estimate $H_{tr}(\text{Fe})$ from data on the hyperfine field on nonmagnetic impurities. However, to the reasons given in Ref. 7 we must add the following. The hyperfine fields $H(Z)$ on the nonmagnetic impurities (Z) in an iron matrix have an oscillating dependence as a function of Z, varying in sign and significantly in magnitude.[15] From this dependence it is clear that only for ^{27}Al and ^{63,65}Cu nuclei is $B(Z) = H(Z)/A_s(Z)$ [here $A_s(Z)$ is the polarization constant for the s electrons, Ref. 18) almost equal to $B(\text{Fe}) = H_{tr}(\text{Fe})/A_s(\text{Fe}) = 0.81 \cdot 10^{-1}$ [$H_{tr}(\text{Fe}) = -14.5$ T]. For other nuclei the values of $B(Z)$ differ from $B(\text{Fe})$ by several-fold. From the equalities $B(\text{Fe}) = B(\text{Cu}) = B(\text{Al})$ we can find a relation between H_{tr} and the experimental hyperfine fields on the ^{27}Al or ^{63,65}Cu impurity nuclei in the investigated iron-based sample, i.e.,

$$H_{tr}(\text{Fe}) = H(Z)A_s(\text{Fe})/A_s(Z), \qquad (2)$$

where $Z = $ Al or Cu. Thus, by measuring the hyperfine fields on the nuclei of ^{27}Al or ^{63,65}Cu impurity atoms occupying Fe sites in the iron-based alloy and using relation (2) it is possible to estimate the induced contribution to the hyperfine fields on the ^{57}Fe nuclei and then $H_{loc}(\text{Fe}) = H(\text{Fe}) - H_{tr}(\text{Fe})$.

The fields $H_{tr}(\text{Fe})$ and $H_{loc}(\text{Fe})$ on ^{57}Fe nuclei in LuFe$_2$ compounds were estimated on the basis of the experimental data for $H(\text{Fe})$ and $H(\text{Al})$ measured in this work. The obtained values of $H(\text{Al})$ and $H(\text{Fe})$ also contained the Lorentz field for LuFe$_2$. Thus, $H(\text{Al}) = 2.88$ T and $H(\text{Fe}) = -21.08$ T; thus $H_{tr}(\text{Fe}) = -5.89$ T [estimated using formula (2)]. Consequently, $H_{loc}(\text{Fe}) = -15.19$ T and $\mu(\text{Fe}) = 1.69\mu_b$. This value of the moments on the Fe atoms is found in agreement with the estimates of $\mu(\text{Fe})$ from polarized neutron scattering measurements in LuFe$_2$ $\mu(\text{Fe}) = 1.67\mu_b$ (Ref. 11). Calculations of the electronic structures of LuFe$_2$ (Ref. 4) gave the following value for the magnetic moment on the states of the Fe atoms: $\mu(\text{Fe}) = 1.64\mu_b$.

In order to accurately estimate the magnetic moments on the A atoms in Laves compounds of the type AFe$_2$ from the hyperfine-field data, it is also necessary to know the values of the hyperfine fields on the nuclei of the s, p, and d impurity atoms occupying the A and Fe sites in the AFe$_2$ lattice. However, such data for LuFe$_2$ alloys are lacking. In LuFe$_2$ $\mu(\text{Lu})$ can be estimated from data on the mean magnetic moment of the alloy μ_f, calculated on the basis of the chemical formula of the compound AFe$_2$ [$\mu_f = 2\mu(\text{Fe}) + \mu(A)$]. It should also be borne in mind that going this route can incur significant variations in $\mu(A)$ since there is a spread in the data on μ_f due to the sensitivity of the values of μ_f to the stoichiometry of the composition and the single-phase character of the samples of AFe$_2$ compounds. The magnetic moments μ_f in LuFe$_2$ were measured in Refs. 12 and 19 and found to lie in the range $\mu_f = (2.85 - 3.00)\mu_b$. Using the obtained value of $\mu(\text{Fe})$, we obtain $\mu(\text{Lu}) = -(0.38 - 0.53)\mu_b$. Estimates of $\mu(\text{Lu})$ in LuFe$_2$ from cal-

culated electronic structures give $\mu(\text{Lu}) = -0.41\mu_b$ (Ref. 4). Thus, the NMR data for $LuFe_2$ point to a ferromagnetic structure in which a significant magnetic moment is found on the Lu atoms, antiparallel to the magnetic moment of the Fe atoms.

[1] H. Yamada and M. Shimizu, J. Phys. F **16**, 1039 (1986).

[2] S. Asano and S. Ishida, J. Magn. Magn. Mater. **70**, 187 (1987).

[3] Sh. Ishida and S. Asano, J. Phys. Soc. Jpn. **54**, 4688 (1985).

[4] M. S. S. Brooks, O. Eriksson, and B. Johansson, J. Phys.: Condens. Matter **1**, 5861 (1989).

[5] C. Ritter, J. Phys.: Condens. Matter **1**, 2765 (1989).

[6] P. Warren, J. B. Forsyth, G. Y. McIntyre, and N. Bernhoeft, J. Phys.: Condens. Matter **4**, 5795 (1992).

[7] V. S. Pokatilov, V. V. Golikova, and E. F. Sidokhin, Zh. Éksp. Teor. Fiz. **95**, 2079 (1989) [Sov. Phys. JETP **95**, 1202 (1989)].

[8] V. S. Pokatilov and V. V. Golikova, Hyperfine Interact. **60**, 533 (1990).

[9] V. S. Pokatilov, V. V. Golikova, A. V. Tchvyatchenko, and L. N. Fomitcheva, Hyperfine Interact. **60**, 529 (1990).

[10] T. Dumelow, P. C. Riedi, P. Mohn, K. Schwarz, and Y. Yamada, J. Magn. Magn. Mater. **54–57**, 1081 (1986).

[11] D. Givord, A. R. Gregory, and Y. Schweizer, J. Magn. Magn. Mater. **15–18**, 293 (1980).

[12] Y. Kasamatsu, J. G. M. Armitage, J. S. Lord, P. C. Riedi, and D. Fort, J. Magn. Magn. Mater. **140–144**, 819 (1995).

[13] M. B. Stearns, Phys. Rev. **162**, 496 (1967).

[14] R. H. Dean and R. J. Urwin, J. Phys. C **3**, 1747 (1970).

[15] M. B. Stearns, Phys. Rev. B **4**, 4081 (1971).

[16] D. A. Shirley, S. S. Rosenblum, and E. Matthials, ds Phys. Rev. **170**, 363 (1986).

[17] M. B. Stearns, Phys. Rev. B **4**, 4069 (1971).

[18] J. A. Cambell, J. Phys. C **2**, 1338 (1969).

[19] K. H. J. Bushow and R. P. Van Stapele, J. Appl. Phys. **41**, 4066 (1970).

Translated by Paul F. Schippnick

Self-consistent calculation of the hole autolocalization barrier in the CuO₂ plane

A. K. Shelkan[*)] and V. V. Hizhnyakov

Institute of Physics, Tartu University, EE2400 Tartu, Estonia

E. Sigmund

Institut für Physik, Technische Universität Cottbus, P. O. Box 101344, 03013 Cottbus, Germany
(Submitted September 14, 1998)
Fiz. Tverd. Tela (St. Petersburg) **41**, 1145–1148 (July 1999)

We examine the behavior of an extra hole added to the ground state of an antiferromagnetically ordered CuO₂ plane with account of the Cu–O and O–O hybridization. We show that spin flipping in the CuO₂ plane will lead to separation of localized and free-hole states by the energy barrier $E_b \sim 0.05\,eV$, which can be manifested in various kinetic phenomena. © *1999 American Institute of Physics.* [S1063-7834(99)00407-4]

Various studies of lightly doped high-temperature superconductors (HTSC's) show that the hole ground state in the antiferromagnetically ordered CuO₂ plane is an autolocalized state.[1,2] Both the spin–charge interaction, arising due to a breakdown of antiferromagnetic (AF) order,[2] and the electron–phonon interaction, leading to a local distortion of the crystal lattice,[1] contribute to the localization. The small dimensions of a hole polaron lead to quantization of levels and to finite excitation energies ($\sim 0.5 - 1$ eV).[3] New studies of HTSC's with a finite hole concentration clearly indicate the existence of hole subsystems in them of both band and polaron type.[4–6]

Holes can be created optically as well as by chemical doping. A wide photo-induced absorption band is observed around ~ 0.5 eV.[7,8] The relatively long lifetime of the absorption band (~ 1 ms) indicates that optically created holes exist for some time as free quasiparticles. This indicates that the free and autolocalized states in the CuO₂ planes are separated by an energy barrier.[9]

In cuprate perovskites holes are quasi-two-dimensional. In this case, formation of a polaron due to the electron–phonon interaction is barrier-free[10] (also see Ref. 11, where an analogous result was obtained for anisotropic bands in the three-dimensional case). In contrast to this, there is a barrier in the spin–polaron model.[9] The difference consists in the nonlinear nature of the local spin excitation: a flipped spin forms a stable topological defect in an antiferromagnetic lattice. Therefore, a wave packet of large radius of a free particle in an antiferromagnetic lattice with one flipped spin forms a metastable state in contrast to a packet in a locally distorted lattice.

The above-indicated metastable state has a larger energy than a wave packet of the same radius in an ideal antiferromagnetic lattice. However, the energy of a small packet is less if one spin in the lattice is flipped. For some value of the size of the wave packet L_b the two energies coincide. Consequently, to calculate the height of the barrier between a free hole state and an autolocalized hole state it is necessary to find the value of L at which the energy of the wave packet of a free hole and the energy of the packet for one flipped spin coincide.

1. FREE HOLE IN AN ANTIFERROMAGNETIC LATTICE

The model Hamiltonian of the CuO₂ plane in the Hartree–Fock approximation of the Hubbard model has the form[12,13]

$$H = \sum_\sigma H_{MF}^\sigma - U \sum_m \langle n_{m\sigma}^d \rangle \langle n_{m-\sigma}^d \rangle, \qquad (1)$$

where

$$H_{MF}^\sigma = \sum_n (\epsilon_d + U\langle n_{m-\sigma}^d \rangle) n_{n\sigma}^d + \epsilon_p \sum_m n_{m\sigma}^p + T$$

$$\times \sum_{nm} (d_{n\sigma}^\dagger p_{m\sigma} + \text{H.c.}) + t \sum_{mm'} (p_{m\sigma}^\dagger p_{m'\sigma} + \text{H.c.}),$$

$$(2)$$

$n_{n\sigma}^d$ and $n_{m\sigma}^p$ are the occupation numbers of the $d_{x^2-y^2}$ and $p_{x,y}$ orbitals of copper and oxygen, respectively, ϵ_d and ϵ_p are the energies of these states, T and t are the Cu–O and O–O overlap integrals, respectively, U is the value of the Hubbard correlation energy on copper. The values of these parameters can be obtained from band calculations: $U \approx 8$ eV, $T \approx 1$ eV, $t \approx 0.3$ eV, and $\epsilon = \epsilon_p - \epsilon_d \approx 3$ eV (Ref. 14).

A free hole in an antiferromagnetic lattice is described by the eigenstates of the Hamiltonian (1) provided that the lower band is filled with holes. The mean values of the occupation numbers $\langle n_\sigma^d \rangle$ are calculated self-consistently.[15] For the above-indicated values of the parameters, the second hole band (empty in the undoped case) has four minima at the points $(\pm \pi/2a, \pm \pi/2a)$ of the Brillouin zone, where a is the lattice constant (see Fig. 1).

In the antiferromagnetically ordered state the unit cell is doubled. Cu₂O₄ cells form a simple cubic lattice with lattice constant $a' = a\sqrt{2}$. The minimum of the hole band is shifted
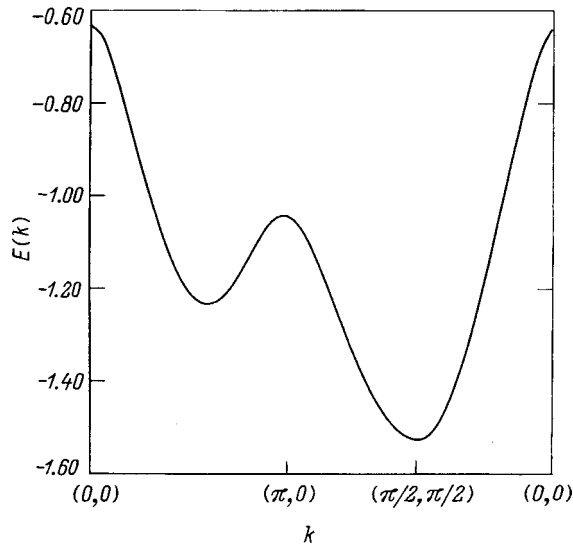
FIG. 1. Band structure of a hole in an antiferromagnetic lattice, calculated in the mean-field approximation.

to the points $(\pm\pi/a',0)$ and $(0,\pm\pi/a')$ of the Brillouin zone. At these points the wave function is a linear combination of the lattice-site functions

$$|\psi\rangle_{\mathbf{m}'}=(-1)^{m_{x'}}(\sin\alpha|d_2\rangle_{\mathbf{m}'}+\cos\alpha|P_1\rangle_{\mathbf{m}'}),\qquad(3)$$

$$|P_1\rangle_{\mathbf{m}'}=\frac{1}{2}(|p_1\rangle_{\mathbf{m}'}-|p_2\rangle_{\mathbf{m}'}+i|p_3\rangle_{\mathbf{m}'}-i|p_4\rangle_{\mathbf{m}'}),\qquad(4)$$

$|p_n\rangle_{\mathbf{m}'}$ denotes the states of the four oxygens surrounding the copper in the unit cell with the indices $\mathbf{m}'$; according to our calculations, $\sin\alpha\approx0.39$. As is well known, the case $t=0$ is degenerate: the minimum of the hole band is found at the boundary of the Brillouin band, but the density of states has a logarithmic divergence at the energy of the minimum. Taking the O–O interaction into account removes the singularity and shifts the maximum of the density of states to a finite energy (see Fig. 2).
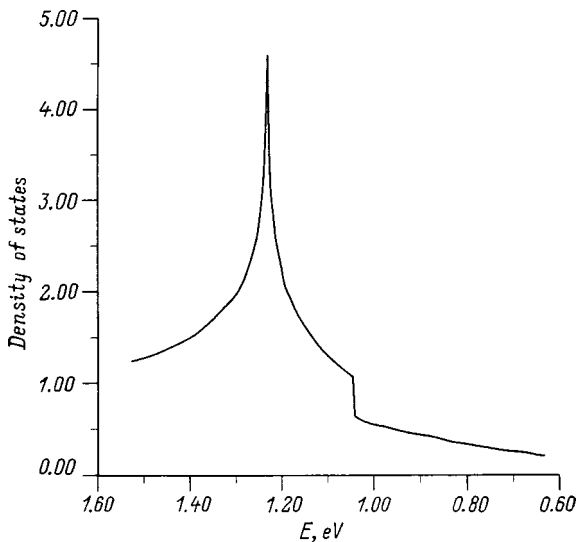
FIG. 2. Density of hole states, calculated in the mean-field approximation.

Below we examine the behavior of the following large-radius hole packet in an antiferromagnetic lattice:

$$|\Psi_L\rangle=\sum_{\mathbf{m}'}A_L\exp[-2(|m_{x'}|+|m_{y'}|)a'/L+i\pi m_{x'}]a_{\mathbf{m}'}^{+}|0\rangle,$$

$a_{\mathbf{m}'}^{+}$ is the creation operator of the state $|\psi_{\mathbf{m}'}\rangle$, $A_L=\tanh\times(2a'/L)$; this form is similar to the form $[\sim\mathrm{sech}(x/L)]$ of a soliton wave packet having minimum energy for a given size $L=(\int|\psi|^4dx)^{-1}\gg a'$. The kinetic energy of the packet is equal to

$$E_{\mathrm{kin}}(L)=\sum_{k_{x'}}\sum_{k_{y'}}E(\mathbf{k}')|\varphi(k_{x'}-\pi/a')\varphi(k_{y'})|^2,\qquad(5)$$

where

$$\varphi(q)=(A_L)^{1/2}\sinh(2a'/L)/(\cosh(2a'/L)-\cos(qa')).$$

For $L\gg a'$ the energy depends quadratically on a'/L despite the above-indicated maximum in the density of states.

To find the total energy of the packet, it is also necessary to calculate the correction E_{SE} to the energy of the packet arising due to the spin–hole interaction. In the limit $L/a'\to\infty$ it depends on the mean hole concentration $\overline{|\psi|^2}=(a'/L)^2$. Therefore, for large L E_{SE} is approximately equal to $1/N_0$ part of the correction to the energy of the state with N_0 additional holes. In the mean-field approximation this energy is calculated as

$$E_{SE}=\frac{1}{N_0}[E^{(s.-c.)}(N_0)-E^{(r)}(N_0)],\qquad(6)$$

where $E^{(r)}(N_0)$ is the energy of the CuO_2 plane with N_0 additional holes of the same spin, added to the rigid antiferromagnetic lattice. When finding $E^{s.-c.}(N_0)$, the values of the polarization $\langle n_\sigma^d\rangle$ are calculated self-consistently with the N_0 additional holes taken into account. Results of calculation of $E_{\mathrm{kin}}(L)$ and the total energy of the packet $\epsilon_L=E_{\mathrm{kin}}(L)+E_{SE}(L)$ are plotted in Fig. 3. It can be seen that ϵ_L grows with decreasing size of the packet. Taking into account that the energy of a spin polaron is less than the energy of the minimum of the hole band,[15] we can conclude that the free hole state is separated from the state autolocalized by the energy barrier.

2. EFFECT OF SPIN FLIPPING ON COPPER

In order to find the height of the barrier, let us consider how the energy of a packet of large radius varies when one spin on a copper atom flips. In this case, we need to take into account two different contributions to the variation of the energy.

1) An increase in the energy due to change in the magnetic interaction upon one spin flip; it is calculated in the mean-field approximation by the Lifshitz' method of localized perturbations (details of the application of this method in the three-band Hubbard model can be found in Ref. 15). For typical values of the parameters we obtain $E^{(S)}\sim0.15\,\mathrm{eV}$, which essentially coincides with the experimental value of this parameter in an antiferromagnetically ordered CuO_2 plane.
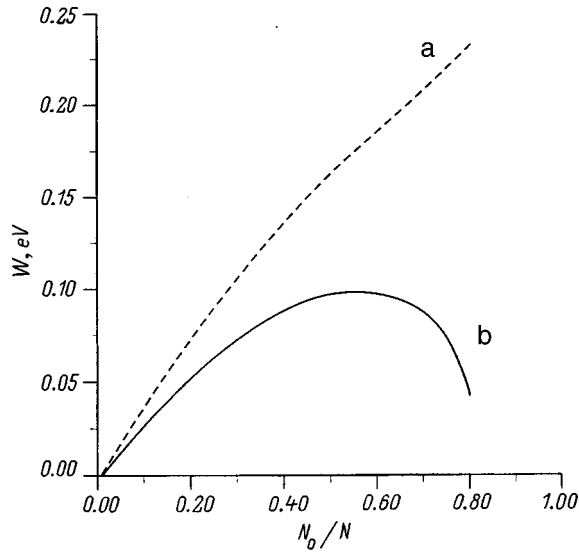
FIG. 3. Dependence of the mean energy W of a hole in the CuO$_2$ plane with N_0 additional holes of identical spin in a rigid (a) and a self-consistent (b) antiferromagnetic lattice, consisting of N unit cells, on the additional hole concentration N_0/N.

2) A decrease in the energy due to hybridization of a copper ion with spin flip $|d_0\rangle$ and the oxygen ions surrounding it, entering into the four nearest packets and forming two orthogonal symmetrized states

$$|\psi_1\rangle = \frac{1}{2}(|P_1\rangle_1 + |P_1\rangle_2 - |P_1\rangle_3 - |P_1\rangle_4),$$

$$|\psi_2\rangle = \frac{1}{2}(|P_2\rangle_1 + |P_2\rangle_2 + i|P_2\rangle_3 + i|P_2\rangle_4);$$

the $|P_1\rangle_m$ states are defined by formula (4),

$$|P_2\rangle_{1,2} = \frac{1}{2\sqrt{3}}(3|p_{1,2}\rangle_{1,2} + |p_{2,1}\rangle_{1,2} \mp i(|p_3\rangle_{1,2} + |p_4\rangle_{1,2})),$$
(7)

$$|P_2\rangle_{3,4} = \frac{1}{2\sqrt{3}}(3|p_{3,4}\rangle_{3,4} + |p_{4,3}\rangle_{3,4} \pm i(|p_1\rangle_{3,4} + |p_2\rangle_{3,4})).$$
(8)

The energy hybridization matrix of a wave packet with $|d_0\rangle$ and $|\psi_2\rangle$ states has the form

$$H_h = \begin{pmatrix} \epsilon_L + E^{(S)} & \frac{T}{\sqrt{2}}A_L\cos\alpha & 0 \\ \frac{T}{\sqrt{2}}A_L\cos\alpha & \epsilon_0 & T\sqrt{3} \\ 0 & T\sqrt{3} & \epsilon_2 \end{pmatrix},$$
(9)

$\epsilon_L + E^{(S)}$ is the energy of a hole wave packet in an antiferromagnetic lattice with one flipped spin, $\epsilon_0 = U\langle n_\downarrow\rangle - \epsilon - \epsilon_{\min}$ is the energy of the copper state relative to the minimum of the hole band, $\epsilon_2 = 2T^2/U - \epsilon - (4/3)t - \epsilon_{\min}$ is the energy of the oxygen $|P_2\rangle_m$ states relative to the minimum of the hole band.[16] The lowest state of this Hamiltonian has energy
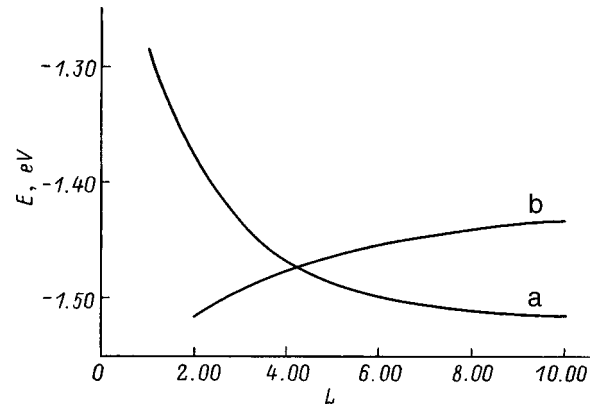

FIG. 4. Dependence of the energy of the free hole state in an antiferromagnetic lattice with one flipped spin (a) and of a ferron state (b) on the size of the states L.

$$E_h \approx E^{(S)} + \frac{1}{2}[\epsilon_L + \varepsilon_1 - \sqrt{(\epsilon_L - \varepsilon_1)^2 + 2(TA_L\cos\alpha\sin\beta)^2}],$$
(10)

where

$$\varepsilon_1 = \frac{1}{2}(\epsilon_0 + \epsilon_2 - \sqrt{(\epsilon_0 - \epsilon_2)^2 + 12T^2}),$$

$$\sin\beta = (\varepsilon_1 - \epsilon_2)/\sqrt{(\varepsilon_1 - \epsilon_2)^2 + 3T^2}.$$

The energy of the wave packet in an antiferromagnetic lattice with a flipped spin calculated in this way, E_h, and the energy of a free wave packet ϵ_L are plotted in Fig. 4 as functions of L. The corresponding curves intersect at the packet size $L_b \approx 4a'$ (i.e., 32 CuO$_2$ cells). The energy at which the curves intersect (reckoned from the energy of the minimum of the band), $E_b \approx 0.05$ eV, is the height of the barrier.

Thus, the mechanism of barrier formation consists in the following: during the initial localization (contraction) of a hole packet of large radius the energy grows. This takes place until the localization energy exceeds $E^{(S)}$, i.e., it becomes sufficient to flip a spin. After this, the hole relaxes to a ferron state.

Thus, we conclude that the spin polaron of a hole in an antiferromagnetically ordered CuO$_2$ plane, in contrast to a phonon polaron in a two-dimensional lattice, is separated from the band hole state by a potential barrier. The found value of the barrier ~0.05 eV allows us to explain the significant lifetime of the photo-induced absorption band near 0.5 eV.

[1] N. F. Mott, J. Phys.: Condens. Matter **5**, 3487 (1993).
[2] V. Hizhnyakov and E. Sigmund, Physica C **156**, 655 (1988).
[3] S. Tajima, H. Ishii, T. Nakahashi, T. Takagi, S. Ushida, and M. Seki, J. Opt. Soc. Am. B **6**, 475 (1989).
[4] A. Bianconi, N. L. Saini, A. Lanzara, M. Missori, T. Rossetti, H. Oyanagi, H. Yamaguchi, K. Oka, and T. Ito, Phys. Rev. Lett. **76**, 3412 (1996).

[5] R. K. Kremer, A. Simon, E. Sigmund, and V. Hizhnyakov, Proc. Estonian Acad. Sci., Phys. **44**, 274 (1995).

[6] Yu. V. Yablokov, T. A. Ivanova, and A. E. Usachev, Fiz. Tverd. Tela (St. Petersburg) **40**, 622 (1998) [Phys. Solid State **40**, 569 (1998)].

[7] D. Mihailović, C. M. Forster, K. Voss, and A. J. Heeger, Phys. Rev. B **42**, 7989 (1990).

[8] A. V. Bazhenov, A. V. Gorbunov, and V. B. Timofeev, Zh. Éksp. Teor. Fiz. **104**, 3193 (1993) [JETP **77**, 500 (1993)].

[9] V. Hizhnyakov, E. Sigmund, and G. Zavt, Phys. Rev. B **44**, 12 639 (1991).

[10] E. I. Rashba, in *Excitons*, edited by E. I. Rashba and M. D. Sturge, Ch. 13 (North-Holland, Amsterdam, 1982).

[11] A. Shelkan and G. Zavt, Izv. AN ÉSSR, Ser. Fiz. **39**, 358 (1990).

[12] A. M. Oleś and J. Zaanen, Phys. Rev. B **39**, 9175 (1989).

[13] G. Seibold, E. Sigmund, and V. Hizhnyakov, Phys. Rev. B **48**, 7537 (1993).

[14] E. B. Stechel and D. R. Jennison, Phys. Rev. B **38**, 4632 (1988).

[15] A. Shelkan, G. Zavt, V. Hizhnyakov, and E. Sigmund, Z. Phys. B **104**, 433 (1997).

[16] V. Hizhnyakov, E. Sigmund, and M. Schneider, Phys. Rev. B **44**, 795 (1991).

Translated by Paul F. Schippnick

Vibrations of copper atoms in Pr_2CuO_4

P. P. Parshin, M. G. Zemlyanov,*) A. S. Ivanov, and L. D. Shustov

Russian Scientific Center ''Kurchatov Institute,'' 123182 Moscow, Russia

G. Chaubert

Institut Laue–Langevin, BP 156, F-38042 Grenoble Cedex 9, France

The method of isotopic contrast in combination with inelastic neutron scattering has been used to investigate the vibrational spectrum of the copper atoms in Pr_2CuO_4. It is shown that the energy positions of the features of the vibrational spectrum of copper in Pr_2CuO_4 and CuO (which also has a planar oxygen coordination of copper) coincide. We conclude that the dynamical behavior of the copper atoms is formed mainly by their interaction with the nearest-neighbor oxygen atoms. © *1999 American Institute of Physics.* [S1063-7834(99)00507-9]

At present it is acknowledged that the presence of conducting CuO_2 planes [a common structural element of all high-temperature superconducting (HTSC) cuprates] is essential for the occurence of high-temperature superconductivity. And although there is no mechanism of charge-carrier attraction providing a transition to the superconducting state at ''high temperatures,'' it is clear that the role of phonons must be taken into account in any case, in particular the influence of vibrations of the copper and oxygen atoms making up the conducting cuprate planes. In this light, the interest in vibrations of these atoms is understandable.

The method of isotopic contrast in combination with inelastic neutron scattering,[1,2] which is based on the difference in the scattering cross sections for chemically equivalent isotopes of the same element, in a number of cases opens up the possibility of experimentally retrieving the partial vibrational spectra of atoms of one kind or another. Unfortunately, the difference in the isotopes for oxygen is so small[3] that, at the present state-of-the-art, it is impossible to determine the partial vibrational spectrum and, therefore the possibilities for obtaining experimental information are limited to atoms of copper and a few other metals.

In experiments measuring the vibrational spectra of copper atoms in HTSC cuprates with hole conductivity and in related compounds ($YBa_2Cu_3O_x$, La_2CuO_4, and $Bi_2Sr_2Ca_{n-1}Cu_nO_{2n+4}$)[2,4–6] it was shown that the dynamical behavior of the copper atoms is shaped primarily by the interaction in the first two coordination spheres. Consequently, the main interactions for copper in these compounds are its interactions with the nearest-neighbor (in the CuO_2 plane) oxygen atoms (Fig. 1) and with apical oxygen (the atoms at the vertices of the oxygen octahedra or tetrahedra surrounding the copper).

In contrast to the mentioned HTSC cuprates, in compounds with electronic conductivity $(R/Ce)_2CuO_4$ (the so-called T' phases, R = Pr, Nd, Sm, Eu, Gd, Ref. 7) the second coordination sphere around the copper atoms does not contain an apical oxygen (Fig. 1) and the purely square oxygen

coordination in the CuO_2 plane is a distinguishing feature of the structure of these compounds. The mutual coordination of the copper and oxygen atoms (first coordination sphere) in this case is similar to that found in the binary oxide CuO, with the difference that in CuO (monoclinic lattice) the environment of copper has rhombic, not square coordination.[8] It follows from optical spectroscopy data and calculation based on the central-force model[9] that in compounds having the structure of the T' phase R_2CuO_4 (R = Pr, Nd, Sm, Gd), in contrast to the other HTSC cuprates, a strong force interaction of the copper atoms does take place, where the strongest bond is formed not with the oxygen atoms but with the rare-earth atoms. On the basis of their calculations, the authors of Ref. 9 conclude that the presence of an apical oxygen in T phases leads to strong screening of the interaction of the copper with the rare-earth atoms. At the same time, calculating in the shell model, which provides a good description of the phonon dispersion curves in Nd_2CuO_4,[10] gives the maximum value of the force constant responsible for the interaction of copper with oxygen, with the interaction of copper with the rare-earth atoms in general not being taken into account. Apparently, an answer to the question of the role of the copper–oxygen interaction in the formation of the dynamics of the copper atoms can be provided by direct measurement of the vibrational spectrum.

To experimentally investigate the vibrational spectrum of the copper atoms specifically with square coordination, we chose the system Pr_2CuO_4, which has the lowest neutron absorption cross section.

1. EXPERIMENT

As is well known,[11] information about the vibrational spectrum of the crystal lattice can be extracted from inelastic incoherent neutron scattering data on a polycrystalline sample. If the investigated material is monoatomic and its nuclei scatter neutrons incoherently (e.g., vanadium), then direct retrieval of the phonon spectrum is possible. For a
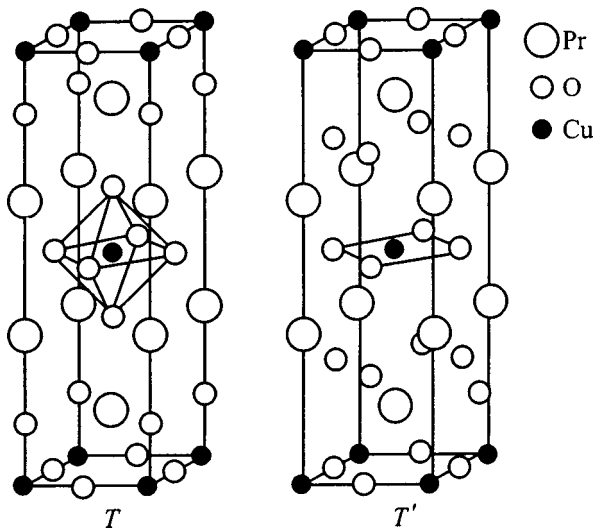
FIG. 1. Unit cells of the T phase (representative compound La$_2$CuO$_4$) and the T' phase (representative compound Pr$_2$CuO$_4$.

monoatomic, incoherently scattering material it is possible to retrieve the generalized (neutron-weighted) vibrational spectrum of the crystal lattice $G(E)$

$$G(E) = \sum (c_i \sigma_i / M_i) g_i(E) \exp(-2W_i), \qquad (1)$$

$$g(E) = \sum c_i g_i(E), \qquad (2)$$

$$W_i \sim \int E^{-1} g_i(E) \coth(E/2kT) dE. \qquad (3)$$

Here c_i, σ_i, M_i, W_i, and $g_i(E)$ are the atomic concentration, neutron incoherent scattering cross section, atomic mass, Debye–Waller thermal factor, and partial vibrational spectrum of the atoms of the ith sort, respectively, and $g(E)$ is the spectral distribution of the vibrations of the crystal lattice (phonon spectrum). The sum in expressions (1) and (2) extends over all atoms of different sort in the unit cell or in a formula unit.

In the case of a material consisting of atoms whose nuclei have a considerable amount of coherent scattering (all HTSC cuprates are like this), the function $G(E)$, in which the total neutron scattering cross section by atoms of the ith sort figures as σ_i, can be obtained from the inelastic neutron scattering spectra of a polycrystalline sample only by averaging the data over a large volume in phase space[12] (the incoherent approximation). In this case, the larger the phase volume V encompassed in the experiment in comparison with the volume of the Brillouin zone V_{BZ}, the better will the average be and the closer will the measured spectrum be to $G(E)$.

The presence in expression (1) of the factor σ_i / M_i opens up the possibility of experimentally separating out the partial vibrational spectra of atoms of a given sort. It is this that is the basis of the method of isotopic contrast in inelastic neutron scattering.
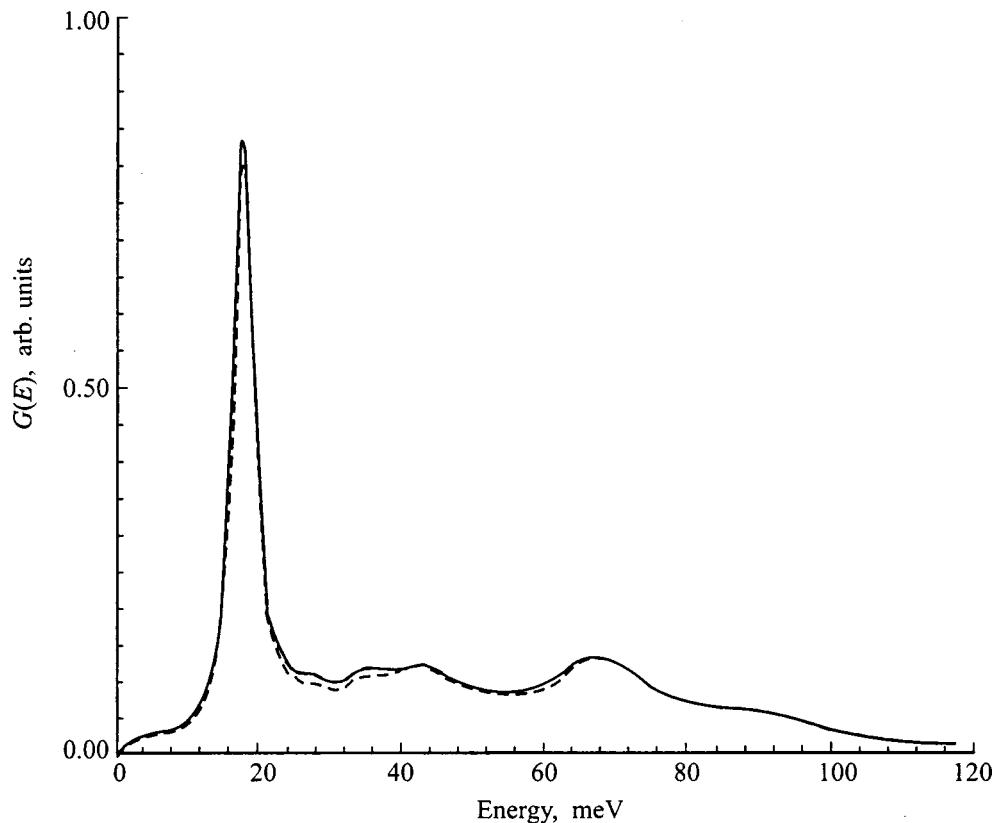
Let us consider this situation in the case of copper

FIG. 2. Neutron-weighted vibrational spectra for Pr$_2$CuO$_4$ containing different copper isotopes: solid line — ^{65}Cu, dashed line — ^{63}Cu.
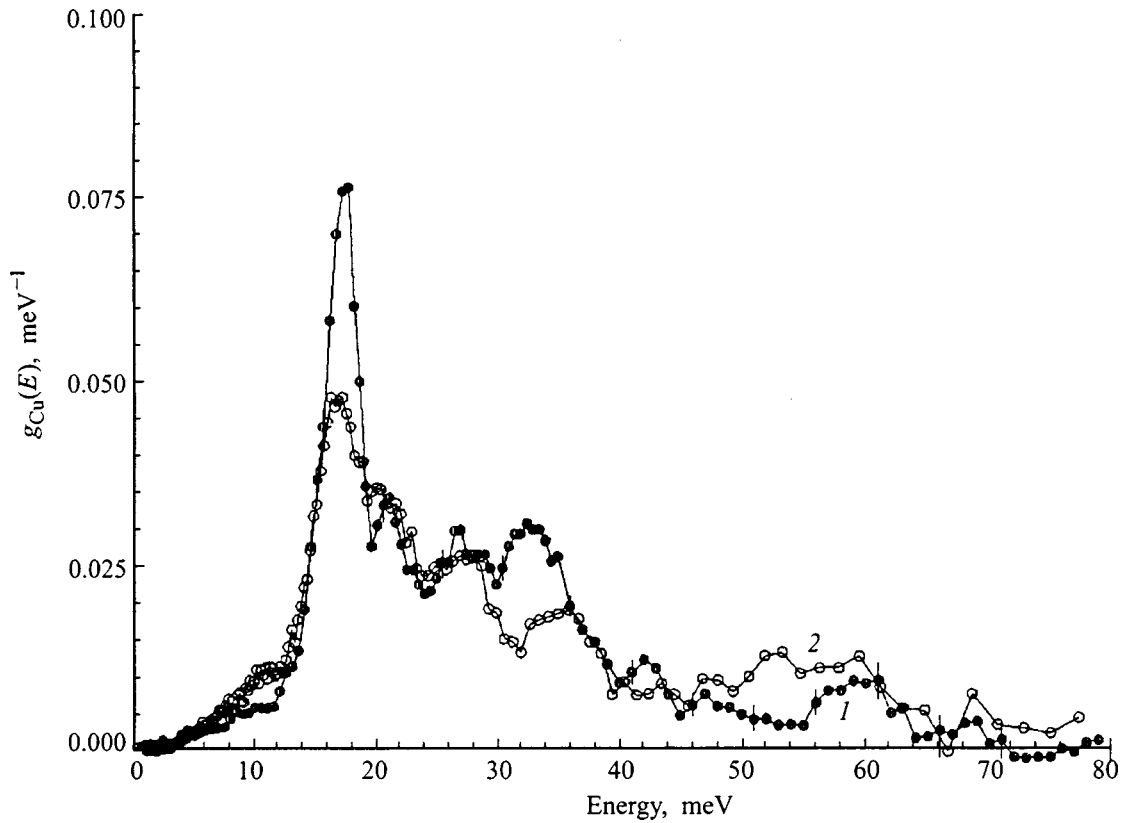
FIG. 3. Partial vibrational spectra of the copper atoms: *1* — in Pr_2CuO_4, *2* — in CuO (Ref. 13).

atoms,[13] which has two stable isotopes: ^{63}Cu ($\sigma=5.2$ barn) and ^{65}Cu ($\sigma=14.5$ barn) with greatly different cross sections. Since the difference in the atomic masses of the copper isotopes is $\sim3\%$, it is possible to neglect differences in the partial vibrational spectrum and, consequently, the thermal factor between the two isotopes. In this case, the partial vibrational spectrum of the copper atoms $g_{Cu}(E)$ is proportional to the difference of the neutron-weighted vibrational spectra $\Delta G(E)$ measured on two samples enriched with ^{65}Cu and ^{63}Cu, respectively

$$g_{Cu}(E)\sim\Delta G(E)\exp(2W_{Cu}). \qquad (4)$$

Since W_{Cu} is a weighted integral of $g_{Cu}(E)$ over energy, simultaneous solution of Eqs. (3) and (4) by the method of successive approximations allows one to experimentally retrieve both the partial vibrational spectrum and the thermal factor for the copper atoms.

From the experimental point of view regarding cuprates containing rare-earth atoms in their makeup, an additional difficulty arises (besides the relatively high neutron absorption cross section $\sigma_a=11.5$ barn for Pr), associated with the strong magnetic scattering by the rare-earth ions. In the doubly differential inelastic neutron scattering cross section of Pr_2CuO_4 there is an intense line at the energy $E\sim18$ meV, responsible for the transition between levels of the Pr^{3+} ion split by the crystal field.[14,15] The intensity of this line, which falls within the band of greatest density of vibrations of the copper atoms (0–40 meV), is comparable with the intensity of the elastically scattered neutrons and significantly exceeds the intensity of scattering by phonons. Under these condi-

tions, it is impossible to retrieve the neutron-weighted vibrational spectrum of the crystal lattice from the inelastic neutron scattering data. However, it is possible to retrieve the partial vibrational spectrum of the copper atoms since it is defined as the difference of spectra measured for two samples with different isotopic composition, but the effect of the crystal field on the rare-earth ion does not depend on the copper isotope. Of course, obtaining reliable data in this case requires especially high statistical accuracy in the measurement of experimental spectra.

With the aim of obtaining the maximum possible contrast in the neutron scattering on the vibrations of the copper atoms in Pr_2CuO_4, we synthesized two samples enriched with ^{65}Cu (99%) and ^{63}Cu (99.7%) weighing 15 g each. Synthesis and heat treatment of the samples took place under identical conditions (to avoid differences in their oxygen content). We found by x-ray analysis that the samples were single-phase and the lattice parameters of the tetragonal T' phase ($a=3.95$ Å, $c=12.21$ Å) agree with the data in the literature.[16]

The inelastic neutron scattering experiments were carried out at room temperature on the IN6 time-of-flight neutron spectrometer with rectilinear geometry mounted on the ILL high-flux reactor (Grenoble, France). The energy of the incident neutrons was 3.12 meV, and the inelastic neutron scattering spectra were recorded in the interval of scattering angles $11-113°$.

Estimates show that since $V_{BZ}=2.6$ Å^{-3} for Pr_2CuO_4 and the volume of phase space over which the IN6 experimental data were averaged was $V=35.8$ Å^{-3} for the elasti-

TABLE I. Integral characteristics of vibrations of copper atoms in a Pr_2CuO_4 lattice.

Compound	$\langle u^2 \rangle$	$\langle E \rangle$	$\langle B \rangle$
Pr_2CuO_4	5.38±0.16	2.87±0.6	2.54±0.18
			0.85, Ref. 9
Nd_2CuO_4			2.73, Ref. 10

Note. $\langle u^2 \rangle$ — Mean-square thermal displacement at 300 K (10^{-3} Å^2); $\langle E \rangle$ — mean vibrational energy at 300 K (meV); $\langle B \rangle$ — mean force interaction constant (mdyn/Å).

cally scattered neutrons and was $V = 831$ Å^{-3} for neutrons with energy 85 meV (near the boundary of the vibrational spectrum), the incoherent approximation works quite well over the entire spectrum although the low-energy region is reproduced less accurately than the high-energy region.

As a result of processing in the one-phonon approximation, with the above qualifications taken into account, we obtained neutron-weighted vibrational spectra $G(E)$ directly from the experimental data for each of the samples, distorted, as was already noted, by the contribution of magnetic scattering (Fig. 2).

2. DISCUSSION

The isotopic contrast in the vibrations of copper atoms, which shows up as a difference in the spectra for samples with ^{65}Cu and ^{63}Cu isotopes (Fig. 2), amounts to 2–5% of the total spectrum, which noticeably exceeds the statistical error of the experiment. The partial vibrational spectrum of the copper atoms (Fig. 3) was obtained as the difference in spectra of samples with different isotopic composition and is normalized to unity to facilitate comparison.

As was already mentioned, the coordination of the copper atoms in Pr_2CuO_4 is similar to their coordination in the binary oxide CuO, and the Cu–O distances are similar. It can be seen from the data plotted in Fig. 3 that the edge energies and the energy positions of all the main features of the copper-atom vibrational spectra in these compounds essentially coincide, while the differences in intensity of these features can probably be explained, but not completely, by the square oxygen coordination of the copper in the case of CuO. The similarity of the spectra in Fig. 3 allows one to conclude that the vibrational spectrum of the copper atoms in Pr_2CuO_4, as in CuO, is formed mainly by a force interaction with the nearest-neighbor oxygen atoms and probably depends weakly on its more distant neighbors, including its interaction with rare-earth atoms. This conclusion is in line with the calculations of Ref. 10 while the conclusion drawn in Ref. 9 on the basis of optical-spectroscopic data that the interaction of copper with the rare-earth atoms predominates are not confirmed by our experiments.

From the partial spectra retrieved from the experimental data we calculated integral characteristics of the vibrations of the copper atoms in the investigated compound: the mean-square thermal displacement and the mean-force interaction constant of the copper atoms in the lattice, which is mainly connected with the Cu–O interaction (see Table I). For comparison, Table I also lists the values of the force interaction constants of Cu–O obtained in Refs. 9 (for Pr_2CuO_4) and 10 (for Nd_2CuO_4).

To summarize, the method of isotopic contrast in combination with inelastic neutron scattering in the presence of a strong contribution from magnetic scattering has been used to experimentally retrieve the partial vibrational spectra of copper atoms in the compound Pr_2CuO_4, which has square oxygen coordination of its copper atoms. It has been shown that the vibrational spectrum of copper in Pr_2CuO_4 is qualitatively similar to the vibrational spectrum of copper in the binary oxide CuO; consequently, the dynamical behavior of the copper atoms in this cuprate, which is related to HTSC compounds with electronic conductivity, is determined to a significant extent by their interaction with just the nearest-neighbor oxygen atoms (a similar result was obtained earlier for HTSC cuprates with hole conductivity).

*)E-mail: zeml@isssph.kiae.ru

[1] Yu. Kagan, Zh. Éksp. Teor. Fiz. **42**, 1375 (1962) [Sov. Phys. JETP **15**, 954 (1962)].

[2] P. P. Parshin, M. G. Zemlyanov, O. E. Parfenov, and A. A. Chernyshev, JETP Lett. **51**, 433 (1990).

[3] F. Sears Varley, Neutr. News **3**, No. 3, 26 (1992).

[4] M. G. Zemlyanov, I. V. Krylov, P. P. Parshin, and P. I. Soldatov, Zh. Éksp. Teor. Fiz. **104**, 2538 (1993) [JETP **77**, 148 (1993)].

[5] P. P. Parshin, M. G. Zemlyanov, A. V. Irodova, P. I. Soldatov, and S. Kh. Suleĭmanov, Fiz. Tverd. Tela (St. Petersburg) **38**, 1665 (1996) [Phys. Solid State **38**, 919 (1996)].

[6] P. P. Parshin, M. G. Zemlyanov, and A. V. Irodova, Fiz. Niz. Temp. **22**, 564 (1996) [Low Temp. Phys. **22**, 435 (1996)].

[7] Z. Fisk, J. D. Thompson, M. F. Hundley, R. B. Schvarz, G. H. Kwei, J. E. Schirber, S.-W. Cheong, A. S. Cooper, P. Bordet, and M. Marezio, J. Less-Common Met. **168**, 31 (1991).

[8] W. Reichardt, F. Compf, M. Ain, and B. M. Wanklyn, Z. Phys. B **81**, 19 (1990).

[9] M. Udagawa, Y. Nagaoka, N. Ogita, M. Masada, J. Akimutsi, and K. Ohbayashi, Phys. Rev. B **49**, 585 (1994).

[10] M. Hofmann, D. Straue, U. Schröder, and E. Rampf, J. Phys.: Condens. Matter **6**, 3669 (1994).

[11] V. F. Turchin, *Slow Neutrons* [in Russian] (Gosatomizdat, Moscow, 1963).

[12] V. S. Oskotskiĭ, Fiz. Tverd. Tela (Leningrad) **9**, 550 (1967) [Phys. Solid State **9**, 420 (1967)].

[13] P. P. Parshin, M. G. Zemlyanov, and P. I. Soldatov, Zh. Éksp. Teor. Fiz. **101**, 750 (1992) [Sov. Phys. JETP **74**, 400 (1992)].

[14] C.-K. Loong and L. Soberholm, J. Alloys Compd. **181**, 241 (1992).

[15] W. Henggeler, T. Chattopadhyay, B. Roessly, P. Vorderwisch, P. Thalmeier, D. I. Zhigunov, S. N. Barilo, and A. Furrer, Phys. Rev. B **55**, 1269 (1997).

[16] Kajitani Tsuyoshi, Higara Kenji, Hosoya Syoichi, Fukuda Tsuguo, Oh-Ishi Katsuyoshi, and Syono Yasuhiko, Physica C **178**, 397 (1991).

Translated by Paul F. Schippnick

Specific heat of the electronic superconductor Pr$_{1.85}$Ce$_{0.15}$CuO$_4$

M. N. Khlopkin,[*] G. Kh. Panova, A. A. Shikov, and N. A. Chernoplekov

Russian Scientific Center ''Kurchatov Institute,'' 123182 Moscow, Russia
(Submitted November 12, 1998)

We have investigated the specific heat of the ceramic Pr$_{1.85}$Ce$_{0.15}$CuO$_4$ in the temperature range 2–800 K in magnetic fields up to 8 T. We have determined the magnitude of the specific-heat discontinuity at the superconducting transition $\Delta C/T_c$ and estimate the coefficient of the electronic specific heat. In the temperature interval 5–800 K we have separated out the phonon contribution to the specific heat, determined the temperature dependence of the characteristic Debye temperature Θ, and calculated the mean frequencies (moments) of the phonon spectrum. We compare the parameter values obtained in this way with data for the compound La$_{1.85}$Sr$_{0.15}$CuO$_4$ having similar crystal structure, but hole conductivity. The magnitude of the specific-heat discontinuity and consequently the effective electron mass in the ''electronic'' superconductor Pr$_{1.85}$Ce$_{0.15}$CuO$_4$ is several times smaller than in the ''hole'' superconductor La$_{1.85}$Sr$_{0.15}$CuO$_4$. The phonon spectrum in Pr$_{1.85}$Ce$_{0.15}$CuO$_4$ in the low-energy region is somewhat ''more rigid,'' and in the high-energy region somewhat ''softer'' than in La$_{1.85}$Sr$_{0.15}$CuO$_4$.
© *1999 American Institute of Physics.* [S1063-7834(99)00607-3]

Comparative studies of compounds with similar crystal structure and carrier concentrations, but different conductivity type are of great significance in elucidating aspects of the properties of high-temperature superconductors (HTSC's).

Compounds of the system Ln$_{2-x}$Ce$_x$CuO$_4$ (Ln=Nd, Pr, Sm) have a crystal structure similar to that of La$_{2-x}$Sr$_x$CuO$_4$. The CuO planes, in which the charge carriers responsible for superconductivity are concentrated, are identical in both cases, and the difference in their structures consists in the fact that in the first case the copper atom is surrounded by four oxygen atoms and has a square–planar environment while in the second case the copper atom is surrounded by six oxygen atoms and is located at the center of an oxygen octahedron.[1] Both measurements of the transport properties[2] and arguments about the formal valence state indicate that, for doping of the La-system with strontium and of the Pr-system with cerium, the majority charge carriers in the first case are holes and in the second electrons.

We have initiated comparative studies of the normal and superconducting properties of samples of the system of ceramic compounds Pr$_{2-x}$Ce$_x$CuO$_4$ with differing Ce content $(0.13 < x < 0.17)$ and the system of ceramic compounds La$_{2-x}$Sr$_x$CuO$_4$ (Ref. 3). These studies include measurements of the thermal voltage, Hall effect, magnetic properties, and specific heat measurements.

Measurements of the temperature dependence of the specific heat of Pr$_{1.85}$Ce$_{0.15}$CuO$_4$ samples were carried out in Refs. 4 and 5, where primary attention was given to the behavior of the specific heat near the superconducting transition temperature T_c and in the low-temperature region. However, the expected specific-heat discontinuity at T_c was not observed, apparently because of the large width of the transition. These references gave an estimate of the Sommerfeld coefficient, which was obtained from the temperature

dependence of the specific heat of the nonsuperconducting sample in the low-temperature region.

With the aim of refining the parameters characterizing the electronic and vibrational subsystems, the present work looks at the specific heat of the ceramic compound Pr$_{1.85}$Ce$_{0.15}$CuO$_4$ over a wide temperature range (2–800 K) in magnetic fields of 0, 2, 4, 6, and 8 T. We detected a discontinuity in the specific heat at T_c and examined the behavior of the specific heat in the low-temperature region, which enabled us to estimate the density of electronic states. We separated out the phonon contribution to the specific heat and determined the characteristic Debye temperature over a wide temperature range, and also calculated the moments of the phonon spectrum. We compared the parameters of the compound Pr$_{1.85}$Ce$_{0.15}$CuO$_4$ with those of the compound La$_{1.85}$Sr$_{0.15}$CuO$_4$, investigated earlier.[6]

1. PREPARATION OF SAMPLES AND EXPERIMENTAL TECHNIQUE

A sample of Pr$_{1.85}$Ce$_{0.15}$CuO$_4$ was prepared by solid-phase synthesis from a mixture of oxides Pr$_2$O$_3$ (purity 99.9%), CeO (99.9%), and CuO (99.6%), which after careful grinding was annealed for 14 hours in air at a temperature of 950 °C. The obtained material was ground anew and pressed under a pressure of 5 kbar into pellets 12 mm in diameter and 2 mm in thickness, which were annealed in air at $t = 1100$ °C for 18 hours and cooled to room temperature at a rate of 20 °C per minute. Then, to achieve the superconducting state the pellets were placed in a reducing anneal under conditions of dynamical vacuum of 10^{-3} Torr at a temperature of 920 °C for seven hours with subsequent cooling to room temperature at a rate of 10 °C per minute.

A chemical analysis performed using the method of plasma fluorescence spectroscopy confirmed the formula
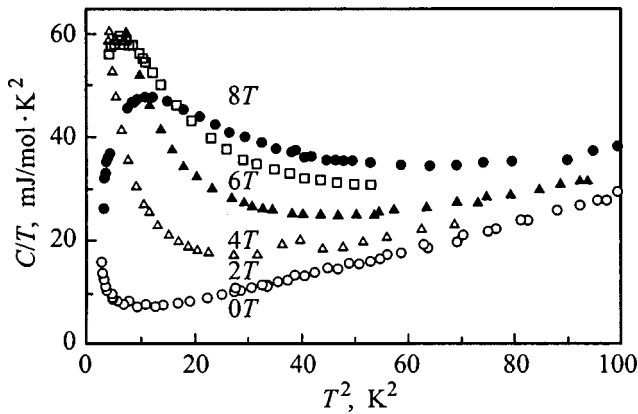
FIG. 1. Temperature dependence of the specific heat of $Pr_{1.85}Ce_{0.15}CuO_4$ in magnetic fields of 0, 2, 4, 6, and 8 T in the temperature range 2–10 K.

FIG. 2. Temperature dependence of the specific heat of $Pr_{1.85}Ce_{0.15}CuO_4$ near the superconducting transition in zero field (*1*) and in a magnetic field of 4 T (*2*). Below: superconducting transition curve from the ac magnetic susceptibility.

composition of the sample. According to x-ray analysis, the sample was single-phase and had tetragonal structure.

The critical temperature T_c of the superconducting transition, determined from ac magnetic susceptibility measurements, was 18 K, and the width of the transition was 2 K. The curve of the superconducting transition is shown in Fig. 2.

Studies of the Meissner effect in $Pr_{1.85}Ce_{0.15}CuO_4$ at helium temperature ($T = 4.2$ K) by the technique described in Ref. 7 enabled us to estimate the volume fraction of the superconducting phase in the sample to be 40%.

The specific heat of the sample in magnetic fields up to 8 T was measured using the adiabatic method with pulsed heating.[8] The experimental error was around 2% in the temperature range 1.5–4 K, 1% in the range 4–10 K, and 0.2–0.5% in the range 10–150 K. In the temperature range 130–800 K the specific heat measurements were performed using the method of differential calorimetry, which allowed us to measure microsamples (10–200 mg) with an accuracy of 2%. The operation of the differential scanning calorimeter is described in Ref. 9.

2. EXPERIMENTAL RESULTS

Results of our study of the specific heat of $Pr_{1.85}Ce_{0.15}CuO_4$ are shown in Figs. 1–3 and in Tables I and II. The temperature dependence of the specific heat at low temperatures (2–10 K) in fields of 0, 2, 4, 6, and 8 T is shown in Fig. 1. In the temperature range 5–9 K in zero field the temperature dependence of the specific heat obeys the law $C = \gamma^* T + \beta T^3$, which corresponds to a straight line in the coordinates C/T vs T^2. At temperatures below 3 K in zero field an anomaly is observed in the temperature dependence of the specific heat of $Pr_{1.85}Ce_{0.15}CuO_4$ consisting in a deviation from the law $C = \gamma^* T + \beta T^3$: the specific heat grows with decreasing temperature. As the magnetic field is increased, the anomaly shifts toward higher temperatures. A quantitative analysis shows that the anomaly can be satisfactorily described by a dependence characteristic of a Schottky anomaly with a gap, that depends almost linearly on the magnetic field. An estimate of the magnitude of this gap in a
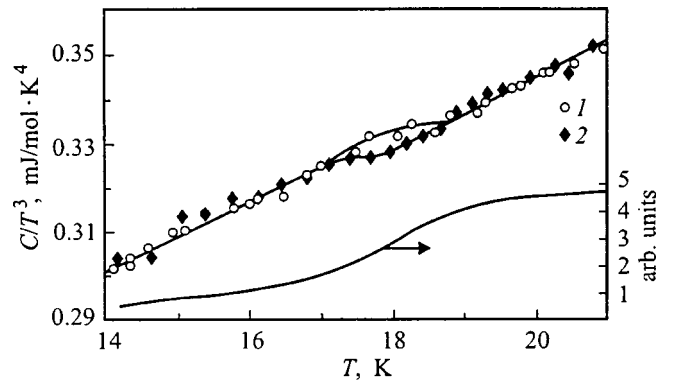
field of 8 T gives 10 K, and the concentration of magnetic-moment carriers is of the order of 0.02 per unit cell.

Figure 2 shows a graph of the specific heat of the sample in the vicinity of the superconducting transition. A discontinuity is observed in the temperature dependence of the specific heat of $Pr_{1.85}Ce_{0.15}CuO_4$ in zero field around 18 K. Application of a magnetic field of 4 T shifts the specific-heat discontinuity toward lower temperatures, but above T_c, within the limits of experimental error, the magnetic field has no effect on the specific heat. The suppression of the specific-heat discontinuity by a magnetic field, and also the closeness of the temperature of the specific-heat discontinuity to the superconducting transition temperature determined
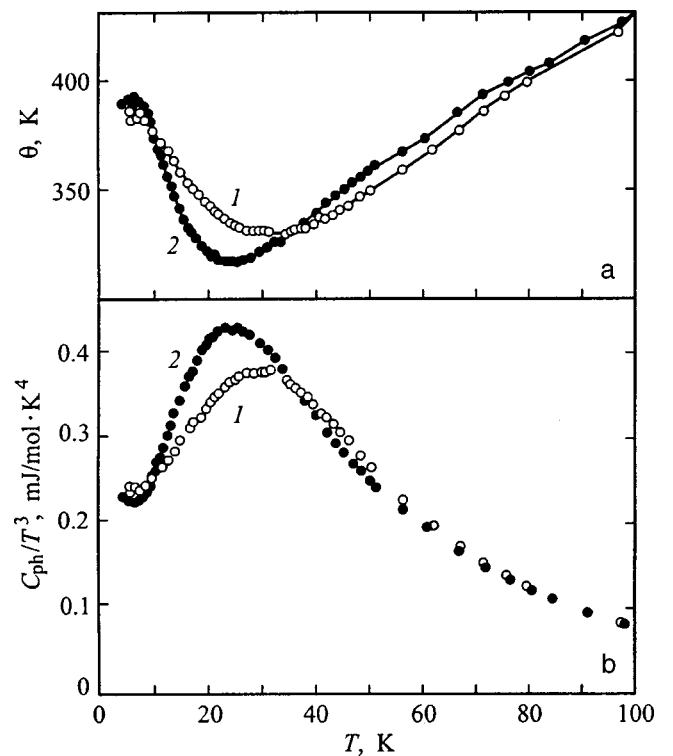

FIG. 3. Temperature dependence of the characteristic Debye temperature Θ (a) and the phonon specific heat (b) for $Pr_{1.85}Ce_{0.15}CuO_4$ (*1*) and $La_{1.85}Sr_{0.15}CuO_4$ (*2*) in the temperature range 5–100 K.

TABLE I. Smoothing of the molar specific heat C_P of $Pr_{1.85}Ce_{0.15}CuO_4$ (1 mol=409.2 g) and $La_{1.85}Sr_{0.15}CuO_4$ (1 mol=397.7 g) in zero magnetic field.

	C_P, J/(mol K)	
T, K	$Pr_{1.85}Ce_{0.15}CuO_4$	$La_{1.85}Sr_{0.15}CuO_4$
2	0.020	0.0037
3	0.022	0.0086
4	0.031	0.0171
5	0.048	0.0310
6	0.072	0.0515
8	0.150	0.123
10	0.285	0.261
15	1.050	1.176
20	2.82	3.31
25	5.70	6.70
30	10.02	11.05
35	15.80	16.00
40	21.6	20.90
45	27.5	26.24
50	33.4	33.0
60	44.6	43.0
70	54.7	53.5
80	64.9	63.5
90	73.4	72.5
100	80.7	80.4
150	106.6	106.0
200	128.5	126.4
250	143.0	140.0
300	154.6	150.0
400	171.5	163.6
500	179.5	172.5
600	186.0	175.3
700	192.0	178.8
800	194.0	182.6

TABLE II. Characteristics of superconducting transitions and specific heat of $Pr_{1.85}Ce_{0.15}CuO_4$ and $La_{1.85}Sr_{0.15}CuO_4$ samples.

Parameter	$Pr_{1.85}Ce_{0.15}CuO_4$	$La_{1.85}Sr_{0.15}CuO_4$
T_c, K	18	39
$\Delta C/T_c$, mJ/mol K^2	2	12
γ_n, mJ/mol K^2	1.4	9
γ^*, mJ/mol K^2	3.3	0.5
β, mJ/mol K^4	0.244	0.230
Θ_L, K	382	390
Θ_H, K	550	560
A, mJ/mol K^2	26.5	14
$\Omega_{\log}$, K	211	209
Ω_{-2}, K	209	207
Ω_{-1}, K	259	259
Ω_1, K	393	390
Ω_2, K	426	434
Ω_*, K	464	475

Note. T_c — superconducting transition temperature. $\Delta C/T_c$ — amplitude of the specific heat discontinuity and γ_n — coefficient of the electronic specific heat of the superconductor in the normal state, normalized to 100 % of the superconducting phase. The coefficients γ^* and β fit the specific heat in the temperature range $5-9$ K with the dependence $C=\gamma^*T+\beta T^3$. Θ_L and Θ_H — low-temperature and high-temperature values of the Debye temperature, A — coefficient of the linear term at high temperatures. $\Omega_{\log}$, Ω_{-2}, Ω_{-1}, Ω_1, Ω_2, and Ω_* characterize the mean frequencies (moments) of the phonon spectrum as defined by relations (6)–(8), expressed in temperature units.

from the ac magnetic susceptibility give reason to conclude that the specific-heat discontinuity is due specifically to a superconducting transition in the bulk of the sample. The amplitude of the jump $\Delta C/T_c$ for the investigated sample is 1 mJ/mol $\cdot$ K^2. Since the superconducting phase, according to the data on the Meissner effect, occupies only about 40% of the volume of the sample, the amplitude of the specific-heat discontinuity for content of the superconducting phase equal to 100% will be around 2 mJ/mol $\cdot$ K^2.

Figure 3 plots the temperature dependence of the phonon specific heat and characteristic Debye temperature Θ for $Pr_{1.85}Ce_{0.15}CuO_4$ (*1*) and $La_{1.85}Sr_{0.15}CuO_4$ (*2*) in the temperature range $5-100$ K.

3. DISCUSSION

As is well known, the specific-heat discontinuity $\Delta C/T_c$ at the superconducting transition is connected with the renormalized density of electron states at the Fermi level $N(E_F)$. Estimation of the Sommerfeld coefficient γ_n for $Pr_{1.85}Ce_{0.15}CuO_4$ according to the BCS relation $\Delta C/T_c = 1.43\gamma_n$ gives $\gamma_n = 1.4$ mJ/mol $\cdot$ K^2 and correspondingly $N(E_F) = 0.042$ states/eV $\cdot$ spin. Comparison of our data for $Pr_{1.85}Ce_{0.15}CuO_4$ with the data obtained in Ref. 10 for $Nd_{1.85}Ce_{0.15}CuO_4$ shows that these quantities are similar: for $Nd_{1.85}Ce_{0.15}CuO_4$ $\Delta C/T_c = 1.7-2$ mJ/mol $\cdot$ K^2 and $\gamma_n = 1.2 - 1.4$ mJ/mol $\cdot$ K^2 (Refs. 6 and 11). These same parameters

for the system $La_{2-x}Sr_xCuO_4$ have a substantially larger values than for electronic superconductors and have the values $\Delta C/T_c = 11-12$ mJ/mol $\cdot$ K^2 and $\gamma_n = 8-10$ mJ/mol $\cdot$ K^2. This shows that the effective mass of the carriers in an electron-doped system is much smaller than in a hole-doped system.

The obtained data allowed us to separate out the phonon contribution from the experimentally measured specific heat over a wide temperature range and determine the temperature dependence of the characteristic Debye temperature Θ [Fig. 3(a)] and also calculate the values of some mean frequencies (moments) of the phonon spectrum.

When separating out the phonon contribution to the specific heat, we assumed that the phonon component of the specific heat in the harmonic approximation C_{ph} is related to the experimentally measured specific heat at constant pressure C as

$$C = C_{ph} + C_a, \tag{1}$$

$$C_a = \{\gamma + (A-\gamma)(C_{ph}/3nR)^2\}T, \tag{2}$$

where C_a combines within itself contributions to the specific heat having a linear temperature dependence and due to anharmonic effects, thermal lattice expansion, and also conduction electrons. Here γ is the coefficient of the electronic specific heat of the superconductor in the normal state at low temperatures, A is the coefficient of the linear term at high temperatures, R is the gas constant, and n is the number of atoms per formula unit (in our case $n=7$).

The interpolation formula (2) for C_a gives the corresponding linear asymptotic limits both at high and at low temperatures and provides a smooth transition between the low- and high-temperature asymptotic limits according to a

law similar to the Nernst–Lindeman equation.[12] Note that the contribution C_a to the total specific heat in the temperature range 20–120 K does not exceed a few percent of the phonon background, and therefore the simplicity of formula (2) applied to the description of C_a is completely justified.

The values of the coefficients γ and A were determined by successive approximation of the experimental data by the corresponding asymptotic expansions.

In the low-temperature region we used the standard relation $C = \gamma T + \beta T^3$, which allowed us to describe the experimental data in the temperature interval 5–9 K with standard deviation $\sim 1.5\%$. The quantities γ and β and also the limiting low-temperature value of the characteristic Debye temperature Θ_L, related to β by the formula $\beta = 12\pi^4 nR/(5\Theta_L^3)$, are listed in Table II.

In the high-temperature region the total specific heat was described by a relation with three variable parameters: Ω_2, Ω_*, and A

$$C = C_{ph} + C_a$$

$$= 3Rn\left\{ 1 - \frac{1}{12}\left(\frac{\Omega_2}{T}\right)^2 + \psi\left(\frac{\Omega_*}{T}\right)\right\} + A\left(\frac{C_{ph}}{3nR}\right)^2 T, \quad (3)$$

where

$$\psi(z) = \frac{z^2 \exp(z)}{(1 - \exp(z))^2} - \left(1 - \frac{z^2}{12}\right). \quad (4)$$

Here, to describe the phonon component of the specific heat we used an approach that is similar to that employed in Refs. 13 and 14; specifically, we used the asymptotic expansion of the phonon specific heat in the small parameter $z = \Omega/T$, where Ω is the characteristic energy of the phonons and T is the temperature

$$C_{ph} = 3nR\left\{ 1 - \sum_{k=2}^{\infty} \frac{(k-1)B_k}{k!}\left(\frac{\Omega_k}{T}\right)^k\right\}. \quad (5)$$

Here B_k are the Bernoulli numbers, where all B_k with odd $k > 2$ are equal to zero.

In formula (3) the second-order correction in Ω/T is written separately, and the function $\psi(\Omega_*/T)$ includes all higher corrections in the ''Einstein'' approximation, i.e., by setting $\Omega_k = \Omega_*$ for all $k \geq 4$.

The quantities Ω_k are the moments (mean frequencies) of the phonon spectrum and are defined as

$$(\Omega_k)^k = \langle \omega^k \rangle = \int_0^{\infty} g(\omega)\omega^k d\omega \bigg/ \int_0^{\infty} g(\omega)d\omega. \quad (6)$$

Here $g(\omega)$ is the energy density of phonon states, and ω is the energy, expressed in temperature units.

Note that in expansion (3) the term containing Ω_* describes the higher-order corrections with $k \geq 4$, and therefore the quantity Ω_* is determined primarily by the fourth and sixth moments of the spectrum, i.e.,

$$\omega_* \cong \Omega_4, \Omega_6. \quad (7)$$

The quantities Ω_2, Ω_*, and A were determined by least squares using formula (3) over the temperature range 115–800 K. In this temperature range we were able to describe the

experimental results with a standard deviation around 1.3%. The values of the parameters A, Ω_2, and Ω_* are given in Table II. Table II also gives the limiting high-temperature value of the Debye temperature Θ_H related to the second moment of the phonon spectrum by the formula $\Omega_2 = \Omega_H (3/5)^{1/2}$.

The above analysis allows us to separate out from the total specific heat the phonon background C_{ph} in the harmonic approximation by eliminating the electronic and anharmonic components using relations (1) and (2), and to estimate the values of A and γ by successive approximation.

Some moments of the phonon spectrum are expressed directly in terms of integrals of the phonon specific heat[15]

$$\langle \omega \rangle = 2 \int_0^{\infty} \left(1 - \frac{C_{ph}}{3nR}\right) dT,$$

$$\langle \omega^{-1} \rangle = \frac{3}{\pi^2} \int_0^{\infty} \frac{C_{ph}}{3nR} T^{-2} dT,$$

$$\langle \omega^{-2} \rangle = 0.138651 \int_0^{\infty} \frac{C_{ph}}{3nR} T^{-3} dT,$$

$$\langle \omega^{-1} \log \omega \rangle = \frac{3}{\pi^2} \int_0^{\infty} \frac{C_{ph}}{3nR} \log\left(\frac{T}{0.70702}\right) T^{-2} dT.$$

The indicated moments were determined numerically, where the integration was carried out over the experimental points in the temperature interval 10–800 K, outside of which we extrapolated the specific heat using the low-temperature asymptotic limit $C_{ph} = \beta T^3$ and the high-temperature asymptotic limit in the model of the Debye spectrum, as in Ref. 16.

The mean frequencies corresponding to these moments are listed in Table II, where all the frequencies are expressed in temperature units. The quantities Ω_2, Ω_1, Ω_{-1}, and Ω_* were determined above by Eqs. (6) and relation (7), and parameter $\Omega_{\log}$ is defined as

$$\log(\Omega_{\log}) = \frac{\langle \omega^{-1} \log \omega \rangle}{\langle \omega^{-1} \rangle}$$

$$= \int_0^{\infty} \frac{g(\omega)\log \omega}{\omega} d\omega \bigg/ \int_0^{\infty} \frac{g(\omega)}{\omega} d\omega. \quad (8)$$

Note that the moments of higher orders (Ω_2 and Ω_*) reflect the characteristics of the phonon spectrum in the region of higher energies and are determined primarily by the behavior of the specific heat at high temperatures. The moments $\Omega_{\log}$, Ω_{-2}, and Ω_{-1} characterize the low-energy region and are determined mainly by the specific heat at low temperatures. In the given systems, for example, the moment Ω_{-2} is determined mainly by the temperature region up to 50 K and characterizes the spectrum in the energy region from 0 to 25 meV.

The experimental data on the specific heat of the previously investigated sample, $La_{1.85}Sr_{0.15}CuO_4$ (Ref. 6), were processed using the same procedure as for $Pr_{1.85}Ce_{0.15}CuO_4$, which made it possible to perform a correct comparative analysis of the parameters for these two samples. The analy-

sis of the obtained numerical values of the mean frequencies (moments) of the phonon spectrum in $Pr_{1.85}Ce_{0.15}CuO_4$ and $La_{1.85}Sr_{0.15}CuO_4$ shows that the quantities characterizing the low-frequency region of the vibrational spectrum ($\Omega_{\log}$, ω_{-2}, and Ω_{-1}) in $La_{1.85}Sr_{0.15}CuO_4$ are smaller than in $Pr_{1.85}Ce_{0.15}CuO_4$ and, thus, the low-frequency region of the phonon spectrum of $La_{1.85}Sr_{0.15}CuO_4$ is "softer." As for the moments Ω_2 and Ω_*, which characterize the higher-frequency region of the spectrum, here the reverse is true: $Pr_{1.85}Ce_{0.15}CuO_4$ has the "softer" spectrum.

As is well known, the low-temperature specific heat carries sufficient information to draw conclusions about the low-frequency region of the vibrational spectrum. Toward this end, it is advantageous to plot the phonon component of the specific heat in the coordinates C_{ph}/T^3 vs T since the detailed analysis carried out in Ref. 17 showed that the quantity C_{ph}/T^3 gives a good approximate picture of the function $\omega^{-2}g(\omega)$ for $\omega = 4.93\,T$. This implies that vibrations in the energy region $E \sim 5kT$, where k is the Boltzmann constant, make a substantial contribution to the phonon specific heat at the temperature T.

Since the information content of the analyzed dependence decreases with increasing temperature due to the rapid falloff of C_{ph}/T^3, it would be more appropriate to discuss the temperature dependence of the specific heat with the help of the temperature dependence of the characteristic Debye temperature Θ, which is a more sensitive characteristic, governing, as it does, in particular, the rate of convergence of $C_{ph}(T)$ to its asymptotic limit. The temperature dependence of $C_{ph}(T)/T^3$ for $Pr_{1.85}Ce_{0.15}CuO_4$ passes through a wide maximum at $T \sim 30$ K [Fig. 3(b)], which corresponds to the presence in the phonon spectrum of an intense low-frequency mode at the energy $E \sim 15$ meV. For $La_{1.85}Sr_{0.15}CuO_4$ the corresponding maximum is observed at $T \sim 20$ K, which corresponds to a low-frequency mode at $E \sim 10$ meV. Figure 3(a) plots the dependence of the characteristic parameter Θ on the temperature. The shift of the maximum in the dependence $C_{ph}(T)/T^3$ and the corresponding minimum in the dependence $\Theta(T)$ toward higher temperatures in $Pr_{1.85}Ce_{0.15}CuO_4$ in comparison with $La_{1.85}Sr_{0.15}CuO_4$ is evidence of an increase in the rigidity of the phonon spectrum in the energy region 10–15 meV in the Pr-system.

Our measurements of the specific heat of $Pr_{1.85}Ce_{0.15}CuO_4$ over a wide range of temperatures and magnetic fields allows us to make the following conclusions.

1) For the first time, a discontinuity in the specific heat at the transition to the superconducting state has been observed in $Pr_{1.85}Ce_{0.15}CuO_4$, equal in magnitude to $\Delta C/T_c = 2$ mJ/mol$\cdot$K^2, which has made it possible to estimate the Sommerfeld coefficient $\gamma_n = 1.4$ mJ/mol$\cdot$K^2. The discontinuity in the specific heat at T_c and the corresponding value of the Sommerfeld coefficient in the investigated $Pr_{1.85}Ce_{0.15}CuO_4$ sample is several times smaller than in the $La_{1.85}Sr_{0.15}CuO_4$ sample. This fact indicates that the effective electron mass in an "electronic" superconductor is several times smaller than in a "hole" superconductor.

2) The phonon component of the specific heat has been separated out. Within the framework of a more accurate analysis of the specific-heat data in the region of intermediate and high temperatures, we have calculated the mean phonon frequencies (moments) of the phonon spectrum and have determined the characteristic Debye temperature Θ over a wide range of temperatures. In the low-energy region the phonon spectrum of the system $La_{1.85}Sr_{0.15}CuO_4$ is "softer" than the phonon spectrum of the system $Pr_{1.85}Ce_{0.15}CuO_4$. In the high-energy region the spectrum of the system $Pr_{1.85}Ce_{0.15}CuO_4$ is "softer."

*)E-mail: khlopkin@ismain.isssph.kiae.ru

[1] Y. Tokura, H. Takagi, and S. V. Uchida, Nature (London) **337**, No. 6205, 345 (1989).

[2] M. E. Lopez-Morales, R. S. Savoy, and P. M. Grant, Solid State Commun. **71**, 1079 (1989).

[3] M. N. Khlopkin, J. Toth, G. Kh. Panova, R. O. Zaitsev, N. A. Babushkina, J. A. Arnold, and S. E. Voinova, Solid State Commun. **87**, 213 (1993).

[4] M. Sera, S. Shamoto, and M. Sato, Solid State Commun. **72**, 749 (1989).

[5] A. Iwai, A. Masaaki, H. Nakajima, and K. Kumagai, Physica C **185–189**, Part II, 1349 (1991).

[6] B. E. Balbashov, D. A. Shulyatev, G. Kh. Panova, M. N. Khlopkin, N. A. Chernoplekov, A. A. Shikov, and A. V. Suetin, Physica C **256**, 371 (1996).

[7] V. S. Egorov and A. A. Teplov, Sverkhprovodimost: Fiz., Khim., Tekh. **1**, No. 2, 44 (1988).

[8] M. N. Khlopkin, N. A. Chernoplekov, and P. A. Cheremnykh, Preprint IAÉ, No. 3549/10. Moscow (1982).

[9] G. Kh. Panova, A. A. Shikov, T. Kemen', B. Fogarashi, Yu. V. Efimov, and E. M. Savitskiĭ, Preprint IAÉ, No. 3246/10, Moscow (1980).

[10] B. Buffeteau, T. Hargreaves, B. Grevin, and C. Marin, Physica C **294**, 55 (1998).

[11] A. Junod, A. Bezinge, D. Cattani, J. Cors, M. Decroux, O. Fisher, P. Genoud, L. Hoffmann, J.-L. Jorda, J. Muller, and E. Walkerz, Jpn. J. Appl. Phys. **26**, No. 26–3, 1119 (1987).

[12] L. A. Reznitskiĭ, *Solid State Calorimetry* [in Russian] (Moscow, 1981).

[13] V. N. Naumov, Phys. Rev. B **49**, 13 247 (1994).

[14] M. I. Katsnelson, I. I. Naumov, A. V. Trefilov, M. N. Khlopkin, and K. Yu. Khromov, Philos. Mag. B **75**, 389 (1997).

[15] A. Junod, Solid State Commun. **33**, 55 (1980).

[16] A. V. Mirmel'shteĭn, A. E. Kar'kin, V. E. Arkhipov, and V. I. Voronin, Fiz. Met. Metalloved. **58**, 1008 (1984).

[17] A. Junod, T. Jarlborg, and J. Muller, Phys. Rev. B **27**, 1568 (1983).

Translated by Paul F. Schippnick

On the decay of generalized Swihart waves

A. S. Malishevskiĭ,*) V. P. Silin, and S. A. Uryupin

P. N. Lebedev Physical Institute, Russian Academy of Sciences, 117924 Moscow, Russia
(Submitted September 29, 1998; accepted for publication November 17, 1998)
Fiz. Tverd. Tela (St. Petersburg) **41**, 1160–1167 (July 1999)

For Josephson junctions in sandwich geometry and in thin-film geometry we formulate the equations of nonlocal electrodynamics which take account of the influence of normal electrons in superconductors. On the basis of these equations we examine the spectrum and decay of generalized Swihart waves. We find that the decay of these waves by normal electrons becomes especially prominent in the short-wavelength region. Comparison of various dissipation mechanisms has revealed the conditions for efficient emission of electromagnetic waves from Josephson structures with finite dimensions. © *1999 American Institute of Physics.*
[S1063-7834(99)00707-8]

The properties of Swihart waves have attracted continuous attention from the moment they were predicted at the beginning of the 1960's (Ref. 1). The interest in these waves has been motivated by studies of the spectral properties both of solitary Josephson junctions (see, e.g., Refs. 2–4) and layered Josephson structures.[5] Ordinary Swihart waves are described by the Klein–Gordon–Fock equation with dissipation

$$\frac{\partial^2}{\partial t^2}\varphi - \nu_s^2 \frac{\partial^2}{\partial z^2}\varphi + \omega_j^2 \varphi = -\beta \frac{\partial}{\partial t}\varphi + \alpha \frac{\partial^3}{\partial t\, \partial z^2}\varphi, \qquad (1)$$

where $\varphi = \varphi(z,t)$ is the phase difference of the wave functions of the Cooper pairs on different sides of the junction,

$$\nu_s \equiv c\sqrt{d/\varepsilon\lambda} \qquad (2)$$

is the Swihart velocity, and

$$\omega_j \equiv \left(\frac{16\pi}{\hbar\varepsilon}\left|e\right|dj_c\right)^{1/2}$$

is the Josephson frequency. Here j_c is the critical Josephson current density, e is the charge of the electron, $2d$ is the thickness of the junction, ε is the dielectric constant of the nonsuperconducting layer, $\hbar$ is Planck's constant, c is the speed of light, λ is the London length. The right-hand side of Eq. (1) contains terms describing dissipation of Swihart waves. The term containing

$$\beta \equiv 4\pi\sigma/\varepsilon,$$

describes dissipation in the nonsuperconducting layer with conductivity σ, and the term containing

$$\alpha \equiv \frac{2\pi}{\varepsilon}\sigma_n\lambda d = \frac{4\pi\sigma_n}{\varepsilon}\left(\frac{2d}{\lambda}\right)\frac{\lambda^2}{4},$$

describes dissipation in the superconductors with conductivity of the normal electrons σ_n. Neglecting dissipation, Eq. (1) gives the following relation for the spectrum of the Swihart waves:

$$\omega^2 = \omega_j^2 + k^2\nu_s^2.$$

Taking the small dissipative terms on the right-hand side of Eq. (1) into account leads to the following expression for the decay decrement:

$$\gamma = \frac{\beta}{2} + \frac{\alpha}{2}k^2. \qquad (3)$$

With increasing magnitude of the wavelength $2\pi/k$, the second term in Eq. (3) falls away. Therefore, for long enough waves, when

$$\frac{1}{R_n} \equiv \frac{\sigma_n}{\lambda}\left(\frac{1}{2}k\lambda\right)^2 \ll \frac{\sigma}{2d} \equiv \frac{1}{R_\sigma}, \qquad (4)$$

the influence of normal electrons on the decay of Swihart waves is negligibly small. In Eq. (4) we have used the notation R_n for the resistance per unit area of the superconductor, and R_σ for the resistance per unit area of the junction. The quantity R_n in Eq. (4) depends on the London length λ. Note that in those cases when the field penetration depth of the superconductor is different from λ the expression for R_n contains λ_{eff} or λ_e (see below).

Equation (1) describes Josephson junctions within the framework of local electrodynamics. The development of the description of Josephson structures within the framework of nonlocal electrodynamics[6–21] has made it possible to reveal the conditions under which the need for a nonlocal description of the wave properties of Josephson junctions arises. In particular, according to Ref. 11 (see also Refs. 10 and 12) for a Josephson junction between bulk superconductors the local description becomes unsuitable when the characteristic scale $L_\varphi \equiv |\partial \ln \varphi/\partial z|^{-1}$ of spatial variation of the phase difference is small in comparison with the London length $L_\varphi \ll \lambda$. For a junction on a thin superconducting film of thickness D, when the effective penetration depth of a static magnetic field λ_e significantly exceeds the London length[22]

$$\lambda_e \equiv \lambda^2/D \gg \lambda,$$

an adequate description of the properties of the junction is possible only within the framework of nonlocal electrodynamics.[8,9,13,14,17,20] Spatial nonlocality has as its result that

Eq. (1) must be replaced by an integral equation over the spatial variables. Another reason for nonlocality of the electrodynamics of Josephson junctions has to do with the possibility of emission of Swihart waves from a sandwich as well as from a thin film.[21]

As was already mentioned, a considerable number of works[6–21] have been dedicated to a description of Josephson junctions within the framework of nonlocal electrodynamics. Here dissipation of the electromagnetic energy is connected either with losses in the nonsuperconducting layer[10–14] or with losses to radiation of waves to the vacuum.[21] In contrast to these works, Ref. 23 takes account in the equations of nonlocal electrodynamics of the dissipation associated with the conductivity of the normal electrons of superconductors. Note that already in relations (3) and (4) it is clear that with growth of the Swihart wave vector the role of the normal electrons becomes more and more important.

In what follows we consider Swihart waves on the basis of the equations of nonlocal electrodynamics, where the term ''generalized Swihart waves'' is used for such waves. We present results of a study of the spectrum of such generalized waves and regularities of their decay. The paper is organized as follows. Section 1 discusses consequences of London's electrodynamics. It is found that at temperatures not too close to T_c (the superconducting transition temperature), dissipation by normal electrons of the superconductor is comparatively small and it can be described using expansion (10). Section 2 considers the wave properties of a superconducting sandwich. A nonlocal equation (specifically, nonlocal in space) is derived for the phase difference which takes account of ohmic losses in the junction and superconducting electrodes. It considers the spectrum of generalized Swihart waves and provides a description of their decay. Conditions are revealed under which absorption of waves by normal electrons of the superconductor plays a defining role. Section 3 gives a description of radiative decay of Swihart waves in the region of long wavelengths. A comparison is given of the radiative decay decrement and contributions to the total decrement by normal electrons, superconducting electrons, and by losses in the junction. This enables one to judge the emission efficiency of Swihart waves from a sandwich. This section also finds the spectrum and decay decrement of surface waves. Section 4 is dedicated to the theory of a Josephson junction in a thin film. It derives a nonlocal equation for the phase difference which, in contrast to the known equation,[8,9] takes account of the influence of normal electrons in the film and makes it possible to determine their influence on the decay of generalized Swihart waves. Section 5 derives the corresponding equation for the phase difference that takes account both the influence of normal electrons and the effect of emission of waves from the film. This latter process makes this equation nonlocal in time. Temporal nonlocality also arises as a result of the interaction of Swihart waves with surface waves of the film. Conditions are revealed, under which the decay decrement of the Swihart waves is governed by radiative losses, and the decay due to the influence of normal electrons in the film and losses in the junction are comparatively small. In other words, we have identified the

conditions for efficient emission from a Josephson junction in a superconducting film.

1. MATERIAL EQUATION OF LONDON'S ELECTRODYNAMICS

The electric current density in a superconductor is equal to the sum of the superconducting current density and the current density of the normal electrons

$$\mathbf{j}(\mathbf{r},t) = -\frac{c}{4\pi\lambda^2}\left\{\frac{\phi_0}{2\pi}\,\mathrm{grad}\,\Phi(\mathbf{r},t) + \mathbf{A}(\mathbf{r},t)\right\} + \sigma_n\mathbf{E}(\mathbf{r},t). \quad (5)$$

Here $\phi_0 \equiv \pi\hbar c|e|^{-1}$ is the magnetic flux quantum, $\Phi(\mathbf{r},t)$ is the phase of the wave function of the Cooper pairs, $\mathbf{A}(\mathbf{r},t)$ is the vector potential, and $\mathbf{E}(\mathbf{r},t)$ is the electric field vector. In Eq. (5) the current density of the normal electrons as it is written assumes that the characteristic time of variation of the electric field is large in comparison with the inverse collision frequency of the normal electrons while the characteristic spatial scale of variation of the field is much greater than their mean free path. Taking into account the condition of gauge invariance in the theory (see, e.g., Ref. 24)

$$V(\mathbf{r},t) = \frac{\phi_0}{2\pi c}\frac{\partial}{\partial t}\Phi(\mathbf{r},t),$$

where $V(\mathbf{r},t)$ is the scalar potential, we rewrite Eq. (5) for the current density in the form (see, e.g., Ref. 25)

$$\frac{\partial}{\partial t}\mathbf{j}(\mathbf{r},t) = \left(\frac{c^2}{4\pi\lambda^2} + \sigma_n\frac{\partial}{\partial t}\right)\mathbf{E}(\mathbf{r},t). \quad (6)$$

Taking the Fourier transforms for time, Eq. (6) yields

$$\mathbf{j}(\mathbf{r},\omega) = \frac{\omega}{4\pi i}\varepsilon(\omega)\mathbf{E}(\mathbf{r},\omega), \quad (7)$$

where the dynamic dielectric constant $\varepsilon(\omega)$ is described by the expression

$$\varepsilon(\omega) = -\frac{c^2}{\omega^2\lambda_*^2} \equiv -\frac{c^2}{\omega^2\lambda^2} + i\frac{4\pi}{\omega}\sigma_n. \quad (8)$$

Taking into account the relation between the London length and n_s (the number density of the superconducting electrons),

$$\lambda^2 = mc^2/4\pi e^2 n_s$$

and of the conductivity σ_n with n_s (the number density of the normal electrons),

$$\sigma_n = e^2 n_n/m\nu,$$

where m is the effective electron mass and ν is their collision frequency, we have from Eq. (8)

$$\varepsilon(\omega) = -\frac{4\pi e^2}{m\omega^2}n_s(1 - i\omega\tau), \quad (9)$$

where $\tau \equiv n_n/\nu n_s$ is the characteristic relaxation time of the field. At temperatures of the superconductor T less than the critical temperature T_c, the ratio of n_n to n_s falls with decreasing temperature (see, e.g., Ref. 25)

$$\frac{n_n}{n_s} \simeq \frac{T_c}{2(T_c - T)} - 1, \quad T_c - T \ll T_c,$$

$$\frac{n_n}{n_s} \simeq \left(2\pi \frac{\Delta}{T}\right)^{1/2} \exp\left(-\frac{\Delta}{T}\right), \quad T \ll T_c.$$

Here Δ is the width of the energy gap at $T=0$, $\Delta \sim T_c$. In addition, within the limits of applicability of relation (5) $\omega \ll \nu$. This implies that at temperatures of the superconductor that are not too close to critical the imaginary part of the dielectric constant (8), (9) is small in comparison with the real part. Under these conditions, we may use the approximate expression

$$\lambda_* \equiv \lambda(1 - i\omega\tau)^{-1/2} \simeq \lambda\left(1 + \frac{i}{2}\omega\tau\right). \quad (10)$$

for the complex London length λ_*. According to the material equations (7) and (8), in the following treatment of the electrodynamics of superconductors λ can be replaced by λ_*.

2. SLOW WAVES IN A SANDWICH

Consider a Josephson junction in a sandwich formed by two identical superconducting electrodes of thickness L, separated by a nonsuperconducting layer of thickness $2d$ with dielectric constant ε and conductivity σ. Assuming that the junction is characterized by a real dielectric constant $\varepsilon > 0$ and conductivity σ, in what follows we will digress from a discussion of non-ohmic energy losses in it. Following Ref. 15 and taking account of the relation between the current density and the electric field (6) and making use of expansion (10) we have the following equation for the phase difference of the wave functions of the electrodes:

$$\omega_j^2 \sin\varphi(z,t) + \beta\frac{\partial}{\partial t}\varphi(z,t) + \frac{\partial^2}{\partial t^2}\varphi(z,t)$$

$$= \hat{L}[\varphi(z,t)] \equiv \frac{\partial^2}{\partial z^2}\int_{-\infty}^{\infty}dz' Q(z-z')\varphi(z',t)$$

$$- \tau\frac{\partial^3}{\partial t\partial z^2}\int_{-\infty}^{\infty}dz' Q_n(z-z')\varphi(z',t), \quad (11)$$

where the kernels of the integral terms are given by

$$\left\{\begin{matrix} Q(z) \\ Q_n(z) \end{matrix}\right\} = \int_{-\infty}^{\infty}\frac{dk}{2\pi}\exp(ikz)\left\{\begin{matrix} Q(k,\lambda) \\ Q_n(k,\lambda) \end{matrix}\right\}, \quad (12)$$

$$Q(k,\lambda) \equiv \frac{\nu_s^2}{\lambda}\lambda(k)\tanh\left[\frac{L}{\lambda(k)}\right], \quad (13)$$

$$Q_n(k,\lambda) \equiv \frac{\lambda}{2}\frac{\partial}{\partial\lambda}Q(k,\lambda), \quad (14)$$

$$\lambda(k) \equiv \lambda/\sqrt{1+k^2\lambda^2}. \quad (15)$$

If the thickness of the electrodes L is much larger than the London length, the kernels (12) of the integral terms in Eq. (11) take the form (cf. Ref. 23)

$$Q(z) = \frac{\nu_s^2}{\pi\lambda}K_0\left(\frac{|z|}{\lambda}\right), \quad (16)$$

$$Q_n(z) = \frac{\nu_s^2}{\pi\lambda}\left[\frac{|z|}{2\lambda}K_1\left(\frac{|z|}{\lambda}\right) - K_0\left(\frac{|z|}{\lambda}\right)\right], \quad (17)$$

where $K_\nu(x)$ is the McDonald function, and the velocity ν_s has the form (2). In the case when the characteristic spatial scale of variation in the phase difference L_φ significantly exceeds the London length, relations (16) and (17) allow us to represent the right-hand side of Eq. (11) in local form

$$\hat{L}[\varphi(z,t)] = \nu_s^2\frac{\partial^2}{\partial z^2}\varphi(z,t) + \frac{1}{2}\nu_s^2\tau\frac{\partial^3}{\partial t\partial z^2}\varphi(z,t). \quad (18)$$

In this case, of course, Eq. (11) reduces to Eq. (1) (see, e.g., Refs. 3 and 4) in the local electrodynamics of Josephson junctions. In the opposite limiting case, when $L_\varphi \ll \lambda$, using relations (16) and (17) we find for the operator $\hat{L}[\varphi]$

$$\hat{L}[\varphi(z,t)] = \frac{\nu_s^2}{\pi\lambda}\left(1 + \tau\frac{\partial}{\partial t}\right)\text{P.V.}\int_{-\infty}^{\infty}\frac{dz'}{z'-z}\frac{\partial}{\partial z'}\varphi(z',t), \quad (19)$$

where the integral over z' is understood in the sense of its principal value. In essence, relations (16)–(19), which do not contain any dependence on the thickness of the superconducting electrodes, conform to the electrodynamics of Josephson junctions in bulk superconductors. The dependence of the kernels $Q(z)$ and $Q_n(z)$ on L can be manifested in the case of thin electrodes, when $L \ll \lambda$. Then, to describe phase difference distributions that have scales less than the London length $L_\varphi \ll \lambda$, we find from relations (12)–(14)

$$Q(z) = -Q_n(z) = \frac{\nu_s^2}{\pi\lambda}\ln\left[\coth\left(\frac{\pi|z|}{4L}\right)\right].$$

In turn, the integral operator in Eq. (11) takes the form

$$\hat{L}[\varphi(z,t)] = \frac{\nu_s^2}{2\lambda L}\left(1 + \tau\frac{\partial}{\partial t}\right)\text{P.V.}$$

$$\times \int_{-\infty}^{\infty}\frac{dz'}{\sinh\left[\frac{\pi(z-z')}{2L}\right]}\frac{\partial}{\partial z'}\varphi(z',t), \quad (20)$$

where the difference from Ref. 15 lies in taking dissipation into account. Obviously, for $L_\varphi \ll L$ expression (20) goes over to expression (19). Another possible way of manifesting the finite thickness of the electrodes is realized for $L_\varphi \gg \lambda \gg L$. Under these conditions the functional $\hat{L}[\varphi]$ takes the form

$$\hat{L}[\varphi(z,t)] = \nu_{sL}^2\left(1 + \tau\frac{\partial}{\partial t}\right)\frac{\partial^2}{\partial z^2}\varphi(z,t). \quad (21)$$

The main difference between expressions (21) and (18) consists in a change in the Swihart velocity, which in the case of thin electrodes depends on the effective length $\lambda_{\text{eff}} \equiv \lambda^2/L \gg \lambda$

$$\nu_{sL} \equiv c\sqrt{d/\varepsilon\lambda_{\text{eff}}} \ll \nu_s.$$

We will use Eqs. (11)–(14) to describe linear waves in a sandwich. The corresponding dispersion relation looks comparatively simple

$$\omega^2 + i\beta\omega = \omega_j^2 + k^2 Q(k,\lambda) + i\omega\tau k^2 Q_n(k,\lambda). \quad (22)$$

Here the Fourier components of the kernels $Q(k,\lambda)$ and $Q_n(k,\lambda)$ are described by expressions (13) and (14). Setting $\omega \equiv \omega' - i\gamma$, where $\gamma \ll \omega'$, for the real part of the frequency Eq. (22) yields[19]

$$\omega'^2 = \omega_j^2 + k^2 \nu_s^2 \frac{\lambda(k)}{\lambda} \tanh\left[\frac{L}{\lambda(k)}\right]. \quad (23)$$

Next, taking the imaginary corrections in Eq. (22) into account, we obtain the decay decrement of the generalized Swihart waves, whose dispersion law is given by relation (23)

$$\gamma = \gamma_d + \gamma_n. \quad (24)$$

The term γ_d in expression (24) describes wave decay due to ohmic losses in a Josephson junction

$$\gamma_d = \beta/2 = 2\pi\sigma/\varepsilon. \quad (25)$$

The term γ_n in expression (24) is related to energy losses in the superconducting electrodes, due to scattering of normal electrons

$$\gamma_n = -\frac{\tau}{4}(k\lambda)^2 \nu_s^2 \frac{\partial}{\partial\lambda}\left\{\frac{\lambda(k)}{\lambda^2}\tanh\left[\frac{L}{\lambda(k)}\right]\right\}$$

$$\equiv \frac{1}{2}\tau k^2 \nu_s^2 \left[\frac{\lambda(k)}{\lambda}\right]^3 \tanh\left[\frac{L}{\lambda(k)}\right]$$

$$\times\left\{\frac{1}{2} + (k\lambda)^2 + \frac{L}{\lambda(k)}\sinh^{-1}\left[2\frac{L}{\lambda(k)}\right]\right\}. \quad (26)$$

Let us compare the decay decrements (25) and (26). For $k\lambda \sim 1$ and $L \gg \lambda$ the decay decrement of the waves is mainly caused by normal electrons if the effective resistance per unit area of the superconductor $R_n \equiv \lambda/\sigma_n \ll R$, where $R \equiv 2d/\sigma$ is the resistance per unit area of the Josephson junction. Similarly for $k\lambda \sim 1$, but in the case of thin electrodes, when $L \ll \lambda$, because of the fact that in the theory we are using $\lambda_{\text{eff}} \equiv \lambda^2/L \gg \lambda$ and the resistance R_n is increased, decay of the waves is governed by the normal electrons provided the more restrictive condition $R \gg R_n \equiv \lambda_{\text{eff}}/\sigma_n \gg \lambda/\sigma_n$ is met. Also note that for $k\lambda \ll 1$, as can be seen from Eq. (26), the decay decrement on the normal electrons decreases in proportion to $(k\lambda)^2$, and for $k\lambda \gg 1$ it grows in proportion to $k\lambda$. In the short-wavelength region, when $k\lambda \gg 1$, the decrement γ is governed by the normal electrons if $R \gg (2/k\sigma_n)$ coth(kL). In this case, Eqs. (23) and (26) yield

$$\gamma_n = \frac{1}{2}\tau\nu_s^2\frac{k}{\lambda}\tanh(kL),$$

$$\omega' = \frac{\nu_s}{\lambda}\sqrt{k\lambda}[\tanh(kL)]^{1/2},$$

$$\frac{\gamma}{\omega'} = 2\pi\sigma_n\frac{\lambda\nu_s}{c^2}[k\lambda\tanh(kL)]^{1/2} \equiv \frac{1}{2}\omega'\tau \ll 1. \quad (27)$$

According to Eq. (27), in the short-wavelength region, when the phase velocity of the generalized Swihart wave is substantially decreased, wave decay by normal electrons is manifested quite dramatically. However, within the limits of applicability of the basic approximate relation (10), the decay of generalized Swihart waves turns out to be comparatively small.

3. FAST WAVES IN A SANDWICH

Equations (11)–(15) are suitable only for describing waves with phase velocity less than the speed of light. To consider fast waves with $\omega/k \gg c$, it is necessary to use a more general equation for the phase difference that allows for the possibility of radiation of electromagnetic waves into the vacuum. The corresponding equation is obtained within the framework of the approach of Ref. 21 if we use the material equations linking the current density with the field in the superconductors (6). In this case, in contrast to Eqs. (11)–(15) an equation that is nonlocal in time as well as space arises

$$\omega_j^2 \sin\varphi(z,t) + \beta\frac{\partial}{\partial t}\varphi(z,t) + \frac{\partial^2}{\partial t^2}\varphi(z,t)$$

$$= \hat{L}[\varphi(z,t)]$$

$$\equiv \int_{-\infty}^{\infty}dz'\int_{-\infty}^{\infty}dt'\frac{\partial^2}{\partial z^2}\left[Q(z-z',t-t')\right.$$

$$\left. -\tau\frac{\partial}{\partial t}Q_n(z-z',t-t')\right]\varphi(z',t'), \quad (28)$$

where for the kernels of the integral term we have the relations

$$\left\{\begin{array}{c}Q(z,t)\\Q_n(z,t)\end{array}\right\} = \int_{-\infty}^{\infty}\frac{dk}{2\pi}\int_{-\infty}^{\infty}\frac{d\omega}{2\pi}\exp(-i\omega t + ikz)$$

$$\times\left\{\begin{array}{c}Q(k,\omega,\lambda)\\Q_n(k,\omega,\lambda)\end{array}\right\}, \quad (29)$$

$$Q(k,\omega,\lambda) \equiv \nu_s^2\frac{\lambda(k)}{\lambda}\tanh\left[\frac{L}{\lambda(k)}\right]$$

$$\times\frac{\coth\left[\dfrac{L}{\lambda(k)}\right] - \dfrac{c^2}{\lambda^2\omega^2}\lambda(k)\psi(k,\omega)}{\tanh\left[\dfrac{L}{\lambda(k)}\right] - \dfrac{c^2}{\lambda^2\omega^2}\lambda(k)\psi(k,\omega)}, \quad (30)$$

$$Q_n(k\omega,\lambda) \equiv \frac{\lambda}{2}\frac{\partial}{\partial\lambda}Q(k,\omega,\lambda), \quad (31)$$

and the function $\psi(k,\omega)$ associated with the possibility of emission of waves is given by

$$\psi(k,\omega)\equiv[\,\eta(c^2k^2-\omega^2)-i\,\eta(\omega^2-c^2k^2)\,\text{sign}\,\omega]$$
$$\times\sqrt{|\omega^2/c^2-k^2|}. \qquad (32)$$

$\eta(x)$ in Eq. (32) is the Heaviside function.

Since it is usually the case that $\omega_j\lambda\ll c$, the phase velocity of the generalized Swihart waves [see Eq. (23)] exceeds the speed of light only in the range of wavelengths much larger than the London length, when $k\lambda\ll1$. To describe long-wavelength ($k\lambda\ll1$) low-frequency ($\omega\lambda\ll c$) variations of the phase difference, instead of relation (30) we can use the approximate relation

$$Q(k,\omega,\lambda)\simeq\nu_s^2\tanh\!\left(\frac{L}{\lambda}\right)\!\left[1-2i\frac{\omega}{c}\lambda\sinh^{-1}\!\left(\frac{2L}{\lambda}\right)\right],\quad(33)$$

where $\omega\gg ck$. Expressions (31) and (33) allow us to express the right-hand side of Eq. (28) in the form

$$\hat{L}[\varphi(z,t)]=\nu_s^2\tanh\!\left(\frac{L}{\lambda}\right)\frac{\partial^2}{\partial z^2}\varphi(z,t)$$

$$+\left\{\frac{\lambda}{c}\cosh^2\!\left(\frac{L}{\lambda}\right)+\frac{\tau}{2}\tanh\!\left(\frac{L}{\lambda}\right)\right.$$

$$\left.\times\left[1+\frac{2L/\lambda}{\sinh(2L/\lambda)}\right]\right\}\nu_s^2\frac{\partial^3}{\partial t\,\partial z^2}\varphi(z,t).\quad(34)$$

Substituting expression (34) into Eq. (28) and replacing $\sin\varphi$ by its argument φ, it can be seen that for $\omega'\gg ck$ the dispersion law of the generalized Swihart waves has the form

$$\omega'^2=\omega_j^2+k^2\nu_s^2\tanh(L/\lambda).\qquad(35)$$

Function (35) joins well with function (23), which describes the relation between the frequency and the wave vector for $\omega\ll ck$. The decay decrement of fast waves has three parts

$$\gamma=\gamma_d+\gamma_n+\gamma_r.\qquad(36)$$

In Eq. (36) γ_d describes decay due to energy loss in the junction (25). The term

$$\gamma_n\equiv\frac{\tau}{4}k^2\nu_s^2\tanh\!\left(\frac{L}{\lambda}\right)\!\left[1+\frac{2L/\lambda}{\sinh(2L/\lambda)}\right]$$

describes energy losses due to scattering by normal electrons. Finally, γ_r describes decay of Swihart waves due to radiation to the vacuum

$$\gamma_r\equiv\frac{\lambda}{2c}(k\nu_s)^2\cosh^{-2}(L/\lambda).$$

In the case of thick electrodes the inequality $L\gg\lambda$ is fulfilled and the radiative decay decrement is exponentially small. On the contrary, for $L\ll\lambda$ losses to radiation are very large. In particular, for $L\ll\lambda$ in the limit under discussion here, the long-wavelength limit ($k\lambda\ll1$), the ratio γ_n/γ_r does not depend on the wave number

$$\frac{\gamma_n}{\gamma_r}=\frac{c\tau}{\lambda_{\text{eff}}}\equiv\frac{c}{\lambda\nu}\frac{L}{\lambda}\frac{n_n}{n_s}.\qquad(37)$$

For typical values of λ and ν: $\lambda\sim3\times10^{-5}$ cm and $\nu\sim10^{15}\,\text{s}^{-1}$, the ratio (37) is much less than unity if the temperature of the electrodes is substantially less than critical and $n_n\ll n_s$. Under these conditions, the radiative decay decrement exceeds the decay decrement on normal electrons. The quantity γ_r also exceeds γ_d if

$$k\lambda\gg\frac{c}{\nu_s}\left(\frac{4\pi\sigma\lambda}{\varepsilon c}\right)^{1/2},$$

which is fulfilled comparatively easily (see Ref. 21).

In the case of thick electrodes, when $L\gg\lambda$ and radiative losses are negligibly small, the decay decrement is governed by the normal electrons if

$$k\lambda\gg\frac{\lambda}{\nu_s}\left(\frac{8\pi\sigma}{\varepsilon\tau}\right)^{1/2}.$$

To complete the picture, note that Eq. (28) with kernels of the form (29)–(31) is solved not only by generalized Swihart waves, but also by surface electromagnetic waves in the sandwich. The dispersion law for these waves is determined by the zeros of the denominator of kernel (30), and decay, by the Fourier component of kernel (31). Since the phase velocity of the surface waves is less than the speed of light, to find their dispersion law and decay we have the equation

$$\frac{\omega^2}{c^2}\left(1+i\omega\tau\frac{\lambda}{2}\frac{\partial}{\partial\lambda}\right)\frac{\lambda^2}{\lambda(k)}\tanh\!\left[\frac{L}{\lambda(k)}\right]=\sqrt{c^2k^2-\omega^2}.$$

Hence we find a relation between the frequency ω' and the wave vector

$$\omega_s'=\frac{c}{\sqrt{2}\lambda^2}\lambda(k)\coth\!\left[\frac{L}{\lambda(k)}\right]$$

$$\times\left\{\sqrt{1+4k^2\frac{\lambda^4}{\lambda^2(k)}\tanh^2\!\left[\frac{L}{\lambda(k)}\right]}-1\right\}^{1/2}\qquad(38)$$

and the decay decrement due to absorption on the normal electrons

$$\gamma_s=\frac{\tau}{4}c^2\frac{\lambda^4(k)}{\lambda^6}\coth^2\!\left[\frac{L}{\lambda(k)}\right]$$

$$\times\left\{1+2k^2\lambda^2-\frac{2L}{\lambda(k)}\text{csch}\!\left[\frac{2L}{\lambda(k)}\right]\right\}$$

$$\times\left\{\frac{1+2k^2\lambda^4\lambda^{-2}(k)\tanh^2[L/\lambda(k)]}{\sqrt{1+4k^2\lambda^4\lambda^{-2}(k)\tanh^2[L/\lambda(k)]}}-1\right\}.$$

The interaction of a surface wave with a Swihart wave can be manifested at those wave numbers at which their phase velocities are similar. The dependences of the frequencies on the wave vector obtained above, (23), (35), and (38), hold far from the intersection points of the dispersion curves.

4. SLOW WAVES IN A FILM

Let us turn now to the problem of a Josephson junction in a thin film whose thickness D is much less than the London length. As is well known,[22] the effective penetration

depth of the field into the film in this case is $\lambda_e \equiv \lambda^2/D \gg \lambda$. Taking into account the presence of normal electrons in the film and using relation (10), it is necessary in our treatment of the electrodynamics of a film to replace λ_e by

$$\lambda_{e*} \equiv \lambda_e (1 - i\omega\tau)^{-1} \simeq \lambda_e (1 + i\omega\tau). \tag{39}$$

Next, repeating the derivation of the equation for the phase difference proposed in Refs. 8 and 9 and taking into account the redefinition of λ_e (39), we obtain an equation of the form (11)–(14) for $\varphi(z,t)$ in which the Fourier components of the kernels of the integral operator are given by the expressions

$$Q(k,\lambda_e) \equiv \nu_s^2 \frac{8}{\pi} \frac{\lambda}{D} F(2k\lambda_e),$$

$$Q_n(k,\lambda_e) \equiv \lambda_e \frac{\partial}{\partial\lambda_e} Q(k,\lambda_e), \tag{40}$$

and the function $F(x)$ has the form

$$F(x) \equiv \frac{1}{\sqrt{x^2-1}} \arctan \frac{\sqrt{x^2-1}}{1+|x|}, \quad |x| \geqslant 1;$$

$$F(x) \equiv \frac{1}{2\sqrt{1-x^2}} \ln \frac{1+\sqrt{1-x^2}}{|x|}, \quad |x| \leqslant 1.$$

When the spatial scale of variation of the phase difference L_φ is much less than λ_e, we can replace expressions (40) by the approximate expressions

$$Q(k,\lambda_e) = -Q_n(k,\lambda_e) = \frac{\nu_s^2}{k\lambda},$$

which allow us to represent the integral terms in Eq. (11) in the form (19). If, on the other hand, $L_\varphi \gg \lambda_e$, then

$$Q(k,\lambda_e) \simeq \frac{4}{\pi} \nu_s^2 \lambda_D \ln \frac{1}{|k\lambda_e|}, \quad Q_n(k,\lambda_e) \simeq \frac{4}{\pi} \nu_s^2 \frac{\lambda}{D},$$

and the operator $\hat{L}[\varphi]$ takes the form

$$\hat{L}[\varphi(z,t)] = \frac{4}{\pi} \nu_s^2 \frac{\lambda_e}{\lambda} \tau \frac{\partial^3}{\partial t \partial z^2} \varphi(z,t) + \frac{2}{\pi} \frac{\lambda_e}{\lambda} \nu_s^2 \frac{\partial^2}{\partial z^2}$$

$$\times \int_{-\infty}^{\infty} dz' \, \text{sign} \, (z-z')$$

$$\times \left[C + \ln \left(\frac{|z-z'|}{\lambda_e} \right) \right] \frac{\partial}{\partial z'} \varphi(z',t), \tag{41}$$

where $C \simeq 0.577$ is the Euler constant. As can be seen from Eqs. (11) and (41), the equation for the phase difference describing a Josephson junction in a film remains nonlocal in the coordinate also for $L_\varphi \gg \lambda_e$. At the same time, the first term on the right-hand side of Eq. (41), which is due to the influence of normal electrons, has local form, but in contrast to its analog for a junction in bulk superconductors, it contains an additional large factor $8\lambda_e/\pi\lambda \gg 1$, which is due to the increase in the effective penetration depth of the field into the film.

The dispersion relation for waves propagating along the Josephson junction in a film, as before, has the form (22) but

with new kernels Q and Q_n (40). This relation leads to the well-known dispersion law for the generalized Swihart waves[17]

$$\omega'^2 = \omega_j^2 + \frac{8}{\pi} \frac{\lambda_e}{\lambda} k^2 \nu_s^2 F(2k\lambda_e) \tag{42}$$

and a decay decrement of the form (24), where the contribution to the decay decrement due to the normal electrons is given by

$$\gamma_n = \frac{2}{\pi} \frac{\lambda_e}{\lambda} \tau \frac{k^2 \nu_s^2}{4k^2\lambda_e^2-1} \{8k^2\lambda_e^2 F(2k\lambda_e) - 1\}. \tag{43}$$

For $2k\lambda_e \sim 1$ the decay decrement associated with the normal electrons γ_n (43) exceeds γ_d (25) if $R \gg R_n \equiv \lambda_e/\sigma_n$, where the resistance per unit area, R_n, exceeds its value in bulk electrodes by a factor of $\lambda/D = \lambda_e/\lambda \gg 1$. As in a sandwich, in the long-wavelength region $(2k\lambda_e \ll 1)$ the decrement γ_n (43) decreases $\propto (2k\lambda_e)^2$, and for $2k\lambda_e \gg 1$ it increases $\propto 2k\lambda_e$. When $2k\lambda_e \gg 1$, the total decrement γ (24) is governed by the normal electrons for $R \gg R_n \sim 1/k\sigma_n \ll \lambda_e/\sigma_n$. In the short-wavelength region $(2k\lambda_e \gg 1)$ the ratio of the total decay decrement $\gamma \sim \gamma_n$ (43) to the frequency ω' (42) has the form [cf. Eq. (27)]

$$\frac{\gamma}{\omega'} = 2\pi\sigma_n \frac{\lambda\nu_s}{c^2} \sqrt{k\lambda} \equiv \frac{1}{2} \omega'\tau \ll 1. \tag{44}$$

It can be seen from Eq. (44) that the ratio of $\gamma \sim \gamma_n$ to the frequency ω' is small.

5. FAST WAVES IN A FILM

To consider fast waves in a Josephson junction in a thin film, we will use the approach of Ref. 21. Taking into account the material equation (6), we obtain an equation of the form (28), (29) for the phase difference of the wave functions. In this case, the Fourier components of the kernels of the integral operator $\hat{L}[\varphi]$ have the forms

$$Q(k_z,\omega,\lambda_e) \equiv 4 \frac{\lambda}{D} \nu_s^2 \int_{-\infty}^{\infty} \frac{dk_x}{2\pi} \frac{1}{k_x^2 + k_z^2}$$

$$\times \left[\frac{\psi}{1+2\psi\lambda_e} - \frac{\omega^2 k_x^2/k_z^2}{c^2\psi - 2\omega^2\lambda_e} \right],$$

$$Q_n(k_z,\omega,\lambda_e) \equiv \lambda_e \frac{\partial}{\partial\lambda_e} Q(k_z,\omega,\lambda_e),$$

$$\psi \equiv \psi(\sqrt{k_x^2 + k_z^2}, \omega), \tag{45}$$

and the integral over k in Eq. (29) must be replaced by an integral over k_z. As can be seen from the dispersion law (42), the phase velocity of the generalized Swihart waves can become comparable with the speed of light only for $k\lambda_e \ll 1$, when the frequency ω' is close to the Josephson frequency ω_j. This means that to examine fast waves with $\omega' \gg ck_z$ we can use a comparatively simple approximate expression for the Fourier components of the kernels

$$Q(k_z,\omega,\lambda_e)\simeq 4\frac{\lambda}{D}k_z^{-2}\nu_s^2\left[\frac{k_z^2}{\pi}\ln\frac{c}{|\omega|\lambda_e}\right.$$

$$\left.-\frac{\omega^2}{\pi c^2}\ln\frac{c}{|\omega|d}-i\frac{\omega|\omega|}{2c^2}\right],$$

$$Q_n(k_z,\omega,\lambda_e)\simeq -\frac{4}{\pi}\frac{\lambda}{D}\nu_s^2. \tag{46}$$

In this case the operator $\hat{L}[\varphi]$ has the form

$$\hat{L}[\varphi(z,t)]=\frac{4}{\pi}\tau\frac{\lambda_e}{\lambda}\nu_s^2\frac{\partial^3}{\partial t\,\partial z^2}\varphi(z,t)$$

$$+\frac{2}{\pi}\frac{\lambda}{D}\left(\frac{\nu_s}{c}\right)^2\frac{\partial}{\partial t}\text{P.V.}\int_{-\infty}^{\infty}\frac{dt'}{t'-t}\frac{\partial}{\partial t'}\varphi(z,t')$$

$$-\frac{4}{\pi}\frac{d}{\varepsilon D}\ln\frac{\lambda_e}{d}\frac{\partial^2}{\partial t^2}\varphi(z,t)+\frac{2}{\pi}\frac{\lambda}{D}\nu_s^2$$

$$\times\left(\frac{\partial^2}{\partial z^2}-\frac{1}{c^2}\frac{\partial^2}{\partial t^2}\right)\int_{-\infty}^{\infty}dt'\,\text{sign}\,(t-t')$$

$$\times\left[C+\ln\left(\frac{c|t-t'|}{\lambda_e}\right)\right]\frac{\partial}{\partial t'}\varphi(z,t'). \tag{47}$$

The first term in Eq. (47) is due to the influence of the normal electrons, the second term describes radiation of waves into the vacuum, and the last two terms in Eq. (47) describe, in particular, dispersion of fast generalized Swihart waves with allowance for their interaction with surface waves in the film. The influence of surface waves on the spectrum of the Swihart waves is also evident for $\omega'\ll ck_z$ and leads to a decrease in the square of the frequency (42) and in the decay decrement (25) by a factor of

$$\Lambda(k_z)\equiv 1+\frac{4}{\pi}\frac{d}{\varepsilon D}\ln\frac{1}{k_z d}.$$

For $\omega'\gg ck_z$, replacing $\sin\varphi$ by φ, we have from Eqs. (28), (29), and (46)

$$\omega'^2=\frac{1}{\Lambda}\left[\omega_j^2+\frac{4}{\pi}\frac{\lambda}{D}k_z^2\nu_s^2\ln\left(\frac{c}{\lambda_e\omega_j}\right)\right],$$

where $\Lambda\equiv\Lambda(\omega_j/c)$, and the expression for the decay decrement is of the form (36) with

$$\gamma_d=\beta/2\Lambda,$$

$$\gamma_r=\frac{\lambda}{\Lambda D}\left(\frac{\nu_s}{c}\right)^2\omega', \tag{48}$$

$$\gamma_n=\frac{2}{\pi\Lambda}\tau\frac{\lambda_e}{\lambda}\nu_s^2 k_z^2. \tag{49}$$

It can be seen from relations (48) and (49) that the ratio of the radiative decay decrement γ_r to the decay decrement on the normal electrons is much greater than unity if $\omega'\gg ck_z$

$$\frac{\gamma_r}{\gamma_n}=\frac{\pi}{2}\left(\frac{\omega'}{ck_z}\right)^2\frac{1}{\omega'\tau}>\frac{\pi}{2}\left(\frac{\omega'}{ck_z}\right)^2\gg 1.$$

As the phase velocity of the waves approaches the speed of light, γ_r falls off in proportion to $(\omega'^2-c^2k_z^2)\eta(\omega'^2-c^2k_z^2)$, and for large k_z it can be neglected. In this case, wave decay is governed by the quantity γ_n if the resistance of the junction is large enough: $R\gg(\pi/2)R_n/(\lambda_e k_z)^2$, where $R_n\equiv\lambda_e/\sigma_n$.

The parameter τ also governs the decay of surface waves, the dispersion relation for which follows from the condition that the denominator of the Fourier component of the kernel (45) vanish

$$2\frac{\lambda_e}{c}(1-i\omega\tau)\omega^2=\sqrt{c^2k^2-\omega^2},\quad k^2\equiv k_x^2+k_z^2. \tag{50}$$

Setting $\omega\equiv\omega'_s-i\gamma_s$, we find from relation (50) the frequency

$$\omega'^2_s=\frac{c^2}{8\lambda_e^2}(\sqrt{1+16k^2\lambda_e^2}-1) \tag{51}$$

and decay decrement

$$\gamma_s=\frac{\tau}{8}\frac{c^2}{\lambda_e^2}\left[\frac{1+8k^2\lambda_e^2}{\sqrt{1+16k^2\lambda_e^2}}-1\right]. \tag{52}$$

Within the applicability limits of relations (51) and (52), when $\omega'\tau\ll 1$, the ratio γ_s/ω'_s is much less than unity.

To summarize, the treatment presented here makes it possible to obtain information about the influence of the normal electrons in a superconductor on the decay of generalized Swihart waves. The influence of the normal electrons in this case is especially large for short waves. A comparison of various decay mechanisms allowed us to find the conditions in which emission of waves from a Josephson junction in a sandwich and from a junction in a thin film takes place efficiently.

APPENDIX A

In any treatment of linear waves in a sandwich it is sufficient to use Eqs. (11) and (28), in which the phase difference depends on one coordinate, z, which corresponds to choosing the direction of propagation of the wave to be along the z axis. At the same time, to examine nonlinear, two-dimensional vortex structures, it is necessary to utilize an equation for the phase differences that depends on the two coordinates in the junction plane. A two-dimensional equation for the phase difference that allows for ohmic energy losses in the Josephson junction, energy losses to radiation, and small dissipation by the normal electrons, and is nonlocal in time and space, has the form

$$\omega_j^2 \sin \varphi(\mathbf{r}_\parallel, t) + \beta \frac{\partial}{\partial t} \varphi(\mathbf{r}_\parallel, t) + \frac{\partial^2}{\partial t^2} \varphi(\mathbf{r}_\parallel, t)$$

$$= \frac{\partial^2}{\partial \mathbf{r}_\parallel^2} \int d\mathbf{r}_\parallel' \int_{-\infty}^{\infty} dt' Q(\mathbf{r}_\parallel - \mathbf{r}_\parallel', t - t') \varphi(\mathbf{r}_\parallel', t')$$

$$- \tau \frac{\partial^3}{\partial t \partial \mathbf{r}_\parallel^2} \int d\mathbf{r}_\parallel' \int_{-\infty}^{\infty} dt' Q_n(\mathbf{r}_\parallel - \mathbf{r}_\parallel',$$

$$\times t - t') \varphi(\mathbf{r}_\parallel', t').$$

Here $\mathbf{r}_\parallel$ is the two-dimensional position vector in the junction plane, and the kernels of the integral terms are given by

$$\left\{ \begin{array}{c} Q(\mathbf{r}_\parallel, t) \\ Q_n(\mathbf{r}_\parallel, t) \end{array} \right\} = \int \frac{d\mathbf{k}}{(2\pi)^2} \times \int_{-\infty}^{\infty} \frac{d\omega}{2\pi} \exp\left(-i\omega t + i\mathbf{k}\mathbf{r}_\parallel\right)$$

$$\times \left\{ \begin{array}{c} Q(\mathbf{k}, \omega, \lambda) \\ Q_n(\mathbf{k}, \omega, \lambda) \end{array} \right\},$$

which contain Fourier transforms of the kernels of the form (30)–(32). Here it is necessary to set $k = \sqrt{k_y^2 + k_z^2}$ in expressions (30)–(32), where k_y and k_z are the components of the wave vector in the junction plane.

*)E-mail: malish@sci.lebedev.ru

[1] J. C. Swihart, J. Appl. Phys. **32**, 461 (1961).
[2] K. L. Ngai, Phys. Rev. **182**, 555 (1969).
[3] A. Barone and G. Paterno, *Physics and Applications of the Josephson Effect* (John Wiley & Sons, New York, 1982).
[4] K. K. Likharev, *Introduction to the Dynamics of Josephson Junctions* [in Russian] (Nauka, Moscow, 1985).
[5] S. Sakai, A. V. Ustinov, H. Kohlstedt, A. Petraglia, and N. F. Pedersen, Phys. Rev. B **50**, 12,905 (1994).
[6] G. M. Lapir, K. K. Likharev, L. A. Maslova, and V. K. Semenov, Fiz. Niz. Temp. **1**, 1235, (1975) [Sov. J. Low Temp. Phys. **1**, 590 (1975).
[7] M. Yu. Kupriyanov, K. K. Likharev, and V. K. Semenov, Fiz. Niz. Temp. **2**, 706 (1976) [Sov. J. Low Temp. Phys. **2**, 346 (1976)].
[8] Yu. M. Ivanchenko and T. K. Soboleva, JETP Lett. **51**, 114 (1990).
[9] Yu. M. Ivanchenko and T. K. Soboleva, Phys. Lett. A **147**, 65 (1990).
[10] A. Gurevich, Phys. Rev. B **46**, 3187 (1992).
[11] Yu. M. Aliev, V. P. Silin, and S. A. Uryupin, Sverkhprovodimost: Fiz., Khim., Tekh. **5**, 228 (1992).
[12] Yu. M. Aliev and V. P. Silin, Zh. Éksp. Teor. Fiz. **104**, 2526 (1993) [JETP **77**, 142 (1993)].
[13] R. G. Mints and I. B. Snapiro, Physica A **200**, 426 (1993).
[14] R. G. Mints and I. B. Snapiro, Phys. Rev. B **49**, 6188 (1994).
[15] G. L. Alfimov and A. F. Popkov, Phys. Rev. B **52**, 4503 (1995).
[16] Yu. E. Kuzolev and A. I. Lomtev, Zh. Éksp. Teor. Fiz. **111**, 1803 (1997) [JETP **84**, 986 (1997)].
[17] R. G. Mints and I. B. Snapiro, Phys. Rev. B **51**, 3054 (1995).
[18] Yu. M. Aliev, K. N. Ovchinnikov, V. P. Silin, and S. A. Uryupin, Zh. Éksp. Teor. Fiz. **107**, 972 (1995) [JETP **80**, 551 (1995)].
[19] V. P. Silin and S. A. Uryupin, Zh. Éksp. Teor. Fiz. **108**, 2163 (1995) [JETP **81**, 1179 (1995)].
[20] R. G. Mints, J. Low Temp. Phys. **106**, Nos. 3/4, 183 (1997).
[21] K. N. Ovchinnikov, V. P. Silin, and S. A. Uryupin, Fiz. Met. Metalloved. **83**, No. 5, 14 (1997).
[22] J. Pearl, Appl. Phys. Lett. **5**, No. 4, 65 (1964).
[23] Zh. D. Genchev and V. I. Vas'kivs'kiĭ, Zh. Éksp. Teor. Fiz. **113**, 955 (1998) [JETP **86**, 521 (1998)].
[24] B. I. Ivlev and N. B. Kopnin, Adv. Phys. **33**, No. 1, 47 (1984).
[25] A. A. Abrikosov, *Fundamentals of the Theory of Metals* (North-Holland, Amsterdam, 1988).

Translated by Paul F. Schippnick

Electron and phonon effects in superconducting tunnel detectors of x-radiation

V. A. Andrianov,[*] V. P. Gor'kov, M. G. Kozin, I. L. Romashkina, S. A. Sergeev, and
V. S. Shpinel'

*Scientific-Research Institute of Nuclear Physics, M. V. Lomonosov Moscow State University,
119899 Moscow, Russia*

P. N. Dmitriev and V. P. Koshelets

Institute of Radio Engineering, Russian Academy of Sciences, 103907 Moscow, Russia
(Submitted December 11, 1998)
Fiz. Tverd. Tela (St. Petersburg) **41**, 1168–1175 (July 1999)

Nb/Al/AlO$_x$/Nb superconducting tunnel junctions were investigated in the role of x-ray
detectors. Amplitude spectra of pulses arising upon irradiation of tunnel junctions of different
sizes by ^{55}Mn x-radiation were recorded at a temperature $T = 1.4$ K. We also analyzed
the temporal shape of the pulses. We considered the influence of diffuse motion of nonequilibrium
quasiparticles, the inverse tunneling effect, and exchange of 2Δ phonons between electrodes,
on the characteristics of the tunnel detectors. It is shown that phonon processes can
bring about changes in the amplitude, duration, and polarity of the signal. © *1999 American
Institute of Physics.* [S1063-7834(99)00807-2]

Superconducting tunnel junctions (STJ's) are promising devices for detectors of x-ray and ultraviolet radiation possessing high energy resolution and a low threshold of operation.[1] The record characteristics of such devices are linked with the substantially larger number of current carriers (quasiparticles) arising in the superconductor upon the absorption of a quantum of radiation as compared to conventional semiconductors. At present, prototype detectors have already been constructed possessing an energy resolution of 29 eV at the x-ray line of 6 keV energy (Ref. 2) in the statistical limit of 4 eV, along with detectors having a threshold of operation around 1 eV (Ref. 4).

The energy resolution that it is possible to achieve in STJ detectors is limited by various loss mechanisms of the nonequilibrium quasiparticles. The most important are diffusive escape of quasiparticles from the tunneling region and their loss on the boundaries of the STJ,[5] capture of quasiparticles in the region with decreased width of the superconducting gap, and also quasiparticle recombination and escape of 2Δ phonons. The reverse tunneling effect can also have a substantial influence on the operation of STJ detectors, by which we mean the possibility of the quasiparticles to tunnel multiply from one electrode to the other (Gray effect, Ref. 6). This makes it possible to amplify the output signal of the detector, with simultaneous degradation of the energy resolution, however.[7]

At present, questions regarding diffusion of quasiparticles, reverse tunneling, and exchange of 2Δ phonons have been investigated for superconducting tunnel junctions having the simple structure Nb/Al/AlO$_x$/Nb. In this construction, the additional trap-layer used to increase the effective tunneling probability[8] was not deposited near the tunneling barrier, which allowed us to study the indicated processes under simpler conditions.

1. EXPERIMENTAL TECHNIQUE

The superconducting tunnel junctions were fabricated by magnetron sputtering. A diagram of a superconducting tunnel junction is shown in Fig. 1. A buffer layer of amorphous Al$_2$O$_3$ 90 nm thick was first sputtered onto a silicon substrate, followed by the three-layer structure Nb/Al/AlO$_x$/Nb with layer thicknesses 240/8/2/120 nm. Five STJ's having different areas of the tunnel barriers were formed on one chip: 400, 400, 1800, 6400, and 20,000 μm^2. The tunnel junctions had rhombic shape in the plane of the layers with ratio of the diagonals 1 : 2 and 1 : 4. The dimensions of the upper electrode coincided with the dimensions of the tunnel barrier. The dimensions of the lower electrode exceeded the dimensions of the tunnel barrier by 5 μm along the short diagonal, forming a belt, or ''skirt,'' of width $\approx 2~\mu$m not in direct contact with the barrier. The current-lead strips had a width of 6 μm near the STJ. The normal resistivity of the tunnel barrier was equal to $2 \times 10^{-5}\,\Omega \cdot$cm^2.

Current–voltage characteristics (CVC's) of the superconducting tunnel junctions were measured in the temperature range $1.4 - 4.2$ K using the four-probe method. Superconducting tunnel junctions with areas of 400, 800, and 6400 μm^2, which we will denote as samples A, B, and C from here on, had CVC's of the same shape and differed only in the scale of the currents. STJ's with a barrier area of 20,000 μm^2 had too high a level of leakage currents and will not be considered further. We determined the values of the superconducting gap from the CVC's: for the lower (base) electrode $\Delta_b = 1.33(2)$ meV, and for the upper (counter) electrode $\Delta_c = 1.48(2)$ meV. The smaller value of Δ_b is due to the influence of the Al layer adjacent to the tunnel barrier.

Spectroscopic measurements were taken at the temperature $T = 1.4$ K under irradiation of the STJ's with Mn
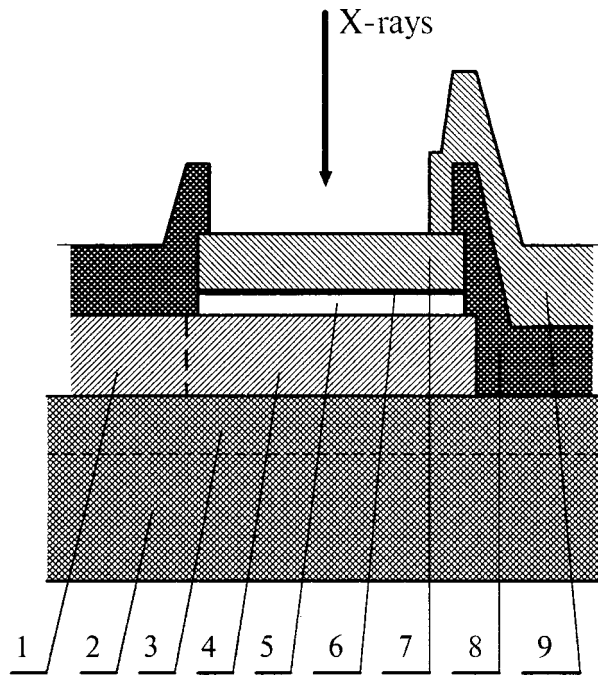
1064   Phys. Solid State **41** (7), July 1999

Andrianov *et al.*

FIG. 1. Schematic sectional view of a tunnel detector. *1* — Current lead to the lower electrode; *2* — silicon substrate (0.5 mm); *3* — amorphous Al_2O_3 layer (90 nm); *4* — lower Nb electrode (240 nm); *5* — aluminum layer (8 nm); *6* — AlO_x tunnel barrier (2 nm); *7* — upper Nb electrode (120 nm); *8* — insulating layer of SiO; *9* — current lead to the upper electrode.

5.89 keV $K\alpha$ (88%) and 6.49 keV $K\beta$ (12%) x-radiation accompanying radioactive decay of ^{55}Fe. To suppress the Josephson current, we applied a magnetic field with field strength up to 200 Oe, lying in the plane of the tunnel barrier and oriented along the short diagonal of the rhombus. In these measurements we used a charge-sensitive preamplifier, kept at room temperature and connected to the STJ by means of a coaxial cable. To measure the amplitudes of the generated pulses, we used a multichannel analyzer. Simultaneous with recording of the amplitude spectra, we encoded and wrote on disk the temporal shape of the pulses at the output of the preamplifier. Thus, each measurement produced an amplitude spectrum and a dataset of roughly 200 pulse files. Some details of the experiment are given in Ref. 9.

2. AMPLITUDE SPECTRA

Figure 2 shows typical spectra of pulses from samples *A*, *B*, and *C*. The spectra are superpositions of contributions corresponding to absorption of photons in the counter and base electrodes of the STJ. The narrow peak in the small-amplitude region corresponds to the counter electrode. The wide distribution in the large-amplitude region, which has the form of a trapezium, corresponds to absorption in the base electrode. A small ''step'' is observed on the right side of the spectra, which arises thanks to absorption of the $K\beta$ line in the base electrode. The spectra of all the samples have a similar form and differ only in the scale of the collected charge.

As a characteristic of the spectra we can use the maximum charge Q_m corresponding to absorption of the more intense $K\alpha$ line. Table I lists values of Q_m for both elec-

trodes, corresponding to spectra measured with the bias voltage $V_b = 0.75(1)$ mV. For other values of the bias voltage V_b the structure of the spectra remained the same and the maximum charge Q_m varied in a similar way as in Ref. 10.

Table I also shows exponential-growth times of the pulses of the lower electrode τ_b, which are equivalent to the effective lifetimes of the nonequilibrium quasiparticles in this electrode. The values of τ_b were obtained by processing averaged pulses of maximum amplitude. The pulses of the counter electrode have shorter duration; however, their shape is not described by exponential growth (see the following section). It follows from the data of Table I that increasing the geometrical dimensions of the STJ leads to an increase in the collected charges Q_m and quasiparticle lifetimes τ_b.

To first order, the shape of the pulses can be described by the diffusion model.[5] This model takes account of diffusive motion of the nonequilibrium quasiparticles in the STJ electrodes, their loss in the bulk and at the boundaries of the electrodes, and escape of quasiparticles from the tunneling region to the peripheral regions (''skirts''). Since the linear dimensions of the electrodes are significantly larger than their thickness, the problem can be treated as two-dimensional. Propagation of the cloud of nonequilibrium quasiparticles formed upon absorption of one quantum of radiation at the point with coordinates $\mathbf{r} = (x_0, y_0)$ is described by

$$\frac{\partial n}{\partial t} = D\left(\frac{\partial^2 n}{\partial x^2} + \frac{\partial^2 n}{\partial y^2}\right) - \gamma n, \tag{1}$$

where n is the two-dimensional quasiparticle density, t is time, x and y are the spatial coordinates, D is the diffusion coefficient, and γ is the effective rate of quasiparticle losses. $\gamma = \tau_T^{-1} + \tau_L^{-1}$, where τ_T and τ_L are the quasiparticle tunneling and loss times in the bulk of the electrode, respectively.

The initial and boundary conditions have the following form:

$$n(x, y, t=0) = N_0 \delta(x - x_0) \delta(y - y_0),$$

$$D\left.\frac{\partial n}{\partial N}\right|_b = -\alpha n, \tag{2}$$

where N_0 is the initial number of quasiparticles formed upon absorption of a quantum with energy 6 keV ($N_0 = 2.4 \times 10^6$, Ref. 3), $(\partial n / \partial N)|_b$ is the derivative along the normal to the electrode boundary, and α is the probability of loss of a quasiparticle in the region of the boundary.

The collected charge is given by the integral

$$Q(x_0, y_0) = e\tau_T^{-1} \int_0^\infty dt \int_A n(x, y, t) dx\, dy, \tag{3}$$

where e is the electron charge, and the integral is taken over the area of the tunnel barrier A.

In the given model, broadening of the spectra is caused by the dependence of the collected charge on the coordinates of the point at which a quantum of radiation is absorbed. The maximum charges Q_m correspond to absorption of a quantum in the center of the electrode. Results of a calculation for
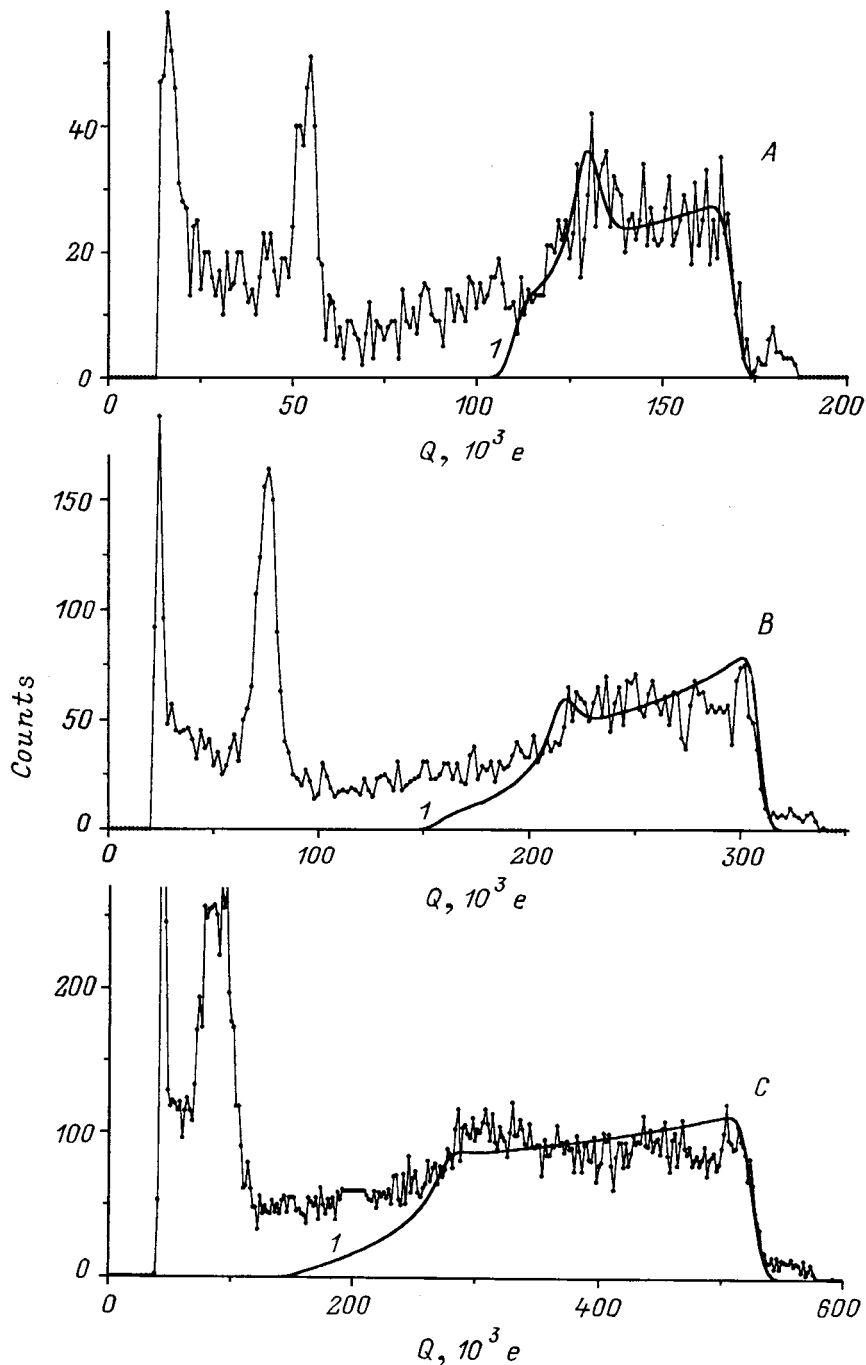
FIG. 2. Spectra of pulses arising upon irradiation of samples *A*, *B*, and *C* by a ^{55}Fe source (bias voltage at the detector $V_b = 0.75$ mV). *1* — calculation using the diffusion model.

the base electrode are depicted in Fig. 2, based on analytical expressions obtained in Ref. 5 for square-shaped electrodes, (curve *1*). It can be seen that the diffusion model provides a satisfactory description of the experimental data. The obtained values of the diffusion coefficient *D* are listed in the table. The distinguishing difference of the spectra of the counter electrode has to do with the shorter diffusion length in it, due to the short quasiparticle lifetime in this electrode, and also with the absence of a ''skirt.''

At the same time, the simple diffusion model does not give a self-consistent quantitative description of the spectra of the counter and base electrodes, and of spectra of STJ's of different dimensions.

3. REVERSE TUNNELING

An important mechanism affecting the operation of a STJ detector is reverse tunneling, i.e., multiple tunneling of nonequilibrium quasiparticles from one electrode to the other.[7,11] The collected charge in this case is given by the expression

$$Q_1 = \frac{eN_0\left(\dfrac{\tau_{d1}}{\tau_{T1}}\right)\left(1 + \dfrac{\tau_{d2}}{\tau_{T2}}\right)}{1 - \left(\dfrac{\tau_{d1}}{\tau_{T1}}\right)\left(\dfrac{\tau_{d2}}{\tau_{T2}}\right)}, \tag{4}$$

where τ_{T1} and τ_{T2} are the tunneling times, and τ_{d1} and τ_{d2}

TABLE I. Parameters of STJ detectors.

Sample	A	B	C
S_T, μm^2	400	1800	6400
Q_m^b, $10^4 e$	16.8(2)	30.2(4)	51.8(4)
Q_m^c, $10^4 e$	5.5(1)	7.6(2)	9.6(2)
τ_b, μs	0.45(1)	0.78(1)	1.36(2)
D, cm^2/s	1.0	2.6	3.7
τ_{c1}, μs	0.15(2)	0.20(2)	0.33(4)
τ_{c2}, μs	0.45(3)	0.74(3)	1.35(6)
f, %	45(3)	61(1)	71(4)
K, %	15	15	13

Notes. S_T — Area of tunnel barrier; Q_m^b and Q_m^c — maximum collected charges for base and counter electrodes; D — quasiparticle diffusion coefficient; τ_b, τ_{c1}, and τ_{c2} — time constants of pulses of base and counter electrodes; f — contribution of reverse tunneling to the signal of the counter electrode; K — fraction of quasiparticles arising in the base electrode upon absorption of a photon in the counter electrode.

are the effective quasiparticle lifetimes. The subscript 1 pertains to the electrode in which the quantum was absorbed, and the subscript 2, to the opposite electrode.

It follows from expression (4) that the contribution of reverse tunneling is governed by the ratio τ_{d2}/τ_{T2}. These quantities can be estimated from the values of the maximum charges Q_m: $\tau_d/\tau_T \approx Q_m/eN_0$. For the STJ's investigated in the present work, these ratios are substantially less than 1. In addition, the effective quasiparticle lifetimes in the counter and base electrodes are significantly different. Under these conditions, the time dependence of the collected charge is given by the expression

$$Q_1(t) \cong eN_0\left(\frac{\tau_{d1}}{\tau_{T1}}\right)[(1-f)(1-\exp(-\tau_{d1}^{-1}t))$$
$$+f(1-\exp(-\tau_{d2}^{-1}t))], \qquad (5)$$

where $f = \tau_{d2}/\tau_{T2}$.

It follows from relation (5) that, under conditions of reverse tunneling, the leading edge of the pulse should be described by a superposition of two exponentials with growth times roughly equal to the effective quasiparticle lifetimes in the STJ electrodes. For pulses of the counter electrode, the contribution of reverse tunneling f should be ≈ 7, 13, and 22 % for samples A, B, and C, respectively. For pulses of the base electrode, reverse tunneling should not exceed 3 %.

To obtain data on the effects of reverse tunneling, the shape of the recorded pulses was analyzed using expression (5). To enhance accuracy, pulses belonging to the counter and base electrodes were selected from the experimental set of pulses and averaged. For the base electrode we selected pulses that had maximum amplitude, which corresponded to absorption of quanta in the center of the electrode. For the counter electrode, in addition to the amplitude criterion we selected for a shorter duration of the leading edge in comparison with the pulses of the base electrode.

We fit the pulses by the method of least squares. Toward this end, expression (5) was modified to take account of discharge currents through the resistance of the tunnel junction and load, and also to take account of the effect on the signal of the differentiating circuit of the preamplifier

($\tau_{dif} = 22 \, \mu s$). We varied the following parameters: the amplitude of the pulse Q, the times τ_1 and τ_2, and the contribution of reverse tunneling f. To describe the shape of the pulses of the base electrode, it turned out to be sufficient to use an expression with one growth time τ_b (i.e., we set the parameter $f=0$). This result is in line with the above estimates of the small contribution of reverse tunneling to the signals of the base electrode.

Processing of the pulses in the counter electrode showed that, for a correct description of the shape, it is necessary to take account of the contribution of reverse tunneling. Figure 3(a) displays a pulse of sample B, obtained with a bias voltage $V_b = 0.74 \, mV$. The solid curve depicts the result of fitting, the dashed curves are contributions with different growth times. The obtained values of the times τ_{c1} and τ_{c2} and the parameter f are given in the table. Note that the time τ_{c2} coincides within the limits of error with the time τ_b, obtained by processing the pulses of the base electrode. The time τ_{c1}, corresponding to the effective quasiparticle lifetime in the counter electrode, is substantially shorter, in line with the form of the amplitude spectrum in the diffusion model.

However, the values of the parameter f describing the contribution of tunneling from the base electrode significantly exceed the values calculated in the reverse tunneling model (5) and vary from 45 % to 71 % as the area of the tunnel barrier is increased. This implies that, along with quasiparticle tunneling, there is another channel leading to redistribution of nonequilibrium quasiparticles between the STJ electrodes. Without going into specific mechanisms, the collected charge in the counter electrode upon absorption of one quantum in the counter electrode can be described in simplest form by

$$Q_c \cong eN_0\left[(1-K)\left(\frac{\tau_{c1}}{\tau_{T1}}\right) + K\left(\frac{\tau_b}{\tau_{T2}}\right)\right], \qquad (6)$$

where K is the fraction of quasiparticles belonging to the base electrode. Values of K were calculated for all of the processed pulses based on the obtained values of the parameter f ($K = fQ_m^c/Q_m^b$). It turned out that the number of quasiparticles formed in the base electrode upon absorption of one quantum in the counter electrode is essentially independent of the dimensions of the STJ and other parameters and is equal roughly to 14 %.

4. EXCHANGE OF 2Δ PHONONS

An additional process leading to redistribution of nonequilibrium quasiparticles between electrodes appears to be exchange of 2Δ phonons. It is well known that a dynamical equilibrium between quasiparticles and 2Δ phonons is maintained in superconductors[12,13]

$$\tau_R^{-1} n = 2\tau_{pb}^{-1} p \quad \text{and} \quad \tau_R^{-1} = Rn. \qquad (7)$$

Here n and p are the quasiparticle density and the 2Δ-phonon density, respectively, τ_{pb} is the pair-breaking time, τ_R is the quasiparticle recombination time, and R is the recombination constant. For Nb $\tau_{pb} = 4.17 \, ps$ and $R = 2 \times 10^{-9} \, cm^3 s^{-1}$ (Ref. 14).
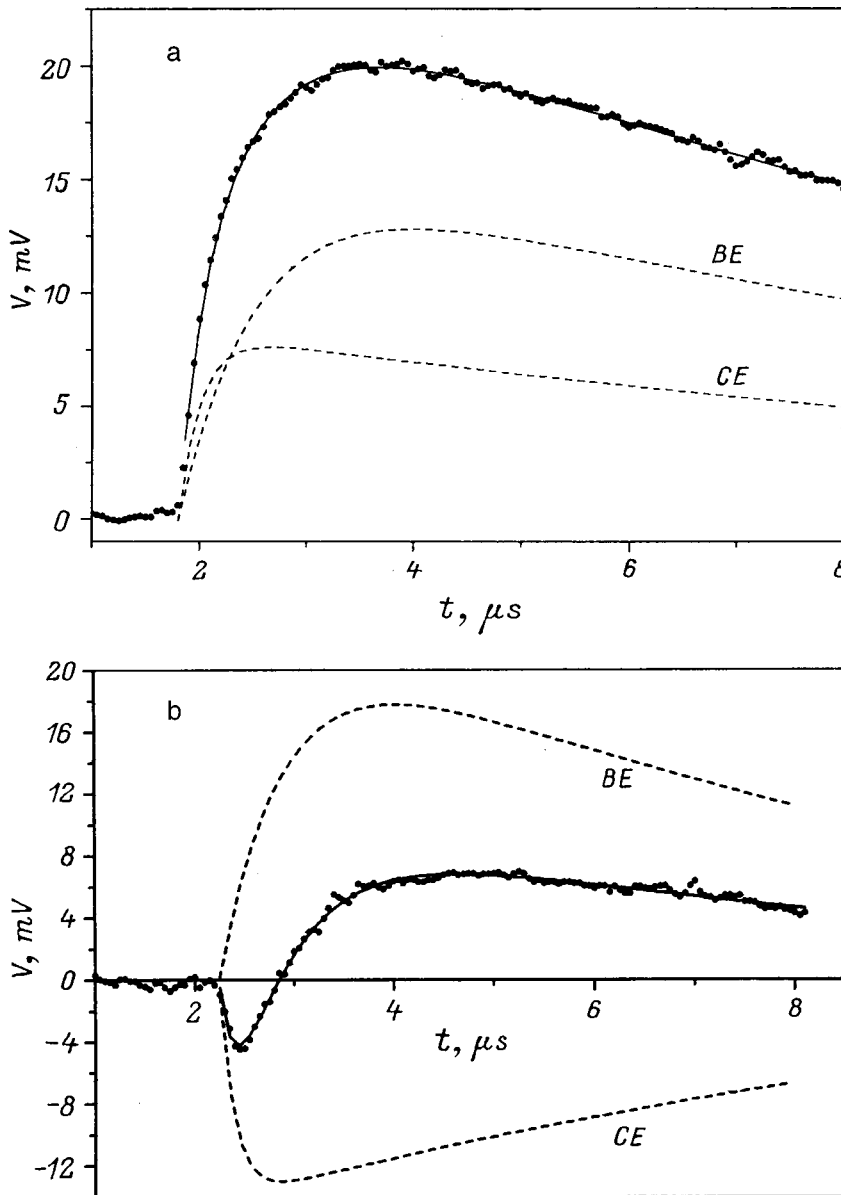
FIG. 3. Shape of the pulses arising upon absorption of radiation in the upper electrode. V_b, mV: *a* — 0.75, *b* — 0.09. Solid curves — result of fitting, taking reverse tunneling into account according to Eq. (5). Dashed curves plot the contributions of the lower (*BE*) and upper (*CE*) electrodes.

In thermal equilibrium at $T = 1.4\,\mathrm{K}$ $\tau_R \approx 1\,\mu s$. In this case the number of 2Δ phonons is less than the number of quasiparticles—by six orders of magnitude, and they cannot have a noticeable effect on the operation of a STJ detector. However, upon absorption of an x quantum the density of the formed quasiparticles significantly exceeds their thermal density; therefore, recombination proceeds primarily by non-equilibrium carriers, i.e., self-recombination occurs. Estimates show that the recombination rate in this case grows by several orders of magnitude, which according to relations (7) results in an increase in the 2Δ-phonon density.

At low temperatures ($T \ll T_C$), scattering processes with decrease of energy are attenuated for 2Δ phonons; therefore, the main loss mechanism for 2Δ phonons is their escape to the other electrode and/or substrate. The characteristic time of this process is given by the expression[15]

$$\tau_{p,tr}^{-1} = \frac{\eta c}{4d}, \tag{8}$$

where d is the thickness of the electrode, η is the transparency of the interface, and c is the speed of sound (in Nb $c_L = 5.1 \times 10^5\,\mathrm{s}^{-1}$ and $c_T = 2.8 \times 10^5\,\mathrm{s}^{-1}$).

For the case under consideration $\tau_{p,tr} \approx 1$. When the density of 2Δ phonons is increased, this mechanism can provide a noticeable redistribution of the excitation energy between the two electrodes. Note that after relocating to the second electrode the 2Δ phonons, by virtue of relation (7), are almost completely converted into quasiparticles. A diagram of the exchange of quasiparticles and 2Δ phonons in a STJ detector is shown in Fig. 4.

Let us estimate the 2Δ-phonon flux from the counter electrode to the base electrode for the superconducting tunnel junctions investigated in the present work. We assume that the nonequilibrium quasiparticle density in the counter electrode, $n(\mathbf{r},t)$, can be represented as the solution of the diffusion equation
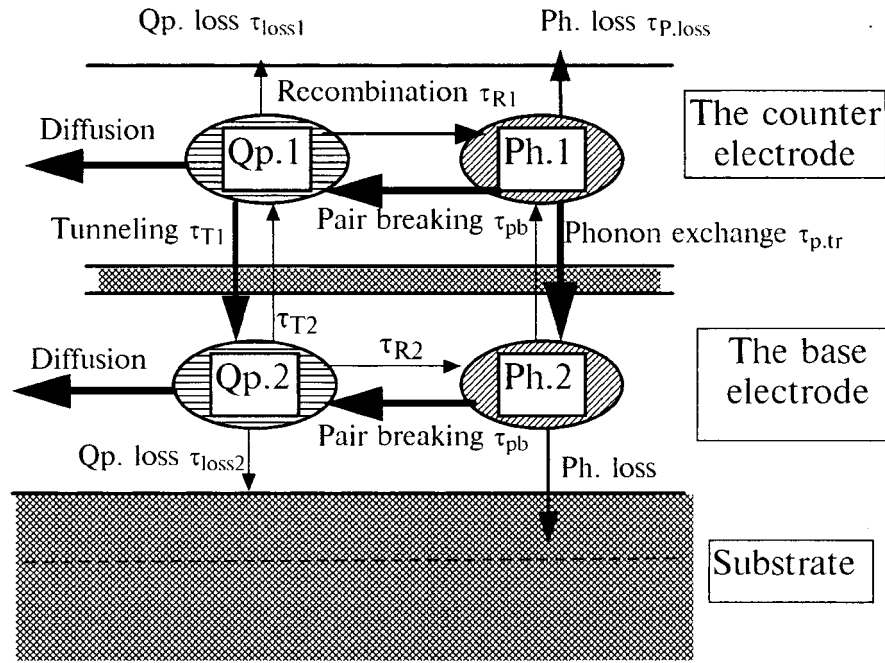
FIG. 4. Diagram of electron and phonon processes in a STJ detector upon the absorption of radiation in the upper electrode: diffusion, tunneling, recombination, and other losses of quasiparticles (Qp.); breaking of Cooper pairs by phonons (pair breaking) , phonon exchange between electrodes (Ph. exchange), loss of phonons to the substrate. Characteristic times and the role of these processes for each of the electrodes are discussed in text. Thickness of arrows reflects the intensity of the processes.

$$n(\mathbf{r},t)=\frac{N_0}{4\pi Dt}\exp\left[-\frac{(\mathbf{r}-\mathbf{r}_0)^2}{4Dt}-\frac{t}{\tau_{c1}}\right]. \qquad (9)$$

Since expression (9) falls off rapidly with time, we will neglect boundary effects and we will consider the problem in an infinite plane. According to relations (7)–(9), the 2Δ-phonon flux from the counter electrode to the base electrode is equal to

$$I_{2\Delta}=\frac{N_0^2 R}{16\pi dDt}\left(\frac{\tau_{pb}}{\tau_{p,tr}}\right)\exp\left(-\frac{2t}{\tau_{c1}}\right). \qquad (10)$$

Expression (10) diverges as $t\to 0$; therefore to obtain the total number of relocated 2Δ phonons, $P_{2\Delta}$, the integration over time should start from the time t_0 at which quasi-equilibrium is established in the system after absorption of a quantum. We finally obtain

$$P_{2\Delta}=\frac{N_0^2 R\tau_{pb}c\,\eta}{64\pi d^2 D}\left[\ln\left(\frac{\tau_{c1}}{2t_0}\right)-0.57\right]. \qquad (11)$$

If we adopt the values $t_0=2$ ns (Ref. 3), $D\approx 1$ cm·s^{-1}, and $\tau_{c1}\approx 0.2\ \mu$s, then using Eq. (11) we can estimate the value of the coefficient η for which the 2Δ phonon flux stimulates the formation in the base electrode of KN_0 quasiparticles. These estimates give a value around 0.1 for η, which is entirely acceptable taking into account the multilayer structure of the tunnel barrier.

The influence of phonon exchange can explain a series of experimental facts regarding the operation of STJ detectors which have not yet received a consistent interpretation. In particular, it is well known that in asymmetric STJ's with electrodes having different superconducting gaps ($\Delta_1\neq\Delta_2$), anomalous polarity signals should be observed.[9,16,17] These signals arise upon the absorption of quanta of radiation in the electrode with the larger gap for $V_b<(\Delta_1-\Delta_2)/e$ thanks to a competition between the electron and hole tunneling chan-

nels. However, in Refs. 10 and 18 anomalous polarity pulses were not observed. In the present study, the appearance of anomalous pulses of negative polarity could be expected for the counter electrode ($\Delta_c>\Delta_b$). However, instead of this, for small bias voltages we observed anomalous bipolar pulses with a short negative excursion [see Fig. 3(b)].

According to the model of exchange of 2Δ phonons, the pulses in the counter electrode are formed by the sum of tunnel currents from both STJ electrodes. In this case, the contribution of the counter electrode is around 40 %, and the contribution of the base electrode, due to phonon exchange, is roughly 60 %. For small bias voltages $V_b<(\Delta_1-\Delta_2)/e$ the tunneling current from the base electrode has the usual positive polarity and the tunneling current from the counter electrode should have negative polarity. In conjunction with the different duration of the currents from the counter and base electrodes this should lead to the formation of a bipolar output signal.

In Fig. 3(b) the solid curve depicts the result of fitting expression (5) to the experimental pulse assuming a negative contribution of the counter electrode. The variable parameters—the effective lifetimes τ_1 and τ_2 and the contribution of reverse tunneling f—agree with the data obtained by processing pulses observed in large fields. Apparently, the absence of anomalous-polarity pulses in Refs. 10 and 18 can also be explained by compensation of signals from different electrodes, brought about by phonon exchange.

Phonon processes can also have an effect on signals of the base electrode. In the investigated samples, escape of phonons to the counter electrode upon absorption of a quantum of radiation in the base electrode gives a small contribution to the signal as a consequence of smallness of the ratio τ_{d2}/τ_{T2} for the counter electrode. Escape of 2Δ phonons to the substrate requires a separate treatment. First of all it should be noted that the lifetime of the 2Δ phonons

in an insulating substrate in contrast to a superconductor is larger than the typical duration of the pulsed tunneling current ($\tau_d \approx 1 \mu$s). If the substrate is a high-purity single-crystal wafer (e.g., silicon or sapphire), then the 2Δ phonons can propagate ballistically across the wafer to the opposite face.[19] In this case, since the thickness of the substrate is usually much greater than the linear dimensions of the electrode, the back flux of 2Δ phonons is negligibly small, and escape of 2Δ phonons to the substrate is one of the channels of quasiparticle loss. The efficiency of this channel is governed by the acoustic transparency of the boundary.

In the tunnel junctions investigated in the present work, we deposited a layer of amorphous Al_2O_3 of thickness 90 nm between the silicon substrate and the niobium electrode. An analogous buffer layer is usually present in the designs of STJ detectors of other authors. If the acoustic transparency of the buffer layer–substrate boundary is small, the 2Δ phonons will be localized in the buffer layer, whose thickness is comparable with the thickness of the electrodes. In this case, the back flux of phonons from the buffer layer to the electrode becomes important. This flux can have a considerable effect on the effective lifetime and diffusion of quasiparticles in the base electrode.

The study presented here shows that upon absorption of a quantum of x radiation in an electrode of a tunnel detector an electron–phonon nonequilibrium state is formed, which then not only propagates throughout the volume of the electrode, but also redistributes between the two electrodes of the detector.

Diffuse propagation of nonequilibrium quasiparticles throughout the volume of an electrode and their loss at the boundaries of the electrode are a source of inhomogeneous broadening of the spectra. In the investigated superconducting tunnel junctions this mechanism governs the shape of the spectra of the base electrodes and is described by the two-dimensional diffusion model. Loss of quasiparticles on the boundaries is due to capture to traps which are defect regions with reduced value of the order parameter. Inhomogeneous broadening of the spectra can also have a phonon origin if the escape probability for 2Δ phonons is not identical over the surface of the electrode.

Analysis of the temporal shape of the pulses shows that redistribution of nonequilibrium quasiparticles between the electrodes of the detector proceeds via two channels: by tunneling of quasiparticles and by exchange of 2Δ phonons. In the investigated superconducting tunnel junctions the phonon channel is dominant. We have shown that exchange of 2Δ phonons between the electrodes, and also between the electrodes and the substrate, can alter the amplitude, duration,

and also the polarity of the observed signals. The intensity of the phonon processes depends on the acoustic transparency of the interfaces and, consequently, on the choice of materials and technology. These issues must be taken into account in the development of new designs of STJ detectors.

*)E-mail: andrva@srdlan.npi.msu.su

[1] N. E. Booth and D. J. Goldie, Supercond. Sci. Technol. **9**, 493 (1996).

[2] C. A. Mears, S. E. Labov, M. Frank, M. A. Lindeman, L. J. Hiller, H. Netel, and A. T. Barfknecht, Nucl. Instrum. Methods Phys. Res. A **370**, 53 (1996).

[3] N. Rando, A. Peacock, A. van Dordrecht, C. Foden, R. Engelhardt, B. G. Taylor, P. Gare, J. Lumley, and C. Pereira, Nucl. Instrum. Methods Phys. Res. A **313**, 173 (1992).

[4] P. Verhoeve, N. Rando, A. Peacock, A. van Dordrecht, M. Bavdaz, J. Verveer, D. J. Goldie, M. Richter, and G. Ulm, *Proceedings of the Seventh International Workshop on Low-Temperature Detectors (LTD-7)*, edited by S. Cooper (Munich, 1997), p. 97.

[5] O. J. Luiten, M. L. van den Berg, J. Gomez Rivas, M. P. Bruijn, F. B. Kiewiet, and P. A. J. de Korte, *Proceedings of the Seventh International Workshop on Low-Temperature Detectors (LTD-7)*, edited by S. Cooper (Munich, 1997), p. 25.

[6] K. E. Gray, Appl. Phys. Lett. **32**, 392 (1978).

[7] D. J. Goldie, P. L. Brink, C. Patel, N. E. Booth, and G. L. Salmon, Appl. Phys. Lett. **64**, 3169 (1994).

[8] N. E. Booth, Appl. Phys. Lett. **50**, 293 (1987).

[9] V. A. Andrianov, M. G. Kozin, S. A. Sergeev, V. S. Shpinel', V. P. Koshelets, and I. V. Abramova, Fiz. Niz. Temp. **23**, 1187 (1997) [Low Temp. Phys. **23**, 889 (1997)].

[10] E. P. Houwman, A. A. Golubov, J. G. Gijsbertsen, J. Flokstra, H. Rogalla, J. B. le Grand, M. P. Bruijn, and P. A. J. de Korte, J. Low Temp. Phys. **93**, 677 (1993).

[11] O. J. Luiten, H. L. van Lieshout, F. A. Michels, P. Valko, M. P. Bruijn, F. Kiewiet, P. A. J. de Korte, D. J. Adelerhof, A. W. Hamster, C. G. S. Brons, and J. Flokstra, Nucl. Instrum. Methods Phys. Res. A **370**, 72 (1996).

[12] J. B. le Grand, Ph. D. Thesis, Utrecht, The Netherlands (1994).

[13] V. F. Elesin and Yu. V. Kopaev, Usp. Fiz. Nauk **133**, 259 (1981) [Sov. Phys. Usp. **24**, 116 (1981)].

[14] S. B. Kaplan, C. C. Chi, D. N. Langenberg, J. J. Chang, S. Jafarey, and D. J. Scalapino, Phys. Rev. B **14**, 4854 (1976).

[15] S. B. Kaplan, J. Low Temp. Phys. **37**, 343 (1979).

[16] M. Gutsche, P. Hettl, J. Jochum, B. Kemmather, and H. Kraus, Nucl. Instrum. Methods Phys. Res. A **370**, 91 (1996).

[17] S. Lemke, J. Martin, J. B. le Grand, R. Gross, R. P. Huebener, P. Videler, N. Rando, T. Peacock, P. Verhoeve, and F. A. Jansen, Nucl. Instrum. Methods Phys. Res. A **370**, 119 (1996).

[18] J. B. le Grand, M. P. Bruijn, C. Patel, P. A. J. de Korte, S. Lemke, R. Gross, and R. P. Huebener, Physica C **279**, 85 (1997).

[19] F. Probst, Th. Peterreins, F. V. Feilitzsch, and H. Kraus, Nucl. Instrum. Methods Phys. Res. A **288**, 125 (1990).

Translated by Paul F. Schippnick

SEMICONDUCTORS. DIELECTRICS

A new bound-exciton emission band in ZnSe crystals and multiplasmon optical transitions

V. S. Vavilov, M. V. Chukichev, and R. R. Rezvanov

M. V. Lomonosov Moscow State University, 119899 Moscow, Russia

A. A. Klyukanov,*) K. D. Sushkevich, and A. Z. Avavdekh

Moldavian State University, 277009 Kishinev, Moldava

We have investigated cathodoluminescence both in unannealed ZnSe crystals and in crystals annealed in a Bi melt at a temperature of 1200 K for 120 h with subsequent quenching. In the wavelength range $450-480$ nm we have detected a new line series $I_i^s - nLO - mPl$ consisting of the bound-exciton emission line I_i^s with wavelength $\lambda = 455.9$ nm and its plasmon and LO-phonon echoes $I_i^s - LO$ ($\lambda_1 = 461.3$ nm), $I_i^s - 2LO$ ($\lambda_2 = 466.8$ nm), $I_i^s - 3LO$ ($\lambda_3 = 472.4$ nm), and $I_i^s - 4LO$ ($\lambda_4 = 478.3$ nm). We have determined the mean number of emitted LO phonons $N_{LO} = 2.2 \pm 0.1$ per photon. It is shown that the observed finer structure of the band may be due to multiphonon optical transitions. At low plasma densities ($\omega_p \ll \omega_{LO}$) the Coulomb interaction causes broadening of the $I_i^s - nLO$ series. In samples with denser plasma, in which the condition $\omega_p \lesssim \omega_{LO}$ is met, multiplasmon satellites of the series $I_i^s - nLO - mPl$ are observed. Theoretical calculations of the shape of the emission band agree with experiment. © *1999 American Institute of Physics.* [S1063-7834(99)00907-7]

Multiphoton optical transitions involving the participation of low-frequency plasmons created by vibrations of the plasma of band charge carriers have been studied under radiative recombination of electrons and holes in the direct-band semiconductor compounds ZnSe, CdS, and ZnTe by the authors of Refs. 1–8. Photo- and cathodoluminescence (CL) spectroscopic studies of free–free, free–bound, and bound–bound recombination transitions with emission of photons, phonons, and plasmons were carried out over a wide temperature range $(4.2-355$ K) at different levels of excitation ($j = 0.01 - 10$ A/cm^2) with different delay times $(0.1-10$ ms).[1-8] New wide composite emission bands, including around ten plasmon echoes, were detected at high levels of excitation in the intervals of lattice temperatures $40-70$ K (ZnSe) and $30-120$ K (ZnTe),[2-4] corresponding to the maximum lifetime of the plasmons and the minimum mobility of the charge carriers. It was shown that the multiplasmon fine structure of the bands is due to recombination of free band electrons and holes strongly interacting with the plasmons.

Multiplasmon optical transitions, showing up in the fine structure and in broadening of the bands, enable one to explain many key features of the emission spectra of II–VI semiconductor compounds. It has been shown that not only the high-temperature series of green luminescence of CdS, which is due to free–bound transitions, but also recombination of electrons and holes at donor–acceptor pairs (DAPs) can be accompanied by emission and absorption of several plasmons.[6] The measured distances between the lines of the

multiplasmon low-temperature series varied from 2 to 10 meV. This is an experimental proof of the participation in the optical transitions of plasmons whose energy $\hbar \omega_p$ depends on the plasma density and, therefore, varies with the level of excitation and from sample to sample.[6]

A striking manifestation of multiplasmon radiative transitions during recombination of bound excitons is the red cathodoluminescence band in ZnTe (Ref. 7).

The present paper examines multiplasmon transitions that were detected in the cathodoluminescence spectra of ZnSe crystals, both unannealed and annealed in a Bi melt with subsequent quenching. As the starting material, we used ZnSe crystals grown from the vapor phase. The samples were annealed at 1200 K for 120 h. Cooling (quenching) to room temperature took place outside the furnace by submerging the ampoule in water.

Cathodoluminescence was excited at a sample temperature of 4.2 K by an electron beam with energy 40 keV, pulse duration 0.4 μs and a pulse repetition rate of 200 Hz. The emission was analyzed with a DFS-12 monochromator in the wavelength range $0.4-0.8$ μm.

The edge cathodoluminescence of both the unannealed and the annealed samples consists of a series of lines in the exciton region of the spectrum. The most intense line is the EPK line I_i^d (445.8 nm), produced by an exciton localized at a neutral acceptor—a zinc vacancy (V_{Zn}). In Refs. 9–12 it was suggested that the I_i^d line is formed by two acceptors of different nature—V_{Zn} and/or copper substituting for zinc
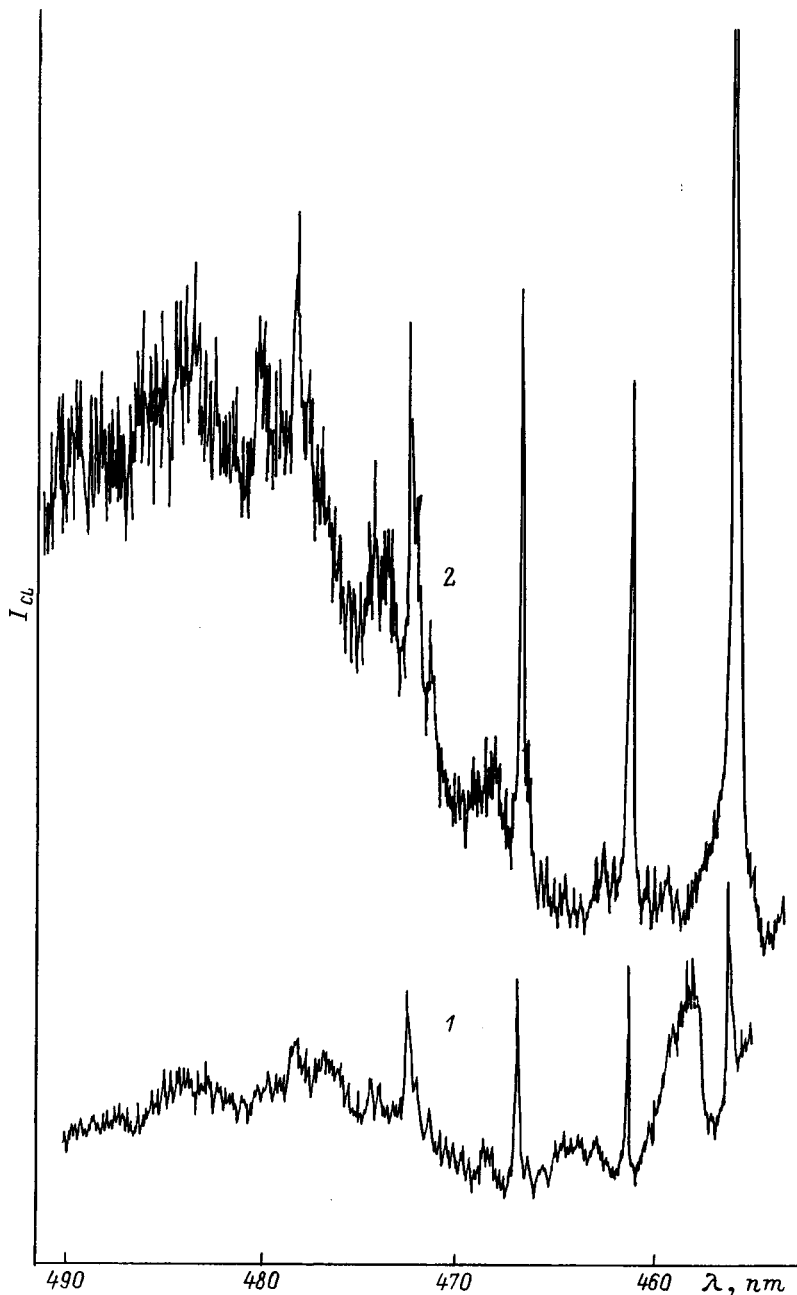
FIG. 1. Cathodoluminescence spectra of ZnSe crystals at $T = 4.2$ K: *1* — sample annealed in a Bi melt with subsequent quenching; *2* — starting sample.

(Cu_{Zn}). For undoped samples, I_i^d is due to zinc vacancies. For copper-doped samples, defects based on Cu_{Zn} are responsible for I_i^d.

In the wavelength region $450-480$ nm at low levels of excitation, we detected a new emission band $I_i^s - nLO - mPl$ (Fig. 1), consisting of the emission line of a bound exciton I_i^s with wavelength $\lambda = 455.9$ nm and its plasmon and LO-phonon echoes $I_i^s - LO$ ($\lambda_1 = 461.3$ nm), $I_i^s - 2LO$ ($\lambda_2 = 466.8$ nm), $I_i^s - 3LO$ ($\lambda_3 = 472.4$ nm), and $I_i^s - 4LO$ ($\lambda_4 = 478.3$ nm). Besides the LO-phonon echoes, we also observed a finer band structure, due to multiplasmon transitions (curves *1* and *2* in Fig. 1, and curve *1* in Fig. 2).

Note that in the samples annealed in a Bi melt, a Bi melt with zinc admixture, and a Zn melt and slowly cooled (by turning off the furnace), the $I_i^s - nLO - mPl$ band was not observed[13] (here n is the number of emitted longitudinal op-

tical phonons, m is the number of plasmons). This points to a substantial role of zinc vacancies in the formation of the centers responsible for emission of the $I_i^s - nLO - mPl$ series.

We will begin our analysis of the emission spectra with a consideration of the emission series of the bound excitons including the I_i^d line and its LO-phonon echoes, for which the radiative recombination rate R_λ can be represented in the form

$$R_\lambda = R_0 \sum_n (N_{LO}^n / n!) \gamma_n / [(x+n)^2 + \gamma_n^2]. \qquad (1)$$

Here R_0 is a constant, $x = (\omega - \omega_0)/\omega_{LO}$, ω is the phonon frequency, ω_0 is the frequency corresponding to the maximum of the I_i^d line, ω_{LO} is the frequency of the LO
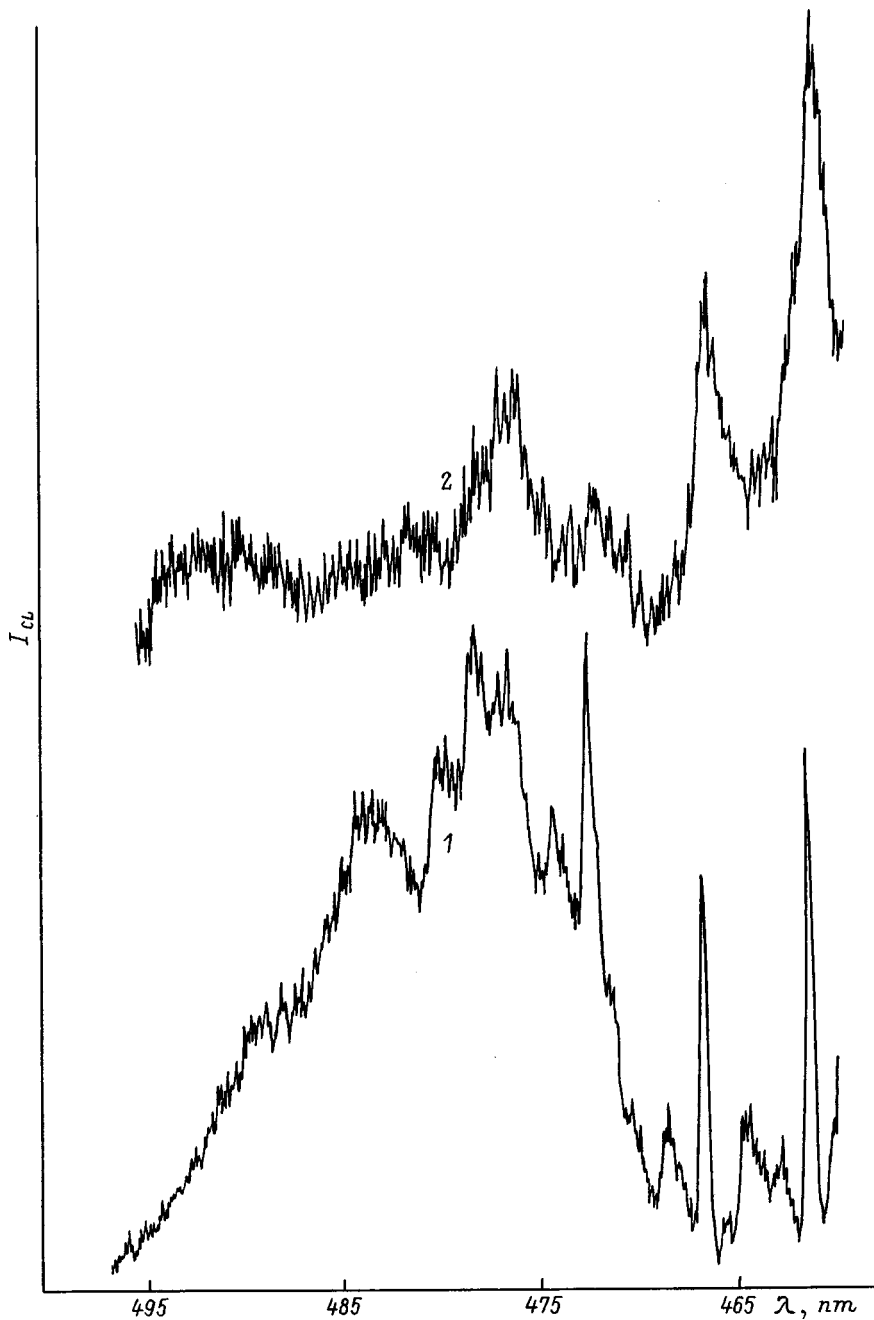
FIG. 2. Cathodoluminescence spectra with different densities of the equilibrium plasma: *1* — dense plasma $\omega_p \lesssim \omega_{LO}$, in which plasmon echoes are observed; *2* — low-density plasma $\omega_p \ll \omega_{LO}$.

phonons, N_{LO} is the number of LO phonons emitted per photon, $2\gamma_n$ is the half-width of the nth phonon echo in units of ω_{LO}. For a series of lines of identical half-width, Eq. (1) corresponds to a Poisson distribution for R_λ at the maxima of the LO-phonon echoes $I_i^d - nLO$. According to our results, $N_{LO} = 0.20 \pm 0.01$ if we define N_{LO} as the ratio of intensities of R_n at the maxima of the non-phonon peak and the single-phonon echo ($R_1^{max}/R_0^{max} = N_{LO}\gamma_0/\gamma_1$). If, on the other hand, we define N_{LO} as the ratio ($R_2^{max}/R_1^{max}) = (1/2)N_{LO}(\gamma_1/\gamma_2)$, then it turns out that $N_{LO} > 0.2$ and it varies from sample to sample within the limits $0.2-0.5$. Yet more striking results obtain if we define N_{LO} in terms of the third and second phonon echoes. According to the cathodoluminescence spectra shown in Fig. 1, $N_{LO} \cong 4$ for sample 1 and $N_{LO} \cong 1$ for sample 2. In addition, for the first sample the half-width of $I_i^d - 2LO$ is greater than the half-width of $I_i^d - 3LO$ (if we

take the line at the wavelength $\lambda = 461.3$ nm to be $I_i^d - 3LO$). As can be seen from Fig. 1 (curve *1*), the $I_i^d - 2LO$ line has a shoulder on its short-wavelength side. All these features are easily sorted out if we note that in the region of the second LO-phonon echo of the I_i^d line there are (superimposed) two $I_i^d - 2LO$ lines and a new non-phonon line I_i^s. For the second sample, this is mainly the line $I_i^d - 2LO$ at $\lambda = 456.0$ nm whereas for the first sample the intensity of the $I_i^d - 2LO$ line is two times greater than the intensity of I_i^s. For the series I_i^s the interaction of a bound exciton with phonons turns out to be stronger than for the series I_i^d. According to the results presented in Fig. 1, for the series of the new line I_i^s and its LO-phonon echoes we find that $N_{LO} = 2.2 \pm 0.1$.

The radiative recombination rate R_λ (Ref. 8) is defined

by a generating function, which in the two-level approxima-tion for a bound exciton has the form

$$I(t) = \exp\left\{ \sum_k (\nu_\kappa/\pi\hbar) \left| \rho_h(\kappa) - \rho_e(\kappa) \right|^2 \right.$$

$$\left. \times \int_0^\infty \mathrm{Im}\{\varepsilon_\infty/\varepsilon^*(\kappa,\omega)\} f(t,\omega)/\omega^2 d\omega. \right\}. \quad (2)$$

The notation here is the same as in Ref. 8. The frequen-cies of the elementary excitations with which the recombin-ing electron and hole interact are determined by the zeros of the dielectric function $\varepsilon(\kappa,\omega)$. At low densities of the plasma of band charge carriers ($\omega_p \ll \omega_{LO}$) these excitations are plasmons ($\kappa < 1/\lambda_0$, where λ_0 is the screening length) and LO phonons. For hydrogenlike centers

$$\rho_{e,h}(\kappa) = \langle e,h | \exp(i\boldsymbol{\kappa} \cdot \mathbf{r}_{e,h}) | e,h \rangle$$

$$= \{1 + (\kappa a_{e,h}/2)^2\}^{-2}. \quad (3)$$

It can be seen from Eq. (2) that, in the case when the radii of the electron and hole states a_e and a_h are of the same order ($a_e \cong a_h$, $\rho_h(\kappa) \cong \rho_e(\kappa)$), the interaction with plasmons and phonons is weak. Thus, we can judge the structure of the center from the cathodoluminescence spectra. A strong inter-action with LO phonons and plasmons is characteristic of centers that strongly bind one of the carriers of an $e-h$ pair, localizing it within the limits of a unit cell, and create a Coulomb field for the second charge carrier. In this case, the region of motion of the second carrier in this field encom-passes hundreds of lattice constants. An I_i^s line and its $LO-$phonon and plasmon echoes, whose shape can be ap-proximated by the expression

$$R_\lambda = \sum_{n,m} (N_{LO}^n/n!)(N_p^m/m!) \gamma_{n,m}/\{(\omega+n+am)^2 + \gamma_{n,m}^2\}, \quad (4)$$

are associated with a center of this type.

Here $a = \omega_p/\omega_{LO}$. Figure 3 displays results of calcula-tions of cathodoluminescence spectra for various values of the mean numbers of LO phonons N_{LO} and plasmons N_p emitted during recombination, various ratios of ω_p and ω_{LO}, and various half-widths of the lines making up the emission band.

Numerical calculations of single-phonon and single-plasmon satellites can be performed using the results of Refs. 1–8 and the generating function $I(t)$ (2) with $\varepsilon(\kappa,\omega)$ in the random phase approximation. It turns out that the half-width of the single-plasmon satellite is greater, as a rule, than that of the single-phonon satellite. This has to do with the large dispersion of the plasmons and with Landau decay. Thus, it is necessary to surmise that the inequality $\gamma_{n,m} > \gamma_{n,0}$ ($m = 1,2, \ldots$) is satisfied and that the quantity $\gamma_{n,m}$ grows with growth of the number of emitted plasmons m. For small plasma densities ($\omega_p \ll \omega_{LO}$) the multiplasmon structure is not resolved. Processes involving emission of several plas-mons lead to a broadening of the I_i^s line and its LO-phonon echoes (curve *3* in Fig. 3), in agreement with experiment (curve *2* in Fig. 2). If, on the other hand, $\omega_p \lesssim \omega_{LO}$, then the plasmon structure can be observed (curves *1* and *2* in Fig. 1,
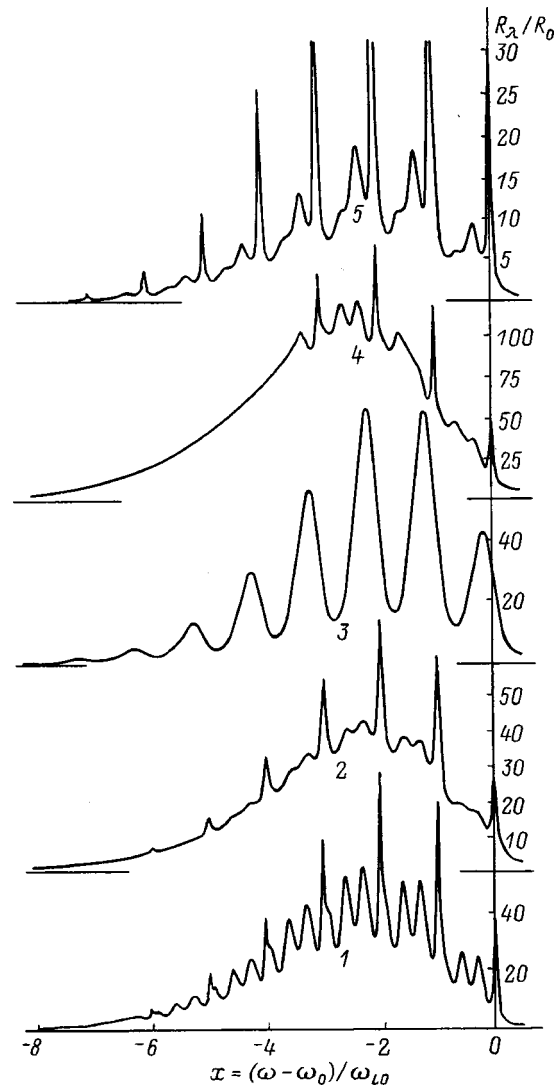

FIG. 3. Shape of the $I_i^s - nLO - mPl$ band R_λ ($a = \omega_p/\omega_{LO}$, b, γ_1, γ_2, N_{LO}, N_p, x) at different plasma densities and different satellite half-widths $\gamma_{n,0} = \gamma_1$, $\gamma_{n,m} = \gamma_2(1+mb)$ ($m=1,2,\ldots$): *1* — R_λ (0.3, 0, 0.03, 0.1, 2, 2, x); *2* — R_λ (0.3, 0, 0.05, 0.2, 2, 2, x); *3* — R_λ (0.1, 0, 0.1, 0.1, 2, 2, x); *4* — R_λ (0.3, 0.35, 0.03, 0.1, 2, 3, x); *5* — R_λ (0.3, 0.35, 0.03, 0.1, 2, 1, x).

and curve *1* in Fig. 2). The numerical calculations (Fig. 3) and experimental cathodoluminescence spectra are found to be in satisfactory agreement, which allows us to conclude that plasmons participate in the emission of the new series of bound-exciton lines $I_i^s - nLO - mPl$ in ZnSe crystals to-gether with emission from donor–acceptor pairs[14] in this re-gion of the spectrum.

Noting that LO-phonon echoes are usually observed during recombination of excitons bound to acceptors, it is natural to suppose that the center responsible for the appear-ance of the I_i^s line is a zinc-vacancy based acceptor. The I_i^s line is observed only in samples subjected to quenching; therefore, it may be concluded that the given acceptor center exists at high temperatures and is frozen in during quench-ing. Upon slow cooling, on the other hand, this center is destroyed and new associates based on it are formed. Such an acceptor center is possibly a complex consisting of two zinc vacancies and one selenium vacancy.

*)E-mail: klukanov@cinf.usm.md

[1] A. A. Klyukanov, Fiz. Tverd. Tela (Leningrad) **29**, 1529 (1987) [Sov. Phys. Solid State **29**, 876 (1987)].

[2] V. S. Vavilov, A. A. Klyukanov, É. A. Senokosov, L. É. Chibotaru, and M. V. Chukichev, Fiz. Tverd. Tela (Leningrad) **30**, 614 (1988) [Sov. Phys. Solid State **30**, 355 (1988)].

[3] A. A. Klyukanov, E. A. Senokosov, and L. E. Chibotaru, Phys. Status Solidi B **155**, 295 (1989).

[4] V. S. Vavilov, A. A. Klyukanov, N. M. Pavlenko, Sabri Dzhasin Mukhammed, É. A. Senokosov, V. G. Stoĭkova, and M. V. Chukichev, Fiz. Tverd. Tela (Leningrad) **31**, *10*, 132 (1989) [Sov. Phys. Solid State **31**, 1726 (1989)].

[5] V. S. Vavilov, A. A. Klyukanov, É. A. Senokosov, L. É. Chibotaru, and M. V. Chukichev, Fiz. Tverd. Tela (Leningrad) **33**, *1*, 63 (1991) [Sov. Phys. Solid State **33**, 35 (1991)].

[6] V. S. Vavilov, A. A. Klyukanov, M. V. Chukichev, O. M. Shapoval, A. Z. Avavdekh, and R. R. Rezvanov, Fiz. Tekh. Poluprovodn. **28**, 2113 (1994) [Semiconductors **28**, 1162 (1994)].

[7] V. S. Vavilov, A. A. Klyukanov, K. D. Sushkevich, M. V. Chukichev, A. Z. Avavdekh, and R. R. Rezvanov, Fiz. Tverd. Tela (St. Petersburg) **37**, *2*, 312 (1995) [Phys. Solid State **37**, 170 (1995)].

[8] V. S. Vavilov, A. A. Klyukanov, K. D. Sushkevich, M. V. Chukichev, R. R. Rezvanov, and S. K. Sushkevich, Fiz. Tverd. Tela (St. Petersburg) **39**, 1526 (1997) [Phys. Solid State **39**, 1358 (1997)].

[9] Shi Min Huang, J. Nozne, and J. C. Igaki, Jpn. J. Appl. Phys. **22**, 1420 (1983).

[10] H. Roppiseher, J. Jacob, and B. V. Novikov, Phys. Status Solidi A **27**, 123 (1975).

[11] P. J. Dean, A. D. Ditt, M. S. Skolnick, P. J. Wright, and J. Blockayne, J. Cryst. Growth **59**, 301 (1982).

[12] P. J. Dean, D. C. Herbert, C. J. Werkhoven, B. J. Fitzpatrick, and R. N. Bhorgava, Phys. Rev. B **23**, 4888 (1981).

[13] A. V. Simashkevich and K. D. Sushkevich, Izv. Akad. Nauk Respubliki Moldaviya, Ser. Fiz. Tekh., **2**(*8*), 28 (1992).

[14] P. J. Dean, Phys. Status Solidi A **81**, 625 (1984).

Translated by Paul F. Schippnick

Effect of IR illumination on photocurrent spectra in CdS crystals

A. S. Batyrev and R. A. Bisengaliev

Kalmyk State University, 358000 Élista, Russia

É. D. Batyrev, B. V. Novikov, and V. S. Anbushinov

Institute of Physics, St. Petersburg State University, 198904 St. Petersburg, Russia
(Submitted October 27, 1998)
Fiz. Tverd. Tela (St. Petersburg) **41**, 1181–1184 (July 1999)

Low-temperature near-band-edge photoconductivity (PC) spectra of CdS crystals were studied as a function of IR illumination intensity in the PC quenching interval. The photocurrent quenching by IR light of the PC response profile has been investigated. An analysis of these relationships permitted establishing a direct connection between the *r* photoconductivity centers and the near-band-edge structure of the spectrum. The effect of ''pinning'' of majority-carrier lifetime on the semiconductor surface has been discovered and interpreted. It is proposed that surface-acceptor states in CdS crystals play the part of surface photoconductivity centers. © 1999 American Institute of Physics. [S1063-7834(99)01007-2]

Additional illumination by IR light in the photoconductivity (PC) quenching region was reported to affect dramatically the low-temperature photocurrent response in CdS crystals.[1–6] However the experimental data and their interpretation presented in Refs. 1–5 exhibit substantial discrepancies. This has stimulated our investigation of the changes in low-temperature ($T=77$ K) near-band-edge spectra of steady-state PC excitation in CdS crystals which are induced by IR illumination in the PC quenching region at different intensity levels.

The PC response measurements were performed on a laboratory setup based on an MDR-2 high-collecting power monochromator. The spectra were recorded automatically with a KSP-4 recorder. The samples were pure (i.e. undoped) CdS plates with the hexagonal **C** axis in the sample surface plane. Cooling down to $T=77$ K took place by immersing the sample into an optical cryostat filled with liquid nitrogen. The IR light for PC quenching was isolated from the continuum of a halogen filament lamp with an IKS-1 color filter. The IR intensity was varied either by controlling properly the lamp power voltage or by diaphragming the objective lens focusing the IR light on the sample at a fixed lamp voltage. The spectra were measured in the $\mathbf{E} \perp \mathbf{C}$ incident (probing) polarization ($\mathbf{E}$ is the light-wave electric vector). The spectral resolution was not worse than 8 Å in all experiments.

1. EXPERIMENTAL RESULTS

Figure 1 shows PC spectra of CdS crystals with a fine (excitonic) structure (FS) of type I (*a*) and type II (*b*) (notation of Ref. 6) obtained without (curves *1*) and with (curves *2* and *3*) additional IR illumination at various intensity levels. As seen from Fig. 1, IR illumination affects PC spectra of the CdS crystals studied in the following way.

(1) IR illumination produces photocurrent quenching throughout the photoconductivity spectral range studied. The quenching increases with increasing IR intensity.

(2) The IR-induced quenching is spectrally selective; namely, the quenching is particularly strong around the so-called additional maxima AM_1 and AM_2 [Ref. 5] (I_1 and I_X, respectively, in the notation of Ref. 2).

(3) In crystals with a peak-shaped FS (type I, *a*), the IR quenching of the photocurrent is accompanied by noticeable changes in the spectrum, namely, by an enhancement of the excitonic and a weakening of the additional photocurrent maxima. For high enough IR intensities, one observes a spectrum with a very sharp peak-shaped FS, with practically no additional maxima visible (curve *3*).

(4) In crystals with a dip-shaped FS (type II, *b*), as the IR illumination intensity increases, the prevailing photocurrent quenching in the region of additional maxima is accompanied by FS transformation to the peak type. The general character of the spectrum also changes under IR illumination to acquire features characteristic of crystals with peak-shaped FS (curve *3*).

(5) The magnitude of IR-induced photocurrent quenching differs substantially (by orders of magnitude) in crystals having different FS types. In crystals exhibiting dip-shaped FS, IR illumination of a sufficiently high intensity may suppress the photocurrent at a fixed wavelength near the fundamental absorption edge by three to four orders of magnitude, and in crystals with peak-shaped FS, by one to 1.5 orders of magnitude in the same conditions.

To complete the picture of the observed effect of IR-induced photocurrent quenching in CdS crystals, one should add to items 3 and 4 the following remarks.

(i) Most of the crystals with type-I FS exhibit a clearly pronounced trend to saturation of the IR quenching effect with increasing IR intensity;

(ii) In crystals with type-II FS, one observes a direct correlation between the relative intensity of the additional maxima in the spectrum and the IR intensity required to change the FS type; indeed, some of the dip-FS crystals re-
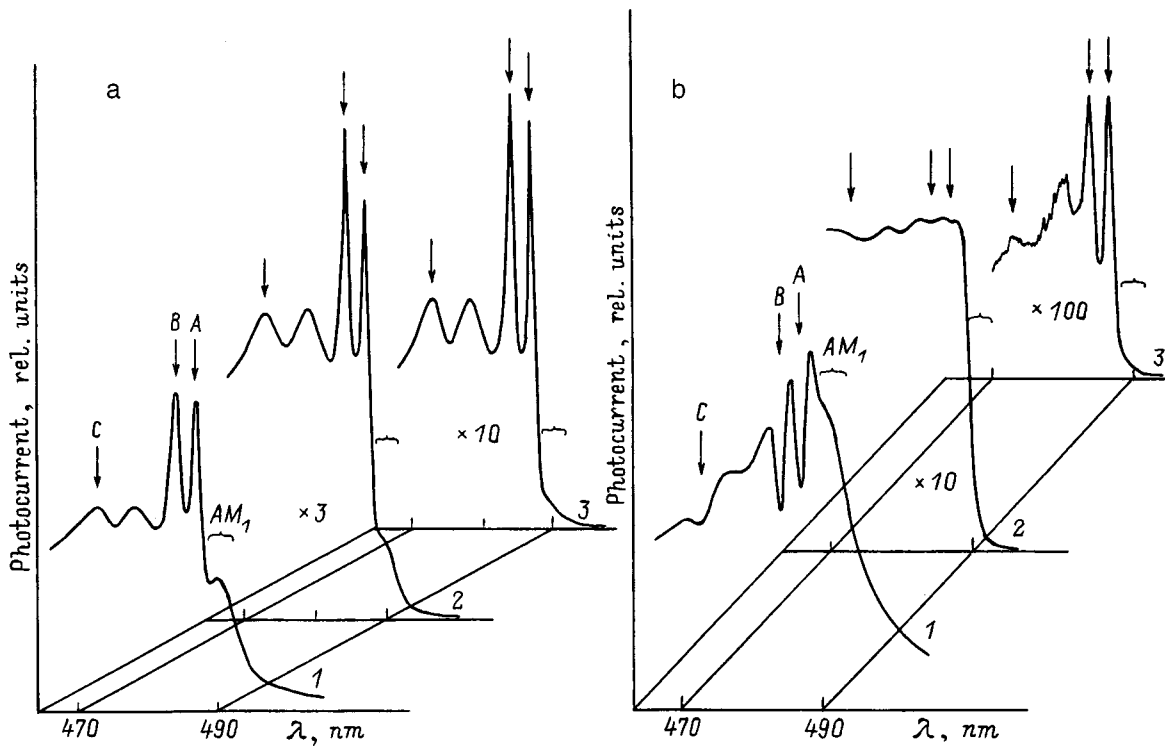
FIG. 1. PC spectra of CdS crystals with (a) type-I FS and (b) type-II FS without (curves *1*) and with (curves *2* and *3*) additional IR illumination at different intensity levels ($T = 77$ K, $\mathbf{E} \perp C$). *a,b*: *1* — $I = I_0$, *2* — $I = 9I_0$, *3* — $I = 90I_0$; I_0 is the IR intensity.

versed their FS type only at extremely high IR illumination intensities.

Figure 2 presents typical peak- and dip-type spectra usually observed at low ($T \cong 77$ K) temperatures in most of the ~ 150 CdS crystals studied (see also Fig. 1 and Refs. 2 and 7).

Note that the relationships of the IR-induced changes in CdS PC spectra established in our experiments (see also Refs. 4 and 5), while exhibiting substantial discrepancies in some aspects, correlate largely with the data obtained in similar studies[1-3]. It should also be pointed out that a number of essential features in the phenomenon of IR-induced photocurrent quenching in CdS have not been mentioned, to our knowledge, in any of the work we are aware of, including the most comprehensive publication of Böer and coworkers.[2]

2. DISCUSSION OF THE EXPERIMENTAL DATA

IR-induced quenching of photocurrent in CdS crystals is a well-studied phenomenon (see, e.g., Ref. 6). It is associated with the presence in CdS of slow-recombination centers (the so-called *r* centers[8]), which are responsible for the high photosensitivity of the semiconductor. In CdS, these are deep compensated acceptors, which possess a high hole-trapping cross section ($\approx 10^{-2} - 10^{-13}$ cm^2) and a low electron-trapping cross section ($\approx 10^{-19} - 10^{-20}$ cm^2). In ''pure'' CdS crystals, intrinsic lattice defects can act as *r* centers.[9,10]

The mechanism of the IR-induced photocurrent quenching in CdS crystals is well known.[6] It is associated with the IR-induced relocalization of photoholes from *r* to *s* centers. The latter are fast recombination centers, which reduce the lifetime of the majority carriers and, hence, bring about a

decrease of the PC. Thus the mechanism of IR-induced PC quenching in CdS reduces actually to an increase of the recombination flow through the *s* centers through suppression by IR light of the recombination channel via the *r* centers.

The IR-induced photocurrent quenching in the CdS crystals studied is observed to occur throughout the spectral range covered, including both the intrinsic region and the region of the additional maxima AM_1 and AM_2, which lies substantially below the excitonic resonance $A_{n=1}$ (see Fig. 1). This implies a decrease in the carrier lifetime both in the bulk (τ_v) and near the surface (τ_s) of the semiconductor under IR illumination. Note that crystals with both peak- and dip-shaped FS exhibit a substantially larger decrease of τ_v than of τ_s.

In crystals with peak-shaped FS, this manifests itself in a relative enhancement of the excitonic maxima in spectra with increasing IR intensity (Fig. 1a). Indeed, an FS appears if τ_s and τ_v are not equal,[11] with the $\tau_s > \tau_v$ case corresponding to the peak-shaped FS, and $\tau_s < \tau_v$, to the dip-shaped one. This model suggests that the relative height of the excitonic maxima above the background in crystals with a peak-shaped FS is determined by the ratio $(\tau_s - \tau_v)/\tau_v$. Therefore an increase of a peak-shaped FS above the background indicates an increase of the τ_s/τ_v ratio. In the conditions where τ_s and τ_v decrease simultaneously, this is possible only if τ_v decreases faster.

The effect of prevailing decrease of τ_v under IR illumination is seen particularly clearly in crystals with dip-shaped FS. It manifests itself in a disappearance of the structure in the PC spectral response at low IR intensities and in the PC type inversion at high enough, and, in some cases, the high-
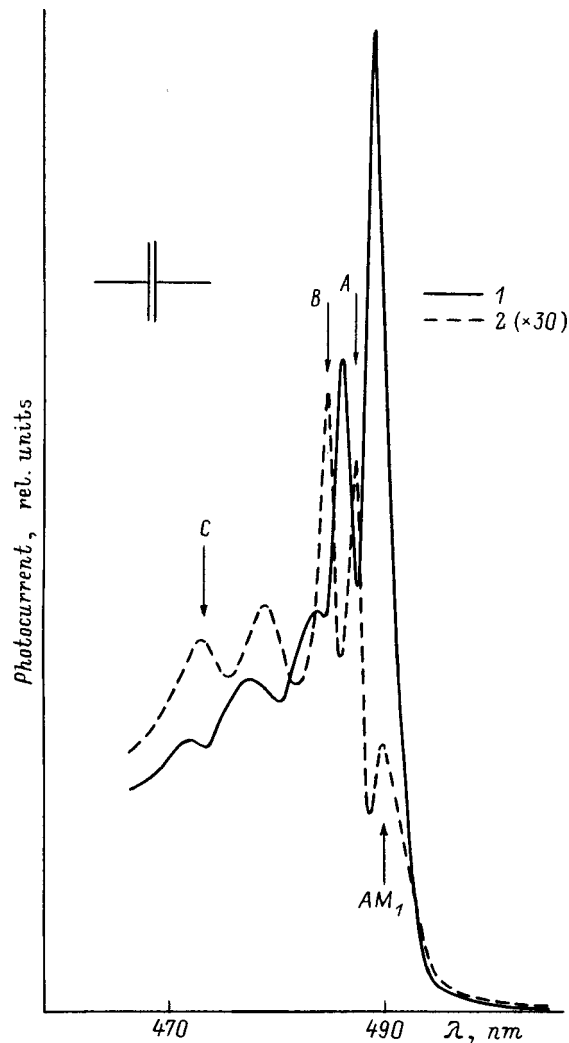
FIG. 2. PC spectra of a CdS crystal obtained at $T = 77$ K and $\mathbf{E} \perp C$. *1* — no IR illumination, *2* — IR illumination with an intensity $I = 60I_0$.

electron and a hole, with subsequent hole localization in a surface state.[15] These states may play a significant part also in the formation of spectra in the region of band transitions by trapping the photoholes and increasing in that way the photoelectron lifetime near the surface.

Thus the stabilization of τ_s in the near-surface layer under discussion may be connected with a sort of pinning of the majority-carrier lifetime on the CdS surface by surface acceptor states. Switching on IR illumination reduces drastically τ_v by suppressing bulk photosensitivity centers, and surface acceptor states, which act as surface photosensitivity centers, may provide a photosensitivity in the near-surface layer of the crystal higher than that in the bulk, which accounts for a response curve with a peak-shaped FS. It should be pointed out that the idea of a possible presence in CdS of surface photosensitivity centers differing in properties from the bulk r centers is in no way new (see Ref. 3).

Of particular interest for the interpretation of the nature of the additional photocurrent maxima AM_1 and AM_2 is the spectrally selective IR-induced quenching of the photocurrent (Fig. 1). Because the action of IR illumination reduces primarily to suppression of the bulk r photosensitivity centers, the IR-induced quenching will be the strongest for the spectral features which are due to the states directly interacting with the r centers. Therefore the selective IR quenching of the photocurrent maxima AM_1 and AM_2, by supporting their bulk nature, argues convincingly for a direct relation of the corresponding states with the r centers. Hence the AM_1 and AM_2 maxima may be considered as indicators of the CdS volume photosensitivity determined by the volume concentration of the r centers. On the other hand, if one identifies the AM_1 and AM_2 maxima with bulk photosensitivity r centers in CdS, they may be used as a probe for studying these centers.

In this connection it should be noted that the AM_1 and AM_2 photocurrent bands in CdS photoconductivity spectra quite frequently cannot be resolved into isolated maxima and, in addition, become superimposed on the excitonic structure to form a broad dominant long-wavelength photocurrent band in crystals with a dip-shaped FS or a long-wavelength tail on the exciton peak A in the case of a peak-shaped FS. In these conditions, states in the PC spectrum, including those responsible for the AM_1 and AM_2 maxima, can be resolved by using IR illumination at moderate intensity levels. This is demonstrated by Fig. 2. One readily sees that illumination of a CdS crystal with a dip-shaped FS with IR light of a moderate intensity results in a good spectral resolution of excitonic states and of the states responsible for the AM_1 maximum due to a good spectrally selective IR-induced photocurrent quenching.

The possibility of reversible switching of a spectrum from type II to type I by suppressing the bulk r centers by IR light suggests that in CdS crystals with a dip-shaped FS the bulk r center concentration exceeds substantially that in peak-shaped-FS ones. This suggestion is buttressed also by the strong difference in the magnitude of this IR quenching effect between crystals having different types of FS, the observed trend to PC quenching saturation under conventional IR illumination levels in type-I crystals (see above), a lower,

est IR intensities tested (curves *2* and *3* in Fig. 1b). Indeed, the transformation of the type-II to type-I FS corresponds to regular changes of τ_s and τ_v resulting in the reversal of the $\tau_s < \tau_v$ inequality (see above). These changes in τ_s and τ_v are equivalent to a monotonic growth of the τ_s / τ_v ratio from a value less than one (type-II curve) to one (structureless curve) to greater to one (type-I curve). Clearly enough, if both τ_s and τ_v decrease, the τ_s / τ_v ratio can grow only if τ_v decreases faster.

The observed pattern of carrier lifetime variation under IR illumination in the near-surface layer and in the bulk of CdS, first, indicates that the carrier lifetime in the bulk, τ_v, is determined by the bulk r centers, and, second, evidences the existence near the surface of a factor that favors stabilization of τ_s and, thus, allows its substantially smaller changes under IR illumination compared with τ_v. Filled acceptor-type surface states could act as such a factor stabilizing τ_s in the presence of IR illumination. The existence of such states was established in a large number of studies (see, e.g., Refs. 12–14). They play a key role in the formation of the excitonic structure in surface photo-emf spectra of CdS by providing conduction-stimulating exciton decay into an

as a rule, integrated photosensitivity of the latter compared to that in crystals with type-II FS, as well as by the presence among the samples with dip-shaped FS of crystals having an extremely high photosensitivity. A similar conclusion was reached also in an analysis[7] of the irreversible transformation of peak- to dip-shaped PC spectra in samples subjected to a thermal treatment.

The above discussion permits an important conclusion that the dip-shaped FS and the corresponding behavior of the photocurrent spectral response in the short-wavelength (intrinsic) region observed in undoped CdS crystals with a ''natural'' surface are due not to the high surface recombination rate, as is usually assumed, but rather to the relatively high concentration of r centers associated with intrinsic lattice defects in the bulk of the crystal, which provide a high volume photosensitivity of a semiconductor compared to its surface characteristic.

Thus the experimental results directly indicate the significant part played in CdS crystals by the volume of the semiconductor in the formation of the near-band-edge low-temperature PC response. This relates primarily to crystals with a dip-shaped FS, where the FS type, the structure of the spectrum, and the high photosensitivity in the AM_1 and AM_2 extrinsic region, which is responsible for the general pattern of the PC response characteristic of these crystals, are due to the bulk r centers. In crystals with a peak-shaped FS, the bulk r centers, provided their concentration is sufficiently

high, can produce a background on which excitonic photocurrent maxima will be seen, as well as give rise to features in the form of long-wavelength AM_1 and/or AM_2 maxima.

[1] V. E. Lashkarev, E. A. Sal'kov, and V. A. Khvostov, *Proceedings of the 3rd International Conference on Photoconductivity* (Stanford, 1969), p. 111.

[2] J. A. Bragagnolo, G. M. Storti, and K. W. Böer, Phys. Status Solidi A **22**, 639 (1974).

[3] A. V. Il'inskiĭ, B. V. Novikov, and S. I. Sutulova, Fiz. Tverd. Tela (Leningrad) **16**, 3029 (1974) [Sov. Phys. Solid State **16**, 1957 (1974)].

[4] A. S. Batyrev, R. A. Bisengaliev, O. E. Botov, N. V. Karasenko, and E. V. Sumyanova, *Abstracts of the International Conference on Optics of Excitons in Condensed Matter* (St. Petersburg, Russia, 1997), p. 64.

[5] A. S. Batyrev, R. A. Bisengaliev, O. E. Botov, N. V. Karasenko, and E. V. Sum'yanova, Fiz. Tverd. Tela (St. Petersburg) **40**, 941 (1998) [Phys. Solid State **40**, 867 (1998)].

[6] E. F. Gross and B. V. Novikov, J. Phys. Chem. Solids **22**, 87 (1961).

[7] J. A. Bragagnolo and K. W. Böer, Phys. Status Solidi A **21**, 291 (1974).

[8] R. H. Bube, *Photoconductivity of Solids* (Wiley, New York, 1960; IL, Moscow, 1962).

[9] *Physics and Chemistry of II-VI Compounds*, edited by M. Aven and J. S. Prener (North-Holland, Amsterdam, 1967; Mir, Moscow, 1970, p. 499).

[10] M. K. Sheĭnkman, N. E. Korsunskaya, I. V. Markevich, and T. V. Torchinskaya, Izv. Akad. Nauk SSSR, Ser. Fiz. **40**, 2290 (1976).

[11] J. Voigt and E. Ost, Physica (Amsterdam) **33**, 381 (1969).

[12] R. Williams, J. Phys. Chem. Solids **23**, 1057 (1962).

[13] S. Baidyaroy and P. Mark, Surf. Sci. **30**, 53 (1972).

[14] J. Łagowski, Surf. Sci. **299/300**, 92 (1994).

[15] A. Morawski and R. Banisch, Surf. Sci. **69**, 444 (1977).

Effect of isotopic disorder on the thermal conductivity of germanium in the region of the maximum

A. P. Zhernov

Kurchatov Institute Russian Scientific Center, 123182, Moscow, Russia Institute of Superconductivity and Solid-State Physics, 123182, Moscow, Russia
(Submitted in final form December 18, 1998)
Fiz. Tverd. Tela (St. Petersburg) **41**, 1185–1189 (July 1999)

This paper discusses the question of how isotopic disorder affects the position of the thermal-conductivity maximum of germanium. The discussion is in terms of a Callaway-type model. Experimental data on the thermal conductivity of a natural Ge crystal and of highly enriched Ge^{70} crystals are analyzed. © *1999 American Institute of Physics.*
[S1063-7834(99)01107-7]

V. I. Ozhogin's group[1] has recently obtained chemically pure, perfect, and highly enriched crystals of Ge^{70} (with 99.99 % enrichment). They simultaneously measured the thermal conductivity $K(T)$ in a wide temperature range not only on a highly enriched sample but also on Ge^{70} samples with 96 % enrichment and a natural sample (see also Ref. 2).They found that the position of the maximum of the thermal conductivity for the ''99.99'' germanium is shifted substantially to the right on the temperature scale compared to the analogous ''96'' germanium and the natural germanium sample.

The effect of isotopic disorder on the thermal conductivity $K(T)$ has been analyzed in many papers. It is well known that isotopic disorder substantially reduces the thermal conductivity of insulating single crystals (see, for example, Refs. 3–5). However, as far as we know, the question of the position of the maximum of $K(T)$ as a function of isotopic composition has not been discussed for crystals with a strongly anisotropic phonon spectrum, such as germanium. This specific question is considered below, using the experimental results of Ref. 1.

1. THE GENERALIZED CALLAWAY MODEL

In considering thermal conductivity, it is usually assumed that the various scattering processes of nonequilibrium phonons, namely boundary scattering at the sample walls and elastic scattering due to isotopic disorder and impurities, as well as inelastic anharmonic collisions, are independent. It is well known in this case that normal (N) anharmonic phonon-scattering processes, i.e., processes in which quasi-momentum is conserved, do not cause finite thermal resistance in themselves. At the same time, in the temperature interval in which resistive scattering processes of phonons by phonons (U processes), with loss of quasi-momentum, freeze out, N processes can determine the structure of the steady-state nonequilibrium phonon distribution, so that their role is extremely important.

Taking this into consideration, the results of Ref. 6 (see also Ref. 7) are widely used in analyzing the influence of various relaxation mechanisms. That paper took into account

the specific role of N processes and obtained a simple and elegant expression for the thermal conductivity. Note that Ref. 8 attempted to assign a different significance to the formation of the steady-state distribution of low- and high-frequency groups of phonons (as $T \rightarrow 0$, the high-frequency phonons must be virtually in equilibrium and have a weak effect on the steady-state distribution).

We note that the phonon spectrum of germanium has been studied in great detail. The theoretical papers can be divided into two groups. The first group develops and modifies phenomenological models. The second group bases their analysis on the theory of the density functional, using the approximations of linear response and ''frozen-in'' phonons (see, for example, Refs. 7 and 9).

In this paper, we shall consider the relatively low-temperature region near the maximum of the thermal conductivity. The contribution from the optical modes can be neglected in this situation, and only acoustic modes need be included. As far as the acoustic modes are concerned, the strong dispersion of the phonon modes needs to be taken into account in the case of Ge-type crystals (see, for example, Ref. 10). Taking this into consideration, a model that included the t modes along with the longitudinal (l) modes was used earlier to describe the thermal conductivity of Ge.

In terms of the two-mode model of Ref. 2, the thermal conductivity is defined as

$$K = K_t + K_l, \tag{1}$$

where subscripts t and l denote the partial contributions to K from the transverse and longitudinal phonons, respectively. According to Refs. 2 and 6, for a cubic crystal in which a temperature gradient exists along one of the crystallographic axes,

$$K_i = \gamma_i \frac{k_B^4}{2\pi^2 h^3 v_i} T^3 \left[\langle \tau_R^{(i)} \rangle + \frac{\langle \tau_c^{(i)}/\tau_N^{(i)} \rangle^2}{\langle \tau_c^{(i)}/(\tau_N^{(i)} \tau_R^{(i)}) \rangle} \right], \tag{2}$$

where $i = t, l$. The quantities h and k_B are the Planck and the Boltzmann constants. γ_i equals 2/3 and 1/3, respectively, in the cases of transverse and longitudinal modes, and v_i is the

group velocity of sound. τ_c and τ_R denote the combined relaxation time and the total relaxation time of the resistive processes, with

$$\tau_c^{-1} = \tau_R^{-1} + \tau_N^{-1}. \tag{3}$$

The symbol $\langle \ldots \rangle$ is defined by

$$\langle f_i \rangle = \int_0^{\theta_i/T} dx \, x^4 \frac{e^x}{(e^x - 1)^2} f_i(x).$$

Here the upper limit is given by $\theta_i = k_B \omega_i / h$, where ω_i is the maximum frequency for polarization i.

It was assumed in the specific calculations that the group velocities equal $v_t = 3.16 \times 10^5$ cm/sec and $v_l = 5.21 \times 10^5$ cm/sec (see, for example, Ref. 2). The characteristic Debye temperatures are also taken from Ref. 2. Here $\theta_t = 101$ and $\theta_l = 330$ K.

Assuming that the various relaxation mechanisms of nonequilibrium phonons act independently, we have

$$\tau_R^{(i)-1} = \tau_b^{-1} + \tau_{is}^{-1} + \tau_U^{(i)-1}. \tag{4}$$

Here τ_b, τ_{is}, and τ_U are the relaxation times of phonons determined, respectively, by boundary scattering at the walls of the sample or the boundaries of the blocks, elastic scattering caused by isotopic disorder, and inelastic anharmonic Umklapp processes.

We should point out that, if the N processes are slower than the processes that result from momentum losses, the main contribution comes from the first term in Eq. (2). Otherwise, the thermal conductivity is determined by the second term.

Note that τ_b for diffuse boundary scattering is determined by an expression of the form

$$\tau_b^{-1} = v_b(1/l_c + 1/l_s). \tag{5}$$

Here l_c is the Casimir length, and l_s is the length of the sample (in the direction in which the heat flows). In this case, for a sample with a rectangular cross section with area S, we have $l_c = 1.12\sqrt{S}$ (see, for example, Refs. 11 and 12). As far as velocity v_b is concerned, it was assumed that

$$v_b^{-1} = b_s^{-1} = \frac{1}{3}[2v_t^{-1} + v_l^{-1}]. \tag{5a}$$

Let us consider the scattering mechanism associated with isotopic disorder. The corresponding relaxation time is defined as

$$\tau_{is}^{-1} = G \frac{\pi V}{6} g(\omega), \tag{6}$$

where G is the isotopic disorder parameter, V is the volume per atom, and $g(\omega)$ is the density of phonon states (all modes). In this case,

$$G = (\langle M^2 \rangle - \langle M \rangle^2)/\langle M \rangle^2, \langle \ldots \rangle = \sum_s \sum_\mathbf{n} c_\mathbf{n}^{(s)} \ldots \, .$$

Here $\mathbf{n}$ is a lattice node, s is the sort of isotope, and $c_\mathbf{n}^{(s)}$ is its concentration (see Refs. 1 and 4 for details).

Note that the situation relative to the frequency dependence of the relaxation rate of the t modes because of isoto-

pic disorder in Ge was analyzed in detail in Ref. 13. Since $\tau_{is}^{-1} \sim \omega^2 g(\omega)$, the relaxation time given by Eq. (6) varies more rapidly than ω^4 in the region of strong frequency dispersion of the transverse vibrational modes. (The partial spectrum of the t modes has a sharp peak at 2.4 THz, and its maximum frequency is ≈ 3.2 THz. However, the spectrum of the l modes is localized at much larger frequencies of ≈ 6 THz.[14]) Nevertheless, since we are using the Debye approximation, it was assumed that

$$\tau_{is}^{-1} = G \frac{V}{4\pi v_s^3} \omega^4. \tag{6a}$$

The parameters of the isotopic scattering mechanism were not varied in the calculations.

The question of the relaxation mechanism due to U processes has also been considered by many authors. In the case of t modes, there are two substantial types of U processes: $t + t \rightarrow l$ and $t + l \rightarrow l$. It was shown that only the first channel plays a substantial role for Ge. In this case,

$$\frac{1}{\tau_U} \sim \begin{cases} \omega^2 T^3 \exp(-B^{(t)}/T), & T \ll \theta_t \\ \omega^2 T \theta_t^2, & T > \theta_t/2 \end{cases} \tag{7}$$

(see, for example, Ref. 2). Let us discuss the quadratic dependence of τ_U^{-1} on frequency. See below for the value of $B^{(t)}$.

In this paper, a representation in the form of

$$\frac{1}{\tau_U^{(t,l)}} = A_U^{(t,l)} \omega^2 T \exp(-B^{(t,l)}/T) \tag{7a}$$

was chosen for the relaxation rate due to U processes for both types of phonon modes. Based on the results in Ref. 4, we obtained $B^{(t)} = 55$ and $B^{(l)} = 180$ K. The B values correlate with the Debye temperatures of the t and l modes and are about $\theta_i/2$.

Note that a representation similar to Eq. (7a) was also used in a recent paper[15] in which the behavior of isotopically enriched diamond samples was studied.

As far as the relaxation rates due to N processes are concerned, it was assumed as usual (see, for example, Ref. 16) that

$$\frac{1}{\tau_N^{(t)}} = A_N^{(t)} \omega T^4, \quad \frac{1}{\tau_N^{(l)}} = A_N^{(l)} \omega^2 T^3. \tag{8}$$

It was found in Ref. 2 from a comparison of the theoretical and experimental results for ''99.99'' germanium that

$$A_N^{(t)} = 2 \times 10^{-13} K^{-4}, \quad A_N^{(l)} = 2 \times 10^{-21} s K^{-3},$$

$$A_U^{(t)} = 1 \times 10^{-19} K^{-4}, \quad A_U^{(l)} = 5 \times 10^{-19} s K^{-3}. \tag{9}$$

Moreover, the specific calculations used the parameters from Table I and assumed that the mean velocity of sound is $v_s = 0.35 \times 10^6$ cm/sec and that the atomic volume is $V = 22.64 \,\text{Å}^3$. The geometrical dimensions of the samples and the corresponding values of the isotopic-disorder param-

TABLE I. Values of the isotopic-disorder parameter G and the geometrical sizes (l_x, l_y, l_z) of the samples.

Sample	G	l_x, l_y, l_z, mm
1	5.87×10^{-4}	$2.515 \times 2.525 \times 40$
2	7.57×10^{-5}	$2.50 \times 2.50 \times 40$
3	8.16×10^{-8}	$2.48 \times 2.47 \times 29$

eter that appeared in Ref. 1 were also used. These are shown in Table I. Note that the three values of G correspond to mean masses of 72.69, 70.11, and 70.0002.

We now turn our attention to the fact that using Eqs. (7) and (8) to represent $\tau_U^{(i)-1}$ and $\tau_N^{(i)-1}$ actually restricts the theory to the region of comparatively low temperatures (about the temperature of the maximum thermal conductivity). Indeed, above liquid-nitrogen temperature, a power-law dependence on temperature must be followed instead of an exponential temperature dependence. The contribution from optical modes must be finite.

Finally, effects associated with a hydrodynamic energy-transport mechanism can show up in sufficiently perfect samples (see, for example, Ref. 1).

In order to elucidate this, let us first determine the free path length l_i corresponding to the i mechanism of phonon scattering. We have

$$\frac{1}{l_i} = \int d\mathbf{q} \, \frac{C_{\mathbf{q}}}{v_{\mathbf{q}} l_{\mathbf{q}}^{(i)}} \int d\mathbf{q} \, \frac{C_{\mathbf{q}}}{v_{\mathbf{q}}}. \tag{10}$$

Here $C_{\mathbf{q}}$ is the partial contribution to the lattice heat capacity from mode $\mathbf{q}$, and $v_{\mathbf{q}}$ is the group velocity.

At low T, let the path lengths l_N and l_R corresponding to normal and resistive processes satisfy conditions of the form

$$l_N \ll d, \quad l_R l_N \gg d^2.$$

Here d is the characteristic geometrical size of the sample. Then, according to Ref. 17, for example, it can be assumed that the motion of the phonon gas under the action of an applied temperature gradient has the character of viscous Poiseuille flow. The effective path length increases in this case. It is determined from

$$l_{ef} \approx 0.1 \, \frac{d^2}{l_N}.$$

As the temperature is reduced further, when

$$l_N, l_R \gg d, \quad l_{ef} \approx d^2/l_N,$$

the phonon gas enters the Knudsen regime, similar to the case of a strongly rarefied gas.

References 18 and 19 established the criteria for Poiseuille flow; namely, it is required that

$$l_R/l_N \geq 10^3, \quad d/l_N \geq 30. \tag{11}$$
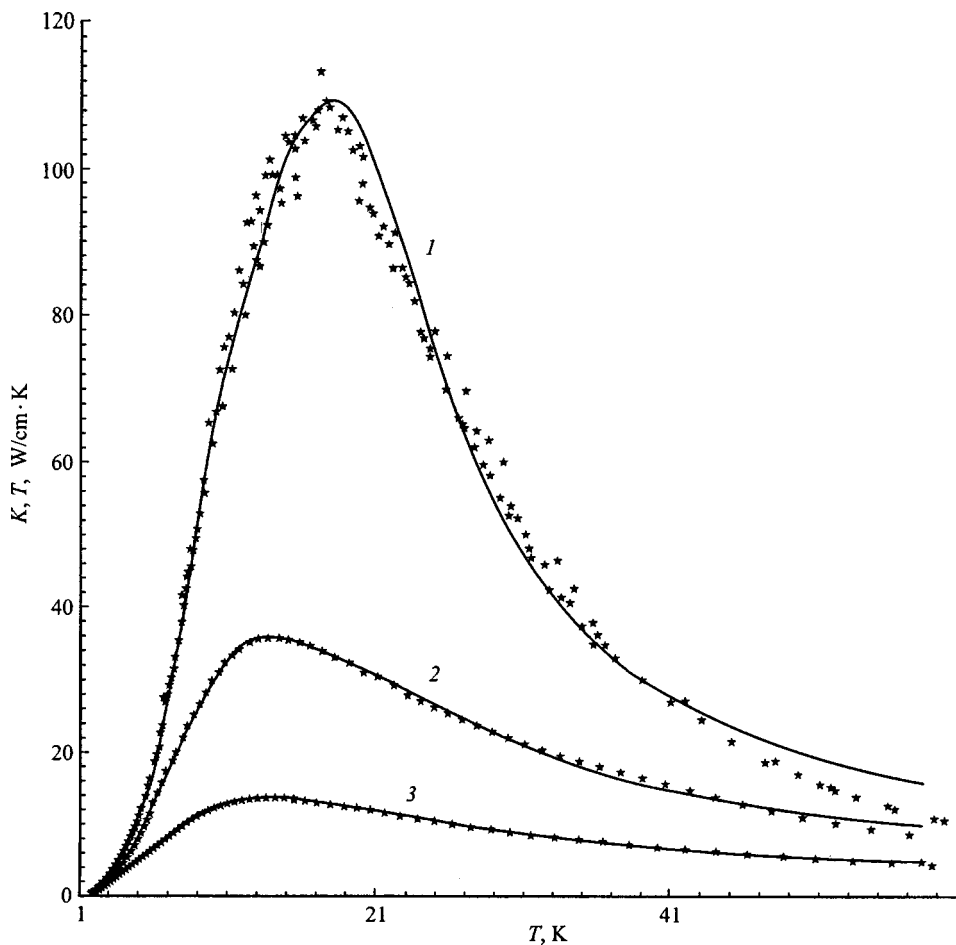
FIG. 1. Thermal conductivity of highly enriched ''99.99'' (*1*) and ''96'' (*2*) Ge^{70} and natural germanium (*3*). The experimental data of Ref. 1 are shown by the points. The solid curves show the calculations.
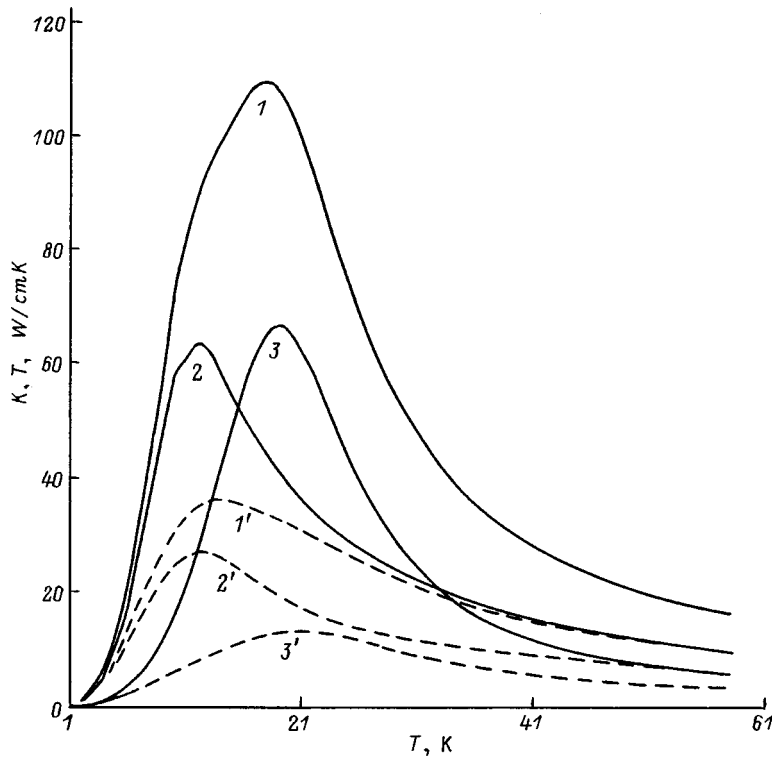
FIG. 2. Partial contributions to the thermal conductivity for Ge^{70} with an enrichment of 99.99 % (solid curves) and 96 % (dashed curves). *2* and *3* correspond to the contributions from the transverse and longitudinal phonons, and *1* is the total thermal conductivity.

Note that Ref. 18 considered the thermal conductivity of extremely perfect and monoisotopic samples of solid He^4 and distinctly detected the features predicted in Ref. 17 in the temperature dependence of $K(T)$ in the region to the left of the maximum. Moreover, the question of the appearance of the hydrodynamic regime in connection with the problem of second sound was analyzed in NaF and Bi crystals, which have no isotopic scattering mechanism. See, for example, Ref. 5 for a discussion of the corresponding results.

The next section briefly discusses the possibility of the appearance of the hydrodynamic effect in germanium.

2. ANALYSIS OF THE THERMAL CONDUCTIVITY OF GERMANIUM

First, the question of the possibility of the appearance of the hydrodynamic regime in perfect and highly enriched samples of "99.99" germanium was studied. Equation (10) was used to calculate the path lengths l_N and l_U. It was then checked whether or not the condition given by inequalities (11) was satisfied. It turned out that the inequality $l_N \ll d \ll l_U$ is not satisfied for the transverse modes in the temperature region to the left of the maximum in the heat conductivity. As far as the longitudinal modes are concerned, the situation is as follows: It can be shown that $l_N^{(l)} \ll l_U^{(l)}$; i.e., the path lengths differ substantially. At the same time, we have

$$\frac{l_c}{l_N} \approx \frac{5 \times 10^8 T^5}{\theta_l^5},$$

where $\theta_l = 330$ K is the Debye temperature for the longitudinal modes. Thus, for $T > 4 - 10$ K, l_c is larger than l_N but of the same order of magnitude. Generally speaking, the condition given by inequalities (11) is not rigorously satisfied.

Thus, no hydrodynamic regime is developed in the case in question, but the effects associated with it manifest themselves to a definite extent for the longitudinal modes. In the temperature interval $\sim 4 - 10$ K, their scale is ~ 10 %. As far as the samples with 96 % enrichment are concerned, as well as those with natural composition, the isotopic scattering mechanism is substantial in the same interval of $\sim 4 - 10$ K. As a result, the diffusion mechanism is ineffective. This question will be considered in detail in another paper, allowing for the possibility that the phonons are specularly reflected from the surface.

Secondly, the experimental results of Ref. 1 in the region of the thermal-conductivity maximum in the temperature region $\sim T_M$ were analyzed, using Eqs. (1)–(9). In this case, Fig. 1 shows the experimental and theoretical curves for the thermal conductivity. Figure 2 shows theoretical curves that illustrate the role of the partial contributions of the *l* and *t* modes to $K(T)$ for the isotopically highly enriched "99.99" and "96" samples.

A few comments regarding the results shown in Figs. 1 and 2 are called for. As can be seen from Fig. 1, the agreement between the experimental and theoretical curves is satisfactory for all the samples studied here. As far as Fig. 2 is concerned, we note that, for the highly enriched "99.99" sample, the main contribution to $K(T)$ right in the T_M region turned out to be connected with the *l* modes, since the influence of the *l* modes is partially veiled because of the isotopic scattering. This explains why the maximum for the "96" sample is shifted toward lower temperatures by several degrees ($\sim 4K$) by comparison with the "99.99" sample. In the case of the natural sample, the role of the *l* modes under conditions of sufficiently strong isotopic scattering increases somewhat relative to the *t* modes, and the maximum is dis-

placed toward higher temperatures by some fraction of a degree.

[1] V. I. Ozhogin, A. V. Inyushkin, A. N. Toldenkov, G. É. Popov, E. Haller, and K. Itoh, Pis'ma Zh. Éksp. Teor. Fiz. **63**, 463 (1996) [JETP Lett. **63**, 490 (1996)].

[2] M. Asen-Palmer, K. Bartkowsky, E. Gmelin, M. Cardona, A. P. Zhernov, A. V. Inuishkin, A. V. Taldenkov, V. I. Ozhogin, K. M. Itoh, and E. E. Haller, Phys. Rev. B **56**, 9431 (1997).

[3] I. Pomeranchuck, J. Phys. USSR **6**, 238 (1942).

[4] J. M. Ziman, *Electrons and Phonons* (Clarendon Press, Oxford, 1960; Moscow, Inostr. Lit., Moscow, 1963).

[5] R. Berman, *Thermal Conduction in Solids* (Clarendon Press, Oxford, 1976).

[6] J. Callaway, Phys. Rev. **113**, 1046 (1959).

[7] Wei Siging and M. Y. Chou, Phys. Rev. B **50**, 2221 (1994).

[8] H. B. Armstrong, Phys. Rev. B **32**, 3381 (1985).

[9] R. Eryigit and I. P. Herman, Phys. Rev. B **53**, 7775 (1996).

[10] A. D. Zdetsis and C. S. Wang, Phys. Rev. B **19**, 2999 (1979).

[11] H. B. Casimir, Physica (Amsterdam) **5**, 495 (1938).

[12] J. W. Wandersande, Phys. Rev. B **15**, 2355 (1977).

[13] S. Tamura, Phys. Rev. B **27**, 858 (1983).

[14] S. Tamura, Phys. Rev. B **31**, 2574 (1985).

[15] L. Wei, P. K. Kuo, R. L. Thomas, T. R. Anthony, and W. F. Banholzer, Phys. Rev. Lett. **70**, 3764 (1993).

[16] C. Herring, Phys. Rev. **195**, 954 (1954).

[17] R. N. Gurzhi, Zh. Éksp. Teor. Fiz. **46**, 719 (1964) [Sov. Phys. JETP **19**, 490 (1965)]; Usp. Fiz. Nauk **94**, 689 (1968) [Sov. Phys. Usp. **11**, 255 (1968)].

[18] L. P. Mezhov-Deglin, Zh. Éksp. Teor. Fiz. **49**, 66, (1965) [Sov. Phys. JETP **22**, 47 (1966)].

[19] L. P. Mezhov-Deglin, Fiz. Tverd. Tela **22**, 1748 (1980) [Sov. Phys. Solid State **22**, 1018 (1980)].

Physical properties of *n*-CdGeAs$_2$ single crystals prepared by low-temperature crystallization

I. K. Polushina, Yu. V. Rud', and T. N. Ushakova

A. F. Ioffe Physicotechnical Institute, Russian Academy of Sciences, 194021 St. Petersburg, Russia

V. Yu. Rud'

St. Petersburg State Technical University, 195251 St. Petersburg, Russia
(Submitted November 12, 1998; resubmitted December 22, 1998)
Fiz. Tverd. Tela (St. Petersburg) **41**, 1190–1193 (July 1999)

The first results obtained in studies of the temperature dependences of electrical conductivity and Hall constant of *n*-CdGeAs$_2$ single crystals prepared by low-temperature crystallization are reported. It has been established that the method developed permits growing single crystals with a free-electron concentration $\simeq (1-2) \times 10^{18}$ cm^{-3} and a Hall mobility $\simeq 10000$ cm^2/(Vs) at $T = 300$ K. It is shown that the temperature dependence of Hall mobility exhibits a behavior characteristic of electron scattering by lattice vibrations, whereas below 150 K a deviation from this law is observed to occur evidencing an increasing contribution of static lattice defects to scattering. The Hall mobility in the crystals prepared was found to reach $\simeq 36000$ cm^2/(Vs) at 77 K. Photosensitive heterojunctions based on *n*-CdGeAs$_2$ single crystals were prepared. The spectral response of the photosensitivity of these structures is analyzed. It is concluded that this method is promising for preparation of perfect CdGeAs$_2$ crystals. © *1999 American Institute of Physics.* [S1063-7834(99)01207-1]

Complication of the atomic composition of diamond semiconductors, in accordance with the criteria of their formation developed by Goryunova,[1] offers a possibility of varying the fundamental properties of these compounds so as to meet the demands of electronics. For instance, substitution of atoms of Groups II and IV for two atoms of Group III of the periodic system paves the way to formation of ternary compounds $A^{II}B^{IV}C_2^{V}$, which are more numerous than the III–V family, and whose physical properties are capable of not only complementing but broadening the potential of the semiconductor electronics, which is presently based primarily on elemental and binary semiconductors.[2,3] Among the most essential of known differences of $A^{II}B^{IV}C_2^{V}$ compounds from their III–V analogs are the anisotropy in physical properties and the record-high nonlinear susceptibility of some ternary semiconductors. Therefore one witnesses at present a revival of interest in chalcopyrite semiconductors, specifically in CdGeAs$_2$.[4–8] The priority in the preparation of CdGeAs$_2$ single crystals and the first studies of their fundamental properties belongs to the Ioffe Institute.[9–11] The main obstacle on the way to a wide application of CdGeAs$_2$ in high-efficiency nonlinear optical converters is the fairly high optical absorption in the transmission window of this compound.[4,7]

It should be stressed that all studies performed until recently were made on single crystals prepared from close to stoichiometric melts at the crystallization temperature of CdGeAs$_2$. In the absence of doping, such crystallization yields *p*-type material.[6,8] This work reports the first measurements of the physical properties of CdGeAs$_2$ single crystals grown by low-temperature crystallization from a nonstoichiometric melt-solution, which permitted us to make a qualitative breakthrough in the technology of this material and surpass the electron mobility limit $U_n \leqslant 3000$ cm^2/(Vs) which had persisted for over 30 years.[6,11–13]

1. CdGeAs$_2$ single crystals were grown from nonstoichiometric melts in the temperature region substantially below the melting point of CdGeAs$_2$ and the temperature of the additional thermal effect, which is frequently seen[11] in DTA curves within the stability region for this compound. The crystals grown exhibit a well developed natural faceting characteristic of chalcopyrite compounds.[10] X-ray diffraction measurements show that the unit-cell parameters of these samples agree within experimental error with those quoted for CdGeAs$_2$ single crystals which were grown at the crystallization temperature from a close-to-stoichiometric melt.[10,11]

2. Parallelepiped-shaped samples about $0.3 \times 0.5 \times 5$ mm were prepared for measurements of the transport coefficients. The electrical conductivity σ and of the Hall constant R were measured by the compensation method in constant weak electric and magnetic fields. The current and potential contacts were pure indium pads. The relative accuracy of σ and R determination within the 77–300 K region studied was 3 and 5%, respectively. Measurements of the sign of the Hall voltage and of the Seebeck coefficient showed that the low-temperature crystallization permits one, similarly to ZnGeP$_2$,[12] to prepare without deliberate doping *n*-type crystals with a free-electron concentration $n = (1-2) \times 10^{18}$ cm^{-3} at $T = 300$ K and a Hall mobility of 10000 cm^2/(Vs).

Figure 1 presents temperature dependences $\sigma(T)$ and $R(T)$ for one of these samples. As the temperature decreases,
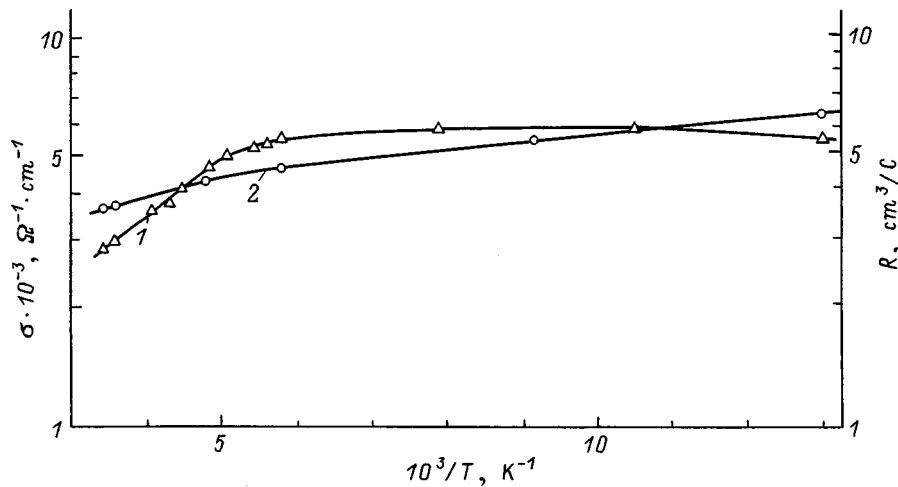
FIG. 1. Temperature dependences of (*1*) electrical conductivity and (*2*) the Hall coefficient for an *n*-CdGeAs$_2$ crystal grown by low-temperature crystallization (sample 2).

the electrical conductivity (curve 1) first grows (down to $T \simeq 180$ K), then remains practically constant, and only for $T < 100$ K exhibits a tendency to decrease with decreasing temperature. On the whole, the behavior of $\sigma(T)$ in the samples studied is apparently associated with changes in the scattering mechanism. At the same time, the Hall constant falls off monotonically with increasing T within the temperature range covered, which can be assigned to shallow-donor center ionization (curve 2 in Fig. 1). Precise determination of the ionization energy of these centers would require extending this investigation to helium temperatures.

As seen from Fig. 2, the electron Hall mobility in our crystals increases with decreasing temperature $T < 300$ K as $U_n \sim T^{-3/2}$ down to $\sim 150 - 160$ K, which, taking into account Ref. 14, gives one grounds to assume electron scattering from lattice vibrations to be dominant. As the temperature is lowered still more, a deviation from the $U_n \sim T^{-3/2}$ relation takes place with the growth of U_n slowing down, so that, at the nitrogen temperature, the electron Hall mobility reaches a level which is not characteristic of CdGeAs$_2$ samples studied earlier[11,13,15] and is fairly high, $U_n = 36000$ cm^2/(Vs). This observation implies a higher quality of material prepared by low-temperature crystallization compared to the traditional[11] high-temperature method.
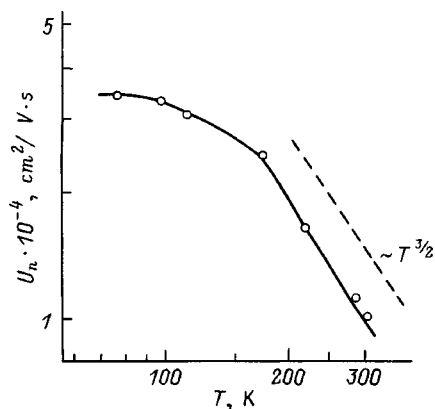
Extrapolation of the empirical relationship $U_n \sim T^{-3/2}$ to $T = 77$ K yields $U_n \simeq 70000$ cm^2/(Vs), which is in accord with the low effective electron mass in this compound[16].

3. Until recently, photosensitive structures of several types were fabricated only from *p*-CdGeAs$_2$ crystals.[16–19] This work reports on the first attempt to prepare such structures using *n*-CdGeAs$_2$ crystals. It was based on a method employed successfully recently in studies of compound semiconductors and requires placing different semiconductors in optical contact, an approach which does not require any postgrowth treatment capable of affecting the properties of these compounds.[20] The heterojunctions (HJ) were produced by bringing in optical contact the natural (112) specular surface of a CdGeAs$_2$ single crystal with a perfect cleaved surface of *n*-InSe. This contact was fixed in a special crystal holder and provided a possibility of illuminating the HJ from both sides. One used undoped InSe single crystals [$n \sim 10^{14}$ cm^{-3}, $U_n \approx 30$ cm^2/(Vs) at $T = 300$ K], which were grown by directed crystallization from a close to stoichiometric InSe melt. The cleaved InSe plates were $\simeq 30\,\mu$m thick. The heterocontact area in the structures thus produced was $\sim 10^{-2}$ cm^2 and was determined by the area of CdGeAs$_2$.

The steady-state I–V characteristics of these isotypic structures were close to linear and practically did not depend on the polarity of the external voltage. For bias voltages $U \geqslant 0.1$ V, the current ratio obtained for opposite voltage polarities did not exceed 1.1–1.2, the resistance was at a level of 10^5 Ω at $T = 300$ K and was determined primarily by the InSe resistance. The steady-state I–V characteristics of the HJ obtained were found to be similar in pattern to those of known[21] isotypic structures.

Illumination of an *n*-CdGeAs$_2$/*n*-InSe heterojunction generates a photovoltaic effect, in which *n*-CdGeAs$_2$ charges negatively relative to InSe, irrespective of the incident photon energy and illumination geometry. The photosensitivity is dominant when the heterojunction is illuminated from the side of its wide-band component *n*-InSe.[22,23] The maximum photosensitivity of the best HJs is 70–100 V/W at $T = 300$ K, which is substantially better than that of previous
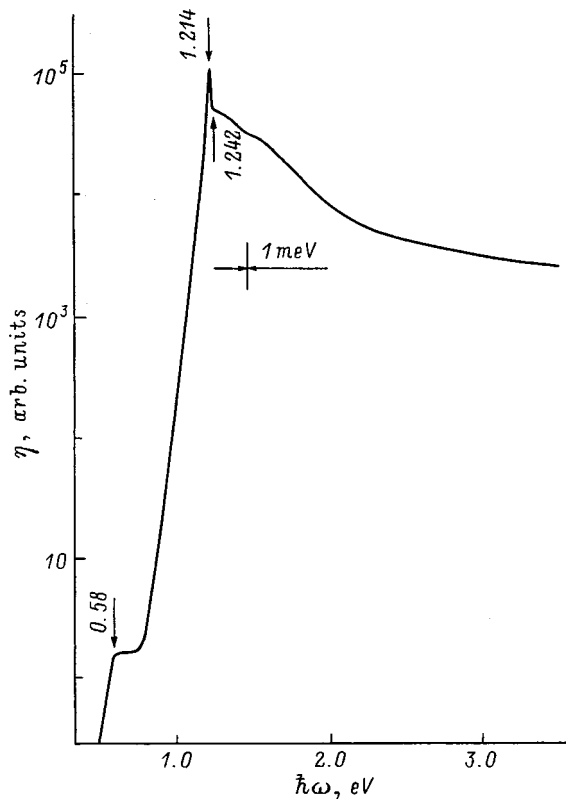

FIG. 2. Temperature dependence of the electron Hall mobility in an *n*-CdGeAs$_2$ crystal (sample 2).

FIG. 3. Spectral response of the relative photoconversion quantum yield of an *n*-CdGeAs$_2$/*n*-InSe heterojunction obtained at $T = 300$ K. (Illumination with polarized light from the InSe side.)

structures[16–19] and argues for a higher perfection of the CdGeAs$_2$ single crystals.

The spectral response of the relative photoconversion quantum yield η, obtained at $T = 300$ K as the ratio of the short-circuit photocurrent to the incident photon number, is presented in Fig. 3 for a typical InSe/CdGeAs$_2$ heterojunction. One readily sees that the photosensitivity of such HJs at $T = 300$ K extends over a broad spectral range from 0.5 to 3.5 eV when illuminated from the InSe side, and is particularly high in the region of their fundamental absorption.[23] The exponential growth of η for $\hbar\omega > 1.18$ eV has a steep slope $s = \partial(\ln \eta)/\partial(\hbar\omega) \simeq 60$ eV^{-1} characteristic of direct interband transitions in InSe.[23] For $\hbar\omega > 1.21$ eV, the growth of η is replaced by a steep short-wavelength drop in photosensitivity, which is accounted for by the effect of optical absorption of radiation in the InSe plate and by the specific features of collection of the photogenerated carriers in the active region of such HJs. Therefore as the thickness of InSe decreases, the maximum in η approaches the band gap width in InSe, and the short-wavelength falloff in the sensitivity becomes smoother.

The long-wavelength photosensitivity threshold of the CdGeAs$_2$/InSe heterojunctions and the break at $\hbar\omega = 0.58$ eV observed when illuminated from the InSe side (Fig. 3) are associated with the onset of interband absorption by the narrow-gap component of these structures.[18,22] The HJ illuminated from the *n*-CdGeAs$_2$ side was found to be photosensitive only around $\hbar\omega \simeq 0.6$ eV. As follows from Fig. 3, the photosensitivity of our HJs in the region of CdGeAs$_2$ inter-

band absorption is lower than that at $\hbar\omega \simeq 1.21$ eV by four to five orders of magnitude. This can be traced to differences in the doping levels of CdGeAs$_2$ and InSe, as a result of which the HJ active region is localized primarily in InSe. Our measurements show also that the photosensitivities of the cleaved InSe interface and of the CdGeAs$_2$ postgrowth surface do not exhibit any signs of degradation.

No natural photopleochroism was observed in our HJs illuminated with linearly polarized radiation in the region of the high photosensitivity ($\hbar\omega > 1.1$ eV). This may be assigned to the fact that incident radiation penetrates into the HJ active region along the isotropic direction in InSe.[23] For intrinsic photopleochroism to become observable in such HJs, one obviously should bring the doping levels in both components closer in magnitude, and in this way assure that polarization photosensitivity arises through anisotropy of absorption in CdGeAs$_2$.

Thus the results presented here demonstrate the potential of the low-temperature crystallization method for improving the quality of CdGeAs$_2$ single crystals.

[1] N. A. Goryunova, *Chemistry of Diamond Semiconductors* [in Russian] (LGU, Leningrad, 1963).

[2] O. M. Madelung, *Physics of III–V Compounds* (Springer, Berlin,: Group IV Elements and III–V Compounds) (Wiley, New York, 1964; Mir, Moscow, 1967).

[3] V. D. Prochukhan and Yu. V. Rud', Fiz. Tekh. Poluprovodn. **12**, 209 (1978) [Sov. Phys. Semicond. **12**, 118 (1978)].

[4] M. C. Ohmer and R. Pandey, Metall. Mater. Trans. B **23**, No. 7, 16 (1998).

[5] P. G. Schunemann and T. M. Pollak, MRS Bull. **23**, No. 7, 23 (1998).

[6] B. H. Bairamov, V. Yu. Rud', and Yu. V. Rud', MRS Bull. **23**, No. 7, 41 (1998).

[7] P. G. Schunemann, K. L. Schepler, and P. A. Budni, MRS Bull. **23**, No. 7, 45 (1998).

[8] B. Kh. Baĭramov, I. K. Polushina, V. Yu. Rud', Yu. V. Rud', P. G. Schunemann, M. C. Ohmer, N. C. Fernelius, G. Irmer, and J. Monecke, Fiz. Tverd. Tela (St. Petersburg) **40**, 212 (1998) [Phys. Solid State **40**, 190 (1998)].

[9] R. F. Mekhtiev, É. O. Osmanov, and Yu. V. Rud', Prib. Tekh. Éksp. No. 2, 179 (1964).

[10] A. A. Vaĭpolin, F. M. Gashimzade, N. A. Goryunova, F. P. Kesamanly, D. N. Nasledov, É. O. Osmanov, and Yu. V. Rud', Izv. Akad. Nauk SSSR, Ser. Fiz. **28**, 1085 (1964).

[11] N. A. Goryunova, F. P. Kesamanly, É. O. Osmanov, and Yu. V. Rud', Izv. Akad. Nauk SSSR, Neorg. Mater. **1**, 885 (1965).

[12] V. Yu. Rud' and Yu. V. Rud', Pisma Zh. Tekh. Fiz. **22**, No. 2, 37 (1996) [Tech. Phys. Lett. **22**, 107 (1996)].

[13] L. B. Zlatkin, Yu. F. Markov, and I. K. Polushina, Fiz. Tekh. Poluprovodn. **3**, 1590 (1969) [Sov. Phys. Semicond. **3**, 1336 (1969)].

[14] F. J. Blatt, *Physics of Electronic Conduction in Solids* (Academic, New York, 1957; Fizmatgiz, Leningrad, 1963).

[15] Ch. Dovletmuradov, Yu. V. Rud', A. Allanazarov, M. Serginov, and É. O. Osmanov, Izv. AN TSSR, Ser. Fiz. Tekh. Khim. Geolog. No. 6, 18 (1975).

[16] A. S. Borshchevskiĭ, N. E. Dagina, A. A. Lebedev, K. Ovezov, I. K. Polushina, and Yu. V. Rud', Fiz. Tekh. Poluprovodn. **10**, 1571 (1976) [Sov. Phys. Semicond. **10**, 934 (1976)].

[17] A. S. Borshchevskiĭ, N. E. Dagina, A. A. Lebedev, I. K. Polushina, and Yu. V. Rud', Fiz. Tekh. Poluprovodn. **10**, 1905 (1976) [Sov. Phys. Semicond. **10**, 1136 (1976)].

[18] A. A. Abdurakhimov, Yu. V. Rud', K. V. Sanin, M. Serginov, and V. E. Skoryukin, Zh. Tekh. Fiz. **53**, 325 (1983) [Sov. Phys. Tech. Phys. **28**, 199 (1983)].

[19] Yu. V. Rud', Yu. K. Undalov, and N. E. Dagina, Fiz. Tekh. Poluprovodn. **13**, 515 (1979) [Sov. Phys. Semicond. **13**, 304 (1979)].

[20] N. N. Konstantinova, M. A. Magomedov, V. Yu. Rud', and Yu. V. Rud', Fiz. Tekh. Poluprovodn. **26**, 558 (1992) [Sov. Phys. Semicond. **26**, 317 (1992)].

[21] A. G. Milnes and D. L. Feucht, *Heterojunctions and Metal-Semiconductor Junctions* (Academic, New York, 1972; Mir, Moscow, 1975).

[22] A. Shileika, Surf. Sci. **37**, 730 (1973).

[23] N. M. Mekhtiev, Yu. V. Rud', and É. Yu. Salaev, Fiz. Tekh. Poluprovodn. **12**, 1566 (1978) [Sov. Phys. Semicond. **12**, 924 (1978)].

Translated by G. Skrebtsov

Local deformation and the structure of the Stark splitting of rare-earth ions

M. M. Chumachkova and A. B. Roĭtsin*)

Institute of Semiconductor Physics, Ukrainian Academy of Sciences, 252650 Kiev, Ukraine
(Submitted September 2, 1998)
Fiz. Tverd. Tela (St. Petersburg) **41**, 1194–1199 (July 1999)

A model for describing the relaxation of ligand ions close to a defect when impurity ions are introduced into a crystal is proposed and verified. The approach assumes that ionic displacements into new equilibrium positions can be regarded as fundamental parameters of impurity crystals that can be determined from experimental data concerning the energy structure of the impurity ion. Direct calculations for rare-earth impurity ions using crystal-field theory showed that the energy spectrum of these ions strongly depends on the equilibrium positions of the nearest matrix ions surrounding them. The results of the calculations are compared with the available experimental data. The parameters of the theory are determined. The possibility of applying this approach to the study of other systems is discussed. © *1999 American Institute of Physics.* [S1063-7834(99)01307-6]

1. The calculation of the energy structure and transition intensities of impurity ions remains one of the main problems of the theoretical study of defects in crystals.[1] This is mainly because they strongly affect the physical properties of diverse substances and because they are therefore widely used in practice. They are also of theoretical interest in themselves, since they can serve as model systems when describing the many-electron defect structure of condensed substances. Among impurity ions, specific features possessed by rare-earth ions,[2–4] are directed mainly toward the use of their optical properties (see, for example, Ref. 5). Ions of this group with a small number of electrons (holes) are especially important. Although they constitute many-electron systems with a complex energy structure, they are easy to describe. Therefore, they in turn can serve as model systems for the study of how the intracrystalline electric field affects them. Most importantly, the Pr^{3+} ion studied in this paper, with two electrons in the *f* shell, is included among such ions.

Various methods are used to calculate the impurity-ion energy structure that describes the absorption and luminescence spectra and other properties of doped crystals:[6,7] MO LCAO, crystal-field theory, the X-α scattered-wave method, various semiempirical methods, and other approaches that are some combination or modification of the methods mentioned above. Because of the complexity and unwieldiness of the problem (its many-atom, many-electron, and multilevel nature, the relaxation of atoms close to the defect, and the presence of various kinds of compensators and complexes), as well as the use of numerous approximations even in ''first-principles'' calculations, it is rarely possible to achieve good agreement between theory and experiment. In this connection, it is worth while to consider simple methods that contain the minimum number of theoretical parameters and at the same time adequately describe the main forms of interaction in the defect structure of crystals. One such approach, used in this paper, was proposed and implemented in Ref. 8, which showed, in particular, that the energy structure of a rare-earth impurity ion with a definite electron configu-

ration can be described by means of a relatively simple approximation of the wave function.

When foreign atoms are introduced into a crystal, a local deformation of the lattice occurs, causing it to expand (compress) close to the defect. This must be taken into account in order to adequately explain the local physical properties. In this connection, a number of papers have been devoted to this question and, in particular, to the determination of the new equilibrium positions of the main lattice ions close to the defect by minimizing the energy. The following have been considered: mixed alkali-halide crystals,[9] alkaline-earth oxides[10] and halides,[11–14] and also semiconductors.[15,16] Various impurity ions, including rare-earth ions, were considered in this case. At the same time, a number of papers (for example, Ref. 11), have noted that estimates of the ion displacements made by different authors for the same substances disagree. Moreover, it has been noted that there is disagreement not only in the quantitative results but even in the qualitative results, including the displacement directions. All this only underlines the complexity of the problem. In this connection, the inverse problem (as an alternative to direct calculations of the new equilibrium positions) is of some interest. Namely, one can consider how the energy structure and the other characteristics depend on a given relative placement of the atoms and can estimate these displacements as the parameters of the theory by comparing theory and experiment. It is important in this case that the displacements be given and that the energy terms depending on them be determined in terms of the same concept. This paper attempts such a treatment.

2. The Pr^{3+} ion is chosen as the object of the study (a sort of probe) for the following two reasons: First, as indicated in the introduction, it is of methodological interest. Second, studies of this ion, especially recent ones, have established that it strongly affects the physical properties of the crystals into which it is introduced. This has made it possible to use it for numerous practical purposes.

Thus, crystals with high concentrations of Pr^{3+} can be used as high-gain media and are therefore suitable for creating compact surface lasers and microlasers.[17] Doping with Pr^{3+} promotes the accumulation of the light sum by luminophores and the amplification or quenching of the luminescence caused by other dopants. The use of Pr^{3+} promotes the creation of an active medium for multicolor lasers in the visible range.[17] New lasing possibilities have recently been found for it, and, in particular, a powerful praseodymium laser has been developed. Crystals doped with Pr can be used as photoluminophors and can convert UV into visible light to create powerful sources of modulated radiation. An amplifier with high output power has been based on a praseodymium-doped fluoride fiber. Intensive studies of the optical properties of this promising ion are continuing.[4]

There is equal interest in the nonoptical properties of the Pr^{3+} ion, which are appreciably different from those of other rare-earth ions. We should point out, most importantly, that Pr^{3+} ions suppress superconductivity in HTSCs and strongly affect T_c by decreasing it as their concentration is increased. They possess specific properties, including anomalous magnetic and other properties, inherent only in them. In this case, there is a correlation between their presence and the characteristic manifestation of their anomalous properties, on one hand, and the suppression of HTSCs on the other. Pr^{3+} ions possess specific transport properties and cause a characteristic metal–insulator transition and a dimensional effect. This list of properties inherent only in Pr^{3+} ions could be extended.

Rare-earth ions are usually found in a low-symmetry neighborhood; this is associated not only with the low spatial symmetry of many crystals but also with the presence of compensators close to the impurity ion. However, the ion is sometimes found in a cubic neighborhood; these are called centers with nonlocal compensation.[13,14,18–21] This produces a simpler level system and facilitates the study of how various factors determine the character and magnitude of the splitting of the free-ion terms. Therefore, this paper discusses a crystal of cubic symmetry containing the Pr^{3+} ion in cubic surroundings, while specific calculations are carried out for alkaline-earth halides, in which the praseodymium ion replaces the metal. This group of crystals, and in particular the fluorides, are chosen because they often serve as model objects when impurity ions are studied[21] and have been widely used in laser technology.[5] However, they are also of interest from a theoretical viewpoint, since they are the most ionic compounds,[22] in which crystal-field theory with the point-charge model is most applicable.[7,23,24]

3. In general, according to group theory, the thirteen terms of the free Pr^{3+} ion are split in an intracrystalline electric field of cubic symmetry into forty levels E_i of the impurity ion. The E_i levels have been calculated in terms of crystal-field theory.[7,25] The interaction-energy operator of the ion with intracrystalline field V was chosen as a perturbation operator, and the corrections ΔE_i to the atomic levels were found in first-order perturbation theory. The latter, using symmetry theory,[26] were expressed in terms of the minimum number of matrix elements (MEs) of potential V on many-electron atomic functions. These MEs in turn were expressed

in terms of the three diagonal MEs $V_{m,m}$ (m is the orbital momentum quantum number) of potential V on the single-electron functions. Finally, the MEs $V_{m,m}$, given in a single coordinate system, were expressed in terms of a linear combination of the MEs of the potential V^k of an individual ligand, given in the coordinate system whose z axis coincides with the direction to the kth ligand.[27] As a result, the expressions for all the ΔE_i were written as a linear combination of the MEs $V^k_{m,m'}$ of potential V^k. The coefficients of these combinations are the numbers and angles that characterize the direction to the kth ion. The MEs $V^k_{m,m'}$ are identical within the coordination sphere and depend only on the distance R_k to the kth ion. The resulting expressions have a general character and are independent of the form of potentials V and V^k.

For specific calculations, a radial function of the form[8]

$$R_{4f} = 2/(3\sqrt{35})\alpha^{9/2} r^3 \exp(-\alpha r) \qquad (1)$$

is chosen for the initial single-electron wave function, where α is the Slater orbital parameter, and the point-charge approximation is chosen as potential V. In this case, the MEs $V^k_{m,m'}$ are computed in analytical form, so that all the ΔE_i are explicitly expressed in terms of parameters γ, q_k, α and R_k, where q_k is the charge of the kth ligand (in units of the electronic charge e), γ is the characteristic ionicity level (for purely ionic crystals, $\gamma = 1$); $\Delta E_i = (E_0 + k_i A + l_i B)$, where $E_0 = -2\alpha \Sigma_k F_0(x_k) q_k$ is the overall shift of the levels,

$$A = (\alpha/44)\sum_k q_k f_4^k F_4(x_k),$$

$$B = (25\alpha/1716)\sum_k q_k f_6^k F_6(x_k), \qquad x_k = \alpha R_k,$$

$$f_4^k = 35n_k^4 - 30n_k^2 + 3,$$

$$f_6^k = 231n_k^6 - 315n_k^4 + 105n_k^2 - 5, \qquad n_k = \cos\theta_k,$$

and θ_k is the polar angle of the direction from the impurity ion (the origin of coordinates) to the kth ligand ion. The expression for $F_n(x)$ includes direct and inverse polynomials in x in combination with $\exp(-2x)$. For simplicity, they are not shown here (see Ref. 8). Coefficients k_i and l_i are numbers that characterize a specific level. Thus, the $^3H_4$ ground term of the free ion is split in the crystal field into four levels: E, T_1, A_1, and T_2 (using the usual notation of irreducible representations). The values for them are, respectively: $-28/33$, $-4/33$, $26/33$, and $-14/33$ for k_i; and $-272/165$, $1088/825$, $-68/165$, and $68/825$ for l_i.

The lattice sum (over k) was carried out twice: directly over the coordination spheres and (as a control) over cubes, using the method of fractional charges,[28] with each cube containing fourteen positive and eight negative charges.

The lattice deformation (the relaxation of the atoms of the surroundings) is allowed for by varying R_k close to its equilibrium position R_k^0, corresponding to the ideal lattice. Assuming that $R_k = a\rho_k$, where a is the lattice constant (equal to 10.32 a.u. for CaF_2, Ref. 29), we get $x_k = a\alpha\rho_k$, $\rho_k = \rho_k^0 + \Delta\rho_k$. Because the lattice can be either compressed or expanded close to the impurity ion, parameter $\Delta\rho_k$ was varied from -0.03 to 0.03 for all the coordination spheres.
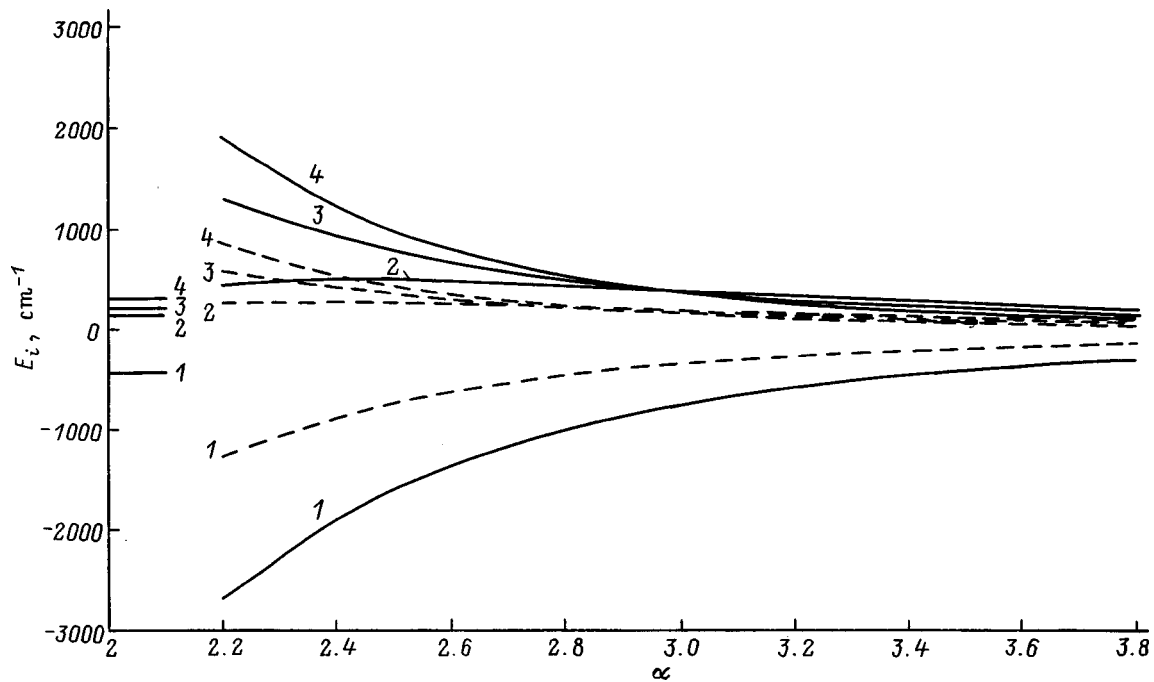
FIG. 1. Dependence of the energy levels on parameter α. The solid curves are for $\Delta\rho_1 = -0.03$, and the dashed curves are for $\Delta\rho_1 = 0.03$. The experimental values here and in the other figures are plotted on the vertical axis. The following notation is introduced here and in Figs. 2 and 4: T_2—1, A_1—2, T_1—3, E—4; $\gamma = 1$.

This interval covers all the fixed displacements of the ions calculated earlier, but is significantly less than the distance between the nearest ions in the undeformed lattice.

4. For brevity, we show below only the results of the calculation of the energy structure of the $^3H_4$ ground atomic term in the crystal (i.e., the E, T_1, A_1, and T_2 levels) as a function of various parameters, including the displacements of the ligand ions from the equilibrium position in an ideal lattice. Figure 1 shows the dependence of the energy levels on parameter α for limiting values of $\Delta\rho_1$ ($\Delta\rho_k = 0$ if $k \neq 1$). The E_i values corresponding to other $\Delta\rho_1$ values are included between the limiting curves. In particular, the $E_i(\alpha)$ curves for $\Delta\rho_1 = 0$ are approximately centered between the curves for $\Delta\rho_1 = 0.03$ and $\Delta\rho_1 = -0.03$. It can be seen from Fig. 1 that, in the region before the A_1, T_1, and E levels cross over (at small α values), where their order corresponds to the experimental data,[13,30] it is quite impossible to match theory and experiment for any α values if $\Delta\rho_k = 0$. Although the relative distance between the A_1, T_1, and E terms in the region of $\alpha = 2.4$–2.7 is close to the experimental value, this entire group of terms is separated from the T_2 term by about a factor of 2 greater than the experimental value. For $\Delta\rho_1 > 0$, the agreement with experiment is improved.

The contribution of the displacements of the atoms of each kth coordination sphere $\Delta\rho_{i \neq k} = 0$ to the positions of the levels is plotted in Fig. 2. It be seen from this that the main contribution comes from the displacement of the atoms of the first sphere. The contributions of the second and third spheres are of the same order of magnitude (the curves virtually merge). The displacements of the atoms also have an effect on the crossover point α_c of the levels. This is illus-

trated in Fig. 3 in more detail, taking into account the contribution of each coordination sphere.

Let us compare the results of our computations with the results of calculations from first principles. In order to do this, we substitute into our equations the results of Ref. 13 for the equilibrium positions of the atoms of the closest four spheres, calculated by the method of Ref. 14. The results of the calculations are shown in Fig. 4. As in the case of $\Delta\rho_1 = 0.03$, $\Delta\rho_{k \neq 1} = 0$ (Fig. 1), the agreement with experiment was improved as compared to neglecting the displacements of the ions. The results of our calculations thus qualitatively confirm the conclusions of Refs. 13 and 14 that the lattice expands when a Pr^{3+} ion is introduced. It should be pointed out here that all the calculations given here and above were carried out for the case $\gamma = 1$, i.e., for ideal ionic compounds. However, even for fluorides, the most ionic compounds, the effective charge of the fluorine, as shown in Ref. 22, equals 0.8. Taking this into account further improves the agreement with experiment (see, for example, Fig. 4).

Recalling that, as shown by the analysis, the displacement of the ions of the first coordination sphere has the largest effect on the energy structure, we determined the region of the optimum values of $\Delta\rho_1$ and α that best satisfy the experimental data for $\gamma = 0.8$: $(\Delta\rho_1)_{opt} = 0.025 \pm 0.005$ for $\alpha_{opt} = 2.62 \pm 0.02$. These were compared with experiment for all three distances between the E, T_1, A_1, and T_2 terms. We should emphasize that $(\Delta\rho_1)_{opt}$ depends on the values of the chosen parameter α_{opt}; the larger is α, the smaller is $(\Delta\rho_1)_{opt}$. The resulting $(\Delta\rho_1)_{opt}$ value was close to that obtained in Ref. 13 by minimizing the energy. It is noteworthy that the value of $\alpha_{opt} = 2.62$ was smaller than the value $\alpha = 4.83$ obtained by using the approximation of the exact ini-
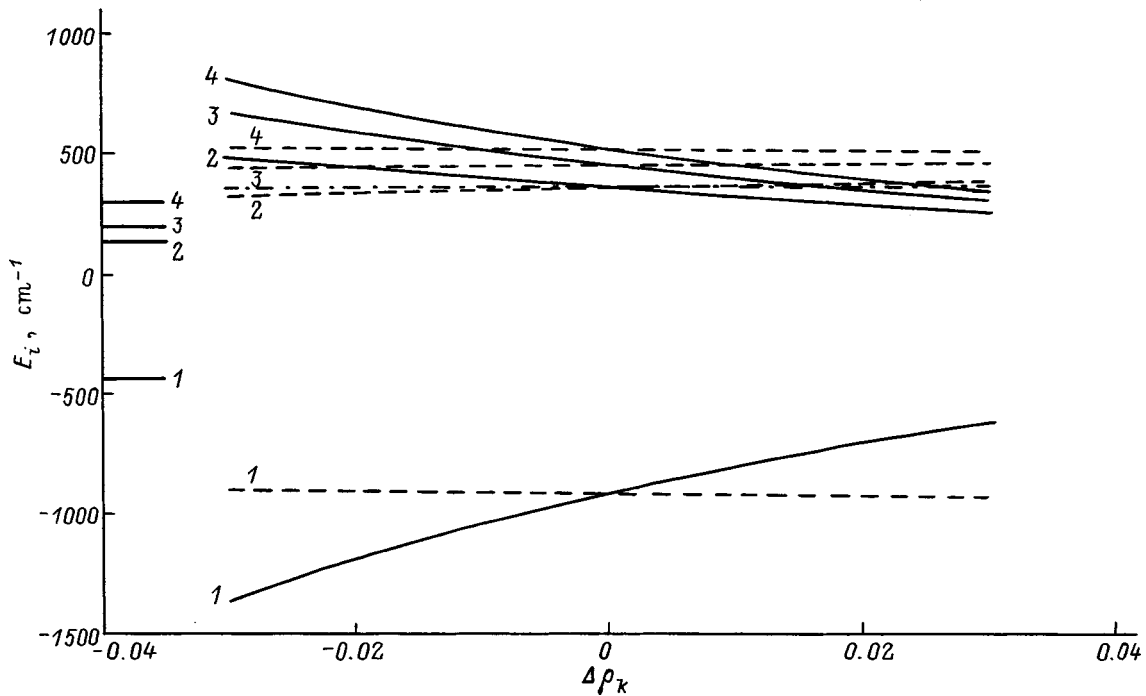
FIG. 2. Dependence of the energy levels on the displacements $\Delta\rho_k$ of the atoms for $\alpha=2.6$. The solid curves correspond to $k=1$, the dashed curves to $k=2$, and the dot–dashed curves to $k=3$. Displacements of the atoms of the fourth sphere within the indicated limits have no effect on the position of the levels; $\gamma=1$.

tial wave function of a free Pr^{3+} ion[31] in Eq. (1).[8] This difference is caused by the ligand field and is the so-called nephelauxetic shift.[1,2]

It thus follows from the above treatment that the ionic displacements can be regarded as theoretical parameters that can be directly determined from experiment. Moreover, this approach makes it possible to estimate the magnitude of the nephelauxetic shift from the α_{opt} data. It also follows from the essence of the work that the above treatment can be applied to other impurity ions and halides, as well as to alkaline-earth oxides with rare-earth impurity ions. Considering the relative simplicity of the method, it can be assumed
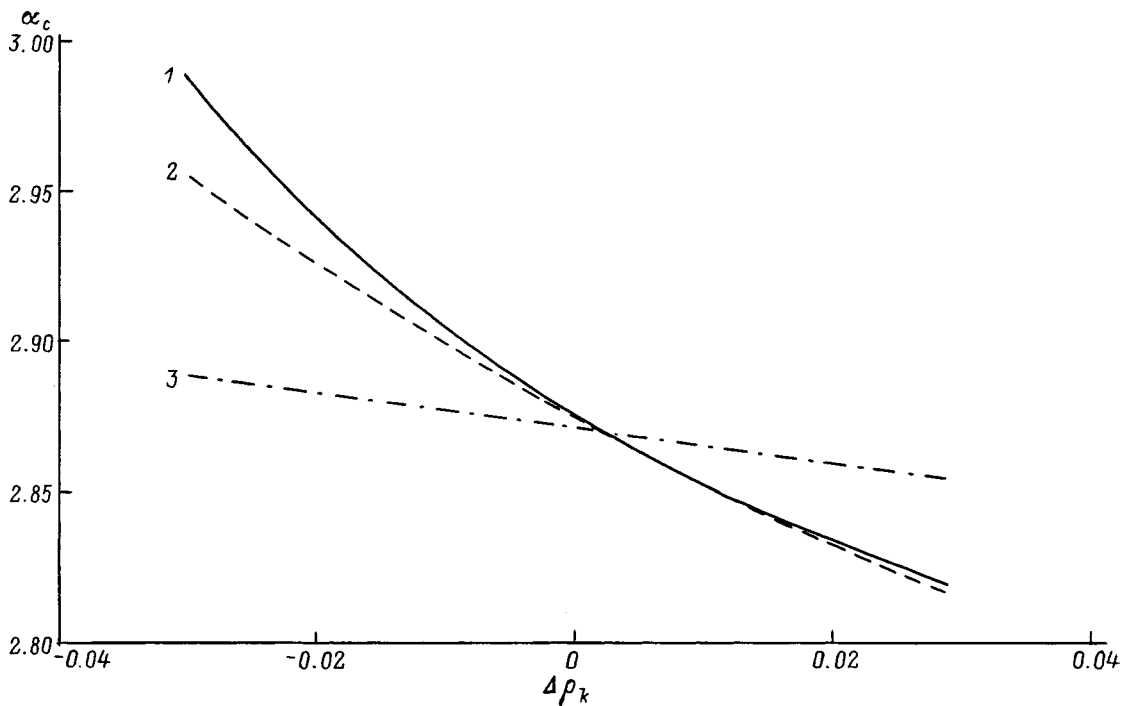
FIG. 3. Dependence of parameter α_c, corresponding to the point where the levels cross over, on the displacements $\Delta\rho_k$ of the atoms (for $\Delta\rho_i=0$, if $i\neq k$). The numbers on the curves correspond to the k values.
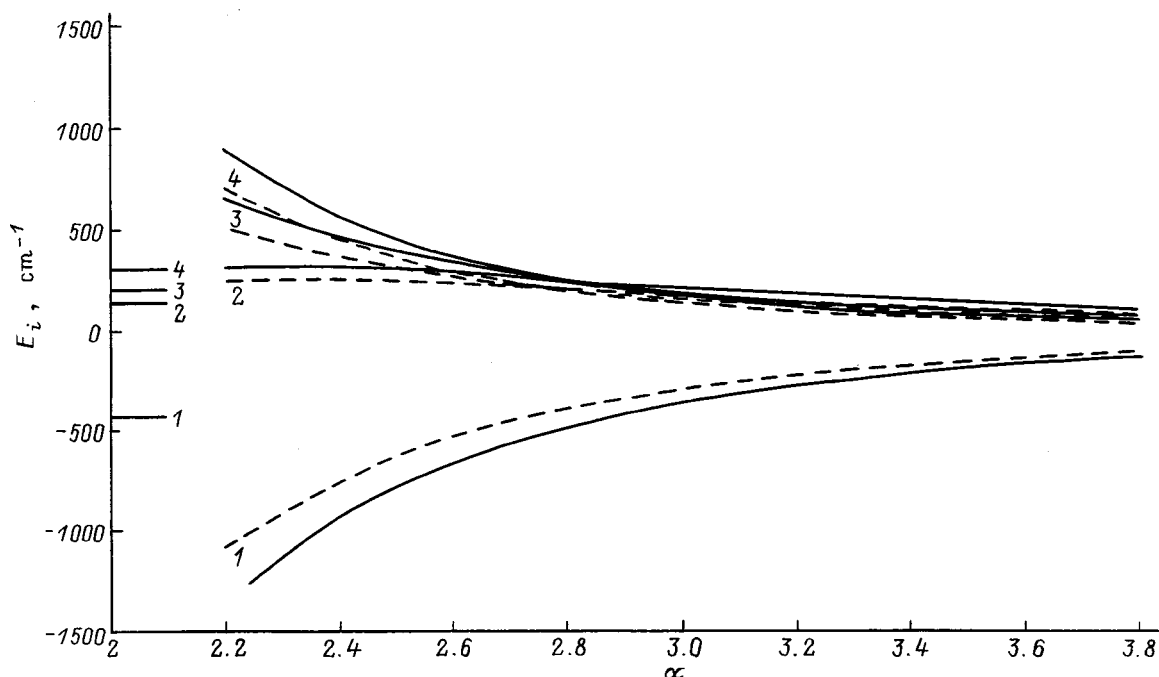
FIG. 4. Dependence of the energy levels on parameter α for $\Delta\rho_1=0.0254$, $\Delta\rho_2=0.0172$, $\Delta\rho_3=-0.0041$, $\Delta\rho_4=0.0044$.[13] The solid curves correspond to $\gamma=1$, and the dashed curves to $\gamma=0.8$.

in this case that it can be used to interpret the experimental data.

The authors express their gratitude to their coauthors on the preceding papers, L. V. Artamonov and A. A. Klimov, for useful collaboration that significantly promoted the completion of this work.

*⁾E-mail: roitsin@roklar.semicond.kiev.ua

[1] N. A. Kulagin and D. T. Sviridov, *Methods of Calculating the Electronic Structure of Free and Impurity Ions* [in Russian] (Nauka, Moscow, 1986).

[2] E. F. Kustov, G. A. Bondurkin, É. N. Murav'ev, and V. P. Orlovskiĭ, *Electronic Spectra of Compounds of the Rare-Earth Elements* [in Russian] (Nauka, Moscow, 1981).

[3] B. Z. Malkin, in *Spectroscopy of Solids Containing Rare Earth Ions*, Vol. 4, edited by A. A. Kaplyanskii and R. M. Macfarlane (Elsevier Sci. Publ., 1987), p. 15.

[4] A. A. Kornienko, ''Differentiated influence of excited configurations on the multiplets of the rare-earth ions,'' Author's abstract of dissertation for the doctorate of physicomathematical sciences, Institute of Molecular and Atomic Physics, Academy of Sciences of Belarus, Minsk, 1997.

[5] A. A. Kaminskiĭ and B. M. Antipenko, *Multilevel Functional Schemes of Crystal Lasers* [in Russian] (Nauka, Moscow, 1989).

[6] A. B. Roĭtsin, Fiz. Tekh. Poluprovodn. **8**, 3 (1974) [Sov. Phys. Semicond. **8**, 1 (1974)].

[7] I. B. Bersuker, *Electronic Structure and Properties of Coordination Compounds* [in Russian] (Khimiya, Leningrad, 1986).

[8] A. A. Klimov, A. B. Roĭtsin, M. M. Chumachkova, and L. V. Artamonov, Ukr. Fiz. Zh. **40**, 866 (1995).

[9] B. G. Dick and T. P. Das, Phys. Rev. **127**, 1053 (1962).

[10] T. P. Das, Phys. Rev. A **140**, 1957 (1965).

[11] C. Fainstein, M. Tovar, and C. Ramos, Phys. Rev. B **25**, 3039 (1982).

[12] M. Tovar, C. Ramos, and C. Fainstein, Phys. Rev. B **28**, 4813 (1983).

[13] M. P. Davydova and A. L. Stolov, Fiz. Tverd. Tela **17**, 329 (1975) [Sov. Phys. Solid State **17**, 203 (1975)].

[14] Z. I. Ivanenko and B. Z. Malkin, Fiz. Tverd. Tela **11**, 1859 (1969) [Sov. Phys. Solid State **11**, 1498 (1970)].

[15] M. Schefler, J. P. Vigneron, and G. B. Bachelet, Phys. Rev. B **31**, 6541 (1985).

[16] F. Bechstedt and W. A. Harrison, Phys. Rev. B **39**, 5041 (1989).

[17] A. M. Tkachuk, in *Spectroscopy of Crystals* [in Russian], edited by A. A. Kaplyanskiĭ (Nauka, Leningrad, 1989).

[18] V. Ranon J. Phys. Chem. Solids **25**, 1205 (1964).

[19] C. D. Cleven, S. H. Lee, and J. C. Wright, Phys. Rev. B **44**, 23 (1991).

[20] I. B. Aĭzenberg, B. Z. Malkin, and A. L. Stolov, Fiz. Tverd. Tela **13**, 2566 (1971) [Sov. Phys. Solid State **13**, 2155 (1972)].

[21] A. A. Kaplyanskiĭ and A. I. Ryskin, in *Spectroscopy of Crystals* [in Russian], edited by A. A. Kaplyanskiĭ (Nauka, Leningrad, 1983).

[22] K. Lesniak, Acta Phys. Pol. A **75**, No. 1, 169 (1989).

[23] R. Boyn, Phys. Status Solidi B **148**, 11 (1988).

[24] W. F. Krupke, Phys. Rev. **1451**, 325 (1966).

[25] N. V. Eremin, in *Spectroscopy of Crystals* [in Russian], edited by A. A. Kaplyanskiĭ (Nauka, Leningrad, 1989).

[26] A. B. Roĭtsin, *Some Applications of the Theory of Symmetry in Microwave Spectroscopy* [in Russian] (Nauk. Dumka, Kiev, 1973).

[27] A. B. Roĭtsin and L. A. Firshteĭn, Theor. Exp. Chem. **2**, 747 (1966).

[28] C. Kittel, *Introduction to Solid State Physics* (Wiley, New York, 1976; Fizmatgiz, Moscow, 1978).

[29] *Fundamental Properties of Inorganic Fluorides. A Handbook* [in Russian], edited by N. P. Galkin, (Atomizdat, Moscow, 1976).

[30] B. M. Tissue and J. C. Wright, Phys. Rev. B **36**, 9781 (1987).

[31] K. N. R. Taylor and M. Darby, *Physics of Rare-Earth Compounds* (Chapman & Hall, London, 1972; Mir, Moscow, 1974); N. V. Starostin and G. A. Sizova, *Spectroscopy of Crystals* [in Russian] (Nauka, Moscow, 1985), p. 70.

Translated by W. J. Manthey

Conductivity of ionic crystals when they are irradiated by picosecond electron beams

B. P. Aduev and V. N. Shvaĭko

Kemerovo State University, 650043 Kemerovo, Russia
(Submitted October 6, 1998)
Fiz. Tverd. Tela (St. Petersburg) **41**, 1200–1203 (July 1999)

This paper discusses the pulsed electron conductivity σ of KCl, KBr, and NaCl crystals when they are excited by an electron beam (0.2 MeV, 50 ps) with current densities in the interval $j = (30–10^4)$ A/cm^2. It is shown that the lifetime of the electrons in the conduction band is $\tau \ll 100$ ps. To explain the experimental $\sigma(j)$ dependences, a model is proposed that includes electron capture by structural defects and stable radiation defects at low excitation densities and electron capture predominantly by unstable radiation defects generated by the excitation pulse at high excitation densities. © *1999 American Institute of Physics.*
[S1063-7834(99)01407-0]

The investigation of radiation-induced electron conductivity of ionic crystals when they are excited by pulsed beams of high-density electrons is an informative method for studying primary energy-dissipation and radiation-damage processes.

A number of papers, summarized in Ref. 1, have discussed the pulsed conductivity of ionic crystals when they are excited by dense beams of electrons of nanosecond pulse width. The authors showed that, under the experimental conditions, the pulse of conduction current follows the excitation pulse with no lag, with the dependence of the conduction amplitude on the excitation density having a complex character. To explain the results, the authors proposed models of two new forms of nonequilibrium conduction. The first of these is associated with conduction-band electrons with energy 1–10 eV in the process of relaxing to the bottom of the band—so-called ''high-energy conductivity.''[1,2] The second is associated with thermalized electrons in the field of the trapping and recombination centers—so-called ''intracenter conductivity.''[3] Both forms of conductivity, according to the models, have a picosecond relaxation time.

However, the nanosecond time resolution used in studying the elementary stages of the radiation damage is clearly inadequate. It is well known, for example, that autolocalized excitons and F centers are formed in alkali-halide crystals in a picosecond time range.[4–8] In this connection, to discriminate the primary processes, excitation pulses of picosecond width must be used in combination with apparatus having good time resolution. The use of excitation pulses with a width of $\tau_p \sim 50$ ps in optical and electrophysical studies has shown that the charge-carrier lifetime before capture or recombination for various objects can lie either in the interval 0.1–1 ns (for example, CsI, Refs. 9–11, and Al$_2$O$_3$, Ref. 12) or in the region $\ll 100$ ps (for example, crystals with a NaCl lattice[8–10]).

Therefore, the results of studies with nanosecond excitation[1–3] used as the basis of fundamental conclusions concerning the presence of two new forms of conductivity need to be experimentally checked with substantially better time resolution. This would allow the possible contribution of subnanosecond processes to be discriminated and would make it possible to more accurately interpret the results.

To solve this problem, we studied the conductivity of crystals with a NaCl lattice when they are excited with 50-ps electron pulses.

1. TECHNIQUE AND EXPERIMENTAL RESULTS

Pure single crystals of KCl, KBr and NaCl were studied, grown from grade-VHP salt by the Kyropoulos method. The samples had dimensions of $10 \times 10 \times 3$ mm. A cylindrical crater 2 mm in diameter was drilled in the center of the sample in such a way that the thickness of the bottom was 50 μm, considerably less than the path length of electrons in the crystal; this is necessary for homogeneity of the excitation. Platinum contacts were sputter-coated into the crater and from the other side.

The sample was mounted in a coaxial cell and irradiated with an electron beam through a collimator 1 mm in diameter. An electron accelerator with a discharger–peaker,[13] having a pulse width of 50 ps and a maximum electron energy of 0.2 MeV, was used as the irradiation source. The design of the measurement cell makes it possible to vary the distance between the sample and the accelerator diode, and this allows the excitation density to be varied in the range $(30–10^4)$ A/cm^2. The time resolution of the measurement channel is 150 ps and is determined by the limiting frequency of an S7-19 oscilloscope with a signal-delay line to the scan-trigger time. The experiments were carried out at room temperature.

The structure of the conduction-current pulse depends on the prehistory of the sample and the excitation current density. This is clearly demonstrated by the oscilloscope tracings for the KBr crystal shown in Fig. 1. If the crystal was not preirradiated, the conduction-current pulse has two components when it is excited with a low-density electron beam ($j \sim 30$ A/cm^2): an inertialess component and a component that relaxes with $\tau \sim 1$ ns (oscilloscope tracing a in Fig. 1). To the extent that the sample is irradiated, the contribution of the inertial component decreases, and essentially only the
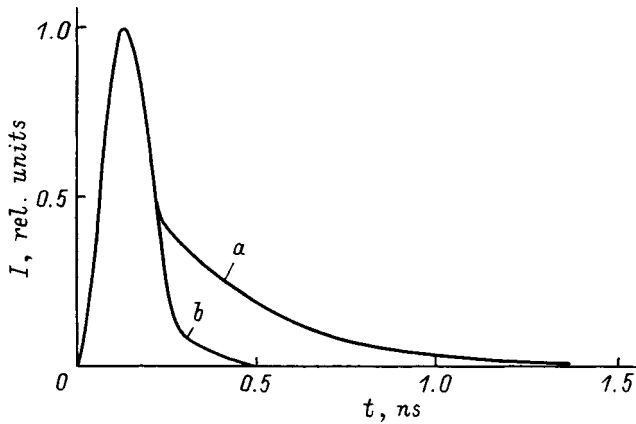
1094   Phys. Solid State **41** (7), July 1999

B. P. Aduev and V. N. Shvaĭko

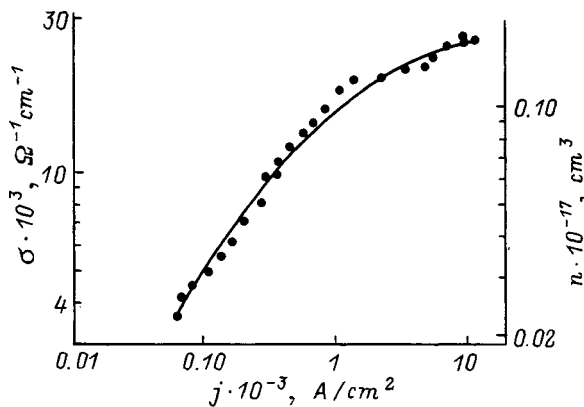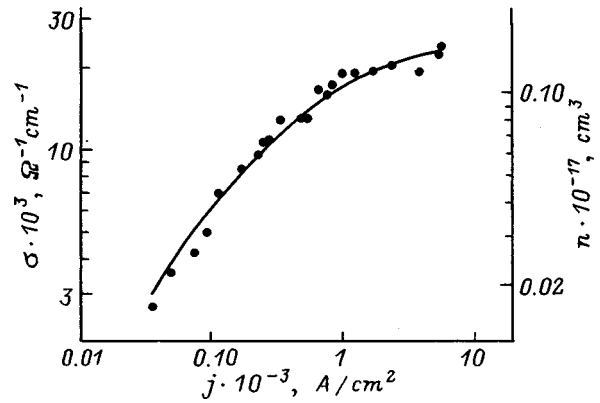FIG. 1. Relaxation of the conduction current in KBr for $j = 30$ A/cm^2 (a) and for $j = 100$ A/cm^2 (b).

FIG. 3. Dependence of conductivity σ and concentration n on the current density j of the beam in KBr.

inertialess component remains (oscilloscope tracing b in Fig. 1). For current densities of $j \geqslant 100$ A/cm^2, the contribution of the inertial component is virtually negligible even in the first irradiation pulses. In the NaCl and KCl crystals, no inertial component of the conduction-current pulse was detected with the excitation densities used here.

The volt–ampere characteristics of the test crystals, measured at the maximum of the conduction-current pulse, are linear in fields up to 5×10^4 V/cm. The slope of the volt–ampere characteristic was used to calculate the resistance of the sample and the conductivity σ. The experiment was carried out in a wide range of excitation densities on a large number of samples.

The following regularities were detected. With irradiation densities of $j < 10^3$ A/cm^2, the increase of σ with increasing j can be approximated by the power law

$$\sigma \sim j^\delta. \tag{1}$$

In this case, the exponent δ lies within the limits (0.5–0.65) for various crystals and depends on the specific sample and the preirradiation dose. As j increases, the increase of the conductivity sharply slows down and reaches a virtually constant value for all samples, beginning with certain j values for all the test samples. Typical results for KCl, KBr, and NaCl are shown in Figs. 2–4. It should be pointed out that

the $\sigma(j)$ dependence is very reproducible for a specific sample after a preirradiation dose ($\geqslant 100$ pulses). Figures 2–4 show just such curves.

2. DISCUSSION OF THE RESULTS

A. Low excitation densities

The structure of the conduction-current pulse in the KBr crystal for low irradiation densities shows that the conduction is associated with thermalized conduction-band electrons whose concentration is commensurate with that of preradiation structural defects (uncontrolled impurities) that are capture centers for electrons. The fast component of the conduction in this case can be associated with bimolecular electron–hole recombination (V_k centers), while the inertial component is associated with electron capture on structural defects. As the sample is irradiated, stable radiation defects build up to some steady-state concentration that exceeds the concentration of structural defects. The lifetime τ_e of the conduction-band electrons before they are captured on stable radiation defects then becomes less than τ_p, and the observed oscilloscope tracing (Fig. 1b) includes recombination processes with the rate constant

$$\alpha = \nu S, \tag{2}$$

FIG. 2. Dependence of conductivity σ and concentration n on the current density j of the beam in KCl.
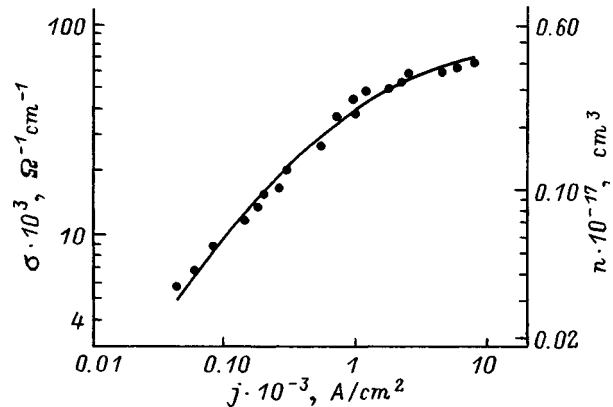

FIG. 4. Dependence of conductivity σ and concentration n on the current density j of the beam in NaCl.

where ν is the thermal electron velocity and S is the $e-V_k$-recombination cross section, and capture processes on the defects with the rate constant

$$\beta = \nu \Sigma S_i N_i, \tag{3}$$

where the S_i and N_i are the effective capture cross sections and concentrations of stable radiation defects and structural defects. The character of the $\sigma(j)$ dependence on the increasing sections (Figs. 2–4) is determined by just these two processes, with the coefficient δ in Eq. (1) being determined by the ratio of the contributions of the processes named above.

B. High excitation densities

It is very difficult to explain the $\sigma(j)$ dependence with increasing excitation density. A weak dependence with $\delta \approx (0.1-0.3)$ in a definite dose interval on the same objects was observed by Vaĭsburd et al.[3] for excitation by electron beams of nanosecond pulse width. To explain this, they proposed the ''intracenter conductivity'' model mentioned above. This effect is expressed more clearly in our experiments: σ is virtually independent of j (Figs. 2–4). To explain this result, we propose another, in our view, simpler model, which is as follows: It is well known that, with pulsed excitation, unstable radiation defects (electron and hole centers) are generated at the instant of irradiation. These relax within nano- and microseconds to $\sim(2-5)\%$ of the initial value per pulse, which corresponds to the stable defects.[14,15] We assume that, for large excitation densities, the electron lifetime in the conduction band is predominantly controlled by capture at just these defects at the instant of the irradiation pulse. The rate constant of this process is

$$\gamma = \nu S N_r, \tag{4}$$

where S and N_r are the effective capture cross section and concentration of unstable defects. It is also assumed that the yield of these defects is proportional to the dose per pulse. In this case, we can write

$$N_\tau = k G \tau_p, \tag{5}$$

where $k \leqslant 1$ is a coefficient, and G is the generation rate of electron–hole pairs. According to Ref. 16,

$$G = \frac{jE}{(1.5-2)E_q d} = Aj, \tag{6}$$

where E is the effective energy of the electrons in the beam, and E_q is the band gap of the test crystal (under our experimental conditions, $A \approx 10^{25}$ cm^{-1}sec$^{-1}A^{-1}$). Using Eqs. (2)–(6), the balance equation for the conduction electrons can be written in the form

$$\frac{dn}{dt} = Aj - \alpha n^2 - (\beta + Bj)n, \tag{7}$$

where

$$B = k \tau_p A \nu S. \tag{8}$$

Since the conduction pulse follows the excitation pulse with no lag, Eq. (7) can be solved by using the quasi-steady-

TABLE I. Values used for the parameters.

Material	KCl	KBr	NaCl
α, 10^{-6} cm^3/sec	(31 ± 5)	(18 ± 4)	(4 ± 1)
β, 10^{11} sec^{-1}	(1.6 ± 0.4)	(1.4 ± 0.4)	(1.2 ± 0.3)
B, 10^8 cm^2 sec^{-1} A^{-1}	(1.12 ± 0.02)	(1.21 ± 0.03)	(0.42 ± 0.01)
S, 10^{-12} cm^2	1.7	1	0.2
τ, 10^{-12} sec	6	7	8

state approximation. However, it follows even from the form of Eq. (7) that the extrapolation of n to high excitation densities gives $n = A/B = $ const. The solution of Eq. (7) has the form

$$n = \frac{1}{2\alpha}(\beta + Bj)\left\{\left[1 + \frac{4\alpha Aj}{(\beta + Bj)^2}\right]^{1/2} - 1\right\}. \tag{9}$$

Using the expression

$$n = \sigma/e\mu, \tag{10}$$

where e is the charge of the electron and μ is the mobility, along with the experimental values of σ and literature values of μ,[17,18] n was calculated from Eq. (9). The solid curves in Figs. 2–4 are constructed from Eq. (9), and parameters α, β, and B for the test crystals are indicated in Table I.

Let us analyze the resulting values of the microscopic parameters α and β. We use Eq. (2) and the value $\nu = 1.75 \times 10^7$ cm/sec at $T = 300$ K to estimate the effective electron–hole recombination cross section S and $1/\beta = \tau$, the electron-capture time on stable radiation defects (both indicated in Table I).

The reasonable values of the microscopic parameters α and β calculated from the experimental data are evidence in favor of the proposed model. We should also point out that, in the range of excitation densities studied here, no high-energy electron conduction[1,2] is detected under the conditions of the experiment.

[1] D. I. Vaĭsburd, B. N. Semin, É. G. Tavanov, S. B. Matlis, I. N. Balychev, and G. I. Gering, *High-Energy Solid-State Electronics* [in Russian] (Nauka, Novosibirsk, 1982).

[2] D. I. Vaĭsburd, Izv. Vyssh. Uchebn. Zaved. Fiz. No. 12, 109 (1996).

[3] D. I. Vaĭsburd, G. A. Mesyats, V. L. Naminov, and É. G. Tavanov, Dokl. Akad. Nauk SSSR **265**, 1113 (1982) [Sov. Phys. Dokl. **27**, 625 (1982)].

[4] Y. Suzuki, H. Ohtani, S. Taragi, and M. Hirai, J. Phys. Soc. Jpn. **50**, 3537 (1981).

[5] Y. Suzuki, M. Okumura, and M. Hirai, J. Phys. Soc. Jpn. **47**, 184 (1979).

[6] R. T. Williams, J. N. Bradford, and W. L. Fast, Phys. Rev. B **12**, 7038 (1978).

[7] R. T. Williams, B. B. Graig, and W. L. Fast, Phys. Rev. Lett. **52**, 1709 (1984).

[8] É. D. Aluker, V. Z. Gorbenko, R. G. Deĭch, G. S. Dumbadze, A. D. Tal'virskiĭ, and V. G. Shpak, Fiz. Tverd. Tela **28**, 3154 (1986) [Sov. Phys. Solid State **28**, 1775 (1986)].

[9] B. P. Aduev, G. M. Belokurov, and V. N. Shvaĭko, Fiz. Tverd. Tela **37**, 2537 (1995) [Phys. Solid State **37**, 1392 (1995)].

[10] B. P. Aduev, A. V. Igolinskiĭ, and V. N. Shvaĭko, Fiz. Tverd. Tela **38**, 947 (1996) [Phys. Solid State **38**, 525 (1996)].

1096   Phys. Solid State **41** (7), July 1999

B. P. Aduev and V. N. Shvaĭko

[11] B. P. Aduev, É. D. Aluker, V. V. Gavrilov, R. G. Deĭch, and S. A. Chernov, Fiz. Tverd. Tela **38**, 3521 (1996) [Phys. Solid State **38**, 1919 (1996)].

[12] B. P. Aduev, É. D. Aluker, and V. N. Shvaĭko, Fiz. Tverd. Tela **39**, 1995 (1997) [Phys. Solid State **39**, 1784 (1997)].

[13] B. P. Aduev and V. G. Shpak, Prib. Tekh. Éksp. No. 2, 49 (1990).

[14] Y. Kondo, M. Hirai, and M. Ueta, J. Phys. Soc. Jpn. **33**, 151 (1972).

[15] I. P. Denisov and V. Yu. Yakovlev, Izv. Akad. Nauk LatvSSR Ser. Fiz. Tekh. Nauk No. 3, 61 (1990).

[16] É. D. Aluker, D. Yu. Lyusis, and S. A. Chernov, *Electronic Excitations and Microwave Luminescence of Alkali-Halide Crystals* [in Russian] (Zinatne, Riga, 1979).

[17] R. K. Ahrenkiel and F. C. Brown, Phys. Rev. A **36**, 223 (1964).

[18] C. H. Seager and D. Emin, Phys. Rev. B **2**, 3421 (1970).

Translated by W. J. Manthey

A comparison of NMR spectral parameters of ^{47}Ti and ^{49}Ti nuclei in rutile and anatase

L. V. Dmitrieva, L. S. Vorotilova, I. S. Podkorytov, and M. E. Shelyapina

L. V. Grebenshchikov Institute of Silicate Chemistry, Russian Academy of Sciences, 199155 St. Petersburg, Russia
(Submitted October 26, 1998)

The paper reports on a measurement of the chemical-shift tensor for ^{47}Ti and ^{49}Ti in TiO$_2$ single crystals (rutile and anatase). The nature of the chemical shift anisotropy is discussed. © *1999 American Institute of Physics.* [S1063-7834(99)01507-5]

NMR has been employed actively in recent years to study new materials containing titanium oxides. In order to identify NMR spectra correctly, it is essential to know the NMR parameters for the principal crystal phases of TiO$_2$, rutile and anatase. We carried out earlier a study of single-crystal anatase and determined the tensors describing NMR spectra of the ^{47}Ti and ^{49}Ti nuclei, namely, those of the quadrupole coupling eQV_{ij} and the chemical shift δ_{ij}.[1] While the quadrupole splitting parameters for rutile were available in the literature,[2] data on the chemical shift were lacking. This work reports determination of the chemical-shift tensor of ^{49}Ti nuclei in rutile and compares the characteristics of spectra in the two crystals.

1. STRUCTURAL DATA

The structure of the two TiO$_2$ phases, the low-temperature anatase and the high-temperature rutile (the transition temperature 800–900 °C), is well studied. They belong to tetragonal symmetry, the space symmetry groups of anatase is $I4_1/amd$ and that of rutile, $P4_2/mnm$.[3] The unit-cell parameters were given by various authors, with refined data cited in Ref. 4. Both crystals are built of Ti^{4+}O$_6$ octahedra, which are distorted in the same way in the anatase and rutile, namely, there are two relatively long Ti–O bonds, i.e. the octahedron is extended along a crystallographic axis. In anatase, the long bonds are directed along [001], and in rutile they are aligned with [110] and [$\bar{1}$10]. The difference consists in the way in which the octahedra are joined and in the number of magnetically inequivalent sites, to wit, one in anatase, and two in rutile. The atomic coordinates are given in Refs. 5 and 6. An investigation[4] of thermal expansion of

these crystals revealed a stronger anisotropy in the thermal expansion coefficient of anatase compared to that of rutile. Table I lists the room-temperature structure parameters of the crystals.

2. EXPERIMENT

The experimental study of NMR spectra was carried out on single crystals grown at the ISC RAS.[7] The samples were parallelepiped shaped, with the long edge along the [001] direction. The side faces of the rutile crystal were identified by x-ray diffraction measurements as (110) and (1$\bar{1}$0). Orientation of the crystals in the magnetic field was based on their faces and refined by the pattern of the spectra.[1]

NMR spectra of the ^{47}Ti and ^{49}Ti nuclei were measured on a Bruker AM 500 spectrometer at a frequency of 28.2 MHz at room temperature using a 10-mm broad-band probehead. Both isotopes have close resonant frequencies if there are no quadrupole effects (for instance, in a liquid). In crystals, the position of the titanium isotope lines varies within a broad range because of large nuclear quadrupole moments: eQ (^{47}Ti) = 0.29 b, $I = 5/2$; eQ (^{49}Ti) = 0.24 b, $I = 7/2$. Because of the difficulties met in measuring the total spectrum, the side bands were not sought and the parameters were calculated based on the orientational dependence of the central line (the $1/2 \leftrightarrow -1/2$ transition).

The conditions for spectral measurements were chosen as follows: pulse duration 33 μs, delay time 1 s, accumulated counts ~1000. TiCl$_4$ was used as a reference for chemical shift determination. The shift was reckoned from the ^{47}Ti signal in the reference.

TABLE I. Room-temperature structure parameters of anatase and rutile crystals.

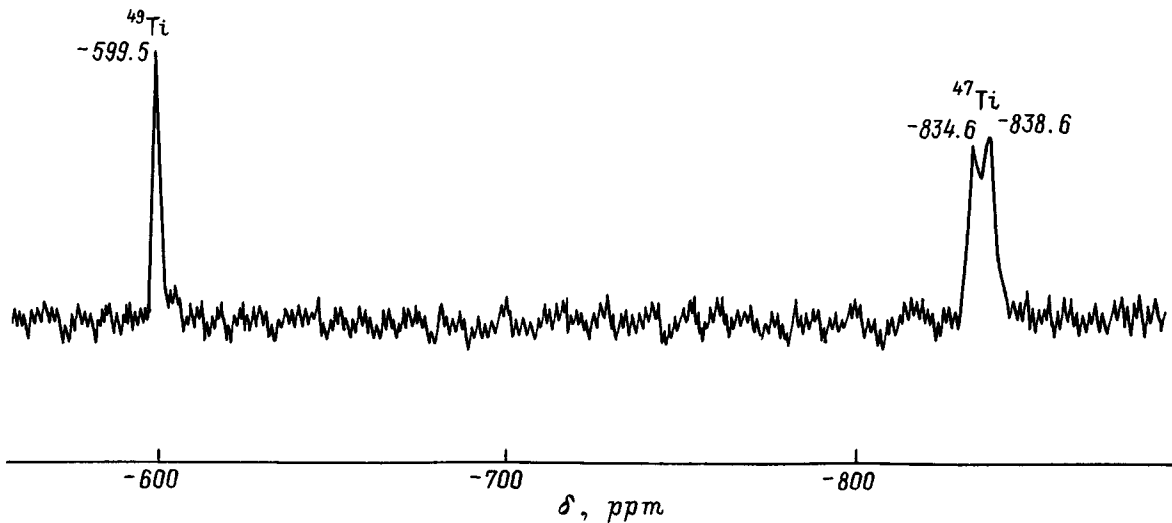| Substance	Cell parameters, Å		Bond lengths, Å	
	a_0	c_0	Ti–O	O–O
Anatase	3.7845±0.0001	9.5143±0.0004	1.934 (R_1) 1.979 (R_2)	2.464×4 (A_1) 2.793×4 (A_2) 3.040×4 (A_3)
Rutile	4.5941±0.0001	2.9589±0.0001	1.948 (R_1) 1.980 (R_2)	2.536×2 (A_1) 2.777×8 (A_2) 2.959×2 (A_3)

FIG. 1. NMR spectrum of ^{47}Ti and ^{49}Ti nuclei measured in an orientation close to $B_0 \| [001]$.

3. DISCUSSION OF THE RESULTS

3.1. Parameters of ^{47}Ti and ^{49}Ti spectra in the anatase

The sites corresponding to the central transition of both isotopes were measured in an anatase single crystal for several magnetic-field orientations in the (100) plane. Because of the quadrupole coupling and chemical shift tensors, eQV_{ij} and δ_{ij}, in this crystal being axially symmetric, the expressions describing the position of the $1/2 \leftrightarrow -1/2$ transition are fairly simple, and have been given in Ref. 1. The possibility of observing the two nuclei at the same site, combined with the knowledge of the ratio of their quadrupole moments $eQ(^{47}\text{Ti})/eQ(^{49}\text{Ti}) = 1.21$, permitted one to determine both the quadrupole coupling parameters and the chemical shift from measurements at one frequency. The values obtained are as follows: $\delta_\| = -840 \pm 10$ ppm, $\delta_\perp = -960 \pm 15$ ppm, $eQV_{zz}/h = 5.90 \pm 0.10$ MHz, and $\eta = 0$ for ^{47}Ti, and $eQV_{zz}/h = 4.85 \pm 0.10$ MHz and $\eta = 0$ for ^{49}Ti.

3.2. Parameters of ^{47}Ti and ^{49}Ti spectra in the rutile

Because of the existence of magnetically inequivalent sites in rutile, its spectra obtained under an arbitrary crystal orientation contain pairs of lines for each titanium isotope, which merge into one in the [100], [010], and [001] orientations (Fig. 1). The principal axes of the eQV_{ij} and δ_{ij} tensors are rotated relative to the crystallographic axes through $45°$ in the (001) plane, so that the principal axial system can be written $x \| [110]$, $y \| [\bar{1}10]$, $z \| [001]$.

We can use the expressions derived by us from Volkov's relation for the quadrupole shift, which describe the position of the central line in spectra of half-integer spin nuclei in the principal orientations:

$$B_0\|x, \quad (\nu - \nu_0)/\nu_0 = 10^{-6}\delta_{xx} + A(I)(3 + \eta)^2 \nu_Q^2/\nu_0^2,$$

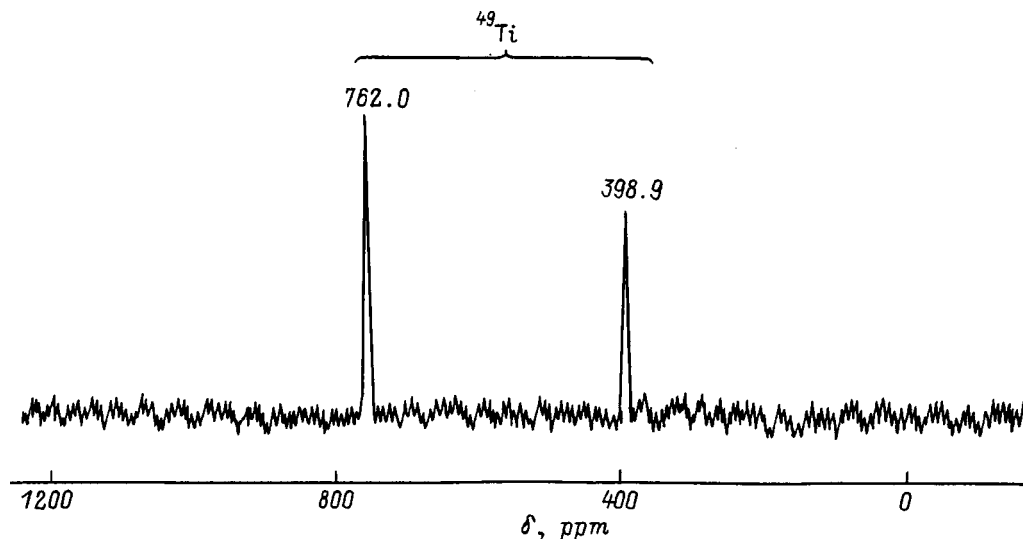$$B_0\|y, \quad (\nu - \nu_0)/\nu_0 = 10^{-6}\delta_{yy} + A(I)(3 - \eta)^2 \nu_Q^2/\nu_0^2,$$

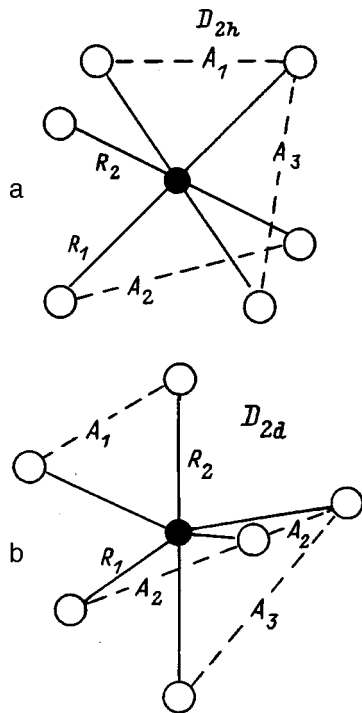FIG. 2. ^{49}Ti NMR spectrum measured in a rutile sample for $B_0 \| [110]$.

FIG. 3. Schematic representation of TiO_6 octahedra in (a) rutile and (b) anatase. The R_i and A_i distances are given in Table I.

$$B_0 \| z, \quad (\nu - \nu_0)/\nu_0 = 10^{-6}\delta_{zz} + B(I)\,\eta^2 \nu_Q^2/\nu_0^2,$$

where δ_{xx}, δ_{yy}, and δ_{zz} are the components of the chemical shift tensor (in ppm), ν_Q, η are the conventional quadrupole splitting parameters, with ν_Q being related to the eQV_{ij} tensor through $\nu_Q = 3eQV_{zz}/2I(2I-1)h$, and $A(I)$ and $B(I)$ are numerical factors depending on the nuclear spin.

For the isotopes of interest here $A(I)$, $B(I)$

^{47}Ti: $I = 5/2$, $A = 1/18$, $B = 2/9$;

^{49}Ti: $I = 7/2$, $A = 5/48$, $B = 5/12$.

Substituting the values of ν_Q and η from Ref. 2 permits one to find the principal values of the chemical shift tensor from measured line positions of one isotope. We chose in the experiment the ^{49}Ti isotope, which has more narrow lines (Fig. 2). For this isotope, $\nu_Q = 0.99$ MHz and $\eta = 0.19$, which yields for δ_{ij} (in ppm): $\delta_{xx} = -815 \pm 10$, $\delta_{yy} = -885 \pm 10$, and $\delta_{zz} = -885 \pm 10$.

Figure 3 shows schematically TiO_6 octahedra in anatase and rutile. The Ti–O bond lengths are listed in Table I. We note immediately that the minimum chemical-shift tensor component (-840 ppm in anatase and -815 ppm in rutile) or, using the terms related to magnetic shielding, the minimum shielding, corresponds to the longest Ti–O bond. Note that the anisotropy of the δ_{ij} tensor in anatase is larger than that in rutile, which also correlates with the scatter in bond lengths in the octahedron, namely, rutile exhibits the smallest difference in the Ti–O bond lengths. Finally, one can compare the average bond length in the octahedron with the isotropic shift $\delta_{iso} = (\delta_{xx} + \delta_{yy} + \delta_{zz})/3$. In rutile, $\delta_{iso} = -860 \pm 10$ ppm for an average bond length of 1.959 Å, and in anatase $\delta_{iso} = -920 \pm 15$ ppm for an average Ti–O bond length of 1.949 Å. Thus a purely qualitative consideration indicates a possibility of establishing direct correlation between the shift and the structural parameters in isotypic crystals. A more rigorous analysis of this problem would require complex calculations invoking quantummechanical models. For crystals such calculations still remain unfeasible.

The isotropic shift and the anisotropy of the δ_{ij} tensor obtained here for the crystal phases of TiO_2 can be used in studies of spectra of ^{47}Ti and ^{49}Ti in more complex oxides for identification of the titanium sites and simulation of spectra of powders and ceramics.

[1] L. V. Dmitrieva, L. S. Vorotilova, and M. V. Razumeenko, Fiz. Tverd. Tela (St. Petersburg) **39**, 1194 (1997) [Phys. Solid State **39**, 1057 (1997)].
[2] O. Kanert and H. Kolem, J. Phys. C **21**, 3909 (1988).
[3] *Minerals* [in Russian], edited by F. V. Chukhrov and É. M. Bondshtedt-Kupletskaya, (Nauka, Moscow, 1965), Vol. 2, Pt. 2, pp. 239, 287.
[4] K. V. Krishna Rao, S. V. Nagender Naidu, and L. Iyengar, J. Am. Ceram. Soc. **53**, No. 3, 124 (1970).
[5] M. Horn, C. F. Schwerdtfeger, and E. P. Meagher, Z. Kristallogr. **136**, 273 (1972).
[6] R. Restori, D. Schwarzenbach, and J. R. Schneider, Acta Crystallogr., Sect. B: Struct. Sci. **43**, 251 (1987).
[7] M. V. Razumeenko, V. S. Grunin, and A. A. Boĭtsov, Kristallografiya **26**, 650 (1981) [Sov. Phys. Crystallogr. **26**, 371 (1981)].

Translated by G. Skrebtsov

Spatial distribution of radiation defects in tooth enamel

S. S. Ishchenko, S. M. Okulov, and I. P. Vorona

Institute of Semiconductor Physics, Ukrainian Academy of Sciences, 252650 Kiev, Ukraine
(Submitted December 15, 1998)
Fiz. Tverd. Tela (St. Petersburg) **41**, 1207–1209 (July 1999)

The spatial distribution of radiation defects in tooth enamel has been investigated using EPR imaging. Plates of enamel irradiated with γ rays and electrons with energy 1.2 and 3.8 MeV have been studied. A falloff of the radiation-defect concentration in the direction in which the radiation acts is detected in the electron-irradiated plates, with the slope of the falloff decreasing with increasing electron energy. The defect distribution was uniform in the γ-irradiated plates. It is shown that the study of tooth enamel by means of EPR imaging can be used to determine the type and energy characteristics of the ionizing radiation that acts on a living organism. © *1999 American Institute of Physics.* [S1063-7834(99)01607-X]

A rather large number of papers have been devoted to the study of tooth enamel (see, for example, Refs. 1–3). This is mainly because it is a unique object—a mineral synthesized directly in a living organism. There is special interest in the centers formed in tooth enamel by the action of ionizing radiations.[4–6] Such centers (radiation defects) serve as probes for studying the microstructure of the enamel. Moreover, they have recently been widely used for dosimetric purposes and for dating archeological sites.[7–9] Since radiation defects in tooth enamel are paramagnetic, the most effective way to study them is by EPR. Earlier papers used the ordinary technique for observing EPR,[10] in which the signal was recorded from the sample as a whole. Below we describe the results of a study of plates of irradiated enamel in an inhomogeneous magnetic field, which made it possible to observe the EPR signals from different sections of the test sample separately. This method is known as EPR imaging.[11,12] It is valuable in that it makes it possible to obtain information concerning the spatial distribution of radiation defects, as well as concerning possible inhomogeneities of the structure of the enamel. Plates irradiated by various types of radiation were studied.

1. EXPERIMENT

The study used three rectangular $1 \times 3 \times 4$-mm^3 plates of enamel, cut from the front surfaces of the teeth. Two of them were irradiated with electrons of various energies, and the third with γ rays from a ^{60}Co source. They were irradiated perpendicular to the 1×3-mm^2 surface, while the other surfaces were protected from the radiation by a special holder. The irradiation dose was about 100 Gy.

EPR was measured in a Radiopan spectrometer equipped with a ZZG-1 tomographic attachment, which made it possible to create a gradient $G_x = dB/dx$ along the main magnetic field **B**. A tomogram corresponding to a definite orientation of the plate relative to the gradient was recorded by sweeping the B field and was a recording of the EPR signal in the inhomogeneous magnetic field $\mathbf{B} - \mathbf{x}G_x$, $\mathbf{x} \| \mathbf{B}$. The computer of the Radiopan spectrometer was connected to an

IBM PC 386/387 computer, which used a special program to process the experimental tomographic curve and to obtain from it the distribution function of the radiation defects in the sample along the magnetic-field gradient. The experiments took place at room temperature, with $G_x = 2$ T/m.

Figure 1 shows tomograms of the test plates of tooth enamel. The plates were oriented so that their length $L = 4$ mm coincided with the direction of gradient G_x. The tomograms then reflected the concentration variation of radiation defects in the plates along the direction in which the radiation acted. It can be seen from Fig. 1 that the form of the tomographic curve depends substantially on the type and energy characteristics of the radiation acting on the sample.

2. THEORETICAL DESCRIPTION AND DISCUSSION OF RESULTS

In the case of a steady-state gradient $G_x = $ const, the EPR tomogram can be described by

$$T(B) = \int_{x_1}^{x_2} R(x)S(B - xG_x)dx, \tag{1}$$

where $R(x)$ is the spatial distribution of paramagnetic centers, $S(B)$ is the shape function of the EPR line, and x_1 and x_2 correspond to the beginning and end of the sample. Equation (1) is a Fredholm equation of the first kind, and therefore finding $R(x)$ is a rather complex problem. Fourier analysis was used to solve it.

Equation (1) can be represented in the form of a convolution

$$T = R * S, \tag{2}$$

where * is the convolution symbol. Since the Fourier transform of the convolution of two functions equals the product of their Fourier transforms, Eq. (2) can be written as
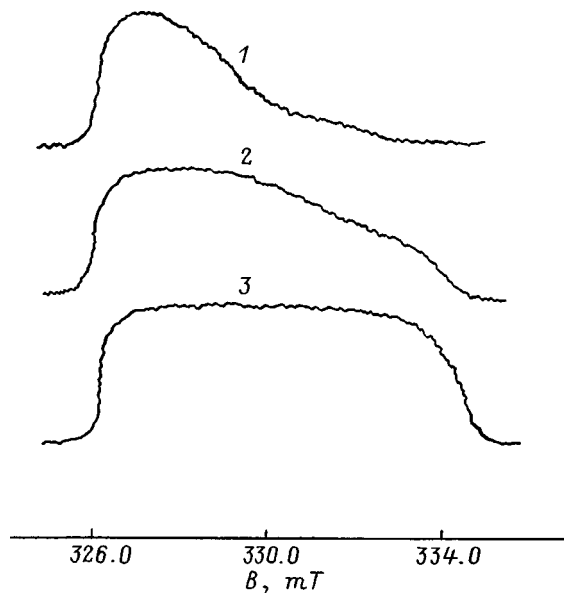
$$F(T) = F(R)F(S), \tag{3}$$

where

FIG. 1. EPR tomograms of plates of tooth enamel irradiated with electrons with energy 1.2 MeV (*1*) and 3.8 MeV (*2*) and γ rays (*3*). The curves correspond to the absorption signal.

FIG. 2. Spatial distribution of radiation defects in a plate of tooth enamel irradiated by a directed electron beam with energy 1.2 MeV.

$$F(T) = \int_{-\infty}^{\infty} T(B)\exp(-i\omega B)dB, \qquad (4)$$

and ω is the independent variable in Fourier space.

$R(x)$ is found from Eq. (3) by the inverse Fourier transformation

$$R(x) = F^{-1}[F(T)/F(S)]. \qquad (5)$$

The main problem of deconvolution is division by zero or a quantity close to it. In fact, actual spectral distributions are described in most cases by a line shape that is Lorentzian, Gaussian, or a linear combination of both. Therefore, $F(S) \to 0$ when $\omega \to \infty$. The actual deconvolution thus results in division by zero at large ω. Moreover, the indicated problem also arises for small ω if the value of $F(S)$ becomes smaller than the noise amplitude. One uses so-called windows to overcome these difficulties. In this case, Eq. (5) becomes

$$R(x) = F^{-1}[F(T)f(\omega)/F(S)], \qquad (6)$$

where $f(\omega)$ is the window function.[13]

We used a computer program in which the Fourier transformation has a rectangular window,

$$f(\omega) = \begin{cases} 1 & \omega \leqslant \omega_f \\ 0 & \omega > \omega_f. \end{cases} \qquad (7)$$

Parameter ω_f depends on the SNR and is determined from the $\Phi(\omega) = F(S)F^*(S)$ spectrum as the maximum value of ω above which $\Phi(\omega)$ does not exceed the noise level.

An analysis of the theoretical expressions shows that, the smaller the width ΔS of the EPR line is by comparison with $G_x L$, the nearer the shape of the $R(x)$ curve is to that of the $T(B)$ curve.

Figure 2 illustrates the distribution of radiation defects in a plate irradiated by electrons with energy 1.2 MeV. This
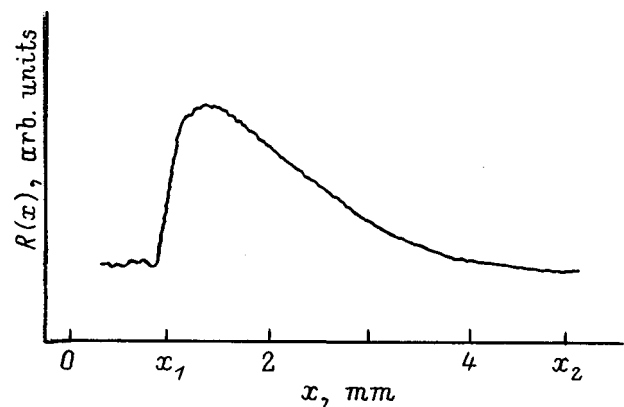
distribution was obtained by the procedure described above from tomogram 1 of Fig. 1. $R(x)$ is near to $T(B)$ in our case because $\Delta S = 0.6$ mT is substantially less than $G_x L = 8$ mT. The $R(x)$ curves obtained from Eq. (6) for the other two plates are also close to the corresponding tomographic curves $T(B)$. The resolving power of the EPR imaging method is determined by the expression $\Delta x = \Delta S/G_x$. This equalled about 0.3 mm in our experiments.

Our studies have thus established that $R(x)$ depends on the form and characteristics of the radiation, and this makes it possible to use tooth enamel to obtain detailed information about the nature of the radiation damage of living organisms. In favorable situations, EPR imaging of tooth enamel can be used to establish not only the type of radiation that acts on an organism but also its energy characteristics (see curves *1* and *2* in Fig. 1). The latter makes it possible to elucidate what radioactive nuclei were the source of the radiation. The smooth behavior of the resulting $R(x)$ curves is evidence that there are no inhomogeneities in the structure of the tooth enamel.

[1] J. E. Glas, Arch. Oral. Biol. **7**, No. 1, 91 (1962).

[2] F. C. M. Driessens and R. M. H. Verbeek, *Biominerals* (CRC Press, Boca Raton, Fla. 1990).

[3] C. Rey, V. Renugopalakrischnan, M. Shimizu, B. Collins, and M. J. Glimcher, Calcif. Tissue Int. **49**, No. 1, 259 (1991).

[4] F. J. Callens, R. M. H. Verbeek, P. F. A. Matthys, L. C. Martens, and E. R. Boesman, Calcif. Tissue Int. **41**, No. 1, 124 (1987).

[5] Y. Doi, T. Aoba, M. Okazaki, J. Takahashi, and Y. Moriwaki, Calcif. Tissue Int. **28**, No. 1, 107 (1979).

[6] S. S. Ishchenko, S. M. Okulov, I. P. Vorona, A. B. Roĭtsin, and A. A. Klimov, Fiz. Tverd. Tela **34**, 2847 (1992) [Sov. Phys. Solid State **34**, 1522 (1992)].

[7] M. Ikeya, Appl. Magn. Res. **7**, 237 (1994).

[8] A. I. Ivannikov, V. G. Skvortsov, V. F. Stepanenko, and A. F. Tsyb, Fiz. Med. **2**, Nos. 3–4, 29 (1992).

[9] A. B. Brik, S. S. Ishchenko, L. G. Rozenfel'd, D. I. Zabolotnyĭ, and I. S. Zaritskaya, Med. Radiologiya **38**, No. 1, 25 (1993).

[10] C. P. Poole, *Experimental Techniques in Electron Spin Resonance* (Wiley, New York, 1966; Mir, Moscow, 1970).

[11] O. E. Yakimchenko and Ya. S. Lebedev, Khim. Fiz. **4**, 445 (1983).

[12] G. R. Eaton, S. S. Eaton, and K. Ohno, *EPR imaging and in vivo EPR* (CRC Press, Boston, 1991).

[13] L. Rabiner and B. Gould, *Theory and Application of Digital Signal Processing* (Prentice–Hall, Englewood Cliffs, N.J., 1975; Mir, Moscow, 1978).

Translated by W. J. Manthey

DEFECTS. DISLOCATIONS. PHYSICS OF STRENGTH

Electroelastic fields of moving dislocations and disclinations in piezoelectric crystals

Sh. Kh. Khannanov

Institute of the Physics of Molecules and Crystals, Ufa Scientific Center, Russian Academy of Sciences,
450075 Ufa, Russia

Integral representations for the electroelastic fields of moving dislocations and disclinations in piezoelectric crystals have been obtained in terms of a four-dimensional formalism of dynamic Green's functions. The cases of continuously distributed and single linear defects are considered. The correctness of the results is confirmed by the fact that they meet the necessary requirements as one goes to the purely elastic solution. © *1999 American Institute of Physics.* [S1063-7834(99)01707-4]

Linear defects of a crystal lattice have been studied from the viewpoint of both the mechanical[1] and the electrical[2] properties. The nature of the electrical activity of the defects depends on the crystal type. Here we are dealing with piezo-electric crystals,[3-5] in which, because of electrical polarization, linear defects possess coupled electroelastic fields.[6-8] The theoretical study of these fields is an extremely critical problem and has attracted the attention of a number of researchers.[6-8]

For a purely elastic body, general solutions for arbitrary distributions of moving dislocations and disclinations have been obtained using Green's functions.[9,10] The elastic fields in this case are completely expressed in terms of the density and flux of the defects. Such a general solution for electroelastic fields of arbitrarily distributed moving linear defects (dislocations and disclinations) has not yet been obtained for the case of a piezoelastic body. The attempt made in Ref. 8 cannot be considered wholly successful, since the solution there is expressed not in terms of the flux of defects but in terms of macroscopic rates of plastic deformation and plastic bending and twisting. The purpose of this paper is to fill in this gap.

1. FORMULATION OF THE PROBLEM

In continuum theory, one starts from the assumption that linear defects (dislocations and disclinations) are equivalent to certain basic plastic (singular) fields.[9] The latter, as will be shown below, can be replaced by distributions of fictitious volume forces f_i and charges g. The problem of determining the electroelastic fields of the defects therefore reduces to some problem of piezoelasticity for given f_i and g.

Let us consider a piezoelastic crystal that is characterized by tensors of elastic λ_{ijkl}, dielectric ε_{ij}, and piezoelectric β_{kij} constants (the notation follows Ref. 3, Sec. 17), satisfying well-known symmetry properties.[3-5] Here and below, except when otherwise indicated, lower-case latin subscripts take the values 1, 2, 3. The constants enter into the linear equations of state that relate the elastic stresses σ_{ij} and

the electric displacements D_i with the elastic strains e_{kp} and the electric field E_k.[3-5] Expressing e_{kp} in terms of the elastic displacement vector u_p in the form $e_{pk} = (u_{p,k} + u_{k,p})/2$ and expressing E_i in terms of the electric potential φ in the form $E_i = -\varphi_{,i}$, the indicated equations of state can be written as follows:[3-5] $\sigma_{ij} = \lambda_{ijkp}u_{p,k} + \beta_{kij}\varphi_{,k}$; $D_i = \beta_{ikp}u_{p,k} - \varepsilon_{ij}\varphi_{,j}$. Here the subscript after the comma denotes differentiation with respect to the corresponding coordinate.

To determine the displacement u_i and the potential φ for given f_i and g, we have the equations of motion of the particles of the body (the equations of elasticity theory)[4] $\sigma_{ij,j} - p\ddot{u}_i = -f_i$ and the equation of electrostatics[3] $D_{i,j} = g$, where ρ is the density of the body, and an overdot denotes differentiation with respect to time. Substituting the expressions for σ_{ij} and D_i into these equations, we get inhomogeneous equations containing only u_k and φ,

$$\lambda_{ijkp}u_{k,pj} - p\ddot{u}_i + \beta_{kij}\varphi_{,kj} = -f_i, \tag{1}$$

$$\beta_{jkp}u_{k,pj} - \varepsilon_{jk}\varphi_{,jk} = -g. \tag{2}$$

Now f_i and g in Eqs. (1) and (2) need to be expressed in terms of the basic plastic fields of the linear defects.

According to Ref. 9, a body with moving dislocations and disclinations is characterized by a set of basic plastic fields: the strain field e_{ij}^p, the bending–twisting field $\varkappa_{ij}^p$, the velocity field v_l^p, and the rotation field ω_q^p. As shown in Ref. 9 (see also Ref. 11), the plastic velocity v_l^p can be set equal to zero for physical defects. The quantities $\varkappa_{ij}^p$ and ω_q^p do not enter into the equations of state. Therefore, f_i and g will actually be determined only by the plastic strain e_{ij}^p. In the presence of $e_{ij}^p \neq 0$, we have

$$e_{kp} = e_{kp}^T - e_{kp}^P = \frac{1}{2}(u_{p,k} + u_{k,p}) - e_{kp}^P, \tag{3}$$

where e_{kp}^T is the total (plastic plus elastic) strain, and we set $f_i = g = 0$ in Eqs. (1) and (2) (the role of the external forces

and electric charges is now played by the basic plastic fields of the defects). Taking this into account, Eqs. (1) and (2) take the form

$$\lambda_{ijkp} = u_{k,pj} - \rho \ddot{u}_i + \beta_{kij} \varphi_{,kj} = \lambda_{ijkp} e^P_{pk,j}, \tag{4}$$

$$\beta_{jkp} u_{k,pj} - \varepsilon_{jk} \varphi_{,jk} = \beta_{jkp} e^P_{pk,j}. \tag{5}$$

Comparing Eqs. (1) and (2) to Eqs. (4) and (5), we see that linear defects in a piezoelectric crystal are equivalent to a distribution of fictitious volume forces f_i and charges g whose magnitude is determined by

$$f_i = -\lambda_{ijkp} e^P_{pk,j}, \tag{6}$$

$$g = -\beta_{jkp} e^P_{pk,j}. \tag{7}$$

The problem is to interpret the inhomogeneous Eqs. (4) and (5). This can be done in general form by using the Green's function formalism.

2. FOUR-DIMENSIONAL GREEN'S-FUNCTION FORMALISM

Because of the symmetry of the material constants and of the equations of the problem, Eqs. (1) and (2), it is convenient to introduce four-dimensional dynamic tensor Green's functions $G_{\alpha\beta}(\mathbf{r},t)$, where $\mathbf{r}$ is the radius vector, and t is the time; subscripts indicated by Greek letters take the values 1, 2, 3, 4. In the static case, such Green's functions were introduced in Ref. 12.

Carrying out the Fourier transformation

$$\bar{f}(\omega,\mathbf{k}) = \int \int f(\mathbf{r},t) \exp[i(\mathbf{k} \cdot \mathbf{r} - \omega \mathbf{t})] d\mathbf{r} \, dt,$$

Eqs. (1) and (2) can be represented in matrix form

$$D_{\alpha\beta}(\omega,\mathbf{k}) \bar{U}_\beta(\omega,\mathbf{k}) = \bar{F}_\alpha(\omega,\mathbf{k}), \tag{8}$$

where the (4×2) matrix $D_{\alpha\beta}(\omega,\mathbf{k})$ has the form (δ_{ik} is the Kronecker delta)

$$D_{ik} = \lambda_{ijkp} k_p k_j - \rho \omega^2 \delta_{ik},$$

$$D_{i4} = D_{4i} = \beta_{kij} k_k k_j, \quad D_{44} = -\varepsilon_{jk} k_j k_k,$$

and the components of the four-dimensional vectors U_α and F_α equal

$$U_i = u_i, \quad U_4 = \varphi,$$

$$F_i = -f_i, \quad F_4 = -g.$$

Starting from the form of Eq. (8), we define the Fourier transform of the Green's function $\bar{G}_{\alpha\beta}(\omega,\mathbf{k})$ by

$$D_{\alpha\beta}(\omega,\mathbf{k}) \bar{G}_{\beta\gamma}(\omega,\mathbf{k}) = \delta_{\alpha\gamma}, \tag{9}$$

where $\delta_{\alpha\gamma}$ is the four-dimensional analog of the Kronecker delta. Multiplying both sides of Eq. (9) by the matrix $D^{-1}_{\alpha\beta}(\omega,\mathbf{k})$, we find

$$\bar{G}_{\alpha\beta}(\omega,\mathbf{k}) = \frac{d_{\beta\alpha}(\omega,\mathbf{k})}{D(\omega,\mathbf{k})}, \tag{10}$$

where $D(\omega,\mathbf{k})$ is the determinant of the matrix $D_{\alpha\beta}(\omega,\mathbf{k})$, and $d_{\alpha\beta}(\omega,\mathbf{k})$ is the algebraic complement of element $D_{\alpha\beta}(\omega,\mathbf{k})$.

In accordance with the form of Eqs. (8) and (9), the Green's function $G_{\alpha\beta}$ describes various types of responses of a piezoelastic body: a displacement force (components G_{ik}), a potential force (components G_{4k}), a displacement charge (components G_{i4}), and a potential charge (components G_{44}).

In what follows, we also need an equation for $G_{\alpha\beta}(\mathbf{r},t)$. By applying an inverse Fourier transformation to Eq. (9), we get

$$\hat{D}_{\alpha\beta}\left(-i\frac{\partial}{\partial t}, \ i\frac{\partial}{\partial x_p}\right) G_{\beta\gamma}(\mathbf{r},t) = \delta_{\alpha\gamma} \delta(\mathbf{r}) \delta(t), \tag{11}$$

where $\hat{D}_{\alpha\beta}(-i\,\partial/\partial t, i\,\partial/\partial x_p)$ is the matrix with operator elements that is obtained from matrix $D_{\alpha\beta}(\omega,\mathbf{k})$ by substituting $\omega \to -i\,\partial/\partial t$ and $k_p \to i\,\partial/\partial x_p$.

3. ELECTROELASTIC FIELDS OF LINEAR DEFECTS

The solution of the fundamental Eq. (8) is given by the equality

$$U_\gamma = G_{\gamma\alpha} F_\alpha$$

or, after inverse Fourier transformation,

$$U_\alpha(\mathbf{r},t) = \int \int G_{\alpha\beta}(\mathbf{r}-\mathbf{r}', t-t') F_\beta(\mathbf{r}',t') \, d\mathbf{r}' dt',$$

where $U_\alpha = (u_i, \varphi)$, and $F_\beta = (-f_i, g)$. Substituting here Eqs. (6) and (7) for the density of the fictitious volume forces f_i and charges g, we get expressions for the displacements u_i and the electric potential φ created by moving defects

$$u_i(\mathbf{r},t) = -\int \int \{G_{iq}(\mathbf{R},T) \lambda_{qjkp} e^P_{pk,j'}(\mathbf{r}',t')$$

$$+ G_{4i}(\mathbf{R},T) \beta_{ikp} e^P_{pk,j'}(\mathbf{r}',t')\} d\mathbf{r}' dt', \tag{12}$$

$$\varphi(\mathbf{r},t) = -\int \int \{G_{4q}(\mathbf{R},T) \lambda_{qjkp} e^P_{pk,j'}(\mathbf{r}',t')$$

$$+ G_{44}(\mathbf{R},T) \beta_{ikp} e^P_{pk,j'}(\mathbf{r}',t')\} d\mathbf{r}' dt', \tag{13}$$

where $\mathbf{R} = \mathbf{r} - \mathbf{r}'$, $T = t - t'$.

Eqs. (12) and (13) contain the macroscopic characteristic e^P_{pk}—the plastic strain tensor. In order to eliminate macroscopic characteristics and express the electroelastic fields in terms of the characteristics of the defects (the density and flux tensors), it is necessary to transform the solution of Eqs. (12) and (13), and this procedure is largely analogous to the transformations in Ref. 10 in the case of pure elasticity. In this case, one uses Eqs. (11) for the Green's function and also the defining relations for the density tensors α_{ik} and θ_{ik} and the flux tensors J_{kl} and S_{kq} of the dislocations and disclinations[9] (see also Ref. 11):

$$\alpha_{pl} = -\varepsilon_{pmk}(e^P_{kl,m} + \varepsilon_{klq} \varkappa^P_{mq}),$$

$$\theta_{pq} = -\varepsilon_{pmk} \varkappa^P_{kq,m},$$

$$J_{kl} = \dot{e}^P_{kl} + \varepsilon_{klq} \omega^P_q,$$

$$S_{kq} = -\omega^P_{q,k} + \dot{\varkappa}^P_{kq}.$$

Here, as above, we have set the plastic velocity equal to zero, $v_l^p = 0$, and this has no effect on the final results.

Without showing the detailed calculations, we immediately write the final expressions for elastic strain tensor e_{mn} and electric field vector E_k:

$$e_{mn}(\mathbf{r},t) = \int \int \{ [\varepsilon_{pmk} C_{\alpha ikl} G_{\alpha n,i} \alpha_{pl} - \rho \dot{G}_{ln} J_{ml}]$$
$$- \varepsilon_{pmk} [\varepsilon_{qsl} C_{\alpha ikl} H_{\alpha n,is} \theta_{pq}$$
$$- \rho \dot{H}_{kn,s} S_{sp}] \}_{(mn)} d\mathbf{r}' dt', \qquad (14)$$

$$E_m(\mathbf{r},t) = \int \int \{ [\varepsilon_{pmk} C_{\alpha ikl} G_{\alpha 4,i} \alpha_{pl} - \rho \dot{G}_{l4} J_{ml}]$$
$$- \varepsilon_{pmk} [\varepsilon_{qsl} C_{\alpha ikl} H_{\alpha 4,is} \theta_{pq}$$
$$- \rho \dot{H}_{k4,s} S_{sp}] \}_{(mn)} d\mathbf{r}' dt', \qquad (15)$$

where mn is the symmetrization operation, ε_{pmk} is the unit antisymmetry tensor, and for simplicity the arguments $(\mathbf{R}, T)$ are omitted from the Green's functions $G_{\alpha\beta}$ and the potentials $H_{\alpha\beta}$, as well as the arguments $(\mathbf{r}', t')$ from the functions α_{pl}, θ_{pq}, J_{ml}, and S_{sp}. Here we have introduced the tensor of the material constants $C_{\alpha\beta\delta\gamma}$, in which $C_{jikl} = \lambda_{jikl}$, $C_{4ikl} = \beta_{ikl}$, and the other components equal zero. Potentials $H_{\alpha\beta}(\mathbf{r},t)$ are determined according to Ref. 10:

$$H_{\alpha\beta}(\mathbf{r},t) = \int G_{\alpha\beta}(\mathbf{r}',t)(2\pi R)^{-1} d\mathbf{r}'.$$

In going to the purely elastic case, in which $C_{4ikl} = \beta_{ikl} = 0$, $G_{\alpha 4}$ and $H_{\alpha 4}$ go to zero in accordance with Eq. (9), while electric field E_m disappears according to Eq. (15). In this case, Eq. (14) leads to the expression

$$e_{mn}(\mathbf{r},t) = \int \int \{ [\varepsilon_{pmk} \lambda_{jikl} G_{jn,i} \alpha_{pl} - \rho \dot{G}_{ln} J_{ml}]$$
$$- \varepsilon_{pmk} [\varepsilon_{qsl} \lambda_{jikl} H_{jn,is} \theta_{pq}$$
$$- \rho \dot{H}_{kn,s} S_{sp}] \}_{(mn)} d\mathbf{r}' dt',$$

which coincides with Eq. (4.6) from Ref. 10. This confirms the correctness of the results obtained here.

The solutions given by Eqs. (14) and (15) are valid for an arbitrary distribution of moving dislocations and disclinations. From this it is easy to obtain solutions for the case of single defects. To do this, it is necessary to substitute into Eqs. (14) and (15) known expressions[10] for the densities

$$\alpha_{pl}(\mathbf{r},t) = \oint_{L(t)} \delta(\mathbf{R}) \{ b_l + \varepsilon_{lqr} \Omega_q (x_r' - x_r^0) \} dL_p',$$

$$\theta_{pq}(\mathbf{r},t) = \oint_{L(t)} \delta(\mathbf{R}) \Omega_q dL_p'$$

and fluxes

$$J_{kl}(\mathbf{r},t) = \oint_{L(t)} \varepsilon_{pmk} \delta(\mathbf{R}) \{ b_l + \varepsilon_{lqr} \Omega_q$$
$$\times (x_r' - x_r^0) \} v_m(\mathbf{r}',t') dL_p',$$

$$S_{kq}(\mathbf{r},t) = \oint_{L(T)} \varepsilon_{pmk} \delta(\mathbf{R}) \Omega_q v_m'(\mathbf{r}',t) dL_p'$$

of the dislocations and disclinations of a single linear defect and to carry out the integration. Here $L(t)$ is a defect line, x_r^0 is the coordinate of a point on the rotation axis, b_l is the Burgers vector of the dislocation associated with the defect line, Ω_q is the Franck vector, and v_m is the velocity with which $L(t)$ moves. As a result of the integration, taking into account the properties of the delta function, we get

$$e_{mn}(\mathbf{r},t) = \int \int_{L(t)} \{ \varepsilon_{pmk} (C_{\alpha ikl} G_{\alpha n,i} + \rho \dot{G}_{ln} v_k')$$
$$\times (b_l + \varepsilon_{lqr} \Omega_q (x_r' - x_r^0)) - \varepsilon_{qmk} \varepsilon_{psl} (C_{\alpha ikl} H_{\alpha n,is}$$
$$+ \rho \dot{H}_{kn,s} v_l') \Omega_q \} dL_p' dt'_{(mn)}, \qquad (16)$$

$$E_m(\mathbf{r},t) = \int \int_{L(t)} \{ \varepsilon_{pmk} (C_{\alpha ikl} G_{\alpha 4,i} + \rho \dot{G}_{l4} v_k')$$
$$\times (b_l + \varepsilon_{lqr} \Omega_q (x_r' - x_r^0)) - \varepsilon_{qmk} \varepsilon_{psl}$$
$$\times (C_{\alpha ikl} H_{\alpha 4,is} + \rho \dot{H}_{k4,s} v_l') \Omega_q \} dL_p' dt', \qquad (17)$$

In going to the purely elastic case, electric field E_m disappears, and Eq. (16) coincides with Eq. (5.7) from Ref. 10. The elastic stress tensor σ_{ij} and the electric displacement vector D_i created by moving linear defects can be found from the equations of state,[3–5] by substituting in them Eqs. (14) and (15) or Eqs. (16) and (17) obtained for elastic strains e_{mn} and electric field vector E_m.

General solutions have thus been obtained for the electroelastic fields of moving dislocations and disclinations in piezoelectric crystals. The physically observed fields in this case are determined in terms of the density and flux tensors of the dislocations and disclinations, which should be regarded as given.

[1] B. I. Smirnov, *Dislocation Structure and the Hardening of Crystals* [in Russian] (Nauka, Leningrad, 1981).

[2] Yu. A. Osip'yan and V. F. Petrenko, in *Problems of the Strength and Plasticity of Solids* [in Russian], edited by S. N. Zhurkov (Nauka, Leningrad, 1979), pp. 118–128.

[3] L. D. Landau and E. M. Lifshitz, *Electrodynamics of Continuous Media* [in Russian] (Nauka, Moscow, 1982).

[4] Yu. I. Sirotin and M. P. Shaskol'skaya, *Fundamentals of Crystal Physics* [in Russian] (Nauka, Moscow, 1975).

[5] J. F. Nye, *Physical Properties of Crystals* (Clarendon Press, Oxford, 1957; Mir, Moscow, 1960).

[6] A. M. Kosevich, L. A. Pastur, and É. P. Fel'dman, Kristallografiya **12**, 916 (1967) [Sov. Phys. Crystallogr. **12**, 797 (1967)].

[7] I. S. Smirnova, Phys. Status Solidi B **126**, 177 (1984).

[8] S. Minagawa, Phys. Status Solidi B **124**, 565 (1984).

[9] E. Kossecka and R. De Wit, Arch. Mech. **29**, 633 (1979).

[10] E. Kossecka and R. De Wit, Arch. Mech. **29**, 749 (1979).

[11] Sh. Kh. Khannanov, Fiz. Met. Metalloved. **49**, No. 1, 59 (1980).

[12] N. A. Pertsev and K. V. Smirnov, Kristallografiya **33**, 1335 (1988) [Sov. Phys. Crystallogr. **33**, 795 (1988)].

Translated by W. J. Manthey

Amplitude-dependent elastic-modulus defect in the main dislocation-hysteresis models

A. B. Lebedev

A. F. Ioffe Physicotechnical Institute, Russian Academy of Sciences, 194021 St. Petersburg, Russia
(Submitted November 11, 1998; resubmitted December 22, 1998)
Fiz. Tverd. Tela (St. Petersburg) **41**, 1214–1221 (July 1999)

The amplitude-dependent defect of the elastic modulus has been calculated for the three main dislocation-hysteresis models: (i) breakaway hysteresis of Granato–Lücke, (ii) Davidenkov hysteresis, and (iii) friction hysteresis without restoring force (WRF). The ratio r of the amplitude-dependent decrement to the modulus defect has been considered for all three types of loops, and it is shown that, in a general case, r depends on the vibration amplitude. In the particular case of power-law amplitude dependences of the decrement and the modulus defect, r does not depend on amplitude and depends only on the exponent n. Expressions have been obtained for the $r(n)$ dependence for the three hysteresis-loop types, and it is demonstrated that r can serve to identify the loop shape. A comparison of calculated curves with experimental data accumulated to date shows that most of them lie closer to the Davidenkov and WRF hystereses. An analysis has been made of the applicability of the secant modulus-defect approximation used to derive the dislocation strain from internal-friction measurements. © *1999 American Institute of Physics.* [S1063-7834(99)01807-9]

In 1938 Davidenkov, in an analysis of the reasons for the dependence of sound damping in crystalline solids on vibration amplitude, put forward a hypothesis that this dependence is the result of a hysteresis in microplastic strain ε_d .[1] Davidenkov suggested that the hysteresis loop has a two-fold symmetry axis, and that the nonlinearity in the microplastic strain can be approximated by a power-law stress function

$$\varepsilon_d = (\sigma + \sigma_0)^m - 2^{m-1}\sigma_0^m, \quad \text{for increasing } \sigma,$$

$$\varepsilon_d = -(\sigma_0 - \sigma)^m + 2^{m-1}\sigma_0^m, \quad \text{for decreasing } \sigma, \qquad (1)$$

where σ_0 is the vibration stress amplitude varying according to the harmonic law. Accordingly, for the vibration decrement one obtained also a power-law function $\delta_h \propto \sigma_0^n$, where $m = n+1$.

Read[2,3] was the first to relate the amplitude dependences of internal friction and of the elastic modulus defect in zinc and copper directly to dislocation motion. Because modern concepts consider microplastic deformation to be the result of a small and, as a rule, reversible displacement of dislocations, one can say that the experiments of Read provided direct support for the hypothesis of Davidenkov. Besides, Read established experimentally for the first time a proportionality between the amplitude-dependent decrement δ_h and the elastic-modulus defect $(\Delta M/M)_h$, which was subsequently confirmed by a number of researchers

$$\delta_h = r(\Delta M/M)_h, \qquad (2)$$

where the coefficient of proportionality r did not depend on the vibration amplitude but varied strongly (by about a factor ten) in zinc with variation of the sample orientation with respect to the basal plane of the hcp lattice.

Nowick[4] showed theoretically that the mechanism of simple (frequency-independent) hysteresis results in Eq. (2), where coefficient r does not depend on vibration amplitude

and can vary from zero to four (for the particular case of quadratic amplitude dependences of the decrement and modulus defect). He obtained different values of r for annealed and prestressed copper. The proportionality (2) was obtained also in the theory of Granato–Lücke,[5] where a conclusion was drawn that the ratio r should be of order unity, but no exact expression was presented. In later theories based both on the breakaway model of Granato–Lücke[5] and on various friction models (see, e.g., Ref. 6) attention was focused primarily on the vibration decrement.

Nowick[4] and Ishii[7] demonstrated that the behavior of the modulus defect and of the r ratio carry significant information, but these parameters, which allow experimental testing, have not been adequately studied in present theories of dislocation hysteresis. In most cases (see, e.g., Ref. 7) one used the approximate relation[8]

$$(\Delta M/M) \approx \varepsilon_{dm}/\varepsilon_0, \qquad (3)$$

where $\varepsilon_{dm} = \varepsilon_d(\sigma_0)$ is the amplitude value of the dislocation-induced strain, and ε_0, that of the elastic one, without analyzing the validity of this approximation.

An exact expression for the modulus defect measurable by acoustic methods can be derived by taking into account only the component of ε_d which is in phase with the applied vibration stress, i.e., by Fourier transformation. Nowick[4] employed this approach to analyze $(\Delta M/M)_h$ and r for the case of quadratic amplitude dependences of the decrement, Boser,[9] for the linear dependences, and Naimi[10] considered the amplitude dependences of δ_h and $(\Delta M/M)_h$ for the case of work against the generalized friction forces of Peierls–Nabarro. Granato used in his thesis[11] Fourier analysis for the breakaway model, but the mathematical difficulties associated with substitution of Koehler's distribution function[12] forced him to limit himself to an approximate expression,
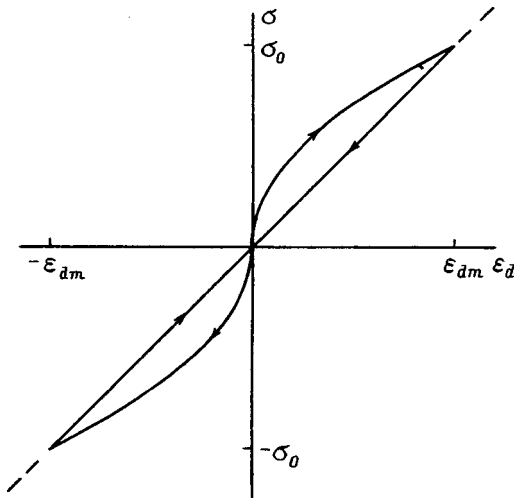
FIG. 1. Schematic representation of a generalized Granato–Lücke loop[5,6] drawn in the stress (σ) — dislocation strain (ε_d) coordinates.
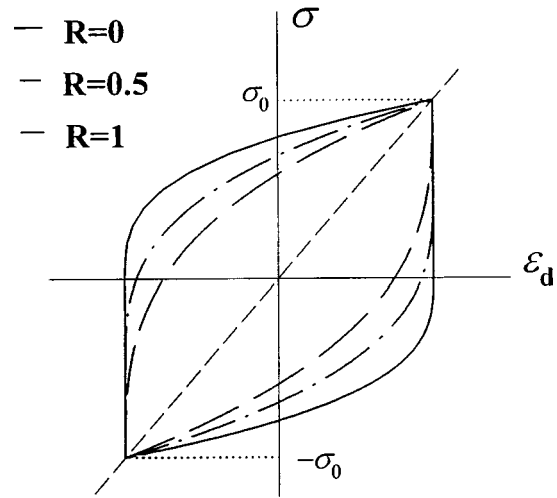

FIG. 2. Schematic presentation of various friction hystereses: Davidenkov loop ($R=1$), loop without restoring force ($R=0$), and a loop with partial restoring-force efficiency (a case of $R=0.5$). The dashed line passing through the origin illustrates the secant modulus defect (as in Fig. 1).

which led to the conclusion that the quantities δ_h and $(\Delta M/M)_h$ are practically equal, i.e., that $r \approx 1$.

This work deals with a theoretical consideration of the amplitude-dependent modulus defect and of the r ratio in various models of dislocation hysteresis. The work generalizes and complements the results reported by the author earlier in Ref. 13 (where the breakaway hysteresis is discussed in detail) and a short communication[14].

1. MAIN MODELS OF DISLOCATION HYSTERESIS

In the initial stages of amplitude-dependent internal friction (ADIF), vibration energy is lost in reversible hysteretic motion of dislocations in the force fields of barriers acting against it. The ADIF theories based on the string dislocation model of Koehler–Granato–Lücke[5,12] are presently enjoying the most widespread use. In these theories (see, e.g., Refs. 15–17), dislocation hysteresis occurs by breakaway followed by repinning at the same point defects during each vibration halfperiod. The associated displacements from the position of equilibrium are considered to be small, and it is assumed that the dislocation breaks away only from one row (linear array) of the weakest pinners, but that it cannot snap loose from strong point defects (dislocation network nodes, impurity precipitates etc.).

In other ADIF theories, a dislocation overrides several rather than one row (planar array) of point defects (c.f. Refs. 7,18,19) and even overcomes long-range internal stress fields[20,21] (one can find many relevant references in Ref. 21). Following the classification of Asano,[6] models of the first type are referred to as breakaway, and those of the second, as friction theories, because dislocation damping can be assigned here to an effective friction force.

Following Asano,[6] we shall call the generalized Granato–Lücke (or breakaway) model any model in which the stress–dislocation-strain diagram has the following pattern: the absolute value of ε_d grows nonlinearly from zero to a maximum $|\varepsilon_{dm}|$ with increasing absolute magnitude of stress σ, and falls off linearly from $|\varepsilon_{dm}|$ to zero when $|\sigma|$ decreases (Fig. 1). The reason for the nonlinearity of $\varepsilon_d(\sigma)$

is not specified. The general expression for the breakaway hysteresis can be written[6]

$$\delta_h(\sigma_0) = \frac{M}{\sigma_0}\left[\varepsilon_d(\sigma_0) - \frac{2}{\sigma_0}\int_0^{\sigma_0}\varepsilon_d(\sigma)\,d\sigma\right]. \qquad (4)$$

The principal difference between the friction and breakaway models consists in the shape of the hysteresis loop. In friction models (Fig. 2), a steady-state loop does not pass through the origin. The dashed line in Fig. 2 shows the Davidenkov loop; its main feature is the existence of a restoring force, so that the absolute value of the dislocation-induced strain starts to decrease as soon as the absolute magnitude of the stress has begun to decrease. The loop without restoring force (WRF) is shown in Fig. 2 with a solid line. Here the dislocation strain changes only after the stress has started to increase in absolute magnitude, and it remains constant when the absolute magnitude of stress decreases.

Asano[6] derived an expression for the generalized Davidenkov loop

$$\delta_h(\sigma_0) = \frac{M}{\sigma_0^2}\left[2\sigma_0\varepsilon_d(2\sigma_0) - 2\int_0^{2\sigma_0}\varepsilon_d(\sigma)\,d\sigma\right]. \qquad (5)$$

This relation is written for the origin located at the loop corner. The generalization consists actually in that $\varepsilon_d(\sigma)$ can be here any nonlinear function. Thus Eq. (5) can be formally applied to any loop having a twofold-symmetry axis, among which are both the WRF and Granato-Lücke hystereses (the actual form of this relation is determined by the choice of the origin, which, in its turn, is governed by physical considerations). For the WRF hysteresis, Eq. (5) can be conveniently recast in the coordinates of Fig. 2, so that the $\varepsilon_d(\sigma)$ function under the integral contains only the nonlinear portion

$$\delta_h(\sigma_0) = \frac{M}{\sigma_0^2}\left[4\sigma_0\varepsilon_d(\sigma_0) - 2\int_0^{\sigma_0}\varepsilon_d(\sigma)\,d\sigma\right]. \qquad (6)$$

2. THE TRUE AND SECANT MODULUS DEFECT AND THE *r* RATIO

The monograph of Lazan[22] makes use of the concept of the secant elasticity modulus, which is determined by the slope of the straight line connecting the ends of a hysteresis loop in the stress–total-strain coordinates. Because the amplitude value of total strain is a sum of the elastic, $\varepsilon_0 = \sigma_0/M$, and dislocation-induced, ε_{dm}, parts, and Figs. 1 and 2 present only the part associated with dislocations, the straight lines passing through the origin and the ends of the hysteresis loops in these figures correspond obviously to the modulus defect determined by Eq. (3); we shall call it the secant modulus and denote by $(\Delta M/M)_{\mathrm{sec}}$. Accordingly, the ratio of δ_h to $(\Delta M/M)_{\mathrm{sec}}$ will be denoted by r_{sec}. Now Eqs. (3) and (4) yield for the breakaway hysteresis

$$r_{\mathrm{sec}} = 1 - \frac{2}{\sigma_0 \varepsilon_d(\sigma_0)} \int_0^{\sigma_0} \varepsilon_d(\sigma)d\sigma. \tag{7}$$

In the case of the Davidenkov hysteresis we have to recall that Eq. (5) is written for the origin located in the lower left corner of the loop presented in Fig. 2. Nishino and Asano used a trivial expression for the secant modulus in these coordinates, $(\Delta M/M)_{\mathrm{sec}} = M\varepsilon_d(2\sigma_0)/2\sigma_0$, to obtain[23]

$$r_{\mathrm{sec}} = 4 - \frac{4}{\sigma_0 \varepsilon_d(2\sigma_0)} \int_0^{2\sigma_0} \varepsilon_d(\sigma)d\sigma. \tag{8}$$

Here $\varepsilon_d(\sigma)$ is the equation for the upper branch of the loop (for increasing stress). Assuming the condition $r_{\mathrm{sec}} = $ const, the integral equations (7) and (8) allow straightforward solution. Indeed, differentiating, for instance, Eq. (8) with respect to σ_0 yields

$$\frac{d\varepsilon_d}{\varepsilon_d} = \left(\frac{4 + r_{\mathrm{sec}}}{4 - r_{\mathrm{sec}}}\right) \frac{d(2\sigma_0)}{2\sigma_0}. \tag{9}$$

Next, taking into account that σ and σ_0 are actually the same stress (σ varies from zero to $2\sigma_0$), the subscript 0 on σ_0 can be dropped. Then if the $\varepsilon_d(\sigma)$ function and its derivative are continuous, integration of (9) yields a power-law relation $\varepsilon_d \propto \sigma^m$, where $m = (r_{\mathrm{sec}} + 4)/(4 - r_{\mathrm{sec}})$, and

$$r_{\mathrm{sec}} = 4(m-1)/(m+1). \tag{10}$$

Substituting $\varepsilon_d \propto \sigma^m$ in Eqs. (3) and (5) gives power-law relations for the decrement and the secant modulus defect with an exponent $n = m - 1$:

$$\delta_h = r_{\mathrm{sec}}(\Delta M/M)_{\mathrm{sec}} \propto \sigma_0^n. \tag{11}$$

In other words, if $r_{\mathrm{sec}} = $ const, then the generalized Davidenkov hysteresis for a continuous $\varepsilon_d(\sigma)$ function with a continuous derivative reduces to the simple Davidenkov hysteresis. The relation between r_{sec} and n follows from Eq. (10):

$$r_{\mathrm{sec}} = 4n/(n+2). \tag{12}$$

Similarly, Eq. (7) solved for $r_{\mathrm{sec}} = $ const likewise yields (11), where

$$r_{\mathrm{sec}} = n/(n+2). \tag{13}$$

Equations (10) and (12) for the original Davidenkov model were derived earlier[23–25] by direct substitution of ε_d

$\propto \sigma^m$ in equations of the type (3) or (8). This work deals with a more general problem, namely, one looked for a function $\varepsilon_d(\sigma)$ which is necessary and sufficient to meet the $r_{\mathrm{sec}} = $ const condition. As follows from the above, for continuous $\varepsilon_d(\sigma)$ and $\varepsilon_d'(\sigma)$ it is a power-law function. However even if one assumes the existence of a discontinuity in the derivative, as is the case, for example, with WRF hysteresis, it can be shown using Eqs. (3) and (6) that the necessary and sufficient condition for $r_{\mathrm{sec}} = $ const is a power-law course of the nonlinear portions in the $\varepsilon_d(\sigma)$ function. This results naturally in power-law amplitude dependences of the decrement and secant modulus defect (11), and one obtains the following relation for their ratio

$$r_{\mathrm{sec}} = 4(n+1)/(n+2). \tag{14}$$

Obviously enough, the absence of restoring force is actually equivalent to the case where this force is balanced by dislocation pinning at points farthest away from the equilibrium position (for $\varepsilon_d = \varepsilon_{dm}$). Introduce parameter R characterizing the efficiency of the restoring force. We write the loop equation in the form

$$\varepsilon_d = -\varepsilon_{dm}, \quad -R\sigma_0 > \sigma \geq -\sigma_0 \text{ and } \varepsilon_d$$
$$= \varepsilon_{d1}(\sigma), \quad \sigma \geq -R\sigma_0 \text{ for increasing } \sigma,$$
$$\varepsilon_d = \varepsilon_{dm}, \quad R\sigma_0 < \sigma \leq \sigma_0 \text{ and } \varepsilon_d$$
$$= \varepsilon_{d2}(\sigma), \quad \sigma \leq R\sigma_0 \text{ for decreasing } \sigma.$$

A loop with a partial efficiency of the restoring force is illustrated in Fig. 2 with a dot-dashed line (for $R = 0.5$). If $\varepsilon_{d1}(\sigma)$ and $\varepsilon_{d2}(\sigma)$ are power-law functions such that

$$\varepsilon_{d1} = (\sigma + R\sigma_0)^m - \sigma_0^m(1+R)^m/2,$$
$$\varepsilon_{d2} = -(R\sigma_0 - \sigma)^m + \sigma_0^m(1+R)^m/2,$$

one readily obtains

$$\delta_h = 2M(1+R)^m \sigma_0^{m-1}(m-R)/(m+1), \tag{15a}$$

$$(\Delta M/M)_{\mathrm{sec}} = M\sigma_0^{m-1}(1+R)^m/2, \tag{15b}$$

$$r_{\mathrm{sec}} = 4(m-R)/(m+1) = 4(n+1-R)/(n+2). \tag{15c}$$

For $R = 1$, Eqs. (15) yield δ_h, $(\Delta M/M)_{\mathrm{sec}}$, and r_{sec} for the Davidenkov hysteresis, and for $R = 0$, those for a pure WRF loop. Theoretically, R can vary from 1 to -1. The smaller is R, the weaker is the restoring force (or the stronger is the pinning force at the $\varepsilon_d = \varepsilon_{dm}$ points). For $R = -1$, the loop becomes a rectangle, which yields amplitude-independent hysteretic damping.

There are grounds to assume that any loop having a twofold symmetry axis, where the $\varepsilon_d(\sigma)$ function has a linear and a nonlinear portion with increasing σ, will yield power-law amplitude dependences of the decrement and modulus defect and independence of r_{sec} on amplitude. As an illustration, one may consider not only the friction but also the breakaway hysteresis, because Eq. (5) is valid for any symmetric loop, in particular, for the Granato–Lücke loop.

Let us consider now the actual modulus defect which can be measured by acoustic methods.

A. Granato-Lücke hysteresis

The diagram for the breakaway hysteresis is shown in Fig. 1, and the decrement is expressed by Eq. (4). The amplitude-dependent modulus defect is obtained from the Fourier transform

$$\left(\frac{\Delta M}{M}\right)_h = \frac{2M}{\sigma_0 \pi}\left[\int_0^{\pi/2}\varepsilon_d(\sigma_0 \sin\theta)\sin\theta d\theta\right.$$

$$\left.+\int_{\pi/2}^{\pi}\varepsilon_d(\sigma_0)\sin^2\theta d\theta\right],$$

and after substituting $\sigma=\sigma_0\sin\theta$

$$\left(\frac{\Delta M}{M}\right)_h = \frac{2M}{\sigma_0 \pi}\left[\int_0^{\sigma_0}\varepsilon_d(\sigma)\frac{\sigma d\sigma}{\sigma_0\sqrt{\sigma_0^2-\sigma^2}}+\frac{\pi}{4}\varepsilon_d(\sigma_0)\right]. \tag{16}$$

The r ratio follows from Eqs. (4) and (16):

$$r = \frac{2\varepsilon_d(\sigma_0)-\dfrac{4}{\sigma_0}\displaystyle\int_0^{\sigma_0}\varepsilon_d(\sigma)d\sigma}{\varepsilon_d(\sigma_0)+\displaystyle\int_0^{\sigma_0}\varepsilon_d(\sigma)\dfrac{\sigma d\sigma}{\sigma_0\sqrt{\sigma_0^2-\sigma^2}}}. \tag{17}$$

Because the integrals in the numerator and denominator of (17) are non-negative, we obviously come to $r \leq 2$.

If $r=$ const (i.e. it does not depend on vibration amplitude), the solution of integral equation (17) is a power-law function $\varepsilon_d(\sigma)\propto\sigma^m$.[13] Substituting $\varepsilon_d(\sigma)\propto\sigma^m$ in (4), (16), and (17) and replacing $m=n+1$ yields

$$\delta_h = r(\Delta M/M)_h \propto \sigma_0^n, \tag{18}$$

$$r = \frac{2n}{n+2+\dfrac{2(n+2)}{\pi}B\left(\dfrac{n+3}{2},\dfrac{1}{2}\right)}, \tag{19}$$

where $B(x,y)=\Gamma(x)\Gamma(y)/\Gamma(x+y)$ is the beta function, and Γ is the gamma function.

An $r(n)$ graph plotted using Eq. (19) is shown in Fig. 3 (curve a). Curve a' constructed using Eq. (13) depicts $r_{\text{sec}}(n)$. For $n\to\infty$, r tends to two, and r_{sec}, to unity.

It should be pointed out that Eq. (17) yields the r ratio for the generalized breakaway model, irrespective of the particular mechanisms and features responsible for the nonlinearity of $\varepsilon_d(\sigma)$, for instance the breakaway mechanism (a catastrophe, or detachment of double, triple etc. segments) or the shape of the distribution (of dislocation segments in length, or of pinning points in pinning force). Thus one can make two significant statements for any breakaway-model variant: (i) the r ratio does not exceed 2, and (ii) the independence of the r ratio of vibration amplitude is accounted for by the power-law form of the amplitude dependences of the decrement and modulus defect (18); if in the first and third quarters of the period the $\varepsilon_d(\sigma)$ function is continuous and has a continuous derivative, the relation between n and r is given by Eq. (19).
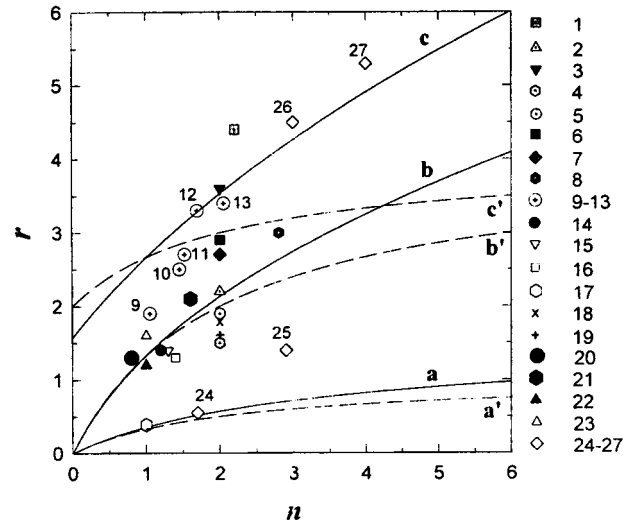

FIG. 3. Comparison of experimental values of $r(n)$ for materials given in Table II (the symbols are numbered in accordance with the lines) with theoretical curves for r (a,b,c) and r_{sec} (a',b',c'): a and a' correspond to the Granato–Lücke loop [Eqs. (19) and (13), respectively]; b and b' — to the Davidenkov loop [Eqs. (23) and (12)]; and c and c' — to the WRF loop [Eqs. (14) and (26)].

B. Davidenkov hysteresis

Using Fourier transformation, one can obtain the following general expression for the modulus defect within the generalized Davidenkov hysteresis model (Fig. 2, $R=1$):

$$\left(\frac{\Delta M}{M}\right)_h = -\frac{2M}{\pi\sigma_0^2}\int_{-\sigma_0}^{\sigma_0}\varepsilon_d(\sigma)\frac{\sigma d\sigma}{\sqrt{\sigma_0^2-\sigma^2}}. \tag{20}$$

For the r ratio one can write

$$r = \frac{\pi\displaystyle\int_{-\sigma_0}^{\sigma_0}\varepsilon_d(\sigma)d\sigma}{\displaystyle\int_{-\sigma_0}^{\sigma_0}\varepsilon_d(\sigma)\dfrac{\sigma d\sigma}{\sqrt{\sigma_0^2-\sigma^2}}}. \tag{21}$$

Substituting $\sigma=\sigma_0\cos\theta$ and the power-law relation (1) in (20) yields a power-law relation for the modulus defect:

$$(\Delta M/M)_h = (2M/\pi)\sigma_0^{m-1}\int_0^{\pi}(1+\cos\theta)^m\cos\theta d\theta. \tag{22}$$

Denoting $n=m-1$, we obtain for r

$$r = 2^{n+1}n\pi/\left[(n+2)\int_0^{\pi}(\cos\theta+1)^{n+1}\cos\theta d\theta\right]. \tag{23}$$

Equations (12) and (23) are also plotted in Fig. 3 (curves b' and b, respectively). We readily see that in the case of the Davidenkov hysteresis (as for the breakaway models) the secant modulus defect is a good approximation for the modulus defect derived from acoustic measurements, if the exponent is small ($n<5$). The error grows with increasing n (if $n\to\infty$, $r\to\infty$ and $r_{\text{sec}}\to4$).

TABLE I. The r and r_{sec} ratios of the amplitude-dependent decrement to modulus defect calculated for some values of n in the case of a power-law form of the $\delta_h = r(\Delta M/M)_h \propto \sigma_0^n$ relations.

n	Granato–Lücke hysteresis		Davidenkov hysteresis		WRF hysteresis	
	r	r_{sec}	r	r_{sec}	r	r_{sec}
0	0	0	0	0	1.57	2
0.5	0.21	0.20	0.79	0.80	2.16	2.40
1	0.36	0.33	1.33	1.33	2.67	2.67
2	0.57	0.50	2.13	2.00	3.53	3.00
3	0.71	0.60	2.74	2.40	4.27	3.20
4	0.82	0.67	3.25	2.67	4.91	3.33
5	0.90	0.71	3.69	2.86	5.49	3.43
6	0.97	0.75	4.09	3.00	6.01	3.50
7	1.03	0.78	4.46	3.11	6.50	3.56
8	1.07	0.80	4.79	3.20	6.95	3.60
9	1.11	0.82	5.11	3.27	7.39	3.64
10	1.15	0.83	5.41	3.33	7.80	3.67

C. Hysteresis without restoring force

The modulus defect for the WRF hysteresis can be written

$$\left(\frac{\Delta M}{M}\right)_h = \frac{2M}{\pi\sigma_0}\left[\int_0^{\sigma_0}\varepsilon_d(\sigma)\frac{\sigma d\sigma}{\sigma_0\sqrt{\sigma_0^2-\sigma^2}} + \varepsilon_d(\sigma_0)\right], \tag{24}$$

and the r ratio can be obtained from Eqs. (6) and (24):

$$r = \frac{2\pi\sigma_0\varepsilon_d(\sigma_0) - \pi\int_0^{\sigma_0}\varepsilon_d(\sigma)d\sigma}{\sigma_0\varepsilon_d(\sigma_0) + \int_0^{\sigma_0}\varepsilon_d(\sigma)\frac{\sigma d\sigma}{\sqrt{\sigma_0^2-\sigma^2}}}. \tag{25}$$

As in the two preceding cases, the solution of Eq. (25) for $r=\mathrm{const}$ is a power-law stress–dislocation-strain relation, which results in amplitude dependences of the decrement and modulus defect of the form (18). The expression for r can be written

$$r = \left[(n+1)^2\sqrt{\pi}\,\Gamma\left(\frac{n+1}{2}\right)\right]\Big/\left[(n+2)\Gamma\left(\frac{n+2}{2}\right)\right]. \tag{26}$$

Equation (26) yields $r=\pi/2$ for $n=0$ (linear WRF hysteresis). In this case we have amplitude-independent hysteretic damping, as, say, in the LDWRF mechanism (limited displacement without restoring force) proposed by Gremaud[26] to account for the internal-friction background in solid solutions.

Figure 3 shows $r(n)$ and $r_{\mathrm{sec}}(n)$ graphs, with curve c being a plot of Eq. (26), and curve c', that of Eq. (14). As in the case of the Davidenkov hysteresis, $r=r_{\mathrm{sec}}$ for $n=1$, and if $n\to\infty$, then $r\to\infty$ and $r_{\mathrm{sec}}\to 4$. As n increases, the secant modulus approximation for the WRF hysteresis yields a larger error than in the two preceding cases. The magnitude of this error can be judged from Table I listing numerical values of r and r_{sec} for some n from zero to 10 calculated for the three loops considered here.

3. AMPLITUDE-DEPENDENT INTERNAL FRICTION AND DISLOCATION STRAIN

Baker proposed in 1962 a simple algorithm for determining the mean dislocation velocities from ADIF data and demonstrated the relation of amplitude-dependent decrement to dislocation strain.[27] He made use of the proportionality between the decrement and the modulus defect (2), as well as of the approximate expression (3) for the dislocation-induced modulus defect. Then

$$\varepsilon_{dm} = \varepsilon_0\delta_h/r. \tag{27}$$

For steady-state vibrations, the dislocation strain rate $\dot\varepsilon_d$ is proportional to strain ε_{dm}, namely, $\dot\varepsilon_d = 4f_0\varepsilon_{dm}$, where f_0 is the vibration frequency. Then the average dislocation velocity V_{av} can be obtained using the well-known Orowan relation: $\dot\varepsilon_d = \Lambda b V_{av}$. Note that Eq. (27) does not depend on the shape of the hysteresis loop.

Asano[6] used another way to obtain the dislocation strain, namely, he obtained the solution to integral equation (5) in the form

$$\varepsilon_d(\sigma) = \frac{\sigma}{M}\left[\frac{1}{4}\delta_h(\sigma/2) + \int_0^{\sigma/2}\frac{\delta_h(\sigma_0)}{\sigma_0}\right]. \tag{28}$$

Nishino and Asano[28] used Eq. (28) to derive the $V_{av}(\sigma)$ relations from ADIF data and stressed that this procedure does not require any information concerning the modulus defect.

In the particular case of a power-law dependence of decrement on amplitude, $\delta_h \propto \sigma_0^n$, Eq. (28) yields the Davidenkov hysteresis. As follows from Sec. 2, however, the Davidenkov hysteresis is not the only solution to Eq. (5). In particular, for a power-law behavior of the nonlinear portions of the loops in Fig. 2 with exponent m, all of the loops yield a power-law amplitude dependence of decrement with an exponent $n=m-1$. Thus one cannot extract absolute values of dislocation strain and, accordingly, the average velocities of dislocation motion solely from data on the amplitude-dependent decrement. To be precise, using Eq. (28) may result in error in determining ε_d and V_{av}.

The method of Baker[27] was used[29,30] to derive the microyield stress σ_ε as the vibration amplitude providing a constant ε_{dm} level from ADIF data. One revealed a proportionality (called the similarity law) between the temperature dependences of micro- and macroyield stresses for a broad class of crystals.[29,30] The similarity law stems, in particular, from separation of variables in the amplitude and temperature dependences of the vibration decrement, $\delta_h = f_1(\sigma_0)f_2(T)$.

It is essential, however, that in the particular case of power-law relations (18) the error in determining ε_d depends only on the exponent n and, if n does not change under variation of external factors, the method of Baker[27] yields a constant error by a factor r_{sec}/r (which is small in cases of practical interest). The method of Asano[6] is capable of providing more information, because it permits one to obtain not only the amplitude value of dislocation strain ε_{dm} but the total response σ vs ε_d as well, but only provided one knows the shape of the loop, at least qualitatively. If, however, it is

TABLE II. Ratio r of the amplitude-dependent decrement to modulus defect for various crystals calculated for the case of power-law approximation $\delta_h = r(\Delta M/M)_h \propto \sigma_0^n$.

Line No.	Material	Impurities, %	T, K	f, kHz	r	n	Ref. (see Refs. 13, 14 for unspecified references)
1	Cu, s., ps.	0.002	293	33.5	4.4	2.1	Read, 1941 Ref. 3
2	Cu, s., ann.	0.01	293	39.8	2.2	2	Nowick, 1950 Ref. 4
3	Cu, s., ps.		213–306		3.6		
4	Cu, s., ann.	0.01 Si	5	80	1.5	2	Saul, Bauer, 1968
5		0.01 Si	81		1.9		
6		0.01 Si	294		2.9		
7		0.005 Ge	76–210		2.7		
8	Cu–Al, p., q.	1.38 Al	293	1	3	2.8	Takahashi, 1956
9	Cu–P, p.	0.002 P	293	2.7	1.8	1.05	*ibid.*
10		0.006 P			2.3	1.44	
11		0.021 P			2.7	1.52	
12		0.062 P			3.1	1.69	
13		0.207 P			3.3	2.05	
14	Cu–Si–Mn, p., ps.	1.6 Si, 1.4 Mn	7-293	100	1.4	1.2	Lebedev, Pilecki, 1995
15	Al, s.	0.66 Si, 0.22 Fe	6.5-293	100	1.4	1.3	Lebedev, Ivanov, 1993
16	Al–Al$_2$Cu, eu.	composite	6.5-293	100	1.3	1.4	Lebedev, Nikanorov, 1996
17	6061Al/SiC/Gr	composite	343	0.001	0.39	1	Zhang *et al.*, 1997 Ref. 31
18	NaF, s., ps.	0.01	293	100	1.8	2	Lebedev *et al.*, 1989
19	NaF, s., ps.	0.01	4.2-295	100	1.6	2	Kardashev *et al.*, 1974
20	LiF, s., ps.	0.01	293	0.0005	1.3	0.8	Kustov *et al.*, 1988
21	NaCl, s., ps.	0.01	293	0.0005	2.1	1.6	*ibid.*
22	MgO, s., ps.	0.2	65-295	100	1.2	1	Kardashev *et al.*, 1985
23	Zn, s., $\theta=0°$, ps.	0.003	293	100	1.6	1	Lebedev *et al.*, 1993
24	Zn, s., ann., $\theta=88°$	0.001	293	39	0.55	1.7	Read, 1940 Ref. 2
25	$\theta=20°$				1.4	2.9	
26	$\theta=74.5°$				4.5	3	
27	$\theta=61.3°$				5.3	4	

Note. s — single crystal, p — polycrystal, eu — eutectic alloy, ann — annealed, q — quenched, ps — prestressed, θ — angle between the normal to basal plane and sample axis.

unknown, the error in determining ε_d can become appreciable even for small n (although it should be pointed out that in this case too, the error depends only on n).

4. COMPARISON WITH EXPERIMENT

Most of the available experimental data exhibit a proportionality of the type (2) between δ_h and $(\delta M/M)_h$, which, as mentioned in the introduction, was first observed[2] by Read for zinc single crystals. This proportionality (see Sec. 2) is a consequence of the power-law form of Eq. (18) relating the amplitude dependences of the decrement and modulus defect, which is observed in a large number of experiments (see Table II).[a] Thus there is a possibility to compare theoretical $r(n)$ curves obtained for different types of hysteresis loops with experiment.

The available data are listed in Table II, and Fig. 3 displays them in a graphical form together with curves calculated for the three types of hysteresis loops depicted in Figs. 1 and 2. A comparison shows that most of the experimental points do not fall on the curve corresponding to the breakaway model and lie instead (although with a large scatter) around the $r(n)$ curves calculated for the Davidenkov and WRF hystereses. Only two out of 27 points lie on the curve corresponding to the Granato–Lücke model. We may recall that this model was developed for relatively pure crystals, and therefore a question arises about the origin of the

Granato–Lücke hysteresis in such a complex composite material as aluminum–silicon-carbide–graphite (line 17). This question remains unanswered.

Note that the orientational dependence of the r parameter observed by Read[2] as far back as 1940 finds, for the first time, a reasonable explanation. This dependence may quite possibly be due to the dislocation hysteresis mechanism by the Granato–Lücke breakaway model for a pyramidal slip system being replaced by WRF hysteresis for basal dislocations. For the orientations where both systems operate (line 25 in Table II), r acquires an intermediate value, which depends on the relative contribution of the two systems to hysteresis damping.

Interestingly, the data of Nowick[4] (lines 2 and 3 in Table II) for annealed copper are in accord with the Davidenkov hysteresis, and those for prestressed copper, to hysteresis without restoring force. This means that the restoring force in annealed copper originates from the Cottrell atmosphere formed in the course of annealing. A slight plastic deformation at room temperature releases old dislocations from these atmospheres and gives rise to new dislocations, which are initially free of impurities. Because the room-temperature mobility of point defects in copper is low,[34] the dislocation free paths become substantially larger than the radius of action of the Cottrell atmospheres responsible for the restoring force.

In Cu–P alloys (lines 9–13), an increase in phosphorus concentration to 0.06% reduces the restoring-force efficiency parameter to $R=0$, which implies that this force is fully balanced by the impurity pinning of dislocations at points of their maximum displacement from the positions of equilibrium, i.e., that we have here a pure WRF loop.

Thus a comparison of theoretical curves with experimental data shows that all types of dislocation-hysteresis loops considered here can be realized, and that the ratio of the r decrement to the modulus defect may serve to identify the loop shape.

One could add the following points to the main conclusions:

(1) The same functional form of $\delta_h(\varepsilon_0)$ may be observed with dislocation hysteresis loops of different shapes, but for a given amplitude-dependent vibration decrement there is a one-to-one correspondence between modulus defect and the shape of the hysteresis loop having a two-fold symmetry axis;

(2) Amplitude dependences of the modulus defect, as well as the r ratio, have been derived for all three types of dislocation hysteresis; it was shown that, in a general case, r depends on the vibration amplitude and that, in the breakaway models, r does not exceed two, and it can vary from zero to infinity in the friction models; also that in the particular case of power-law (18) relations for the decrement and modulus defect, r does not depend on vibration amplitude and is dependent only on the exponent n;

(3) While the dislocation strain derived from ADIF data with the use of Baker's algorithm[27] differs from actual values, in the case of the amplitude relations (18) having a power-law form both Eq. (27) and the method of Asano (28) may yield a difference in ε_d only in constant factors which are functions of n.

[a]ADIF curves exhibit, as a rule, the presence of more than one stage within a broad range of amplitudes (see, e.g., Refs. 32 and 33). Power-law (18) functions are observed usually in the initial stage.

[1] N. N. Davidenkov, Zh. Tekh. Fiz. **8**, 483 (1938).
[2] T. A. Read, Phys. Rev. **58**, 371 (1940).
[3] T. A. Read, Trans. AIME **143**, 30 (1941).
[4] A. S. Nowick, Phys. Rev. **80**, 249 (1950).
[5] A. V. Granato and K. Lücke, J. Appl. Phys. **27**, 583 (1956).
[6] S. Asano, J. Phys. Soc. Jpn. **29**, 952 (1970).
[7] K. Ishii, J. Phys. Soc. Jpn. **52**, 141 (1983).
[8] A. S. Nowick and B. S. Berry, *Anelastic Relaxation in Crystalline Solids* (Academic Press, New York, 1972).
[9] O. Boser, J. Appl. Phys. **54**, 2338 (1983).
[10] E. K. Naimi, Phys. Status Solidi A **72**, 825 (1982); Fiz. Met. Metalloved. **54**, 601 (1982).
[11] A. V. Granato, PhD Thesis, Brown University, Providence (1955).
[12] J. S. Koehler, *Imperfections in Nearly Perfect Crystals*, edited by W. Shockley, J. H. Hollomon, R. Mauerer, and F. Seitz (Wiley, New York, 1952), p. 197.
[13] A. B. Lebedev, Philos. Mag. A **74**, 137 (1996).
[14] A. B. Lebedev, J. Phys. IV **6**, C8-325 (1996).
[15] V. L. Indenbom and V. M. Chernov, Phys. Status Solidi A **14**, 347 (1972).
[16] A. V. Granato and K. Lücke, J. Appl. Phys. **52**, 7136 (1981).
[17] M. Gabbay, A. Vincent, and G. Fantozzi, Phys. Status Solidi A **100**, 121 (1987).
[18] R. B. Schwarz, Acta Metall. **29**, 311 (1981).
[19] V. I. Belan and A. I. Landau, Fiz. Met. Metalloved. **65**, 259 (1988).
[20] H. Kressel and N. Brown, *Dislocation Dynamics*, edited by A. R. Rosenfield, G. T. Hahn, A. L. Bement, and R. I. Jaffe (McGraw-Hill, New York, 1968), p. 337.
[21] S. B. Kustov and S. N. Golyandin, M_3D *III: Mechanics and Mechanisms of Materials Damping*, edited by A. Wolfenden and V. K. Kinra (ASTM, 1997), p. 22.
[22] B. J. Lazan, *Damping of Materials and Members in Structural Mechanics* (Pergamon Press, Oxford, 1968).
[23] Y. Nishino and S. Asano, Phys. Status Solidi A **138**, K9 (1993).
[24] S. B. Kustov, Cand. Sci. Thesis, Ioffe Institute (Leningrad, 1989).
[25] A. B. Lebedev and S. B. Kustov, Phys. Status Solidi A **136**, K85 (1993).
[26] G. Gremaud, J. Phys. (France) **48**, C8-15 (1987).
[27] G. S. Baker, J. Appl. Phys. **33**, 1730 (1962).
[28] Y. Nishino and S. Asano, Phys. Status Solidi A **151**, 83 (1995).
[29] A. B. Lebedev and S. B. Kustov, Phys. Status Solidi A **116**, 645 (1989).
[30] A. B. Lebedev, J. Alloys Compd. **211-212**, 177 (1994); J. Phys. IV **6**, C8-255 (1996).
[31] J. Zhang, R. J. Perez, and E. J. Lavernia, M_3D *III: Mechanics and Mechanisms of Materials Damping*, edited by A. Wolfenden and V. K. Kinra (ASTM, 1997), p. 313.
[32] S. P. Nikanorov and B. K. Kardashev, *Elasticity and Dislocation Anelasticity of Crystals* [In Russian] (Nauka, Moscow, 1985).
[33] B. I. Smirnov, V. A. Chelnokov, and N. L. Kuz'min, Fiz. Tverd. Tela (Leningrad) **25**, 519 (1983) [Sov. Phys. Solid State **25**, 293 (1983)].
[34] R. B. Schwarz, J. Phys. (France) **46**, C10-207 (1985).

Translated by G. Skrebtsov

Kinetics of periodic processes during plastic flow

S. A. Barannikova, L. B. Zuev, and V. I. Danilov

Institute of the Physics of Strength and Materials Science, Siberian Division, Russian Academy of Sciences, 634021 Tomsk, Russia

This paper establishes the dependence of the velocity of the self-consistent motion of the foci of inhomogeneous plastic deformation on the strain-hardening coefficient during the stretching of single-crystal γ Fe. It is shown that the relationship between the velocity and the indicated quantity is inversely proportional at the linear-hardening stage. An interpretation of the observed regularities is proposed on the basis of the concept of the autowave character of the plastic flow of solids and of self-organization in a deformed medium. The dispersion law of the plastic-deformation autowaves is established. © *1999 American Institute of Physics.* [S1063-7834(99)01907-3]

It has been established reliably in experimental studies of the inhomogeneity of plastic deformation of single crystals and polycrystalline materials that there is a close connection between the observed shape of the inhomogeneity and the nature of strain hardening of a material at the stage under consideration. The observed periodic regularities in the density distribution of dislocations and the strain over the sample have been interpreted[1,2] as the result of self-organization of a deformable medium in the shape of various forms of autowaves. Such an explanation[2] is based on the concept that a deformable medium is active, i.e., capable of self-organization in the sense of the spontaneous appearance of spatial, temporal, or functional inhomogeneities in it.[3] From the general standpoint of the theory of open systems,[4] such a situation is quite realistic for loaded deformable bodies through which an energy flux passes from the loading device.

The observed localization zones of plastic flow move along the sample during loading with a velocity of about $(10^{-4}–10^{-5})$ m/sec.[5,6] However, the question of the factors that determine the velocity V with which they are displaced remains open. There is special interest here in the case in which the plastic deformation is accompanied by a collection of equidistant strain-localization foci that simultaneously move along the sample. The task of this paper is to establish and analyze the possible shape of the dependence of V in this situation on the force parameters of the loading process, in particular on the generally accepted dynamic characteristic— the strain-hardening coefficient of the material, $\theta = d\sigma/d\varepsilon$.

1. EXPERIMENTAL CONDITIONS

As shown by the data published earlier,[2,5,6] a stable periodic pattern of plastic-deformation inhomogeneity is observed at the linear stages of the strain hardening of single crystals and polycrystalline materials under the condition θ=const. An equidistant sequence of from 3–6 foci of plastic flow is formed in the sample in this case, separated from each other by 5–10 mm and self-consistently moving with

constant velocity V. For experiments to determine how the strain-hardening coefficient affects V, a material is needed in which comparatively moderate actions that do not substantially alter the structure can be used to alter efficiently θ while maintaining the linear relationship between the strain and the stress. In this sense, it is convenient to use single crystals of highly doped γ iron grown from the melt by the Bridgman method and maintaining an fcc lattice at 300 K because of their high Ni concentration. By orienting the stretching axis along [100] or [111] and by also using diffusion saturation with nitrogen up to 0.3–0.5 wt.%, it was possible to obtain fairly long linear stages of flow in them, with the strain-hardening coefficient varying within the limits $1.2 \times 10^3 \leqslant \theta \leqslant 4.2 \times 10^3$ MPa, i.e., $\sim (0.5–2.0) \times 10^{-2} G$ (G is the shear modulus). The samples were stretched at a constant rate of $d\varepsilon/dt = 3.4 \times 10^{-5}$ sec^{-1} on an Instron-1185 test apparatus.

2. EXPERIMENTAL RESULTS

The speckle interferometry technique described in Refs. 2 and 5 was used to study the strain of such single crystals. This made it possible to determine the field of the components of the plastic-distortion tensor over the entire deformed sample, to display the configuration of the strain-localization zones, and to establish the following regularities for the stages of linear strain hardening: (1) The observed space–time pattern of the plastic-flow inhomogeneity in all cases has the shape of a wave travelling along the sample with constant velocity (Fig. 1). (2) The propagation velocity of this wave is $2 \times 10^{-5} \leqslant V \leqslant 7 \times 10^{-5}$ m/sec. (3) The propagation velocity varies as $V \sim \theta^{-1}$ (Fig. 2); i.e.,

$$V(\theta) = V_0 + J/\theta. \tag{1}$$

Such a shape of the dependence indicates that the observed wave processes are fundamentally different from known plasticity waves,[7] whose velocity is $V_p = (\theta/\rho_0)^{1/2}$; i.e. $V_p \sim \theta^{1/2}$ (ρ_0 is the density of the material). A simple estimate moreover indicates that $V_p \gg V$. It will be assumed
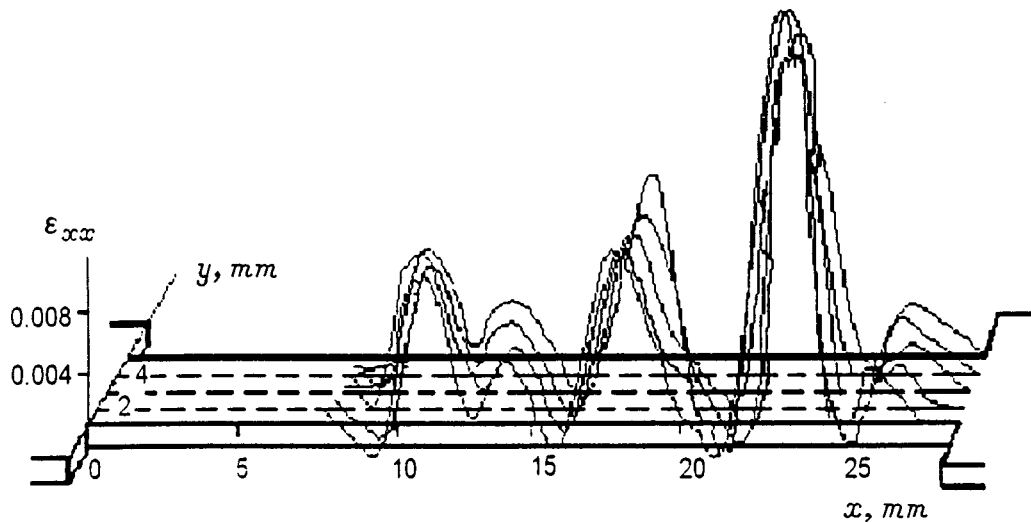
FIG. 1. Typical pattern of the strain distribution over the sample during stretching at the stage of linear hardening.

in what follows that the proportionality coefficient *J*, whose dimension is $[\mathrm{Pa \cdot m/sec}] = [\mathrm{J/m^2 \cdot sec}]$ (here θ has the dimension of σ), has the meaning of the energy flux passing through the strained object fastened in a loading device. All this means that the observed periodic space–time regularities of the inhomogeneous plastic flow must be assigned to the class of autowave phenomena[8] (self-organization processes in a deformable medium) alternative to ordinary waves. In this case, as is well known,[3,4,8] it is the presence of an energy flux flowing through the medium that allows it to possess self-organization processes. The elucidation of the character of the $V(\theta)$ relationship can contribute to the understanding of the nature of the periodic processes observed during deformation at least by comparing it to the shape of the analogous relationships for elastic and plastic waves.

3. DISCUSSION OF THE RESULTS

To understand the physical meaning of the dependence given by Eq. (1), we use the concept of the nature of θ proposed by Roitburg,[9] who regarded the strain-hardening coefficient as a ratio of energies:

$$\theta/G \sim W/Q \approx Gb^2\rho_s/\sigma bL\rho_m. \qquad (2)$$
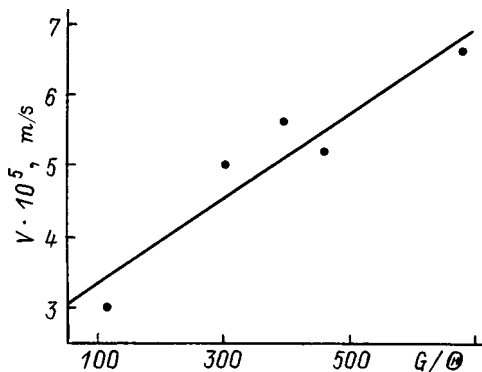
FIG. 2. Propagation velocity of autowaves vs the strain-hardening coefficient of single crystals.

Here $W \approx Gb^2\rho_s$ is the energy of the dislocations accumulated in the course of plastic deformation per unit volume, while $Q \approx \sigma bL\rho_m$ is the energy scattered into heat by the movable dislocations also per unit volume (*b* is the Burgers vector of the dislocations; ρ_s and ρ_m are the densities of the accumulated and movable dislocations, respectively; and *L* is their path length). When $J = $ const, increasing the density of the accumulated defects (increasing the strain hardening), according to Eq. (1), reduces the propagation velocity *V* of the autowaves. Conversely, increasing the amount of thermal energy scattered in the sample causes it to become heated, and this increases the probability of elementary events of thermally activated plastic deformation and promotes the increase in *V*. A similar separation of the contributions accords with the two-factor model of self-organization processes (the generation of autowaves) in an active medium, explained in Ref. 8. It is well known that such a process can be implemented in general when autocatalytic and damping factors with different kinematic and spatial characteristics act simultaneously. The data on the shape of the $V(\theta)$ dependence also make it possible to choose plastic deformation as the activating factor and elastic stresses as the damping factor. In accordance with the above, quantity $Q \sim L$, associated with the motion of dislocations during the deformation, serves as the autocatalytic factor of the process. Conversely, an increase of $W \sim \rho_s$ results in an increase of internal stresses of a dislocation nature ($\sigma_i \approx Gb\rho_s^{1/2}$); i.e. *W* should actually be regarded as a damping factor. Such an opposition of the roles of plastic deformation and elastic stresses in the self-organization of plastic flow was introduced for the first time by Nikolis and Prigozhin,[10] who then applied it in Refs. 2, 6, and 11. In terms of this approach, the linear stage of strain hardening corresponds to a steady-state ratio of the autocatalytic and damping factors that control the self-organization kinetics in an active medium.

From the resulting experimental data, it is possible to obtain the dispersion law of the observed autowaves, whose wavelength λ was directly determined from patterns analogous to those shown in Fig. 1, while the frequency ω of the
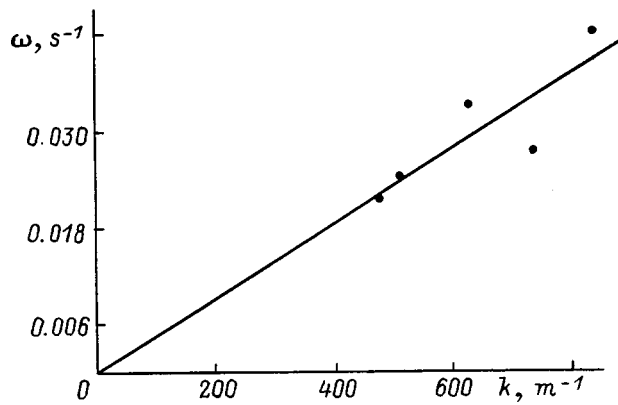
FIG. 3. Dispersion relationship for plastic-deformation autowaves.

periodic process was determined from sequences of them. Figure 3 shows the dependence of ω on wave number $k = 2\pi/\lambda$. Its linear character indicates the absence of dispersion in the case studied here; this is characteristic of autowave processes in nonlinear[12] or active[4,8] media. A numerical estimate shows that the slope of the straight line of $\omega(k)$ in Fig. 3 is $\omega/l \approx V_0$. In this case, Eq. (1) can be transformed to

$$V \approx \omega/k + J/\theta, \tag{3}$$

where the first term on the right characterizes the dispersionless character of the autowaves in a deformable medium, and the second term reflects the influence of the external deformation conditions on the value of V. In such a case, V can be understood as the signal-transport velocity in a deformable medium subjected to plastic stretching. Information concerning the beginning of the deformation process in a localized volume propagates with this velocity in the system.

The relationships established for the velocity $V(\theta)$ and the dispersion $\omega(k)$ of periodic vibrational processes of plastic flow are thus extremely important for the understanding of their nature. Most importantly, they allow the observed effects to be reliably excluded from the class of wave effects

and allow them to be regarded as self-organization processes in a deformable medium (autowave processes). The quantitative parameters of the $V(\theta)$ relationship then make it possible to also take into account the role of the factors that control the self-organization process and their connection with the loading conditions. Finally, the nondispersive nature of autowaves (the linear dispersion law) explains the observed stability of such structures during the linear stage of the plastic flow process. The sequential transition of one type of autowaves into another as the stages of plastic flow change is caused in this case by the change of state (structure) of the deformable medium. Here it is essential to keep in mind that the observed systems of localized strain foci appear when they are generated from the chaotic distribution of local strains characteristic of the transitional stages of the process; i.e., this is an ordering process in a deformable medium.

[1] G. A. Malygin, Fiz. Tverd. Tela **37**, 3 (1995) [Phys. Solid State **37**, 1 (1995)].

[2] L. B. Zuev and V. I. Danilov, Int. J. Solids Struct. **34**, 3795 (1997).

[3] H. Haken, *Information and Self-Organization. A Macroscopic Approach to Complex Systems* (Springer-Verlag, Berlin, 1988; Mir, Moscow, 1991).

[4] Yu. L. Klimontovich, *Statistical Theory of Open Systems* (Kluwer Academic, Dordrecht, 1995; Yanus TOO, Moscow, 1995).

[5] V. I. Danilov, L. B. Zuev, N. M. Mnikh, V. E. Panin, and L. V. Shershova, Fiz. Met. Metalloved. No. 3, 188 (1991).

[6] L. B. Zuev, V. I. Danilov, N. V. Kartashova, and S. A. Barannikova, Mater. Sci. Eng., A **234−236**, 699 (1997).

[7] H. Kolsky, *Stress Waves in Solids* (Clarendon Press, Oxford, 1953; Inostr. Lit., Moscow, 1995).

[8] V. A. Vasil'ev, Yu. M. Romanovskiĭ, and V. G. Yakhno, *Autowave Processes* [in Russian] (Nauka, Moscow, 1987).

[9] *The Physics of Strain Hardening of Single Crystals* [in Russian], edited by V. I. Startsev and V. Z. Bengus (Nauk. Dumka, Kiev, 1972), p. 5.

[10] G. Nikolis and I. Prigozhin, *Perception of the Complex* [in Russian] (Mir, Moscow, 1990).

[11] L. B. Zuev and V. I. Danilov, Fiz. Tverd. Tela **39**, 1399 (1997) [Phys. Solid State **39**, 1241 (1997)].

[12] A. M. Kosevich and A. S. Kovalev, *Introduction to Nonlinear Physical Mechanics* [in Russian] (Nauk. Dumka, Kiev, 1989).

Translated by W. J. Manthey

Determining the microhardness throughout the depth in a sample

A. B. Gerasimov, G. D. Chiradze, N. G. Kutivadze, A. P. Bibilashvili, and
Z. G. Bokhochadze

Tbilisi State University, 380028 Tbilisi, Georgia

In order to improve the accuracy of the microindentation mechanism, experimental data on the influence of the spectral composition and intensity of light on the microhardness of single-crystal Si and theoretical calculations have been analyzed to establish that a thin layer of high hardness exists near the surface of Si. This layer has a different influence on the microhardness, depending upon how deeply the indenter penetrates into the substance. © *1999 American Institute of Physics.* [S1063-7834(99)02007-9]

Knowing the mechanism by which an indentation forms under the action of an indenter has great significance not only for estimating the microhardness H but also for understanding the physical processes that occur when a crystal is damaged by an indenter. Even though quite a few papers have been devoted to this problem and significant successes have been achieved,[1–12] unfortunately it has not yet been fully solved.[11] This paper is devoted to a further study in this direction.

As is well known,[4] the microhardness at small loads is substantially greater than at high loads, when it approaches a steady-state value (Fig. 1a). As previously assumed,[4] this can be caused by the presence of defects in the surface layer. However, regardless of the nature of this phenomenon, it is of interest to determine the value of H throughout the depth. It can exhibit two kinds of behavior: (1) H gradually decreases until it reaches a steady-state value, or (2) a thin layer of high hardness exists near the surface and affects the value of the microhardness even when the indenter penetrates more deeply.

Since H is the mean value of the contact pressure on the area of the indentation, it is clear that a steady-state value of H will be reached when the pressure applied to the indenter by the part of the crystal with a constant microhardness value H is significantly larger than the analogous pressure produced by the harder upper layers. The hardness of these layers can be selectively changed by light. Therefore, in determining the correct model for the distribution of H over depth and in estimating its value, it can be very useful to study how the photomechanical effect (the variation of the microhardness under the influence of light)[1] depends on the spectral composition and intensity of the light.

The experiments were done on dislocation-free, single-crystal samples of n-type Si with resistivity $\rho = 200\,\Omega \cdot \text{cm}$, doped with Sb to give an impurity concentration of $N_d = 2.3 \times 10^{13}\,\text{cm}^{-3}$. The samples were cut along the (100) surface planes, and the misorientation did not exceed $0.3°$. The microhardness was measured on a Durimet apparatus by impressing with a standard four-sided Knoop pyramid. Before the measurement, the surface of the samples was subjected to chemical–mechanical processing, followed by annealing in vacuum. To ensure the constancy of the elastic recovery, the load was removed a definite time after the formation of the indentation.[3] In all the experiments, the large diagonal of the Knoop pyramid always coincided with the $\langle 100 \rangle$ direction of the (100) test plane, to prevent anisotropy from affecting the size of the indentation.[8] A DRSh-1000 lamp was used as the UV light source, and a K21-150 incandescent lamp with a tungsten filament and silicon ($\rho \sim 150\,\Omega \cdot \text{cm}$) filters $300\,\mu\text{m}$ thick was used as the IR source. The intensity was varied by changing the number of lamps and neutral-density filters. To prevent thermal effects, the system of lamps, filters, and the test crystal was cooled by an air flow. The thickness of the SiO_2 film on the Si test surface, measured by an ellipsometric microscope, did not exceed $30\,\text{Å}$. Special experiments were run to show that a SiO_2 layer up to $60\,\text{Å}$ had no effect on the shape of $H = \varphi(P)$.

It was shown in Ref. 10 that light with a quantum energy of $h\nu > \Delta E_g$ (where ΔE_g is the band gap) acts at low loadings, i.e., for small penetration depths of the indenter, while light with quantum energies $h\nu < \Delta E_g$ acts in the entire load interval that we studied. This results from the different penetration depths of the light. It can be seen from Fig. 1b that H decreases linearly as the intensity of the IR radiation increases. This is because the IR radiation has a low absorption coefficient and penetrates into the entire region of the crystal damaged by the indenter for any penetration depths of the indenter. However, when UV light acts on the system, the linear falloff of H transforms into saturation because the UV light is absorbed in a thin surface layer of the crystal, and the influence of this layer on the value of H decreases as the penetration depth of the indenter increases.

As can be seen from Fig. 1a (curve *2*), the UV light stops acting when the loadings are greater than $100\,\text{g}$. Starting from the absorption coefficient of the UV radiation into Si and recalling that the penetration depth of the UV light is less than $0.1\,\mu\text{m}$, it can be assumed that the value of H in the loading regions beyond $100\,\text{g}$ is mainly determined by the part of the crystal that is not subjected to the action of the light. Thus, the surface layer with increased H must be less than $0.1\,\mu\text{m}$ thick, and the value estimated from curve *1* in
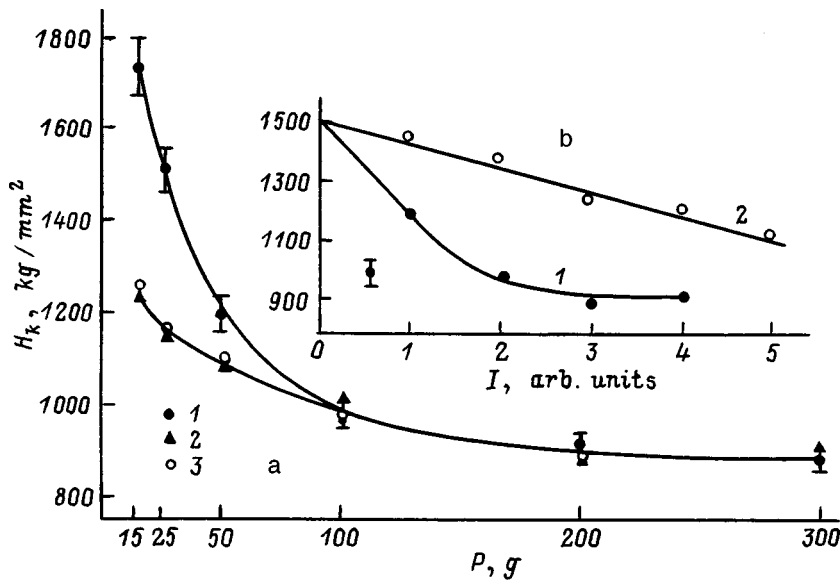
FIG. 1. (a) Experimental and calculated curves of the load dependence of the microhardness of Si: *1*—in the dark, *2* and *3*—under the action of UV radiation (experimental and calculated, respectively). The measurement error indicated in the dark for the given load also relates to the illuminated system. (b) Microhardness of Si vs illumination intensity, under the action of photons with *1*—$h\nu > \Delta E_g$, *2*—$h\nu < \Delta E_g$, (*I* is the intensity of the light sources in arbitrary units, and 0 corresponds to darkness).

Fig. 1a when it is extrapolated[1)] to a load of 1 g is $H \approx 3000 \, \text{kg/mm}^2$.

Starting from these premises, if H is represented as changing from one layer to another with definite values of the layer thickness h_j and H_j (Fig. 2a), the mean value of H can be calculated for a given load (and the dependence of H on load P can thereby be determined) by the following technique: One must compute the force with which each layer acts on the indenter for the corresponding load and then sum all the forces and divide by the area over which the embedded part of the indenter contacts the material: $H = \Sigma F_j / S$, where $F_j = H_j / S_j$ is the force exerted by the jth layer, S_j is the area of the jth layer, and H_j is the microhardness of the jth layer. Keep in mind in this case that the friction and the damage around the indentation is observed to increase as the load increases.[7] This is because, when the force of the lower layer (F_3) with a steady-state value of H is greater than the

force of the upper thin layers ($F_1 + F_2$) with high values of H by comparison with the steady-state values, the substance extruded from the lower layer will disturb or break open the upper layers and will thereby reduce the influence of the upper layers, Fig. 2a. The larger the difference of these forces, the larger will be the damage of the upper layers and the smaller will be their contribution to the mean microhardness. This can be taken into account quantitatively if the force of the upper layers is reduced by the factor by which the force of the lower layer is greater than the sum of the forces of the upper layers, i.e., by introducing the coefficient

$$\alpha = F_3 / (F_1 + F_2).$$

It should be pointed out that $\alpha > 1$ in this particular case for loads of 50 g and above. The $H = \varphi(P)$ dependence calculated by this technique is shown in Fig. 2b (curve *2*), where
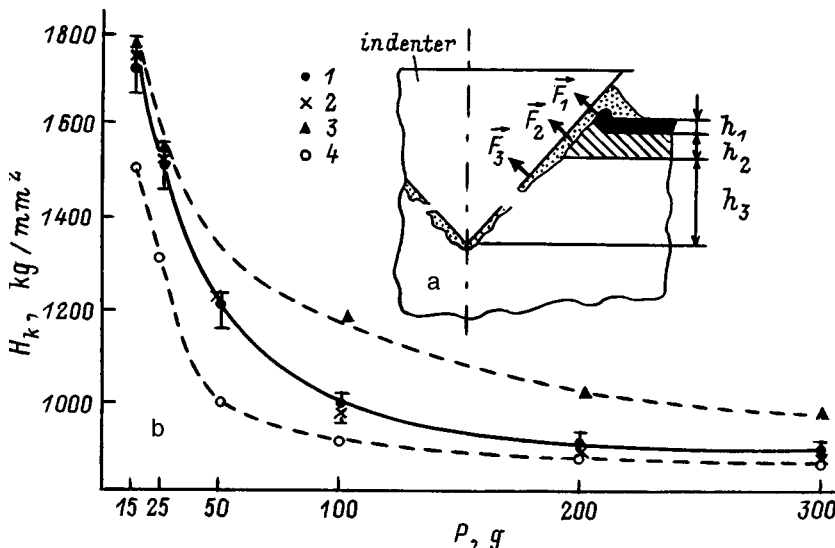
FIG. 2. (a) Schematic image of the penetration of the indenter into the material: h_1 and h_2 are, respectively, the thicknesses of the surface layer and the transition layer, and h_3 is the thickness of a layer with the steady-state value of H. F_i are the forces acting on the indenter from the corresponding layer. (b) Load dependence of the microhardness of Si in the dark: *1*—experimental, *2*—calculated, taking into account coefficient α, with $h_1 = 0.03$ and $h_2 = 0.07 \, \mu\text{m}$, $H_1 = 2900$, $H_2 = 2600$ and $H_3 = 900 \, \text{kg/mm}^2$, *3* and *4*—neglecting coefficient α.

it can be seen that, to within experimental error, it completely coincides with curve *1*, obtained by experiment. It should be pointed out that it is impossible to obtain such agreement for any variation of parameters h_j and H_j (curves *3* and *4* in Fig. 2b) if the breaking open of the upper solid layers is neglected. Evidence in favor of the above considerations concerning the depth and magnitude of layers with increased H is provided by experiments on the dependence of the photomechanical effect on the intensity and quantum energy of the light, Fig. 1. Actually, if one takes into account the absorption coefficient of UV and the depth of the first layer h_j, its influence on H when it is illuminated by UV light must be negligible. In this way, the calculated $H = f(P)$ curve agrees well with the experimental results shown in Fig. 1a (curves *3* and *2*).

Evidence of the presence of a thin layer in which H is significantly higher than the steady-state value is provided by the data of Ref. 11.

It can thus be concluded that a thin layer of high hardness exists near the Si surface that affects the value of H differently, depending on the penetration depth of the indenter into the substance.

[1]It should be pointed out that it is very difficult to obtain reliable experimental values of H in Si for loads less than 5 g.

[1] G. C. Kuczynsky and R. H. Hochman, Phys. Rev. **108**, 946 (1957).

[2] P. P. Kuz'menko, N. N. Novikov, N. R. Gorid'ko, and L. I. Fedorenko, Fiz. Tverd. Tela **8**, 1732 (1966) [Sov. Phys. Solid State **8**, 1381 (1966)].

[3] V. M. Glazov and V. N. Vigdorovich, *Microhardness of Metals and Semiconductors* [in Russian] (Metallurgiya, Moscow, 1969).

[4] V. K. Grigorovich, in *Test Methods for Microhardness* [in Russian] (Nauka, Moscow, 1965), p. 35.

[5] V. I. Kruglov, Uch. Zap. Leningr. Gos. Univ. No. 386, 119 (1976).

[6] V. P. Alekhin ''Physical regularities of microplastic deformation of the damage of the surface layers of a solid'' Author's abstract of dissertation, Kiev, 1978.

[7] Yu. S. Boyarskaya and M. I. Val'kovskaya, *Microhardness* [in Russian] (Shtiintsa, Kishinev, 1981), p. 67.

[8] P. D. Uoren, S. G. Roberts, and P. B. Khirsh, Izv. Akad. Nauk SSSR, Ser. Fiz. **51**, 812 (1987).

[9] A. B. Gerasimov, Z. V. Dzhibuti, and G. D. Chiradze, Soobshch. Akad. Nauk Gruzii **142**, No. 1, 53 (1991).

[10] A. B. Gerasimov and G. D. Chiradze, Soobshch. Akad. Nauk Gruzii **142**, No. 1, 61 (1991).

[11] Yu. I. Golovin and A. I. Tyurin, Fiz. Tverd. Tela **37**, 1562 (1995) [Phys. Solid State **37**, 849 (1995)].

[12] A. B. Gerasimov, G. D. Chiradze, N. G. Kutivadze, A. P. Bibilashvili, and Z. G. Bokhochadze, Fiz. Tverd. Tela **40**, 503 (1998) [Phys. Solid State **40**, 462 (1998)].

Translated by W. J. Manthey

MAGNETISM AND FERROELECTRICITY

Long-lived induction signal in antiferromagnets with a dynamic NMR frequency shift

V. S. Rukhlov[*]

Kazan Physicotechnical Institute, Russian Academy of Sciences, 420029 Kazan, Russia
(Submitted June 26, 1998)
Fiz. Tverd. Tela (St. Petersburg) **41**, 1228–1230 (July 1999)

This paper discusses manifestations of the singularities that appear in the frequency distribution when an acoustic NMR mode is excited by an rf pulse. The conditions are found for observing the power-law decay of the homogeneous precession. The macroinhomogeneous-broadening suppression effect is predicted. It is found that the nuclear spin–spin relaxation rate can be measured from the long-lived component of the induction signal. © *1999 American Institute of Physics.* [S1063-7834(99)02107-3]

1. A number of problems of pulsed NMR in weakly anisotropic antiferromagnets are associated with reconstructing the inhomogeneously broadened spectrum of the acoustic NMR mode of mixed vibrations of the electronic and nuclear spins.[1] The dependence of the spectrum on the excitation level is caused by the dynamic frequency shift (DFS) of the NMR,[2,3] which determines the substantially nonlinear nature of the spin dynamics and plays a key role in the mechanisms by which the frequency-modulated (FM) echo is formed.[4] However, the possibility of obtaining reliable information concerning the kinetic properties of the spin system by means of the FM echo when there is strong nonlinearity does not have an adequate theoretical basis. The questions that appear here have a general character for nonlinear spin systems with large deviations from equilibrium and are also being actively studied in experiments of the nuclear spin echo in solid ^{3}He.[5,6]

This paper is the first to discuss one of the main consequences of the nonisochronism of the precession during an rf pulse, which consist of the appearance of singularities in the perturbed frequency distribution, namely, points with an infinitely large density of the isochromatic curves. This matter is important because the position and nature of the singularities largely determine both the spectral content and the damping rate of the response.

Unlike Ref. 3, here we study a substantially nonlinear situation, in which the variations of the NMR resonance frequencies are comparable to the initial detunings. We are mainly interested in the appearance of the primary singularity of the perturbed distribution in the simplest case of single-pulse rf excitation.

2. We use the two-sublattice model of an easy-plane antiferromagnet and consider the case of transverse pumping, in which the gain $\eta = |\mathbf{H}_n|/|\mathbf{H}|$ is maximized, where $\mathbf{H}_n$ is the hyperfine field at the nucleus. In this case, the constant magnetic field $\mathbf{H}$ that determines the equilibrium orientation of the magnetic moments of the sublattices and the rf field $\mathbf{H}_1(t) = 2\mathbf{h}\cos\Omega t$ perpendicular to it, with amplitude $2|\mathbf{h}|$

$\ll |\mathbf{H}|$ and frequency $\Omega = 2\pi\nu$, lie in a plane with small magnetic anisotropy.

The equations that describe the precession of the nuclear magnetization m of the sublattice, taking into account the Suhl–Nakamura interaction,[7,8] look especially simple in a rotating system of coordinates connected to the sublattice,[3]

$$\begin{cases} m_x = -[\Delta\Omega + \Omega_p m_z/m_0]m_y - m_x/T_2, \\ m_y = [\Delta\Omega + \Omega_p m_z/m_0]m_x + \Omega_1 m_z - m_x/T_2, \\ m_z = -\Omega_1 m_y - (m_z - m_0)/T_1, \end{cases} \quad (1)$$

where $\Delta\Omega = 2\pi\Delta\nu = \Omega - \Omega_n^0$ is the detuning relative to the undisplaced NMR frequency $\Omega_n^0 \approx \gamma|\mathbf{H}_n|$, $\Omega_p = 2\pi\nu_p$ is the equilibrium value of the DFS, and $T_{1,2}$ are the spin–lattice and spin–spin relaxation times, respectively. The **Z** axis is directed along the equilibrium magnetization $\mathbf{m_0}$ ($m_0 = |\mathbf{m_0}|$) of the nuclear sublattice, while the **X** axis is along the circularly polarized resonance component of the amplified rf field at the nucleus, whose amplitude in frequency units is $\Omega_1 = 2\pi\nu_1 = \gamma\eta|\mathbf{h}|$, where γ is the nuclear gyromagnetic ratio.

In actual samples, the NMR line is inhomogeneously broadened and has a Gaussian shape. It is assumed that the main contribution to the inhomogeneous line width $\delta\Omega = 2\pi\delta\tilde{\nu}$ is introduced by the scatter $\delta\Omega_p = 2\pi\delta\nu_p = \Omega_p - \Omega_p^0$ of the Ω_p values at distances that substantially exceed the Suhl–Nakamura interaction radius r_{SN}.[1] The DFS $\Omega_p^0 = 2\pi\nu_p^0 = \langle\Omega_p\rangle$ averaged over the sample determines the displaced NMR frequency $\Omega_n^0 - \Omega_p^0$.

3. Let us limit the width t_p of the rf pulse by the condition that the conservative approximation $t_p \ll T_{1,2}$ can be used. Then Eqs. (1) reduce to the equation for a nonlinear oscillator.[9] Allowing for macroinhomogeneous broadening, the spin system when such a pulse acts is an ensemble of noninteracting nonlinear oscillators with different resonance frequencies.

Let us transform Eqs. (1) to dimensionless variables: the dynamic detuning $\zeta = (\nu_p m_z/m_0 + \Delta\nu)3|\Delta\nu\nu_1^2|^{1/3}$, the transverse components of the magnetization $\zeta^{x,y}$

$=(\nu_p/3|\Delta\nu^2\nu_1|^{1/3})(m_{x,y}/m_0)$, and the pulse width τ_p $=3|\Delta\Omega\Omega_1^2|^{1/3}t_p$. The solution of the system of Eqs. (1) is well known in the conservative approximation.[9] Under ordinary experimental conditions,[4,10,11] we restrict ourselves to studying it in the zeroth approximation in the small parameter

$$(\nu_1/\Delta\nu)^{2/3}\ll 1, \tag{2}$$

and we consider the initial equilibrium detunings $\zeta_0=(\nu_p+\Delta\nu)/3|\Delta\nu\nu_1^2|^{1/3}$ lying to the left of the separatrix value $\zeta_s=2^{-2/3}$. The region $\zeta_0<\zeta_s$ contains the maximum amplitudes $\varkappa_r(\zeta_0)=-(2/3)[\varkappa_+(\zeta_0)+\varkappa_-(\zeta_0)]^2$ of the deviations of ζ from their equilibrium values ζ_0, where $\varkappa_\pm(\zeta_0)=[1/2\pm(1/4-\zeta_0^3)^{1/2}]^{1/3}$.

The approximate solution $\zeta(\zeta_0,\tau_p)$ is a single-parameter family of mappings[12] of equilibrium detunings ζ_0 into perturbed detunings ζ. The distribution of the perturbed resonance frequencies, with formation of a single-pulse FM echo,[10,11] is modulated because they are crowded together at the compressing sections of the mapping, $|\partial\zeta(\zeta_0,\tau_p)/\partial\zeta_0|<1$, and are thinned out at the stretching sections of the mapping, $|\partial\zeta(\zeta_0,\tau_p)/\partial\zeta_0|>1$.

It is clear that, when the width of the compressing sections is comparable to the equilibrium width of the line, it is possible to suppress the macroinhomogeneous broadening. Moreover, the suppression is most efficient when the detuning from the center of the equilibrium NMR line, $\zeta_0^0=\langle\zeta_0\rangle$, coincides with the critical points of function $\zeta(\zeta_0,\tau)$, at which the maximum number of its first derivatives with respect to ζ_0 go to zero.

The first degenerate critical point ζ_{03}^*, in which two first derivatives go to zero simultaneously, appears in the region of small detunings when the threshold value $\tau_p=\tau_p^*$ is reached. In order to find τ_p^*, it is sufficient to investigate the approximate solution in the neighborhood of the turning point $\zeta_r(\zeta_0)=\zeta_0-\varkappa_r(\zeta_0)$ of the oscillator. For equilibrium initial conditions $m_{x,y}=0$ and $m_z=m_0$, it has the form

$$\zeta(\zeta_0,\tau_p)=\zeta_r(\zeta_0)-\{\zeta_r(\zeta_0)[\zeta_r^2(\zeta_0)-\zeta_0^2]+8/27\}$$
$$\times[\tau_p-\theta(\zeta_0)]^2,$$

where the rf pulse width τ_p is close to the half-period of the vibrations of the nonlinear oscillator, $\theta(\zeta_0)\cong7.286(1+0.615\zeta_0+0.250\zeta_0^3)$.

4. From the condition that two first derivatives of $\zeta(\zeta_0,\tau_p)$ go to zero, we find $\zeta_{03}^*\cong-0.210$ and $\tau_p^*=\theta(\zeta_{03}^*)\cong6.312$. After an rf pulse with parameters $\zeta_0^0=\zeta_{03}^*$ and $\tau_p=\tau_p^*$, the perturbed detunings equal $\zeta_3(\zeta_0,\tau_p^*)=\zeta(\zeta_0^*+\delta\zeta_0,\tau_p^*)\cong\zeta_3^*+\delta\zeta_3$. The critical value $\zeta_3^*=\zeta(\zeta_{03}^*,\tau_p^*)\cong0.630$ is the center of the distribution of the perturbed resonance detunings ζ_3, whose scatter $\delta\zeta_3\equiv\zeta_3-\zeta_3^*$ is associated with the scatter of the equilibrium DFS values $\delta\zeta_0\equiv\zeta_0-\zeta_0^0=\delta\nu_p/3|\Delta\nu\nu_1^2|^{1/3}$ by the relationship $\delta\zeta_3=C_3\delta\zeta_0^3$, where $C_3\cong1.86$.

The distribution density of the perturbed detunings after pulsed excitation at a degenerate critical point is divergent, and, for a Gaussian shape of the unperturbed NMR line, has the form

$$g(\delta\zeta_3)=(1/3\sqrt{2\pi}\sigma_0C_3^{1/3})\exp(-\delta\zeta_3^{2/3}/2C_3^{2/3}\sigma_0^2)\delta\zeta_3^{-2/3}.$$

It follows from a comparison of the equilibrium rms values $\sigma_0=\langle\delta\zeta_0^2\rangle^{1/2}=\delta\tilde\nu/6\sqrt{2\ln2}|\Delta\nu\nu_1^2|^{1/3}$ and the perturbed rms values $\sigma=\langle\delta\zeta^2\rangle^{1/2}=\sqrt{15}C_3\sigma_0^3$ of the scatter of the detunings that, to efficiently suppress the broadening, the inequality

$$\delta\tilde\nu/|\Delta\nu|\leqslant(\nu_1/\Delta\nu)^{2/3}\ll1 \tag{3}$$

needs to be satisfied.

Estimates based on the data of Ref. 4 show that the scatter in the frequencies can be made substantially less than the homogeneous line width.

We shall describe the decay of the induction signal because the perturbed inhomogeneity in the resonance approximation by means of the circularly polarized component of the dimensionless magnetization averaged over the ensemble, $\langle\zeta^+(\tau_f)\rangle=\langle\zeta_x(\tau_f)+i\zeta_y(\tau_f)\rangle$, where τ_f is the dimensionless time, measured from the instant of turning off the pulse. Omitting the details of the computations, we note only that, when dissipation is neglected, this component is expressed in terms of rapidly oscillating integrals.[12]

The main consequence of the power-law divergence of the perturbed distribution is that a long-lived component of the induction signal (IS) appears, whose decay is described by the power-law asymptotic expression

$$|\langle\zeta_3^+(\tau_f)\rangle|\cong\frac{3^{1/2}\Gamma(1/3)}{2(2\pi)^{1/2}\sigma_0C_3^{1/3}}[(\zeta_3^*)^2-(\zeta_{03}^*)^2]\tau_f^{-1/3}.$$

With such a character of the decay, Bloch relaxation becomes the dominant damping factor of the long-lived component at times $\sim T_2$. Therefore, to observe the power law, it is necessary that the time to reach the asymptote be less than the spin–spin relaxation time. Recalling that $|\Delta\nu|\simeq\nu_p^0$, this condition is expressed by the inequality

$$((\nu_1^2\nu_p^0)^{1/3}/\delta\tilde\nu)^2<T_2\delta\tilde\nu/3, \tag{4}$$

which limits the pulse amplitude from above. When inequality (3) is satisfied, the damping rate of the IS is virtually completely determined by the spin–spin relaxation, and no power-law section is observed.

5. When $\tau_p>\tau_p^*$, the degenerate critical point ζ_{03}^* is split into two nondegenerate points $\zeta_{0+}^*(\Delta\tau_p)$ and $\zeta_{0-}^*(\Delta\tau_p)$, where $\Delta\tau_p=\tau_p-\tau_p^*$. For $0<\Delta\tau_p\leqslant1$, their position is described by

$$\zeta_{0\pm}^*(\Delta\tau_p)\simeq\zeta_{03}^*\pm0.26\sqrt{\Delta\tau_p}+0.12\Delta\tau_p.$$

Analogously to the preceding treatment, it is shown that, for critical detuning values of the rf pulse from the center of the equilibrium NMR line, $\zeta_0^0=\zeta_{0\pm}^*(\Delta\tau_p)$, the perturbed distribution has asymmetric square-root singularities at the points $\zeta_\pm^*(\Delta\tau_p)=\zeta[\zeta_{0\pm}^*(\Delta\tau_p),\tau_p^*+\Delta\tau_p]$. These correspond to the long-lived components of the IS, which decay according to the law

$$|\langle\zeta_\pm^+(\tau_f)\rangle|\sim\tau_f^{-1/2}.$$

6. There is special interest for the experiment in how the frequencies $\zeta_\pm^*(\Delta\tau_p)$ of the long-lived harmonics in the IS depend on the pulse width. The graph of this dependence is

the caustic of the single-parameter family of functions $\zeta(\zeta_0, \tau_p)$,[12,13] which is described close to the turning point ζ_3^*, τ_p^* by the semicubic parabola

$$(\zeta^* - \zeta_3^*)^2 \simeq 3.8 \times 10^{-3} (\tau_p - \tau_p^*)^3.$$

Note that this analysis is equivalent in mathematical terms to the constructions of catastrophe theory used in analyzing diffraction caustics in optics.[12,13] In this case, the surface of the perturbed detunings $\zeta(\zeta_0, \tau_p)$ close to the caustic and its turning point gives the normal shape of the fold and assembly catastrophes, respectively.

7. The condition for the appearance of singularities with large detunings, $|\zeta_0^0| > 1$, has the form $\tau_p \cong 27(\zeta_0^0)^2$ and is more rigorous. For the long-lived IS to be observed in this region, the power of the rf pulse needs to be 3–4 orders of magnitude higher than for small detunings. Therefore, such a possibility is not discussed here.

The question of the possible relaxation manifestations of the singularities of a perturbed frequency distribution is also not touched on. The treatment above depends only on the experimental fact that, even with a fairly strong pulsed perturbation, the character of the signal damping because of spin–spin relaxation remains approximately exponential, even though the value of T_2 can vary.[4]

8. Unfortunately, the published experimental data are insufficient for a reliable check of the results given here. The studies in Ref. 11 of the Fourier spectrum of the rf response by the parametric-echo method are the closest to the subject of this article. However, they were carried out only for τ_p values less than the threshold τ_p^*, when the role of nonlinearity is small. Nevertheless, the results of Ref. 11 for zero detuning $\zeta_0^0 = 0$ reflect, in our view, a tendency for the perturbed spectrum to narrow with increasing τ_p.

The most persuasive confirmation of the theoretical conclusions obtained here would be the experimental observation of the power-law sections in the falloff of the IS and, in particular, the dependence $t_f^{-1/3}$. Taking into account the results of our analysis and the experimental possibilities,[4,10,11] it seems convenient to use pulses for this purpose whose parameters are close to the values $\Delta\nu + \nu_p^0 = -0.21\delta\tilde{\nu}$, $\nu_1 = (\delta\tilde{\nu}/3)^{3/2}\nu_p^{-1/2}$, and $t_p = 1/\delta\tilde{\nu}$. Moreover, since the power-law asymptotic dependence is masked by the spin–spin relaxation, samples with the maximum T_2 are necessary.

The optimum parameters of the rf pulses for measuring T_2, as follows from Eq. (3), must be close to the values $\nu_1 = \delta\tilde{\nu}^{3/2}\nu_p^{-1/2}$, $t_p = 1/3\delta\tilde{\nu}$, and $\Delta\nu + \nu_p^0 = -0.63\delta\tilde{\nu}$. From the viewpoint of variations of the frequencies of the long-lived harmonics, the most informative portion must be the "tail" of the IS at times $t_f \gtrsim T_2$.

9. The general conclusion is that the long-lived components of the IS and FM echo must serve as an information source concerning spin relaxation for highly nonlinear excitation regimes. The long-lived IS must be observed in the region of small detunings, where there is no single-pulse FM echo.[4] Its use can therefore substantially increase the analytical possibilities of the pulse method in nonlinear NMR. The formation mechanism of the long-lived IS is just as universal as the formation mechanism of the echo because of anharmonicity,[14] while the conditions needed for observing it do not go beyond the framework of known experiments.[4,10,11]

In conclusion, the author expresses his gratitude to G. V. Teĭtel'baum, N. K. Solovarov, and V. N. Lisin for useful discussions.

*)E-mail: rukhlov@dionis.kfti.kcn.ru

---

[1] A. S. Borovik-Romanov, Yu. M. Bun'kov, B. S. Dumesh, M. I. Kurkin, M. P. Petrov, and V. P. Chekmarev, Usp. Fiz. Nauk **142**, 537 (1984) [Sov. Phys. Usp. **27**, 235 (1984)].

[2] P. G. de Gennes, P. A. Pincus, F. Hartman-Boutron, and M. Winter, Phys. Rev. **129**, 1105, (1963).

[3] M. I. Kurkin and E. A. Turov, *NMR in Magnetically Ordered Substances and Its Application* [in Russian] (Nauka, Moscow, 1990).

[4] Yu. M. Bun'kov and B. S. Dumesh, Zh. Éksp. Teor. Fiz. **68**, 1161 (1975) [Sov. Phys. JETP **41**, 576 (1975)].

[5] G. Deville, M. Bernier, and J. M. Delrieux, Phys. Rev. B **19**, 5666 (1979).

[6] T. Matsushita, R. Nomura, H. H. Hensley, H. Shida, and T. Mizusaki, J. Low Temp. Phys. **105**, 67 (1996).

[7] H. Suhl, Phys. Rev. **109**, 606 (1958).

[8] T. Nakamura, Prog. Theor. Phys. **20**, 542 (1958).

[9] E. A. Turov, M. I. Kurkin, and V. V. Nikolaev, Zh. Éksp. Teor. Fiz. **64**, 283 (1973) [Sov. Phys. JETP **37**, 147 (1973)].

[10] V. P. Chekmarev and M. P. Petrov, Zh. Éksp. Teor. Fiz. **71**, 377 (1976) [Sov. Phys. JETP **44**, 197 (1976)].

[11] Yu. M. Bun'kov and S. O. Gladkov, Zh. Éksp. Teor. Fiz. **73**, 2181 (1977) [Sov. Phys. JETP **46**, 1141 (1977)].

[12] V. I. Arnol'd, *Catastrophe Theory* (Springer-Verlag, Berlin, 1986; Nauka, Moscow, 1990).

[13] R. Gilmore, *Catastrophe Theory for Scientists and Engineers* (Wiley, New York, 1981; Mir, Moscow, 1984), vol. 1.

[14] R. M. Gould Astrophys. J., Suppl. **37**, 585 (1969).

Translated by W. J. Manthey

Features of the motion of a 180° domain boundary in a thin ferromagnetic film with defects

Yu. I. Dzhezherya and M. V. Sorokin

Institute of Magnetism, Ukrainian Academy of Sciences, 252680 Kiev, Ukraine
(Submitted July 20, 1998)
Fiz. Tverd. Tela (St. Petersburg) **41**, 1231–1235 (July 1999)

For a thin ferromagnetic film, the braking process of a 180° domain boundary in a field of randomly distributed point defects is studied using perturbation theory. It is established that, for low velocities, the motion of the boundary is nonsteady-state. It is shown that the critical velocity of steady-state motion depends substantially on film thickness and the defect concentration. © *1999 American Institute of Physics.* [S1063-7834(99)02207-8]

Questions regarding the braking of domain boundaries (DBs) play a central role in the theory of magnetically ordered systems. Dissipation processes have been widely studied by various authors in terms of a phenomenological approach[1–6] based on the introduction of relaxation terms of relativistic and exchange nature into the equation of the magnetization dynamics. However, DB-braking mechanisms exist that cannot be considered on the basis of the principles of a phenomenological approach. One of them is associated with the interaction of moving DBs with magnetic-structure defects. To more accurately determine the nature of the magnetization dynamics, the effect of this process should be considered in detail.

This paper discusses the influence of structural defects on the DB-braking processes in a thin ferromagnetic film. The character of the DB motion has been studied in the entire range of velocities in terms of the model used here, for materials with various magnetic and relaxation parameters.

It can be shown on the basis of a simple analysis that, for small velocities, the nature of the DB motion is determined by interactions with the defect field.

It is obvious that the variation of the kinetic energy of the DBs caused by an external magnetic field has the form

$$\frac{\partial E_{\text{kin}}}{\partial v} \dot{v} = 2M_0 H S v - P(v), \tag{1}$$

where E_{kin} is the kinetic energy of the DB, H is the external magnetic field; M_0 is the saturation magnetization, S is the area of the DB, v is the velocity of the DB, and $P(v)$ is the power lost by the DBs.

To determine the condition of steady-state motion, we represent the velocity of the DB in the form

$$v = v_0 + v_1(t), \tag{2}$$

where $v_0 = \text{const}$ is the velocity of the steady-state motion, determined by the equation

$$2M_0 H S v_0 - P(v_0) = 0. \tag{3}$$

Here v_1 are small corrections $|v_1| \ll v_0$ that satisfy the equation

$$\frac{\partial E_{\text{kin}}}{\partial v_o} \dot{v}_1 = 2M_0 H S v_1 - \frac{\partial P(v_0)}{\partial v_0} v_1, \tag{4}$$

whose solution has the form

$$v = \text{const} \exp(\gamma^* t),$$

$$\gamma^* = \left(P(v_0) - \frac{\partial P(v_0)}{\partial v_0} v_0 \right) \bigg/ \frac{\partial E_{\text{kin}}}{\partial v_0} v_0. \tag{5}$$

The sign of γ^* determines whether the small addition to the constant velocity increases or decreases as time passes. If $\gamma^* < 0$, v_1 damps out, and the DB will move with constant velocity. Eliminating from γ^* factors known to be positive and using Eq. (3), we can write the criterion of steady-state motion as

$$\gamma(v_0) = P(v_0) - \frac{\partial P(v_0)}{\partial v_0}] v_0 \leqslant 0. \tag{6}$$

In describing the dissipation processes by the Hilbert relaxation term in the Landau–Lifshitz equation, the power lost because a thermostat absorbs the energy of the moving DBs is proportional to the square of the velocity, and a DB moves uniformly at any velocity less than the Walker velocity. It was obtained in Ref. 7 that, for small velocities, the power lost by DBs when they interact with a defect field is proportional to $\sqrt{v}$. Inequality (6) is not satisfied in this case, and the motion of the DB is not steady-state. This paper discusses the possibility of implementing regions of nonsteady-state motion for a wider range of velocities, all the way to the Walker value.

In studying the character of the motion of a flat DB, we assume that the energy density of a ferromagnetic film has the following form:

$$w = \frac{1}{2} M_0^2 \Bigg\{ \alpha \left(\frac{\partial \mathbf{M}}{\partial x_i} \right)^2 - \beta M_z^2 + \frac{1}{4\pi} \mathbf{H}_m^2$$

$$+ \Delta\alpha \Delta V \sum_n \left(\frac{d\mathbf{M}}{\partial x_i} \right)^2 \delta(\mathbf{x} - \mathbf{x}_n) \Bigg\}, \tag{7}$$

where α and β are the exchange-interaction constant and the easy-axis anisotropy, $\mathbf{M}$ is the unit magnetization vector, and $\mathbf{H}_m$ is the magnetostatic field; the constant term in Eq. (7) is

associated with the presence of point defects whose interaction potential with the magnetization field has a δ-form localization and is associated with a change in a small neighborhood with volume ΔV of the exchange-interaction constant by a value $\Delta\alpha$; $\mathbf{x}_n$ is the radius vector of a defect.

We shall study the dynamics of the magnetization in a coordinate system whose Z axis is orthogonal to the plane of the ferromagnetic film, while the surface of the DB is parallel to YZ. Then the magnetization distribution in the ground state will depend upon one spatial variable x.

For a thin ferromagnetic film, the magnetostatic field can be represented with good accuracy in the Winter approximation,[4]

$$\mathbf{H}=-4\pi M_x\mathbf{e}_x, \tag{8}$$

where $\mathbf{e}_x$ is the unit vector along X.

To find the solution, it is convenient to use the variables $\mathbf{m}=(m_x,m_y,m_z)$, connected with $\mathbf{M}$ by

$$\mathbf{M}=\begin{pmatrix} \cos\chi & 0 & \sin\chi \\ 0 & 1 & 0 \\ -\sin\chi & 0 & \cos\chi \end{pmatrix}\begin{pmatrix} \cos\theta & \sin\theta & 0 \\ -\sin\theta & \cos\theta & 0 \\ 0 & 0 & 1 \end{pmatrix}$$

$$\times\begin{pmatrix} m_x \\ m_y \\ 1+m_z \end{pmatrix}. \tag{9}$$

Vector $\mathbf{m}$ corresponds to the perturbations of the DB caused by the interaction with the defect field. In this case, the ground state is determined by the Walker solution

$$\mathbf{M}_w=\begin{pmatrix} \cos\chi_0\sin\theta \\ \sin\chi_0\sin\theta \\ \cos\theta \end{pmatrix},$$

$$\theta=2\arctan\exp(\xi-\xi_0),$$

$$\xi=x/\delta, \quad \delta=\sqrt{\alpha/\beta^*}, \quad \beta^*=\beta+4\pi\cos^2\chi_0,$$

$$\frac{\partial\chi_0}{\partial\tau}=\alpha_G v^*, \quad \alpha_G\frac{\partial\chi_0}{\partial\tau}+v^*+\frac{2\pi}{\beta^*}\sin2\chi_0, \quad \frac{\partial\xi_0}{\partial\tau}=v^*,$$

$$v^*=v/\omega_0\delta, \quad \tau=\omega_0 t, \quad \omega_0=2\beta^*\mu_B M_0/\hbar, \tag{10}$$

where μ_B is the Bohr magneton.

If the film is thin, magnetic moment oscillations along the perpendicular to its plane can be neglected. From the condition $|\mathbf{M}|=1$ and using Eq. (9), we get that $m_z=-\frac{1}{2}(m_x^2+m_y^2)$ is an order of magnitude smaller than m_x and m_y. The Landau–Lifshitz equation in the linear approximation will then look like

$$\left(-v^*\frac{\partial}{\partial\xi}+\frac{\partial}{\partial\tau}\right)\sigma_{ij}m_j+\hat{G}_{ij}m_j=f_i,$$

$$\sigma_{ij}=\begin{pmatrix} \alpha_G & -1 \\ 1 & \alpha_G \end{pmatrix}, \quad \mathbf{m}=(m_x,m_y),$$

$$\hat{G}_{xx}=\hat{B}^+-\frac{\partial^2}{\partial\eta^2}, \quad \hat{G}_{xy}=\hat{G}_{yx}=-\frac{1}{2}Q^{-1}\sin2\chi\tanh\xi,$$

$$\hat{G}_{yy}=\hat{G}_{xx}-Q^{-1}\cos2\chi, \quad Q=\beta^*/4\pi,$$

$$\hat{B}=\frac{\partial}{\partial\xi}+\tanh\xi,$$

$$\mathbf{r}=(\xi,\eta,\zeta), \quad \eta=\frac{y}{\delta}, \quad \zeta=\frac{z}{\delta},$$

$$f=\begin{pmatrix}1\\0\end{pmatrix}\left[\sum_n\varepsilon\frac{\sinh\xi}{\cosh^2\xi}\delta(\mathbf{r}-\mathbf{r}_n+\xi_0\mathbf{e}_x)-\frac{\dot\chi-\dot\chi_0}{\cosh\xi}\right],$$

$$\varepsilon=(\Delta\alpha/\alpha)(\Delta V/\delta^3). \tag{11}$$

When the size of the defects is much less than the thickness of the DB, the form of the right-hand side is independent of the nature of the defects and is caused by the distribution of the magnetization in the DB itself. An equation identical to Eq. (10) was obtained in Ref. 7 for the variables m_x and m_y, and it was shown that, in first order in ε, the scattering at the defects does not change the dynamic properties of the DB ($\dot\chi=\dot\chi_0$).

For highly anisotropic films, the solution of Eq. (11) in zeroth approximation in $Q^{-1}\ll1$ can be written as an expansion in the eigenfunctions (EFs) of the operator $\hat{B}^+\hat{B}$, which have the form

$$\varphi(\xi)=\frac{1}{\sqrt{2}}\sec h\xi, \tag{12.1}$$

$$\psi_k(\xi)=\frac{\exp(i\mathbf{k}\cdot\mathbf{r})\{-ik_\xi+\tanh\xi\}}{(2\pi)^{3/2}(1+k_\xi)^{1/2}}, \tag{12.2}$$

where $\mathbf{k}=\mathbf{q}\delta$, $\mathbf{q}$ is the wave vector, $\varphi(\xi)$ is an EF of the discrete spectrum, describing the surface distortions of the DB, and $\psi_k(\xi)$ corresponds to the volume vibrations of the magnetization. As shown in Ref. 8, the contribution of volume spin waves to the energy dissipation of DBs moving in a defect field is negligible for highly anisotropic materials, and only the effect of the surface perturbations of the DBs will be included in what follows. We thus write the value of $\mathbf{m}(\mathbf{r},\tau)$ in the form

$$\mathbf{m}(\mathbf{r},\tau)=\mathbf{m}(\eta,\tau)\varphi(\xi). \tag{13}$$

Averaging Eq. (11) over the thickness L_z of the film and finding the scalar product with the EF given by Eq. (12.1), we get an equation for $\mathbf{m}(\eta,\tau)$:

$$\left[\frac{\partial^2}{\partial\tau^2}+2\alpha_G\left(-\frac{\partial^2}{\partial\eta^2}-\frac{2\pi}{\beta^*}\cos2\chi\right)\frac{\partial}{\partial\tau}\right.$$

$$\left.-\frac{\partial^2}{\partial\eta^2}\left(-\frac{\partial^2}{\partial\eta^2}-\frac{4\pi}{\beta^*}\cos2\chi\right)\right]\mathbf{m}(\eta,\tau)=\mathbf{F}(\eta,\tau),$$

$$\mathbf{F}(\eta,\tau)=\varepsilon\frac{\delta}{L_z}\left(\begin{array}{c}-\dfrac{\partial^2}{\partial\eta^2}-\dfrac{4\pi}{\beta^*}\cos 2\chi \\ \\ \dfrac{\partial}{\partial\tau}\end{array}\right)\sum_n\frac{\sinh(\xi_n-\xi_0)}{\cosh^3(\xi_n-\xi_0)}\delta(\eta-\eta_n). \tag{14}$$

For the Fourier transform of the components of the magnetization, we get from Eq. (14) the simple algebraic equation

$$\left[-\omega^2-2\alpha_G\left(k^2-\frac{2\pi}{\beta^*}\cos 2\chi\right)i\omega+k^2\left(k^2-\frac{4\pi}{\beta^*}\cos 2\chi\right)\right]\mathbf{m}(k,\omega)=\mathbf{F}(k,\omega),$$

$$\mathbf{F}(k,\omega)=\varepsilon\frac{\delta}{L_z}\frac{i}{8\pi v^{*3}}\left(\begin{array}{c}k^2-\dfrac{4\pi}{\beta^*}\cos 2\chi \\ \\ -i\omega\end{array}\right)\frac{\omega^2}{\sinh\dfrac{\pi\omega}{2v^*}}\sum_n\exp\left[i\left(\omega\frac{\xi_n}{v^*}-k\eta_n\right)\right], \tag{15}$$

whose solution has the form

$$\mathbf{m}(k\omega)=\varepsilon\frac{\delta}{L_z}\sum_n\mathbf{a}(k,\omega)\exp\left[i\left(\omega\frac{\xi_n}{v^*}-k\eta_n\right)\right],$$

$$\mathbf{a}(k,\omega)=\frac{(-i)}{8\pi v^{*3}}\left(\begin{array}{c}k^2-\dfrac{4\pi}{\beta^*}\cos 2\chi \\ \\ -i\omega\end{array}\right)\frac{\omega^2\sinh^{-1}\left(\dfrac{\pi\omega}{2v^*}\right)}{\left[\omega^2+2\alpha_G\left(k^2-\dfrac{2\pi}{\beta^*}\cos 2\chi\right)i\omega-k^2\left(k^2-\dfrac{4\pi}{\beta^*}\cos 2\chi\right)\right]}. \tag{16}$$

Using the inverse Fourier transformation, we write $\mathbf{m}(\eta,r)$ as

$$\mathbf{m}(\eta,r)=\varepsilon\frac{\delta}{L_z}\sum_n\int\int dk d\omega\,\mathbf{a}(k,\omega)$$

$$\times\exp\{i[k(\eta-\eta_n)-\omega(\tau-\xi_n/v^*)]\}. \tag{17}$$

To determine the power lost by the DB, we use the dissipative function

$$P(v)=\int d\mathbf{r}\left\{\frac{\delta w}{\delta\mathbf{M}}\frac{\partial}{\partial t}\mathbf{M}\right\}. \tag{18}$$

In the given case, two terms can be distinguished in the expression for the lost power:

$$P(v)=P_1(v)+P_2(v). \tag{19}$$

The former term, $P_1(v)$, corresponds to the absorption by the thermostat of the energy of the moving unperturbed DB

$$P_1(v)=2\alpha_G\omega_0 M_0^2\beta^* S\delta v^{*2}. \tag{20}$$

The latter term, $P_2(v)$, describes the energy losses that result from the emission of spin waves excited when the DBs interact with the defects of the magnetic structure

$$P_2(v)=\alpha_G\omega_0 M_0^2\beta^* L_z\delta^2\int d\eta\left|\frac{\partial\mathbf{m}(\eta,\tau)}{\partial\tau}\right|^2. \tag{21}$$

Knowing the explicit form of the deviation of the magnetization from the ground state, we get the following expression for $P_2(v)$:

$$P_2(v)=\alpha_G\omega_0 M_0^2\beta^*\frac{\delta^4}{L_z}\varepsilon^2$$

$$\times\sum_{n,m}\int\int d\eta\,dk d\omega\,dk'd\omega'\,\omega\,\omega'\,\mathbf{a}^+(k',\omega')$$

$$\times\mathbf{a}(k,\omega)+\exp\{i[(k-k')(\eta-\eta_n)-(\omega-\omega')$$

$$\times(\tau-\xi_n/v^*)]\}. \tag{22}$$

We assume that the defects are randomly distributed in the film, with a contribution to the sum being given only by the diagonal terms ($m=n$). We introduce into the discussion the defect concentration n and transform in Eq. (22) from summation to integration over the spatial variables. After some simple transformations, we get the following expression for the power lost:

$$P_2(v)=4\pi^2\omega_0\alpha_G M_0^2\beta^* L_y\delta^5\varepsilon^2 nv^*$$

$$\times\int dk d\omega\,\omega^2\,|\mathbf{a}(k,\omega)|^2. \tag{23}$$

It is easy to see that, in the thin-film approximation, the losses $P_2(v)$ are independent of the thickness of the film.

Analysis shows that inhomogeneities whose size is of the order of the volume of the crystal cell make no appreciable contribution to the relaxation processes.

Therefore, substantial variations in the character of the motion of the DBs are possible if the ferromagnet contains a large number of defects, $n\delta^3\sim 1$, of sufficiently large size $\Delta V\approx(0.1\delta)^3$.
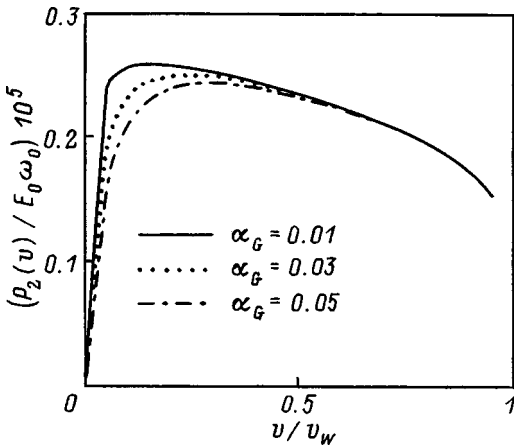
FIG. 1. Power lost by DBs because of their interaction with defects vs velocity when $L_z = \delta$ and $n\delta^3 = 1$ ($E_0 = 2\beta^* M_0^2 L_y \delta^2$, and $v_w = \dfrac{2\pi}{\beta^*}\omega_0\delta$ is the Walker velocity).

We shall carry out further studies for materials with magnetic parameters $\alpha = 10^{-8}\,\mathrm{cm}^2$, $\beta = 100$, and $M_0 = 10\,\mathrm{G}$, in which we assume that $\Delta\alpha \approx \alpha$.

Figure 1 shows how the power lost by a DB in the form of kinetic energy depends on the velocity of its motion in materials with various dissipative characteristics α_G.

As the velocity of the DB increases, the losses of kinetic energy initially increase proportionally to $\sqrt{v}$, which agrees with the results of Ref. 7. It is noteworthy that power $P_2(v)$ decreases with increasing dissipative constant α_G. This is caused by the decrease of the amplitude of the DB perturbations in a dissipative medium. The presence of a maximum of $P_2(v)$ is observed in the figure, and its decrease can be traced in the high-velocity region. From a physical viewpoint, this is associated with the influence of the DB velocity on the dispersion law of spin waves.[8] As the velocity increases, the energy of a spin wave excited by defects decreases. When this occurs, the role of the given relaxation channel decreases.

An analysis of the $\gamma(v)$ dependence shown in Fig. 2 in terms of the model used here makes it possible to speak of the features of the DB motion. Thus, the point where the graph of $\gamma(v)$ intersects the horizontal axis determines the critical velocity v_c, which depends on the magnetic proper-

FIG. 3. Critical velocity of steady-state motion vs defect concentration when $\alpha_G = 0.02$, $L_z = \delta$.

ties of the material and the defect density. The decrease of v_c as the relaxation constant α_G increases can be explained by the strengthening of the role of relativistic and exchange relaxations in the DB-braking process.

Figure 3 shows a graph of $v_c(n)$ for a film with thickness $L_z = \delta$, which shows that increasing the defect density causes the critical velocity to increase. It can be seen from an analysis of the expression for the power losses given by Eq. (23) that, as the film gets thicker, just as with an increase of the relativistic constant, the relativistic and exchange braking processes, which have a stabilizing effect on the DB motion, become more important. Thus, Fig. 4 shows the result of calculating the dependence of the critical velocity v_c on the film thickness.

Our studies have thus shown that, for small DB velocities, the braking mechanism at defects is the main one, and it causes the appearance of the region of nonsteady-state motion. As α_G increases, the power lost by the DBs because of their interaction with the defect field declines, and the critical velocity of steady-state motion decreases accordingly. It is found that v_c increases with increasing defect density and decreasing film thickness.

In conclusion, the authors thank Professor Yu. I. Gorobets for useful discussions of the results.

FIG. 2. Criterion for steady-state motion of the DBs vs velocity when $L_z = \delta$, $n\delta^3 = 1$ ($E_B = 2\beta^* M_0^2 L_y \delta^2$ is the energy of a Bloch DB).
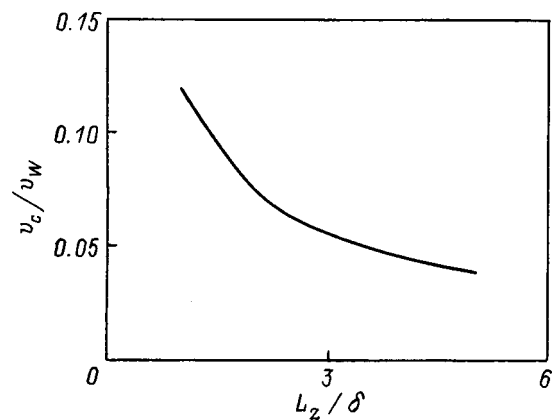
FIG. 4. Critical velocity of steady-state motion vs film thickness when $\alpha_G = 0.02$, $n\delta^3 \approx 0.3$.

[1] V. G. Bar'yakhtar, Zh. Éksp. Teor. Fiz. **87**, 1501 (1984) [Sov. Phys. JETP **60**, 863 (1984)].

[2] V. G. Bar'yakhtar, Zh. Éksp. Teor. Fiz. **91**, 1454 (1986) [Sov. Phys. JETP **64**, 857 (1986)].

[3] V. G. Bar'yakhtar, Fiz. Tverd. Tela **29**, 1317 (1987) [Sov. Phys. Solid State **29**, 754 (1987)].

[4] A. Malozemoff and J. C. Slonczewski, *Magnetic Domain Walls in Bubble Materials* (Academic Press, New York, 1979; Mir, Moscow, 1982).

[5] V. G. Bar'yakhtar and Yu. I. Gorobets, *Cylindrical Magnetic Domains and Their Lattices* [in Russian] (Nauk. Dumka, Kiev, 1988).

[6] E. G. Galkina, B. A. Ivanov, and K. A. Safaryan, Zh. Éksp. Teor. Fiz. **111**, 158 (1997) [JETP **84**, 87 (1997)].

[7] Yu. I. Gorobets, Yu. I. Dzhezherya, and V. I. Finokhin, Fiz. Tverd. Tela **35**, 335 (1993) [Phys. Solid State **35**, 170 (1993)].

[8] Yu. I. Gorobets, V. I. Finokhin, and Yu. I. Dzhezherya, Ukr. Fiz. Zh. **36**, 1215 (1991).

Translated by W. J. Manthey

Spin-glass ordering in amorphous Tb–Cr alloys

O. V. Stogneĭ,*) I. V. Zolotukhin, and O. Rapp

Voronezh State Technical University, 394026 Voronezh, Russia
(Submitted October 12, 1998)

This paper discusses amorphous Tb_xCr_{100-x} alloys ($x = 16$, 28.5, 43, and 59 at. %) obtained by quenching from the vapor phase. It is found that the structure of the alloys is heterogeneous: the coexistence of two amorphous phases, characterized by different short-range order, is observed. The short-range order of these phases qualitatively corresponds to the structure of pure components (Cr or Tb). In the low-temperature region, the alloys transform to the spin-glass state. It is established that the transition temperatures to the spin-glass state depends on the composition linearly, increasing as the terbium concentration increases. It is shown that the magnetic properties of amorphous Tb–Cr alloys are determined by the random magnetic anisotropy associated with the Tb atoms. © *1999 American Institute of Physics.* [S1063-7834(99)02307-2]

It is well known that, except for gadolinium and europium, the heavy rare earth metals and their compounds possess giant magnetic anisotropy.[1] If an alloy that contains a rare-earth (RE) element has an amorphous structure, the distribution of the local electrostatic fields acting on the RE ions will be random as a consequence of the atomic disorder. The orientation of the easy magnetization axes of the RE ions will then also have a random character. Terminologically, such a state is defined as a state with random magnetic anisotropy. It has been theoretically shown[2] that random magnetic anisotropy can cause a magnetically ordered phase with the properties of a spin glass to form in amorphous RE-based alloys. Studies of amorphous alloys of RE metals with ferromagnetic and paramagnetic metals show that phases with the properties of a spin glass are actually formed in such systems in wide concentration ranges.[3,4] On the other hand, there are virtually no data on alloys of RE metals with antiferromagnetic metals. This paper discusses therefore the possibility of forming a magnetically ordered phase with the properties of a spin glass in amorphous Tb–Cr alloys, i.e., in an RE–antiferromagnet system, in an alloy region with a low concentration of the RE component.

1. EXPERIMENTAL TECHNIQUE

All the alloys studied here were obtained by ion–plasma sputtering of composite targets in an atmosphere of spectrally pure argon. Before admitting the argon, the vacuum chamber was prepumped to a pressure of 6.65×10^{-4} Pa, which ensured that the films were not contaminated by residual gases. The material was deposited on aluminum substrates cooled to 77 K. The targets were fabricated from metallic terbium and chromium with a purity of 99.8 and 99.9 at. %, respectively.

The resulting samples were $10-12 \,\mu$m thick and 10×20 mm in area. The amorphousness of the samples was monitored by x-ray structure analysis, which was carried out at room temperature immediately before investigating the

magnetic characteristics. The recording was done by the Debye–Scherrer method in monochromatic Cu Kα radiation. The composition of the alloys was determined by energy-dispersive electron-probe analysis. The results of the studies of our samples show that the argon concentration in the films does not exceed 1 at. %, and no traces of other gases were detected. The magnetic properties of the alloys were studied on a vibrating-sample magnetometer in the temperature range 4.2–300 K.

2. RESULTS AND DISCUSSION

Four Tb_xCr_{100-x} alloys ($x = 16$, 28.5, 43, and 59 at. %) were produced for the studies. Figure 1 shows x-ray diffraction patterns that confirm that the fabricated samples had an amorphous structure. It is obvious that the amorphous phase is not homogeneous in the given alloys, and that the first peak on the diffraction patterns (the amorphous halo) is a superposition of two peaks (two haloes), each of which is the result of the diffraction of x rays by different regions of the alloy having short-range orders that differ from each other. These regions can be defined conventionally as amorphous phases AI and AII. It is well known that the mean closest interatomic distance D_m for amorphous alloys of transition metals can be estimated from the angular position of the halo by means of the simple relationship

$$D_m = \sqrt{\frac{3}{2}} \frac{\lambda}{2 \sin \theta},$$

where λ is the wavelength of the radiation being used, and θ is the Bragg angle.[5]

Figure 2 shows the D_m values for the amorphous Tb–Cr alloys, as well as the closest interatomic distances in the pure metals, chromium and terbium. Extrapolating the mean closest atomic distances in the amorphous phase AI to 100 at. % Tb gives a value that coincides with the smallest interatomic distance in crystalline Tb. The same is true for amorphous phase AII, whose D_m values are close to those in crystalline
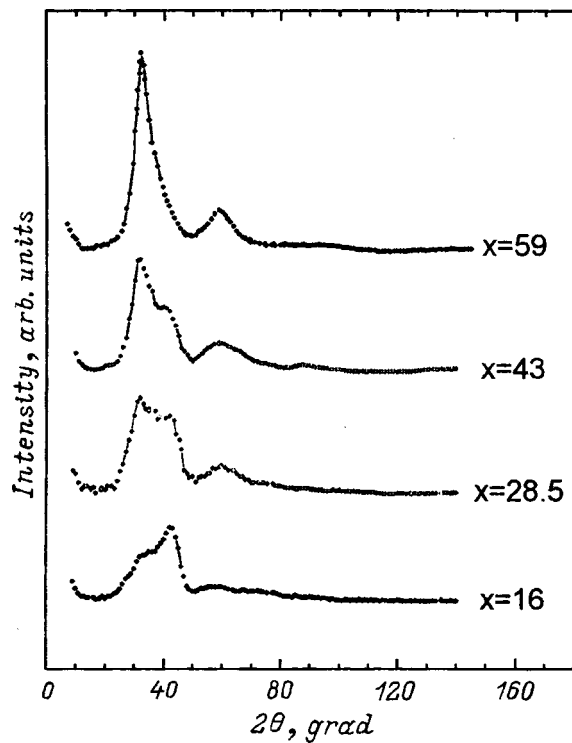
FIG. 1. X-ray diffraction patterns of amorphous Tb–Cr alloys. The numbers in the figure show the concentration of Tb in the alloy (at. %).
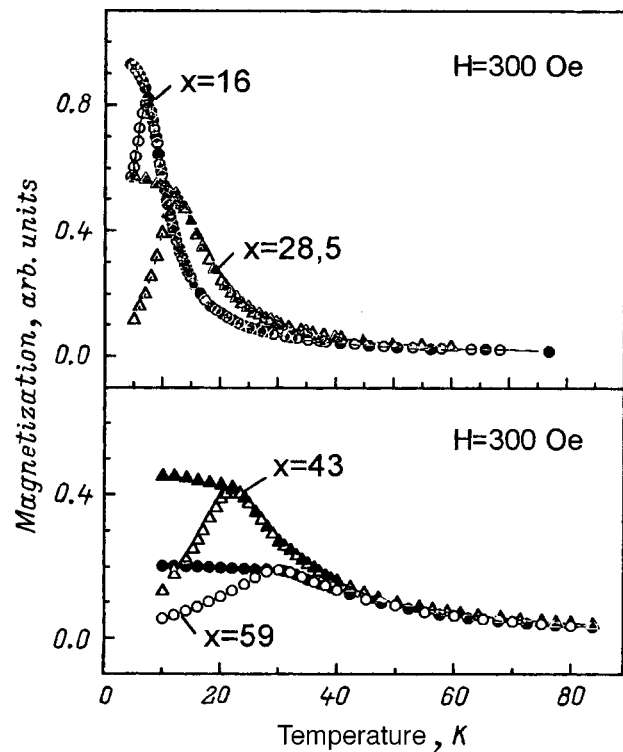

FIG. 3. Temperature dependence of the magnetization of amorphous Tb–Cr alloys. The white symbols correspond to ZFC, and the black symbols to FC.

chromium. This shows, at least qualitatively, that the short-range order of the amorphous phases corresponds to the structure of the pure metals. This fact is apparently due to the mutual solubility of the components being extremely low (under equilibrium conditions, the solubility of Tb and Cr does not exceed 0.13 at. %).[6] At the same time, it can hardly be assumed that the structure of the alloys is a kind of analog to a finely dispersed eutectic, since the alloys are formed under extremely nonequilibrium conditions, and atoms condensing on a cold substrate (77 K) quickly lose diffusional mobility and with it the capability of forming equilibrium structures.

3. MAGNETIC PROPERTIES

The magnetization of Tb–Cr amorphous alloys was studied in two standard regimes: FC involves cooling the sample in an external constant magnetic field to a temperature of 4.2 K and subsequently heating it in the same field; ZFC involves heating the sample in a magnetic field after cooling in zero field. It was established that thermomagnetic hysteresis occurs in the low-temperature region in all the alloys (Fig. 3); i.e., the sample's magnetization depends on the conditions under which it was cooled. These results are evidence that a transition to a magnetically ordered phase with the properties of spin glass occurs in Tb–Cr alloys.[7] Since both components in the alloy are magnetic materials (i.e., the concentration of magnetic atoms is 100 at. %), the resulting low-temperature phase is a speromagnet.[8]

It is well known that the formation of the spin-glass state can have two causes in amorphous alloys. First, it can be caused by competition between ferromagnetic and antiferromagnetic ordering. The competition is due to fluctuations of the exchange interaction (sign fluctuations of the exchange integral) as a consequence of the structure of disordered alloys. This mechanism mainly occurs in amorphous alloys based on magnetic $3d$ metals. Second, it can be caused by random distribution of the local magnetic anisotropy axes. This characterizes amorphous alloys based on the majority of heavy RE metals.

The Tb–Cr alloys are heterogeneous, and two amorphous phases AI and AII coexist in them (Figs. 1 and 2). This gives a basis for assuming that some one mechanism is dominant in each phase. It is also obvious that this mechanism is determined both by the short-range order of the

FIG. 2. Concentration dependence of the mean closest interatomic distance D_m in amorphous Tb–Cr alloys (black and white circles), as well as the closest interatomic distances in pure crystalline Tb and Cr. The straight lines are obtained by linear regression.
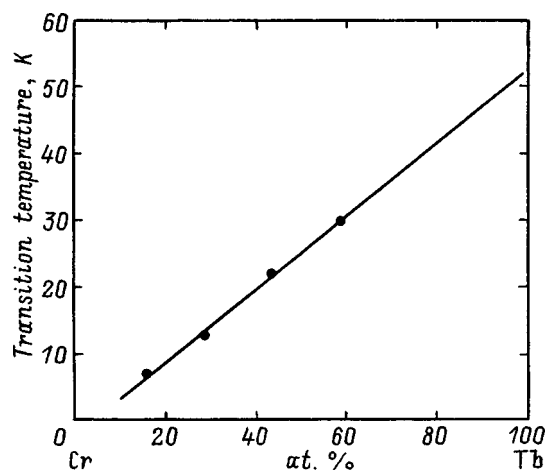
FIG. 4. Concentration dependence of the transition temperature to the spero-magnetic state of amorphous Tb–Cr alloys. The straight line is obtained by linear regression.

FIG. 5. Concentration dependence of the reduced specific magnetization of amorphous Tb–Cr alloys.

amorphous phase and by the nature of the component that predominates in this amorphous phase. We thus assume that an interaction corresponding to that in a pure component (Tb or Cr) occurs in each amorphous phase (AI or AII). In this connection, we need to decide whether the macroscopic properties of the amorphous Tb–Cr alloys result from the simultaneous action of different mechanisms or whether one of the mechanisms prevails over the other.

Metallic terbium is characterized by giant magnetic anisotropy, which determines its magnetic properties. In the crystalline state, it is a helicoidal antiferromagnet with a Néel temperature $T_N = 229$ K and goes to the ferromagnetic state at 222 K. On the other hand, terbium, with a disordered structure, displays spin-glass properties with a transition temperature of 53 K.[9] The amorphous alloy $Tb_{90}Si_{10}$ (i.e., the alloy as close as possible in composition to ideal amorphous terbium) goes to a state with the properties of spin glass at 58 K.[10] The amorphization of terbium thus leads to the appearance of speromagnetic ordering of the magnetic moments instead of the ferro- or antiferromagnetic ordering observed in hcp Tb. This is so because, in the amorphous material, the interatomic distances in the first coordination sphere, as well as the number of nearest neighbors itself, varies randomly. The electrostatic interaction of the $4f$ shell, therefore, also varies randomly with the local crystal field of the neighboring ions. As a result, the orientation of the local axes of easy magnetization vary from ion to ion chaotically (or with some correlation).

Figure 4 shows the concentration dependence of the transition temperature T_t to a magnetically ordered phase with spin-glass properties. The resulting experimental dependence is strictly linear, and this fact is strong evidence that a single magnetic-ordering mechanism acts in the entire concentration interval studied here. Extrapolating T_t to 100 at. % Tb gives a transition temperature equal to 52 K. This value coincides with the 53 K for amorphous terbium[9] and is close to 58 K for the amorphous $Tb_{90}Cr_{10}$ alloy.[10] Consequently, the mechanism that orders the moments is the same in both pure amorphous terbium and amorphous Tb–Cr alloys—a
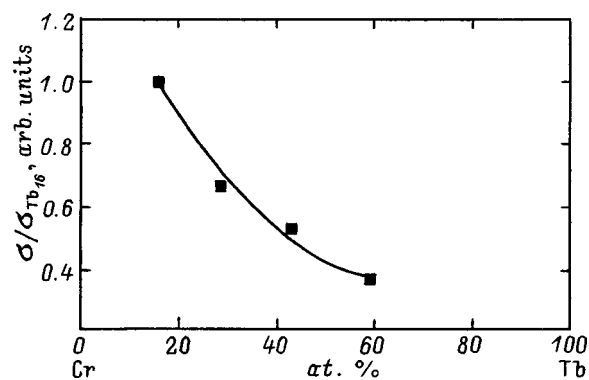
random orientation of the local axes of easy magnetization. Figure 5 shows the dependence of the reduced specific magnetization of the amorphous Tb–Cr alloys on composition (all the values are relative to the magnetization of the $Tb_{16}Cr_{84}$ alloy). The magnetization was determined at 4.2 K after cooling from room temperature in an external magnetic field of 300 Oe. According to these data, the magnetization of the alloys decreases as the terbium concentration increases. This fact is easy to explain only from the viewpoint of random magnetic anisotropy. It is well known that the random magnetic anisotropy constant increases as the concentration of RE metal in an alloy increases.[3,11] As a consequence, the system of magnetic moments becomes more rigidly oriented along the local anisotropy axes, and it becomes less labile and less subject to the action of an external magnetic field (to known limits, of course, when the field simply breaks down the spin-glass phase). Therefore, other external conditions being equal, the total magnetization of such a material must be less than in an alloy with a lower concentration of RE metals, since the orientation of the local anisotropy axes is random. Moreover, increasing the random magnetic anisotropy constant must increase the ordering temperature, since a large thermal energy ($\sim kT$) is needed to break down the magnetic order in this case. Such a dependence is observed in amorphous Tb–Cr alloys (Figs. 4 and 5).

The resulting experimental data are thus explained by the action of only one mechanism, which orders the magnetic moments of the alloys. This mechanism is caused by the random magnetic anisotropy associated with the terbium atoms.

*)E-mail: sto@sci.vrn.ru

[1] S. A. Nikitin, *Magnetic Properties of Rare-Earth Metals and Their Alloys* (Izd. Mosk. Gos. Univ., Moscow, 1989).
[2] A. Aharony and E. Pytte, Phys. Rev. Lett. **45**, 1583 (1980).
[3] Y. Hattori, K. Fukamichi, K. Suzuki, H. Aruga–Katori, and T. Goto, J. Phys.: Condens. Matter **7**, 4193 (1995).
[4] H. Bouchiat and D. Mailly, J. Appl. Phys. **57**, 3453 (1985).

[5] A. Williams and W. L. Johnson, J. Non-Cryst. Solids **34**, 121 (1979).

[6] R. P. Elliot, first suppl. to M. Hansen and K. Anderko, *Constitution of Binary Alloys* (McGraw-Hill, New York, 1965; Mettalurgiya, Moscow, 1970).

[7] K. H. Fisher, Phys. Status Solidi B **116**, 357 (1983).

[8] K. M. Kherd, Usp. Fiz. Nauk **142**, 331 (1984).

[9] J. J. Hauser, Solid State Commun. **55**, 163 (1985).

[10] J. J. Hauser, Phys. Rev. **34**, 3212 (1986).

[11] A. S. Andrienko, S. A. Nikitin, and Yu. I. Spichkin, J. Magn. Magn. Mater. **118**, 142 (1993).

Translated by W. J. Manthey

Phase diagram of multilayer ferromagnet–layered-antiferromagnet structures

A. I. Morozov[*)] and A. S. Sigov

Moscow State Institute of Electronic Engineering. Electronics, and Automatics, 117454 Moscow, Russia

This paper discusses the thickness–roughness phase diagram of a three-layer system consisting of two ferromagnetic layers separated by an antiferromagnetic interlayer. It is shown that the stability region of single-domain ferromagnetic layers is determined by the ratio between the width of the atomic steps that appear at the interfaces of the layers during their growth and the thicknesses of the layers, and also by the values of the interlayer and intralayer exchange interactions. A basis is provided for the phenomenological ''magnetic closeness'' model proposed by Slonczewski, and an expression is obtained for the constants of this model. © *1999 American Institute of Physics.* [S1063-7834(99)02407-7]

Sandwiches consisting of alternating thin ferromagnetic (Fe, Co) and nonmagnetic (Cr, Cu) metallic layers became an object of the close attention of researchers after it was discovered that they display the phenomenon of giant magnetoresistance.[1] A tremendous number of papers have been devoted to these systems, but only a small part of them relate to the case in which the role of the interlayer between the ferromagnetic layers is played by a layered antiferromagnet. At the same time, it is just this case that is of special interest, since the presence of long-range antiferromagnetic order in the interlayer changes the character of the indirect interaction between the ferromagnetic layers.

In the case of a nonmagnetic interlayer, the exchange between adjacent ferromagnetic layers is caused by the RKKY interaction and falls off with the thickness d of the nonmagnetic interlayer as d^{-2}.[2] However, if the sandwich consists of alternating ferromagnetic and antiferromagnetic layers, a long way from the Néel temperature, the exchange between the ferromagnetic layers is provided by correlation of the ferromagnetic and antiferromagnetic order parameters and, as will be shown below, falls of as d^{-1}.

If the antiferromagnetic interlayer consists of ferromagnetic atomic planes with antiparallel orientation of the spins in adjacent planes, an antiparallel orientation of the adjacent ferromagnetic layers is energetically favorable when the number of such planes in the interlayer is even, and a parallel orientation is favorable when the number of planes is odd (Fig. 1).

An example of such a layered antiferromagnet is chromium, in which, for thicknesses $32 < d < 150$ Å, a commensurate transverse spin-density wave appears as the temperature decreases.[3] An analogous structure is obtained when iron impurities with a concentration that exceeds 2% are introduced into the chromium.[4]

Since the interfaces of the layers in a multilayer structure are not smooth but contain atomic steps that alter the thickness of the interlayer by one monatomic layer, it is impossible in the case of a homogeneous distribution of the ferromagnetic and antiferromagnetic order parameters in the layers to optimally orient the magnetizations of the ferro-

magnetic layers on the entire interface of the layers: frustrations appear (Fig. 2).

If the characteristic distance R between atomic steps exceeds some critical value, it is energetically favorable to break up the layers into domains. The roughness-induced domain walls differ from ordinary domain walls, whose width depends on the ratio of the exchange energy and the anisotropy energy. The width of these ''unusual'' domain walls in multilayer structures is determined by the ratio between the intralayer and interlayer exchange interactions. The widths of the unusual walls can therefore be substantially less than in ordinary domain structures.[5]

In an earlier paper,[6] we discussed the conditions for the appearance and structure of domain walls in a ferromagnetic film on the surface of an antiferromagnet, as well as the inhomogeneous distribution of the order parameter in an antiferromagnetic layer placed between two homogeneously magnetized ferromagnetic layers. A distinguishing feature of the domain walls in a ferromagnetic film, generated by roughness of the substrate, is that they become wider as one goes away from the substrate (Fig. 3).

In a three-layer structure, the distortions of the antiferromagnetic order parameter extend to the entire space of the antiferromagnetic layer between two atomic steps (Fig. 4). However, the ferromagnetic layers remain homogeneous only when the exchange interaction in them is much greater than that in the antiferromagnetic layers.

The goal of this paper is to construct a phase diagram of multilayer ferromagnet–layered-antiferromagnet structures with arbitrary ratios between the exchange interactions as well as between the layer thicknesses and the characteristic distance between the steps at their boundaries.

1. DESCRIPTION OF THE MODEL

We shall investigate the distribution of the order parameters in the layers in the mean-field approximation. We shall introduce an order parameter for each layer: the magnetization vector for the ferromagnetic layers and the antiferro-
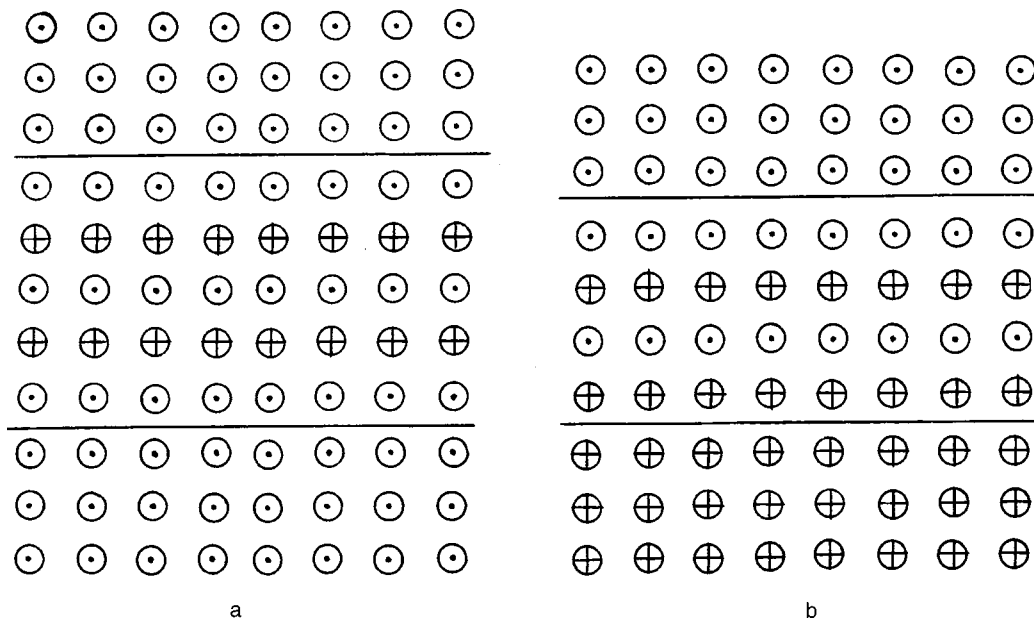
FIG. 1. Orientation of spins in a three-layer system consisting of two ferromagnetic layers and an antiferromagnetic interlayer, in the case of smooth interfaces and an odd (a) or even (b) number of atomic planes in the interlayer.

magnetism vector equal the difference in the magnetizations of the sublattices, for the antiferromagnetic layers.

In the case of sufficiently thin layers, the spins of the atoms lie in the plane of the layer and, therefore, the orientation of the vector order parameter can be given by the angle θ that it forms with the x axis, which lies in the plane of the layer.

Far from the Curie and Néel temperatures, the exchange energy W_i caused by the interaction inside the ith layer can be written as

$$W_i = \frac{A_i}{2} \int (\nabla \theta_i)^2 dV, \qquad (1)$$

where the integral is taken over the volume of the layer, and A_i is the corresponding exchange constant. In order of magnitude, $A_i \sim J_i S_l^2 / b$, where J_i is the exchange integral between adjacent atoms, S_i is the mean spin of the atom, and b is the interatomic distance.

The energy of the exchange interaction between adjacent layers with numbers i and $i+1$ can be written

$$W_{i,i+1} = \pm B \int \cos(\theta_i - \theta_{i+1}) dS, \qquad (2)$$

where the integration is over the interface of the layers, $B \sim J_{f,af} S_i S_{i+1} / b^2$, $J_{f,af}$ is the exchange integral between adjacent atoms belonging to different layers, and the sign on the right-hand side of Eq. (2) is opposite for different sides of the atomic step at the interface of the layers.
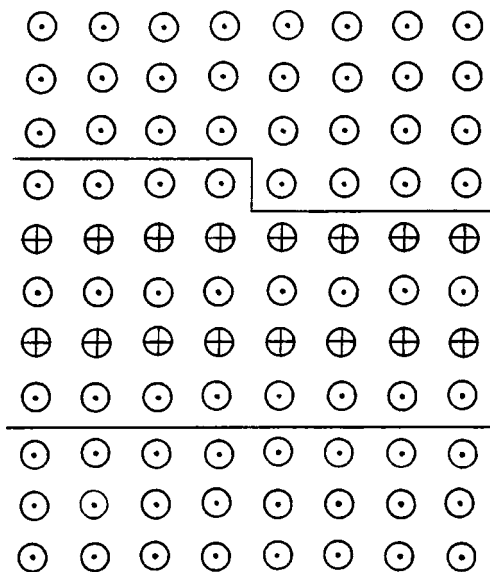
FIG. 2. Frustration in a three-layer system, resulting from the presence of an atomic step at the interface.
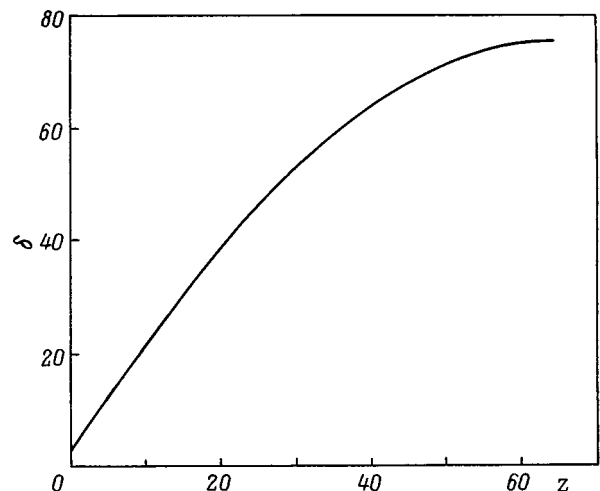
FIG. 3. Width of a domain wall vs the distance to the interface of the layers in a two-layer system.
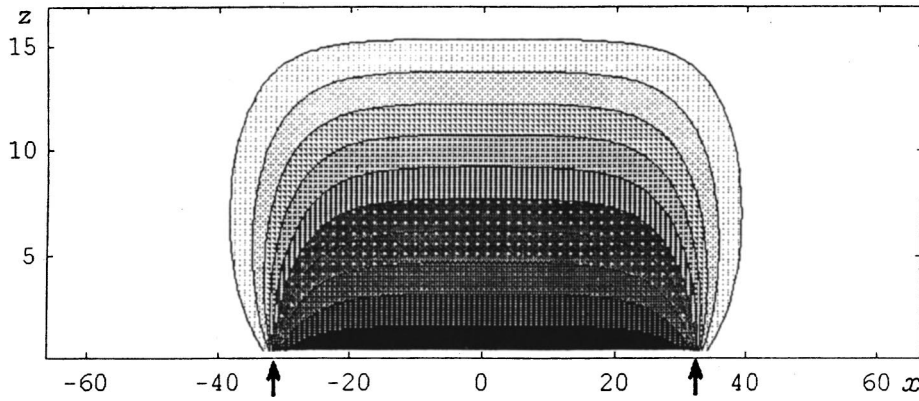
FIG. 4. Distortions of the antiferromagnetic order parameter in a three-layer structure in the case of collinearly and homogeneously magnetized ferromagnetic layers and $a\alpha \gg 1$. The arrows indicate the position of the atomic steps at the interface of the layers. The lines of constant θ_{af} are drawn every $\pi/10$.

We divide all distances by the lattice constant b, assuming it to be virtually identical in both sorts of layers and all energies by the constant A_{af} for the antiferromagnetic layer. We introduce the following dimensionless parameters:

$$\alpha = \frac{J_{f,af}S_f}{J_{af}S_{af}} \qquad (3)$$

and

$$\gamma = \frac{J_f S_f^2}{J_{af}S_{af}^2}, \qquad (4)$$

where subscripts f and af correspond to the ferro- and the antiferromagnet.

By varying Eq. (1) in parameter θ_i, we get a differential equation that describes the distribution of the order parameter in the layer,

$$\Delta \theta_i = 0. \qquad (5)$$

A more careful procedure is needed to obtain the correct conditions at the interface of the layers. The energies of the intralayer and interlayer interactions must be varied in a discrete model, and then we must go to the continuum limit. As a result, we get

$$\tilde{\Delta}\theta_i - \frac{\partial \theta_i}{\partial n} = \mp \frac{B}{A_i b}\sin(\theta_i - \theta_{i+1}), \qquad (6)$$

where $\tilde{\Delta}$ is the two-dimensional Laplacian in the plane of the layer, $\partial/\partial n$ is the derivative in the direction of the outer normal to the boundary of the ith layer, and the upper and lower signs in Eq. (6) correspond to those in Eq. (2). Varying the sum of Eqs. (1) and (2), over θ_i corresponding to the continuum approximation, causes the first term on the left side of Eq. (6) to disappear. This makes it impossible to carry out the limiting transition from Eq. (6) to Eq. (5) when the ith and $i\pm 1$st layers are identical in composition.

Thus, to find the distribution of the order parameters in a multilayer structure, it is necessary to solve the system of linear differential Eqs. (5), related by the nonlinear boundary conditions given by Eq. (6). The distribution will depend on the values of α and γ, on the thicknesses of the layers, and also on the characteristic distance R between the steps at the interface of the layers.

2. DISTORTIONS OF THE ORDER PARAMETER IN AN ANTIFERROMAGNETIC LAYER

We shall first consider the case of $\gamma l \gg a$, where l and a are the dimensionless thicknesses of the ferro- and antiferromagnetic layers, respectively. In this case, the order parameter remains virtually homogeneous in the ferromagnetic layers, while the distortions of the order parameter in different antiferromagnetic layers are not associated with each other and can be considered independently.

When the characteristic distance between the steps exceeds the width δ_0 of the domain wall close to a step, roughness of the interfaces of the layers induces strong inhomogeneity of the order parameter in the antiferromagnetic interlayer. We recall that the width of the domain wall increases as one goes away from the interface of the layers. According to Ref. 6, this condition has the form

$$R \gg \delta_0 = \begin{cases} \sqrt{a/\alpha}, & \text{for} \quad \alpha a \ll 1, \\ (1+\alpha)/\alpha, & \text{for} \quad \alpha a \gg 1. \end{cases} \qquad (7)$$

Let the magnetizations of adjacent ferromagnetic layers form angle ψ. The entire area of the antiferromagnetic interlayer is divided by steps into two types of regions represented as being equally probable. The interlayer consists of an odd number of atomic planes in regions of the first type, and of an even number in regions of the second type.

The character of the resulting distortions is fundamentally differentiated into two limiting cases $a\alpha \gg 1$ and $a\alpha \ll 1$.

(a) $a\alpha \gg 1$. In this limit, the difference at the layer boundaries is $\theta_i - \theta_{i+1} = 0, \pi$, depending on the sign in Eq. (2); i.e., the interaction energy of the layers is a minimum, while all the distortions occur in the volume of the antiferromagnetic interlayer.

Reference 6 obtained a numerical solution of Eq. (5) with the boundary conditions given by Eq. (6) for the case of two steps (Fig. 4). It is easy to see that, in the overwhelming majority of the volume of the interlayer, θ_i varies virtually linearly from one layer boundary to the other. This variation equals ψ in regions of the first type and $\pi - \psi$ in regions of the second type.

The additional energy given by Eq. (1) per one two-

dimensional unit cell in the plane of the layer has the mean value

$$\tilde{W} = \frac{1}{4a}[\psi^2 + (\pi - \psi)^2]. \tag{8}$$

Thus, the exchange interaction of the ferromagnetic layers through an antiferromagnetic interlayer with $a\alpha \gg 1$, like $\tilde{W}$, is proportional to a^{-1}.

The boundary energy between regions of the first and second types in terms of the same cell equals

$$W_b \sim R^{-1} \ln a\alpha \tag{9}$$

and makes no substantial contribution to the energy when $R \gg a$.

The minimum of energy $\tilde{W}$ corresponds to $\psi = \pi/2$; i.e., the magnetizations of the adjacent ferromagnetic layers have a 90° orientation in this region of R values.

To explain such an orientation, Ref. 7 proposed the phenomenological ''magnetic-closeness'' model, in which an expression for energy $\tilde{W}$ was proposed in the form of a linear combination of ψ^2 and $(\pi - \psi)^2$ with independent coefficients C_+ and C_-. The example of the analysis given above makes it possible to determine these parameters from first principles

$$C_+ = C_- = 1/4a. \tag{10}$$

(b) $a\alpha \ll 1$. In this case, the dependence of θ_i on the z coordinate, which is perpendicular to the plane of the layers, can be neglected, and a one-dimensional problem can be solved when the edge of the step is a straight line. Let the x axis of the Cartesian coordinate system be perpendicular to the edge of the step and lie in the plane of the layer, while the magnetizations of the ferromagnetic layers form angle ψ. Measuring angle θ_i from the direction of the magnetization of the lower ferromagnetic layer and integrating over z, we get from Eqs. (5) and (6) that

$$a\frac{\partial^2 \theta_i}{\partial x^2} = \alpha[\sin \theta_i + \sin(\theta_i - \psi)], \quad x > 0,$$

$$a\frac{\partial^2 \theta_i}{\partial x^2} = \alpha[\sin(\theta_i - \pi) + \sin(\theta_i - \psi)], \quad x < 0, \tag{11}$$

where it is assumed that the edge of the step is at the boundary with the lower layer and coincides with the straight line $x = z = 0$.

It is easy to see that, a long way from the step, $\theta_i = \psi/2$ for $x > 0$ and $\theta_i = (\pi + \psi)/2$ for $x < 0$. The solution of Eq. (11) has the form

$$\cos\frac{\theta - \dfrac{\pi}{2}}{2} = \tanh\frac{x - x_1}{\delta_1}, \quad x > 0, \tag{12}$$

$$\cos\frac{\theta - \dfrac{\pi + \psi}{2}}{2} = -\tanh\frac{x - x_2}{\delta_2}, \quad x < 0, \tag{13}$$

where

$$\delta_1 = \sqrt{\frac{a}{2\alpha \cos\dfrac{W}{2}}}, \tag{14}$$

$$\delta_2 = \sqrt{\frac{a}{2\alpha \cos\dfrac{\pi - \psi}{2}}}. \tag{15}$$

The values of the constants x_1 and x_2 are found from the condition that the quantity θ_i and its derivative are continuous at $x = 0$.

If ψ is not too close to 0 or π, the distortions of the antiferromagnetic order parameter fall off at a distance of the order of $\delta_0 \sim \sqrt{a/\alpha}$. The energy of the domain wall per 1 m length is about $\sqrt{a\alpha}$.

However, if $\psi \to 0$ or $\psi \to \pi$, the distortions of the order parameter on one side of the step behave as for arbitrary x, while they fall off much more slowly on the other side of the step. The characteristic length at which the distortions of the order parameter fall off can be obtained only in the next order in αa, i.e., taking into account the dependence of the quantity θ_i on z. The energy of the domain wall in this case is of the same order as for arbitrary ψ.

When $R \gg \delta_0$, the energy of the domain walls is negligible by comparison with the interaction energy of the layers given by Eq. (2), which, per one two-dimensional unit cell, is

$$\tilde{W} = \alpha\left[1 - \cos\frac{\psi}{2}\right] + \alpha\left[1 - \cos\frac{\pi\psi}{2}\right]$$

$$= 2\alpha - \sqrt{2}\alpha\sin\left(\frac{\psi}{2} + \frac{\pi}{4}\right). \tag{16}$$

It is easy to see that the energy of the system is a minimum for $\psi = \pi/2$; i.e., as in the case $a\alpha \gg 1$, the magnetization of adjacent ferromagnetic layers has a 90° orientation. In this thickness region, the exchange interaction between the ferromagnetic layers is independent of the thickness of the antiferromagnetic interlayer and is $J_{f,af}$ in order of magnitude. Since the dependence given by Eq. (16) is not identical to that given by Eq. (8), the phenomenological constants C_+ and C_- can be estimated by comparing the energy difference of the collinear and 90° orientations in the given microscopic model and in the magnetic-closeness model.

$$C_+ = C_- = \frac{2(\sqrt{2} - 1)}{\pi^2}\alpha. \tag{17}$$

It should be pointed out that, in the case of a nonmagnetic interlayer, when the interaction between the ferromagnetic layers is caused by the RKKY interaction, the probability of a 90° orientation of the magnetization of homogeneous ferromagnetic layers is extremely low.[8] To accomplish this, the exchange interaction between the homogeneous ferromagnetic layers, averaged over the surface of the layers, needs to be close to zero. However, when the exchange is via the antiferromagnetic order parameter, this condition is ensured by the equal probability of the appearance of regions of the first and second types (with an even and odd number of atomic planes in the antiferromagnetic interlayer).

As one approaches the Néel temperature T_N, the antiferromagnetic order parameter S_{af} decreases as $\sqrt{\tau}$, where $\tau = (T_N - T)/T_N$ is a dimensionless parameter that characterizes the closeness to the phase-transition point. Let us estimate the value τ^* at which the interaction of the ferromagnetic layers via directed spin polarization (the RKKY interaction) is comparable in order of magnitude with the interaction via the mean order parameter in the antiferromagnetic interlayer. Setting the expression for the RKKY exchange interaction between the ferromagnetic layers equal to Eqs. (8) and (16),

$$J_{\text{RKKY}} = \frac{J_{s-d}^2}{\varepsilon_F a^2}, \tag{18}$$

where J_{s-d} is the exchange integral between the s and d electrons (iron or cobalt), while ε_F is the Fermi energy of the s electrons, we get

$$\tau^* = \begin{cases} \dfrac{J_{s-d}^2}{J_{af}\varepsilon_F} \dfrac{1}{a}, & a\alpha \gg 1, \\[3mm] \dfrac{J_{s-d}^4}{J_{f,af}^2 \varepsilon_F^2 a^4}, & a\alpha \ll 1. \end{cases} \tag{19}$$

For the realistic values $J_{f,af} \sim J_{af}$ and $a \sim 10$, we get the estimate $\tau^* \sim 10^{-2}$.

In the temperature region $T < T^*$ $[T^* = T_N(1 - \tau^*)]$, the determining interaction channel between the ferromagnetic layers is the interaction via the antiferromagnetic order parameter.

When $T > T^*$, the system behaves as though the interlayer were nonmagnetic.

3. DOMAIN WALLS IN A FERROMAGNET

For the subsequent treatment, we restrict ourselves to the case of a three-dimensional system consisting of two ferromagnetic layers separated by an antiferromagnetic interlayer.

In the case of large R values, a homogeneous distribution of the magnetizations of the ferromagnetic layers does not correspond to the case with the lowest energy. Actually, since the distortions of the antiferromagnetic order parameter considered in the preceding section occupy the entire volume of the layer when $a\alpha \gg 1$, and the interaction energy of the layers is proportional to the area of the layers when $a\alpha \ll 1$, the excess energy per unit area of the layers is independent of R.

However, if the ferromagnetic layers are broken up into domain regions whose boundaries coincide with the edges of the atomic steps, the orientation of the magnetizations of the ferromagnetic layers (parallel or antiparallel) in each such region can be chosen so that there are no distortions of the order parameters in the volume of a domain and no excess energy at the boundaries of the layers inside the domain. The excess energy in this case is associated with the presence of the domain walls; its magnitude per unit surface of the layers equals

$$W = \frac{\varepsilon}{R}, \tag{20}$$

TABLE I. Domain-wall parameters in a three-layer structure with identical thicknesses of the layers and values of $\gamma \gg 1$.

Parameter	Region		
	$a\alpha \gg \gamma$	$a\alpha \ll \gamma \ll (a\alpha)^3$	$(a\alpha)^3 \ll \gamma$
$\dfrac{\partial \delta_{af}}{\partial z}$	$\gamma^{1/2}$	$(\gamma a\alpha)^{1/4}$	$\gamma^{1/3}$
$\dfrac{\partial \delta_f}{\partial z}$	1	$\left(\dfrac{a\alpha}{\gamma}\right)^{1/2}$	$\left(\dfrac{a\alpha}{\gamma}\right)^{1/2}$
$\tilde{\delta}_0$	γ/α	$(\gamma a/\alpha)^{1/2}$	$(\gamma a/\alpha)^{1/2}$
ε	$\gamma \ln \dfrac{a\alpha}{\gamma}$	$(\gamma a\alpha)^{1/2}$	$(\gamma a\alpha)^{1/2}$

where ε is the energy of a domain wall per unit length. Therefore, for sufficiently large R values, it becomes energetically favorable to break up the ferromagnetic layers into domains.

As one goes from a domain with parallel orientation of the magnetizations of the ferromagnetic layers (a domain of the first type) to a domain with antiparallel orientations of the magnetizations (a domain of the second type) the magnetizations of the ferromagnetic layers rotate to different sides in the domain wall. The antiferromagnetic order parameter rotates along with the magnetization of the ferromagnetic layer on the boundary with which there is no step at the given site.

In the case of identical ferromagnetic layers and when $\gamma l \gg a$, the magnetizations rotate to different sides by an angle of 90°. However, if one ferromagnetic layer is much thicker than the other, the magnetization of the thin ferromagnetic layer rotates by an angle of 180°, and the thick ferromagnetic layer remains virtually homogeneous.

When $\gamma l \ll a$, the magnetization rotates by 180° in the ferromagnetic layer at whose boundary a step appeared, while the other layers remain virtually homogeneous at the given site.

In order to find the critical value R^* at which the transition occurs from an almost homogeneous magnetization distribution in the ferromagnetic layers to a domain structure in them, we find the value of ε. As in the case of a two-layer system,[6] its order of magnitude can be estimated on the basis of a simple model that assumes that the width δ of the domain wall depends linearly on the distance z to the layer interface that contains a step. The parameters $\tilde{\delta}_0$ (the width of the domain wall near a step) and $\partial\delta/\partial z$ in the ferromagnetic and antiferromagnetic layers are found by minimizing the total energy. We should point out that $\tilde{\delta}_0$ is not the same as the δ_0 in Eq. (7), which is found for the condition of homogeneous ferromagnetic layers.

The results of such a calculation are given in Table I for the case of interest to us, where $l \sim a$.

Comparing Eq. (20) with the energies given in Eqs. (8) and (16), we find the critical step size R^*. It should be recalled here that Eqs. (8) and (16) are valid for $R \ll \delta_0$, a. Finally, we obtain
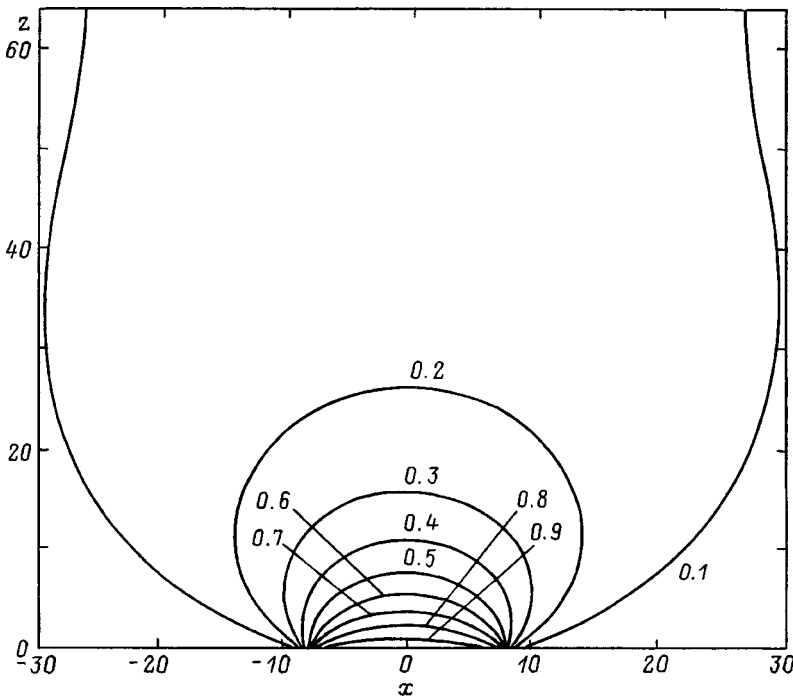
FIG. 5. Spin vortex that arises when $R \ll a$. The value of θ_{af} is indicated on the lines of constant θ_{af} in units of π.

$$R^* = \begin{cases} a\gamma \ln \dfrac{a\alpha}{\gamma}, & \text{for} \quad a\alpha \gg \gamma \gg 1; \\[2mm] \sqrt{\gamma a^3 \alpha}, & \text{for} \quad \gamma \gg a\alpha \gg 1; \\[2mm] \sqrt{\gamma a/\alpha}, & \text{for} \quad \gamma \gg 1 \gg a\alpha. \end{cases} \qquad (21)$$

The case $\gamma \ll 1$ is of no interest, since here distortions appear in the ferromagnetic layers, while the antiferromagnetic order parameter remains homogeneous. There is no coupling between the ferromagnetic layers.

For an arbitrary ratio between the layer thicknesses, the number of possible variants sharply increases.

Close to the Néel temperature, according to Eqs. (3) and (4), $\alpha(T) \propto \tau^{-1/2}$, while $\gamma(T) \propto \tau^{-1}$, and therefore for $T \to T_N$

$$R^*(T) \propto \tau^{-3/4}. \qquad (22)$$

Thus, close to T_N (but not too close, since $\tau > \tau^*$), the ferromagnetic layers can be homogeneously magnetized, and, if $R > R^*(0)$, a first-order phase transition occurs with decreasing temperature, accompanied by the breaking up of the ferromagnetic layers into domains. For realistic values of the parameters $\alpha(0) \sim \gamma(0) \sim 1$, we get $R^*(0) \sim a$, i.e., tens of angstroms. Such a phase transition was observed in the numerical experiment of Ref. 9.

4. PHASE DIAGRAM OF A THREE-LAYER SYSTEM

We have so far assumed that the characteristic distance R between the steps in the plane of the layer is much greater than the thickness of the antiferromagnetic interlayer ($R \gg a$). However, the opposite situation is possible in the case of thick layers. If $R \gg \delta_0$, a static spin vortex arises at the boundary of the layer and connects the two closest steps at the boundary of the given layer.[6] Distortions of the order parameter appear mainly in the antiferromagnetic layer when

$\gamma \gg 1$ (Fig. 5) and in the ferromagnetic layer when $\gamma \ll 1$. In practice, they do not reach the opposite boundary of the layer. The coupling between the ferromagnetic layers even when $\gamma \gg 1$ is therefore substantially weakened [by a factor of $(R/a)^2$] in this region of thicknesses.

When $R \ll \delta_0$, only weak distortions appear in the layers, on a background of homogeneous distributions of the order parameters.

By carrying out a treatment similar to that in the preceding section, it can be shown that the smallest energy of the layers when $R \ll a$ corresponds to an orientation for which the antiferromagnetism vector a long way from the boundaries of the layer is perpendicular to the magnetizations of the ferromagnetic layers. Actually, since the spin vortices are localized close to the interfaces of the layers, the boundary conditions for θ_i are given by the orientation of the order parameters in the depth of the layers.

The magnetizations of the ferromagnetic layers in this case are collinear, while the energies of their parallel and antiparallel orientations are virtually identical.

The phase diagram in the variables layer thickness and roughness is shown in Fig. 6 for a three-layer system with $l \sim a$. Phase *1* is characterized by the presence of vortices and a collinear orientation of the magnetizations of the ferromagnetic layers. In phase *2*, the magnetizations of the ferromagnetic layers are homogeneous and, in the absence of an external magnetic field, are oriented at 90° to each other. Phase *3* corresponds to a multidomain structure of the ferromagnetic layers.

The phase diagram can be compared with experimental data by studying the state of the ferromagnetic layers using a magnetic-force microscope with various ratios between R and a, as well as at different temperatures (because of the temperature dependence of parameters γ and α).
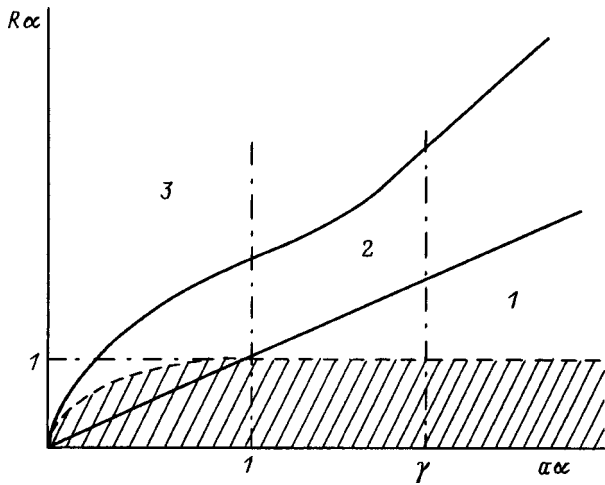
FIG. 6. Thickness–roughness phase diagram for a three-layer system consisting of layers of identical thickness. Phase *1* corresponds to the presence of vortices and collinear orientation of the magnetization of the ferromagnetic layers. The magnetization of the ferromagnetic layers is oriented at 90° in phase *2*, and the ferromagnetic layers break up into domains in phase *3*. The region of weak distortions of the order parameters is hatched.

5. EFFECT OF A MAGNETIC FIELD

The magnetic flux reversal of the ferromagnetic layers in phase *1* (Fig. 6) occurs virtually independently, and the hysteresis loops must coincide with those in a two-layer system consisting of one ferromagnetic and one antiferromagnetic layer. Here and below we assume that the maximum magnetic field is much less than the exchange field in the antiferromagnet. Therefore, the magnetization of the antiferromagnetic layers can be neglected.

In phase *2*, in a weak magnetic field that exceeds the anisotropy field in the plane of the ferromagnetic layers, the magnetizations of the ferromagnetic layers orient themselves at 45° to the field while remaining virtually perpendicular to each other. In this case, the magnetization of the system is $M_{max}/\sqrt{2}$, where M_{max} is the maximum magnetization of the ferromagnetic layers. Its further evolution can be studied by minimizing the sum of the interaction energies of the ferromagnetic layers with each other [Eqs. (8) or (16)] and with the magnetic field. The energy of the ferromagnetic layer in an external magnetic field with induction B is given by

$$W_f = -2\mu l B \cos \frac{\psi}{2}, \tag{23}$$

where μ is the magnetic moment of an atom of the ferromagnet.

For angle ψ between the magnetization of the layers, when $R \gg \delta_0$ and when $a\alpha \gg 1$, we have the transcendental equation

$$\frac{J_{af}S_{af}^2}{a}\left(\frac{\pi}{2} - \psi\right) = \mu l B \sin \frac{\psi}{2}. \tag{24}$$

The characteristic field B^* at which a substantial change of the magnetization occurs is

$$B^* \sim \frac{J_{af}S_{af}^2}{\mu a l}. \tag{25}$$

Not too close to T_N, its value is much less than the exchange field of the antiferromagnet $\sim J_{af}S_{af}^2/\mu_{af}$ (μ_{af} is the magnetic moment of an atom of the antiferromagnet).

However, if $a\alpha \ll 1$, we get

$$\tan \frac{\psi}{2} = \frac{J_{f,af}S_{af}S_f}{J_{f,af}S_f S_{af} + 2\mu l B}, \tag{26}$$

and the characteristic field B^* equals

$$B^* \sim \frac{J_{f,af}S_{af}}{\mu_B l}, \tag{27}$$

where μ_B is the Bohr magneton.

In phase *3*, in a weak magnetic field, domains of the first type, with parallel orientation of the magnetization of the layers, are oriented along the field. The magnetization of the system in this case is $M_{max}/2$. The magnetizations of the ferromagnetic layers in domains of the second type, with their antiparallel orientation in zero field, behave similarly to the magnetizations of the sublattices in the volume of the antiferromagnet. They are oriented virtually perpendicular to the external field.

As B increases, angle ψ between them decreases. The characteristic value of the induction B^* of the external magnetic field in which the angle varies substantially, when $R \gg R^*$, is found by a method similar to that for phase *2* and is given in order of magnitude by Eqs. (25) and (27). Therefore, the form of the hysteresis loops in phases *2* and *3* differs only in the magnitude of the magnetization in weak fields.

The proposed theory can be compared with experimental data by studying the dependence of B^* on the thicknesses of the layers. The resulting $B^*(a,l)$ dependences differ from those for the case in which the interaction of the ferromagnetic layers is caused by the RKKY interaction ($B^* \propto a^{-2}l^{-1}$).

Unfortunately, such studies, as far as we can tell from the literature, have not been carried out.

In conclusion, we summarize the main results of this paper.

(1) The form of the distortions of the order parameter that arise in an antiferromagnetic interlayer between two ferromagnetic layers as a consequence of the roughness of the interfaces of the layers has been studied. The phenomenological magnetic-closeness model proposed by Slonczewski has been confirmed in terms of the microscopic theory, an expression has been obtained for the constants of this model, and the region where it is applicable has been found.

(2) The critical width of the atomic steps at the interface of the layers has been found. When this width is exceeded, it becomes energetically favorable for the ferromagnetic layers to break up into domains, so that a multidomain phase appears.

(3) The thickness–roughness phase diagram has been constructed for a three-layer system consisting of two ferromagnetic layers separated by an antiferromagnetic interlayer, with identical thicknesses of the layers.

(4) The form of the hysteresis loops in the different phases has been studied.

*)E-mail: morosov@eot-gw.eot.mirea.ac.ru

―――――

[1] M. N. Baibich, J. M. Broto, A. Fert, Nguyen van Dau, F. Petroff, P. Etienne, G. Creuzet, A. Friederich, and J. Chazelas, Phys. Rev. Lett. **61**, 2472 (1988).

[2] P. Bruno and C. Chappet, Phys. Rev. B **46**, 261 (1992).

[3] E. E. Fullerton, S. D. Bader, and J. L. Robertson, Phys. Rev. Lett. **77**, 1382 (1996).

[4] E. Fawcett, H. L. Albert, V. Yu. Galkin, D. R. Noakos, and J. V. Yakhmi, Rev. Mod. Phys. **66**, 25 (1994).

[5] A. I. Morozov and A. S. Sigov, JETP Lett. **61**, 911 (1995).

[6] V. D. Levchenko, A. I. Morozov, A. S. Sigov, and Yu. S. Sigov, Zh. Éksp. Teor. Fiz. **114**, No. 5, 1817 (1998) [JETP **87**, 985 (1998)].

[7] J. C. Slonczewski, J. Magn. Magn. Mater. **150**, 13 (1995).

[8] A. I. Morozov and A. S. Sigov, Fiz. Tverd. Tela **39**, 1244 (1997) [Phys. Solid State **39**, 1104 (1997)].

[9] A. Berger and E. E. Fullerton, J. Magn. Magn. Mater. **165**, 471 (1997).

Translated by W. J. Manthey

Magnetic contribution to the Debye temperature and the lattice heat capacity of ferromagnetic rare-earth metals (using gadolinium as an example)

V. Yu. Bodryakov, A. A. Povzner, and O. G. Zelyukova

Ural State Technical University, 620002 Ekaterinburg, Russia
(Submitted August 20, 1998; resubmitted November 12, 1998)
Fiz. Tverd. Tela (St. Petersburg) **41**, 1248–1253 (July 1999)

A thermodynamic approach that describes the spontaneous magnetic contribution to the Debye temperature of a ferromagnetic metal has been developed using the theory of second-order Landau phase transitions. It is shown that the essential cause of the formation of the spontaneous magnetic contribution to the Debye temperature is the magnetostrictive variation of the volume. By using an expression for the spontaneous magnetic contribution to the Debye temperature, the magneto–phonon contribution to the lattice specific heat is found. The resulting generalized expression for the Debye temperature is found to be in good agreement with experimental data concerning the elastic constants of the ferromagnetic phase of gadolinium. The magneto-phonon heat capacity makes an appreciable contribution to the heat-capacity anomaly of gadolinium close to the Curie point. © *1999 American Institute of Physics.* [S1063-7834(99)02507-1]

Rare-earth magnets possess obvious anomalies of their physical properties, which result from phase transitions to the magnetically ordered state and are associated with giant (by comparison with conventional $3d$ ferromagnets) magnetostrictive and magnetoelastic interactions. It has been experimentally established[1–3] that, during the magnetic ordering of rare-earth (RE) ferromagnets, the entire complex of their physical properties, such as the magnetization, thermal expansion (magnetostriction), heat capacity, sound velocity, and elastic moduli, undergo mutually consistent variations. The Debye temperature Θ also varies in a consistent manner in this case.[4] Moreover, it was found in the experimental study of Refs. 1–3 and 5 that the external magnetic field appreciably affects the elastic moduli, and that this manifests itself directly in the variation of the magnetization of the samples. This variation indicates directly that there is a magnetic contribution both to the elastic moduli and to the Debye temperature Θ associated with them, whose variations also correlate with the magnetization variation of the RE metals.[4]

However, strictly speaking, the problem of using experimental data to discriminate the magnetic contribution to the elastic moduli and then to the Debye temperature has not yet been solved. There is no conclusive explanation even for the mechanisms of the temperature dependences of the elastic moduli in the paramagnetic (PM) phase, from which an extrapolation (usually linear) is made into the ferromagnetic region in a number of papers just in order to distinguish the magnetic contribution to the indicated properties.

The first attempts to describe theoretically the dependence of the Debye temperature on the magnetization were undertaken in Refs. 6 and 7. However, these papers actually approached the computation of the compression modulus and the Debye temperature only in terms of the Stoner model of band ferromagnetism, which in principle is inapplicable to the heavy RE metals, with their localized magnetic moments. In the generalization of this approach, proposed later on the basis of the theory of second-order Landau phase transitions,[8] a self-consistent calculation of the Debye temperature was not carried out. Instead of this, it was proposed to determine its dependence on the magnetization via the essentially postulated magnetic components of Young's modulus and the shear modulus, and it was even initially asserted (see, for example, Ref. 7) that the magnetic component of the shear modulus can be neglected.

Since the question of the interconnection of the Debye temperature and the magnetization has not yet been satisfactorily solved, it also did not seem possible to analyze adequately the various components of the total measurable heat capacity of the solid, $C_P(T)$. This is associated in particular with the lack of reliable data on the electronic component of the heat capacity of RE magnets. Data obtained by different methods sometimes differ by a considerable factor,[9] and this is associated just with the problem of separating the magnetic and electronic contributions in the low-temperature region.

This paper uses the theory of second-order Landau phase transitions to describe how the magnetization affects the Debye temperature. The role of the magnetostrictive interactions specific to the magnetically ordered heavy RE metals is analyzed, and the magnetic contribution to the lattice heat capacity associated with this mechanism is considered. Using the ferromagnetic phase of gadolinium as an example, it is shown that the magnetic contribution to the lattice heat capacity associated with the dependence of the Debye temperature on the magnetization has an appreciable effect on the formation of a heat-capacity anomaly close to the Curie point.

1. THE FREE ENERGY OF A FERROMAGNET

We shall start by writing the free energy $\nu F(V,T,M)$ of a free single-domain isotropic ferromagnet in the theory of second-order phase transitions,[10] supplemented by the contribution associated with the energy of acoustic phonons (ν is the number of modes of the substance):

$$\nu F = \nu F_0 + \nu F_p + \nu F_e + \nu F_m. \tag{1}$$

Here $F_0 = F_0(V)$ is the molar free energy of the crystal lattice of the PM phase, extrapolated to zero temperature.

The molar phonon (Debye) part of the free energy is

$$F_p = (9/8)R\Theta + 3RTf(z), \tag{2}$$

where $z = \Theta/T$, and

$$f(z) = \ln[1 - \exp(-z)] - (1/3)D(z). \tag{3}$$

The standard tabulated Debye function is

$$D(z) = (3/z^3) \int_0^z \frac{y^3 dy}{\exp(y) - 1}, \tag{4}$$

while the Debye temperature Θ is a function of the volume of the body, its temperature, and the molar magnetization: $\Theta = \Theta(V,T,M)$, under the conditions that the external pressure equals atmospheric pressure and that the external magnetic field induction is constant.

The molar magnetic part of the free energy is

$$F_m = \alpha M^2 + \beta M^4 - BM, \tag{5}$$

where α and β are the molar thermodynamic coefficients (the Landau coefficients), M is the molar magnetization, and B is accordingly the normalized magnetic induction.

The molar electronic part of the free energy is

$$F_e = -(1/2)\zeta T^2, \tag{6}$$

and, as is well known, its dependence on the magnetization can be neglected, while the weak dependence of the molar coefficient of the electronic heat capacity on the volume should be taken into account only in special cases when analyzing the elastic moduli in the PM region $[\zeta = \zeta(V)]$.

2. THE DEBYE TEMPERATURE

It has been experimentally established that the variation of the Debye temperature because of the magnetic ordering of RE ferromagnets is relatively small (see, for example, Ref. 4). Thus, in the case of gadolinium, the variation of the Debye temperature in the entire interval of magnetic ordering is several kelvin, with the Debye temperature itself being $\Theta \sim 180\,\text{K}$ close to This allows the Debye temperature to be expanded close to the Curie point T_C in two small parameters: the magnetostrictive strain ∂V and the square molar magnetization M^2 (the order parameter) at constant temperature:

$$\Theta = \Theta_{pm} + \left[\left(\frac{\partial \Theta}{\partial V} \right) \partial V + \left(\frac{\partial \Theta}{\partial M^2} \right) M^2 \right]_T + \frac{1}{2} \left[\left(\frac{\partial^2 \Theta}{\partial V^2} \right) (\partial V)^2 \right.$$
$$\left. + 2 \left(\frac{\partial^2 \Theta}{\partial V \partial M^2} \right) \partial V M^2 + \left(\frac{\partial^2 \Theta}{\partial (M^2)^2} \right) M^4 + \dots, \right]_T \tag{7}$$

where Θ_{pm} is the Debye temperature of the PM phase close to $T = T_C$. Generally speaking, Θ_{pm} depends on temperature. It is obvious, however, that this (usually weak) dependence does not contradict the isothermal expansion given by Eq. (7). When there is no magnetic ordering (for a paramagnet) or in the PM region of a ferromagnet, we have that

$$\Theta = \Theta_{pm}(T), \tag{8}$$

where the $\Theta_{pm}(T)$ dependence is described by the equations in Ref. 11.

We should point out that the expansion of the Debye temperature must contain just those terms that are proportional to the powers of M^2, and not simply M, since the Debye temperature, being averaged over the volume by the parameter of the local characteristics of the magnet, obviously cannot depend on the direction of the magnetization, but is determined only by its magnitude. Therefore, in particular, it should be expected that the magnetic component of the Debye temperature does not go exactly to zero at the Curie point but remains nonzero even some way into the PM region. This is because regions of short-range magnetic order are maintained in the PM region after the long-range magnetic order has broken down, while the size of the maintained regions of local magnetic ordering gradually decreases with heating above T_C. Another interpretation of this well-known fact is that the rms value of the local magnetic moment remains nonzero in a certain region above T_C as a consequence of magnetic fluctuations.

As will be seen in what follows, to analyze the experimental data in the case of gadolinium, it is sufficient to restrict ourselves to the terms of the expansion in Eq. (7) containing the first derivative. Recalling that

$$\left(\frac{\partial \Theta}{\partial V} \right)_T = \left(\frac{\Theta}{V} \frac{\partial \ln \Theta}{\partial \ln V} \right)_T = -\gamma \Theta V^{-1}, \tag{9}$$

where

$$\gamma = -(\partial \ln \Theta / \partial \ln V)_T \tag{10}$$

is the Grüneisen constant,[12] while the relative magnetostrictive strain ω is

$$\omega = \left(\frac{\partial V}{V} \right)_T. \tag{11}$$

According to Eq. (7), taking Eqs. (9)–(11) into consideration, for the magnetic part of the Debye temperature, $\Theta_m = \Theta - \Theta_{pm}$, close to $T = T_C$ we have

$$\Theta_m \approx \Theta_{pm} \left[-\gamma \omega + \frac{1}{\Omega_{pm}} \left(\frac{\partial \Theta}{\partial M^2} \right) M^2 \right]_T. \tag{12}$$

The first term here corresponds to the magnetostrictive variation of the Debye temperature, and the second corre-

sponds to the explicit dependence of the Debye temperature on the magnetization as a consequence of the corresponding dependence of the sound velocity, i.e., in the final analysis, of the elastic modulus.

It has been established experimentally[3] that the magnetostriction ω for a wide class of ferromagnets is proportional to the square of the magnetization; i.e.,

$$\omega = \omega' M^2, \tag{13}$$

where the magnetostrictive constant is

$$\omega' = \left(\frac{\partial \omega}{\partial M^2}\right)_T. \tag{14}$$

Also introducing the notation

$$\Theta' = \frac{1}{\Theta_{pm}}\left(\frac{\partial \Theta}{\partial M^2}\right)_T. \tag{15}$$

we finally get for the magnetic part of the Debye temperature the expression

$$\Theta_m \approx \Theta_{pm}[-\gamma\omega' + \Theta']M^2, \tag{16}$$

whose coefficients can be estimated by minimizing the free energy.

3. MINIMIZING THE FREE ENERGY

In the spirit of the theory of second-order Landau phase transitions,[10] we minimize the molar free energy given by Eq. (1) in the square magnetization M^2 at a fixed temperature close to $T = T_C$

$$\left(\frac{\partial F}{\partial M^2}\right)_T = 0. \tag{17}$$

As a result, we get a generalization of the Belov–Arrott equation:[1]

$$\frac{B}{2M} = \alpha + (2\beta - \omega'\alpha\gamma_\alpha)M^2 + W_p\Theta' - \omega'\gamma(W_p + W_e), \tag{18}$$

where terms of higher order than M^2 are omitted from the right-hand side. We also omit the term proportional to $(\partial F_0/\partial M^2)_T = (\partial F_0/\partial V)_T(\partial V/\partial M^2)_T$ and that containing the external pressure $p_0 = -\nu(\partial F_0/\partial V)_T$.

We introduce the following symbols for the phonon and electron molar energies of a ferromagnet, respectively:

$$W_p = \frac{9}{8}R\Theta + 3RTD(z), \tag{19}$$

$$W_e = \frac{1}{2}\zeta T^2. \tag{20}$$

By analogy with the Grüneisen constant given by Eq. (10), it is convenient to call the quantity γ_α corresponding to the logarithmic derivative of the Landau parameter α with respect to the volume of the magnet,

$$\gamma_\alpha = \left(\frac{\partial \ln \alpha}{\partial \ln V}\right)_T, \tag{21}$$

the α-magnetic Grüneisen constant.

For the spontaneous (in the absence of an external magnetic field) molar magnetization M_s, Eq. (18) gives

$$M_s^2 = -[\alpha + W_p\Theta' - \omega'\gamma(W_p + W_e)]/[2\beta - \omega'\alpha\gamma_\alpha]. \tag{22}$$

Equation (22) differs from the well-known result $M_s^2 = -\alpha/2\beta$ obtained in the framework of the conventional theory of second-order phase transitions by terms that take into account, first, the magnetostrictive strain and, second, the variation of the Debye temperature with magnetization, associated with the corresponding variation of the elastic moduli.

The conditions for the applicability of the conventional approach of the Landau theory will be the following:

$$\alpha \gg [W_p\Theta' - \omega'\gamma(W_p + W_e)],$$

$$2\beta \gg \omega'\alpha\gamma_\alpha.$$

In other words, the conventional theory will work well for ferromagnets with comparatively weak magnetostriction and a weak dependence of the elastic moduli on the magnetization. Moreover, the molar phonon energy W_p also must not be too large.

Assuming below, in the spirit of Landau theory, that the square of the spontaneous magnetization goes to zero at the Curie point T_C as

$$M_s^2 = a_m(T_C - T), \quad a_m > 0, \tag{23}$$

we get, in accordance with Eq. (22), that the following conditions must be satisfied close to T_C:

$$\alpha = \alpha_0 - a_\alpha(T_C - T), \quad a_\alpha > 0 \tag{24}$$

$$\Theta' = \Theta_0' + a_\Theta(T_C - T), \tag{25}$$

$$\omega' = \omega_0' + a_\omega(T_C - T). \tag{26}$$

The free terms in Eqs. (24)–(26) are not independent but are connected by the following approximate relationship, neglecting the electronic contribution to the energy of the crystal, as well as the terms $\omega'\alpha\gamma_\alpha$, by comparison with 2β:

$$-\alpha_0 + W_p(\Theta_0' - \omega_0'\gamma) = 0. \tag{27}$$

In accordance with Eqs. (16) and (24)–(26), in the expression for the spontaneous magnetic part of the Debye temperature

$$\Theta_m \approx -\Theta_{pm}\frac{\alpha + 2\beta M_s^2}{W_p}M_s^2 \tag{28}$$

it is possible to distinguish the terms proportional to M_s^2 and $(T_C - T)M_s^2$:

$$\Theta_{ms} \approx \Theta_{m0}M_s^2 + \Theta_{m1}(T_C - T)M_s^2. \tag{29}$$

The expression for Θ_{ms} ensures that the magnetic part of the Debye temperature equals zero at the Curie point. In this case, by substituting the expression for the magnetic part of the Debye temperature into Eq. (2) for the phonon part of the
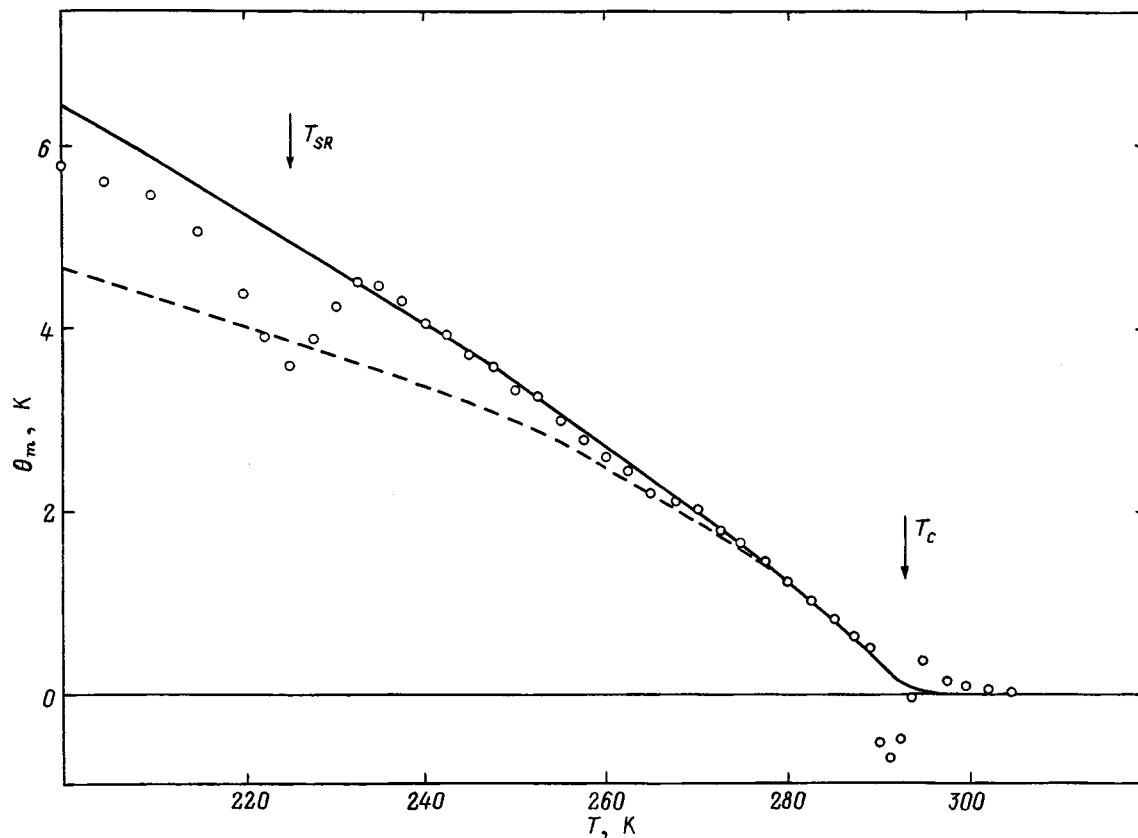
FIG. 1. Temperature dependence of the spontaneous magnetic contribution to the Debye temperature of gadolinium. The circles show the result of processing the experimental data of Ref. 4. The solid curve shows the result of calculation in terms of the theory developed here. The dashed curve shows the result of a calculation using the equation in Ref. 8.

free energy and then expanding in powers of magnetization, one can obtain magnetoelastic contributions to the free energy similar to those used in Refs. 5 and 7 and can also take into account the temperature dependences of the magnetostrictive parameters.

4. ANALYSIS OF THE EXPERIMENT

Figure 1 shows the temperature dependence of the spontaneous (in the absence of an external magnetic field) magnetic contribution to the Debye temperature of gadolinium. The Debye temperature $\Theta(T)$ is computed on the basis of measurements of the velocities of ultrasound.[4] The magnetic contribution to the Debye temperature was defined as the difference between the experimental values of $\Theta(T)$ in the ferromagnetic region and the values extrapolated from the PM region. The legitimacy of using a linear extrapolation is determined by the fact that the Curie temperature of $T_C \approx 293$ K and the spin reorientation temperature of $T_{SR} \approx 230$ K are appreciably higher than the Debye temperature.

According to our calculations and in accord with Eqs. (7), (8), and (29), the Debye temperature Θ (in K) that appears in Eq. (2), for the free energy of the lattice, in the case of gadolinium, can be described by

$$\Theta(M,T) = \Theta_{pm}(T) + \Theta_m(T,M_s^2) = 174.2 - 4.918$$

$$\times 10^{-3}T + 7.779 m_s^2 + 10.887 \tau m_s^2, \qquad (30)$$

where $m_s = M_s(T)/M_s(0)$ is the reduced magnetization, and $\tau = 1 - T/T_C$ is the reduced temperature. The expression for Θ_m works well (the correlation coefficient is $R = 0.9054$) in the wide temperature interval of $232.5 \leqslant T \leqslant 282.5$ K, i.e., in virtually the entire region of ferromagnetic ordering of gadolinium. An additional confirmation of the legitimacy of the mechanism considered here for the dependence of the Debye temperature on the magnetization follows from an analysis of the temperature–field dependences of Young's modulus of gadolinium.[13]

According the equation obtained here, there are appreciable deviations in the dependence of the magnetic part of the Debye temperature from the linear behavior of the dependence of Θ on M_s^2 predicted by Kim[6] and subsequently by Zverev[7] (Fig. 1). At the same time, the region in which our approach is applicable is restricted to the temperature intervals of the spin reorientation and the temperature region close to the Curie temperature (Fig. 1).

This temperature dependence of the magnetic contribution to the Debye temperature shows up in the formation of anomalies in the physical properties in the ferromagnetic region. In this paper, this is shown by the example of the lattice heat capacity of gadolinium, the magnetic contribution to which was determined by a relationship following from the Debye theory. The molar heat capacity of a ferromagnet at constant pressure can be found from well-known thermodynamic relations[10] if one considers the known tem-
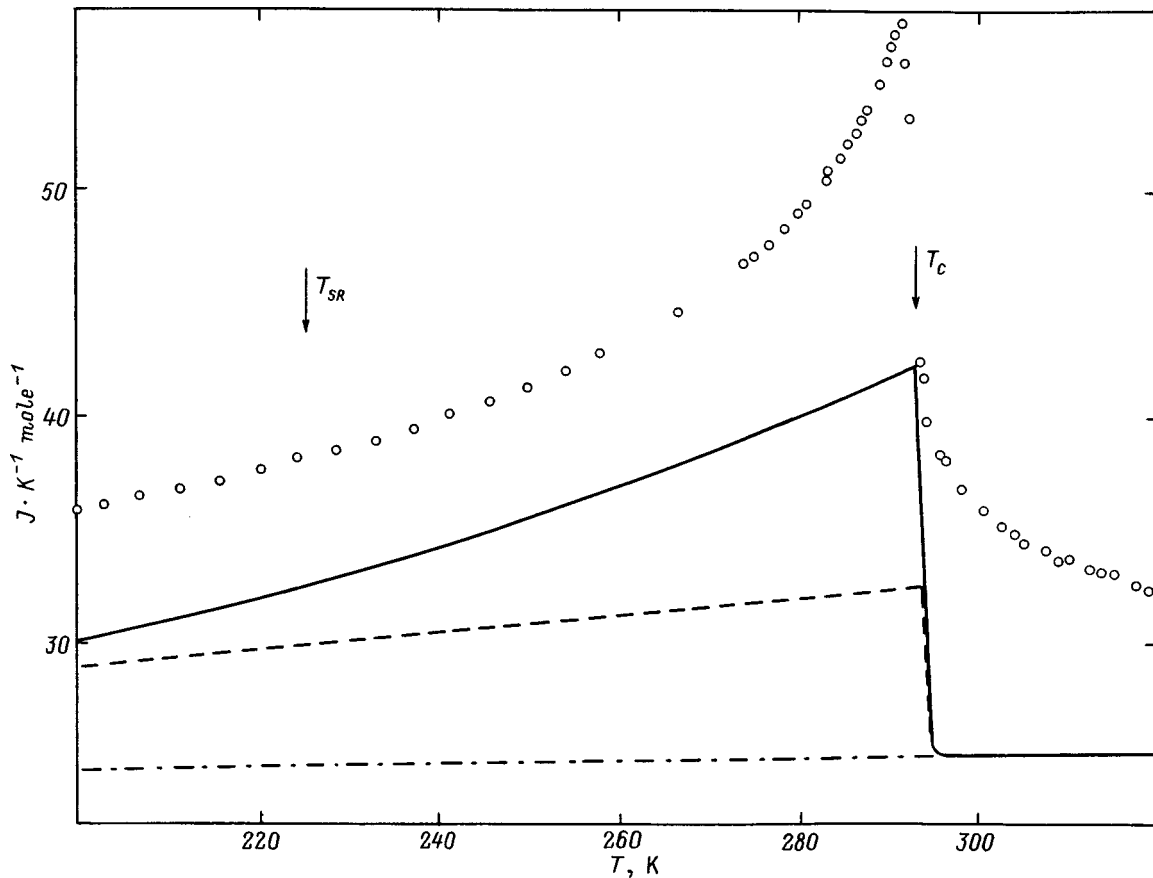
FIG. 2. Temperature dependence of the heat capacity of gadolinium. The circles show the experimental data of Ref. 14. The curves show calculations. The solid curve shows the calculation with the Debye temperature determined from Eq. (30). The dashed curve shows the calculation with the Debye temperature determined from the equation of Ref. 8. The dot–dashed curve shows the calculation with the Debye temperature found by extrapolating from the PM region (neglecting the magnetic contribution).

perature dependence (30) of the Debye temperature $\Theta(T)$:

$$C_p(T,\Theta) = C_V(T/\Theta)\left[1 - \frac{T}{\Theta}\frac{\partial\Theta}{\partial T}\right]^2$$

$$- 3RT\left[\frac{3}{8} - \frac{T}{\Theta}D(T/\Theta)\right]\frac{\partial^2\Theta}{\partial T^2}. \qquad (31)$$

The magneto-phonon contribution to the lattice heat capacity of gadolinium, associated with the spontaneous magnetic contribution to the Debye temperature, has been calculated on the basis of the data reflected in Fig. 1 and is shown in Fig. 2. This figure shows experimental data on the heat capacity,[14] as well as the results of the calculations. The dot–dashed line shows the lattice heat capacity computed on the basis of data on the Debye temperature, which is obtained after linearly extrapolating the $\Theta(T)$ dependence from the PM region. The solid curve describes the computed lattice heat capacity including the magnetic contribution of Eq. (29) to the Debye temperature. Finally, the dashed curve corresponds to the results of a calculation of the lattice heat capacity in which the magnetic part of the Debye temperature contains the incomplete magnetic contribution following from Refs. 7 and 8. The electronic contribution is neglected in the calculations in this case. A comparison of these data shows that the magneto–phonon contribution in the ferro-

magnetic region of gadolinium is extremely large and is comparable with the usual magnetic contribution, proportional to dM_s^2/dT.[1] We should also emphasize that it is important to take into account in Eq. (29) the magnetic contribution proportional to $(T_C - T)M_s^2$, which appreciably increases the magneto–phonon component of the heat capacity (the solid and dashed curves in Fig. 2).

In conclusion, it should be emphasized that the $M_s \sim \tau^\beta$ dependence of the order parameter with $\beta = 0.5$ used in the calculations [see Eq. (23)] following the Landau theory was in fact postulated. It is obvious that the computation of the critical index β lies beyond the possibilities of the thermodynamic approach. The latter only makes it possible to obtain noncontradictory relationships between the various physical parameters and to be in satisfactory agreement with experiment.

Moreover, the deviations of the experimental points from the calculated curve shown in the figures in the immediate neighborhood of the Curie point are evidently associated with the amplification of the fluctuation contribution, which is not considered in the theory of second-order phase transitions. In this connection, the immediate problem is to develop methods for taking the magnetic fluctuations into account in terms of the approach proposed here.

Another important problem requiring a separate treat-

ment is the theoretical investigation of the magnetic component of the elastic moduli in noncollinear magnetic structures, particularly in the spin-reorientation region of gadolinium.

[1] S. V. Vonsovskiĭ, *Magnetism. The Magnetic Properties of Dia-, Para-, Ferro-, Antiferro-, and Ferrimagnetic Materials* [in Russian] (Nauka, Moscow, 1971).

[2] T. E. Scott, in *Handbook on the Physics and Chemistry of Rare Earths, Vol. 1, Metals*, edited by K. A. Gschneidner and L. R. Eyring (North-Holland, Amsterdam, 1982), p. 592.

[3] S. A. Nikitin, *Magnetic Properties of Rare-Earth Metals and Their Alloys* [in Russian] (Mosk. Gos. Univ., Moscow, 1989).

[4] M. Rosen, Phys. Rev. **174**, 504 (1968).

[5] V. Yu. Bodryakov, ''Magnetoelastic and inelastic properties of rare-earth magnets,'' dissertation for candidate of physicomathematical sciences, Moscow State University, Moscow, 1995.

[6] T. J. Kim, Phys. Rev. **25**, 6919 (1982).

[7] V. M. Zverev and V. P. Silin, Zh. Éksp. Teor. Fiz. **93**, 709 (1987) [Sov. Phys. JETP **66**, 401 (1987)].

[8] V. M. Zverev, Zh. Éksp. Teor. Fiz. **112**, 1863 (1997) [JETP **85**, 1019 (1997)].

[9] V. E. Zinov'ev, *Thermophysical Properties of Metals at High Temperatures* [in Russian] (Sprav. Izd. Mettalurgiya, Moscow, 1989).

[10] L. D. Landau and E. M. Lifshitz, *Statistical Physics* (Pergamon Press, Oxford, 1980; Russian original, Nauka, Moscow, 1976), part 1.

[11] V. Yu. Bodryakov, A. A. Povzner, and O. G. Zelyukova, Fiz. Tverd. Tela **40**, 1581 (1998) [Phys. Solid State **40**, 1433 (1998)].

[12] S. I. Novikova, *Thermal Expansion of Solids* [in Russian] (Nauka, Moscow, 1974).

[13] V. Yu. Bodriakov, A. A. Povzner, and S. A. Nikitin, Eur. Phys. J. B **4**, 441 (1998).

[14] R. E. Griffel, F. H. Skochdopole, and F. H. Spedding, Phys. Rev. **93**, 657 (1954).

Translated by W. J. Manthey

Characteristic features of ferromagnetic resonance in iron-garnet films with orthorhombic magnetic anisotropy

V. V. Randoshkin, V. I. Kozlov, V. Yu. Mochar, N. V. Vasil'eva, N. A. Es'kov, and Yu. A. Durasova

Joint Self-Supporting Laboratory ''Magneto-Optoelectronics,'' Institute of General Physics, Russian Academy of Sciences, Mordovia State University, 430000 Saransk, Russia

The characteristic features of ferromagnetic resonance (FMR) were studied in bismuth-containing single-crystal iron-garnet films (BSIGFs) with no rapidly relaxing ions and relatively weak orthorhombic magnetic anisotropy (ORMA). The films were grown on (110) and (210) substrates by liquid-phase epitaxy from a supercooled flux solution. Attention is focused mainly on the unidirectional magnetic anisotropy in the film plane and on the effect of the film/substrate transitional surface layer on the FMR spectrum. © *1999 American Institute of Physics.*
[S1063-7834(99)02607-6]

One way to increase the operating speed of magneto-optic devices based on bismuth-containing single-crystal iron-garnet films (BSIGFs) is to use BSIGFs with orthorhombic magnetic anisotropy (ORMA).[1–7] In general these materials possess an easy magnetization axis, making a certain angle with the normal to the film plane,[8,9] as well as a magnetic anisotropy in the film plane much larger than the crystallographic cubic anisotropy. Such a magnetic anisotropy occurs, specifically, if films with orientation different from (111) contain, besides Bi^{3+}, also Y^{3+} ions.[2,10–13]

Investigations of the dynamics of domain walls (DWs) in BSIGFs with ORMA[2–7,10–14] revealed a number of features: a) absence of the production of microdomains in front of a moving DW in SIGFs with ORMA even when the film does not contain rapidly relaxing rare-earth ions;[7,12,13] b) unusual rhombiform dynamic domains;[12] c) so-called unidirectional anisotropy of the DW velocity;[7,13,14] d) strong dependence of the form of the dynamic domains and velocity of DWs on the magnetic field H_{in} applied in the film plane (in-plane magnetic field).[13]

The unusual dynamical properties of BSIGFs with ORMA, including also the unidirectional anisotropy of the velocity of DWs, can be explained on the basis of the spin-wave mechanism of the motion of DWs,[15,16] if it is assumed that the range of magnetic fields, where spin waves are emitted, and the damping parameter depend on direction in the film plane.[17,18]

When studying BSIGFs with ORMA by FMR, films containing rapidly relaxing rare-earth ions (for example, Dy^{3+}, as in Ref. 19) are chosen to prevent the excitation of spin-wave resonance (SWR).

Our objective in the present work is to study FMR in BSIGFs with ORMA and without rapidly relaxing ions. BSIGFs with the compositions $(Bi,Y)_3(Fe,Ga)_3O_{12}$ (I) and $(Bi,Y,Lu)_3(Fe,Ga)_3O_{12}$ (II) were chosen for the investigations.

Type-I films were grown by liquid-phase epitaxy from a $PbO–Bi_2O_3–B_2O_3$-based supercooled fluxed solution on

$(Gd,Ca)_3(Mg,Zr,Ga)_5O_{12}$ substrates with (210) orientation. In contrast to Pr-containing films with ORMA,[20] the BSIGFs studied possess relatively weak in-plane anisotropy. This makes it possible to observe FMR for any orientation of the external magnetic field.

Type-II films were grown on (110) $Ca_3(Nb,Ga)_5O_{12}$ substrates using the same solvent. The process of epitaxial growth of BSIGFs on this substrate has a number of characteristic features, including the need for strong dilution of the fluxed and large supercooling $\Delta T \geqslant 100$ K.[21,22] It has also been observed[21,22] that the quality of SIGFs is higher if (110) and not (111) substrates are used (for other substrates, specifically, $(Gd,Ca)_3(Mg,Zr,Ga)_5O_{12}$, the situation is reversed). Moreover, films grown on $Ca_3(Nb,Ga)_3O_{12}$ substrates possess a relatively thick (2–10 μm) film–substrate (FS) transitional surface layer.[21,22] In our investigations of type-II films, we focused our attention mainly on the effect of this circumstance on the FMR spectrum.

The content of iron and gallium oxides during the growth of films of both compositions was approximately the same. The content of lutecium in the type-II films was approximately an order of magnitude lower than that of yttrium. The chemical composition of the experimental films was not analyzed. We note that, because the crystal-forming properties of the bismuth-containing fluxed solution degrade, which changes the chemical composition and parameters of BSIGFs grown successively in the same directions,[23] there is no unique relation between the properties of the charge and the films grown.

The experimental samples were usually disk-shaped with a diameter of 2–3 mm and films on both sides of the substrate. FMR was observed at 9.24 GHz. The scanning range of the FMR spectrometer was 0–9000 Oe. The derivatives of the absorption with increasing external magnetic field were recorded. The resonance fields with the external magnetic field oriented perpendicular ($H_\perp$, perpendicular resonance) and parallel ($H_\parallel$, parallel resonance) to the film plane was determined. The in-plane anisotropy was judged according to
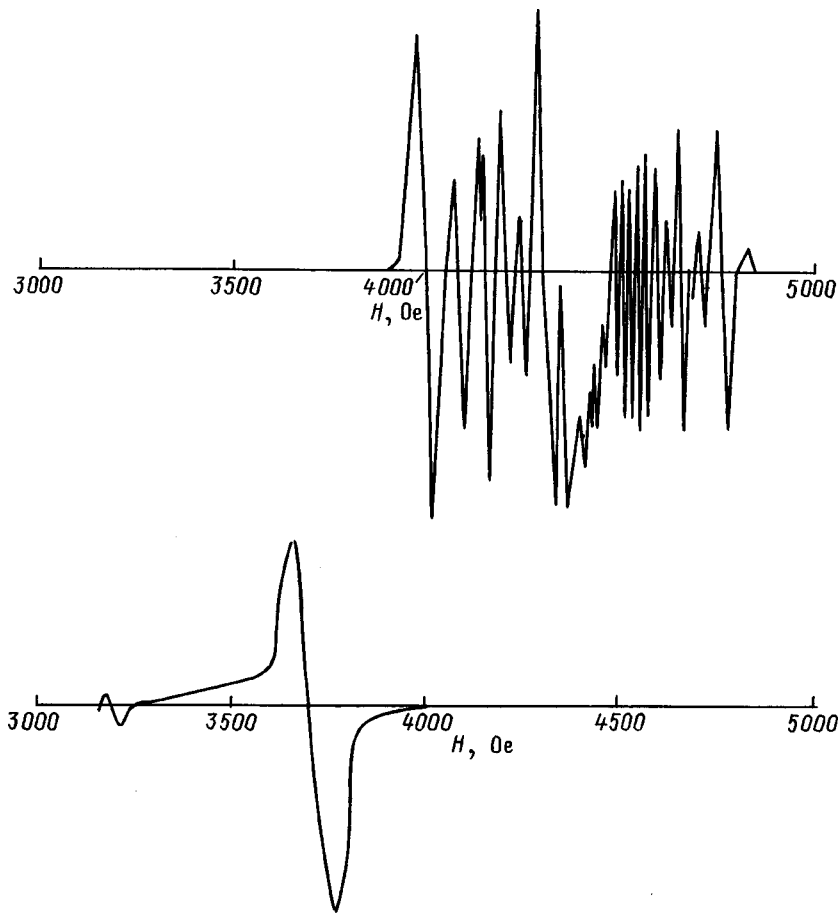
FIG. 1. FMR spectra with parallel resonance for type-I BSIGFs for two mutually opposite directions.

the azimuthal dependence $H_\parallel(\varphi)$ for parallel resonance.

Since the experimental BSIGFs do not contain rapidly relaxing magnetic ions and the only slowing relaxing ions are Fe^{3+}, the effective gyromagnetic ratio γ in the films is the same as for iron ions: (1.76×10^7 $Oe^{-1}\cdot s^{-1}$). In contrast to Refs. 24 and 25 this permits determining the effective magnetic-anisotropy field H_{eff} only from the data on the perpendicular resonance for which the resonance relation can be written

$$\omega/\gamma = H_{eff} + H_\perp,\tag{1}$$

where ω is the angular FMR frequency. However, if the resonance field for parallel resonance is known, then

$$H_{eff} = H_\parallel - (\omega/\gamma)^2/H_\parallel.\tag{2}$$

Figure 1 shows the parallel-resonance spectra for type-I BSIGFs. The spectra were obtained for two values of φ differing by 180°, the lower spectrum corresponding to the direction for which the resonance field of the left-most line in the spectrum is minimal. It is evident that the upper spectrum contains more than 20 lines, which is also characteristic for films which do not contain rapidly relaxing ions and do not exhibit ORMA.[26] However, the linewidth, which exceeds 10 Oe, is much larger than the values (of the order of 1 Oe) that characteristic for films without ORMA that do not contain rapidly relaxing ions.[26] This confirms that the damping parameter depends on the presence of an effective in-plane internal magnetic field.[17,18] When the direction of the external magnetic field is reversed, only two lines, differing in inten-

sity by an order of magnitude and the lines themselves being substantially broadened compared to any line in the upper spectrum, remain in the FMR spectrum.

Following Refs. 17 and 18, the broadening of the FMR lines can be explained by an increase in the dimensionless Gilbert damping parameter α in the presence of an effective magnetic-anisotropy field in the film plane and by the dependence of the damping parameter on this film. The large difference in the parallel-resonance spectra for mutually opposite directions in the film plane attests to the presence of both unidirectional magnetic anisotropy and unidirectional linewidth anisotropy in the FMR spectrum in the film plane. The dependence of the FMR linewidth on the orientation of the external field in the film plane with parallel resonance correlates with the anisotropic broadening of the image of a moving DW (the transitional region between dynamic domains with opposite polarity where local magnetization rotation occurs; this region can be visualized by means of the Faraday magnetooptic effect with crossed polarizer and analyzer) in a BSIGF with ORMA, resulting in unidirectional anisotropy of the DW velocity.[7,13,14]

For a perpendicular resonance the FMR spectrum likewise contains a series of quite wide lines (Fig. 2). It follows from this spectrum that the effective uniaxial magnetic-anisotropy field for this sample lies in the range 2100–2500 Oe (it is impossible to give the exact value of H_{eff}, since additional investigations, including layer-by-layer thinning of the film, are required in order to determine which line is
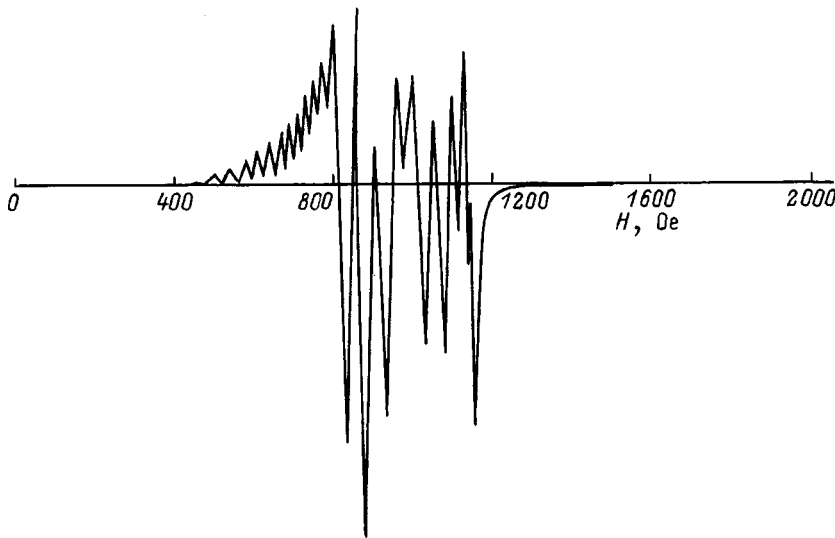
FIG. 2. FMR spectrum with perpendicular resonance for a type-I BSIGF.

the ''zeroth'' mode for the interior volume of the film). However, it is clear that the FMR spectrum (Fig. 2) includes both zero modes for the interior volume of the films on both sides of the substrate and transitional surface layers as well as SWR modes.

The quite large width of the FMR lines with a perpendicular resonance correlates with the absence of micro-domain generation in front of a moving DW in BSIGFs with ORMA without rapidly relaxing ions.[7,12,13]

The parameters of type-II BSIGFs, the results of investigations of which are discussed in the present paper, are presented in Table I, where $2h$ is the total width of the films on both sides of the substrate, Θ_F is the specific Faraday rotation at wavelength 633 nm, and P_0 is the equilibrium period of the stripe domains. The table also gives data for a sample grown on a (110) $Nd_3Ga_5O_{12}$ substrate.

Figure 3 shows the parallel-resonance spectrum for a SIGF grown from a fluxed solution I (sample No. 1 in Table I). It is evident that the spectrum contains two FMR lines with different widths. The first line corresponds to a lower resonance field (low-field line), it is approximately two times wider and belongs to the film (or layer) with ''easy plane'' anisotropy ($H_{eff} = -1050$ Oe). The second line corresponds to a higher resonance field (high-field line) and belongs to the film (layer) with ''easy axis'' anisotropy ($H_{eff} = 2920$ Oe). However, it is difficult to imagine that the difference in the conditions of film growth on the bottom and top sides of the substrate[27] can lead to such a radical change in the magnetic anisotropy. At the same time there exist physical mechanisms that lead to the formation of an FS layer whose magnetic anisotropy differs strongly from that of the interior

volume of the film. They include etching of the substrate at the initial stage of epitaxial growth, followed by incorporation of the dissolved components of the substrates in the epitaxial films.[28,29] Moreover, dissolution of the substrate can occur on some sections of the film while at the same time epitaxial growth occurs on other sections. We note that such ''island'' growth of the BSIGFs studied and the intense dissolution of the $Ca_3(Nb,Ga)_5O_{12}$ substrate have been observed in growth experiments.[21,22] Moreover, as the BSIGFs build up, solid-state diffusion can occur, producing a strong change in the chemical composition of the FS layer.[30]

The values of H_{eff} obtained from the data in Fig. 3 make it possible to calculate the resonance field for a perpendicular resonance: $H_\perp = 410$ Oe for the narrow FMR line and 4380/Oe for the wide line. Even though the computed values of $H_\perp$ do not fall outside the scan limits of the FMR spectrometer, the perpendicular resonance is not observed in sample No. 1. On switching from an orientation where the external magnetic field is applied in the film plane to an orientation where it is perpendicular to this plane (as the angle θ between the direction of the external magnetic field and the plane of the SIGF increases), the amplitude of the FMR signal decreases sharply and the resonance line broadens at the same time, so that the signal vanishes at $\theta = 20°$.

TABLE I. Parameters of the type-II experimental samples.

Sample No.	Substrate	$2h$, μm	Θ_F, grad/μm	P_0, μm
1	$Ca_3(Nb,Ga)_5O_{12}$	6.0	1.7	7.8
2	$Ca_3(Nb,Ga)_5O_{12}$	4.8	1.5	13.0
3	$Ca_3(Nb,Ga)_5O_{12}$	5.8	2.1	5.7
4	$Nd_3Ga_5O_{12}$	1.8	1.8	5.7
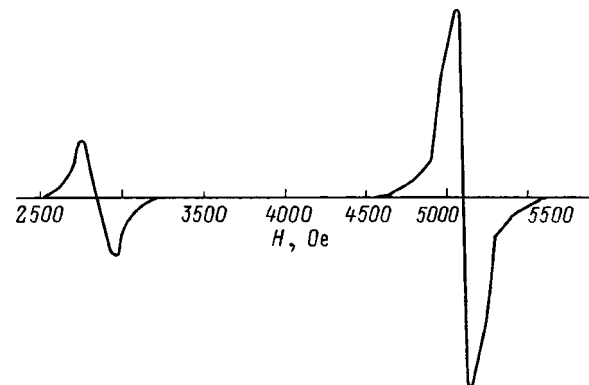
FIG. 3. Parallel-resonance spectrum for a type-II BSIGF (sample No. 1 in Table I).
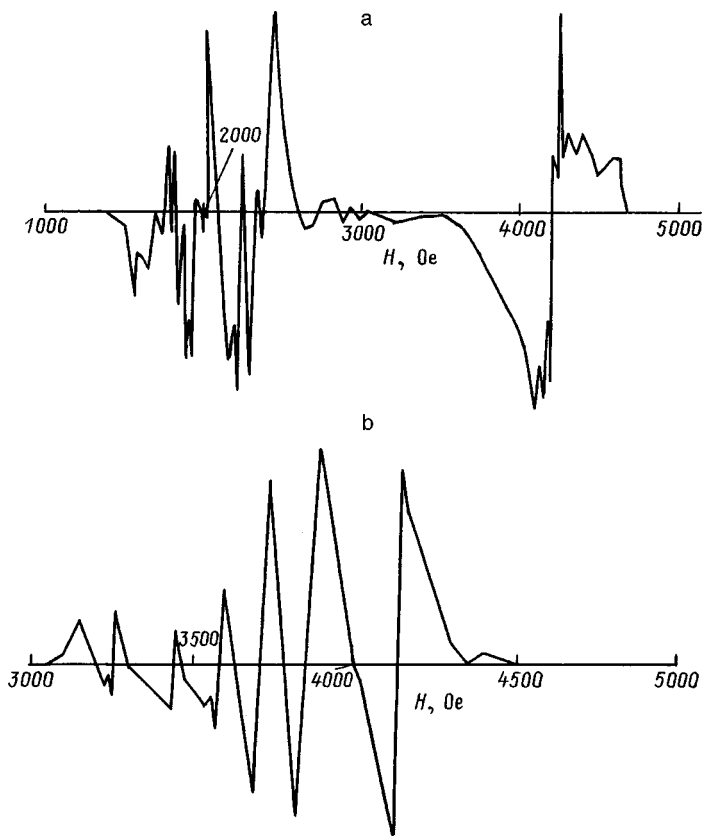
FIG. 4. Parallel-resonance (a) and perpendicular-resonance (b) spectra for a type-II BSIGF (sample No. 3 in Table I).

Only one FMR line with $H_\parallel = 5300$ Oe was observed for the thinner sample No. 2 with parallel resonance. This gives the computed value $H_\perp = 130$ Oe. For it, just as for sample No. 1, the perpendicular resonance is not observed.

However, a perpendicular resonance is observed for sample No. 3 synthesized from a fluxed solution with lower Y_2O_3 and Lu_2O_3 concentrations, and there are two quite separate packets of FMR lines (we associate these packets with the interior volume of the film and the FS layer, respectively) with the resonance fields for the strongest lines equal to 2100 and 4200 Oe (Fig. 4a). The values of H_{eff} and $H_\parallel$ calculated from these data are 1230 and 4000 Oe, respectively, for the first line and -870 and 2930 Oe for the second line. The existence of two packets of lines with approximately the same intensity attests to a relatively large thickness of a transitional FS surface layer with ''easy plane'' anisotropy.

For a parallel resonance the experiment (Fig. 4b) gives a series of lines in the range 3000–4500 Oe, the strongest line lying closer to the upper limit of this range.

For comparison, the FMR spectrum with parallel resonance for a BSIGF grown on a $Nd_3Ga_5O_{12}$ substrate, for which the characteristic features of epitaxial growth that are characteristic for $Ca_3(Nb,Ga)_5O_{12}$ are not observed, is displayed in Fig. 5. As expected, because the FS layer is thinner for sample No. 4 the FMR spectrum is more ''regular'' than the spectrum presented in Fig. 4. On account of the high uniaxial magnetic anisotropy in this sample ($H_{eff} \geqslant 3200$ Oe) the FMR signal with perpendicular resonance is not observed.

Anisotropy in the film plane is observed for all type-II

samples. However, the anisotropy is small (~ 150 Oe) compared to the average resonance field, but the unidirectional magnetic anisotropy is absent. For films on a $Ca_3(Nb,Ga)_5O_{12}$ substrate the azimuthal dependence of the resonance field contains four almost equidistant peaks which reflects the crystallographic anisotropy of the film. This correlates with the elliptic shape of the dynamic domains in the experimental films. For a film on a $Nd_3Ga_5O_{12}$ substrate, the azimuthal dependence of the resonance field is more complicated. This is explained by excitation of SWRs, leading to the appearance of a quite large number of lines in the FMR spectrum (Fig. 5).

For type-I films (Figs. 1 and 2) as well as for type-II films (Figs. 3, 4 and 5) the FMR linewidth is much larger than for films without ORMA which do not contain rapidly relaxing ions (see, for example, Ref. 26).
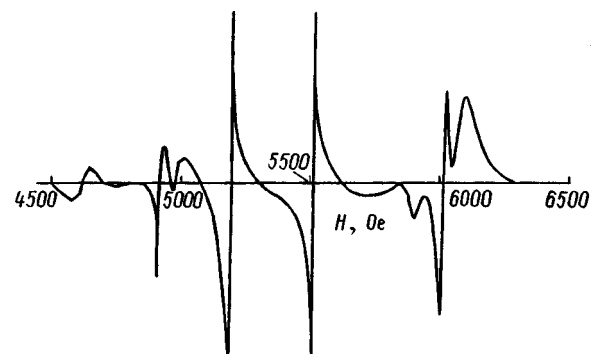
FIG. 5. Perpendicular-resonance spectrum for a type-II BSIGF (sample No. 4 in Table I).

In summary, it has been shown in this work that: a) in type-I BSIGFs grown on (210) $(Gd,Ca)_3(Mg,Zr,Ga)_5O_{12}$ substrates unidirectional magnetic anisotropy and FMR linewidth anisotropy are observed in the film plane; b) in type-II BSIGFs grown on (110) $Ca_3(Nb,Ga)_5O_{12}$ substrates the unidirectional magnetic anisotropy in the film plane is absent; c) in type-II BSIGFs grown on $Ca_3(Nb,Ga)_5O_{12}$ substrates the thickness of the film/substrate transitional surface layer is comparable to the thickness of the bulk of the film; and, d) in type-I and -II BSIGFs with ORMA the lines in the FMR spectrum are much wider than in the films without ORMA.

[1] V. V. Randoshkin and A. Ya. Chervonenkis, *Applied Magneto-Optics* [in Russian] (Énergoatomizdat, Moscow, 1990).

[2] V. V. Randoshkin, V. I. Chani, M. V. Logunov, V. P. Klin, B. P. Nam, A. G. Solov'ev, and A. Ya. Chervonenkis, Pis'ma Zh. Tekh. Fiz. **15**(14), 42 (1989) [Sov. Tech. Phys. Lett. **15**, 553 (1989)].

[3] V. V. Randoshkin, Proc. SPIE **1307**, 10 (1990).

[4] V. V. Randoshkin, Proc. SPIE **1469**, 796 (1991).

[5] V. V. Randoshkin, Trudy IOFAN **45**, 49 (1992).

[6] V. V. Randoshkin, Defektoskopiya , No. 6, 58 (1997).

[7] V. V. Randoshkin, M. V. Logunov, and Yu. N. Sazhin, Zh. Tekh. Fiz. **66**(4), 201 (1996) [Tech. Phys. **41**, 404 (1996)].

[8] E. N. Il'icheva, A. V. Dubova, V. K. Peterson, Yu. N. Fedyunin, and A. G. Shishkov, Fiz. Tverd. Tela (St. Petersburg) **35**, 1167 (1993) [Phys. Solid State **35**, 594 (1993)].

[9] E. N. Il'icheva, A. G. Shishkov, A. M. Balbashov, Yu. N. Fedyunin, and A. V. Klushina, Zh. Tekh. Fiz. **63**(11), 143 (1993) [Sov. Phys. Tech. Phys. **38**, 1005 (1993)].

[10] T. Hibiya, H. Makino, and S. Konishi, J. Appl. Phys. **52**, 7347 (1981).

[11] S. Kikukawa, S. Isomura, and S. Iwata, J. Appl. Soc. Jpn. **7**(2), 83 (1983).

[12] V. V. Randoshkin, V. B. Sigachev, V. I. Shani, and A. Ya. Chervonenkis, Fiz. Tverd. Tela (Leningrad) **31**(7), 70 (1989) [Sov. Phys. Solid State **31**, 1138 (1989)].

[13] M. V. Logunov, V. V. Randoshkin, and Yu. N. Sazhin, Fiz. Tverd. Tela (Leningrad) **32**, 1456 (1990) [Sov. Phys. Solid State **32**, 849 (1990)].

[14] F. V. Lisovskiĭ, A. S. Logginov, G. A. Nepokoĭchitskiĭ, and T. V. Rozanova, JETP **45**, 430 (1987).

[15] G. E. Khodenkov, Fiz. Met. Metalloved. **39**, 466 (1975).

[16] V. V. Randoshkin and V. B. Sigachev, Fiz. Tverd. Tela (Leningrad) **28**, 1522 (1986) [Sov. Phys. Solid State **28**, 859 (1986)].

[17] V. V. Randoshkin, Izv. Vyssh. Uchebn. Zaved. Fiz. No. 9, 45 (1997).

[18] V. V. Randoshkin, Fiz. Tverd. Tela (St. Petersburg) **39**, 1421 (1997) [Phys. Solid State **39**, 1260 (1997)].

[19] V. N. Van'kov and A. M. Zyuzin, Zh. Tekh. Fiz. **62**, 15 (1992) [Sov. Phys. Tech. Phys. **37**, 548 (1992)].

[20] V. V. Randoshkin and Yu. N. Sazhin, Zh. Tekh. Fiz. **66**(8), 83 (1996) [Sov. Phys. Tech. Phys. **41**, 790 (1996)].

[21] V. V. Randoshkin, N. A. Es'kov, and V. I. Chani, Pis'ma Zh. Tekh. Fiz. **15**(2), 27 (1989) [Sov. Tech. Phys. Lett. **15**, 49 (1989)].

[22] N. V. Vasiljeva, V. I. Chani, V. V. Randoshkin, and N. A. Es'kov, Proc. SPIE **1126**, 99 (1989).

[23] V. V. Randoshkin, N. V. Vasil'eva, K. V. Stashun, and M. V. Stashun, Neorg. Mater. **35**, 1 (1999).

[24] K. Gangulee and R. J. Kobliska, J. Appl. Phys. **51**, 3333 (1980).

[25] N. A. Loginov, M. V. Logunov, and V. V. Randoshkin, Fiz. Tverd. Tela (Leningrad) **31**(10), 58 (1989) [Sov. Phys. Solid State **31**, 1684 (1989)].

[26] V. D. Dudorov and V. V. Randoshkin, Fiz. Tverd. Tela (St. Petersburg) **36**, 1790 (1994) [Phys. Solid State **36**, 981 (1994)].

[27] V. V. Randoshkin and V. I. Chani, Defektoskopiya , No. 4, 55 (1995).

[28] Yu. V. Starostin, *Magnetic Bubble Memory and Logical Devices* [in Russian] (INÉUM, Moscow, 1981), pp. 85–93.

[29] Yu. V. Starostin, *Problems of Magnetic Bubble Device Construction* [in Russian] (INÉUM, Moscow, 1982), pp. 15–18.

[30] N. A. Groshenko, A. M. Prokhorov, V. V. Randoshkin, M. I. Timoshechkin, A. N. Shaposhnikov, A. V. Shirkov, and Yu. I. Stepanov, Fiz. Tverd. Tela (Leningrad) **27**, 1712 (1986) [Sov. Phys. Solid State **27**, 1029 (1986)].

Translated by M. E. Alferieff

Random anisotropy in R$_2$CuO$_4$ (R=Nd, Pr, Sm, Gd, Eu) quasi-*2D* antiferromagnets

E. I. Golovenchits and V. A. Sanina

A. F. Ioffe Physicotechnical Institute, Russian Academy of Sciences, 194021 St. Petersburg, Russia
(Submitted November 13, 1998)
Fiz. Tverd. Tela (St. Petersburg) **41**, 1259–1263 (July 1999)

The mechanisms of random anisotropy produced by an an effective coupling between rare-earth
ion moments and orbital momenta of Cu^{2+} ions through spin fluctuations is studied in
R$_2$CuO$_4$ crystals. The effective random-anisotropy fields are estimated from an analysis of
experimental data for R$_2$CuO$_4$ crystals (R=Eu, Pr, Gd). © *1999 American Institute of Physics.*
[S1063-7834(99)02707-0]

Crystals of the R$_2$CuO$_4$ family, where (R=Pr, Nd, Gd, Sm, and Eu), belong to the class of quasi-2D Heisenberg antiferromagnets made up of square lattices of Cu^{2+} ions with spin $S=1/2$ in the CuO$_2$ layers. All crystals of the family, with the exception of Gd$_2$CuO$_4$, possess tetragonal symmetry T' ($I4/mmm$).[1] Gd$_2$CuO$_4$ undergoes phase transition at $T\sim 660$ K from the high-temperature tetragonal phase, T', to the low-temperature orthorhombic phase with space group $Acam$.[2]

Neutron diffraction measurements of Bragg peak intensities (see, e.g., Ref. 3) yield $T_N \simeq 250-300$ K for the Néel temperature of the R$_2$CuO$_4$ antiferromagnets. It is assumed that below T_N the Cu subsystem has a *3D* uniform antiferromagnetic long-range order.

Studies of microwave spin dynamics in R$_2$CuO$_4$ crystals (R=Eu, Pr) revealed, however, the existence of *2D* uniform, well pronounced spin-wave excitations of the spin-wave type within a broad range of temperatures, both for $T \ll T_N$ and for $T \gg T_N$.[4,5] Simultaneous observation of the appearance of *2D* and *3D* states for temperatures $T < T_N$ suggests the existence of a quasi-*2D* random-field (RF) state in R$_2$CuO$_4$ tetragonal crystals. It is thus assumed that, for $T < T_N$, 3D antiferromagnetic ordering exists in regions of a limited extent, and that there are 2D Heisenberg antiferromagnetic spin fluctuations with large correlation lengths.[5,7]

The presence of *2D* Heisenberg antiferromagnetic spin fluctuations is characteristic of the whole class of quasi-*2D* compounds involving CuO$_2$ layers in the absence of *3D* uniform long-range antiferromagnetic order.[8] The correlation length of these fluctuations is given by[8]

$$\xi = a \exp(2\pi \rho_s / k_B T),\qquad (1)$$

where a is the lattice constant, and $2\pi\rho_s \simeq 1500$ K is the 2D antiferromagnetic spin stiffness. The quantity $2\pi\rho_s \simeq J$, and J is the 2D Heisenberg antiferromagnetic-exchange constant. For $T=200$ K, $\xi \simeq 2000\,a$.

2D Heisenberg antiferromagnetic spin fluctuations were observed experimentally in inelastic neutron scattering in La$_2$CuO$_4$ only for temperatures $T \gtrsim T_N$.[9] No similar studies have been carried out for the R$_2$CuO$_4$ tetragonal crystals. Note that while the CuO$_2$ layers in all the above-mentioned crystals have similar properties, the nature of the interlayer and anisotropic coupling in the La$_2$CuO$_4$ and R$_2$CuO$_4$ crystals is essentially different, and there are no grounds to expect total analogy among the characteristics of these crystals. Indeed, in contrast to La$_2$CuO$_4$, in the R$_2$CuO$_4$ crystals Cu^{2+} ions in adjacent layers are arranged in such a way that the interlayer molecular fields are zero in the mean-field approximation. The layers are coupled through fluctuation interactions. In R$_2$CuO$_4$ with magnetic rare-earth (RE) ions there are also $3d-4f$ interactions.

The nature of the interlayer and anisotropic interactions and of the 3D antiferromagnetic ordering in R$_2$CuO$_4$ tetragonal crystals was studied theoretically.[10–12] An analysis was made[12] of pseudo-dipole interactions in the Cu subsystem, which can account for the noncollinear 3D antiferromagnetic order observed to exist by neutron diffraction experiments. The mechanisms of anisotropy in R$_2$CuO$_4$ tetragonal crystals originating from both interactions within the Cu subsystem and the interaction between R^{3+} magnetic RE ions with Cu^{2+} ions were considered.[10,11] One investigated also the contribution of anisotropic interactions to the formation of quasi-2D states. However all these examinations of the crystals under study considered uniform 3D antiferromagnetic ordering for temperatures $T \lesssim T_N$.

Now, if one assumes the existence in R$_2$CuO$_4$ tetragonal crystals of a quasi-2D RF state, and that, for $T < T_N$ there are 2D spin fluctuations with large correlation lengths $\xi \gg a$, then an analysis of interlayer coupling and of anisotropic interactions should include also effective interactions through these fluctuations. This is the effective R^{3+}–R^{3+} exchange coupling through 2D antiferromagnetic spin fluctuations ($f-d-f$ exchange) and the orbit-orbit interaction of Cu^{2+} ions through the same fluctuations. The objective of this work is to study the influence of such effective interactions on the anisotropy of the R$_2$CuO$_4$ crystals.

Earlier studies of $3d-4f$ anisotropic interactions and of the $f-d-f$ exchange were made on RE orthoferrites, orthochromites, and garnets (see Refs. 13 and 14). It was shown that the anisotropy of the $3d$ subsystem is dominated by the state of the $4f$ magnetized ions. Direct $4f-4f$ exchange coupling results in $4f$ ion ordering usually only for temperatures $T \lesssim 10$ K. However in RE magnets containing $3d$ ions there is also polarization-induced (fluctuation) $f-d-f$ exchange (see Refs. 14–16), and taking it into account may give rise to
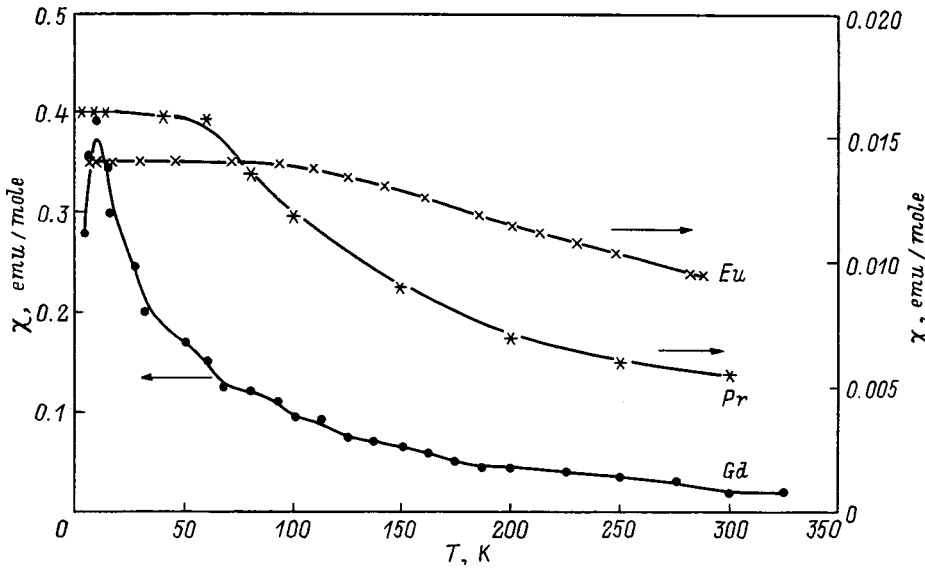
FIG. 1. Temperature dependences of the static magnetic susceptibility for Gd$_2$CuO$_4$ (χ_{ab}, Gd line), Eu$_2$CuO$_4$ (χ_c, Eu line), and Pr$_2$CuO$_4$ (χ_{ab}, Pr line).

$4f$ ion ordering at higher temperatures than is the case with the direct $4f$–$4f$ exchange. As a result, there may appear for $T \gtrsim 10$ K an internal effective anisotropy field in the $3d$ subsystem, which is stimulated by the RE subsystem ordered through the f–d–f interaction.

R$_2$CuO$_4$ crystals, with magnetic RE ions revealed at temperatures $T \gtrsim 10$ K, RE-ion magnetization maxima (for instance, for Gd$_2$CuO$_4$ $T_{max} \simeq 20$ K, and there is a strong magnetization tail extending up to 200 K, see Fig. 1).[17,18] It was assumed[17,18] that the observed features are due to R–Cu and Cu–Cu exchange interactions. We believe that the maxima in question may be identified with $4f$-ion ordering temperatures through the f–d–f exchange.

The existence in R$_2$CuO$_4$ tetragonal crystals of orbit-orbit interaction through 2D Heisenberg antiferromagnetic spin fluctuations requires a degenerate orbital ground state of Cu^{2+} ions (d_{xz}, d_{yz} tetragonal doublet) or an admixture of an excited tetragonal doublet to the ground singlet.[6] We shall assume the existence of such an orbital ground state in R$_2$CuO$_4$ tetragonal crystals. Note that the assumption of the existence of an orbital ground state in the form of $d_{x^2-y^2}$ with an admixture of a d_{xz}, d_{yz} tetragonal doublet was put forward[10] to account for the anisotropy in the ab plane observed in the R$_2$CuO$_4$ tetragonal crystals. An orbital ground state in Eu$_2$CuO$_4$ in the form of a d_{xz}, d_{yz} tetragonal doublet (or of a singlet with a strong admixture of such a doublet) follows from experimental data.[19]

We are going to show below that both anisotropy mechanisms, which originate from effective interactions of RE ions or of orbital momenta of Cu^{2+} ions through 2D antiferromagnetic spin fluctuations, give rise to a fairly large random anisotropy.

The paper is organized as follows: Section 1 deals with effective f–d–f exchange and the random anisotropy caused by this exchange, in Section 2 one takes into account spin-orbit coupling and considers effective orbit-orbit interaction of Cu^{2+} ions through 2D spin fluctuations and the associated random anisotropy, and Section 3 presents an analysis of

mechanisms of random anisotropy for the R$_2$CuO$_4$ crystals (R=Eu, Pr, and Gd).

1. ANISOTROPY CAUSED BY f–d–f EXCHANGE INTERACTION IN R$_2$CuO$_4$ CRYSTALS

Consider the Hamiltonian

$$\mathcal{H} = \sum_{ij} \mathbf{J}_{ij}^{d-d} S_i S_j + \sum_{\alpha\beta, ik} J_{\alpha,i;\beta,k}^{d-f} S_i^\alpha I_k^\beta . \quad (2)$$

Here J_{ij}^{d-d} is the constant of 2D Heisenberg antiferromagnetic exchange between nearest-neighbor Cu^{2+} ions occupying sites i and j in the CuO$_2$ layers, and $J_{\alpha,i;\beta,k}^{d-f}$ is a component of the d–f exchange coupling tensor between the projections of Cu^{2+} spins in the i and j lattice sites (S_i^α) and of the moments (I_k^β) of RE ions in the k,l sites immediately above and below the CuO$_2$ layer. In our case, $J_{ij}^{d-d} \gg J_{\alpha,i;\beta,k}^{d-f}$. We can also write an effective Hamiltonian for the $4f$ subsystem to second order in perturbation theory

$$\mathcal{H}_{eff}^f = \sum_{\alpha,i;\beta,k} J_{\alpha,i;\beta,k}^{d-f} \langle S_i^\alpha \rangle I_k^\beta$$

$$- \sum_{\alpha,l;\beta,k} [J_{\alpha,k;\gamma,i}^{f-d} K_{\gamma,i;\eta,j}^{d-d} J_{\eta,j;\beta,l}^{d-f}] I_k^\alpha I_l^\beta . \quad (3)$$

Here $\langle S_i^\alpha \rangle$ is the configuration-averaged spin of Cu^{2+} ions, and $K_{\gamma,i;\eta,j}^{d-d} = 1/J(\langle S_i^\gamma S_j^\eta \rangle - \langle S_i^\gamma \rangle \langle S_j^\eta \rangle)$ is the correlation function of Cu^{2+} ion spin fluctuations in the CuO$_2$ layers. The indices α, β, γ, and η relate to the $x, y,$ and z projections of the corresponding moments.

The first sum in Eq. (3) describes magnetization of the RE magnetic moments by the mean field $H_{MF}^d = J_{\alpha,i;\beta,k}^{d-f} \cdot \langle S_i^\alpha \rangle$. For $T \leq T_N$, $\langle S_i^\alpha \rangle \neq 0$ and $H_{MF}^d \neq 0$ only in the case where 3D uniform long-range magnetic order persists in the Cu subsystem of the crystal. If there is an RF state in the $3d$ subsystem, these quantities are zero, which leaves only the second term in Hamiltonian (3).

The second term in (3) describes effective $4f-4f$ exchange interaction through spin fluctuations having large correlation lengths (1) in the CuO_2 layers, i.e. $f-d-f$ exchange. Taking into account the Heisenberg nature of these spin fluctuations, as well as the relative magnitude of the $3d-4f$ exchange coupling constants characteristic of RE magnets ($J_{\alpha,i;\beta,k}^{d-f} \ll J_{\alpha,i;\alpha,k}^{d-f}$), we can present the $f-d-f$ exchange interaction in the form[14]

$$\mathcal{H}_{\text{eff}}^f = -\sum_{\alpha;kl} (J_{\alpha,i;\alpha,k}^{d-f})^2 K_{\alpha,i;\alpha,j}^{d-d} I_k^\alpha I_l^\alpha = \sum_{\alpha;kl} A_{\alpha,k;\alpha,l}^{f-f} I_k^\alpha I_l^\alpha . \tag{4}$$

As a result, RE ions can become ordered through $f-d-f$ exchange with the corresponding ordering temperature. This process will give rise to a mean moment $\langle I_k^\alpha \rangle \neq 0$ and an effective anisotropy field due to the $4f$ subsystem, which acts upon the Cu^{2+} ions

$$H_{\alpha,i}^A = J_{\alpha,i;\alpha,k}^{d-f} \langle I_k^\alpha \rangle . \tag{5}$$

Because summation in Eq. (4) is done over all lattice sites, $A_{\alpha,k;\alpha,l}^{f-f}$ is a long-range interaction (the correlation length $\xi \gg a$). Note that the $A_{\alpha,k;\alpha,l}^{f-f}$ interaction is enhanced by its being long range, so that the RE ion ordering temperature due to $f-d-f$ exchange may exceed substantially that due to direct $f-f$ exchange. The $A_{\alpha,k;\alpha,l}^{f-f}$ interaction reverses its sign with a period of the lattice constant (because of the antiferromagnetic nature of the spin fluctuations). We have thus a complete analogy with the situation considered in Ref. 6, and $H_{MF}^f = A_{\alpha,k;\alpha,l}^{f-f} \cdot \langle I_k^\alpha \rangle$ is a random field. It can be added that as a result of $f-d-f$ exchange the $4f$ ion ordering can be either RF or glass type, and the associated phase transition will be diffuse. Obviously enough, the anisotropy caused by the $H_{\alpha,i}^A$ field is likewise random.

However if there is 3D uniform long-range antiferromagnetic order in the $3d$ subsystem, the RE ion state will be determined both by the molecular magnetization field H_{MF}^d and by the $f-d-f$ exchange interaction. In this case $f-d-f$ exchange for $T < T_N$ will be realized through spin waves in the $3d$ subsystem. In this case, the correlator $K_{\alpha,i;\alpha,j}^{d-d} = -1/J$, and $A_{\alpha,k;\alpha,l}^{f-f} = (J_{\alpha,i;\alpha,k}^{d-f})^2/J$. The $4f$ ion ordering through $f-d-f$ exchange turns out to be ferromagnetic. Note, however, that the magnetization field $H_{MF}^d \propto \langle S_i^\alpha \rangle$ gives rise to antiferromagnetic correlations among the RE ion moments. As a result, if the $f-d-f$ exchange contribution is not negligible compared to the magnetization field, the conditions in a uniformly ordered $3d$ subsystem will also be favorable for the onset of the RF state for RE ions and, hence, for development of random anisotropy in the $3d$ subsystem.

Thus taking into account $f-d-f$ effective exchange coupling in R_2CuO_4 crystals both with uniform $3D$ antiferromagnetic ordering (Gd_2CuO_4) for $T < T_N$, and with a quasi-2D RF state [for instance $(Eu,Pr)_2CuO_4$] can give rise to random anisotropy in the $3d$ subsystem, which will be due to the influence of the $4f$ ions. This is what makes a qualitative difference between the anisotropy mechanisms considered in Ref. 11 and in the present work.

2. ANISOTROPY CAUSED BY ORBIT-ORBIT COUPLING THROUGH 2D HEISENBERG ANTIFERROMAGNETIC SPIN FLUCTUATIONS

We write the interaction Hamiltonian for R_2CuO_4 crystals by adding to Hamiltonian (2) the spin-orbit coupling for the Cu^{2+} ions

$$\mathcal{H}_1 = \mathcal{H} + \sum_i \lambda S_i^z \sigma_i^z . \tag{6}$$

Here $\mathcal{H}$ is Hamiltonian (2), λ is the spin-orbit coupling constant for Cu^{2+} ions, and σ_i^z is the projection of the Cu^{2+} orbital momentum (L) on the ground tetragonal doublet (i.e. one assumes the orbital ground state of the Cu^{2+} ion to be a d_{xz}, d_{yz} tetragonal doublet, or an admixture of such a doublet to the orbital ground singlet).

In our case, $J_{ij}^{d-d} \gg J_{\alpha,i;\beta,k}^{d-f}$ and $J_{ij}^{d-d} > \lambda$. We assume J^{d-f} and λ to be of the same order of magnitude. To understand the significance of the Cu-R anisotropic and spin-orbit interactions, consider them separately in addition to the main 2D Heisenberg antiferromagnetic exchange among the Cu^{2+} ion spins. The Cu-R interaction has been considered in the preceding Section. The orbit-orbit coupling through the 2D Heisenberg antiferromagnetic spin fluctuations was analyzed in Refs. 6 and 7 for the Eu_2CuO_4 crystal. This interaction is essentially an analog of the $f-d-f$ exchange, in which in place of the RE ion moment one considers the orbital momentum of Cu^{2+} ions in the CuO_2 layers.

The effective Hamiltonian describing the orbital subsystem can be written (see Ref. 6)

$$\mathcal{H}_{\text{eff}}^\sigma = \sum_i \lambda \langle S_i^x \rangle \sigma_i^z - \sum_{ij} (\lambda)^2 K_{ij}^{zz} \sigma_i^z \sigma_j^z . \tag{7}$$

Here K_{ij}^{zz} is the correlation function of the 2D spin fluctuations in the CuO_2 layers. In the case of interest to us here (the quasi-2D RF state), there remains in (7) only the second term, which describes the effective orbit-orbit interaction through 2D antiferromagnetic spin fluctuations, i.e. $V_{ij}^{zz} = \lambda^2 K_{ij}^{zz}$. As pointed out in Ref. 6, the V_{ij}^{zz} interaction is long range and alternating at each lattice constant, and it is responsible for the onset of the orbit glass state.

Thus taking into account the V_{ij}^{zz} interaction in the R_2CuO_4 tetragonal crystals results in a random uniaxial anisotropy

$$H_{A,i}^z = \lambda \langle \sigma_i^z \rangle , \tag{8}$$

where $\langle \sigma_i^z \rangle$ is the frozen-in local orbital momentum.

3. ANALYSIS OF RANDOM ANISOTROPY MECHANISMS IN R_2CuO_4 CRYSTALS

An analysis of the anisotropy mechanisms carried out in Sections 1 and 2 permits the following conclusions:

1. Taking into account the $f-d-f$ exchange interaction can give rise to random anisotropy in R_2CuO_4 crystals both with uniform quasi-2D long-range magnetic order for $T < T_N$ and with a quasi-2D RF state. It is necessary that there be magnetic RE ions, and that the $f-d-f$ exchange coupling is not negligible compared to the interactions re-

sulting in uniform anisotropy. The f–d–f exchange coupling may be significant in both tetragonal crystals and in crystals with rhombic distortions.

2. Taking into account effective orbit-orbit interaction through 2D spin fluctuations gives rise to random uniaxial anisotropy along the c axis in the R_2CuO_4 tetragonal crystals having a tetragonal doublet for the orbital ground state (or a strong enough admixture of an excited tetragonal doublet to the orbital ground singlet).

Let us estimate now the magnitude of random anisotropy based on experimental data obtained for the R_2CuO_4 crystals (R=Eu, Pr, Gd). To estimate the anisotropy fields $H_{\alpha,i}^A$ (5), consider the temperature dependences of the static magnetic susceptibility for these crystals. Figure 1 presents the susceptibilities for the crystallographic directions in which they are maximal[17,20,21]. Note that the susceptibilities for all three crystals exceed $\chi_\perp \sim 10^{-3}-10^{-4}$ emu/mole, the susceptibility for La_2CuO_4,[22] whose only magnetic system is formed by Cu^{2+} ions in the CuO_2 layers. Assuming the properties of the CuO_2 layers to be similar for all these crystals, we come to a conclusion that one measures actually the susceptibility of the RE subsystem in crystals with RE magnetic ions. In these conditions, $\langle I_k^\alpha \rangle \propto \chi$. By analogy with the situation in other magnetic crystals with RE ions,[13,14] we shall assume the d–f exchange coupling constants for R_2CuO_4 crystals with different RE ions to be close in magnitude. Then for the effective anisotropy fields we obtain $H_{\alpha,i}^A \propto \chi$ too. As seen from Fig. 1, $\chi_{ab}^{Gd} \gg \chi_{ab}^{Pr} \sim \chi_c^{Eu}$, which yields for the relative magnitude of the anisotropy fields $H_{\alpha,i}^A(Gd) \gg H_{\alpha,i}^A(Eu) \simeq H_{\alpha,i}^A(Pr)$.

Estimation of the anisotropy field $H_{A,i}^z$ (8) for Eu_2CuO_4, which is generated by orbit-orbit coupling among the Cu^{2+} ions through spin fluctuations in the CuO_2 layers, yielded $T_a \simeq 250$ K for the effective anisotropy temperature.[4,5] We shall assume that, in all R_2CuO_4 tetragonal crystals which have the same nearest-neighbor environment around Cu^{2+} ions in the lattice and, hence, orbital ground states of the same kind, the constants of orbit-orbit coupling through spin fluctuations are close in magnitude. Indeed, studies of microwave-range spin dynamics in Pr_2CuO_4 showed[5] that the situation in this crystal is similar to that observed in Eu_2CuO_4, and that the uniaxial anisotropy fields $H_{A,i}^z$ in these crystals are close in magnitude.

The random anisotropy field $H_{A,i}^z$ does not depend on temperature for $T \ll 2\pi\rho_s \sim 1500$ K. At the same time the anisotropy field $H_{\alpha,i}^z$ due to f–d–f exchange is essentially temperature dependent, because it is determined by the average RE moment and can play a significant role only at comparatively low temperatures. As a result, a change in temperature can induce in R_2CuO_4 crystals phase transitions originating from switching of the mechanism of dominant anisotropy. Such phase transitions may bring about a change in both magnetic and structural properties of a crystal. Indeed, orbit-orbit interaction through spin fluctuations produces structural lattice distortions as well.[6,7]

We shall assume the structural and magnetic phase transformation in Eu_2CuO_4 occurring at $T \sim 150$ K to be a phase transition in which an anisotropy mechanism switching takes place, namely, for $T \gtrsim 150$ K the dominant anisotropy field is

$H_{A,i}^z$, and for $T < 150$ K it is $H_{\alpha,i}^A$. At $T \simeq 150$ K, these fields become equal in magnitude $[H_{\alpha,i}^A(T=150 \text{ K}) \simeq H_{A,i}^z]$.

R_2CuO_4 crystals (R=Eu, Pr, Gd) revealed[4,5] a reversal of the real part of dynamic magnetic susceptibility along the c axis $[Re(\chi_c)]$ in sign at temperatures $T \simeq T^*$ ($T^*=90$ K for Pr, 120 K for Eu, and 290 K for Gd). This reversal of the sign of $Re(\chi_c)$ is caused by a change in the nature of magnetic anisotropy at the corresponding temperatures.[4,5] Assuming the change in anisotropy to be initiated by the above switching from the effective field $H_{\alpha,i}^A$ (for $T \lesssim T^*$) to $-H_{A,i}^z$ (for $T \gtrsim T^*$), the static magnetic susceptibilities at $T=T^*$ should be close in magnitude for all the three crystals. An inspection of Fig. 1 shows that indeed $\chi_{ab}^{Gd}(T=290 \text{ K}) \simeq \chi_{ab}^{Pr}(T=90 \text{ K}) \simeq \chi_c^{Eu}(T=120 \text{ K})$.

Thus we have shown that R_2CuO_4 crystals exhibit random anisotropy mechanisms initiated by f–d–f exchange and orbit-orbit interaction through spin excitations. Competition between these anisotropy mechanisms may give rise to phase transitions in which the nature of the magnetic anisotropy and of local structural distortions undergo changes.

[1] H. K. von Müller-Buschbaum and W. Wollschläger, Z. Anorg. Allg. Chem. **414**, 76 (1975).

[2] M. Braden, W. Paulus, A. Cousson, P. Vigoureux, G. Heger, A. Goukassov, P. Bourges, and D. Petitgrand, Europhys. Lett. **25**, 625 (1994).

[3] T. Chattopadhyay, J. W. Lynn, N. Rosov, T. E. Grigereit, S. N. Barilo, and D. I. Zhigunov, Phys. Rev. B **49**, 9944 (1994).

[4] E. I. Golovenchits, S. L. Ginzburg, V. A. Sanina, and A. V. Babinskiĭ, Zh. Éksp. Teor. Fiz. **107**, 1641 (1995) [JETP **80**, 915 (1995)].

[5] E. I. Golovenchits and V. A. Sanina, Fiz. Tverd. Tela (St. Petersburg), in press.

[6] A. V. Babinskiĭ, S. L. Ginzburg, E. I. Golovenchits, and V. A. Sanina, JETP Lett. **57**, 289 (1993).

[7] E. I. Golovenchits, V. A. Sanina, and A. V. Babinskiĭ, Zh. Éksp. Teor. Fiz. **110**, 714 (1996) [JETP **83**, 386 (1996)].

[8] S. Chakravarty, B. I. Halperin, and D. R. Nelson, Phys. Rev. B **39**, 2344 (1989).

[9] Y. Endoh, K. Yamada, R. J. Birgenau, D. R. Gabbe, H. P. Jenssen, M. A. Kastner, C. J. Peters, P. J. Picone, T. R. Thurston, J. M. Tranquada, G. Shirane, Y. Hidaka, M. Oda, Y. Enomoto, M. Suzuki, and T. Murakami, Phys. Rev. B **37**, 7443 (1988); K. Yamada, K. Kakurai, Y. Endoh, T. R. Thurston, M. A. Kastner, R. J. Birgenau, G. Shirane, Y. Hidaka, and T. Murakami, *ibid.*, **40**, 4557 (1989).

[10] T. Yildirim, A. B. Harris, A. Aharony, and O. Entin-Wohlman, Phys. Rev. B **52**, 10239 (1995).

[11] R. Sachidanandam, T. Yildirim, A. B. Harris, A. Aharony, and O. Entin-Wohlman, Phys. Rev. B **56**, 260 (1997).

[12] D. Petitgrand, S. V. Maleev, Ph. Bourges, and A. Ivanov, Phys. Rev. B (to be published).

[13] A. K. Zvezdin, V. M. Matveev, A. A. Mukhin, and A. I. Popov, *Rare-Earth Ions in Magnetically Ordered Crystals* [in Russian] (Nauka, Moscow, 1985).

[14] E. I. Golovenchits and V. A. Sanina, Fiz. Tverd. Tela (Leningrad) **26**, 1640 (1984) [Sov. Phys. Solid State **26**, 996 (1984)].

[15] E. I. Golovenchits, B. D. Laĭkhtman, and V. A. Sanina, JETP Lett. **31**, 223 (1980).

[16] E. F. Shender, Zh. Éksp. Teor. Fiz. **83**, 326 (1982) [Sov. Phys. JETP **56**, 178 (1982)].

[17] J. D. Thompson, S.-W. Cheong, S. E. Brown, Z. Fisk, S. B. Oseroff, M. Tovar, D. C. Vier, and S. Schultz, Phys. Rev. B **39**, 6660 (1989).

[18] S. B. Oseroff, D. Rao, F. Wright, M. Tovar, D. C. Vier, S. Shultz, J. D. Thompson, Z. Fisk, and S.-W. Cheong, Solid State Commun. **70**, 1159 (1989).

[19] E. I. Golovenchits, V. A. Sanina, A. A. Levin, Yu. I. Smolin, and Yu. F. Shepelev, Fiz. Tverd. Tela (St. Petersburg) **39**, 1600 (1997) [Phys. Solid State **39**, 1425 (1997)].

[20] A. V. Babinskiĭ, E. I. Golovenchits, N. V. Morozov, V. A. Sanina, and L. M. Sapozhnikova, Fiz. Tverd. Tela (St. Petersburg) **34**, 60 (1992) [Phys. Solid State **34**, 31 (1992)].

[21] P. Allenspach, S.-W. Cheong, A. Dommann, P. Fisher, Z. Fisk, A. Furrer, H. R. Ott, and B. Rupp, Z. Phys. B **77**, 185 (1989).

[22] T. Thio, T. R. Thurston, N. W. Preyer, P. J. Picone, M. A. Kastner, H. P. Jenssen, D. R. Gabbe, C. Y. Chen, R. J. Birgenau, and A. Aharony, Phys. Rev. B **38**, 905 (1988); T. Thio, C. Y. Chen, B. S. Freer, D. R. Gabbe, H. P. Jenssen, M. A. Kastner, P. J. Picone, N. W. Preyer, and R. J. Birgenau, *ibid.*, **41**, 231 (1990).

Translated by G. Skrebtsov

Tunneling of magnetic domain walls in the quasirelativistic limit

V. V. Makhro

Bratsk Industrial Institute 665728 Bratsk, Russia
(Submitted November 24, 1998)
Fiz. Tverd. Tela (St. Petersburg) **41**, 1264–1266 (July 1999)

An additional mechanism which increases the probability of tunneling of magnetic domain walls through defects of a crystal is discussed. In contrast to the thermally stimulated tunneling mechanisms described previously (c.f. Refs. 7 and 8), which arise when the wall acquires additional energy from the thermal system of the crystal, the latter mechanism is produced by the change in the structure of the walls themselves at high energies, which changes the character of their interaction with defects. The results of analytic and numerical analyses of this effect are reported. A discussion and an interpretation of existing experimental results.[3]   © *1999 American Institute of Physics.* [S1063-7834(99)02807-5]

Tunneling of magnetic domain walls has been attracting intense interest in recent years as one of a few examples of macroscopic quantum effects. Existing experimental results[1–3] show quite definitely that the depinning of walls at liquid-helium temperatures (1–10 K) has a tunneling character. Such experimental observations have been indirect thus far. For example, the electrical resistance, internal friction, magnetic viscosity, and so on are used as indicators of depinning. An indicator of a change in the type of depinning from thermal-activational to tunneling is saturation of the temperature dependences of these parameters in the low-temperature range. In the theory of the tunneling of magnetic domain walls, a model where the tunneling section of a wall is represented as a quasiparticle with effective mass m is ordinarily used.[4–6] It is assumed that such a quasiparticle is localized in a metastable minimum in front of a potential barrier of height U_0 formed by magnetic defects of the crystal. Therefore the problem of tunneling depinning of a wall reduces to calculating the probability of tunneling of a quasiparticle through a potential barrier.

Unfortunately, at present there are definite difficulties with the agreement between theory and experiment. The experimentally determined parameters of the problem (the quasiparticle mass and the barrier height and width) give vanishingly small computed values of the tunneling probability: the walls are found to be too ''heavy'' and the barriers too wide. In this connection, it is important to discuss the physical mechanisms capable of increasing barrier transmittance. Various interaction processes between walls and the system of thermal excitations of the crystal, as recently decribed in, for example, Refs. 7 and 8, can be considered as such mechanisms.

The present paper calls attention to a different effect which also increases the tunneling probability and, as will be shown below, to a degree sufficient for describing the experimental data adequately. The point is that, in many cases (c.f., Ref. 3) the dynamic characteristics of walls may fall into in the quasirelativistic range (in Walker's sense[9]). Then the basic parameters of the problem become functions of the wall energy: As the energy increases, the barrier height decreases,

the width decreases, and the quasiparticle mass increases. In what follows, I shall discuss how these changes affect the tunneling probability.

1. MODEL AND BASIC PARAMETERS

Confining attention to a specific experimental situation where, in our opinion, quasirelativistic effects could be important, though it is not ruled out that similar effects can also occur in other situations. We shall consider the results of Ref. 3. There the conductivity of a superthin, approximately 4×10^{-6} cm in diameter, nickel wire was investigated as an indicator of wall depinning. It was found that the width of the starting-field distributions saturates in the temperature range from 10 to 4 K. In Ref. 3, this circumstance was interpreted as tunneling-type depinning predominating in this temperature range. According to the data in Ref. 3, the width Δ of the domain walls was about 10^{-5} cm, and the width a of the potential barrier was of the same order of magnitude. Taking the standard value 1×10^{-6} ergs/cm for the exchange constant A and the indicated value of Δ I obtain for the anisotropy constant $K = 5 \times 10^{-3}$ ergs/cm³. The area of the tunneling section can be estimated from the data in Fig. 3 from Ref. 3 as

$$S \approx \frac{k(T_2 - T_1)}{2M_0(H_{r2} - H_{r1})a},$$

where H_{r2} and H_{r1} are the right-hand limits of the starting-field distributions at temperatures T_2 and T_1, respectively. This gives for S a value of the order of 10^{-14} cm². The surface energy density of a Bloch wall is $\sigma = 2\sqrt{AK}$, and its Doring mass is given by the expression $m_D = \sigma/(8\pi A\gamma^2)$, where γ is the gyromagnetic ratio. For the materials under discussion the Doring mass is $m_D = 1.7 \times 10^{-11}$ g/cm², while the effective mass of the tunneling section is $m = m_D S \sim 10^{-25}$ g. Using the same figure from Ref. 3, the ''pure'' starting field can be estimated as $H_c = 290$ Oe, which gives for the barrier height $U_0 S = 4M_0 H_c a S = 1.5 \times 10^{-14}$ ergs, whereas the observed value of H_c is about 220 Oe (the quasiparticle energy is $E = 1.1 \times 10^{-14}$ ergs). It is easy to see that

for such values of the parameters the transmittance is indeed vanishingly small: in any case it does not exceed 10^{-70}. However, I call attention to the fact that here all parameters are for a static domain wall. This is admissable if $E \ll m v_w^2$, where v_w is the limiting Walker velocity. Its value is given in Ref. 9 as

$$v_w = \left(\sqrt{1 + \frac{2\pi M_0^2}{K}} - 1 \right) \frac{2\gamma \sqrt{AK}}{M_0}$$

and in the present case it is 9.2×10^4 cm/s, while $m v_w^2 = 8.5 \times 10^{-16}$ erg. Therefore it is obvious that the quasirelativistic technique must be used in Ref. 3 to analyze the tunneling.

2. THEORY AND CALCULATIONS

I am considering a Bloch-type domain wall in a ferromagnetic wire with the easy axis oriented along the wire axis. In accordance with Walker's exact calculation for a free boundary, the Lagrangian surface densityin this case will be[10]

$$\Lambda_0 = 4\sqrt{AK} \sqrt{1 + \frac{2\pi M_0^2}{K} \sin^2(\chi_0(v))},$$

where χ_0 is the optimal angle of inclination of the magnetization rotation axis from the normal to the surface of the wall and v is the wall velocity. We describe the wall–defect interaction by a potential function $U(v)$. Then the Lagrangian density can be represented as

$$\Lambda(v) = \Lambda_0(v) - U(v). \tag{1}$$

The Hamiltonian corresponding to the Lagrangian (1) has, in terms of the coordinate of the center of the wall, the quasirelativistic form

$$H(p,x) = v_w \sqrt{p^2 + m^2 v_w^2} + U(p,x), \tag{2}$$

where $p = m v / \sqrt{1 - v^2/v_w^2}$ is the canonical momentum.

Following Ref. 3, we assume that the defect is point-like. In the static case the form of $U(x)$ is determined by the exact Landau–Lifshitz solution[11]

$$\sin(\theta) = \tanh(x/\sqrt{AK}).$$

From the assumption that the wall–defect interaction is strictly local follows that the energy of a defect is proportional to $\cos^2 \theta$, so that $U(x)$ can be expressed as

$$U(x) = \frac{U_0}{\cosh^2(x/a)}, \tag{3}$$

where U_0 is the barrier height and a is the effective wall–defect interaction radius ("width"of the barrier). We note that a is essentially identical to the wall width Δ.

In Walker's dynamical solution Δ and therefore a become functions of the velocity of the wall, and U in Eq. (3) becomes

$$U(x) = \frac{U_0}{\cosh^2(x/a\sqrt{1 - v/v_w^2})}, \tag{4}$$

while the Hamiltonian (2) can be rewritten as

$$H(p,x) = v_w \sqrt{p^2 + m^2 v_w^2}$$
$$+ \frac{U_0}{\cosh^2(x\sqrt{p^2 + m^2 v_w^2}/am v_w)}, \tag{5}$$

where U_0 is determined from the observed coercive force H_c as

$$U_0 = \frac{2 M_0 H_c am v_w}{\sqrt{p^2 + m^2 v_w^2}}. \tag{6}$$

We shall assume for definiteness that the wall in front and behind a barrier is in shallow metastable minima. Then, in the present problem the well-known approach developed for the problem of the decay of a metastable vacuum can be used.[12] The energy of the decaying vacuum has an imaginary part which is proportional to the tunneling rate.[13] The transition amplitude in imaginary time $\tau = -it$ from a state x into a state y is given by a Wiener functional integral

$$\rho(x,y) = \int_{(q=x)}^{(q=y)} Dy \int_{(-\infty)}^{(+\infty)} \frac{Dq}{2\pi\hbar}$$
$$\times \exp\left[\frac{1}{\hbar} \int_0^T d\tau(ipq - H(p,q)) \right]. \tag{7}$$

A method for calculating $\rho(x,y)$ for Hamiltonians which are not quadratic in the momentum is proposed in Ref. 6. However, the WKB approximation is used substantially in this method. This approximation is admissable for low barriers if $U_0 \ll m v_w^2$. In the present problem, on the other hand, $U_0 \sim m v_w^2$, so that ρ was calculated by direct numerical integration.

Motion in imaginary time τ in the potential $U(x)$ is equivalent to motion in real time in the reverse potential $-U(x)$. Let x_1 and x_2 be classical turning points for the reverse potential. The energy of the ground state is found from the amplitude $\rho(x,y)$ at $x = y = x_1$ and $T \to \infty$ on the classical trajectories $q \equiv x_1$ and $q \equiv x_{\text{inst}}$. The so-called instanton trajectory x_{inst} starts at the point x_1 as $\tau \to -\infty$, passes through x_2 at $\tau = 0$, and returns to x_1 as $\tau \to \infty$. The tunneling probability Γ is given by the ratio of the integral (7) on the trajectories $q \equiv x_1$ and $q \equiv x_{\text{inst}}$.

Figure 1 shows the computational results for the tunneling probability Γ as a function of the energy W for wall for parameters corresponding to the experiment of Ref. 3. The values obtained are acceptable for an adequate interpretation of the experiment, and in this sense the quasirelativistic analysis is fully self-consistent.

3. DISCUSSION AND CONCLUSIONS

The results obtained have a quite obvious physical meaning: As the wall energy increases, the wall width decreases and the effective mass increases, the first effect predominating. The decrease of the wall width decreases its range of interaction with a defect and decreases the width of the potential barrier, which increases the transmittance of the barrier. We also call attention to the reevaluation of the barrier height according to the magnitude of the coercive force H_c. In accordance with Eq. (6), U_0 is now a function of the
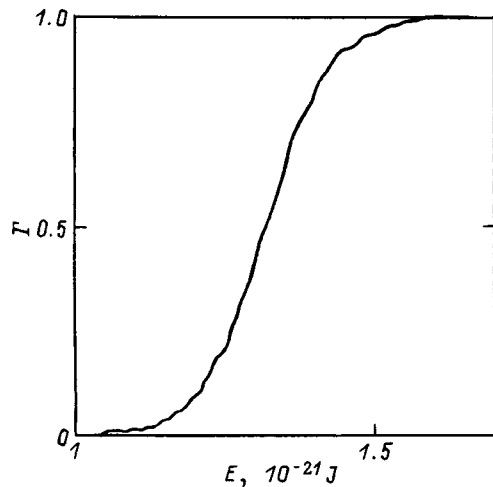
FIG. 1. Barrier transmittance Γ for a point defect as a function of the wall energy E.

momentum (or the total energy) of the particle. For the same value of H_c the barrier height calculated by the quasirelativistic method it is lower than the corresponding height calculated in the classical approximation. Indeed, in the classical approximation U_0 is $U_0 = 4M_0 H_c a$, whereas in the quasirelativistic approximation U_0 is given by

$$U_0 = v_w \sqrt{2M_0 H_c a m}.$$

Ultimately, both factors — narrowing and lowering of the barrier — make the barrier quite transparent, i.e., they make the tunneling probability appreciable.

We now briefly summarize the results. The results of the experimental study of low-temperature relaxation processes demonstrate that depinning of domain walls has a tunneling character. At the same time, theoretical calculations of the corresponding amplitudes of the processes give in most known cases vanishingly small values, which can be interpreted as impossibility of tunneling. It was shown in this paper that this contradiction can be resolved by taking account of the quasirelativistic character of the wall dynamics. A method for calculating the tunneling probability of a wall through a potential barrier in the quasirelativistic limit was proposed and implemented. The application of this method for analyzing a real experimental situation[3] gave satisfactory results: Acceptable values were obtained for the probability of tunneling of a wall, while calculations performed by the conventional method essentially rule out the possibility of tunneling for this situation.

[1] B. Barbara, L. Sampaio, J. Wegrove *et al.*, J. Appl. Phys. **73**, 6703 (1993).
[2] J. Tejada, X. X. Zhang, and L. Balcells, J. Appl. Phys. **73**, 6709 (1993).
[3] Kiming Hong and N. Giordano, J. Phys.: Condens. Matter **8**, L301 (1996).
[4] P. C. E. Stamp, E. M. Cudnovski, and B. Barbara, Int. J. Mod. Phys. B **6**, 1355 (1992).
[5] T. Egami, Phys. Status Solidi B **57**, 211 (1973).
[6] V. V. Dobrovitskiĭ and A. K. Zvezdin, Zh. Éksp. Teor. Fiz. **109**, 1420 (1996) [JETP **82**, 766 (1996)].
[7] V. V. Makhro, Fiz. Tverd. Tela (St. Petersburg) **40**, 1855 (1998) [Phys. Solid State **40**, 1681 (1998)].
[8] V. V. Makhro, J. Phys.: Condens. Matter **10**, 6911 (1998).
[9] L. R. Walker, unpublished (1953); see J. F. Dillon, in *Magnetism*, Vol. 3, edited by G. Rado and H. Suhl (Academic Press, N. Y., 1963).
[10] A. Hubert, *Theorie der Domanenwande in Geordneten Medien* (Springer-Verlag, Berlin, 1974) [Russian translation, Mir, Moscow, 1977].
[11] L. D. Landau and E. M. Lifshitz, Phys. Z. Sowjetunion **8**, 153 (1935).
[12] C. Callan and S. Coleman, Phys. Rev. D **16**, 1762 (1977).
[13] J. S. Langer, Ann. Phys. (N.Y.) **41**, 108 (1967).

Translated by M. E. Alferieff

Weak ferromagnetism in copper metaborate CuB$_2$O$_4$

G. A. Petrakovskiĭ, K. A. Sablina, D. A. Velikanov, A. M. Vorotynov, N. V. Volkov, and
A. F. Bovina

*L. V. Kirenskiĭ Institute of Physics, Siberian Branch of the Russian Academy of Sciences,
660036 Krasnoyarsk, Russia*
(Submitted November 30, 1998)
Fiz. Tverd. Tela (St. Petersburg) **41**, 1267–1271 (July 1999)

CuB$_2$O$_4$ single crystals have been grown and their magnetic and resonance properties have been investigated for the first time. The temperature dependence of the susceptibility was found to contain features at $T = 21$ and 10 K. The CuB$_2$O$_4$ single crystal transformed at $T = 21$ K to a weakly ferromagnetic state. The sharp drop in susceptibility at $T < 10$ K is caused by a transition of the magnetic system of CuB$_2$O$_4$ to an antiferromagnetic state. The effective magnetic moment of the Cu^{2+} ion, determined from the high-temperature part of the magnetic susceptibility, is $1.77\mu_B$. The room-temperature g factors are, respectively, 2.170 and 2.133 for magnetic field parallel and perpendicular to the c axis of the crystal. The antiferromagnetic resonance parameters in the weakly ferromagnetic and antiferromagnetic phases were measured. © *1999 American Institute of Physics.* [S1063-7834(99)02907-X]

Copper oxide compounds are attracting attention due to their unusual low-temperature magnetic properties. Chain, planar, and ladder magnetic structures with nonmagnetic singlet and antiferromagnetic ground states are found in these compounds.[1–3] Since divalent copper ions possess spin $S = 1/2$, quantum effects play a large role in these compounds at low temperatures.

This paper reports the results of the first investigation of the temperature dependence of the magnetization and electronic magnetic resonance of CuB$_2$O$_4$ single crystals.

1. SYNTHESIS OF THE CRYSTALS

The binary system CuO–B$_2$O$_3$ was first studied in Ref. 4. It was established that this system contains two congruently melting compounds: CuB$_2$O$_4$ and Cu$_3$B$_2$O$_6$. In Ref. 5 these same compounds were observed in an investigation of the phase diagram of melting of the ternary system Li$_2$O–CuO–B$_2$O$_3$. Later,[6,7] phase formation was studied and the regions of glass formation in the ternary systems CuO–PbO–B$_2$O$_3$ and CuO–Bi$_2$O$_3$–B$_2$O$_3$, where the compositions CuB$_2$O$_4$ and Cu$_3$B$_2$O$_6$ were also found, were determined. The crystal structure of CuB$_2$O$_4$ was investigated in Ref. 8. Based on these studies, we searched for a technology for growing CuB$_2$O$_4$ single crystals. The system Li$_2$O–CuO–B$_2$O$_3$ was chosen as the basis.

The components CuO, B$_2$O$_3$, and Li$_2$CO$_3$ in the ratios 25, 60, and 15 mole%, respectively, which were pulverized in a ball mill, were placed after mixing into a 50 cm^3 platinum crucible without premelting. The temperature was raised slowly to 800 °C and then rapidly to 1020 °C where it was held for 2 h. Then the melt was cooled to 800 °C at a rate of 1 deg/h.

The crystals were extracted by washing off the contents of the crucible in a 20% boiling-water solution of nitric acid. The crystals were well-faceted prisms, transparent, and violet-blue in color, and their maximum dimensions were $2 \times 1 \times 1$ cm^3. X-ray analysis of a powder obtained by grinding the crystals confirmed that the parameters of the crystals obtained were close to those found in Ref. 8 for CuB$_2$O$_4$.

2. CRYSTAL STRUCTURE

Copper metaborate, CuB$_2$O$_4$, crystallizes in the tetragonal system with space group $I\bar{4}2d$. The unit cell contains 12 formula units. The cell parameters are $a = 11.484$ Å and $c = 5.620$ Å . The computed density of the crystal is 4.022 g/cm^3. The resistivity at 300 K is 10^9 $\Omega \cdot$cm.[6] It is noted in Ref. 5 that CuB$_2$O$_4$ undergoes a structural phase transition at 1000 °C.

The unit cell contains two nonequivalent copper ion positions: four copper ions Cu(1) are located in a planar square environment of oxygen ions; eight copper ions Cu(2) are located in a distorted octahedron of oxygen ions (Fig. 1).

The characteristic O^2–Cu^{2+} distances for two nonequivalent positions of the copper ions are[8]

$$\text{Cu}^{2+}(1) - \text{O}^{2-}(1) = 1.998 \text{ Å},$$

$$\text{Cu}^{2+}(2) - \text{O}^{2-}(2) = 1.902 \text{ Å},$$

$$\text{Cu}^{2+}(2) - \text{O}^{2-}(3) = 1.886 \text{ Å},$$

$$\text{Cu}^{2+}(2) - \text{O}^{2-}(4) = 1.980 \text{ Å},$$

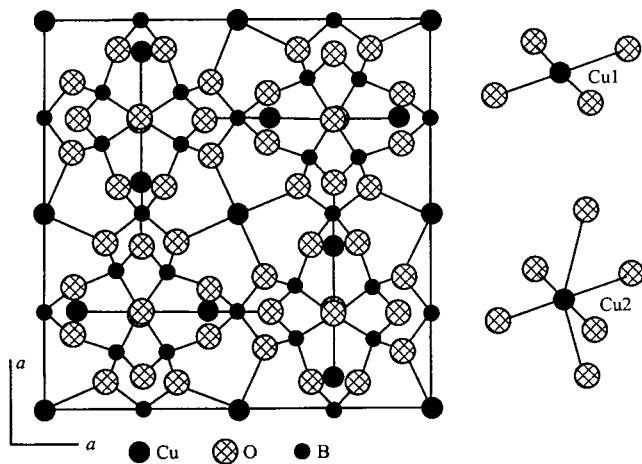$$\text{Cu}^{2+}(2) - \text{O}^{2-}(4') = 1.980 \text{ Å},$$

$$\text{Cu}^{2+}(2) - \text{O}^{2-}(1) = 3.069 \text{ Å}.$$

The Cu^{2+} (2) positions are characterized by the following angles:

$$\text{O}^{2-}(2) - \text{Cu}^{2+}(2) - \text{O}^{2-}(4) = 92.3°,$$

$$\text{O}^{2-}(4) - \text{Cu}^{2+}(2) - \text{O}^{2-}(3) = 87.7°,$$

$$\text{O}^{2-}(3) - \text{Cu}^{2+}(2) - \text{O}^{2-}(4') = 87.7°,$$

FIG. 1. Crystal structure of CuB_2O_4.

$O^{2-}(4') - Cu^{2+}(2) - O^{2-}(2) = 92.3°,$

$O^{2-}(1) - Cu^{2+}(2) - O^{2-}(2) = 73.1°,$

$O^{2-}(1) - Cu^{2+}(2) - O^{2-}(4') = 67.0°.$

3. MAGNETIC SUSCEPTIBILITY

The magnetization of CuB_2O_4 single crystals was measured with a SQUID magnetometer in the temperature 4.2–200 K in magnetic fields of 50 and 330 Oe. The temperature dependence of the magnetic susceptibility for a 50 Oe magnetic field is shown in Fig. 2. The susceptibility is sharply anisotropic: in a magnetic field along the tetragonal c axis of the crystal it increases monotonically with decreasing temperature, while for a field oriented perpendicular to this axis the susceptibility is higher and depends on the temperature nonmonotonically. The paramagnetic Curie temperature and the effective magnetic moment, which are determined from the high-temperature part of the temperature dependence of the reciprocal of the susceptibility, are $\theta = -9.5$ K and 1.77 μ_B for the magnetic field directed along the c axis of the crystal.

At temperatures 21 and 10 K sharp anomalies are observed in the temperature dependence of the susceptibility with the field oriented perpendicular to the c axis. At $T = 21$ K a jump is observed in the temperature dependence of the susceptibility, and as temperature decreases further, the susceptibility increases rapidly. At 10 K the susceptibility decreases abruptly by approximately an order of magnitude. Measurements in a 300 Oe field show qualitatively similar results.

4. ELECTRONIC MAGNETIC RESONANCE

The results of electronic magnetic resonance measurements in the temperature range 80–300 K are displayed in Figs. 3 and 4. The magnetic resonance spectrum is a single Lorentzian line. The angular dependences of the line width and g factor are characteristic for a Cu^{2+} ion in a tetragonal crystal. The linewidth and g factor for magnetic field parallel and perpendicular to the tetragonal axis of the crystal are,
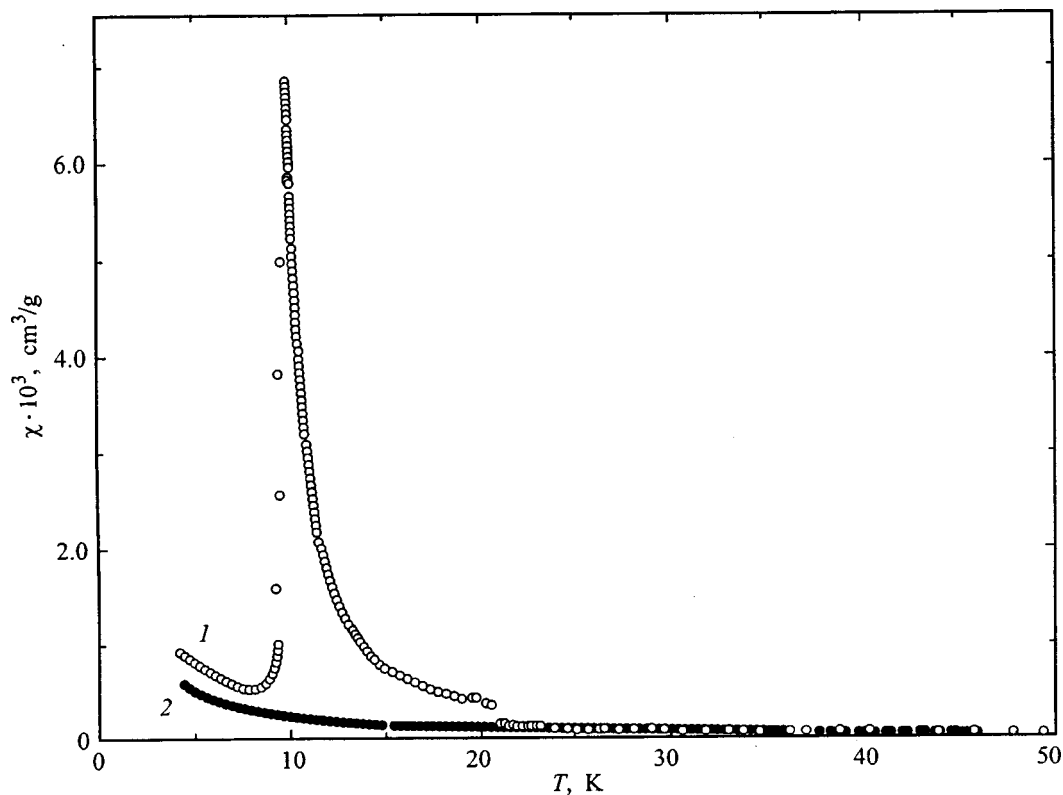
FIG. 2. Temperature dependence of the magnetic susceptibility of a CuB_2O_4 crystal. *1, 2* — Magnetic field H perpendicular and parallel to the c axis of the crystal, respectively.
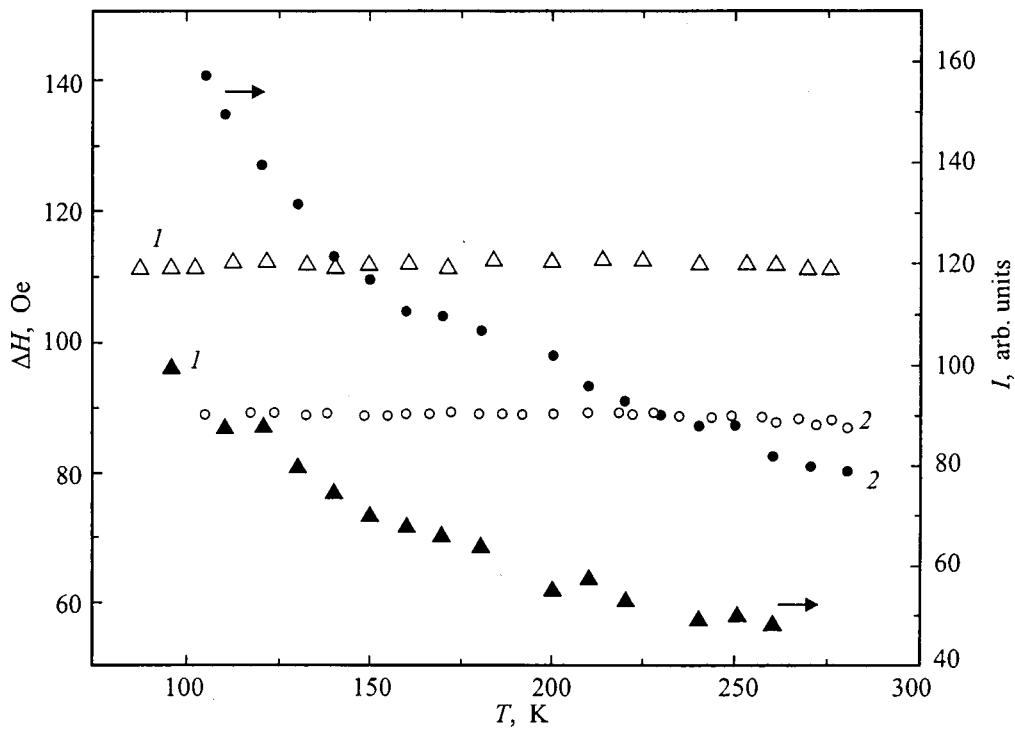
FIG. 3. Temperature dependences of the linewidth and electronic magnetic resonance intensity at frequency $\nu = 9.4$ GHz. *1, 2* — *H* parallel and perpendicular to the *c* axis of the crystal, respectively.

respectively, $\Delta H_{\parallel} = 112$ Oe, $\Delta H_{\perp} = 87$ Oe, $g_{\parallel} = 2.17$, and $g_{\perp} = 2.133$. The single Lorentzian line attests to the existence of an exchange interaction between all copper ions in the crystal.

Anomalies are observed in the magnetic resonance parameters as temperature decreases further. The temperatures of these anomalies correlate with the anomalies in the temperature dependence of the susceptibility (Figs. 5 and 6). The
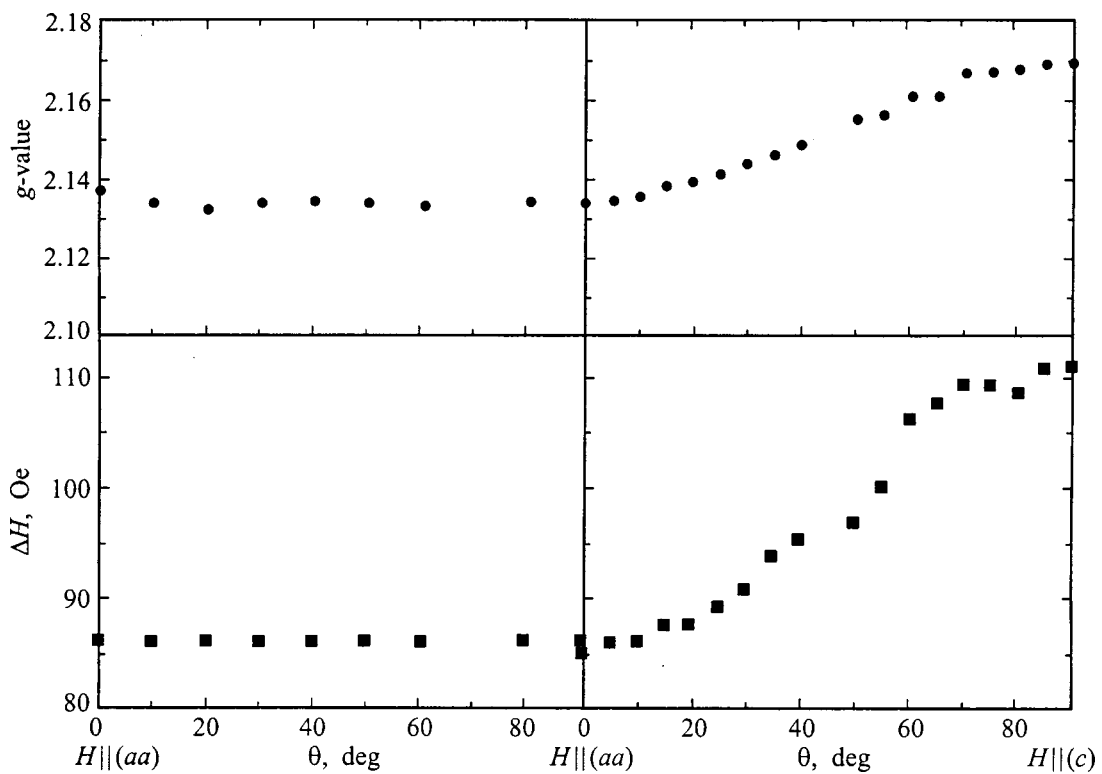
FIG. 4. Angular dependences of the linewidth and *g* factor of the electronic magnetic resonance of a CuB_2O_4 single crystal at room temperature ($\nu = 9.4$ GHz).
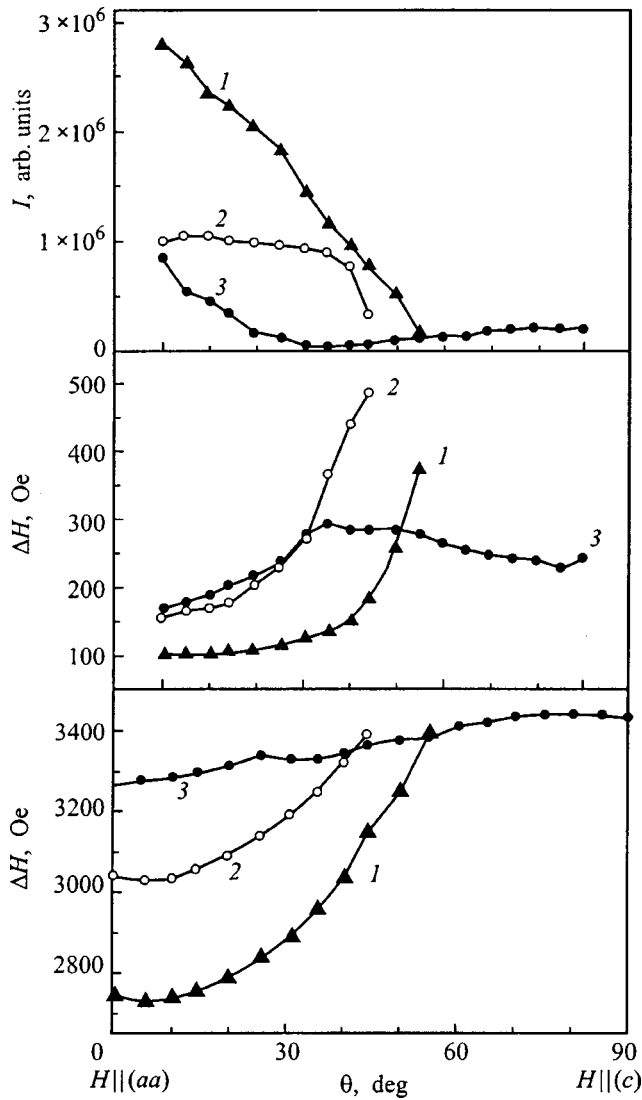
FIG. 5. Angular dependences of the intensity, linewidth, and resonance field of the electronic magnetic resonance signal ($\nu = 10$ GHz) in a CuB_2O_4 single crystal at liquid-helium temperatures T, K: *1* — 10, *2* — 7.5. *3* — 6.
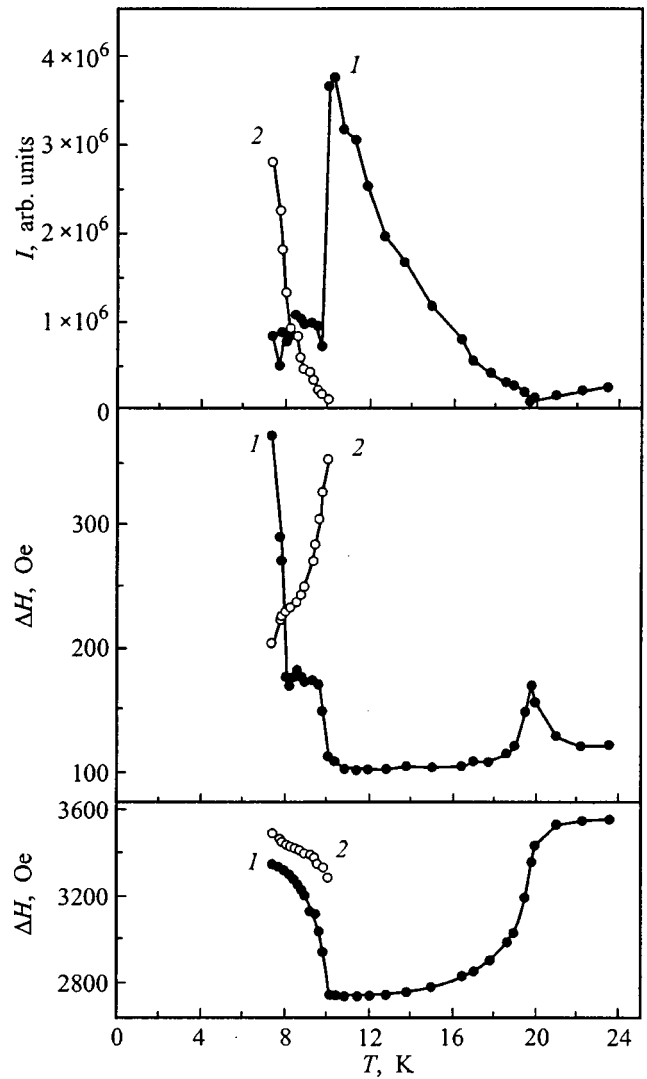
FIG. 6. Temperature dependences of the intensity, linewidth, and resonance field of the electronic magnetic resonance signal ($\nu = 10$ GHz) in a CuB_2O_4 single crystal at liquid-helium temperatures: *1, 2* — H perpendicular and parallel to the c axis, respectively.

resonance field in the tetragonal plane of the crystal decreases gradually from 3560 Oe at $T = 21$ K to 2740 Oe at $T = 10$ K. At temperatures below 10 K, the magnetic resonance signal is observed for any orientation of the magnetic field relative to the crystallographic axes, the resonance field in the plane of the crystal being higher than along the principal axis: $H_r^{\parallel} > H_r^{\perp}$.

5. DISCUSSION

Analysis of the geometry of the arrangement of the Cu^{2+} ions in the CuB_2O_4 crystal lattice shows that an exchange interaction between the nearest neighbors occurs only via the oxgyen and boron ions according to the scheme Cu–O–B–O–Cu. The Cu^{2+} (1) and Cu^{2+} (2) ions have a different number of exchange bonds, so that the parameters of their effective exchange bonds are different. Symmetry analysis of the crystal structure of CuB_2O_4[9] has shown that antiferromagnetic structures admitting the existence of a spontaneous weak ferromagnetic moment in the basal plane

can form in this crystal. The magnetic moments of the Cu^{2+} ions also lie in the basal plane of the crystal. Analysis of the local environment of copper ions based on the Moriya rules[10] suggests the existence of a Dzyaloshinskiĭ–Moriya interaction between the Cu^{2+} ions, which causes canting of the magnetic moments of the sublattices.

In our opinion, at $T = 21$ K a CuB_2O_4 single crystal transforms into a weakly ferromagnetic state. This leads to a strong increase in the magnetization as temperature decreases further.

The magnetic resonance signal in the temperature interval 21–10 K can also be explained by the presence of a weakly ferromagnetic state. The decrease of the resonance field as temperature decreases from 21 to 10 K is apparently caused in this case by an increase in the Dzyaloshinskiĭ field. The angular dependence of the resonance field in a plane containing the tetragonal axis also agrees with this assumption. The Dzyaloshinskiĭ field can be estimated from the temperature dependence of the resonance field as $H_D = 1900$ Oe

at $T = 10$ K. Here the possible existence of a gap in the spectrum of collective excitations and the influence of anisotropy were neglected.

Our data on the magnetization and magnetic resonance allow us to conclude that at a CuB_2O_4 single crystal transforms $T_N = 21$ K from the paramagnetic into a weakly ferromagnetic state. The latter remains as temperature decreases to $T = 10$ K. The sharp drop in the susceptibility at temperature $T_M = 10$ K is due to the transition of the system to an antiferromagnetic state — Morin's transition.

[1] N. Motoyama, H. Eisaki, and S. Uchida, Phys. Rev. Lett. **76**, 3212 (1996).

[2] T. Barnes and J. Riera, Phys. Rev. B **50**, 6817 (1994).

[3] Y. Ueda, J. Phys. Soc. Jpn. **65**, 3142 (1996).

[4] C. E. Weir and R. A. Schroeder, J. Res. Natl. Bur. Stand., Sect. A **68**, 465 (1964).

[5] G. K. Abdullaev, P. F. Rza-Zade, and Kh. S. Mamedov, Zh. Neorg. Khim. **27**, 1837 (1982).

[6] M. I. Zargarova, N. M. Mustafaev, and N. S. Shuster, Izv. Ross. Akad. Nauk, Ser. Neorg. Mater. **32**, 74 (1996).

[7] M. I. Zargarova, N. M. Mustafaev, S. A. Mekhtieva, and N. S. Shuster, Izv. Ross. Akad. Nauk, Ser. Neorg. Mater. **33**, 1235 (1997).

[8] M. Martinez-Ripoll, S. Martinez-Carrera, and S. Garcia-Blanco, Acta Crystallogr., Sect. B: Struct. Crystallogr. Cryst. Chem. **27**, 677 (1971).

[9] E. A. Turov, *The Physical Properties of Magnetically Ordered Crystals* [in Russian] (Nauka, Moscow, 1963).

[10] T. Moriya, Phys. Rev. **120**, 91 (1960).

Translated by M. E. Alferieff

Soliton regimes of surface magnetostatic wave propagation in a magnet–semiconductor structure

A. S. Kindyak

Minsk Scientific-Research Institute of Radio Materials 220024 Minsk, Belorus

V. V. Kindyak

Institute of Solid-State and Semiconductor Physics, Belorussian Academy of Sciences, 220072 Minsk, Belorus

The nonlinear properties of exchange-free surface magnetostatic spin waves in a layered structure containing films of a ferromagnet and a semiconductor are investigated theoretically. The stability of nonlinear surface magnetostatic waves relative to longitudinal disturbances is investigated using the envelope evolution equation in the weak-nonlinearity approximation.
It is shown that, under certain conditions, a surface spin-wave pulse propagates in the form of an envelope soliton. Calculations are performed for the case of an yttrium iron-garnet–indium antimonide structure. © *1999 American Institute of Physics.*
[S1063-7834(99)03007-5]

1. In the last few years the modern ideas of nonlinear wave processes have been actively penetrating the physics of magnetic phenomena. Special attention is being given to magnetostatic spin waves. This is because investigations of spin waves are of interest to both fundamental and applied solid-state physics — due to the possibility of producing new devices employing the nonlinear properties of spin waves and operating in the technologically important microwave range (1–20 GHz).

The nonlinear effects arising during the propagation of a magnetostatic wave (MSW) in a ferromagnetic film have been investigated experimentally and theoretically. It has been shown experimentally that these waves become strongly nonlinear even for low microwave signal excitation powers.[1–7] In turn this leads to a variety of effects: self-modulation, self-focusing of MSWs, instabilities of waves relative to decay into new waves,[1,2] and existence of envelope solitons.[3–7] The instability of surface magnetostatic waves (SMSWs) in thin ferromagnetic films is discussed theoretically in Refs. 8–13. It is shown that these waves are stable with respect to longitudinal disturbances and are unstable with respect to transverse disturbances, which lead to self-focusing. The conditions under which envelope solitons of surface magnetostatic waves have been investigated theoretically in Refs. 10–13.

Primarily, thin ferromagnetic films have been studied in experiments and theoretical investigations, though it is known that multilayer structures provide greater possibilities for controlling the characteristics of MSWs. Examples are ferrite semiconductor structures,[14,15] which make it possible to control the parameters of these waves effectively on account of their interaction with current carriers in the semiconductor layer.[16]

In the present paper the conditions for envelope soliton surface-magnetostatic spin-wave propagation in a planar ferrite-semiconductor structure are investigated theoretically.

2. A necessary condition for the existence of an envelope soliton in a nonlinear dispersive medium was formulated in Ref. 17 and is known as the Lighthill criterion

$$\left(\frac{dk}{d|A|^2}\right)_\omega \left(\frac{d^2k}{d\omega^2}\right)_\omega < 0. \tag{1}$$

The quantity $(d^2k/d\omega^2)$ describes the dispersion of the system and $(dk/d|A|^2)$ describes the change in the wave vector as a function of pulse power. In reality such changes exist for all nonzero values of the pulse amplitude, but they are neglected in the linear regime. For this reason, the first step in investigating a medium for the possibility of soliton formation in it is to check condition (1).

Let an SMSW have a complex amplitude A, and let the second-order nonlinear effects be small. Then the nonlinear dispersion equation can be formally written[9,11,13]

$$f(\omega, k, |A|^2)A = 0. \tag{2}$$

A magnetostatic wave propagates in the form of a pulse with amplitude $A(y,t)$ and envelope along the Y axis. Here t is the time and rapid changes in the wave are described by the function $\exp(i(\omega t - ky))$. Because of dispersion and nonlinearity, the value of the wave vector changes from $k_0 = (0,k_0,0)$ to $k = K + k_0$, where $K = (0,K_y,0)$ and $K_y \ll k_0$, while the frequency changes from ω_0 to $\omega = \omega_0 + \Omega$, where $\Omega \ll \omega_0$. A Taylor series expansion of the dispersion equation neglecting absorption gives[9,11]

$$\left[k - k_0 - \left(\frac{dk}{d\omega}\right)_\omega \Omega - \frac{1}{2}\left(\frac{d^2k}{d\omega^2}\right)_\omega \Omega^2 - \gamma_k|A|^2\right]A = 0, \tag{3}$$

where $\gamma_k = (dk/d|A|^2)_{A=0}$ is the nonlinear coefficient and $(d^2k/d\omega^2)_{\omega_0}$ is the dispersion of the group velocity. Replacing $\omega - \omega_0$ in Eq. (3) by $i(d/dt)$, and K_y by $-i(d/dy)$, we obtain the nonlinear Schrödinger equation

$$i\frac{dA}{dy} + i\left(\frac{dk}{d\omega}\right)_\omega \frac{dA}{dt} - \frac{1}{2}\left(\frac{d^2k}{d\omega^2}\right)_\omega \frac{d^2A}{dt^2} + \gamma_k|A|^2A = 0. \quad (4)$$

The substitutions $T = t - y/v_g$ and $y = y$ transform Eq. (4) into

$$i\frac{dA}{dy} - \frac{1}{2}\beta_2\frac{d^2A}{dt^2} + \gamma_k|A|^2A = 0, \quad (5)$$

where β_2 is the dispersion of the group velocity v_g.

The analytic solution of Eq. (5) has the form

$$A = A_0 \operatorname{sech}\left[\frac{(t-y/v)}{\tau}\right]\exp(i\Delta ky), \quad (6)$$

where $|A_0|^2 = -\beta_2/(\gamma\tau^2)$, $v = v_g$, $\Delta k = -\beta_2\tau^{-2}/2$, Δk is the shift of the wave number, and v is the pulse velocity.

Since the shape, velocity, and evolution length of a soliton are determined by the dispersion law, the dispersion of the group velocity, and the nonlinear coefficient, which in turn are determined by the characteristics of the medium, there is an explicit possibility of controlling the soliton parameters by varying the characteristics of the propagation medium.

3. The starting equations for investigating surface spin waves in a ferrite-semiconductor structure are: for the ferrite layer, Maxwell's equations and the Landau–Lifshitz equation in the magnetostatic approximation, while for a semiconductor layer, Maxwell's equations and the Lorentz equation. On the basis of these equations and the standard boundary conditions, we obtain a dispersion equation of a linear SMSW propagating in a ferrite-semiconductor structure[15]

$$e^{-2kd} = \frac{(\mu^- + k)(\delta\mu^+ + k)\tanh(k_s t) + (\mu^+ + k)\sqrt{\delta}}{(\mu^+ - k)(\delta\mu^- - k)\tanh(k_s t) + (\mu^- - k)\sqrt{\delta}}. \quad (7)$$

Here $\mu^\pm = k(\mu \pm \mu_a)$, $k_s^2 = \delta k^2$, $k = k_1 + ik_2$, and d and t are, respectively, the thickness of the ferrite and semiconductor layers, and μ and μ_a are, respectively, the diagonal and off-diagonal elements of the magnetic susceptibility tensor of the ferrite. The quantity δ determines the nature of the interaction of an SMSW with the semiconductor layer and is given by

$$\delta = 1 - \frac{\omega^2\varepsilon_{zz}}{k^2c^2}. \quad (8)$$

Here $\varepsilon_{zz} = \varepsilon_{zz}^e + \varepsilon_{zz}^h$, $\varepsilon_{zz}^{e(h)}$ is an element of the permittivity tensor of the semiconductor in a magnetic field H

$$\varepsilon_{zz}^e = \varepsilon_s\left(1 - \frac{\omega_p^2}{\omega(\omega - i\nu)}\right), \quad (9)$$

where ε_s is the permittivity of the semiconductor due to the lattice contribution, ν is the electron collision frequency,

$\omega_p = (4\pi e^2N/m^*\varepsilon_s)^{1/2}$ is the plasma frequency, and N is the electron density. For $\delta = 1$ Eq. (7) becomes the Damon–Eshbach equation.[18]

Equation (6) can be put into the form

$$G = AD - BC = 0, \quad (10)$$

where

$$A = \frac{1}{2}[\delta(1+\alpha) + \delta(1-\alpha)],$$

$$D = \omega^2 - \omega_0^2 - \frac{\omega_m^2}{4}(1-\beta), \quad (11)$$

$$B = \frac{1}{4}(\alpha - 1)(\delta - 1),$$

$$C = \omega^2 - \omega_0^2 + \frac{\omega_m}{2}(\omega + \omega_h)(1-\beta), \quad (12)$$

$\delta = \delta^{1/2}$, $\alpha = \exp(-2kt\delta^{1/2})$, $\beta = \exp(-2kd)$, and $\omega_0^2 = w_h^2 + \omega_h\omega_m$. Then the expression for the dispersion β_2 of the group velocity of SMSWs can be determined from the linear dispersion law (10) as

$$\beta_2 = \frac{d^2k}{d\omega^2} = -\frac{1}{G_k^3}(G_{\omega\omega}G_k^2 - 2G_{\omega k}G_\omega G_k + G_{kk}G_\omega^2). \quad (13)$$

In Eq. (13) G_{xy} denote the partial derivatives of the function G with respect to the variables x and y and are too complicated to present here.

Since the nonlinearity is assumed to be weak, the deviation of the magnetization from the equilibrium state will be small, and the z component of the magnetization can be put into the form

$$M_z \cong M_0\left(1 - \frac{|M_x|^2 + |M_y|^2}{2M_0^2}\right), \quad (14)$$

where M_0 is the saturation magnetization and the M_i are the components of the ac magnetization ($i = x, y, z$). Then, in the limit $kd \ll 1$ $M_z \cong M_0 - M_0|A|^2$ and $\omega_m \cong \omega_m(1 - |A|^2)$.[9–13] Substituting the latter expression into Eq. (10) we obtain

$$\gamma = -\frac{dG}{d|A|^2}\bigg/\frac{dG}{dk},$$

$$\frac{dG}{d|A|^2} = AD_a - BC_a,$$

$$D_a = \omega_m(\omega_h + \omega_n(1 - \exp(-2kd))/2),$$

$$C_a = \omega_n(\omega_h - \omega)/2,$$

$$\frac{dG}{dk} = A_kD + AD_k - (B_kC + BC_k), \quad (15)$$

where A_k, B_k, C_k, D_k, and δ_k are the derivatives of the functions (8), (11), and (12) with respect to k.

4. Lighthill's criterion (1) for a surface magnetostatic spin wave propagating in a ferrite-semiconductor structure
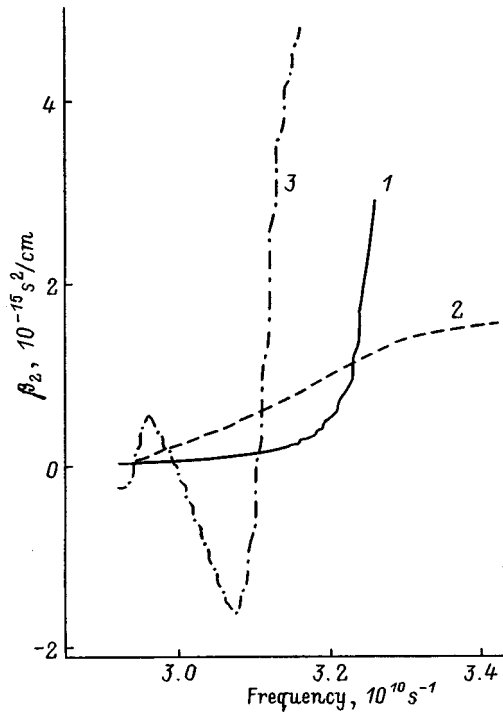
FIG. 1. Curves of the dispersion of the group velocity versus the frequency for electron density in the semiconductor: $1 - N = 10^{14}$, $2 - 2.5 \times 10^{16}$, $3 - 10^{18}$ cm^{-3}.
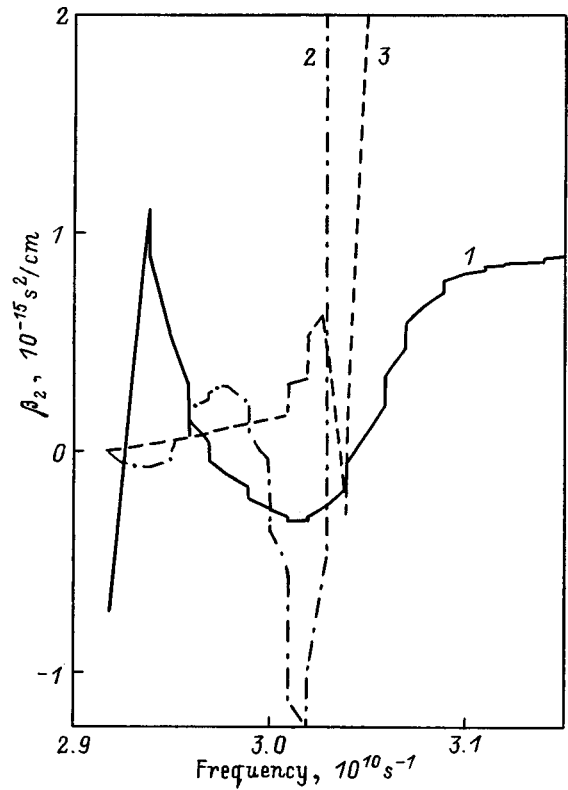

FIG. 2. Dispersion of the group velocity of SMSWs versus the frequency for $H = 1000$ Oe, $d = 0.001$ cm, and $N = 10^{16}$ cm^{-3} for semiconductor layer thickness (10^{-4} cm): $1 - t = 1.0$, $2 - 5.0$, $3 - 10.0$ cm.

was investigated as a function of the carrying frequency for various values of the current-carrier density in the semiconductor layer, the layer thicknesses, and the external magnetic field strength using the equation presented above.

The calculations were performed for an yttrium iron garnet — InSb structure. The following parameters were used: $d = 10^{-3}$ cm, $t = 10^{-4}$ cm, $H = 1000$ Oe, $4\pi M = 1750$ Gs, the electron mobility $\mu_e = 78000$ cm^2/Vs, the hole mobility $\mu_h = 750$ cm^2/Vs, the effective masses $m_e^* = 0.014 m_0$ and $m_h^* = 0.4 m_0$, and $\varepsilon_s = 17.4$. Losses in the ferrite were neglected, and the collision frequency ν in the semiconductor was calculated as $\nu = e/\mu m^*$.

The computed frequency dependences of the dispersion of the group velocity for this system are presented in Figs. 1–3.

Since calculations of the nonlinearity coefficient γ as a function of frequency showed that $\gamma > 0$ in all cases considered here, Lighthill's criterion (1) holds when the dispersion of the group velocity is negative.

As one can see from Fig. 1, for low current-carrier densities the semiconductor film has no effect on the parameters of an SMSW propagating in the structure. The dispersion of the group velocity is positive, and the wave is stable with respect to longitudinal disturbances, in agreement with the data of Refs. 8–13. As the density increases, there appear frequency ranges where β_2 becomes negative and therefore the formation of solitons of the form (6) is possible. As the density increases, these ranges shift toward higher frequencies. However, for certain $N > N_0$ (in our case $N_0 = 5 \times 10^{17}$ cm^{-3}) the propagation of SMSWs once again becomes stable and soliton formation is impossible. This effect of a semiconductor on SMSWs could arise because the finite
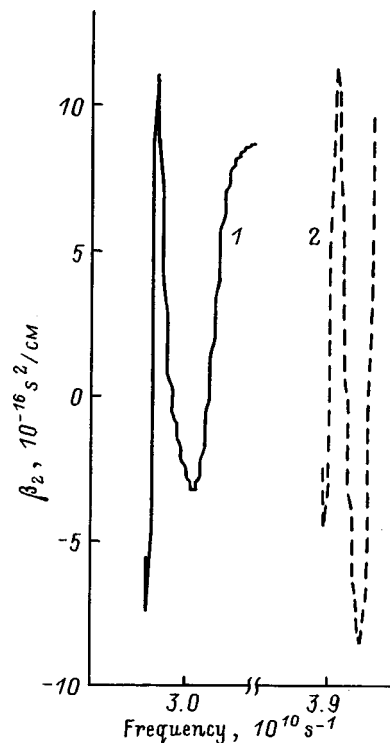
FIG. 3. Dispersion of the group velocity of SMSWs versus the frequency for $t = 0.0001$ cm, $d = 0.001$ cm, and $N = 10^{16}$ cm^{-3} for magnetic fields: $1 - 1.0$ kOe and $2 - 1.5$ kOe.

conductivity causes the semiconductor film to behave like a metal layer located at some distance from the ferrite. As the current-carrier density increases, the dispersion of SMSWs begins to deform and a section of anomalous dispersion appears. For low densities, this deformation appears at low values of the wave number k and, as the density increases, it extends to increasingly larger values of k. On the other hand, for large N, SMSWs are expelled from the semiconductor, the interaction of the waves with the semiconductor layer becomes less efficient, and the properties of the structure approach those of a metallized ferrite plate.

Figure 2 shows the computed frequency dependences of the dispersion of the group velocity of SMSWs for several values of the thickness of the semiconductor layer. One can see that as the thickness of the semiconductor increases, the frequency range of negative values of β_2 becomes narrower, and at the same time these values increase in absolute value. When the thickness of the ferrite is the same as that of the semiconductor, the frequency range where SMSW solitons can exist decreases sharply and shifts into the high-frequency region of the spectrum, where losses to SMSW propagation are large.

Figure 3 shows the frequency dependence of the dispersion of the group velocity for two values of the external magnetic field. It is evident that the frequency range of SMSW solitons in a ferrite-semiconductor structure retains its form as a function of the magnetic field.

In conclusion, we shall estimate the threshold SMSW power required for soliton formation. It is defined as $|A|^2 = -\beta_2/\gamma_k\tau^2$, where τ is the pulse duration. Using the asymptotic expression for the SMSW power[9,11] $P = \pi L d^2 \omega M^2 |A|^2$ (L is the width of the structure), we find that for the parameters used and $N = 2.5\times10^{16}$ cm^{-3}, $\omega = 4.78$ GHz, $\tau = 5\times10^{-7}$ s, and $\beta_2 = -1.4\times10^{-16}$ s^2/cm the threshold power for soliton formation is $P = 8.4$ mW.

In summary, it has been shown in this paper by analyzing the solutions of the nonlinear Schrödinger equation that envelope soliton formation is, in principle, possible during the propagation of an SMSW pulse in a ferrite-semiconductor structure. Investigation of the effect of charge-carrier density in the semiconductor and the thickness of this layer on the soliton-formation conditions showed that the width and location of the frequency range in which passage of an SMSW pulse in the form of a soliton is possible can be controlled effectively by varying the carrier density and/or the thickness of the semiconductor.

[1] Yu. V. Gulyaev, P. E. Zil'berman, S. A. Nikitov, and A. G. Temiryazev, Fiz. Tverd. Tela (Leningrad) **28**, 2774 (1986) [Sov. Phys. Solid State **28**, 1553 (1986)].

[2] A. M. Mednikov, Fiz. Tverd. Tela (Leningrad) **23**, 242 (1981) [Sov. Phys. Solid State **23**, 136 (1981)].

[3] B. A. Kalinikos, N. G. Kovshikov, and A. N. Slavin, Fiz. Tverd. Tela (Leningrad) **27**, 226 (1985) [Sov. Phys. Solid State **27**, 135 (1985)].

[4] P. De Gasperis, R. Morcelli, and G. Miccolli, Phys. Rev. Lett. **59**, 481 (1987).

[5] B. A. Kalinikos, N. G. Kovshikov, *et al.*, Solid State Commun. **74**, 989 (1990).

[6] B. A. Kalinikos, N. G. Kovshikov, and A. N. Slavin, IEEE Trans. Magn. **26**, 1477 (1990).

[7] B. A. Kalinikos, N. G. Kovshikov, and A. N. Slavin, J. Appl. Phys. **67**, 5633 (1990).

[8] V. P. Lukomskiĭ, Ukr. Phys. J. **23**, 134 (1978).

[9] A. K. Zvezdin and A. F. Popkov, Zh. Éksp. Teor. Fiz. **84**, 606 (1983) [Sov. Phys. JETP **57**, 350 (1983)].

[10] A. D. Boardman and S. A. Nikitov, Phys. Rev. B **38**, 11444 (1988).

[11] A. D. Boardman, Yu. V. Gulyaev, and S. A. Nikitov, Zh. Éksp. Teor. Fiz. **95**, 2140 (1989) [Sov. Phys. JETP **68**, 1238 (1989)].

[12] A. D. Boardman, Q. Wang, S. A. Nikitov, *et al.*, IEEE Trans. Magn. **30**, 14 (1994).

[13] A. D. Boardman, S. A. Nikitov, K. Xie, *et al.*, J. Magn. Magn. Mater. **145**, 357 (1995).

[14] Yu. V. Gulyaev and P. E. Zil'berman, Radiotekh. Elektron. **23**, 897 (1978).

[15] A. S. Kindyak, Zh. Tekh. Fiz. **64**(11), 99 (1994) [Tech. Phys. **39**, 1143 (1994)].

[16] A. S. Kindyak, Mater. Lett. **24**, 359 (1995).

[17] M. J. Lighthill, J. Inst. Math. Appl. **4**, 269 (1965).

[18] R. W. Damon and J. R. Eschbach, J. Phys. Chem. Solids **19**, 308 (1961).

Translated by M. E. Alferieff

Phase transitions in the ferroelectrics (Sn$_{1-x}$In$_{(2/3)x}$)$_2$P$_2$S$_6$ at high pressures

P. P. Guranich, P. M. Lukach, V. V. Tovt, E. I. Gerzanich, A. G. Slivka, V. S. Shusta, and V. M. Kedyulich

Uzhgorod State University 294000 Uzhgorod, Ukraine

New ferroelectric solid solutions (Sn$_{1-x}$In$_{(2/3)x}$)$_2$P$_2$S$_6$ were investigated at high hydrostatic pressures. The range in which the incommensurate structure exists was determined. A dynamic shift of the incommensurate–ferroelectric phase transition temperature with increasing rate of change of temperature and the appearance of ''reverse hysteresis'' were observed. The characteristic features in the appearance of the latter effect in these crystals are investigated. © *1999 American Institute of Physics.* [S1063-7834(99)03107-X]

Sn$_2$P$_2$S$_6$ crystals are so far the only intrinsic ferroelectrics in which the isomorphic substitution S → Se (Ref. 1) and hydrostatic pressure[2] produce a new polycritical point in the phase diagram — the Lifshitz point (LP) — leading to the formation of an incommensurate phase (IP). In the present work the effect of substituting of ions Sn → In on the coordinates of the LP and the dielectric properties near incommensurate phase transitions in the new solid solutions (Sn$_{1-x}$In$_{(2/3)x}$)$_2$P$_2$S$_6$ were investigated.

Tin hexathiohypodiphosphate (Sn$_{1-x}$In$_{(2/3)x}$)$_2$P$_2$S$_6$ based single crystals of solid solutions were investigated. The crystals were grown by the chemical transport method. Highly pure elemental components were used for synthesis and iodine was used as the carrier. The temperature regimes were identical to the optimal regimes for growing Sn$_2$P$_2$S$_6$ crystals. Single crystals of the solid solutions (Sn$_{1-x}$In$_{(2/3)x}$)$_2$P$_2$S$_6$ with $x=0.028$, 0.05, and 0.07 and dimensions $2\times2\times2$ mm^3 were obtained. The solid solutions were identified as substitutional solid solutions with subtraction, i.e. when indium is substituted for tin, vacancies form in the tin sublattice ($3\text{Sn}^{2+}\rightarrow2\text{In}^{3+}$) for charge compensation. The obtained crystals had sharply pronounced faceting.

Investigations of the permittivity ε and the tangent $\tan\delta$ of the dielectric loss angle were performed with an E7-12 bridge at 1 MHz in the dynamic range with rate of temperature change 0.5–11 K/min. Pressure was produced by a high-pressure hydrostatic chamber with a working volume of 5 cm^3. The sample was heated and cooled together with the chamber. The sample temperature was measured with a copper-constantan thermocouple. The pressure was monitored to within ±1 MPa. Kerosene was used as the pressure-transmitting medium. The measurements were performed on samples oriented in the [100] crystallographic direction.

At atmospheric pressure, an anomaly corresponding to a ferroelectric phase transition (PT) was observed in the temperature dependences of ε in (Sn$_{1-x}$In$_{(2/3)x}$)$_2$P$_2$S$_6$ crystals with $x=0.028$, 0.05, and 0.07. The PT temperature determined from the maximum values of ε decreases very little with increasing In content (≈0.5 K per mole%). The maximum value of ε is $\varepsilon_{max}=7000$. Figure 1 shows the temperature dependences of the reciprocal of the permittivity of a (Sn$_{1-x}$In$_{(2/3)x}$)$_2$P$_2$S$_6$ crystal with $x=0.028$ for various hydrostatic pressures and the (p,T) phase diagram. As pressure increases, the PT shifts into the low-temperature range. Just as in Sn$_2$P$_2$S$_6$,[3] kinks appear in the curves of ε^{-1}. These kinks attest to splitting of the PT at T_0 in two: a paraelectric — IP phase PT at T_i and an IP — ferroelectric phase PT at T_c. In addition, just as in crystals of the solid solutions Sn$_2$P$_2$(Se$_y$S$_{1-y}$)$_6$ and (Pb$_y$Sn$_{1-y}$)$_2$P$_2$S$_2$,[3,4] the pressure dependences of the Curie–Weiss constant $C_W(p)$ and of the function $\varepsilon_{max}(p)$ show anomalous behavior at the point of splitting ($p=p_L$). The initial pressure coefficients of the shift of the phase transition temperatures for $x=0$, 0.028, and 0.05 are, respectively, $\partial T_0/\partial p=-220$, -225, and -237 K/GPa. As the In content increases, the Lifshitz point shifts into the higher-pressure range. For $x=0$, 0.028, and 0.05 the pressure coordinates of the LP are: $p_L=180$, 210, and 250 MPa. The temperature range of existence of the incommensurate phase increases under compression more rapidly for crystals with a high In content (at $p=400$ MPa, $T_i-T_c=15$ K for $x=0.028$).

In (Sn$_{1-x}$In$_{(2/3)x}$)$_2$P$_2$S$_6$ crystals, the relaxation of the permittivity osberved near the PT is stronger than in pure Sn$_2$P$_2$S$_6$. To study these processes in detail the temperature dependences of ε and $\tan\delta$ obtained in heating and cooling regimes were investigated for different rates of temperature change along the (p,T) phase diagram of the given crystals.

A ''reverse hysteresis'' was observed in the crystals investigated at pressures $p>p_L$. Here the temperature of the commensurate–incommensurate PT on heating is less than the temperature of the PT on cooling. Figure 2 shows the temperature dependences $\varepsilon(T)$ near T_c ($p=420$ MPa) for (Sn$_{1-x}$In$_{(2/3)x}$)$_2$P$_2$S$_6$ crystals with $x=0.028$. The rate of temperature change was 3.3 K/min. The temperatures of the PTs on heating and cooling are, respectively, $T_c^h=248.5$ and $T_c^c=255.7$ K.

Similar phenomena have been observed for the commensurate–modulated PT in proustite[5] and Sn$_2$P$_2$S$_6$ crystals[6] at atmospheric pressure. They can be explained by the influence of the subsystem of electrons localized in attachment levels of the lattice subsystem, where the PT
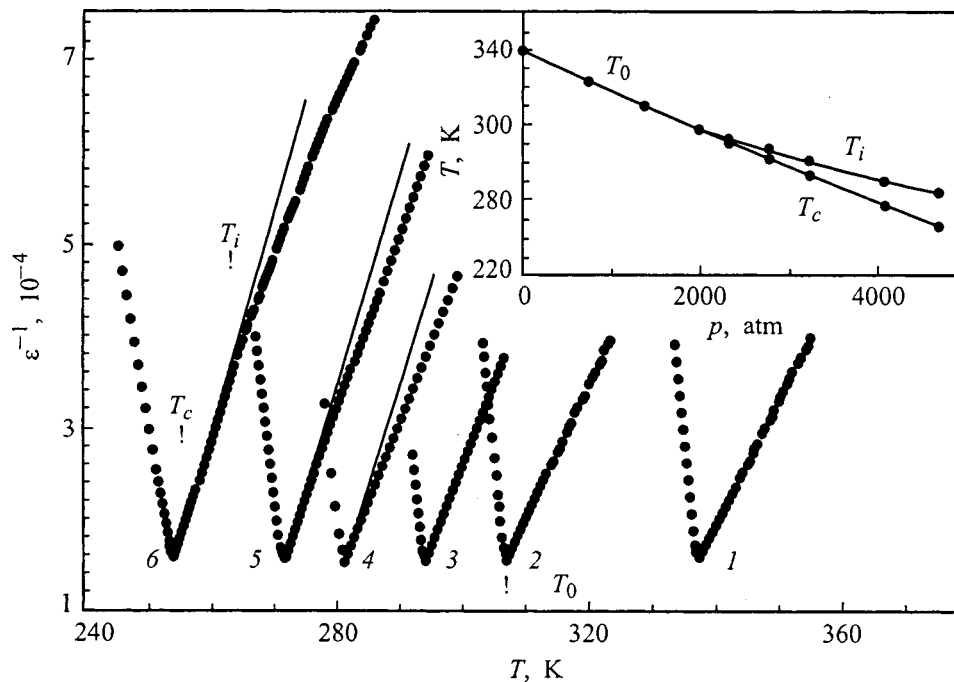
FIG. 1. Temperatures of the reciprocal ε^{-1} of the permittivity of an $(Sn_{1-x}In_{(2/3)x})_2P_2S_6$ crystal with $x=0.028$ for various values of the hydrostatic pressure p, MPa: *1* — 0.1, *2* — 130, *3* — 215, *4* — 278, *5* — 324, *6* — 400. Inset: (p,T) diagram of an $(Sn_{1-x}In_{(2/3)x})_2P_2S_6$ crystal with $x=0.028$.

occurs.[6] These phenomena have not been observed in $Sn_2P_2S_6$ crystals. Therefore their appearance in the solid solutions $(Sn_{1-x}In_{(2/3)x})_2P_2S_6$ ($x=0$) is obviously due to the substitution of In for Sn ions in the cationic sublattice. Compared with Ag_3AsS_3 and $Sn_2P_2Se_6$, the shift of the PT temperatures in $(Sn_{1-x}In_{(2/3)x})_2P_2S_6$ crystals exhibits its own peculiarities. Just as in proustite, a large shift of the PT tem-

perature occurs for rates of temperature change $V=0-10$ K/min, in contrast to $Sn_2P_2S_6$ where V is an order of magnitude higher. In $(Sn_{1-x}In_{(2/3)x})_2P_2S_6$ crystals, as distinct from Ag_3AsS_3 and $Sn_2P_2Se_6$, as the rate of temperature change increases, the temperature T_c^h, similarly to T_c^c, also increases (see inset in Fig. 2). The temperature shift of the PT on cooling and heating does not depend on the initial
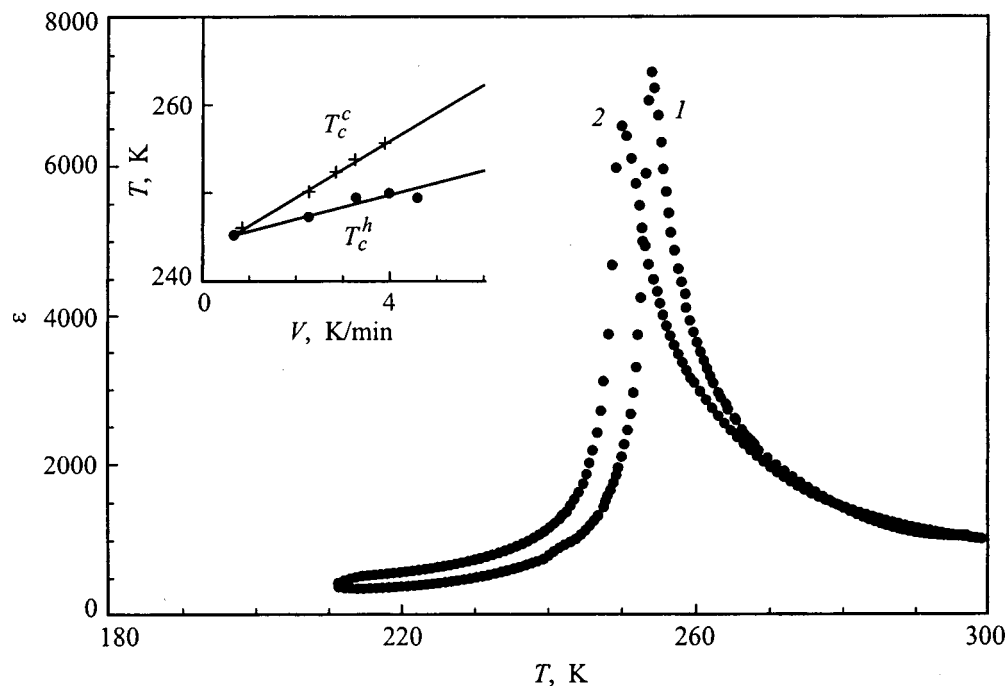
FIG. 2. Temperature dependences of the permittivity ε for an $(Sn_{1-x}In_{(2/3)x})_2P_2S_6$ crystal with $x=0.028$ for $p=420$ MPa. The curves were measured with the rate of temperature change $V=3.3$ K/min: *1* — cooling, *2* — heating. Inset: Temperature of the commensurate–incommensurate PT on heating — T_c^h and cooling — T_c^c versus the rate V of temperature change.

measurement temperature, and a large relaxation of the permittivity is observed over a fairly wide temperature range $T_c \pm 40$ K near the PT (for $p = 420$ MPa). For constant values of V, the temperature difference $T_c^c - T_c^h$ decreases with p and vanishes at pressures $p \approx p_L$. This indicates additionally that the ''reverse hysteresis'' phenomenon is evidently characteristic of only incommensurate phase transitions.

[1] T. K. Parsyamyan, S. S. Khasanov, and V. Sh. Shekhtman, Fiz. Tverd. Tela (Leningrad) **27,** 858 (1985) [Sov. Phys. Solid State **27**, 525 (1985)].

[2] A. G. Slivka, E. I. Gerzanich, P. P. Guranich, and V. S. Shusta, Ferroelectrics **103**, 71 (1990).

[3] A. G. Slivka, E. I. Gerzanich, P. P. Guranich, V. S. Shusta, and V. M. Kedyulich, Ukr. Fiz. Zh. **42**, 211 (1997).

[4] V. S. Shusta, E. I. Gerzanich, A. G. Slivka, P. P. Guranich, and V. A. Bobela, Ferroelectrics **143**, 61 (1993).

[5] I. M. Smyt'ko, V. Sh. Shekhtman, B. Sh. Bagautdinov, and N. S. Afonikova, Fiz. Tverd. Tela (Leningrad) **32**, 2441 (1990) [Sov. Phys. Solid State **32**, 1416 (1990)].

[6] Yu. S. Greznev, R. F. Mamin, and S. F. Motrya, Fiz. Tverd. Tela (St. Petersburg) **35**, 96 (1993) [Phys. Solid State **35**, 51 (1993)].

Translated by M. E. Alferieff

Electron spin resonance on enantiomorphic centers in $PbZrO_3$:Gd^{3+} crystals

A. V. Leyderman

Physics Department, University of Puerto Rico at Mayaguez, PR 00680, USA

V. G. Zaletov

Scientific-Research Institute of Physical and Organic Chemistry Rostov-on-Don State University, 344090 Rostov-on-Don, Russia

O. E. Fesenko[*)]

Scientific-Research Institute of Physics Rostov-on-Don State University, 344090 Rostov-on-Don, Russia

I. N. Leont'ev

Rostov-on-Don State University, 344090 Rostov-on-Don, Russia

N. G. Leont'ev

Azov-Black Sea State Agricultural Mechanization Academy, 344720 Zernograd, Russia
(Submitted October 23, 1998)
Fiz. Tverd. Tela (St. Petersburg) **41**, 1279–1281 (July 1999)

The Gd^{3+} ESR spectrum of the antiferroelectric phase of a $PbZrO_3$ single crystal contains at least one pair of magnetically equivalent components. The angular dependences of the resonance magnetic field that were constructed for them transform into one another by mirror reflection in a plane perpendicular to the antipolarization axis of the crystal. The constants in the spin Hamiltonians for the corresponding pair of paramagnetic centers are determined assuming monoclinic symmetry. © *1999 American Institute of Physics.*
[S1063-7834(99)03207-4]

This work continues the investigations of the antiferroelectric (AFE) phase of $PbZrO_3$ single crystals using ESR of Gd^{3+} ions substituting for Pb^{4+}.[1]

The investigations were performed at room temperature, since available published x-ray- and neutron-diffraction data[2,3] required for interpreting the ESR spectra were obtained at room temperature.

For the investigations we endeavored to select a large crystal, which is certain to possess strong resonance absorption and, when possible, is single-domain so as to rule out twinning-associated multiplication of the spectral lines. Unfortunately, the conditions for the crystal to be single-domain and large dimensions are incompatible, and only small (1.5 $\times$ 1.5 $\times$ 0.70 mm) single-domain samples could be found among the crystals grown. As a result, the resonance lines were relatively weak. This affected the quality of the experimental data so that individual sections of the angular dependences are unreliable: Some lines are missing in the spectrum, probably because of broadening; on the other hand, the close spacing of a large number of relatively weak lines from several paramagnetic centers makes the spectrum complicated in individual spots.

We denote by $H_p(\theta,\varphi)$ the resonance value of the magnetic field as a function of the angles θ and φ. The angle φ was measured from the B axis in the AB plane of the crystallographic coordinate system A,B,C of the orthorhombic cell of the AFE phase, while the angle θ was measured from the C axis. For magnetic field **H** oriented along A — θ $=90°$ and $\varphi=90°$, for **H** along B — $\theta=90°$ and $\varphi=0°$, and for **H** along C — $\theta=0°$.

Figure 1 shows four angular dependences $H_p(90°,\varphi)$ in the range of angles where they are clearly distinguishable. These dependences refer to paramagnetic centers *1, 2, 3,* and *4* — four positions of Gd^{3+} in the $PbZrO_3$ crystal lattice. For angular dependence 1, $H_p^{(1)}(\theta,\varphi)$, reliable data could be obtained even outside the range of polar angles shown in Fig. 1. For this center we have data in the following angular ranges: $100°>\varphi>-20°$ and $90°>\theta>0°$. For the angular dependence 2, $H_p^{(2)}(\theta,\varphi)$, $H_p^{(2)}$ could be measured for $15°>\varphi>-20°$, $100°>\varphi>60°$, and $90°>\theta>0°$.

The curves 1 and 2 are characteristic in that the directions of the vector **H** that correspond to minima of the functions $H_p^{(1)}(\theta,\varphi)$ and $H_p^{(2)}(\theta,\varphi)$ are different from the directions of A and B axes. This, as well as the fact that the extrema of H_p are different for different spectral lines of the fine structure, indicates a low local symmetry for positions corresponding to the paramagnetic centers 1 and 2.

These effects are much weaker for paramagnetic centers 3 and 4, whose local symmetry can be characterized as pseudorhombic. (Some characteristics of these centers and the corresponding angular dependences were presented in Ref. 1, but an exhaustive analysis of these characteristics can be made only on the basis of a more careful experimental investigation using higher-quality samples, which we already possess.)
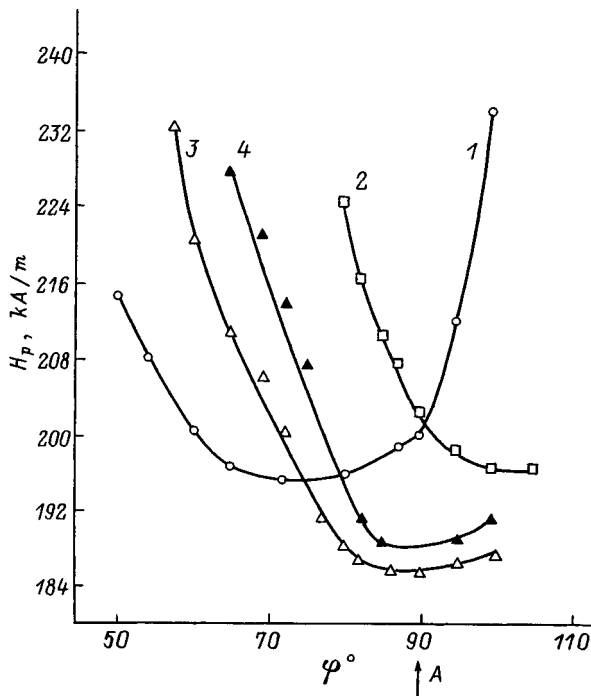
FIG. 1. Angular dependences $H(90°,\varphi)$ for the spectral transition $M=3/2 \rightarrow M=1/2$ in four paramagnetic centers Gd^{3+} in $PbZrO_3$, denoted in the text and in the figures by the numbers *1*, *2*, *3*, and *4*.

In contrast to the dependences $H_p(90°,\varphi)$, the direction of the vector **H** corresponding to the extrema of the dependences $H_p^{(1)}(\theta,0°)$ and $H_p^{(2)}(\theta,0°)$ is the same as the direction of the C axis in Fig. 2. This attests to a local symmetry of the Gd^{3+} positions in the paramagnetic centers *1* and *2* and the corresponding coordination polyhedra is monoclinic m, where m is parallel to the AB plane in agreement with our conclusions[4] based on structural data.[3]

The spin Hamiltonian[5]
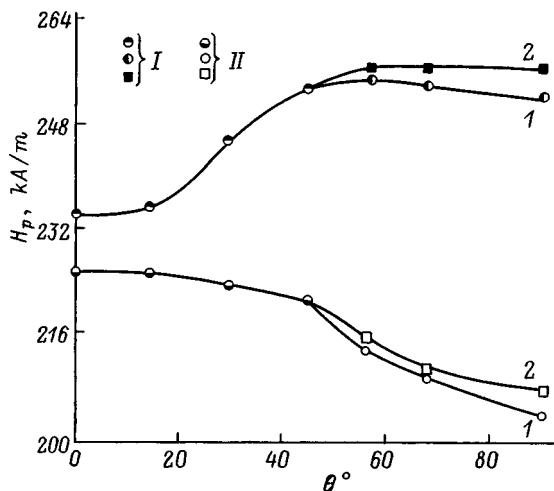
FIG. 2. Angular dependences $H_p(\theta,0°)$ for the spectral transitions $M=3/2 \rightarrow M=1/2$ and $M=1/2 \rightarrow M=-1/2$ in the paramagnetic centers *1* and *2* Gd^{3+} in $PbZrO_3$. The designations *I* and *II* refer to the spectral transitions $1/2 \rightarrow -1/2$ and $3/2 \rightarrow 1/2$, respectively.

$$\mathcal{H}=\beta HgS+\frac{1}{3}(b_2^0 O_2^0+b_2^2 O_2^2+\tilde{b}_2^2 \tilde{O}_2^2)+\frac{1}{60}(b_4^0 O_4^0$$

$$+b_4^2 O_4^2+\tilde{b}_4^2 \tilde{O}_4^2+b_4^4 O_4^4+\tilde{b}_4^4 \tilde{O}_4^4), \tag{1}$$

was used for paramagnetic center 1, for which the most complete dependence $H_p^{(1)}(\theta,\varphi)$ was obtained. This Hamiltonian was tested previously[6] in a number of crystals where paramagnetic centers with monoclinic local symmetry were formed on activation with Gd^{3+} ions. In the expression (1) O_n^m are well-known operators,[6] and the operators $\tilde{O}_n^m$ can be found by multiplying O_n^m by $-i$ and replacing all factors of the form $(S_+^k + S_-^k)$ by $(S_+^k - S_-^k)$. The operators $\tilde{O}_n^m$ must be included in the spin Hamiltonian only for polyhedron symmetry lower than orthorhombic. The Fourier expansion coefficients A_k and B_k of the function $H_p^{(1)}(90°,\varphi)$ were compared with the parameters b_n^m on the basis of the relation obtained between them by diagonalizing the spin Hamiltonian (1). This relation together with the least-squares method for finding A_k and B_k from the experimental curve gave the following values of the coefficients b_n^m in MHz (for $g_x \approx g_y \approx g_z \approx 1.97$): $b_2^0=-510$; $b_2^2=690$; $b_4^0=-80$; $b_4^2 =-540$; $b_4^4=-650$; $\tilde{b}_4^4=330$; $\tilde{b}_2^2+\frac{3}{2}\tilde{b}_4^2=1230$.

Analysis of these seven quantities shows that the coefficients $\tilde{b}_n^m$ and b_n^m are of the same order of magnitude. This confirms the conclusion that the coordination polyhedron has a low symmetry. From the fact that the values of b_4^m are comparable to b_2^m follows that terms with O_4^m must be included in the Hamiltonian. Otherwise it would be impossible to describe the experimental dependence $H_p^{(1)}(\theta,\varphi)$ satisfactorily.

The Fourier expansions of the experimental dependences $H_p^{(1)}(90°,\varphi)$ and $H_p^{(2)}(90°,\varphi)$ have the form

$$H_p^{(1)}(90°,\varphi)=\sum_{k=0}^{4} \{A_k\cos(k\varphi)+B_k\sin(k\varphi)\} \text{ and}$$

$$H_p^{(2)}(90°,\varphi)=\sum_{k=0}^{4} \{A_k\cos(k\varphi)-B_k\sin(k\varphi)\}.$$

It is easy to see that these functions transform into one another when the sign of the angle φ is changed. In the angular ranges indicated above, for which we have reliable data for $H_p^{(1)}(\theta,\varphi)$ and $H_p^{(2)}(\theta,\varphi)$, this conditions is indeed satisfied: $H_p^{(1)}(90°,\varphi)=H_p^{(2)}(90°,-\varphi)$. The spin Hamiltonian for the paramagnetic center 2 can be obtained from expression (1) by changing the sign of the coefficients $\tilde{b}_2^2$, $\tilde{b}_4^2$, and $\tilde{b}_4^4$. In addition, the same spectral pattern with **H** along C and the same values at the minima of the functions $H_p^{(1)}(90°,\varphi)$ and $H_p^{(2)}(90°,\varphi)$ (Fig. 2) are characteristic for both centers. These data show that the centers *1* and *2* differ by a mirror arrangement of the nearest-neighbor atoms of Gd^{3+} relative to the coordinate plane BC and correspond to an antiparallel arrangement of the Pb^{4+} (Gd^{3+}) ions, which is responsible for the antiferroelectric ordering.[7]

*)E-mail: ofesenko@uic.rnd.runnet.ru

[1] A. V. Leyderman, V. G. Zaletov, I. N. Leontiev, O. E. Fesenko, N. G. Leontiev, and V. G. Smotrakov, J. Korean Phys. Soc. **32**, S703 (1998).

[2] F. Iona, G. Shirane, F. Mazzi, and R. Pepinsky, Phys. Rev. **105**, 849 (1957).

[3] H. Fujishita, Yo. Shiozaki, N. Achiva, and E. Sawaguchi, J. Phys. Soc. Jpn. **51**, 3583 (1982).

[4] A. V. Leyderman, I. N. Leont'ev, O. E. Fesenko, and N. G. Leont'ev, Fiz. Tverd. Tela (St. Petersburg) **40**, 1324 (1998) [Phys. Solid State **40**, 1204 (1998)].

[5] M. L. Meĭl'man and M. I. Samoĭlovich, *Introduction to the ESR Spectroscopy of Activated Single Crystals* (Atomizdat, Moscow, 1977), p. 165.

[6] M. M. Zaripov and L. Ya. Shekun, in *Parametric Resonance* (Kazan' State University Press, Kazan', 1964), p. 5.

[7] E. Sawaguchi, H. Maniwa, and S. Hoshino, Phys. Rev. **83**, 1078 (1951).

Translated by M. E. Alferieff

Unique features of the crystal structure of the $(PbMg_{1/3}Nb_{2/3}O_3)_{0.6}-(PbTiO_3)_{0.4}$ solid solution

S. B. Vakhrushev

A. F. Ioffe Physicotechnical Institute, Russian Academy of Sciences, 194021 St. Petersburg, Russia

S. G. Zhukov and V. V. Chernyshev

M. V. Lomonosov Moscow State University, 119899 Moscow, Russia
(Submitted November 12, 1998)
Fiz. Tverd. Tela (St. Petersburg) **41**, 1282–1285 (July 1999)

An x-ray diffraction study of the paraphase of the $(PbMg_{1/3}Nb_{2/3}O_3)_{0.6}-(PbTiO_3)_{0.4}$ solid solution has been found to exhibit a clearly pronounced ferroelectric transition. It is shown that Pb^{2+} ions occupy a special position (000), as opposed to pure PMN and other relaxor ferroelectrics, where they are displaced from it in random directions. The absence of these displacements indicates suppression of frozen-in random electric fields in this compound. © *1999 American Institute of Physics.* [S1063-7834(99)03307-9]

Relaxor ferroelectrics or ferroelectrics having a diffuse phase transition were discovered 40 years ago. While hundreds of papers have been devoted to investigating the physical properties of these compounds,[1,2] detailed information on their structure was lacking until 1989 (Ref. 3). Most of the relaxors are cubic perovskite-like compounds with a general formula $AB'_x B''_{1-x}O_3$, where the equivalent sites on the B sublattice are randomly occupied by different, as a rule nonisovalent, ions. The lead magnoniobate crystal $PbMg_{1/3}Nb_{2/3}O_3$ (PMN) may be considered as a model for studying the properties of relaxors. The PMN structure was studied more than once, both at high[3,4] (above the freezing point $T_F \approx 230$ K) and low[5] temperatures. It was found[3] that even at high temperatures ($>2T_F$) lead ions, rather than occupying special symmetry positions (000), are displaced from them, and these displacements were shown[4] to be in random directions, which means that in an ''averaged'' crystal the probability density of finding a lead ion forms a spherical layer around the (000) position. Similar distortions of the ideal perovskite-like structure were observed in other relaxors as well, for instance, in $PbSc_{1/2}Ta_{1/2}O_3$ (PST) and $PbIn_{1/2}Nb_{1/2}O_3$ (PIN) (Refs. 6 and 7, respectively). Until recently, however, experimental evidence for the observed structural distortions being related to the specific ''relaxor'' behavior of the crystals was lacking.

Experimental investigation and theoretical description of relaxors is extremely complicated, in particular, because they are stoichiometric compounds rather than solid solutions, so that one cannot vary their composition at will. Thus we have no information on the behavior of ''pure'' compounds which could be used as starting data, because crystals of the type $PbMgO_3$ and $PbNbO_3$ just cannot exist. There are two possibilities for following the variation of the main characteristics of mixed perovskites as their behavior crosses over from relaxor to normal ferroelectric. One of them consists in studying ordered compounds of the type of PST and PIN. However the structure of the ordered phase exhibiting a clear

phase transition differs from that of disordered compounds (ordering results in doubling of the unit cell volume), and annealing needed to transform the PIN crystal to the ordered state may bring about formation of a new modification with antiferroelectric properties. Another possibility, which we believe to be more effective, lies in using solid solutions of relaxors and classical ferroelectrics. The best known system of such solid solutions, $(PMN)_{1-x}(PbTiO_3)_x$ (PMNPT), changes its character from relaxor to typically ferroelectric with increasing content of PT (for $x>0.3$). Investigation of these solid solutions has been attracting recently considerable interest, but until the present no relation between the microscopic structure of these crystals and the character of the corresponding phase transition has been revealed. This work presents the results of an x-ray diffraction study of a PMNPT crystal with $x=0.4$ (PMNPT40), which was aimed at finding this relation.

The crystals for the study were provided by the Institute of Physics at Rostov State University. They were prepared by spontaneous crystallization from a solution melt. PMNPT40 undergoes a ferroelectric transition at about 450 K.[8] Accordingly, at room temperature the crystals are in tetragonal modification with considerable internal stresses, which does not permit fabrication of samples of spherical shape. The samples used in the measurements were irregularly shaped fragments of a single crystal, with a characteristic size of about 0.2 mm. The experiments were carried out on a CAD-4 four-circle diffractometer (Mo $K\alpha$ radiation, graphite monochromator, $\omega/2\theta$ scanning) at 500 K using an FR559 Enraf–Nonius high-temperature device. In accordance with available literature data, the measurements showed the crystal to be in a cubic paraphase at this temperature, with the averaged structure corresponding to the $Pm\bar{3}m$ group. The integrated intensities were measured in an Ewald hemisphere down to $\sin\theta/\lambda=1.2$ Å^{-1}. An array of averaged structural amplitudes with $I>3\sigma(I)$ was obtained from 98
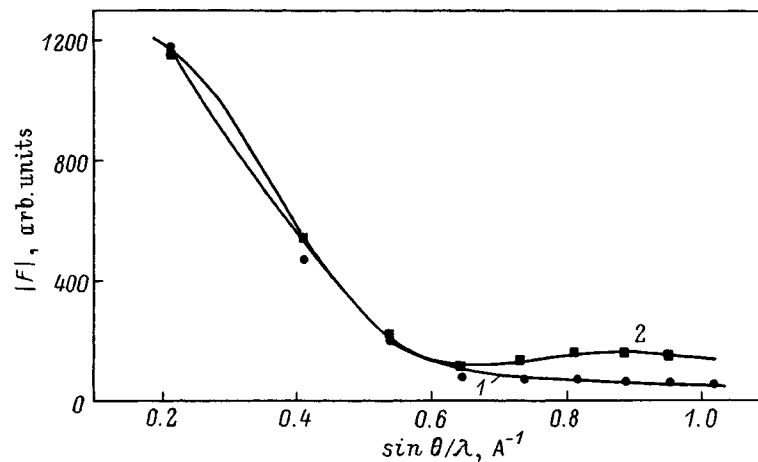
FIG. 1. Dependence of the structure amplitude F of $(h+1k+1l+1)$-type reflections on $\sin\theta/\lambda$ for PMNPT40 obtained at 500 K (curve *1*) and for pure PMN at 293 K (curve *2*).

reflections. A RRKhA program was used for data treatment and structure refinement.[9]

Figure 1 presents the dependences of structure amplitudes F of $(h+1k+1l+1)$-type reflections on $\sin\theta/\lambda$, which is proportional to the length of the scattering vector τ, for PMNPT40 and for pure PMN. In the case of pure PMN, one observes a characteristic non-Gaussian curve with a local minimum in the region of 0.65 Å^{-1}. This pattern of the relationship indicates the existence of local ion displacements from their high-symmetry sites. Note that the intensities of all reflections of a given family fall on the same smooth curve irrespective of the direction of τ, an observation reported earlier in Ref. 4, which implies the absence of any preferred direction of displacement and validates the use of the above-mentioned spherical-layer model. The $I(\sin\theta/\lambda)$ curves of the PMNPT6 and PMNPT10 compounds exhibiting relaxor properties have the same pattern.[a)] The $I(\sin\theta/\lambda)$ dependence obtained for PMNPT40 has a radically different shape, without clearly pronounced extrema. Such a relation does not permit unambiguous conclusions for or against the existence of ion displacements.

We carried out a refinement of the PMNPT40 structure using three different models. The first model assumed the lead ion to occupy a parabolic potential well with the center in the special position (000). The second model took into account a possible nonparabolicity of the potential, with fourth-order anharmonic coefficients d_{1111} and d_{1122} included in the parameters to be refined (third-order anharmonicity is forbidden because the structure is centrosymmetric). The third model was a spherical layer with the average magnitude of local displacements r_{sph} (radius of the sphere) and the isotropic thermal factor U_{iso} determining the effective layer thickness serving as fitting parameters. The quality of the model was estimated from the unweighted R factor, $R=\Sigma(I_{exp}-I_{calc})/\Sigma I_{exp}$. The calculations showed that the harmonic model does not permit adequate description of the experimental data. The anharmonic model yielded $U_{iso}^{anh}=0.042$ Å^2, $d_{1111}=-5.1\times10^{-6}$, $d_{1122}=-1.9\times10^{-6}$, and $R=5\%$. The parameters obtained in the spherical-layer model are $r_{sph}=0.16$ Å, $U_{iso}^{sph}=0.053$ Å^2, and $R=9.9\%$.

The large values of the R factors in both models are due to the large experimental errors in the averaged set of intensities; they were associated with the irregular sample shape, which complicated introducing corrections for absorption and extinction.

Despite the large difference between the values of R obtained within the above models, the χ^2 criterion was in both cases about unity, which precludes unambiguous selection in favor of the anharmonic description. A more detailed analysis reveals, however, that for the above parameters the models differ only quantitatively rather than qualitatively. We calculated the probability density function ρ for the lead ion as a function of its displacement δ from the (000) position using the expressions of Ref. 10. The results of the calculation made for the anharmonic and spherical-layer models are displayed in Fig. 2. The scale on the vertical axis was chosen based on the normalization condition $\int_{-\infty}^{+\infty}\rho(\delta)d^3\delta=1$. Shown for comparison is a $\rho(\delta)$ curve for pure PMN (spherical-layer model, $r_{sph}=0.286$ Å, $U_{iso}^{sph}=0.0196$ Å^2, $R=3.7\%$, Ref. 10) obtained at room temperature. One readily sees that the center of gravity of the curve for pure PMN is displaced from the (000) position by an amount equal to the layer radius, and that the probability density at $\delta=0$ is negligible. At the same time in the case of PMNPT40 both models give a broad bell-shaped distribution centered at $\delta=0$.

The nonparabolicity of the potential well and the large width of the probability-density distribution function indicate that it is this ion which is ferroelectric, as in pure PMN. Most significant is the result implying disappearance in PMNPT40 of clearly pronounced lead-ion displacements from the special position (000). It was conjectured that the Pb^{2+} displacements are a direct consequence of the presence of random electric fields in PMN and other relaxors.[4] The question of a possible dominant role for such fields in the behavior of relaxors, in particular, in PMN was discussed in literature.[11,12] Following these works, one could suggest several sources of random fields. Besides random molecular fields favoring formation of an ordered ferroelectric phase,[12] one could expect generation in PMN-type crystals of
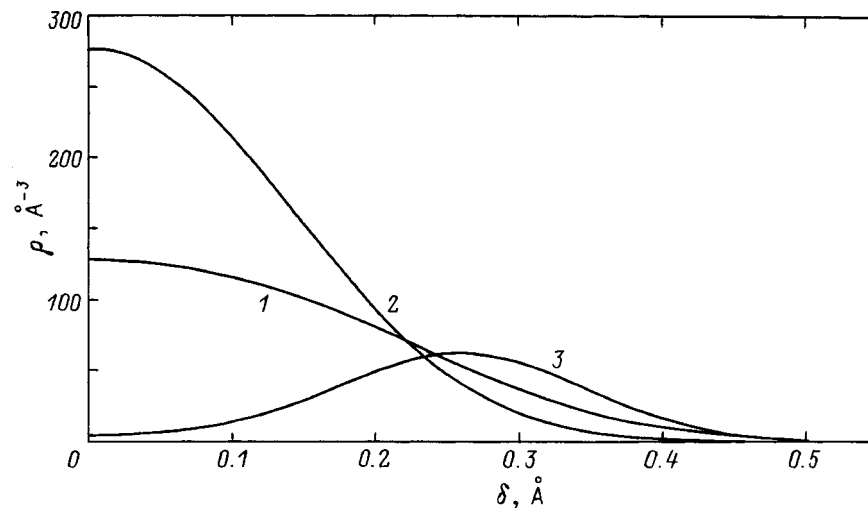
FIG. 2. Probability density function for a lead ion plotted against displacement δ from the (000) position. Curves *1,2* — PMNPT40 at 500 K (anharmonic and spherical-layer model, respectively), curve *3* — pure PMN at 293 K, spherical-layer model.

frozen-in random electric fields due to randomly distributed nonisovalent ions[13,14] (i.e. as a result of charged point defects). It may be conjectured that incorporation of a sufficiently large number of Ti^{4+} ions in PMN having a valence equal to the mean valence of the *B* ions changes appreciably the shielding conditions of uncompensated charges and gives rise to disappearance of the frozen-in local random fields, or at least to their substantial suppression. Because the random fields are linearly related to the ferroelectric mode where lead-ion displacements play a major role,[15] such fields should inevitably produce local Pb^{2+} displacements and, if the concentration of these ions is high enough, to a distortion of the average structure. The absence in PMNPT40 of static displacements of lead ions from special positions is direct evidence of suppression of random electric fields.

Thus the above structure study of the paraelectric phase in the PMNPT40 solid solution, combined with a comparison of the results obtained from the structure of compounds exhibiting relaxor properties, have revealed for the first time a direct relation between the nature of the phase transition and the nature of the low-temperature state, on one hand, and features in the microscopic structure of the paraphase, on the other. An analysis provides support for the hypothesis of a dominant role played by frozen-in random fields in the specific features of relaxor ferroelectrics.

a)After completion of the data treatment involved, the results of the structural study of the PMNPT solid solutions will be published in a separate paper.

---

[1] *Physics of Ferroelectric Phenomena* [in Russian], edited by G. A. Smolenskiĭ (Nauka, Leningrad, 1985).
[2] Z.-G. Ye, Ferroelectrics **184**, 193 (1996).
[3] P. Bonneau, P. Garnier, E. Husson, and A. Morell, Mater. Res. Bull. **24**, 201 (1989).
[4] S. Vakhrushev, S. Zhukov, G. Fetisov, and V. Chernyshov, J. Phys.: Condens. Matter **6**, 4021 (1994).
[5] N. de Mathan, E. Husson, G. Calvarin, J. R. Gavarri, A. W. Hewat, and A. Morell, J. Phys.: Condens. Matter **3**, 8159 (1991).
[6] S. G. Zhukov, V. V. Chernyshev, L. A. Aslanov, S. B. Vakhrushev, and H. Schenk, J. Appl. Crystallogr. **28**, 385 (1995).
[7] S. G. Zhukov, A. V. Yatsenko, and S. B. Vakhrushev, Zh. Strukt. Khim. **38**, 586 (1997).
[8] O. Bunina, I. Zakharchenko, S. Yemelyanov, P. Timonin, and V. Sakhnenko, Ferroelectrics **157**, 299 (1994).
[9] V. V. Chernyshev, G. V. Fetisov, A. V. Laktionov, V. T. Markov, A. P. Nesterenko, and S. G. Zhukov, J. Appl. Crystallogr. **25**, 451 (1992).
[10] V. V. Chernyshev, S. G. Zhukov, A. V. Yatsenko, L. A. Aslanov, and H. Schenk, Acta Crystallogr., Sect. A: Found. Crystallogr. **50**, 601 (1994).
[11] W. Kleemann, Int. J. Mod. Phys. B **7**, 2469 (1993).
[12] M. D. Glinchuk and V. A. Stephanovich, J. Phys.: Condens. Matter **6**, 6317 (1994).
[13] B. I. Halperin and C. M. Varma, Phys. Rev. B **14**, 4030 (1976).
[14] A. D. Bruce and R. A. Cowley, *Structural Phase Transitions* (Taylor & Francis, London, 1981; Mir, Moscow, 1984).
[15] S. B. Vakhrushev, A. A. Naberezhnov, N. M. Okuneva, and B. N. Savenko, Fiz. Tverd. Tela (St. Petersburg) **37**, 3621 (1995) [Phys. Solid State **37**, 1993 (1995)].

Translated by G. Skrebtsov

^{121}Sb and ^{123}Sb NQR and the heterophase structure in the SbSI ferroelectric

S. N. Popov

A. F. Ioffe Physicotechnical Institute, Russian Academy of Sciences, 194021 St. Petersburg, Russia
(Submitted December 1, 1998)
Fiz. Tverd. Tela (St. Petersburg) **41**, 1286–1292 (July 1999)

The temperature dependences of NQR line frequencies and widths of ^{121}Sb (for the $\pm 1/2 \to \pm 3/2$ transition) and of ^{123}Sb (for the $\pm 1/2 \to \pm 3/2$ and $\pm 3/2 \to \pm 5/2$ transitions), as well as of the principal components and the asymmetry parameter of the electric-field-gradient tensor at the ^{123}Sb nucleus have been studied in a SbSI crystal in the 115–325 K range. The dynamic and static factors governing the character of these relations are discussed. The $\pm 1/2 \to \pm 3/2$ line in the ^{121}Sb NQR spectrum splits into a doublet within a narrow (0.5 K) temperature interval near the ferroelectric phase transition ($T_c = 293$ K), which is associated with the formation of a macroscopic heterophase structure in the crystal. © *1999 American Institute of Physics.* [S1063-7834(99)03407-3]

Macroscopic heterophase structures occurring in phase transitions of a number of crystals continue to attract considerable attention. In this connection, investigation of the critical behavior of nuclear quadrupole interactions in the vicinity of phase transitions in ferroelectrics and ferroelastics acquires a particular interest. This work reports a study of ^{121}Sb and ^{123}Sb nuclear quadrupole resonance (NQR) in an antimony sulfoiodide ferroelectric. We have already reported[1] the manifestation of the ferroelectric phase transition in SbSI in NQR. This work deals with a more detailed investigation of antimony NQR in SbSI.

The structure of the SbSI crystal consists of parallel molecular chains. The lattice has rhombic symmetry. At $T_c = 293$ K, SbSI undergoes a first-order structural phase transition $D_{2h}^{16} \to C_{2v}^9$, with spontaneous polarization setting in for $T \leqslant T_c$.[2–4] The unit cell of SbSI contains four formula units. The $(Sb_2S_2I_2)_n$ double chains are oriented along the crystallographic c axis, which in the ferroelectric phase coincides with the ferroelectric axis. The SbSI structure can be described within the model of the $Sb^{3+}S^{2-}I^-$ ionic crystal,[5] allowing, however, the possibility of partially covalent bonding. A model of the outer electronic shells, $(5p)^2$ for Sb^+, $(3p)^4$ for S^-, and $(5p)^6$ for I^-, was proposed.[6] Thus the iodine can exist in the pure ionic state, while the antimony and sulfur may be covalently bonded. Mössbauer studies similarly argue for predominantly ionic halogen bonds and essentially covalent Sb–S bonding.[7]

The present experiment was carried out with an IS-2 pulsed radiospectrometer. The techniques employed are described elsewhere.[8] The measurements were performed on a 45-mm long cylindrical SbSI sample with a 9-mm diameter. The crystallographic c axis was aligned with the cylinder axis.

The static, or inhomogeneous linewidth was determined from the width of the double-pulse spin echo: $\Delta \nu_{1/2} = 0.88/\Delta t_{1/2}$ (here $\Delta \nu_{1/2}$ is the linewidth at half maximum, and $\Delta t_{1/2}$ is the echo full width at half maximum).[8] A clear image of echo shape was obtained by multichannel signal accumulation. To suppress the signals due to electroacoustical (phonon) echo[9] and piezoelectric ringing for $T < T_c$, the sample was placed in a polyethylene container filled with silicone oil.

1. RESULTS OF EXPERIMENT

One studied temperature dependences of three resonant frequencies, ν_1 ($\pm 1/2 \to \pm 3/2$) and ν_2 ($\pm 3/2 \to \pm 5/2$) for ^{123}Sb (spin $I = 7/2$), and ν_3 ($\pm 1/2 \to \pm 3/2$) for ^{121}Sb ($I = 5/2$), as well as those of the corresponding linewidths $\Delta \nu_{1/2}^{(1)}$, $\Delta \nu_{1/2}^{(2)}$, and $\Delta \nu_{1/2}^{(3)}$, including the phase-transition region at $T_c = 293$ K. The experimental values of the ν_1 and ν_2 frequencies were used to calculate the principal components of the electric-field gradient (EFG) tensor, V_{ZZ}, V_{YY}, and V_{XX}, and the EFG asymmetry parameter η for ^{123}Sb by solving the secular equation for quadrupole-coupling energy levels for the $I = 7/2$ spin. A series of ^{121}Sb NQR ($\pm 1/2 \to \pm 3/2$) line measurements were made at different temperatures near the phase transition. The results obtained are as follows.

(1) The $\nu(T)$ experimental relations are linear for all three frequencies, exhibit a clearly pronounced anomaly at $T = T_c$, and behave nonlinearly below T_c;

(2) The $\Delta \nu_{1/2}^{(1)}(T)$, $\Delta \nu_{1/2}^{(2)}(T)$, and $\Delta \nu_{1/2}^{(3)}(T)$ experimental relations, similar to $\nu_1(T)$, $\nu_2(T)$, and $\nu_3(T)$, are practically linear above T_c in the temperature range studied, undergo a sharp anomaly at $T = T_c$, and exhibit nonlinear behavior below T_c;

(3) The temperature dependences of η, V_{ZZ}, V_{YY}, and V_{XX} are linear in the paraelectric phase, and exhibit a sharp anomaly at the phase transition and a nonlinear behavior in the ferroelectric region;

(4) Within a narrow temperature interval (~ 0.5 K) in the vicinity of T_c, the ^{121}Sb NQR ($\pm 1/2 \to \pm 3/2$) line is observed as a doublet with components spaced by more than 1 MHz.
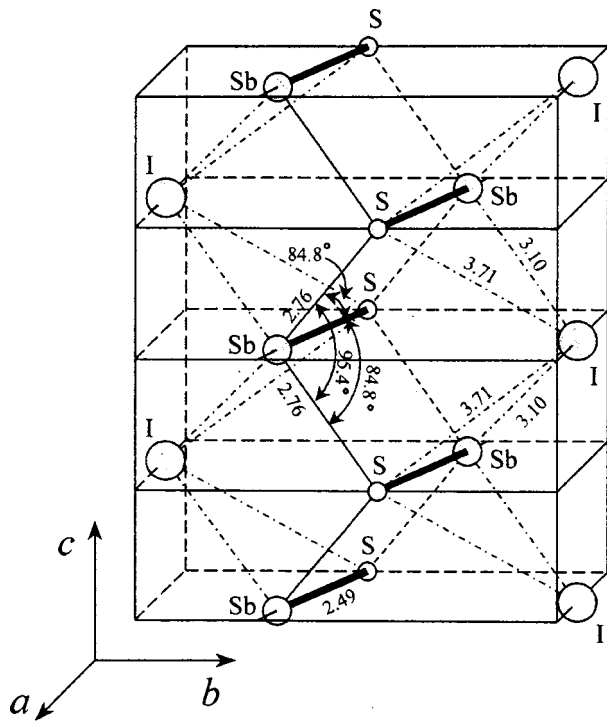
FIG. 1. Schematic presentation of the double molecular chain $(Sb_2S_2I_2)_n$ for the paraelectric state in SbSI. The bond angles and lengths are taken from Ref. 5. The parallelepiped dimensions are not related to the unit cell parameters.

2. DISCUSSION OF RESULTS

In the experiment, the c axis of the SbSI crystal was aligned with the coil axis, i.e. was parallel to the field H_1,

while the $\pm 1/2 \rightarrow \pm 3/2$ transitions can be induced only by the components of the rf field H_1 perpendicular to the principal axis Z of the EFG tensor. Hence the EFG principal component V_{ZZ} is perpendicular to the c axis and oriented along the shortest chemical bond between the antimony and sulfur ions (2.49 Å, Fig. 1), whose outer $5p$ and $3p$ electrons provide the major contribution to the EFG and determine the covalent nature of the bonding.

The Hamiltonian of quadrupole interaction constructed in the frame of the principal EFG tensor axes X, Y, Z can be written

$$H_Q = \frac{e^2 qQ}{4I(2I-1)} \left\{ 3I_Z^2 - I(I+1) + \frac{1}{2} \eta (I_+^2 + I_-^2) \right\}. \quad (1)$$

Here $eq \equiv V_{ZZ}$, $\eta \equiv (V_{XX} - V_{YY})/V_{ZZ}$ is the EFG asymmetry parameter, Q is the nuclear quadrupole moment, $I^2 = I_X^2 + I_Y^2 + I_Z^2$, and $I_\pm = I_X \pm iI_Y$ are nuclear spin operators in the X, Y, Z coordinate frame. The principal EFG components satisfy the relations

$$|V_{ZZ}| > |V_{YY}| > |V_{XX}|,$$

$$V_{ZZ} + V_{YY} + V_{XX} = 0. \quad (2)$$

As seen from Eq. (1), variation of two EFG parameters, V_{ZZ} and η, determines completely that of NQR frequencies with varying crystal temperature.

The experimental $\nu_1(T)$, $\nu_2(T)$, and $\nu_3(T)$ relations in the paraelectric phase of SbSI (Figs. 2–4) are due to anisotropy in the thermal expansion of the lattice.[10] The role played by EFG dynamic Bayer averaging through thermal lattice vibrations, which is efficient primarily for the rocking
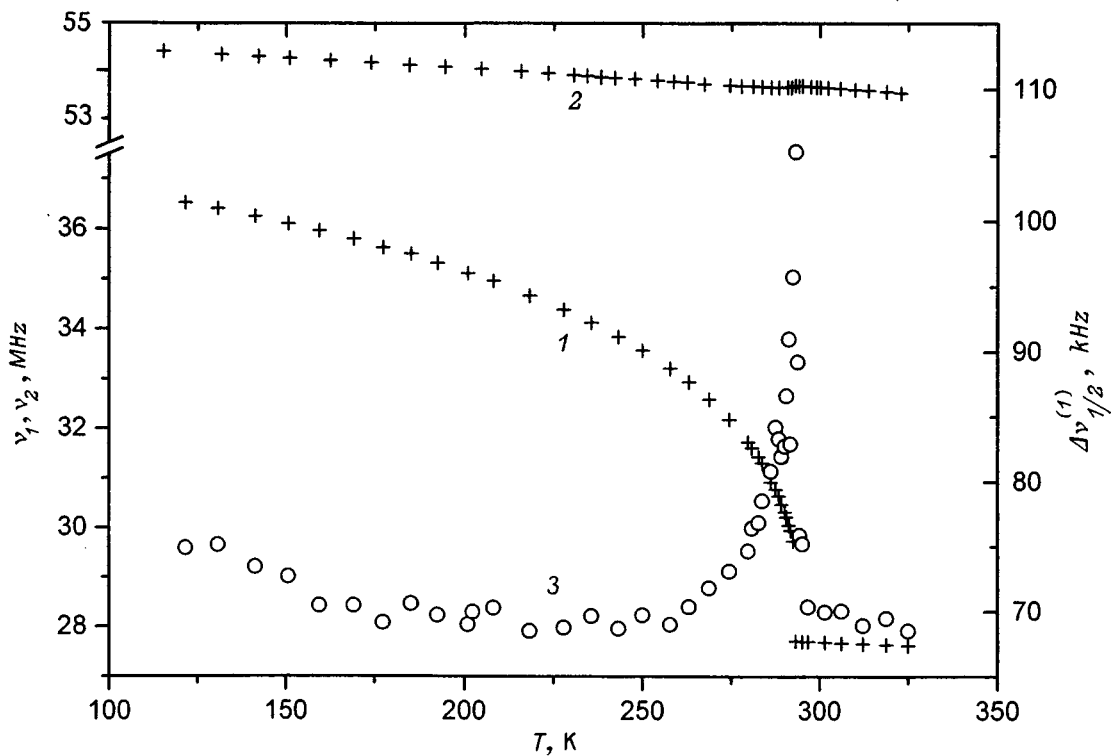

FIG. 2. Temperature dependence of the [123]Sb NQR frequencies (*1*) ν_1 ($\pm 1/2 \rightarrow \pm 3/2$ transition) and (*2*) ν_2 ($\pm 3/2 \rightarrow \pm 5/2$ transition), and (*3*) of the [123]Sb NQR ($\pm 1/2 \rightarrow \pm 3/2$) linewidth $\Delta \nu_{1/2}^{(1)}$ in SbSI.
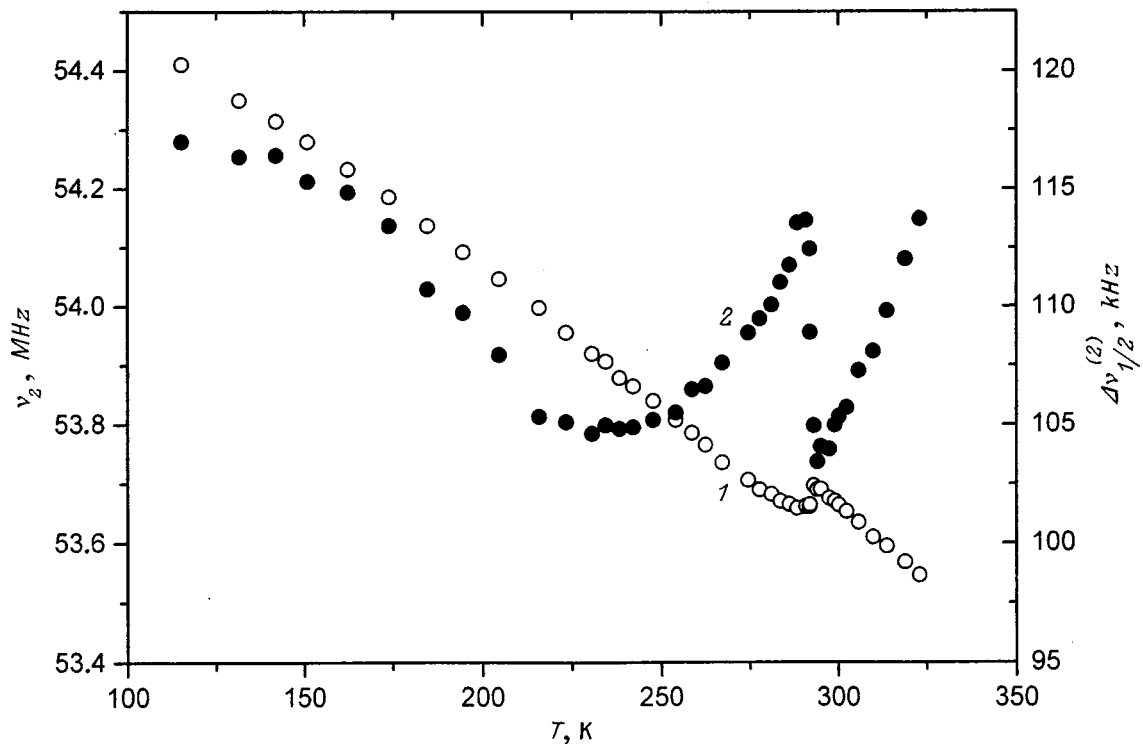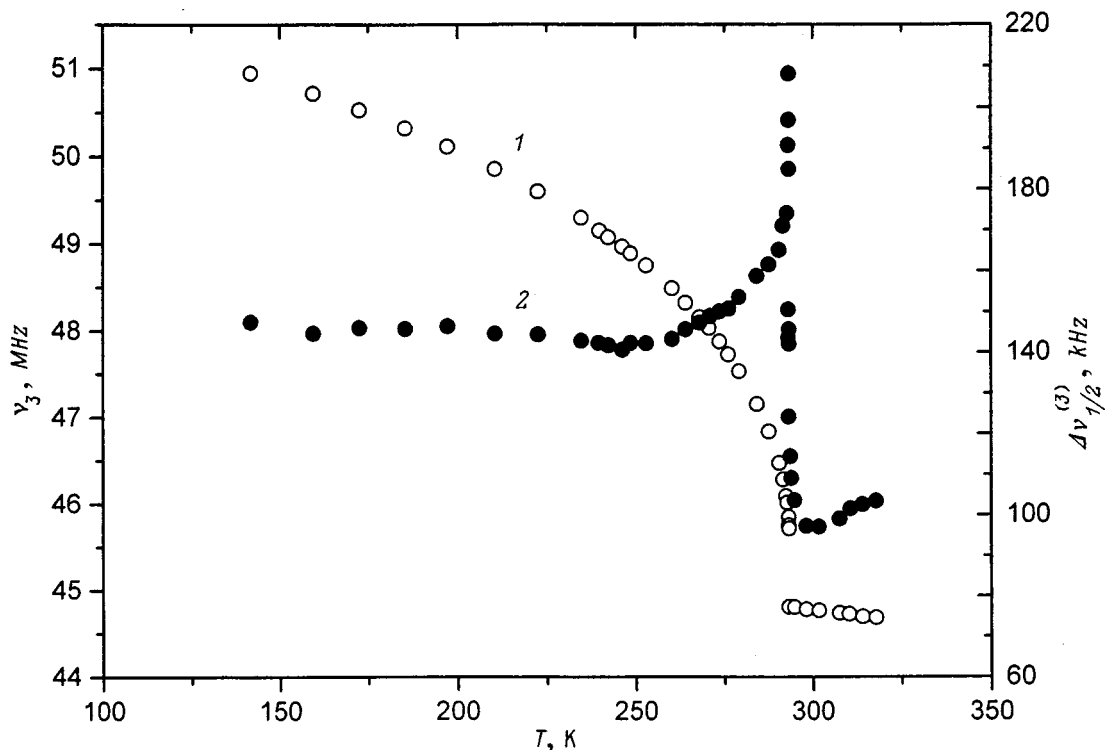
FIG. 3. Temperature dependence of (*1*) ^{123}Sb NQR ν_2 frequency ($\pm 3/2 \rightarrow \pm 5/2$ transition) and (*2*) ^{123}Sb NQR ($\pm 3/2 \rightarrow \pm 5/2$) linewidth $\Delta \nu_{1/2}^{(2)}$ in SbSI.

and torsional motion of molecules, is apparently less significant in the case of SbSI. The distinct anomalies of $\nu(T)$ near T_c are obviously associated with the phase transition. We believe that these anomalies are caused by static distortion of the SbSI rhombic lattice for $T \lesssim T_c$ ($D_{2h}^{16} \rightarrow C_{2v}^{9}$). This static

distortion, which depends on $|T_c - T|$, acts on the principal EFG components and, hence, on the asymmetry parameter η. Note the large difference between the anomalies in $\nu_1(T)$ and $\nu_2(T)$ near T_c, as well as the differences in their behavior below T_c (Fig. 2). This can be explained by the strong

FIG. 4. Temperature dependence of (*1*) ^{121}Sb NQR ν_3 frequency ($\pm 1/2 \rightarrow \pm 3/2$ transition) and (*2*) ^{121}Sb NQR ($\pm 1/2 \rightarrow \pm 3/2$) linewidth $\Delta \nu_{1/2}^{(3)}$ in SbSI.
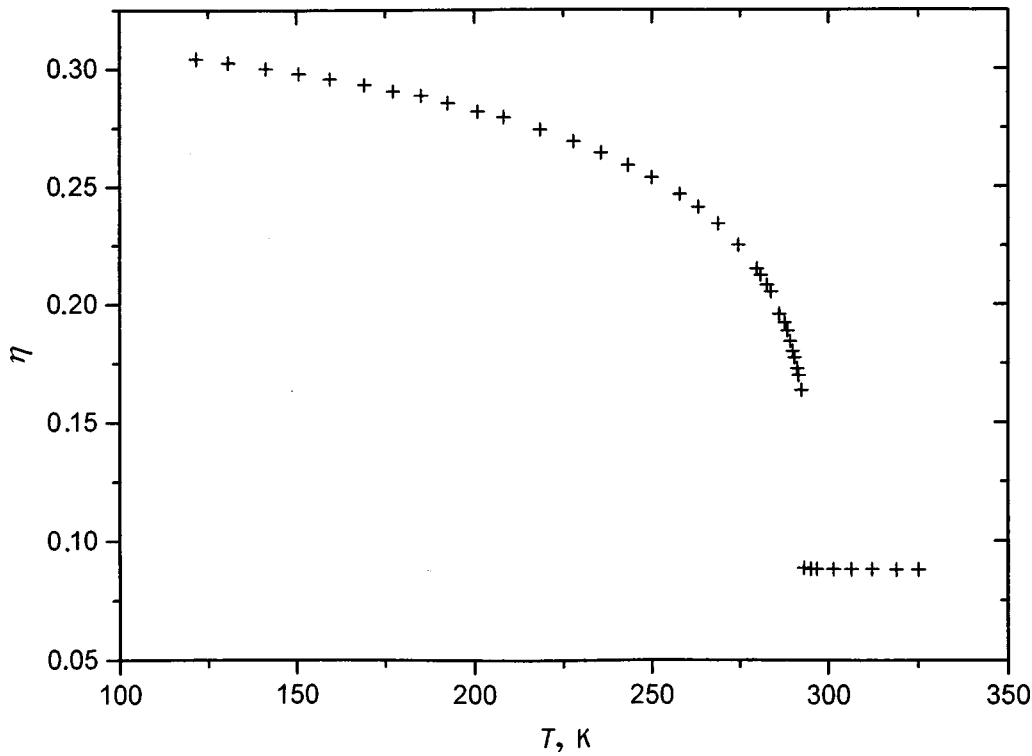
FIG. 5. Temperature dependence of the EFG tensor asymmetry parameter η at the ^{123}Sb nucleus in SbSI.

increase of the asymmetry parameter η (Fig. 5) with variation of local symmetry at the antimony site for $T \leqslant T_c$.[5] The asymmetry parameter was calculated using the secular equation[11] for quadrupole-coupling energy levels for the $I = 7/2$ spin

$$E^4 - 42\left(1 + \frac{\eta^2}{3}\right)E^2 - 64(1 - \eta^2)E + 105\left(1 + \frac{\eta^2}{3}\right)^2 = 0 \tag{3}$$

and the experimental ratio of the frequencies ν_2 and ν_1 for the $\pm 3/2 \rightarrow \pm 5/2$ and $\pm 1/2 \rightarrow \pm 3/2$ transitions in ^{123}Sb, respectively. It is known that as the EFG symmetry changes from axial ($\eta = 0$ for $V_{XX} = V_{YY}$) to off-axial, i.e. the maximally asymmetric ($\eta = 1$ for $V_{XX} = 0$ and $V_{YY} = -V_{ZZ}$), the quadrupole-coupling energy level E_1 ($m = \pm 1/2$) for nuclei with spins $I \geqslant 5/2$ decreases, and the E_2 ($m = \pm 3/2$) level rises.[12] The E_3 ($m = \pm 5/2$) level also rises, but to a lesser extent, and approaches E_2. As a result, the increase in η makes the $\pm 1/2 \rightarrow \pm 3/2$ transition frequency increase, and the $\pm 3/2 \rightarrow \pm 5/2$ frequency, decrease. Note that as η changes from zero to unity, the frequency ratio $\nu(\pm 3/2 \rightarrow \pm 5/2)/\nu(\pm 1/2 \rightarrow \pm 3/2)$ changes from 2 to 0.7. Indeed, as seen from Fig. 6, the pattern of the temperature dependences of the quadrupole coupling levels calculated for ^{123}Sb from Eq. (3) reflects this relationship. The temperature dependences of the principal EFG components V_{ZZ}, V_{YY}, and V_{XX} presented in Fig. 7 complement the general picture, by which the ν_1 frequency in our experiment (Fig. 1) increases with decreasing temperature for $T \leqslant T_c$ both through the increase of V_{ZZ} and by virtue of η, while the behavior of the ν_2 frequency reflects the mutually opposed action of these two factors. The principal components of the EFG created by the

environment of the antimony atom were calculated using the values of η and E_m ($m = 1/2; 3/2; 5/2$) obtained by solving Eq. (3) and the antishielding factor for antimony: $(1 - \gamma_\infty) = 17$ $[q = q_{\text{ext}}(1 - \gamma_\infty)]$. The resonance frequency for the $\pm 1/2 \rightarrow \pm 3/2$ transition can be written in a general form as

$$\nu_1 = (E_{3/2} - E_{1/2})/h \,,$$

and because the quantity E in Eq. (3) is determined through the quadrupole coupling constant e^2qQ in units of $3e^2qQ/4I(2I-1)$,[11] we obtain

$$\nu_1 = \frac{3(E_{3/2} - E_{1/2})e^2qQ}{4I(2I-1)h} \,.$$

Whence, using Eq. (2), we finally come to

$$V_{ZZ} = eq/(1 - \gamma_\infty) = \frac{4I(2I-1)h\nu_1}{51eQ(E_{3/2} - E_{1/2})},$$

$$V_{YY} = -\frac{1}{2}(\eta + 1)V_{ZZ},$$

$$V_{XX} = \frac{1}{2}(\eta - 1)V_{ZZ}.$$

As already mentioned, the V_{ZZ} gradient is directed apparently along the shortest Sb–S bond, which is perpendicular to the c axis (in Fig. 1 this bond is shown with a thicker solid line). Because iodine in SbSI is most probably in a purely ionic state, one may assume the major contribution to the V_{YY} and V_{XX} gradients to be due to the Sb–S bonds forming –S–Sb–S– chains parallel to the c axis of the crystal (Fig. 1). The increase of $|V_{ZZ}|$ and V_{YY}, as well as the decrease of V_{XX} with decreasing temperature for $T \leqslant T_c$ (Fig. 7), accord
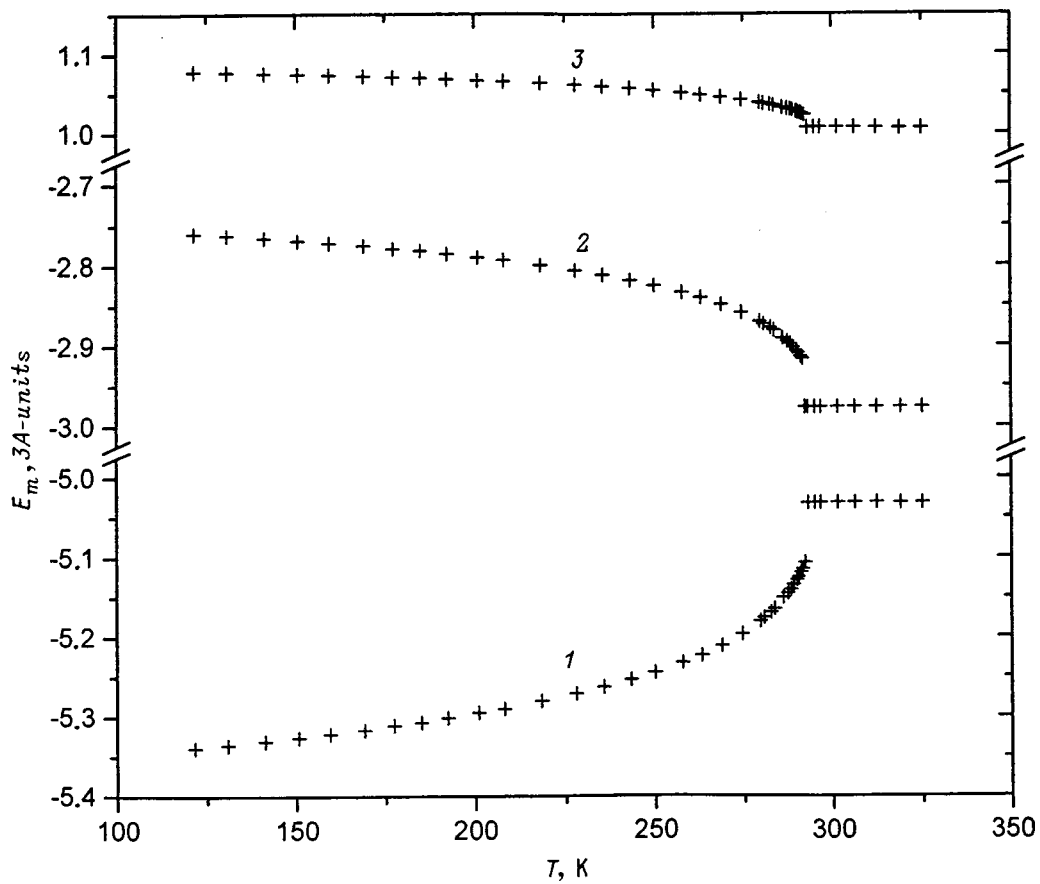
FIG. 6. Temperature dependence of quadrupole-coupling energy levels for ^{123}Sb: $1 — E_{\pm 1/2}$, $2 — E_{\pm 3/2}$, $3 — E_{\pm 5/2}$. Plotted along the vertical axis is $A = e^2 q Q / 4I(2I-1)$.[11]
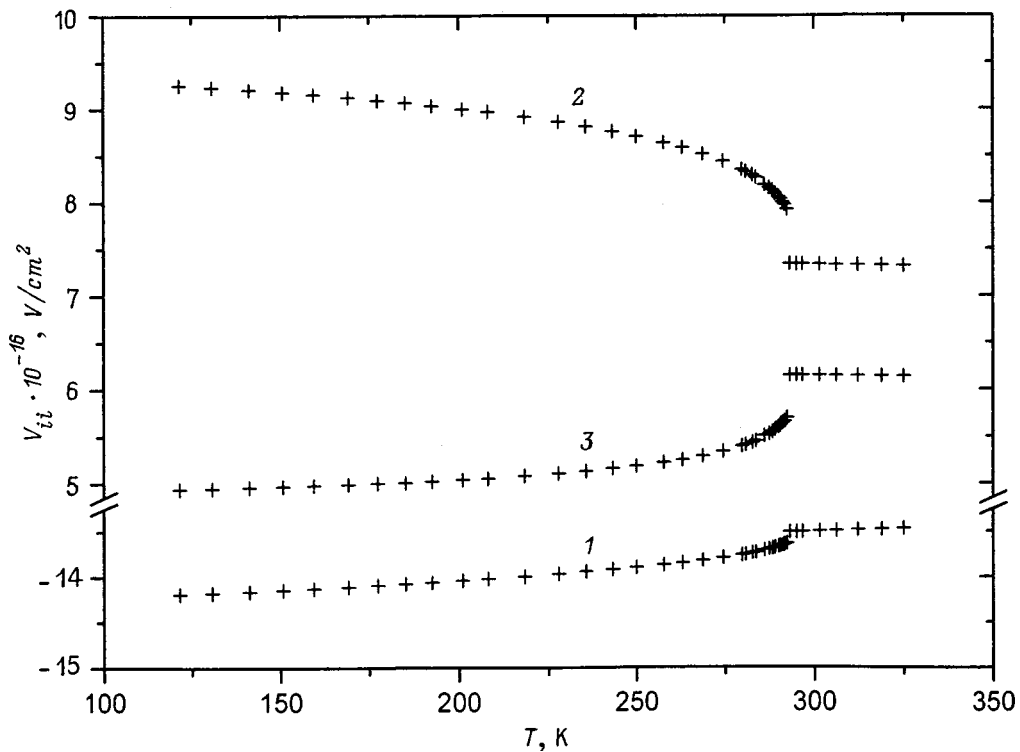

FIG. 7. Temperature dependence of the principal EFG tensor components at the ^{123}Sb nucleus: $1 — V_{ZZ}$, $2 — V_{YY}$, $3 — V_{XX}$.

with x-ray diffraction data obtained[5] for SbSI at $T = 35\,°C$ (in the paraphase) and at $5\,°C$ (in the ferroelectric phase). According to Ref. 5, as the temperature decreases from 35 to $5\,°C$, the Sb–S short bond length decreases ($\Delta L/L \approx -0.68 \times 10^{-2}$), while the other two Sb–S bonds in the –S–Sb–S– chains behave in the opposite manner, namely, one of the bonds shortens ($\Delta L/L \approx -5.75 \times 10^{-2}$), and the other becomes longer ($\Delta L/L \approx 2.57 \times 10^{-2}$). Obviously, the shortening Sb–S bond in the chain is responsible for the increasing gradient, i.e. for V_{YY}, whereas the one growing longer, Sb–S, for V_{XX}. Thus the orientation of the EFG tensor generated by the electric environment of the antimony atom in the SbSI crystal is determined by the direction of antimony chemical bonds with the three sulfur atoms. It should be pointed out that, whereas the direction of the principal axis Z along the shortest Sb–S bond can be specified apparently with sufficiently high probability, the Y and X principal axes do not coincide with the two other Sb–S bonds, while being close to them in direction. This is due to the fact that the three adjoining angles formed by the antimony bonds with the three sulfur atoms are not equal to 90° even in the paraelectric phase of SbSI (one angle is 95.4°, and the other two, 84.8° each,[6] Fig. 1). This is why the EFG tensor asymmetry parameter for $T > T_c$ is not zero but finite ($\eta \approx 0.088$) (Fig. 5), and the V_{YY} and V_{XX} EFG components differ somewhat in magnitude (Fig. 7), despite the corresponding Sb–S bond lengths being equal [2.76 Å (Ref. 6), Fig. 1]. It was not possible to determine more accurately the EFG tensor orientation with respect to the crystallographic axes (from the Zeeman splitting of levels in a magnetic field) because of the disordered directions of a and b axes in the sample used in the measurements.

In the ferroelectric phase of SbSI ($T < T_c$), V_{ZZ} and η are acted upon (i) directly by static atomic displacements originating from lattice instabilities with respect to the soft mode[13] and determined by the order-parameter amplitude $\rho(T_c - T)$, and (ii) by spontaneous ferroelectric lattice strain $\varepsilon(T_c - T)$ appearing for $T < T_c$ ($\varepsilon \propto \rho^2$). As follows from symmetry considerations, both the phase-transition-induced change in the field gradient δV_{ZZ} and the order parameter variation $\delta \eta$ are proportional to ρ^2 and ε. These relations govern to a considerable extent the character of the curves $\nu_1(T)$, $\nu_2(T)$, and $\nu_3(T)$ below T_c. Another factor affecting the temperature dependence of ν_1, ν_2, and ν_3 is the strong anisotropy of thermal expansion of the SbSI lattice for $T \lesssim T_c$.[11] The part played by the already mentioned Bayer averaging of the gradient in the ferroelectric phase of SbSI is still smaller than that in the paraphase, which, generally speaking, is characteristic of ferroelectrics with displacive phase transitions.

The anomalies observed near T_c in the linewidth temperature dependences $\Delta\nu_{1/2}^{(1)}(T)$, $\Delta\nu_{1/2}^{(2)}(T)$, and $\Delta\nu_{1/2}^{(3)}(T)$ (Figs. 2–4) are apparently related to the phase transition. They may be caused by a nonuniform distribution of the static rhombic-lattice distortion induced by the phase transition in the SbSI crystal, which gives rise to a spatial nonuniformity in the phase-transition temperature. The static, or inhomogeneous NQR linewidth is known to be determined by the presence in the crystal of disordered lattice distortions
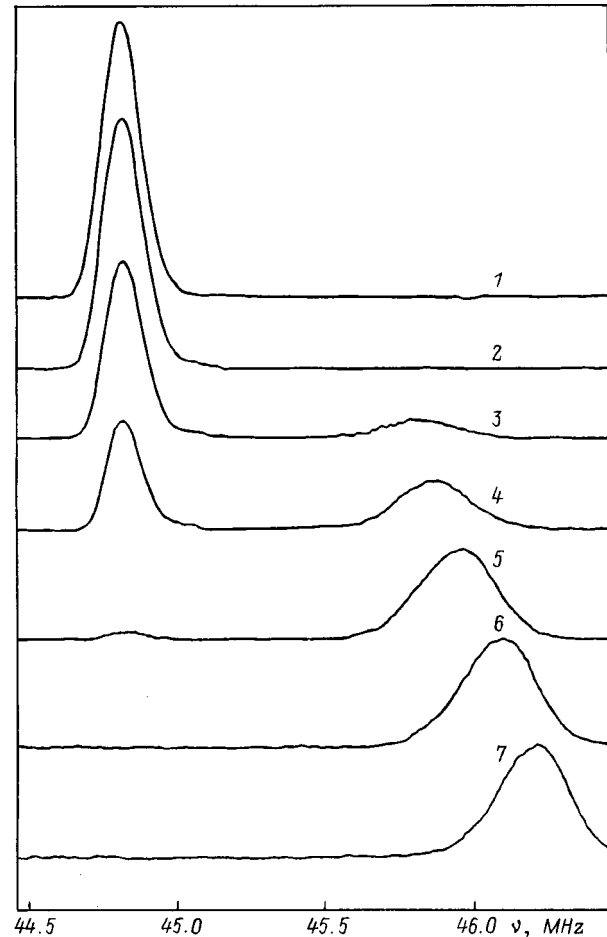

FIG. 8. ^{121}Sb NQR spectrum ($\pm 1/2 \to \pm 3/2$ transition) obtained at different temperatures in the region of the ferroelectric phase transition in the SbSI crystal ($T_c = 293$ K). T(K): 1 — 294.6, 2 — 293.6, 3 — 293.1, 4 — 293.0, 5 — 292.8, 6 — 292.4, 7 — 291.8.

created by point defects, dislocations, and residual stresses, which produce EFG scatter as a result of distorted intramolecular interactions. It is only natural therefore to assume that the nonuniformity in static atom displacements and in spontaneous lattice strain near T_c, which originate from the nonuniform phase-transition temperature distribution, cause a considerable scatter in the field gradient at antimony nuclei, and this is what accounts for the sharp increase in linewidth. The difference between the $\Delta\nu_{1/2}(T)$ anomalies for ν_1 and ν_2 is also obviously associated with different contributions of the change in the asymmetry parameter η to frequency variation.

The doublet structure of the ^{121}Sb NQR ($\pm 1/2 \to \pm 3/2$) line observed within a narrow temperature interval of 292.8–293.1 K (Fig. 8) is obviously associated with the formation of the so-called striated structure[14] in SbSI at the phase transition. This structure is made up of alternating regions of the paraelectric and ferroelectric phases with plane interfaces, which are close in orientation to (101).[14] Macroscopic spatially nonuniform states are known to appear in a number of compounds in structural phase transitions. In most cases, the heterophase structures are irregular. An exception is the calomel crystal (Hg_2Cl_2), whose ferroelastic phase transition ($T_c = 186$ K) gives rise to a regular heterophase

structure causing splitting of the ^{35}Cl NQR line.[8] In contrast to SbSI, however, this splitting is very small ($\Delta\nu \approx 6$ kHz) (the phase transition in Hg$_2$Cl$_2$ is second order and close to the tricritical point) and can be revealed only by the onset of a fine structure in the spin echo in the form of beats.[8]

The general pattern of the antimony NQR line evolution displayed in Fig. 8 reflects the phase-transition kinetics in SbSI: As the temperature decreases, the line corresponding to the paraelectric state of the crystal gradually dies out, and that due to the ferroelectric state grows in strength. As seen from Fig. 8, the temperature interval within which one observes the doublet line is about 0.3 K wide, which accords with literature data on the optical observation[14] of a striated structure in SbSI. According to Ref. 14, the phase transition in SbSI gives rise to nucleation of regions of a new phase, which grows with changing temperature until, at a certain temperature, the crystal splits up into alternating dark and bright bands with plane phase boundaries. This phenomenon is observed within a temperature interval of 0.5 K.

Modern concepts relate the phase-transition-induced formation of large-scale heterophase structures in solids to the fluctuation mechanism for nucleation of a nonsymmetric phase in the vicinity of the tricritical point.

The author owes sincere gratitude to V. V. Lemanov for fruitful discussions.

[1] S. N. Popov, N. N. Kraĭnik, and I. E. Myl'nikova, Izv. Akad. Nauk SSSR, Ser. Fiz. **33**, 271 (1969); S. N. Popov, N. N. Kraĭnik, and I. E. Mylnikova, in *Proceedings of the Second International Meeting on Ferroelectricity* (Kyoto, 1969), J. Phys. Soc. Jpn. **28**, Suppl. 120 (1970).

[2] E. Fatuzzo, G. Harbeke, W. J. Merz, R. Nitsche, H. Roetschi, and W. Ruppel, Phys. Rev. **127**, 2036 (1962).

[3] E. Dönges, Z. Anorg. Allg. Chem. **263**, 112 (1950).

[4] R. Arndt and A. Niggli, Naturwissenschaften **51**, 158 (1964).

[5] A. Kikuchi, Y. Oka, and E. Sawaguchi, J. Phys. Soc. Jpn. **23**, 337 (1967).

[6] Y. Yamada and H. Chihara, J. Phys. Soc. Jpn. **21**, 2085 (1966).

[7] T. A. Khimich, V. F. Belov, O. K. Zhukov, V. A. Yurin, L. N. Korablin, M. N. Shipko, A. N. Lobachev, and V. I. Popolitov, Fiz. Tverd. Tela (Leningrad) **13**, 1507 (1971) [Sov. Phys. Solid State **13**, 1265 (1971)].

[8] S. N. Popov, Fiz. Tverd. Tela (St. Petersburg) **39**, 1287 (1997) [Phys. Solid State **39**, 1143 (1997)].

[9] S. N. Popov and N. N. Kraĭnik, Fiz. Tverd. Tela (Leningrad) **12**, 3022 (1970) [Sov. Phys. Solid State **12**, 2440 (1970)]; G. A. Smolenskii, N. N. Krainik, and S. N. Popov, ''Some phenomena in crystals lacking an inversion center,'' Sov. Sci. Rev. Phys. A. **6**, 261 (1985).

[10] A. V. Gomonnaĭ, B. M. Koperles, I. I. Groshik, and M. I. Gurzan, Fiz. Tverd. Tela (Leningrad) **22**, 930 (1980) [Sov. Phys. Solid State **22**, 546 (1980)].

[11] T. P. Das and E. L. Hahn, Solid State Phys., Suppl. 1 (1958).

[12] M. H. Cohen, Phys. Rev. **96**, 1278 (1954).

[13] M. K. Teng, M. Balkanski, and M. Massot, Phys. Rev. B **5**, 1031 (1972).

[14] S. Kawada and M. Ida, J. Phys. Soc. Jpn. **20**, 1287 (1965).

Translated by G. Skrebtsov

Effect of negative chemical pressure on some displacive-type ferroelectrics

S. V. Baryshnikov, É. V. Bursian, and V. V. Kazakov

Russian State Pedagogical University, 191186 St. Petersburg, Russia
(Submitted October 12, 1998; resubmitted December 21, 1998)
Fiz. Tverd. Tela (St. Petersburg) **41**, 1293–1296 (July 1999)

The effect of embedded helium on the phase-transition temperature and properties of displacive-type ferroelectrics has been studied. It is shown that helium embedded in crystals produces an effect opposite to that of hydrostatic pressure, namely, the temperatures of the ferroelectric phase transitions increase, and those of the antiferroelectric ones, decrease. © *1999 American Institute of Physics.* [S1063-7834(99)03507-8]

When a solid is bombarded by helium ions, helium penetrates into the solid, and, because of their small radius ($r_{atom}=0.291$ Å, Ref. 1), helium atoms can migrate at high temperatures throughout the crystal lattice, to end up distributed fairly uniformly throughout the volume. This entails a change in the physical properties of the crystals,[2–4] in particular, their melting point decreases, the chemical activity increases, and the superconducting transition temperatures change. It was shown that an increase in the concentration of substitutional helium can decrease the binding energy.[2]

We proposed a method of helium incorporation in ferroelectric crystals and showed that the dissolved helium causes an increase of the lattice constant, which can be interpreted as ''negative'' pressure.[5,6] The effect of hydrostatic pressure reducing interatomic distances on the ferroelectric characteristics (spontaneous polarization, dielectric permittivity, and phase-transition temperature) has been studied in considerable detail.[7,8] At the same time information on the variation of ferroelectric properties induced by an increase of the lattice constants is practically lacking. In this connection it appears of interest to follow the variation of the properties of ferroelectric crystals under incorporation of helium.

This communication summarizes the results of a study of the effect of embedded helium on the ferroelectric properties of various crystals, namely, a typical ferroelectric $BaTiO_3$, a paraelectric $SrTiO_3$, an antiferroelectric $NaNbO_3$, and a layered ferroelectric $Sr_2Ta_2O_7$.

Helium was incorporated in an ac discharge. The field in the chamber was 1–2 kV/cm, and the gas pressure was maintained within the 1–10-Pa range. To increase the diffusion coefficient, the samples were heated to 950–1150 K, depending on the type of the crystal. The samples chosen for the studies were platelets, 100–200 μm thick, which ensured a sufficiently uniform distribution of incorporated helium across the sample. The phase-transition temperatures were determined from the maximum in the dielectric permittivity. The transition types referred to below are always denoted in the order of decreasing temperature (the PE–FE notation means that the low-temperature phase is the ferroelectric).

Barium titanate. Following a one-hour long treatment by the above technique carried out at $T=1150$ K, the crystals acquired a greenish color, which transformed to gray-green after two hours of the treatment. After incorporation of helium, the transition temperature of $BaTiO_3$ from the cubic to tetragonal phase (PE–FE) increases.

For barium titanate, the distribution uniformity of embedded helium with depth was studied in the following way. The transition temperature in the sample with helium and a reference sample was determined from observation of the domain structure in a polarizing microscope. When heated, the reference crystal became opaque when viewed under crossed polarizers at a temperature lower by 3–5 K than that for the helium-loaded samples. After this, the sample was thinned on both sides, and the measurements were repeated. The thinning was performed in two ways, by grinding and chemical etching with orthophosphoric acid. Table I lists the transition temperatures of a helium-loaded $BaTiO_3$ sample as a function of sample thickness. It is seen that the phase-transition temperature of $BaTiO_3$:He changes with removal of surface layers by not more than a few tenths of a degree, which implies that the crystals are quite uniform.

The magnitude of the temperature shift depends on the sample treatment chosen. The maximum shift obtained in the experiments is 15 K. The transition temperature from the tetragonal to rhombic phase also increases, while the transition to the rhombohedral phase occurs at a lower temperature. The Curie-Weiss temperature decreases very little, and the temperature hysteresis of the upper phase transition increases from 2 to 8 K. Table II compares the phase-transition temperatures for one of the samples (the data are for $BaTiO_3+0.2$ at.%Fe crystals, and therefore the phase-transition temperatures for the starting sample differ somewhat from those quoted in the literature). Attempts at increasing the concentration of embedded helium still more by raising the temperature and time of bombardment failed because of a dramatic deterioration in the quality of the samples, which became brittle, opaque, and conducting.

After multiple heating of helium-loaded samples in air, the PE–FE transition temperature decreased, which can be explained by helium escaping from the crystal. Note that, in the initial stage, helium evolves from the crystal fairly fast, so that heating for an hour at 520–570 K reduces the transition temperature by about 5–6 K. Thereafter the process slows down and the properties of the crystal do not change for a long time. (At room temperature, the characteristics of

TABLE I. Effect of gradual thinning of a $BaTiO_3$:He crystal on the phase-transition temperature.

	Starting sample	He-loaded sample				
d (μm)	180	180	125	80	50	30
T_{tr} K	390.2	394.8	394.5	394.1	394.0	394.0

the reference sample recovered their original values only in four years.)

X-ray diffraction measurements of the room-temperature parameters of the barium titanate tetragonal lattice yielded the following results. The parameters of the starting sample: $c = 4.019$ Å, $a = 3.984$ Å. The parameters of the helium-loaded sample: $c = 4.023$ Å, $a = 3.985$ Å. The data are averaged over a set of samples grown in the same melt (here and subsequently, the measurement error $\delta \sim 0.001$ Å.) Assuming the lattice expansion to result from a ''negative'' pressure and using the available data[7] on $BaTiO_3$ compressibility, the negative pressure generated by helium can be estimated as 1–1.5 kbar.

Interpretation of the results meets with certain difficulties, because helium ions, depending on their energy, are capable of knocking one of the lattice atoms out to occupy the now vacant site or filling available vacancies and interstices. Considering the accelerating voltages used (~ 10 kV), the knocking out of lattice atoms by helium ions is hardly probable. This statement is supported by data[3] available on metals. According to Ref. 9, interstitial helium generates internal compressive stress and, therefore, helium atoms occupy most likely the vacancies. One could suggest the following mechanism of vacancy formation in $BaTiO_3$. Because the crystals subjected to helium bombardment are kept for a long time at a high temperature and reduced pressure, this is believed[10] to entail partial loss of oxygen. Apparently helium occupies the sites of the evolved oxygen. Note that one vacancy can be filled by more than one helium atom.[11,12] The lattice parameters can increase as a result of formation of $He_m V_n$ helium-vacancy complexes in the crystal.[9] The energy required to detach a vacancy or a helium atom from the complex depends on the relation between m and n and reaches a maximum for $m = n = 1$. The HeV complex possesses the highest stability against thermal and mechanical stresses, and this may account for the decline in helium escape with time.

The increase in the PE–FE transition temperature can be explained within the dynamical theory in the following way. The effective force constant determining the soft-mode frequency depends on the difference between the short-range

TABLE II. Phase-transition temperatures for $BaTiO_3$.

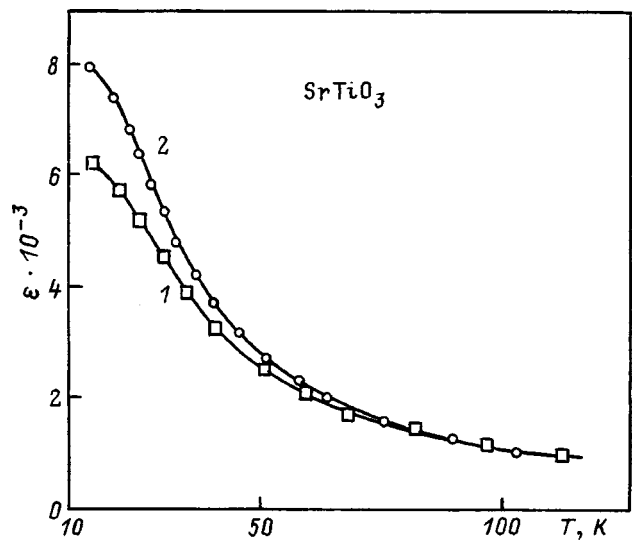| Crystal	T_{tr} (K) (Trigonal-rhombic)	T_{tr} (K) (Rhombic-tetragonal)	T_{tr} (K) (Tetragonal-cubic)
Starting	176	270	380
Helium-loaded	174	273	393

FIG. 1. $\varepsilon(T)$ relation for $SrTiO_3$. *1* — Starting sample, *2* — helium-loaded sample.

restoring and the long-range Coulomb forces: $\omega_{TO}^2 \sim (F_{sr} - F_{coul})$. In normal dielectrics, F_{sr} exceeds by a few times F_{coul}, and this is what accounts for the stability. The stability of a lattice TO vibration can fail if $F_{sr} \lesssim F_{coul}$, and this may occur either if F_{sr} has anomalously decreased, or if F_{coul} has anomalously increased.

The increase in unit-cell volume induced by He incorporation brings about apparently a faster falloff in the short-range forces compared to Coulomb forces, so that their difference decreases.

Strontium titanate is a paraelectric. It does not undergo a transition to the ferroelectric phase down to 0 K and, therefore, one estimated for it only the change in the Curie–Weiss temperature. Figure 1 presents temperature dependences of the dielectric permittivity of pure strontium titanate and of a sample with helium incorporated into it at 1070 K. The graphs show the dielectric permittivity to be higher for the helium-loaded sample.

Using the relation

$$\varepsilon = \frac{C}{(\Theta_1/2)\coth(\Theta_1/2T) - T_C}$$

for the starting $SrTiO_3$ crystal with the parameters $\Theta = 80$ K, $T_C = 27$ K, and $C = 0.84 \times 10^5$ K (Ref. 13), followed by a least-squares procedure, yields 3–4 K for the increase of the Curie-Weiss temperature. The room-temperature cubic-lattice parameter derived from the x-ray measurements increases accordingly from 3.906 to 3.908 Å.

Sodium niobate is of interest because, by the rule of Samara,[8] pressure shifts the phase-transition temperature in an antiferroelectric in the direction opposite to that in ferroelectrics. Therefore, if one accepts the concept of negative pressure, incorporation of helium in antiferroelectrics should reduce the transition temperature.

We studied the transition at 623 K (the transition under cooling from the nonpolar to antiferroelectric phase). Incorporation of helium reduces the temperature of the observed maximum in dielectric permittivity down to 615 K. Interpre-
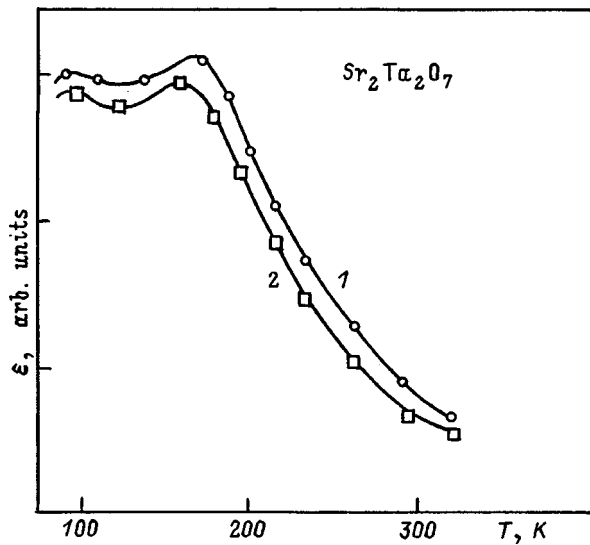
FIG. 2. $\varepsilon(T)$ relation for $Sr_2Ta_2O_7$. *1* — Starting sample, *2* — helium-loaded sample.

tation of this phenomenon meets, however, with difficulties. The actual type of the transition has not been established reliably. The change in the cell volume ν is very small. According to Ref. 14, below the transition ν is slightly smaller than before it, while by Ref. 15 it is somewhat larger. In both cases, however, this difference is within measurement error. Besides, this transition lies close to the transition at 743 K, in which the cell volume undergoes a noticeable decrease upon cooling.

It appears intuitively that the cell volume should increase upon cooling from the para- to ferroelectric phase, because the expansion along the *c* axis is not fully compensated by the contraction in the direction of the *a* axis so that, when cooled to the antiferroelectric phase, the volume should decrease (antiparallel polarization in adjacent cells results in tighter packing). Viewed from the standpoint of microscopic theory, oscillation condensation at the center and edge of the Brillouin zone should also produce opposite results.

If this is so, then our observations agree with both the Samara rule and the thermodynamic relation of Clausius–Mosotti, by which the increments dp and dT_{tr} for $\nu_{low} < \nu_{up}$ should have the same signs, so that generation of negative chemical pressure should induce a decrease in the transition temperature. The above reasoning naturally requires further refinement.

Strontium tantalate is of interest because it is an exception to the Samara rule.[16] The reason for the exception may lie either in the layered structure of the crystal (hydro-

static pressure can be identified effectively with uniaxial compression) or in a transition to the ferroelectric state from an intermediate phase with a superstructure.

Incorporation of helium into $Sr_2Ta_2O_7$ was carried out at 1250 K. The crystal takes on a yellowish color and the conductivity increases, but by not more than an order of magnitude. As seen from the temperature dependence of dielectric permittivity in samples without and with helium in Fig. 2, loading with helium reduces the ferroelectric phase-transition temperature by 7–10 K. Annealing the samples in air at ~850 K restores the phase-transition temperature to its original value. X-ray diffraction measurements showed that the interlayer spacing, i.e. the *b* parameter, undergoes the largest change under helium incorporation in the $Sr_2Ta_2O_7$ layered ferroelectric; it is $b = 27.075$ Å in helium-loaded samples, as compared to $b = 26.997$ Å in the reference samples.

Thus incorporation of helium apparently results in a phase-transition temperature shift opposite to that induced by application of hydrostatic pressure.

[1] M. M. Protod'yakonov and I. L. Gerlovin, *The Electronic Structure and Physical Properties of Crystals* [in Russian] (Nauka, Moscow, 1975), p. 201.
[2] R. Manzke and M. Compagna, Solid State Commun. **39**, 313 (1981).
[3] D. W. Palmer, *From Idea to Application (Some Selected Nuclear Techniques in Research and Development)* (IAEA, Vienna, 1979).
[4] A. V. Khudyakov, available from VINITI, No. 3904-78 (1978).
[5] S. V. Baryshnikov, É. V. Bursian, and V. V. Kazakov, *Abstracts of the Far-Eastern School-Seminar on the Physics and Chemistry of the Solid State* (DVNTs AN SSSR, Blagoveshchensk, 1985), p. 49.
[6] V. V. Kazakov, S. V. Baryshnikov, A. V. Ruzhnikov, and R. M. Rakhmankulov, Izv. Akad. Nauk SSSR, Ser. Fiz. **47**, 736 (1983).
[7] G. A. Samara, J. Phys. Soc. Jpn. **28**, 399 (1970).
[8] G. A. Samara and P. S. Peercy, Solid State Phys., Adv. Res. Appl. **36**, 1 (1981).
[9] A. V. Khudyakov, *Abstracts of the Far-Eastern School-Seminar on the Physics and Chemistry of the Solid State* (DVNTs AN SSSR, Blagoveshchensk, 1985), p. 17.
[10] É. V. Bursian, *Nonlinear Crystal. Barium Titanate* [in Russian] (Nauka, Moscow, 1974), p. 247.
[11] R. Vassen, H. Trinkaus, and P. Jang, Phys. Rev. B **44**, 4206 (1991).
[12] V. V. Kirsanov and A. M. Orlov, Usp. Fiz. Nauk **142**, No. 2, 219 (1984) [Sov. Phys. Usp. **27**, 106 (1984)].
[13] E. Hegenbarth, Phys. Status Solidi **2**, 1544 (1962).
[14] G. Shirane, R. Newnham, and R. Pepinsky, Phys. Rev. **96**, 581 (1954).
[15] S. P. Solov'ev, Yu. N. Venevtsev, and G. S. Zhdanov, Kristallografiya **6**, 218 (1961) [Sov. Phys. Crystallogr. **6**, 171 (1961).
[16] V. V. Kazakov, R. M. Rakhmankulov, Yu. P. Udalov, A. V. Ruzhnikov, and É. V. Bursian, Fiz. Tverd. Tela (Leningrad) **23**, 3449 (1981) [Sov. Phys. Solid State **23**, 2004 (1981)].

Translated by G. Skrebtsov

LATTICE DYNAMICS. PHASE TRANSITIONS

Lattice dynamics of a Rb$_2$KScF$_6$ crystal in unstable cubic and tetragonal phases and in a stable monoclinic phase

V. I. Zinenko[*)] and N. G. Zamkova

L. V. Kirenskiĭ Institute of Physics, Siberian Branch of the Russian Academy of Sciences,
660036 Krasnoyarsk, Russia

The results of a nonempirical calculation of the static and dynamic properties of a Rb$_2$KScF$_6$ crystal with elpasolite structure in cubic, tetragonal, and monoclinic phases are presented. The calculation is performed on the basis of a microscopic model of an ionic crystal that takes account of the deformability and polarizability of the ions. The deformability parameters of the ions are determined from the condition that the total energy of the crystal is minimum. The computational results for the equilibrium lattice parameters are in satisfactory agreement with experimental data. Unstable vibrational modes are found in the vibrational spectrum of the lattice in the cubic and tetragonal phases. These modes occupy the phase space throughout the entire Brillouin zone. The characteristic vectors of the most unstable mode at the center of the Brillouin zone of the cubic phase are related to the displacements of the fluorine ions and correspond to rotation of ScF$_6$ octahedra. Condensation of this mode leads to a tetragonal distortion of the structure. In the tetragonal phase the most unstable mode belongs to the boundary point of the Brillouin zone and condensation of this mode leads to monoclinic distortion with doubling of the unit-cell volume. In the monoclinic phase unstable modes are absent in the vibrational spectrum of the lattice. © *1999 American Institute of Physics.*
[S1063-7834(99)03607-2]

Halides A$_2$BB^{3+}X$_6$ having the elpasolite structure undergo very diverse structural phase transitions associated with the lattice instability of the high-symmetry cubic phase. Uniform nonpolar distortions of the crystal lattice and distortions accompanied by a change in the unit-cell volume of the crystal are observed in the low-temperature phases in these compounds. Structural distortions in most crystals in this family are associated either with the locations of B^{3+}X$_6$ octahedra or a combination of rotations of octahedra and displacements of the A ions.

The instability of a crystal lattice with respect to normal vibrations, corresponding to rotations of octahedra, is apparently a characteristic feature of perovskite-like compounds. In most halides, and in some oxide crystals with perovskite structure, such an instability leads to structural phase transitions in low-symmetry phases with an increase in the unit-cell volume as compared to the volume of the initial cubic phase. The problem of structural instability of perovskite with respect to the ferroelectric lattice vibrational mode and with respect to the vibrational mode associated with rotations of octahedra has been under discussion in experimental and theoretical investigations for several decades now. In the last few years there have appeared many works wherein the phonon frequencies are calculated in one or another approach on the basis of first-principles density functional method for many members of the perovskite family and attempts have been made to understand the nature of this instability.

Virtually no calculations of the phonon spectrum of the crystal have been performed for crystals with elpasolite structure. At the same time these crystals are being intensively investigated by various experimental methods, and there now exist data on the structures of the low-symmetry phases, the physical properties, and the changes in the lattice at phase transitions, for many crystals in this family (see, for example, the recent review in Ref. 1).

Rb$_2$KScF$_6$ belongs to the elpasolite family and its crystal structure in the high-symmetry phase is cubic with space group $Fm3m$ and one molecule per unit cell (Fig. 1). As the temperature decreases, Rb$_2$KScF$_6$ undergoes two successive structural phase transitions: at $T_{c1} = 250$ K to the tetragonal phase with space group $I4/m$ with no change of the cell volume as compared to the volume of the cubic phase and into the monoclinic phase at $T_{c2} = 220$ K with space group $P12_1/n1$ and two molecules per unit cell. Structural investigations of low-symmetry phases[2] show that the distortions of the cubic structure in the tetragonal phase are mainly due to rotations of ScF$_6$ octahedra; these rotations are uniform throughout the entire volume of the crystal. Distortions in the low-temperature monoclinic phase are related to nonuniform rotations of ScF$_6$ octahedra and to displacements of rubidium ions from positions of equilibrium in the tetragonal phase.

Our objectives in the present work are to calculate, from first principles, the equilibrium volume, the total spectrum of lattice vibrations, and the high-frequency permittivity in
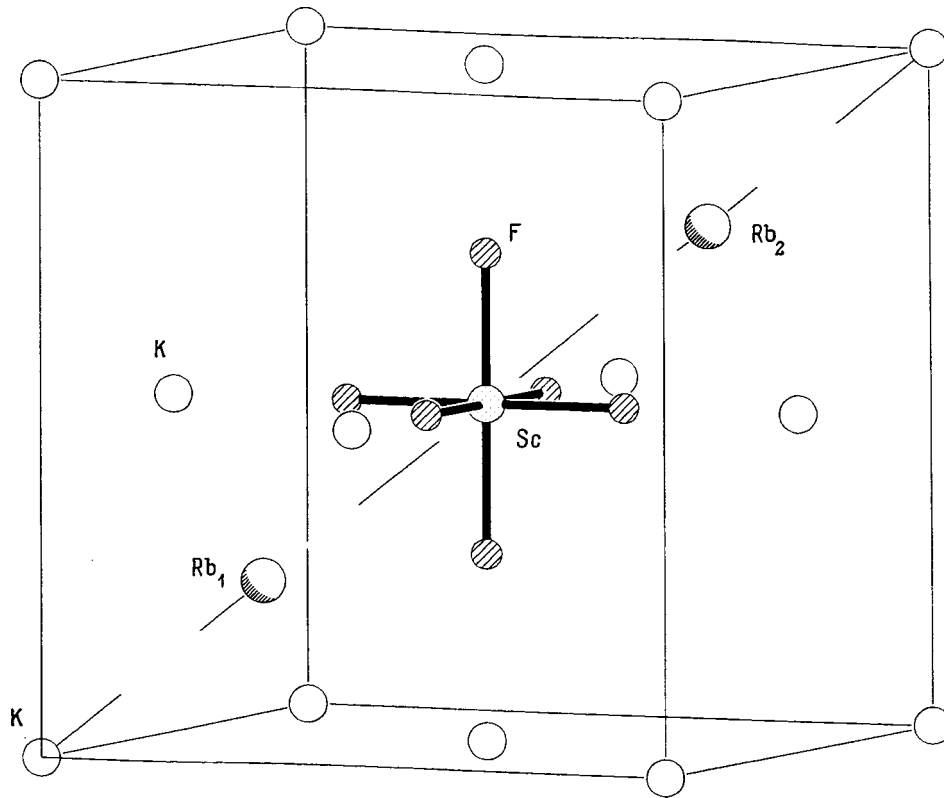
FIG. 1. Crystal structure of Rb_2KScF_6 in the cubic phase. One molecule and the face-centered K lattice are shown.

Rb_2KScF_6 crystals in unstable cubic and tetragonal phases and in the stable monoclinic phase, on the basis of the generalized Gordon–Kim model proposed by Ivanov and Maksimov.[3]

   The model and computational method for calculating the frequencies of the normal lattice vibrations and the high-frequency permittivity are presented in Sec. 1. The computational results and their discussion are presented in Sec. 2.

1. MODEL. COMPUTATIONAL METHOD

   The model proposed by Ivanov and Maksimov[3] for an ionic crystal, taking account of the polarizability of the ions, is used to calculate the phoon frequency spectrum of Rb_2KScF_6. In this model the ionic crystal is modeled by individual, overlapping, spherically symmetric ions. The total electron density of the crystal is written as

$$\rho(\mathbf{r}) = \sum_i \rho_i(\mathbf{r} - \mathbf{R}_i),$$

where the summation extends over all ions in the crystal.

   The total energy of the crystal in the density functional method, taking account of only a pair interaction, has the form

$$E_{cr} = \frac{1}{2} \sum_{i \neq j} \frac{Z_i Z_j}{|\mathbf{R}_i - \mathbf{R}_j|} + Z_i E_i^{self}(R_w^i)$$

$$+ \frac{1}{2} \sum_{i \neq j} \Phi_{ij}(R_w^i, R_w^j, |\mathbf{R}_i - \mathbf{R}_j|), \tag{1}$$

where Z_i is the charge of the i-th ion,

$$\Phi_{ij}(R_w^i, R_w^j, |\mathbf{R}_i - \mathbf{R}_j|) = E\{\rho_i(\mathbf{r} - \mathbf{R}_i) + \rho_j(\mathbf{r} - \mathbf{R}_j)\}$$

$$- E\{\rho(\mathbf{r} - \mathbf{R}_i)\} - E\{\rho(\mathbf{r} - \mathbf{R}_j)\}, \tag{2}$$

the energy $E\{\rho\}$ is calculated by the density functional method[4] using a local approximation for the kinetic and
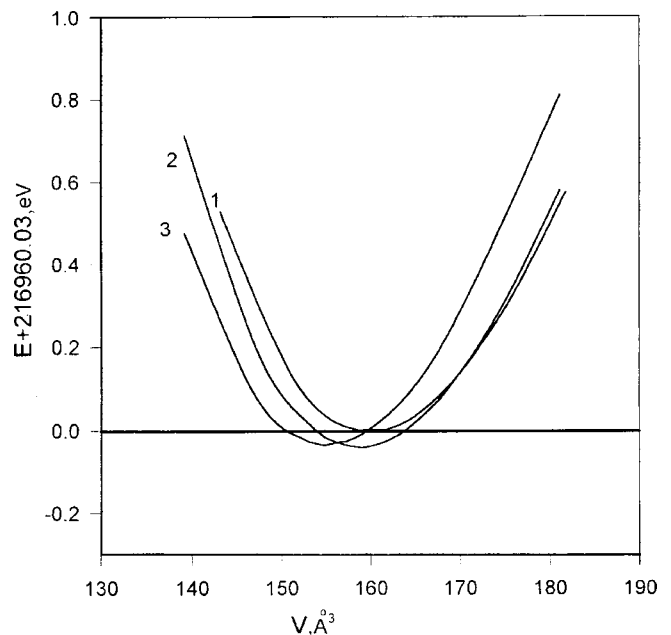

FIG. 2. Total energy (per molecule) of Rb_2KScF_6 versus the volume. Curve 1 — cubic phase, curve 2 — tetragonal phase, curve 3 — monoclinic phase.

TABLE I. The equilibrium values of the lattice parameters.

Phase	Space group	a, Å Calculation	a, Å Experiment	b, Å Calculation	b, Å Experiment	c, Å Calculation	c, Å Experiment
Cubic	$Fm3m$	8.60	9.02	8.60	9.02	8.60	9.02
Tetragonal	$I4/m$	6.08	6.37	6.08	6.37	8.60	9.00
Monoclinic	$P12_1/n1$	6.03	6.36	6.03	6.36	8.52	8.99

Note. Experimental values from Ref. 2.

exchange-correlation energies, and $E_i^{\mathrm{self}}(R_w^i)$ is the self-energy of an ion. The electronic energy and the self-energy of an individual ion are calculated taking account of the crystal potential approximated by a charged sphere (Watson sphere)

$$v(r) = \begin{cases} Z^{\mathrm{ion}_i}/R_w & r < R_w, \\ Z_i^{\mathrm{ion}}/r & r > R_w, \end{cases} \qquad (3)$$

where R_w is the radius of the Watson sphere. The radii R_w^i of the spheres at individual ions are determined so as to minimize the total energy of the crystal.

To calculate the lattice dynamics, terms describing energy changes caused by displacements of the ions from their equilibrium positions must be added to the crystal energy (2). An expression for the dynamical matrix taking account of the electronic polarizability of the ions and the ''breathing'' of an ion in the crystal environment for crystals of arbitrary symmetry is given in Ref. 5. The results of a group-theoretic analysis of the phonon spectrum of crystals having the elpasolite structure are also presented there. We employ the results in Ref. 5 to calculate the vibrational frequencies of the Rb_2KScF_6 lattice and their symmetry classification.

The Coulomb contribution to the dynamical matrix was calculated by Ewald's method. The calculation of an ion was performed using Liberman's program,[6] and the pair interaction energy (3) and polarizability of an ion were calculated using the Ivanov–Maksimov program,[3] the Thomas–Fermi approximation for the kinetic energy, and the Hedin–Lundqvist approximation for the exchange correlation energy. The technique of approximating the energy dependences on the distances **R** and the potentials v of the Watson

sphere were used to calculate the derivatives appearing in the dynamical matrix. Chebyshev polynomials were used for the approximations.[3]

2. RESULTS AND DISCUSSION

In this section the computational results for the total energy, the equilibrium volume, and the phonon spectra of Rb_2KScF_6 in three phases are presented.

2.1. Cubic phase

The equilibrium lattice parameter was determined from the minimum in the volume dependence of the total energy of the crystal (Fig. 2). The lattice parameters together with the experimental values are presented in Table I. It is evident from Table I that the computed values of the lattice parameters (for cubic and tetragonal and monoclinic phases) agree to within 5% with the experimental data. The radii of the Watson spheres found for the ions Rb^+, K^+, and F^- by minimizing the total energy are 2.5, 2.5, and 2.625 a.u., respectively. The Sc^{3+} ion was calculated without a Watson sphere, since our calculations for the cubic phase show that the radii of the scandium ion in a Watson sphere and in the free state are virtually identical. Table II gives the computed polarizabilities of the ions, the high-frequency permittivity, and the dynamic ion charges in an Rb_2KScF_6 crystal.

The computed dispersion curves of the phonon frequencies of Rb_2KScF_6 in the cubic phase are shown in Fig. 3, and the limiting phonon frequencies ($\mathbf{q}=0$) are presented in Table III. Table III table also gives the experimental values

TABLE II. The polarizabilities of the ions, the high-frequency permittivity, and the dynamic charges.

Atom	Cubic $\varepsilon_\infty = 1.91$ α, Å³	Z_{xx}	Z_{yy}	Z_{zz}	Tetragonal $\varepsilon_\infty^{xx}=1.92$, $\varepsilon_\infty^{zz}=1.95$ α, Å³	Z_{xx}	Z_{yy}	Z_{zz}	Monoclinic* $\varepsilon_\infty^{xx}=1.94$, $\varepsilon_\infty^{yy}=1.93$, $\varepsilon_\infty^{zz}=1.94$ α, Å³	Z_{xx}	Z_{yy}	Z_{zz}
Rb	1.35	1.27	1.27	1.27	1.35	1.25	1.25	1.31	1.35	1.01	1.01	1.01
K	0.78	1.21	1.21	1.21	0.78	1.20	1.20	1.21	0.78	1.02	1.02	1.02
Sc	0.29	3.30	3.30	3.30	0.29	3.25	3.25	3.32	0.29	3.0	3.0	3.0
F_1	0.79	−0.97	−0.97	−1.58	0.81	−0.96	−0.96	−1.60	0.81	−0.93	−0.93	−1.16
										−0.94	−0.94	−1.03
F_2	0.79	−0.97	−1.58	−0.97	0.81	−1.33	−1.18	−0.99	0.81	−1.08	−1.02	−0.93
										−1.02	−1.08	−0.93
F_3	0.79	−1.58	−0.97	−0.97	0.81	−1.18	−1.33	−0.99	0.79	−1.02	−1.08	−0.98
										−1.08	−1.02	−0.98

*In the monoclinic phase the dynamic charges of the fluorine ions belonging to different octahedra in the unit cell are different; this is reflected in the table.
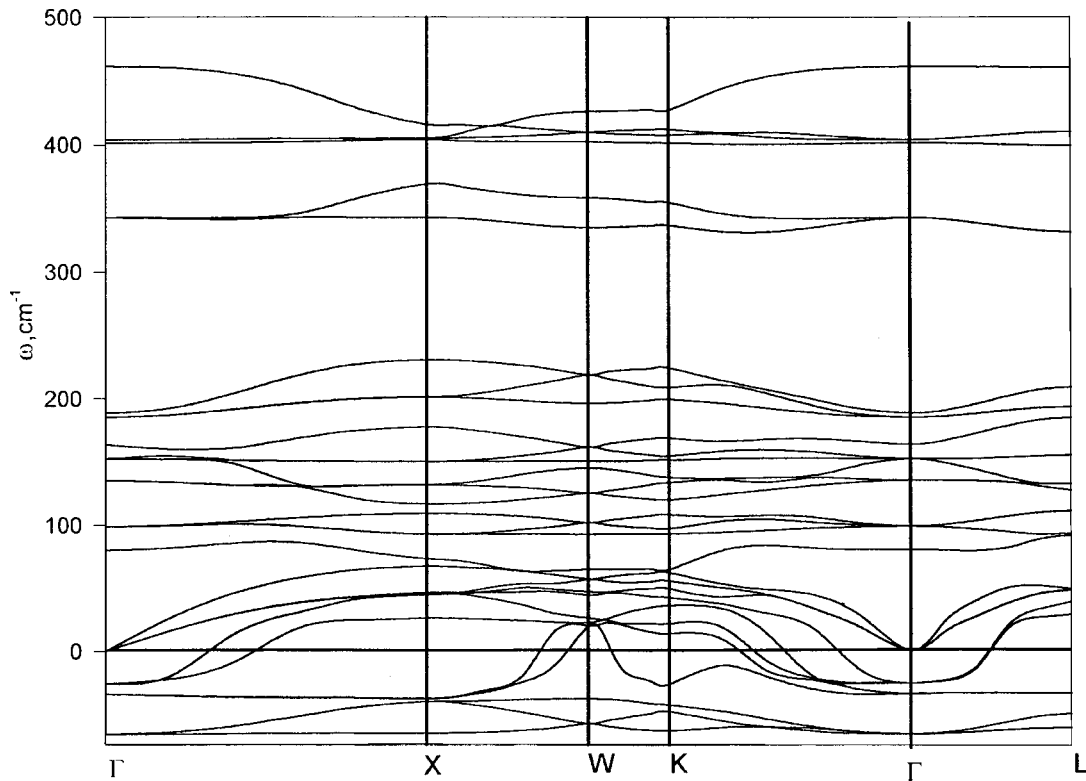
FIG. 3. Computed dispersion curves of Rb_2KScF_6 in the cubic phase. The imaginary frequencies are shown as negative values.

of some Raman-active vibrational frequencies measured in Ref. 7. One can see that the computed values of the Raman-active limiting frequencies are 10–20% less than the experimental values.

As one can see from Fig. 3 and Table III, there exist imaginary phonon frequencies. This attests to structural instability of the cubic phase in this material. It should be underscored that the unstable modes occupy the entire phase

TABLE III. Limiting vibrational frequencies ($\mathbf{q}=0$) in the cubic and tetragonal phases.

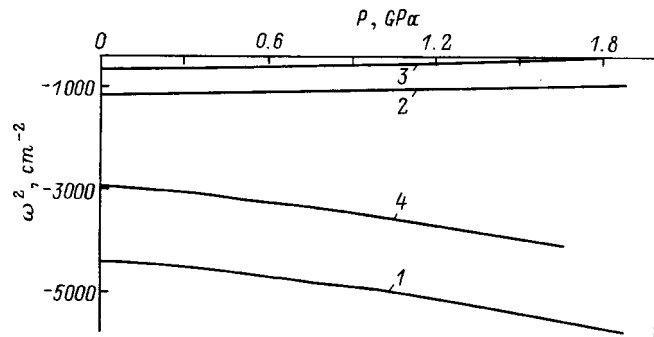| ω_i, cm^{-1}	Cubic				Tetragonal		
	Degeneracy	Vibration type	Frequency	Experiment[7]	Degeneracy	Vibration type	Frequency
ω_1	3	T_{1g}	66.2i		2	E_g	53.6i
					1	A_g	20.1
ω_{2T}	2	T_{1u}	34.3i		1	A_u	14.6i
					1	E_u	14.5
ω_3	3	T_{2g}	26.0i	80.0	1	B_g	18.4
					2	E_g	22.7
ω_4	3	T_{1u}	0.0		1	A_u	0.0
					2	E_u	0.0
ω_{2L}	1	T_{1u}	80.2		1	E_u	82.0
ω_5	3	T_{2u}	98.9		2	E_u	102.9
					1	B_u	111.9
ω_{6T}	2	T_{1u}	135.3		1	A_u	132.7
					1	E_u	136.9
ω_7	3	T_{2g}	152.4	230.0	2	E_g	151.5
					1	B_g	151.7
ω_{6L}	1	T_{1u}	163.7		1	E_u	160.3
ω_{8T}	2	T_{1u}	185.2		1	A_u	180.0
					1	E_u	183.6
ω_{8L}	1	T_{1u}	188.6		1	E_u	187.5
ω_9	2	E_g	342.9	400.0	1	A_g	325.1
					1	B_g	335.7
ω_{11}	1	A_{1g}	401.6	510.0	1	A_g	384.5
ω_{10T}	2	T_{1u}	404.1		1	A_u	390.4
					1	E_u	406.3
ω_{10L}	1	T_{1u}	461.5		1	E_u	443.0

FIG. 4. $\omega_i^2(\mathbf{q})$ versus the pressure. Cubic phase: Curve 1 — $\omega_{T_{1g}}^2$ ($\mathbf{q}=0$); curve 2 — $\omega_{T_{1u}}^2$ ($\mathbf{q}=0$); curve 3 — $\omega_{T_{2g}}^2$ ($\mathbf{q}=0$); tetragonal phase: 4 — $\omega_{X_3}^2$ ($\mathbf{q}=1/2(\mathbf{b}_1+\mathbf{b}_2)$).

FIG. 5. Total energy of Rb_2KScF_6 versus the rotation angle of ScF_6 octahedra in the tetragonal phase.

space in the Brillouin zone and the absolute values of these unstable modes are comparable in magnitude at the symmetric points of the Brillouin zone. The experimentally observed phase transitions in the Rb_2KScF_6 crystal are associated with the instability of the modes at the center and at the boundary point X of the Brillouin zone. In what follows we shall discuss the vibrational modes belonging to these points.

Three types of instability of the cubic structure occur at the center of the Brillouin zone. The greatest instability (the largest, in absolute magnitude, negative value of the squared frequency of the normal mode) is associated with the triply degenerate mode T_{1g}, in which only four fluorine atoms are displaced from positions of equilibrium[5,8]

$$-F_{1y}=F_{2y}=F_{5z}=-F_{6z},$$

$$-F_{1x}=F_{2x}=-F_{3z}=F_{4z},$$

$$-F_{3y}=F_{4y}=-F_{5x}=F_{6x}.$$

These displacements lead to rotation of the ScF_6 octahedra as a whole. The second type of instability, a ferroelectric instability, is associated with transverse vibrations of the polar mode T_{1u}. In this mode all atoms in a unit cell are displaced from positions of equilibrium of the cubic phase. As far as we know, ferroelectric phase transitions in halide crystals with elpasolite structure have not been observed experimentally. Finally, instability of the third type is associated with the triply degenerate mode T_{2g}. In one of the characteristic vectors of this mode, the atomic displacements cause the ScF_6 octahedra to rotate around the body diagonal with a simultaneous displacement of the rubidium atoms located on this diagonal toward one another. It should be noted that
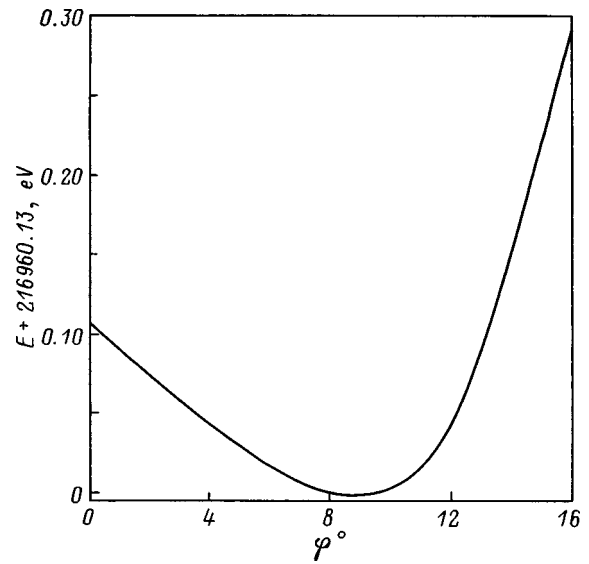
there is also a stable mode with the same symmetry T_{2g} in the phonon spectrum of an Rb_2KScF_6 crystal (see Table III).

The strongest lattice instability at the points X on the Brillouin boundary is related with the nondegenerate X_3 mode, in which the displacements of the four fluorine ions ($F_{3y}=-F_{4y}=F_{5z}=-F_{6z}$) also correspond to rotation of ScF_6 octahedra as a whole, but this rotation is not uniform throughout the crystal and the condensation of this mode results in doubling of the unit-cell volume.

As we have already mentioned in the introduction, as the temperature decreases, a transition to the tetragonal phase associated with condensation of the ''soft'' T_{1g} mode at the center of the Brillouin zone occurs first in the Rb_2KScF_6 crystal. Under hydrostatic pressure the temperature of this phase transition shifts in the direction of high temperatures, with $dT_{c1}/dP=16.6$ K/GPa.[9] We can estimate the derivative dT_{c1}/dP from our calculations assuming that the phase-transition temperature is proportional to the absolute value of the squared frequency of the soft mode T_{1g}. The pressure was determined by differentiating numerically the volume dependence of the total energy. The hydrostatic pressure dependence of the frequencies of the soft modes at the center of the Brillouin zone is shown in Fig. 4. It is evident that the lattice softens under pressure with respect to the T_{1g} mode and hardens with respect to all other unstable modes. The derivative dT_{c1}/dP was found to be ~40 K/GPa, which

TABLE IV. Computed and experimental[2] coordinates of atoms in the tetragonal phase $I4/m$.

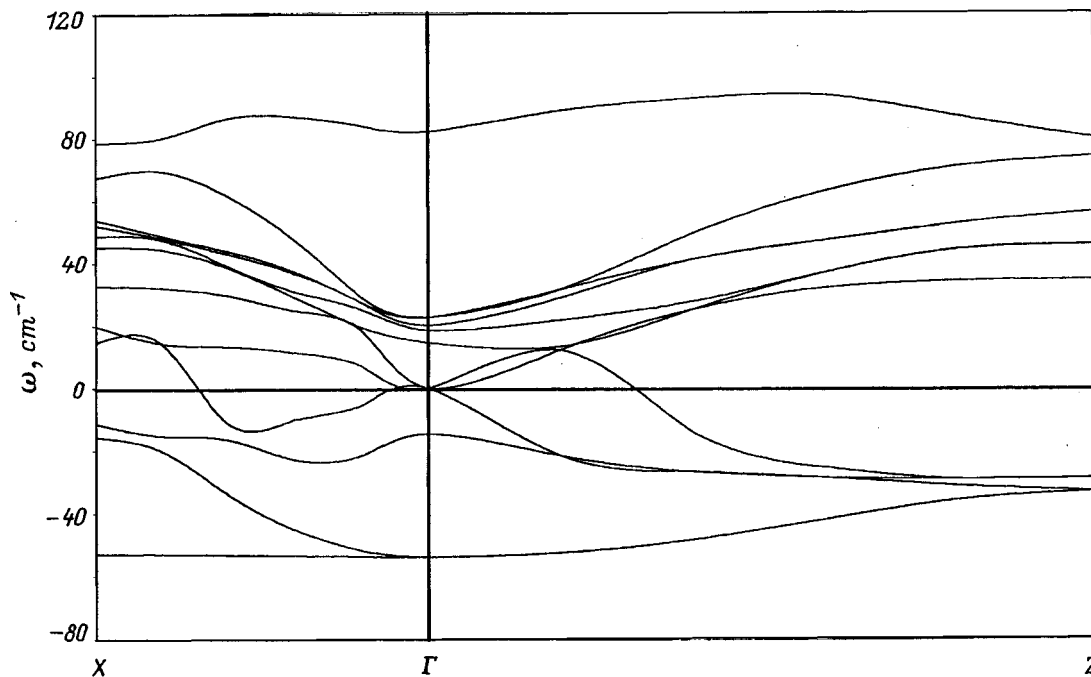| Atom	Position theory	Position experiment	Filling theory	Filling experiment	x/a, theory	x/a, experiment	y/b, theory	y/b, experiment	z/c, theory	z/c, experiment
Rb	$4d$	$4d$	1	1	0.5	0.5	0.0	0.0	0.25	0.25
K	$2b$	$2b$	1	1	0.0	0.0	0.0	0.0	0.25	0.25
Sc	$2a$	$2a$	1	1	0.0	0.0	0.0	0.0	0.0	0.0
F_1	$4e$	$16i$	1	1/4	0.0	0.05	0.0	0.01	0.22	0.22
F_2	$8h$	$16i$	1	1/2	0.19	0.20	0.25	0.24	0.0	-0.03

FIG. 6. Low-frequency part of the computed dispersion spectrum in two symmetric directions in the Brillouin zone of Rb_2KScF_6 in the tetragonal phase. The imaginary frequencies are shown as negative values.

is more than two times larger than the experimental value.

2.2. Tetragonal phase

The phase transition to the tetragonal phase is related to condensation of one component of the triply degenerate T_{1g} mode at the center of the Brillouin zone. This condensation corresponds to rotation of ScF_6 octahedra around a principal axis of the cubic phase. The space group of the tetragonal phase is $I4/m$ and the unit cell contains one molecule. The distortion of the cubic phase (the rotation angle of an octahedron) was determined from the minimum of the total energy as a function of rotation angle, which is shown in Fig. 5. In calculating this dependence, for each fixed value of the rotation of an octahedron, the total energy was minimized with respect to the cell parameters and with respect to the radii of the Watson spheres of the ions. It is evident from Fig. 5 that the minimum of the total energy corresponds to the rotation angle $\varphi = 8°$. However, the calculation is performed at $T = 0$, while the tetragonal phase exists at a finite temperature in a quite narrow temperature range (~ 30 K). The phase transition $Fm3m \rightarrow I4/m$ is of second order[1] and the order parameter in the temperature interval $T/T_{c1} = 0.9$ is far from saturation (for example, in the mean-field approximation it is 0.6), so that distortions corresponding to the rotation angle of an octahedron $\varphi = 5°$ were used to calculate the energy and frequency spectrum in the tetragonal phase. The volume dependence of the total energy in the tetragonal phase is shown in Fig. 2. The equilibrium values obtained for the unit-cell parameters and coordinates of the atoms are presented together with the experimental data in Tables I and IV, whence one can see that the computed values of the cell parameters are approximately 4% lower than the experimental values. At the same time the computed displacements of

the fluorine ions from positions of equilibrium in the cubic phase are larger than the experimental data by approximately the same amount.

The computed values of the permittivity and dynamic Born charges of an Rb_2KScF_6 crystal in the tetragonal phase are presented in Table I. One can see that a tetragonal distortion leads to a redistribution of the dynamic charges on the fluorine ions. We calculated the phonon frequency spectrum of an Rb_2KScF_6 crystal in the tetragonal phase for all symmetry directions and points of the Brillouin zone. However, to save space we do not present here all of the results of these calculations, since the spectrum of ''nonsoft'' modes changes negligibly compared with the spectrum of these modes in the cubic phase (naturally, the lowering of the symmetry lifts the degeneracy of the modes). For this reason, the computed values of the limiting phonon frequencies are presented in Table II and the lower part of the frequency spectrum for two symmetric directions of the Brillouin zone is shown in Fig. 6. As one can see from Table II and Fig. 6, a structural instability ouccrs in the tetragonal phase of Rb_2KScF_6 just as in the cubic phase, but the number of ''soft'' modes in this phasebecomes less than in the cubic phase. It should be underscored that the number of unstable vibrational modes in the tetragonal phase depends strongly on the rotation angle of the ScF_6 octahedra. Figure 7 shows the dependence of the frequencies of several ''soft'' modes at the center and boundary point X of the Brillouin zone versus the rotation angle of the octahedra. It is evident from this dependence that, as the rotation angle of the octahedra increases, the absolute magnitude of the squared frequencies of the ''soft'' modes decreases and for $\varphi \sim 12°$ the squared frequencies become positive (for all modes in the Brillouin
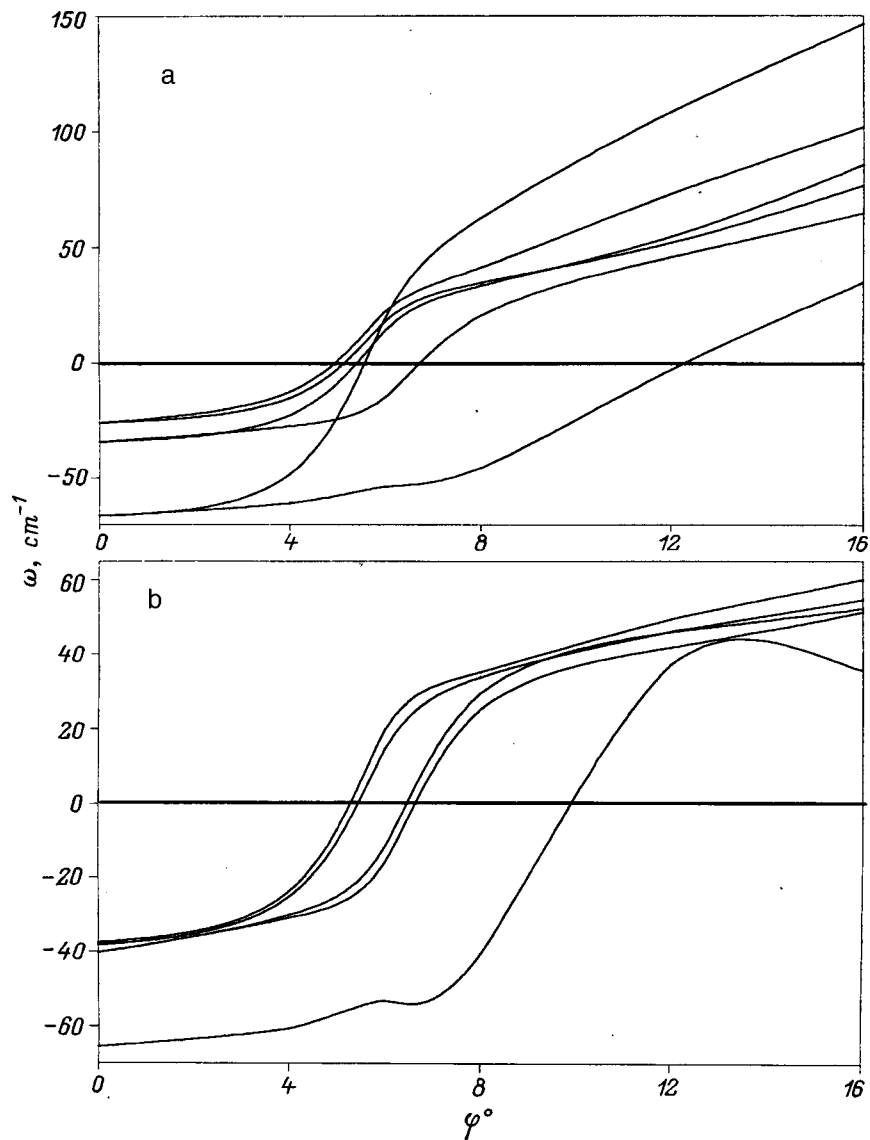
FIG. 7. ''Soft'' lattice vibrational frequencies versus the rotation angle of ScF_6 octahedra in the tetragonal phase: a — Center of the Brillouin zone $\mathbf{q}=0$; b — boundary point X of the Brillouin zone $\mathbf{q}=1/2(\mathbf{b}_1+\mathbf{b}_2)$. The imaginary frequencies are shown as negative values.

zone), i.e. the tetragonal phase is stable for such displacements of the fluorine ions.

As we have already mentioned above, the tetragonal phase in the Rb_2KScF_6 crystal exists at temperatures between 250 and 220 K. At $T_{c2}=220$ K a second phase transition occurs in this crystal into the monoclinic phase, whose unit cell is doubled compared with the cells of the cubic and tetragonal phases. As follows from the results of structural

investigations of the monoclinic phase of Rb_2KScF_6,[2] the cell doubling is due to the condensation of the unstable mode at the boundary point X of the Brillouin zone of the tetragonal group $I4/m$.

As one can see from Fig. 6, the computed frequencies of the unstable modes at the center and at the point X of the Brillouin zone are comparable in absolute magnitude, and

TABLE V. Computed and experimental[2] coordinates of atoms in the monoclinic phase $P12_1/n1$.

Atom	Position	Filling	x/a, theory	x/a, experiment	y/b, theory	y/b, experiment	z/c, theory	z/c experiment
Rb	$4e$	1	0.500	0.504	0.00	−0.02	0.254	0.251
K	$2c$	1	0.0	0.0	0.0	0.0	0.5	0.5
Sc	$2a$	1	0.0	0.0	0.0	0.0	0.0	0.0
F_1	$4e$	1	0.030	0.058	−0.030	0.011	0.220	0.221
F_2	$4e$	1	−0.250	−0.252	0.190	0.189	0.023	0.029
F_3	$4e$	1	0.190	0.184	0.250	0.256	0.000	−0.031

TABLE VI. Limiting vibrational frequencies ($\mathbf{q}=0$) in the monoclinic phase.

ω_i, cm^{-1}	Frequency	ω_i, cm^{-1}	Frequency	ω_i, cm^{-1}	Frequency	ω_i, cm^{-1}	Frequency
1	0.0	16	74.9	31	142.6	46	226.1
2	0.0	17	78.5	32	145.1	47	230.7
3	0.0	18	82.1	33	153.8	48	273
4	21.0	19	87.5	34	161.2	49	316.3
5	26.6	20	90.6	35	163.3	50	317.3
6	33.4	21	93.2	36	173.9	51	319.8
7	41.3	22	102.2	37	181.7	52	353.0
8	41.8	23	108.8	38	197.0	53	391.7
9	42.0	24	114.6	39	199.2	54	398.1
10	46.6	25	118.5	40	206.3	55	400.0
11	49.4	26	122.8	41	206.7	56	402.2
12	54.3	27	127.9	42	209.7	57	403.5
13	55.4	28	131.1	43	216.7	58	406.2
14	66.5	29	131.7	44	221.6	59	439.6
15	68.8	30	134.7	45	224.2	60	461.5

the unstable modes, just as in the cubic phase, occupy a large volume of the phase space. Analysis of the characteristic vectors of the unstable modes shows that vibrational modes in which the displacements of atoms correspond to a ''pure'' rotation of ScF$_6$ octahedra do not exist in the tetragonal phase. At the boundary point X of the Brillouin four fluorine and rubidium ions are displaced in the most unstable mode:

$$F_{1x} = -F_{2x} \approx F_{1y} = -F_{2y},$$

$$F_{5z} \approx -0.75F_{6z},$$

$$Rb_{1z} = Rb_{2z},$$

and these displacements produce a monoclinic distortion of the tetragonal phase with cell doubling.

It has been established experimentally[9] that under hydrostatic pressure the temperature of the phase transition from the tetragonal to the monoclinic phase shifts in the direction of high temperatures. The computed hydrostatic pressure dependence of the squared frequency of the most unstable mode at the boundary point X is shown in Fig. 4, whence it is evident that this dependence agrees qualitatively with the experimental dependence. However, the numerical estimate $dT_{c2}/dP \sim 60$ K/GPa differs strongly from the experimental value of 3.2 K/GPa.[9]

2.3. Monoclinic phase

The coordinates of the atoms in the monoclinic phase, calculated according to the displacements corresponding to condensation of the mode X_3 of the tetragonal phase, are presented in Table V. The table also gives the experimental values of these coordinates. It is evident that the displace-
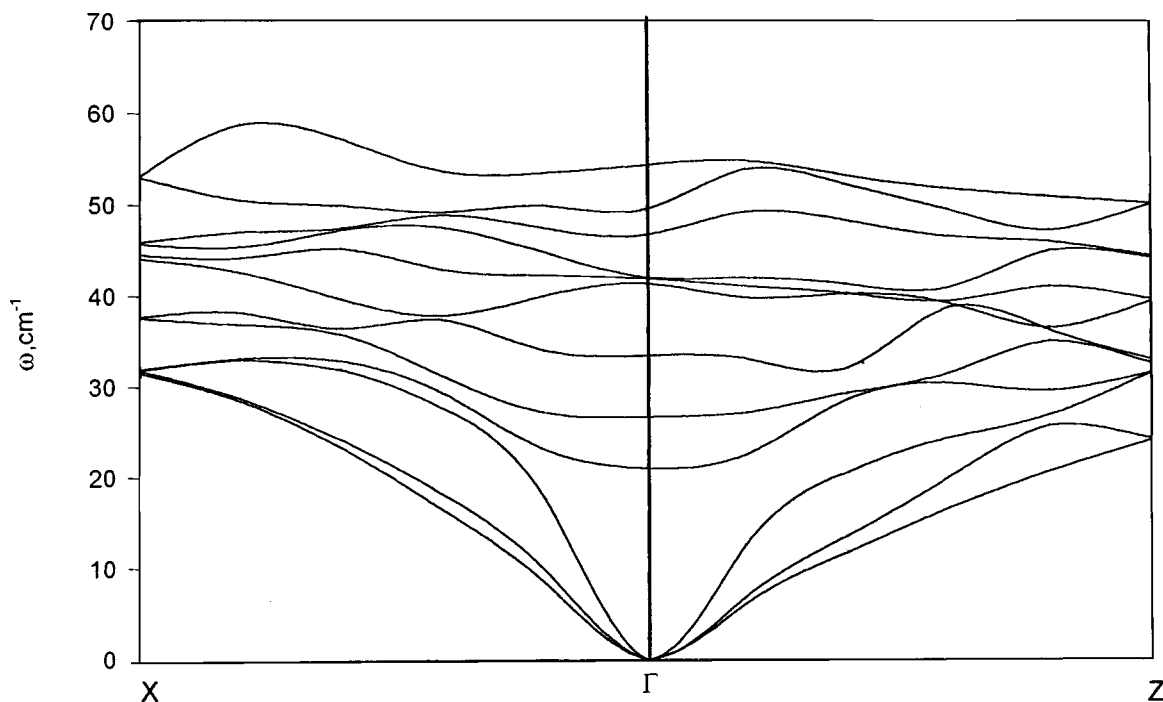

FIG. 8. Low-frequency part of the computed dispersion curve in two symmetric directions in the Brillouin zone of Rb$_2$KScF$_6$ in the monoclinic phase.

ments of the ions F_1 and F_3 in the experimentally determined structure differ substantially from the displacements of these ions as a result of condensation of mode X_3. The computed total energy of Rb_2KScF_6 in the monoclinic phase, for the computed coordinates of the atoms, was found to be 0.14 eV higher than the values of the total energy calculated from the coordinates of the experimental structure. The volume dependence of the energy using the experimental values of the coordinates is presented in Fig. 3, and the values of the unit-cell parameters together with the experimental values are presented in Table I. There are no unstable vibrational modes in the computed phonon frequency spectrum of the monoclinic phase of Rb_2KScF_6. The limiting phonon frequencies are presented in Table VI, and Fig. 8 shows the dispersion curve of the low-frequency part of the spectrum for two symmetric directions in the Brillouin zone of the monoclinic group $P2_1/n1$.

In summary, the static and dynamic properties of a Rb_2KScF_6 crystal with elpasolite structure in the cubic, tetragonal, and monoclinic phases were calculated in the present work on the basis of a fairly simple nonempirical model of an ionic crystal. The computed equilibrium values of the lattice parameters are in satisfactory agreement with the experimental data. At the same time the computed Raman phonon frequencies are 10–20% less than the experimental values. This discrepancy could be due to the fact that, in the present approach, the calculations of the lattice dynamics neglected the higher, specifically the quadrupole, distortions of the electron density, which for the present class of compounds are different from zero even in a static lattice because the fluorine ions are located in a noncubic environment.

The results obtained on the instability of cubic and tetragonal structures, the stability of the monoclinic phase in a Rb_2KScF_6 crystal, and the effect of hydrostatic pressure on the phase transition temperatures describe the experimental situation qualitatively correctly.

*)E-mail: zinenko@iph.krasnoyrsk.su

[1] I. N. Flerov, M. V. Gorev, K. S. Aleksandrov, A. Tressaud, J. Grannec, and M. Couzi, Mater. Sci. Eng. R. **24**, 81 (1998).
[2] H. Faget, J. Grannec, A. Tressaud, V. Rogriguez, T. Roissnel, I. N. Flerov, and M. V. Gorev, Eur. J. Solid State Inorg. Chem. **33**, 893 (1996).
[3] O. V. Ivanov and E. G. Maksimov, Zh. Éksp. Teor. Fiz. **108**, 1841 (1995) [JETP **81**, 1008 (1995)].
[4] W. Kohn and L. J. Sham, Phys. Rev. A **140**, 1113 (1965).
[5] V. I. Zinenko, N. G. Zamkova, and S. N. Sofronova, Zh. Éksp. Teor. Fiz. **114**, 1742 (1998) [JETP **87**, 944 (1998)].
[6] D. A. Liberman, D. T. Cromer, and J. J. Waber, Comput. Phys. Commun. **2**, 107 (1971).
[7] H. Guengard, Doctoral Thesis, Université de Bordeaux (1994).
[8] M. Couzi, S. Khairoun, and A. Tressaud, Phys. Status Solidi A **98**, 423 (1986).
[9] I. N. Flerov, M. V. Gorev, S. V. Mel'nikova, S. V. Misyul', V. N. Voronov, and K. S. Aleksandrov, Fiz. Tverd. Tela (Leningrad) **34**, 2185 (1992) [Sov. Phys. Solid State **34**, 1168 (1992)].

Translated by M. E. Alferieff

LOW-DIMENSIONAL SYSTEMS AND SURFACE PHYSICS

Specific features in low-frequency vibrations of nanocrystals in fluorophosphate glassy matrices

E. P. Denisov, S. V. Karpov, E. V. Kolobkova, B. V. Novikov, A. I. Suslikov,
D. L. Fedorov, and M. A. Yastrebova

Institute of Physics, St. Petersburg State University, 198904 St. Petersburg, Petrodvorets, Russia

A Raman scattering study of low-frequency vibrational spectra of mixed cadmium sulfoselenide nanocrystals in a fluorophosphate glassy matrix is reported. The measurements have revealed a low-frequency feature in the nanocrystal density of states, whose frequency is related to the glass-matrix annealing time and, hence, to the size of the nanocrystals prepared, which is interpreted as a manifestation of the size quantization effect. Besides the line associated with the constraints on the longitudinal acoustic wave in a nanocrystal, a lower-frequency feature assigned to torsional vibrations of a nonspherical nanocrystal has been found. © *1999 American Institute of Physics.* [S1063-7834(99)03707-7]

Zero-dimensional systems (quantum dots or nanocrystals) have been attracting recently increasing attention of researchers, because they exhibit a number of interesting physical properties originating from quantum confinement effects. The progress reached in investigation of the size quantization of electronic states in semiconductor nanocrystals permits one to use the parabolic-band approximation not only to evaluate the size quantization energy but to calculate with a good accuracy the excitonic spectrum near the intrinsic absorption edge as well.[1–4] At the same time description of vibrational excitations (phonons) of such objects is usually based on an *a priori* prescription of the form of spatial decay of the phonon wave function in a limited crystal.[5–7] In this case, the discrete nature of phase space in nanoobjects gives rise to quantization of band vibrational excitations. This manifests itself usually in renormalization of the spectrum and a general line broadening of the vibrational modes. The specific features in vibrational excitations of nanocrystals become observable also in the low-frequency spectral region, where an additional density of vibrational states associated with spatial confinement of acoustic phonons in nanocrystals appears at frequencies close to the matrix boson peak.[8–10] This results in a long-wavelength cutoff of vibrations proportional to the nanocrystal size and in a corresponding rise of the lower phonon-spectrum boundary. These features are not, however, the only changes that can occur in the vibrational spectrum of nanocrystals.

In this connection, we have studied in more detail the low-frequency Raman spectrum of nanocrystals of CdS_xSe_{1-x} mixed semiconductors (for $x=0.35$) in fluorophosphate glassy matrices. The samples, prepared by heating the charge to $1100\,°C$ with its subsequent cooling to room temperature,[11] were colorless before annealing. The annealing was carried out at the matrix-glass-formation temperature T_g for 5 to 120 min. After the anneal, the samples took on

straw-yellow to cherry-red color, which implied formation in them of mixed-semiconductor nanocrystals. One obtained also differential spectra in the exciton absorption region, which indicate size quantization under strong spatial confinement (with the size quantization energy of about 0.1 eV).[12] Raman spectra were obtained on a Model 1404 Spex-Ramalog spectrometer under Ar^+ laser excitation ($\lambda=488.0$ nm, 150 mW) in $180°$ geometry. The low scattered-light intensity in the instrument and the absence of spurious reflections and ghosts in the vicinity of the Rayleigh line permitted taking spectra reliably from $5\ cm^{-1}$ up. The slit spectral width was about $4\ cm^{-1}$. The spectra of the samples studied are presented in Figs. 1 and 2.

The low-frequency feature observed by us in Raman spectra of fluorophosphate glasses is characteristic of nanocrystalline formations. Its frequency and shift in position depending on the glass annealing time observed to occur in samples of the same series (Fig. 1) permit its assignment to a size quantization effect in nanocrystal vibrations. A similar effect was earlier observed in borosilicate glasses.[8,9] The vibration frequency of the lowest spherical mode, ω_{min}, in a Raman spectrum due for a uniform elastic spherical particle embedded in a matrix is inversely proportional to the particle diameter L

$$\omega_{min}=0.9\,\frac{\nu_l}{Lc},\qquad(1)$$

where ν_l and c are the longitudinal acoustic wave velocity and the velocity of light, respectively.

Our data are in a good agreement with this relation, which shows that the average diameter of cadmium sulfoselenide nanocrystals increases from 1.5–2.0 to 6.0 nm with the anneal time increased from 10 to 60 min (curves *2–5* in Fig. 1). The growth in intensity of the observed low-frequency feature indicates an increase in concentration of
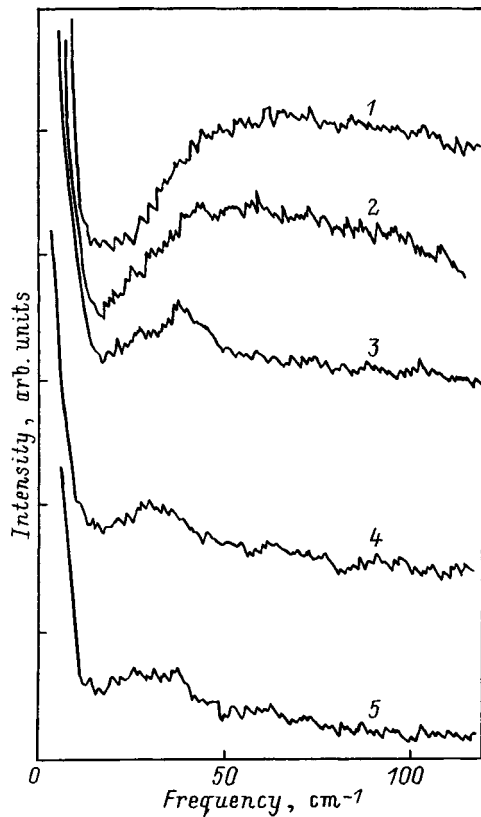
FIG. 1. Raman spectra of cadmium-sulfoselenide–doped fluorophosphate glass samples annealed for different times at 410 °C. Anneal time (min): *1* — matrix, *2* — 10, *3* — 20, *4* — 40, *5* — 60.
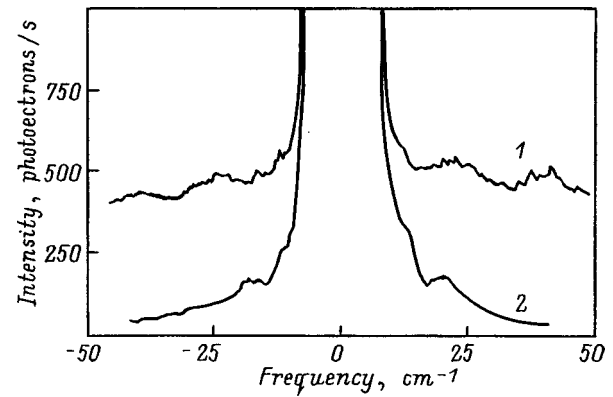

FIG. 2. Raman spectra of two cadmium-sulfoselenide-doped fluorophosphate glass samples. Sulfur concentration 35%. Anneal time (min): *1* — 30, *2* — 10.

the crystalline phase, which correlates well with the variation of the samples in color and spectral changes near the excitonic absorption edge.[12]

Accepting 4070 m/s for the longitudinal acoustic wave velocity in the mixed crystal [obtained by linear interpolation between the sound velocities in CdS (3570 m/s) and in CdSe (4277 m/s)] for the given sulfur concentration ($x = 0.35$, curve *2* in Fig. 2), the frequency of 19 cm^{-1} observed for a sample annealed for 10 min yields about 5.6 nm for the average dimension of a spherical nanocrystal. On the whole, this value is in a good agreement with both the diameters derived from estimates of the size quantization energy in the excitonic region of the spectrum and indirect estimates of the

size of crystalline regions and average distances between their centers obtained by us from high-precision x-ray diffraction measurements.[13]

Besides, some samples of the series studied exhibit in the low-frequency Raman spectrum two lines (Fig. 2). Taking into account the sonic wave velocity and the sample anneal time, the higher-frequency component can be assigned reliably, considering its position and intensity, to the lowest-frequency spherical mode of the nanocrystal. By contrast, the lower-frequency component revealed by us in the Raman spectrum does not allow straightforward identification. The assumption of the presence in fluorophosphate glasses of a semiconductor nanocrystal fraction with sizes of about 10 nm gets no support from either our x-ray diffraction studies or direct electron microscope observations[11]. At the same time attempts to explain the origin of this feature as due to existence, in addition to the longitudinal acoustic mode, of transverse acoustic modes[14] cannot be considered satisfactory. Using Eq. (1) to calculate the transverse modes or a specific size distribution would hardly be reasonable, because it was derived in a rough approximation which shows only that the frequency spectrum of an ideal lattice of a macroscopic crystal lies between $\omega_{min} = \pi \nu_l / L$ and the Debye limit $\omega_{max} = \pi \nu_l / a$ (*a* is the interatomic distance). In this case it would be more appropriate to calculate the vibrational spectrum of a real nanocrystal within a rigorous solu-
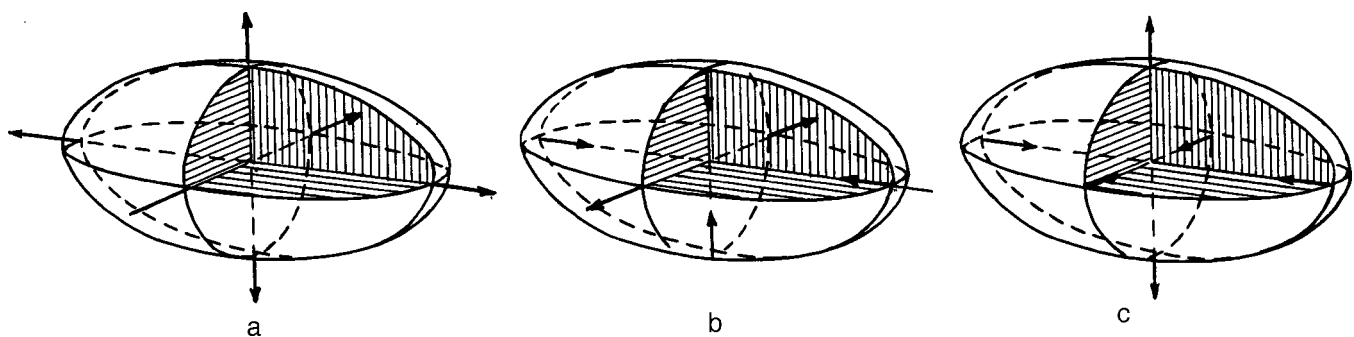

FIG. 3. Low-frequency vibrations of an elastic ellipsoid. (a) Fully symmetric spherical vibration corresponding to the longitudinal acoustic wave LA, (b,c) doubly degenerate ''oblate'' modes due to torsional vibrations corresponding to the transverse acoustic waves TA$_1$ and TA$_2$.
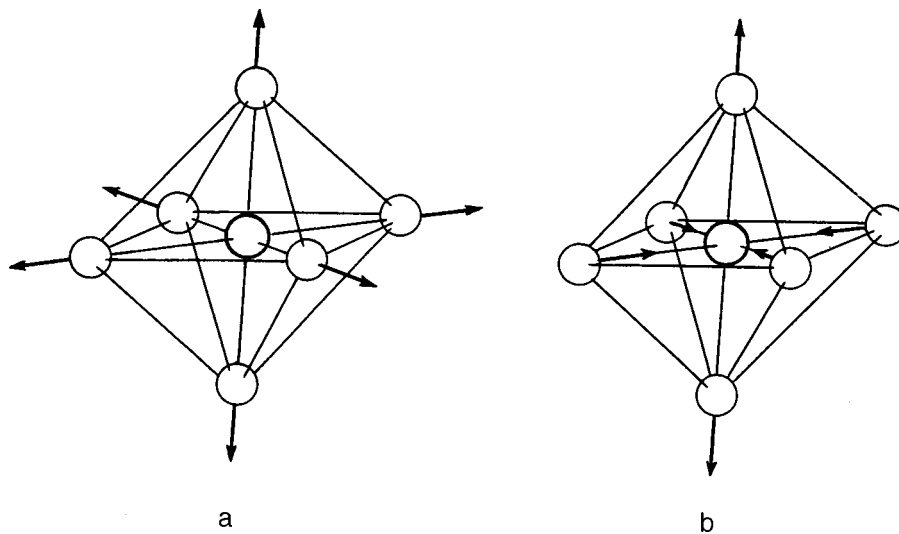
FIG. 4. Fully symmetric, A_g, and doubly degenerate, E_g, vibration of an XY_6 molecule of O_h symmetry. Both vibrations are Raman active in diagonal polarizations.

tion of the dynamic problem, which presently is, in principle, possible, but the question of what boundary conditions should be taken for such a problem is unclear. Besides, studies of nanocrystals 1.5–5 nm in size should inevitably meet with problems similar to excitonic excitation confinement for excitons larger than the nanocrystal dimensions, $d_{exc} > L$. Indeed, any analysis of vibrational excitations made with inclusion of interaction with nearest and next-nearest neighbors in small crystals has to take into account the change in the equations of motion for atoms located in the two outermost crystal layers. The situation where the number of new solutions to this problem becomes one half of the total number of solutions may be considered as a criterion of confinement and, according to the theorem of Lederman,[15] should arise in the case of nanocrystals 10–12 lattice constants in size. Therefore even if the phase space in crystals of one size is divided in identical cells (corresponding to particular boundary conditions), size quantization effects will manifest themselves differently because of different dispersion laws for acoustic phonons in the bulk and in the boundary regions.

Electron microscopy[11] of the fluorophosphate glasses doped with cadmium sulfoselenide and studied by us shows the nanocrystalline formations to differ substantially in shape from nanocrystals in silicate glasses, which are typically spherical. This feature, i.e. the existence of two characteristic sizes of a nanocrystal, may account for the two lines in the Raman spectrum, which correspond to longitudinal waves propagating along the long and the short dimensions of the nanoparticle. However plane acoustic waves cannot exist in a nanocrystal. Therefore when invoking macroscopic representation, one should approximate the elastic vibrations of a volume nanocrystal with vibrations of an elastic sphere,[16] which should include the fundamental harmonics of the longitudinal (LA) mode, two transverse modes (TA$_1$ and TA$_2$), and one surface mode. The ratio of the longitudinal to transverse mode frequencies is approximately proportional to $(E/\tau)^{1/2}$, where E is Young's modulus, and τ is the shear modulus of the crystal. This ratio is close in magnitude to

that of the observed frequencies, 19:12, but in a spherical particle a pure bending mode, for which divergence of the displacement field is zero ($\mathrm{div}\mathbf{W}_t = 0$), cannot be Raman active. At the same time, in the vibrations of an elastic ellipsoid, the transverse (i.e. torsional) vibrations (see Fig. 3b and c) will be active in the scattering spectrum and can change the polarization of scattered light.[17] The symmetry aspects of this problem may be considered and the selection rules obtained by analyzing normal modes of a XY_6 molecule of cubic symmetry O_h.[18] The possible normal modes of such a molecule (Fig. 4) include the Raman-active fully symmetric A_g and the doubly degenerate E_g vibrations. The frequencies of these vibrations differ for most cubic molecules by 20–25% and are active in fully symmetric polarizations:

$$A_g \sim \begin{pmatrix} a & & \\ & a & \\ & & a \end{pmatrix};$$

$$E_g \sim \begin{pmatrix} b & & \\ & b & \\ & & -2b \end{pmatrix} + \begin{pmatrix} b & & \\ & -2b & \\ & & b \end{pmatrix}. \qquad (2)$$

When the molecule symmetry is lowered to D_{2h}, which corresponds to taking into account the particle nonsphericity, the doubly degenerate E_g mode splits into A_g and B_{1g} vibrations, which are observable in both fully symmetric and off-diagonal polarizations. One may therefore expect that the high- and low-frequency lines should have different polarizations. Taking into account the random orientational distribution of the nanocrystals synthesized in the matrix, the degree of depolarization ρ of torsional low-frequency vibrations could be within 0 to 3/4.

[1] A. I. Ekimov, A. A. Onushchenko, and Al. L. Éfros, JETP Lett. **43**, 376 (1986).

[2] G. B. Grigor'yan, E. M. Kazaryan, Al. L. Éfros, and T. V. Yazeva, Fiz. Tverd. Tela (Leningrad) **32**, 1772 (1990) [Sov. Phys. Solid State **32**, 1031 (1990)].

[3] A. I. Ekimov, F. Hache, M. C. Schanne-Klein, D. Ricard, C. Flytzanis, I. A. Kudryavtsev, T. V. Yazeva, A. V. Rodina, and Al. L. Éfros, J. Opt. Soc. Am. B **10**, 100 (1993).

[4] D. J. Norris and M. J. Bawendi, J. Chem. Phys. **103**, 5260 (1995).

[5] H. Richter, Z. P. Wang, and L. Ley, Solid State Commun. **39**, 625 (1981).

[6] I. H. Campbell and P. M. Fauchet, Solid State Commun. **58**, 739 (1986).

[7] V. S. Gorelik, A. V. Igo, and S. N. Minkov, Zh. Éksp. Teor. Fiz. **109**, 2141 (1996) [JETP **82** 1154 (1996)].

[8] E. Duval, A. Boukenter, and B. Champagnon, Phys. Rev. Lett. **56**, 2052 (1986).

[9] B. Champagnon, B. Andrianasolo, A. Ramos, M. Gandais, M. Allais, and J.-P. Benoit, J. Appl. Phys. **73**, 2775 (1993).

[10] T. Bischof, M. Ivanov, A. Materny, and N. Kiefer, J. Raman Spectrosc. **27**, 297 (1996).

[11] E. V. Kolobkova, A. A. Lipovskii, N. V. Nikonorov, and A. A. Sitnikova, Phys. Status Solidi A **147**, K65 (1995).

[12] V. A. Gaĭsin, S. V. Karpov, E. V. Kolobkova, B. V. Novikov, D. L. Fedorov, and M. A. Yastrebova, *Abstracts of the 2nd International Conference on the Chemistry of Highly-Organized Substances and Scientific Fundamentals of Nanotechnology* (Peterhof-St. Petersburg, 1998), p. 53.

[13] E. P. Denisov, S. V. Karpov, E. V. Kolobkova, B. V. Novikov, D. L. Fedorov, and M. A. Yastrebova, *Abstracts of the 2nd International Conference on the Chemistry of Highly-Organized Substances and Scientific Fundamentals of Nanotechnology* (Peterhof-St. Petersburg, 1998), p. 250.

[14] A. I. Ekimov, J. Lumin. **70**, 1 (1996).

[15] A. A. Maradudin, E. W. Montroll, and G. H. Weiss, *Theory of Lattice Dynamics in the Harmonic Approximation* (Academic Press, New York, 1963; IL, Moscow, 1965).

[16] H. Lamb, *The Dynamical Theory of Sound* (Arnold, London, 1931; Fizmatgiz, Moscow, 1960).

[17] V. K. Malinovskiĭ, B. V. Novikov, and A. P. Sokolov, Usp. Fiz. Nauk **163**, No. 5, 119 (1993) [Phys. Usp. **36**, 440 (1993)].

[18] E. B. Wilson, Jr., J. C. Decius, and P. C. Cross, *Molecular Vibrations: The Theory of Infrared and Raman Vibrational Spectra* (McGraw-Hill, New York, 1955; IL., Moscow, 1960).

Translated by G. Skrebtsov

Interband absorption of light in quasi-zero-dimensional semiconductor systems

S. I. Pokutniĭ*)

Ukrainian State Maritime Technical University 237025 Nikolaev, Ukraine
(Submitted August 7, 1998)
Fiz. Tverd. Tela (St. Petersburg) **41**, 1310–1313 (July 1999)

The interband absorption of light in a small semiconductor microcrystal is studied theoretically in the dipole approximation. An expression is obtained for the light absorption coefficient under conditions where the polarization interaction of an electron and a hole with the surface of the microcrystal plays a large role. © *1999 American Institute of Physics.*
[S1063-7834(99)03807-1]

Quasi-zero-dimensional systems — spherical semiconductor microcrystals (SMCs) with sizes $a \simeq 1 - 10$ nm grown in transparent dielectric matrices[1–5] — are attracting attention in connection with their nonlinear optical properties and possible applications in optoelectronics (specifically, as new materials which are promising for developing components that control optical signals[2]). Since the energy gap of a semiconductor is much smaller than the gap in dielectric matrices, the motion of charge carriers in an SMC (''quantum dot'') will be limited by its volume. The sizes a of SMCs will be comparable to the characteristic sizes of quasiparticles in semiconductors. Under these conditions the SMC–dielectric matrix interface can give rise to size quantization of the energy spectrum of electrons and holes in the SMC due to the purely spatial confinement of the quantization region[3] as well as the polarization interaction of charge carriers with the SMC surface.[6–10]

It has been observed experimentally[1,2] that the structure of the interband light absorption spectrum of a small SMC is determined by the size-quantization of the energy spectrum of its quasiparticles.

Interband light absorption by small SMCs has been little studied. The theory developed in Ref. 3 for interband light absorption in SMCs neglected the contribution of the polarization interaction of charge carriers with the SMC surface in the electron and hole spectrum in the SMC. Light absorption and luminescence by nonspherical cadmium selenide nanocrystals have been studied theoretically in Refs. 4 and 5. Just as in Ref. 3, the effect of the polarization interaction of an electron and a hole with the surface of a small SMC on light absorption and luminescence processes in such SMCs was neglected.

To fill this lacuna in the theory, the present paper considers the effect of the polarization interaction of an electron and a hole with the surface of a small SMC on interband light absorption in the SMC. An expression is obtained for the light absorption coefficient as a function of the radius a of the SMC and the parameters of the problem under conditions where the polarization interaction of an electron and a hole with the SMC surface plays a large role. It is shown that the polarization interaction of an electron and a hole with the surface of an SMC shifts the absorption threshold in a small SMC in the short-wavelength direction. It is established that the absorption edge of small SMCs is formed by two transi-

tions of comparable intensity from different hole size-quantization levels to a lower electron size-quantization level.

1. ELECTRON–HOLE PAIR SPECTRUM IN A SMALL MICROCRYSTAL

A simple model of a quasi-zero-dimensional structure was studied in Refs. 6–10: a neutral spherical SMC with radius a and permittivity ε_2 surrounded by a medium with permittivity ε_1. An electron e and a hole h with effective masses m_e and m_h moved in the volume of such an SMC (r_e and r_h are the distances of the electron and hole from the center of the SMC); in addition, the permittivity of the microcrystal and the dielectric matrix differed strongly ($\varepsilon_1 \ll \varepsilon_2$). It was also assumed that the electron and hole bands in the SMC were parabolic.

The following spectrum of an electron-hole pair[6–9] was obtained in the model on the basis of the above-described approximations as well as in the adiabatic approximation ($m_e \ll m_h$) and in the effective-mass approximation using only first-order perturbation theory for the electron wave functions $\Psi_{n_e, l_e, m_e}(r_e, \Theta, \varphi)$ (where Θ and φ are the azimuthal and polar angles) of a spherical potential well of infinite depth:

$$E^{n_h, l_h, m_h}_{n_e, l_e = m_e = 0}(S) = E_g + (\pi^2 n_e^2 / S^2)(m_h / m_e) + S^{-1}(Z_{n_e,0}$$
$$+ P_{n_e,0} + \varepsilon_2 / \varepsilon_1) + \omega_0(S, n_e)(t_h + 3/2),$$
(1)

$$Z_{n_e,0} = 2 \int_0^1 dx \, \sin^2(\pi n_e x)/(1 - x^2).$$

$$P_{n_e,0} = 2 Ci(2\pi n_e) - 2 \ln(2\pi n_e) - 2\gamma + (\varepsilon_2 / \varepsilon_1) - 1, \quad (2)$$

$$\omega_0(S, n_e) = 2(1 + 2/3\pi^2 n_e^2)^{1/2} S^{-3/2} \quad (3)$$

in an SMC of radius

$$(a_0 / a_h) \ll 1 < S \leq (a_e / a_h) \approx (a_{\text{ex}} / a_h) \quad (4)$$

in the state ($n_e, l_e = m_e = 0$; n_h, l_h, m_h), where n_e, l_e, m_e and n_h, l_h, m_h are the radial, orbital, and azimuthal quantum numbers of the electron and hole; $t_h = 2n_h + l_h$ is the principal quantum number of the hole; $S = a/a_h$ is the dimension-

less radius of the SMC; $a_e = \varepsilon_2 \hbar^2/m_e e^2$, $a_h = \varepsilon_2 \hbar^2/m_h e^2$, and $a_{ex} = \varepsilon_2 \hbar^2/\mu e^2$ are the Bohr radii of the electron, hole, and exciton in a semiconductor with permittivity ε_2; $\mu = m_e m_h/(m_e + m_h)$ is the reduced exciton mass; and, a_0 is a characteristic size of the order of the interatomic distance.[11] The energy in the spectrum (1) of an electron–hole pair is measured in the units $\mathrm{Ry} = \hbar^2/2m_h a_h^2$, E_g is the band gap in the semiconductor with permittivity ε_2, $\mathrm{Ci}(y)$ is the cosine integral, and $\gamma = 0.577$ is the Euler constant.

When the conditions (4) are satisfied, the contribution of the polarization interaction of an electron and hole with the surface of an SMC ($\simeq e^2/\varepsilon_2 a$) (the last two terms in Eq. (1)) to the electron–hole pair spectrum (1) will be comparable in order of magnitude to the exciton binding energy ($E_b = \hbar^2/2\mu a_{ex}^2$) in the SMC. The last term in the electron–hole pair spectrum (1) consisted of the spectrum of a heavy hole undergoing oscillations with frequency $\omega_0(S, n_e)$ (3) in the adiabatic electronic potential in the SMC.[8] The hole wavefunction is expressed in terms of odd-numbered Hermite polynomials.[12]

2. INTERBAND LIGHT ABSORPTION IN A SMALL MICROCRYSTAL

Using the approximations described above and the simple model of a quasi-zero-dimensional structure,[6–9] we shall study interband light absorption in an SMC whose radius S satisfies the condition (4). We shall use the dipole approximation in which the absorption length is large compared with the size of the SMC. The relative intensity of optical interband transitions in the SMC with dipole-allowed transitions is determined by the squared overlap integral of the electronic $\Psi_{n_e, l_e, m_e}(\mathbf{r}_e)$ and hole $\chi_{n_h, l_h, m_h}^{n_e, l_e, m_e}(\mathbf{r}_h)$ wave functions[13]

$$K(S, \omega) = A \sum_{\substack{n_e n_h \\ l_e l_h \\ m_e m_h}} \left| \int \Psi_{n_e, l_e, m_e}(\mathbf{r}_e) \chi_{n_h, l_h, m_h}^{n_e, l_e, m_e}(\mathbf{r}_h) \delta(r_e - r_h) dr_e dr_h \right|^2 \delta(\Delta - E_{n_e, l_e, m_e}^{n_h, l_h, m_h}(S)), \quad (5)$$

where $\Delta = \hbar\omega - E_g$, ω is the frequency of the incident light, and A is proportional to the squared modulus of the dipole moment matrix element obtained with Bloch functions.

The quantity $K(S, \omega)$ (5) relates the energy absorbed by the SMC per unit time and the time-averaged squared electric field of the incident wave. In addition, $K(S, \omega)$ (5) multiplied by the number of SMCs per unit volume of the dielectric matrix is the electric conductivity, related in the standard manner with the light absorption coefficient, of the quasi-zero-dimensional systems of interest at the frequency of the field.

Due to the orthogonality of the electron wave functions $\Psi_{n_e, l_e, m_e}(\mathbf{r}_e)$ and hole wave functions $\chi_{n_h, l_h, m_h}^{n_e, l_e, m_e}(\mathbf{r}_h)$ the orbital quantum numbers of the electron and hole ($l_e = l_h$) are conserved in transitions, while the azimuthal number ($m_e = -m_h$) changes sign. The radial quantum numbers n_e and n_h can be arbitrary.

It should be noted that, taking account of the Coulomb and polarization interactions of an electron and hole in a small SMC, changes the selection rules for dipole transitions compared to the rules obtained in an approximation where the Coulomb and polarization interactions were neglected. In this approximation both electron and hole radial and orbital quantum numbers ($n_e = n_h$ and $l_e = l_h$) are conserved, while the azimuthal quantum numbers change sign ($m_e = -m_h$).

We shall now determine $K(S, \omega)$ (5), related to the optical transitions of a hole from a level t_h to the lowest electronic level ($n_e = 1$, $l_e = m_e = 0$). For this case the squared overlap integral of the electronic $\Psi_{1,0,0}(\mathbf{r}_e)$ and hole $\chi_{t_h}^{1,0,0}(\mathbf{r}_h)$ wave functions has been calculated in Ref. 3 as

$$L_{n_h}(S) = \left| \int_0^a \Psi_{1,0,0}(r) \chi_{t_h}^{1,0,0}(r) r^2 dr \right|^2$$

$$= 2\pi^{5/2} \left[\frac{\hbar^2}{m_h \omega_0(S, n_e = 1) a^2} \right]^{3/2} \frac{(n_h + 1)}{2^{2n_h}(n_h!)}. \quad (6)$$

The quantity $L_{n_k}(S)$ with $\omega_0(S, n_e = 1)$ (3) becomes

$$L_{n_h}(S) = \frac{2\pi^{5/2}}{(1 + 2/3\pi^2)^{3/4}} \frac{(n_h + 1)}{2^{2n_h} n_h!} S^{-3/4}. \quad (7)$$

Substituting the expressions (6) and (1) into Eq. (5) we obtain $K(S, \omega)$ in the form

$$K(S, \omega) = A \sum_{n_h} L_{n_h}(S) \delta \left[\Delta - \frac{\pi^2}{S^2} \frac{m_h}{m_e} - \frac{1}{S}\left(Z_{1,0} + P_{1,0} \right. \right.$$

$$\left. \left. + \frac{\varepsilon_2}{\varepsilon_1} \right) - \omega_0(S, n_e = 1)\left(t_h + \frac{3}{2} \right) \right]. \quad (8)$$

It follows from Eq. (8) that, since the Coulomb and polarization interactions of an electron and a hole with a small SMC, whose radius S satisfies condition (4), is taken into account, each line corresponding to prescribed values of the radial n_e and orbital l_e quantum numbers of an electron in the interband optical absorption spectrum of such an SMC transforms into a series of closely-spaced equidistant lines corresponding to different values of the hole principal quantum number t_h. In addition, according to Eq. (3) for $\omega_0(S, n_e)$, the splitting between the equidistant series of lines depends on both the quantum number n_e and the radius S of the SMC. As the electron's radial quantum n_e increases, the splitting between the equidistant series of lines $\omega_0(S, n_e)$ (3) increases ($\omega_0 \sim n_e$), and as the radius S of the SMC increases, this splitting decreases ($\omega_0 \sim S^{-3/2}$).

As follows from Eq. (8), for interband light absorption by a small SMC, the absorption threshold is the light frequency $\bar{\omega}$ given by

$$\hbar\bar{\omega} = E_g + \frac{\pi^2}{S^2} \frac{m_h}{m_e} + \frac{1}{S}\left(Z_{1,0} + P_{1,0} + \frac{\varepsilon_2}{\varepsilon_1} \right)$$

$$+ \frac{3}{2}\omega_0(S, n_e = 1). \quad (9)$$

Equation (9) expresses the law according to which the effective band gap of an SMC increases with decreasing SMC radius S. The polarization interaction [the last two terms in Eq. (9)] makes a positive contribution to Eq. (9), which gives rise to an effective increase of the band gap of a small SMC. In other words, the polarization interaction between charge carriers and the surface of an SMC produces a larger shift of the absorption threshold $\bar{\omega}(S)$ Eq. (9) in a small SMC in the short-wavelength direction than the analogous quantity obtained in Ref. 3 neglecting the polarization interaction.

3. COMPARISON OF THEORY WITH EXPERIMENTS

The experiments performed in Refs. 14 and 15 investigated the low-temperature ($T \simeq 4.2$ K) interband absorption spectra of cadmium sulfide SMCs (with permittivity $\varepsilon_2 \approx 9.3$) of size $a \leqslant a_{\text{ex}}$ dispersed in a transparent dielectric silicate glass matrix (with permittivity $\varepsilon_1 \approx 1.5$). Structure consisting of an equidistance series of levels split by $\Delta E \simeq a^{-3/2}$ was observed near transitions to a lower size-quantization level ($n_e = 1$, $l_e = 0$) of an electron. This structure is due to quantization of the energy spectrum of a heavy hole in the adiabatic electron potential. The effective electron and hole masses in CdS were, respectively, $m_e = 0.205 m_0$ and $m_h = 5 m_0$ (i.e. $m_e / m_h \ll 1$ and m_0 is the electron mass in vacuum).

Indeed, the motion of a heavy hole in the electron potential[7,8] near SMC sizes (4), which also includes the range of SMC radii studied in Refs. 14 and 15, leads to the appearance of an equidistance series of levels whose splitting was determined by the expression ω_0 (3), in the hole energy spectrum. Comparing Eq. (3) (with $n_e = 1$) with the experimental dependence obtained in Refs. 14 and 15 for the splitting $\Delta E(a) = \omega_0(S, n_e = 1)$ on the SMC size a, it follows that for SMCs with radii $a \leqslant a_{\text{ex}}$ the splitting $\omega_0(S, n_e = 1)$ (3) (for $a = 25$ Å $\omega_0 = 37.6$ meV and for $a = 30$ Å $\omega_0 = 28.29$ meV) is in good agreement with the experimental data of Refs. 14 and 15 (correspondingly, for $a = 25$ and 30 Å the splitting $\omega_0 = 40.0$ and 30.1 meV), differing from the latter only negligibly ($\leqslant 6\%$). For the same experimental conditions as in Refs. 14 and 15, we obtain using Eq. (7) the following squared overlap integrals $K(S, \omega)/A$ (8) for transitions of a hole from an equidistant series of levels ($n_h = 0$; $l_h = m_h = 0$), ($n_h = 1$; $l_h = m_h = 0$), ($n_h = 2$; $l_h = m_h = 0$), and ($n_h = 3$; $l_h = m_h = 0$) to a lower electron size-quantization level ($n_e = 1$; $l_e = m_e = 0$)

$$K(S, \omega)/A = \sum_{n_h = 0}^{3} L_{n_h}(S) = 7.659 S^{-3/4}(1 + 0.5$$
$$+ 9.4 \times 10^{-2} + 1.0 \times 10^{-2}). \tag{10}$$

From Eq. (10) follows

$$L_0 = 7.659 S^{-3/4}, \quad L_1 = 0.5 L_0,$$

$$L_2 = 9.4 \times 10^{-2} L_0, \quad \text{and} \quad L_3 = 10^{-2} L_0.$$

TABLE I. The squared overlap integrals $L_{n_h}(S)$ ($n_h = 0, 1, 2, 3$) and light absorption coefficient $K(S, \omega)/A$ as functions of the radius S of a small CdS SMC (a — radius of SMC in angstroms).

S (a, Å)	L_0	L_1	L_2	L_3	K/A
30.43(30)	0.591	0.295	0.056	0.0059	0.942
35.5 (35)	0.527	0.263	0.05	0.0053	0.845
40.57(40)	0.476	0.238	0.045	0.0048	0.764
45.64(45)	0.436	0.218	0.041	0.0044	0.6994
50.71(50)	0.403	0.202	0.038	0.004	0.647

The values $L_{n_h}(S)$ (11) (where $n_h = 0, 1, 2, 3$) together with $K(S, \omega)/A$ (10) for SMCs with radii $30.43 \leqslant S \leqslant 50.71$ ($30 \leqslant a \leqslant 50$ Å) satisfying the condition (4) are presented in Table I.

It follows from the results presented in Table I that spectral lines of holes with quantum numbers ($n_h = 0$; $l_h = m_h = 0$) and ($n_h = 1$; $l_h = m_h = 0$), for which the transition oscillator strengths are maximum, make the main contribution to the light absorption coefficient $K(S, \omega)/A$ (8) of small CdS SMCs with sizes S (4). The contributions of the highly excited hole lines ($n_h \geqslant 2$; $l_h = m_h = 0$) relative to the contribution of the line ($n_h = 0$; $l_h = m_h = 0$) are negligibly small ($\leqslant 9 \times 10^{-2}$).

In summary, it has been shown on the basis of the given model of quasi-zero-dimensional systems that the absorption edge of small CdS SMCs is formed by two transitions of comparable intensity from different hole size-quantization levels ($n_h = 0$; $l_h = m_h = 0$) and ($n_h = 1$; $l_h = m_h = 0$) into a lower electron size-quantization level ($n_e = 1$; $l_e = m_e = 0$).

*)E-mail: vika@ineco.comcentre.nikolaev.ua

[1] A. I. Ekimov and A. A. Onushchenko, JETP Lett. **40**, 1136 (1984).
[2] Yu. V. Vandyshev, V. S. Dneprovskiĭ, and V. I. Klimov, Zh. Éksp. Teor. Fiz. **101**, 270 (1992) [Soy. Phys. JETP **74**, 144 (1992)].
[3] Al. L. Éfros and A. L. Éfros, Fiz. Tekh. Poluprovodn. **16**, 1209 (1982) [Sov. Phys. Semicond. **16**, 772 (1982)].
[4] A. L. Efros and A. V. Rodina, Phys. Rev. B **47**, 10005 (1993).
[5] M. Nirmal, D. Norris, and A. L. Efros, Phys. Rev. Lett. **75**, 3728 (1995).
[6] N. A. Efremov and S. I. Pokutniĭ, Fiz. Tverd. Tela (Leningrad) **27**, 48 (1985) [Sov. Phys. Solid State **27**, 27 (1985)]; *ibid.* **32**, 1637 (1990) [*ibid.* **32** 955 (1990)].
[7] S. I. Pokutniĭ, Fiz. Tekh. Poluprovodn. **25**, 628 (1991) [Sov. Phys. Semicond. **25**, 381 (1991)]; *ibid.* **30**, 1952 (1996) [*ibid.* **30**, 1015 (1996)].
[8] S. I. Pokutnyi, Phys. Lett. A **168**, 433 (1992).
[9] S. I. Pokutniĭ, Fiz. Tverd. Tela (St. Petersburg) **38**, 2667 (1996) [Phys. Solid State **38**, 1463 (1996)].
[10] N. V. Tkach and V. A. Golovatskiĭ, Fiz. Tverd. Tela (Leningrad) **32**, 2512 (1990) [Sov. Phys. Solid State **32**, 1461 (1990)].
[11] Yu. E. Lozovik and D. R. Musin, Preprint No. 20, IS AN SSR (1981).
[12] V. M. Agranovich, *The Theory of Excitons* [in Russian] (Moscow, 1968).
[13] G. B. Grigoryan, É. M. Kazaryan, and Al. L. Éfros, Fiz. Tverd. Tela (Leningrad) **32**, 1772 (1990) [Sov. Phys. Solid State **32**, 1031 (1990)].
[14] A. I. Ekimov, A. A. Onushchenko, and Al. L. Éfros, JETP Lett. **43**, 376 (1986).
[15] D. Chepic, A. Efros, and A. Ekimov, J. Lumin. **47**, 113 (1990).

Translated by M. E. Alferieff

Differential thermopower of a superlattice in a strong electric field

A. S. Bulygin, G. M. Shmelev, and I. I. Maglevannyĭ

Volgograd State Pedagogical University 400013 Volgograd, Russia

The effect of an electric field on the differential thermopower $\alpha(E)$ of a one-dimensional superlattice is investigated in the semiclassical approximation. A nonmonotonic temperature dependence of $\alpha(0)$ is established for a degenerate electron gas. It is shown that, in principle, an electric field can be used to control the thermoelectric properties of superlattices. © *1999 American Institute of Physics.* [S1063-7834(99)03907-6]

There are many published papers devoted to the calculation of the thermopower of an electron gas with a cosinusoidal dispersion law. We call attention to Refs. 1–4 (see also Ref. 5 and the references cited there). We also call attention to a recent experiment[6] that also contains a review of investigations of the thermopower in low-dimensional structures. In Refs. 1–4, 6, and other works, the thermopower was studied in a regime with a weak electric field **E,** so that α does not depend on **E**. The properties of the indicated structures in strong fields, causing nonlinear effects to appear and, correspondingly, the Q of the material to be controlled by means of the fields, could also be of practical interest. In Ref. 5 the effect of ac and dc electric fields on the thermopower of a one-dimensional superlattice (SL) was investigated. The results of Ref. 5 are valid for a nondegenerate electron gas and not too strong fields so that the parameter $eEd\tau/\hbar T$ $\leqslant 1$, where d is the period of the SL, 2Δ is the miniband width, τ is the relaxation time, and T is the temperature in energy units. In the present paper a method free of the indicated limitations is used to calculate α.

In the one-miniband approximation, the electron energy in a one-dimensional SL has the form

$$\varepsilon(\mathbf{p}) = \frac{p_\perp^2}{2m} + \Delta\left(1 - \cos\frac{p_x d}{\hbar}\right), \tag{1}$$

where $p_\perp$ and p_x are, respectively, the components of the quasimomentum p perpendicular and parallel to the SL axis and m is the carrier mass in the plane of the SL layers. We assume that **E** and ∇T ($T = T(x)$ is the local temperature) are directed along the SL axis (OX). In the semiclassical approximation ($2\Delta \gg \hbar/\tau$, eEd, $d\nabla_x T$) the electron distribution function $f(\mathbf{p},\mathbf{r})$ can be found from Boltzmann's equation. We choose the collision integral in the τ approximation, and assume $\tau =$const. The most convincing argument in favor of this condition is the results of Ref. 7, where it is established experimentally that the relaxation time $\tau =$const in a GaAs/AlAs SL above 40 K and is temperature-independent.

We write the kinetic equation in the form

$$\hat{L}_{\mathbf{p}} f + \text{div}(\mathbf{v}f) = \frac{f_0(\mathbf{p},\mathbf{r})}{\tau}, \tag{2}$$

where the operator

$$\hat{L}_p = \left(\frac{d\mathbf{p}}{dt}, \frac{\partial}{\partial\mathbf{p}}\right) + \frac{1}{\tau}, \tag{3}$$

$f_0(\mathbf{p},\mathbf{r})$ is the Fermi distribution function with temperature and chemical potential μ varying in space, and $\mathbf{v(p)}$ $= \partial\varepsilon(\mathbf{p})/\partial\mathbf{p}$ is the electron velocity.

The solution of Eq. (2) must satisfy the condition

$$\sum_{\mathbf{p}} f(\mathbf{p},\mathbf{r}) = n(\mathbf{r}), \tag{4}$$

where $n(\mathbf{r})$ is the electron density. The current density is calculated from

$$\mathbf{j}(\mathbf{r}) = e\sum_{\mathbf{p}} \mathbf{v(p)}f(\mathbf{p},\mathbf{r}), \tag{5}$$

and in the steady state

$$\text{div}\,\mathbf{j}(\mathbf{r}) = 0. \tag{6}$$

We assume the second term on the left side of Eq. (2) to be small. Then the solution of Eq. (2) in the zeroth approximation has the form

$$f^{(0)}(\mathbf{p},\mathbf{r}) = \hat{L}_{\mathbf{p}}^{-1}\left(\frac{f_0(\mathbf{p},\mathbf{r})}{\tau}\right), \tag{7}$$

where the inverse operator $\hat{L}_{\mathbf{p}}^{-1}$ is given by

$$\hat{L}_{\pm\mathbf{p}}^{-1}\psi(\mathbf{p}) = \int_0^\infty \psi(\mathbf{p}\mp\mathbf{p}(t))\exp\left(-\frac{t}{\tau}\right)dt, \tag{8}$$

where $\mathbf{p}(t)$ is the solution of the equation of motion

$$\frac{d\mathbf{p}}{dt} = F \tag{9}$$

with the initial condition $\mathbf{p}(0)=0$, **F** is the constant force acting on the particle, and $\mathbf{F}=e\mathbf{E}$.

To perform correctly [without violating condition (4)] the iteration procedure for finding $f(\mathbf{p},\mathbf{r})$ in the form of a powers series in $\nabla_x T(\mathbf{r})$ or $\nabla_x n(\mathbf{r})$, we add to the right-hand side of Eq. (2) the term $f^{(0)}(\mathbf{p},\mathbf{r})\text{div}\,\mathbf{j}/en$, which is zero. A similar device has been used in a theoretical investigation of
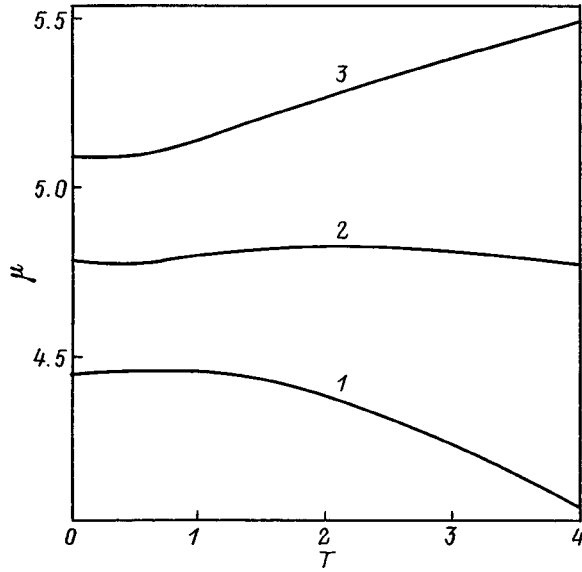
FIG. 1. Chemical potential μ versus the temperature T (arbitrary units). The curves correspond to the values of the parameter $N=\pi^3\hbar^2 nd/m\Delta$: *1* — $N=0.55$; *2* — $N=0.6$; *3* — $N=0.65$.
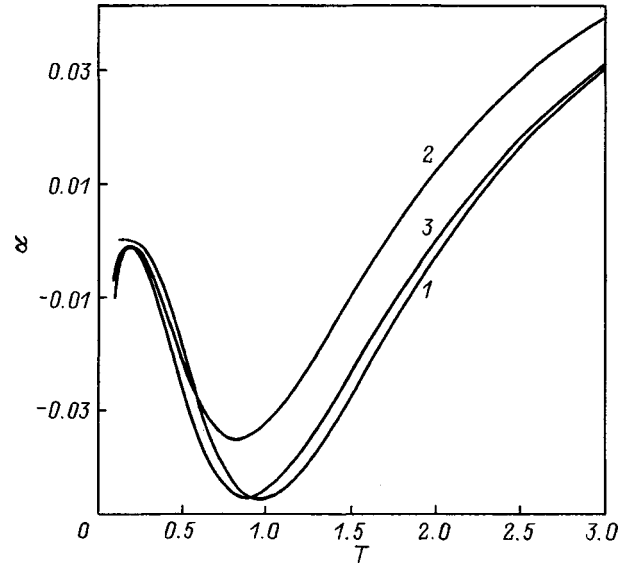

FIG. 2. Thermopower α versus the temperature T for $N=0.6$. The curves correspond to the parameter values: *1* — $E=0$; *2* — $E=1$; *3* — $E=10$.

nonequilibrium fluctuations in an electron gas obeying a parabolic dispersion law (c.f., Ref. 8). Therefore we find, to a first approximation

$$f(\mathbf{p},\mathbf{r})=f^{(0)}(\mathbf{p},\mathbf{r})+\hat{L}_{\mathbf{p}}^{-1}\varphi(\mathbf{p},\mathbf{r})$$

$$\equiv f^{(0)}(\mathbf{p},\mathbf{r})+\hat{L}_{\mathbf{p}}^{-1}\left\{\frac{1}{en}f^{(0)}(\mathbf{p},\mathbf{r})\mathrm{div}\,\mathbf{j}^{(0)}(\mathbf{r})\right.$$

$$\left.-\mathrm{div}\,(\mathbf{v}(\mathbf{p})f^{(0)}(\mathbf{p},\mathbf{r}))\right\}, \tag{10}$$

where $\mathbf{j}^{(0)}(\mathbf{r})$ is the current density obtained from Eq. (5) with $f=f^{(0)}$. The equation for the current density corresponding Eq. (10) is

$$\mathbf{j}(\mathbf{r})=\mathbf{j}^{(0)}(\mathbf{r})+e\sum_{\mathbf{p}}\varphi(\mathbf{p},\mathbf{r})\hat{L}_{-\mathbf{p}}^{-1}\mathbf{v}(\mathbf{p}). \tag{11}$$

Using Eqs. (11), (10), (8), and (1) we find $j_x\equiv j$. We shall represent the result in a dimensionless form, making the transformations $Ee\tau d/\hbar\to E$, $j/env_0\to j$, $\mu/\Delta\to\mu$, $T/\Delta\to T$, $v_0\tau\nabla_x\to\nabla_x$ ($v_0=\Delta d/\hbar$ is the maximum electron velocity along OX).

For $T(\mathbf{r})=$ const we have from Eq. (11) in the linear approximation in $\nabla_x n$

$$j=C_1\frac{E}{1+E^2}-D\frac{\nabla_x n}{n}, \tag{12}$$

where the diffusion coefficient (in units of $v_0^2\tau$) is

$$D(E)=\frac{1}{2(1+E^2)}\left[1+C_2\frac{2E^2-1}{4E^2+1}-4C_1^2\frac{E^2}{(E^2+1)^2}\right], \tag{13}$$

and

$$C_k=C_k(T)=\left\langle\cos\frac{kp_x d}{\hbar}\right\rangle, \tag{14}$$

where the brackets indicate averaging using the function $f_0(\mathbf{p},\mathbf{r})$.

We note that Eq. (13) (for nondegenerate carriers) was first obtained in Ref. 9 by a different method: using Boltzmann's equation with the Bathnagar–Gross–Crook collision integral.

For $n=$ const we find from Eq. (11) in the linear approximation in $\nabla_x T$

$$j=\frac{C_1}{1+E^2}[(E-\nabla_x\mu)-\alpha\nabla_x T], \tag{15}$$

where the differential thermopower (in units of k_B/e) is

$$\alpha(E)=\frac{B_2}{2C_1}\left(\frac{2E^2-1}{1+4E^2}\right)-\frac{2B_1E^2}{(1+E^2)^2}-\frac{d\mu}{dT}, \tag{16}$$

where

$$B_k=\frac{dC_k}{dT}. \tag{17}$$

For a nondegenerate electron gas, where

$$\exp\left(\frac{\mu}{T}\right)=\frac{n}{n_0}\exp\left(\frac{1}{T}\right)I_0^{-1}\left(\frac{1}{T}\right)\ll1, \tag{18}$$

($I_k(z)$ is a modified Bessel function, $n_0=mT\Delta/2\pi\hbar^2 d$) and $f_0(\mathbf{p},\mathbf{r})\approx\exp((\mu-\varepsilon(\mathbf{p}))/T)$, the coefficients C_k and B_k can be calculated analytically as

$$C_k=I_k\left(\frac{1}{T}\right)\bigg/I_0\left(\frac{1}{T}\right),$$

$$2T^2 B_k=2C_1 C_k-C_{k-1}-C_{k+1}. \tag{19}$$
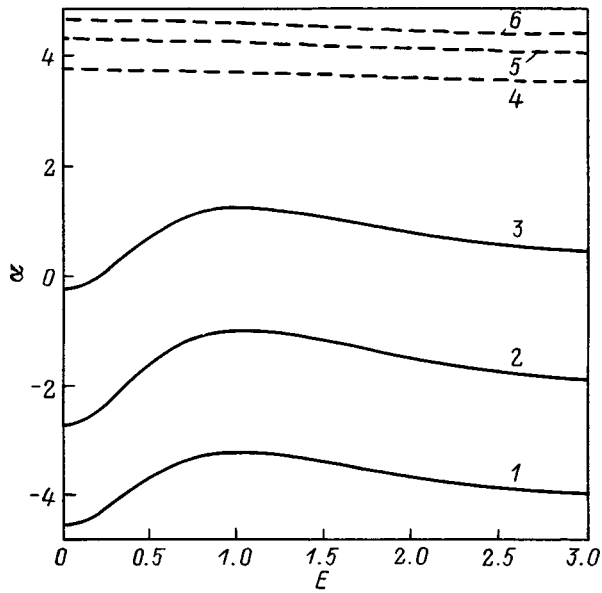
For $E\ll1$ we obtain from Eq. (16)

FIG. 3. Thermopower versus the field E. The solid curves ($10^2\alpha$) correspond to $N=0.6$ and the temperatures: 1 — $T=0.5$; 2 — $T=1$; 3 — $T=1.5$. The dashed curves (α) correspond to $N=0.01$ and temperatures: 4 — $T=0.5$; 5 — $T=1$; 6 — $T=1.5$.

$$\alpha(0)=3+\frac{1}{T}\left(1-\frac{1}{C_1}\right)-\frac{\mu}{T}. \qquad (20)$$

For wide bands and/or low temperatures ($T\ll 1$), from Eq. (20) follows the expression $\alpha=5/2-\mu/T$, corresponding to the standard dispersion law. This is natural, since in this case the band top no longer plays a role. In the opposite limiting case ($T\gg 1$) we have from Eq. (20)

$$\alpha(0)=1-\frac{\mu}{T}. \qquad (21)$$

We note that for $T\gg 1$ and $E\gg 1$ the function $\alpha(E)$ can also be expressed by Eq. (21).

For arbitrary degeneracy of the electron gas, the coefficients $C_k(T)$ can be found using the Fermi distribution function, in which the temperature dependence of the chemical potential $\mu=\mu(T)$ is determined from condition (4). Figure 1 shows the numerical results for $\mu=\mu(T)$ for various values of the dimensionless parameter $N=\pi^3\hbar^2nd/m\Delta$. Figure 2 shows the temperature dependence of the thermopower for several values of the field E. Note the nonmonotonic behavior of $\alpha(0)$ at low temperatures. This character of $\alpha(0)$ has been observed in a GaAs/Ga$_{1-x}$Al$_x$As SL.[6] Figure 3 shows $\alpha(E)$ for various temperatures.

The numerical estimates of the results obtained (including those presented in the figures) reduce to estimating the scale which was used here for the electric field strength ($E_0=\hbar/e\tau d$). For $d=10^{-6}$ cm and $\tau=10^{-12}$ s we have $E_0\approx 660$ V/cm.

[1] A. G. Samoĭlovich and M. I. Klinger, Zh. Tekh. Fiz. **25**(12), 2050 (1955).
[2] A. Ya. Shik, Fiz. Tekh. Poluprovodn. **7**(2), 261 (1973) [Sov. Phys. Semicond. **7**, 187 (1973)].
[3] B. M. Askerov, N. F. Gashimzade, and M. M. Panakhov, Fiz. Tverd. Tela (Leningrad) **29**(3), 818 (1987) [Sov. Phys. Solid State **29**, 465 (1987)].
[4] S. S. Kubakaddi, P. N. Butcher, and B. G. Mulimani, J. Phys.: Condens. Matter **3**, 5445 (1991).
[5] G. M. Shmelev, I. A. Chaĭkovskiĭ, and S. I. Mensa, Fiz. Tekh. Poluprovodn. **23**, 712 (1989) [Sov. Phys. Semicond. **23**, 447 (1989)].
[6] R. Fletcher, P. T. Coleridge, and Y. Feng, Phys. Rev. B **52**, 2823 (1995).
[7] H. T. Grahn, K. von Klitzing, K. Ploog, and G. H. Döhler, Phys. Rev. B **43**, 12 095 (1991).
[8] I. M. Dykman and P. M. Tomchuk, *Transport Phenomena and Fluctuations in Semiconductors* [in Russian] (Naukova Dumka, Kiev, 1981).
[9] A. A. Ignatov and V. I. Shashkin, Fiz. Tekh. Poluprovodn. **18**, 721 (1984) [Sov. Phys. Semicond. **18**, 449 (1984)].

Translated by M. E. Alferieff

Kronig–Penney problem for a biparabolic potential: Quasifree particle motion

A. Zh. Muradyan

Erevan State University 375049 Erevan, Armenia

The Bloch states of a particle in a one-dimensional, periodic, biparabolic field are determined. The solutions are expressed in terms of confluent hypergeometric functions. It is shown that the first term of the Tricomi expansion for confluent hypergeometric functions represents the quasifree above-barrier motion of a particle and is identical to the exact Kronig–Penney solution for a square potential. © *1999 American Institute of Physics.* [S1063-7834(99)04007-1]

The one-dimensional periodic potential[1] in the theory of solids is the foundation for the qualitative (rough) description of the band structure of the energy spectrum and wave functions of electrons.[2–4] The weak-coupling approximation is well known for describing quasifree motion. This approximation actually employs a Taylor expansion in terms of a parameter proportional to the interaction energy. A modified perturbation theory, which is essentially the analog of the Lennard–Jones method,[6] has been proposed in Ref. 5.

In the present paper, the Bloch (steady-state) solutions for the states of a particle in a biparabolic potential are obtained. To describe quasifree motion, the second Tricomi expansion of the confluent hypergeometric function in terms of Bessel functions is used.[7] It is found that this expansion is "softer" relative to the interaction parameter than is the Taylor expansion, since it preserves the main content of the solutions for a periodic potential — the band structure of the energy spectrum — even in the first approximation.

1. BIPARABOLIC POTENTIAL AND EXACT BLOCH SOLUTIONS

A biparabolic potential is a one-dimensional periodic field in which the potential energy of a particle can be represented as a periodic function consisting of truncated and alternately inverted parabolas (Fig. 1)

$$U(x) = \frac{1 + (-1)^n}{2} U_{\min} + \frac{1 - (-1)^n}{2} U_{\max}$$

$$+ (-1)^n k \left(x - \frac{nl}{2} \right)^2, \tag{1}$$

where $n = 0, \pm 1, \pm 2, \ldots$, and for each n the coordinate x varies in the range

$$\frac{2n-1}{4} l \leqslant x \leqslant \frac{2n+1}{4} l.$$

Even values of n correspond to concave and odd values to convex regions of the potential curve relative to the average value $(U_{\min} + U_{\max})/2$. The quantities $U_{\min}$ and $U_{\max}$ are the minimum and maximum values of the potential energy, and l is its spatial period. The continuity of the potential and its first derivative is ensured by choosing the value of the "elas-

tic" constant $k = 8U/l^2$, where $U = U_{\max} - U_{\min}$ is the depth of the periodic potential energy. The origin of the coordinates is placed at the minimum of the concave region for $n = 0$.

The solution of the steady-state Schrödinger equation (SSE) with the quadratic coordinate dependence (1) of the potential energy is presented using confluent hypergeometric functions Φ. In the first region ($n = 0$, $-l/4 \leqslant x \leqslant l/4$), see Fig. 1, the wave function of the particle is

$$\Psi_I(x) = A_a u_a(x) + A_b u_b(x), \tag{2}$$

where

$$u_a(x) = e^{-\eta^2 x^2/2} \Phi\left(\alpha, \frac{1}{2}; \eta^2 x^2 \right), \tag{3}$$

$$u_b(x) = \eta x e^{-\eta^2 x^2/2} \Phi\left(\alpha + \frac{1}{2}, \frac{3}{2}; \eta^2 x^2 \right) \tag{4}$$

are the two unknown solutions of the SSE and the following notations are used:

$$\eta = 2 \left(\frac{MU}{\hbar^2 l^2} \right)^{1/4}, \quad \alpha = \frac{1}{4}(1 - \lambda + V_{\min}),$$

$$V_{\min} = \frac{l}{2\hbar} \sqrt{\frac{M}{U}} U_{\min}, \quad \lambda = \frac{l}{2\hbar} \sqrt{\frac{M}{U}} E, \tag{5}$$

E and M are the particle energy and mass, and A_a and A_b are the as yet unknown coefficients which will be determined from the continuity of the wave function and its first derivative together with the normalization condition.

It is useful to note that, aside from U, the problem also contains a second energy parameter, which can be written as $E_r = \hbar^2 k^2 / 2M$ by analogy with the recoil energy for absorption–emission of a photon, $k = 2\pi/l$. The arguments in the expressions (3) and (4) and the dimensionless particle energy λ will have the form

$$\eta^2 x^2 = 4\pi \sqrt{\frac{2U}{E_r}} \left(\frac{x}{l} \right)^2, \quad \lambda = \pi \frac{E}{\sqrt{2UE_r}}. \tag{6}$$

The spatial scale of the problem is determined by the ratio of these two parameters U and E_r, while the energy scale is determined by their product.
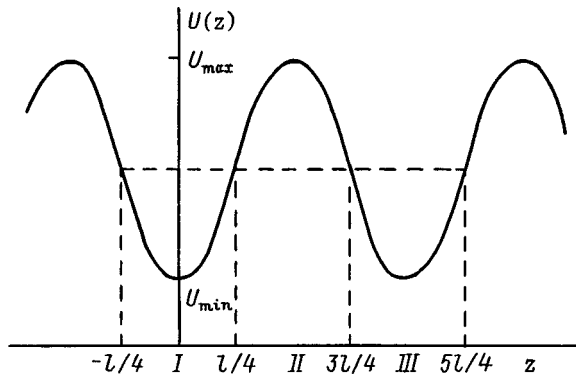
FIG. 1. Biparabolic potential. The first (I; $n=0$), second (II; $n=1$), and third (III; $n=2$) regions are marked at the bottom.

In the second region of the potential energy ($n=1$; $l/4 \leqslant x \leqslant 3l/4$)

$$\Psi_{II}(x) = B_a v_a(x) + B_b v_b(x), \qquad (7)$$

where B_a and B_b are new constants, and $v_a(x)$ and $v_b(x)$ are obtained from the expressions $u_a(x)$ and $u_b(x)$ by replacing α and $V_{\min}$ by

$$\beta = \frac{1}{4}(1 - i(\lambda - V_{\max})), \quad V_{\max} = \frac{l}{2\hbar}\sqrt{\frac{M}{U}} U_{\max}$$

respectively. The independent variable x^2 is replaced by $-i(x-l/2)^2$.

In the third region ($n=2$, $3l/4 \leqslant x \leqslant 5l/4$), according to the Bloch condition the solution of the SSE is

$$\Psi_{III}(x) = e^{\frac{i}{\hbar}pl}\Psi_I(x-l), \qquad (8)$$

where P is the quasimomentum of the particle.

The standard requirements of continuity at the boundary points ($x=1/4$ and $x=3l/4$) yield a dispersion relation of the form

$$\cos\frac{pl}{\hbar} = \frac{G_{ab}G_{ba} + G_{aa}G_{bb}}{G_{ab}G_{ba} - G_{aa}G_{bb}}, \qquad (9)$$

where

$$G_{\mu\nu} = u_\mu v'_\nu - v_\nu u'_\mu \big|_{x=l/2}, \qquad (10)$$

$\mu, \nu = a, b$. The primes on the functions u'_μ and v'_ν denote, as usual, derivatives with respect to the argument (i.e. with respect to x). To obtain the form (10), relations expressing the values of the functions $u_\mu(x)$ and $v_\nu(x)$ and their derivatives at the point $x=3l/4$ in terms of the corresponding values at the point $x=l/4$ were used. These relations were obtained using explicit expressions for the quantities mentioned above. The continuity conditions also establish the following relations between the coefficients A_μ and B_μ:

$$A_b = iA_a\frac{G_{ab}}{G_{bb}}\tan\frac{pl}{2\hbar}, \quad B_a = A_a\frac{G_{ab}}{\Delta}\left(1 + i\tan\frac{pl}{2\hbar}\right),$$

$$B_b = A_a\frac{G_{aa}}{\Delta}\left(-1 + i\cot\frac{pl}{2\hbar}\right), \qquad (11)$$

where Δ is the Wronskian of the solutions for the second region of the potential curve (Fig. 1). To determine the remaining unknown A_a a normalization condition must be added to Eq. (11).[4]

2. QUASIFREE PARTICLE MOTION

For confluent hypergeometric functions, which determine the wave function and energy spectrum of a particle in a periodic biparabolic potential, we make use of the second Tricomi expansion[7]

$$e^{-z/2}\Phi(h, \sigma+1; z) = \Gamma(\sigma+1)(xz)^{-\sigma/2}\sum_{n=0}^{\infty}c_n\left(x, \frac{1+\sigma}{2}\right)$$

$$\times\left(\frac{z}{4x}\right)^{n/2}J_{\sigma+n}(2\sqrt{xz}), \qquad (12)$$

where $\Gamma(\cdot)$ is the gamma function, $x = (1+\sigma)/2 - h$, $J_m(\cdot)$ is a Bessel function, and the coefficients c_n are determined from the recurrence relation

$$(n+1)c_{n+1}(x,r) = (n+2r-1)c_{n-1}(x,r)$$
$$-2xc_{n-2}(x,r), \qquad (13)$$

where $n=2,3,\ldots$ for $c_0=1$ and $c_1=0$ and are polynomials of degree $[n/3]$ in x.

Simple substitutions show that the ratio $z/4x$ appearing in Eq. (12) is less than one in modulus if $E - U_{\max} > U$, i.e. if the particle energy lies above the maximum value of the potential energy. Then the particle undergoes above-barrier motion; the series (12) converges absolutely and a finite number of terms can be retained.

If only the first term is retained in the expansion in all expressions u_μ, u'_μ, v_ν, and v'_ν, then the dispersion relation (9) and the wave functions (2) and (7) assume the elementary form

$$\cos\frac{pl}{\hbar} = \cos\frac{1}{2}k_{\min}l\,\cos\frac{1}{2}k_{\max}l - \frac{1}{2}\left(\frac{k_{\min}}{k_{\max}}\right.$$

$$\left. + \frac{k_{\max}}{k_{\min}}\right)\sin\frac{1}{2}k_{\min}l\,\sin\frac{1}{2}k_{\max}l, \qquad (14)$$

$$\Psi_I(x) = A_a\cos k_{\min}x + \frac{A_b}{2\sqrt{x_{\min}}}\sin k_{\min}x, \qquad (15)$$

$$\Psi_{II}(x) = B_a\cos k_{\max}(x - l/2)$$

$$+ B_b\frac{\sqrt{-i}}{2\sqrt{x_{\max}}}\sin k_{\max}(x - l/2), \qquad (16)$$

where

$$k_{\min,\max} = \frac{1}{\hbar}\sqrt{2M(E - U_{\min,\max})} \text{ and}$$

$$x_{\min,\max} = \frac{\pi(E - U_{\min,\max})}{4\sqrt{E_rU}}.$$

This result is identical to the Kronig–Penney solution for a square potential. A particle in above-barrier quasifree motion
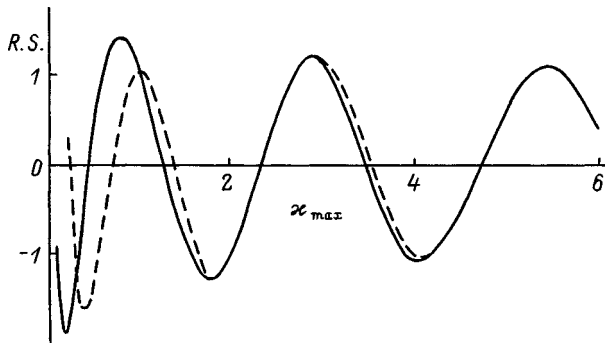
FIG. 2. Right-hand side (*R.S.*) of the dispersion relation (9) as a function of the particle energy (calculated relative to the maximum value of the periodic potential energy). The solid line corresponds to retaining the first and second nonzero terms in the expansion (12), the dashed line corresponds to retaining only the first term. The plots are given for $U_{\min}/E_r = -7$ and $U_{\max}/E_r = -5$.

''feels'' only the depth and period of the periodic potential. It is hoped that this property will remain also in the general case of a periodic potential; however, this must be proved.

Starting with the second term, the second and higher-order terms in the expansion (12) take account of the non-square character of the expansion and contribute, naturally, to states with relatively low-lying energy levels. As an illustration, plots for the first part of the dispersion relation retaining one (square approximation) and two terms of the expansion are presented in Fig. 2. It is evident that, starting with the third or fourth zone, the solutions are virtually identical.

[1] R. L. Kronig and W. Penney, Proc. Roy. Soc. London **130**, 499 (1931).
[2] N. Ashcroft and D. Mermin, *Solid State Physics* (Holt, Rinehart, and Winston, New York, 1976; Mir, Moscow, 1979).
[3] A. S. Davydov, *The Theory of the Solid State* (Nauka, Moscow, 1976), p. 134.
[4] E. M. Lifshitz and L. P. Pitaevskiĭ, *Statistical Physics, Part 2. The Theory of the Condensed State* (Pergamon Press, N. Y., 1980) [Russian original, Nauka, Moscow, 1979, p. 272].
[5] S. Yu. Karpov, O. V. Konstantinov, and M. É. Raĭkh, Fiz. Tverd. Tela (Leningrad) **22**, 3402 (1980) [Sov. Phys. Solid State **22**, 1991 (1980)].
[6] N. Mott and I. Sneddon, *Wave Mechanics and Its Applications* (Dover, New York, 1963) [Russian translation, Nauka, Moscow, 1966].
[7] *Higher Transcendental Functions (Bateman Manuscript Project)*, Vol. 1, edited by A. Erdélyi (McGraw-Hill, New York, 1953; Nauka, Moscow, 1973, p. 265).

Translated by M. E. Alferieff

Enhancement of Raman scattering intensity in porous silicon

M. E. Kompan, I. I. Novak, and V. B. Kulik,

A. F. Ioffe Physicotechnical Institute, Russian Academy of Sciences, 194021 St. Petersburg, Russia

N. A. Kamakova

St. Petersburg State University, St. Petersburg, Russia
(Submitted November 24, 1998)
Fiz. Tverd. Tela (St. Petersburg) **41**, 1320–1322 (July 1999)

An enhancement in inelastic light scattering intensity from porous-silicon quantum wires has been discovered. It is shown that this effect is caused by a decrease in the absorption coefficient of the optical medium formed by quasi-one-dimensional structures, with the crystal structure of the wires themselves remaining unchanged. © *1999 American Institute of Physics.*
[S1063-7834(99)04107-6]

Porous silicon is a macroscopic medium composed of self-organized quasi-one-dimensional formations, the so-called quantum wires.[1] It exhibits a number of unusual properties originating from the smallness of the transverse size of these formations, which is not much in excess of that of the unit cell. As a result, the properties of individual wires exhibit pronounced quantum-mechanical relationships.

In Raman scattering from the wires, these relationships give rise to an uncertainty in the momentum of excited phonons, which is usually seen as a broadening, asymmetry, and shift toward lower energies of the characteristic band in the Raman spectrum. This phenomenon was first considered for the case of thin films, filaments, and small spherical particles.[2] For porous silicon, similar changes in the spectrum are fairly typical and were observed more than once by various authors (see, e.g., Refs. 3 and 4).

Porous silicon is, however, a macroscopic material, and its properties are not identical to those of filaments. Depending on the pattern in which individual wires are arrayed in a material, the latter can exhibit additional properties. Studies of porous silicon revealed new features in the spectral position of the light scattering line and in the scattered polarization.[5,6] This paper reports another feature in the Raman scattering in porous silicon, which manifests itself in an enhancement of the scattered intensity compared to bulk crystalline silicon.

1. EXPERIMENT

The experiments were carried out on samples of porous silicon prepared by radiation-stimulated etching of (100)-oriented silicon plates.[7] The samples used in the study were made from different types of starting silicon and prepared by different technologies and different surface treatment. To facilitate subsequent orientation of the samples with respect to the polarization of exciting light, they were cleaved from the original plates along the $[01\bar{1}]$ and $[011]$ directions. Com-

parative experiments were performed on polished samples of silicon of the same grade.

The phonon spectra excited by a He-Ne laser with a wavelength of 633 nm and power 35 mW were studied in 180° backscattering geometry from the (100) plane using a Ramalog-5 spectrophotometer with computer-controlled data acquisition. To exclude the possible influence of polarization effects on the scattered spectral intensity, no analyzer was used in the detector section of the setup, i.e. the instrument measured the sum of all polarization components. To eliminate the polarizing effect of the gratings, a broad-band quarter-wave phase plate was placed in front of the spectrophotometer entrance slit. To check the absence of polarization effects, the spectra were recorded for two orientations of the electric vector exciting the waves relative to the crystallographic axes, namely, parallel to $[010]$ and to $[01\bar{1}]$.

Figure 1 shows scattering spectra obtained from several samples of porous silicon and one sample of crystalline silicon. In all cases, the spectra showed a single band peaking at about 520 cm^{-1}. The band frequencies in the spectra of crystalline and porous silicon differ only slightly from one another. This can be assigned to the ordered pattern of the quantum-wire array in the samples prepared by the technology of Ref. 5. A similar absence of a frequency shift for a system of oriented quantum wires was reported also in Ref. 8.

As seen from the experimental data, however, the scattered intensity from porous silicon exceeds by far that from samples of crystalline material. Figure 1 presents two sets of spectra corresponding to vector *E* (electric vector of the incident light wave) directed along the $[010]$ axis in the sample plane and parallel to the $[01\bar{1}]$ axis. One readily sees that the polarization of exciting light, as should be expected when all polarization components are combined, affects only weakly the intensity of the scattered spectrum. The maximum difference between the band intensities observed for porous and crystalline silicon was nine times.
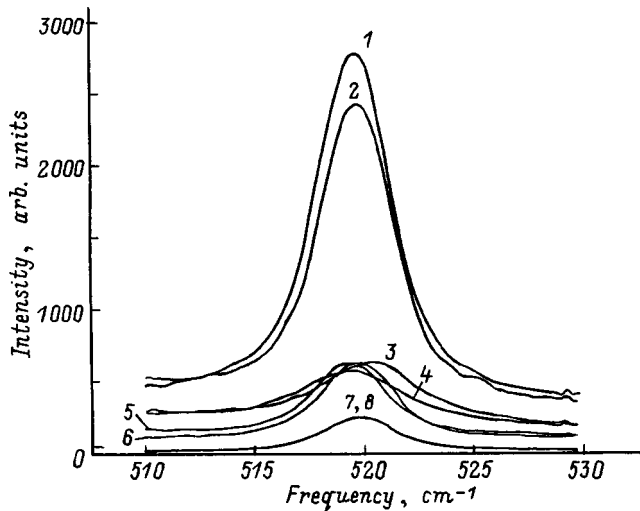
FIG. 1. Raman scattering spectra for three samples of (*1–6*) porous silicon and (*7, 8*) single-crystal silicon. Curves *1*, *3*, *5*, and *7* were obtained with the incident-light polarization oriented along the (010) axis, and curves *2*, *4*, *6*, and *8*, along the (011) axis.

2. DISCUSSION OF RESULTS

Consider a possible reason for the enhancement of Raman scattering intensity in porous silicon. It is known that the intensity of light inelastically scattered from an opaque sample can be written[9]

$$I = \eta (1/K(\omega_i)) \sum_{j=x,y,z} (e_i R_j e_s)^2,$$

where K is the absorption coefficient at the exciting light frequency ω_i, e_i and e_s are the incident and scattered polarization vectors, R_j are the components of the polarizability tensor for light scattering from phonons with polarization j, and η is a constant. The above relation shows that the enhancement in the Raman scattering intensity from porous silicon may result from a change of one of two quantities, namely, the absorption coefficient or the polarizability tensor components.

It can be assumed, however, that the polarizability tensor does not change substantially when transferring from crystalline to porous silicon. The reason for this is that quantum wires and bulk crystalline silicon have identical crystal structures. This conclusion follows from x-ray diffraction data (see, e.g., Refs. 10 and 11) and from the superposition of the lattice vibration bands in the Raman spectrum of porous silicon and c Si. It is also supported by the use of the well-known polarizability tensor of crystalline silicon when interpreting Raman experiments made on porous silicon.[6]

Thus possible reasons for the observed enhancement of Raman scattering intensity reduce to a change in the absorption coefficient of exciting light. This effect is well known. A decrease in visible light absorption in porous silicon compared to crystalline silicon was observed earlier.[12,13] The light absorption coefficient in porous silicon at a wavelength of 633 nm is reported to vary from 4×10^2 to 2.7×10^3 cm^{-1}, whereas for pure crystalline silicon it is 5.6×10^3 cm^{-1}.[14]

There is an obvious reason for an increase in light penetration in porous silicon. This is the decrease of the density in a layer of porous silicon. This factor should bring about a decrease in the absorption coefficient by a factor $(1-k)$ (k is the porosity coefficient of a porous silicon layer) and, hence, an increase of the light penetration depth in the material. However since the density of the material in the absorption layer also decreases $(1-k)$ times because of the pores, the amount of the material within the range of light penetration in porous silicon does not change, and this factor likewise will not produce enhancement in Raman scattering intensity.

This effect can be explained if one recalls the phenomenon of quantum confinement also in an electronic subsystem. The existence of this phenomenon was pointed out in the pioneering work on porous silicon,[1] and relevant numerical calculations can be found in several theoretical papers, for instance, in Ref. 15. Quantum confinement in an electronic subsystem results in a broadening of the band gap of the material. (It underlies the well-known luminescence of porous silicon in the visible.) This phenomenon can increase the light penetration depth in a material additionally by an order of magnitude and even more. Having the same lattice as conventional crystalline silicon, porous silicon behaves with respect to the properties of the electronic subsystem at the exciting-light frequency as a totally different object, namely, it is a transparent crystal with the characteristics of an insulator. The light exciting the scattering will penetrate into a substantially larger volume of the material, and this is what accounts for the enhanced Raman scattering intensity.

As already mentioned, the scattering enhancement observed by us was a factor 1.6 to 9, which is in agreement with the known[12,13] absorption coefficients for porous silicon. Note that the scatter in numerical values appears only natural in this case, because this quantity is known[15] to be different for samples with different quantum-wire cross sections. For this reason one cannot expect exact quantitative agreement of our interpretation of the phenomenon with available data. On the qualitative level, however, one may consider it proven that the anomalously high intensity of inelastically scattered light can be accounted for by a decrease of the absorption coefficient in porous silicon as a result of quantum confinement in the electronic subsystem.

[1] L. T. Canham, Appl. Phys. Lett. **57**, 1046 (1990).

[2] I. H. Campbell and P. M. Fauchet, Solid State Commun. **58**, 739 (1986).

[3] I. Gregora, B. Champagnon, and A. Halimaoui, J. Appl. Phys. **75**, 3034 (1994).

[4] F. Kozlovsky and W. Lang, J. Appl. Phys. **72**, 5401 (1992).

[5] M. E. Kompan, E. G. Kuz'minov, V. B. Kulik, I. I. Novak, and V. I. Beklemyshev, JETP Lett. **64**, 748 (1996).

[6] M. E. Kompan, V. B. Kulik, I. I. Novak, J. Salonen, and A. V. Subashiev, JETP Lett. **67**, 106 (1998).

[7] V. I. Beklemyshev, V. M. Gontar', and V. V. Levenets, Élektron. Prom. **2**, 36 (1994).

[8] D. Papadimitriou and A. G. Nassiopoulou, J. Appl. Phys. **84**, 1059 (1998).

[9] H. Poulet and J.-P. Mathieu, *Spectres de Vibration et Symmetrie des Cristaux* (Gordon and Breach, Paris, 1979) [Russ. transl. Mir, Moscow, 1983].

[10] T. Ugami and M. Seki, J. Exp. Psychol. **125**, 1339 (1978).

[11] A. Nakajima, Y. Ohshima, T. Itakura, and Y. Goto, Appl. Phys. Lett. **62**, 2631 (1993).

[12] L. V. Belyakov, D. N. Goryachev, O. M. Sreseli, and Ya. D. Yaroshetskiĭ, Fiz. Tekh. Poluprovodn. **27**, 1371 (1993) [Semiconductors **27**, 758 (1993)].

[13] M. E. Kompan and I. Yu. Shabanov, Fiz. Tverd. Tela (St. Petersburg) **36**, 2381 (1994) [Phys. Solid State **36**, 1294 (1994)].

[14] S. M. Sze, *Physics of Semiconductor Devices* (Wiley, New York, 1981) [Russ. transl. Mir, Moscow, 1984].

[15] G. D. Sanders and Y.-C. Chang, Phys. Rev. B **45**, 9202 (1992).

Translated by G. Skrebtsov

FULLERENES AND ATOMIC CLUSTERS

Photochromic effect in molybdenum-oxide cluster systems

V. N. Andreev, S. E. Nikitin, V. A. Klimov, and F. A. Chudnovskiĭ

A. F. Ioffe Physicotechnical Institute, Russian Academy of Sciences, 194021 St. Petersburg, Russia

S. V. Kozyrev and D. V. Leshchev

Institute of High-Efficiency Computations and Databases, Russian Ministry of Science, St. Petersburg, Russia

The photochromic effect under UV illumination has been studied in cluster systems of molybdenum oxides in aqueous solutions of citric acid. This paper reports the first observation of two types of systems exhibiting different photochromism. Systematic measurements of the optical characteristics, proton concentration, and photogalvanic emf have been carried out as functions of composition. A model is proposed for the molybdenum-oxide-cluster–citric-acid complex, in which intramolecular electron transfer occurs under UV illumination. © *1999 American Institute of Physics.* [S1063-7834(99)04207-0]

Oxides of transition metals (Mo, W, V) were shown to have a tendency to form cluster structures.[1–9] Cluster formations in solutions may be considered as products of polymerization of ions of transition-metal oxides (molybdates and tungstates), which occurs after the proton concentration has reached a certain level (for a given pH of the solution).[8,10,11] Clusters in amorphous films of tungsten and molybdenum oxides constitute microscopic fragments of a crystal lattice distributed throughout the film.[2,9,12] The properties of clusters should be expected to differ substantially from those of the bulk material. This is due both to lattice distortions in clusters and to the role played by the surface. As a result of the latter, reactions taking place at the cluster surface affect the properties of the cluster as a whole.

Solutions and films containing tungsten and molybdenum oxide clusters were found to exhibit the photochromic effect,[1–4] which consists in a color change of the solution or film when illuminated by UV light. It was shown that the photochromic effect is accompanied by formation of an emf (photogalvanic effect).[4–6] An additional interest in tungsten and molybdenum oxide clusters was initiated by their exhibiting nonlinear optical properties.[13]

Based on EPR and NMR studies of molybdate and tungstate solutions, a structure of the $[Mo_7O_{24}]^{6-}$ cluster was proposed,[3,11] which includes seven types of oxygen ions and three types of molybdenum ions (Fig. 1a).

Present models of coloring of molybdenum and tungsten oxide cluster systems under UV illumination reduce to the following mechanism.[1–5,7] Transition-metal clusters form complexes in interaction with water, protons, and organic substances present in the solution. UV illumination of such a complex may initiate intramolecular electron transfer, which will change the valence state of the metal in the cluster through oxidation of the organic component. The electron

appearing in the metal d orbitals will give rise to an absorption band in optical spectra, which is associated with $d-d$ transitions. Note that, in the reactions proposed in Ref. 1, the organic substance becomes oxidized irreversibly in such a process and the proton concentration decreases.

However the reversible nature of the photochromic effect and the absence of oxidation products of the organic acid revealed in our earlier studies[14,15] do not fit into the scheme proposed in Refs. 1–5 and 7.

The present work reports a study of the photochromic effect in the system of a water solution of citric acid, $C_6H_8O_7$, with ammonium heptamolybdate $(NH_4)_6Mo_7O_{24}$. Systematic studies of the optical characteristics of solutions as functions of composition and proton concentration (pH), as well as measurements of the photogalvanic emf between the illuminated and nonilluminated parts of the solution have been performed for the first time.

1. SAMPLE PREPARATION

A series of aqueous solutions containing ammonium heptamolybdate $(NH_4)_6Mo_7O_{24}$ and citric acid $C_6H_8O_7$ were prepared for the investigation. The citric acid for the solutions was OSCh grade, and the ammonium heptamolybdate was manufactured by Aldrich Chem. Co., USA. In all solutions, pH was measured with a pH-340 meter with a glass electrode. The concentration of $C_6H_8O_7$ in the solutions was 0.071M, and that of $(NH_4)_6Mo_7O_{24}$, 0.018 or 0.027M, and the pH was measured to be, respectively, 1.85 and 2.8.

More concentrated solutions were also prepared, which contained 0.2M $(NH_4)_6Mo_7O_{24}$, and $C_6H_8O_7$ in concentrations of 4M, 3M, 2M, 1.5M, 1M, with the pH values of 0.69, 0.89, 1, 1.2, and 1.4, respectively. A white sediment, presumably molybdenum hydroxide,[10,11] settled down in these
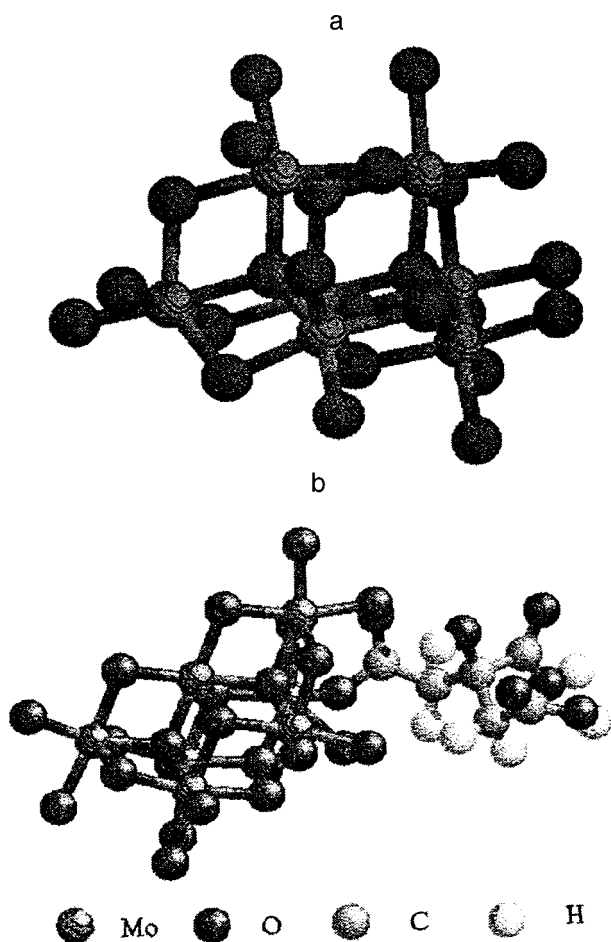
FIG. 1. (a) Structure of the $[Mo_7O_{24}]^{6-}$ cluster; (b) one of possible structures of the $[Mo_7O_{23} \cdot C_6H_7O_7]^{5-}$ complex.

solutions 16–20 h after the preparation. No such phenomenon was observed to occur in less concentrated solutions.

A number of aqueous solutions were prepared for comparison, which contained 0.027M and 0.018M $(NH_4)_6Mo_7O_{24}$ and mineral acids HNO_3 and HCl, which had the same pH values as the $C_6H_8O_7$ solutions.

2. OPTICAL MEASUREMENTS

The solutions were placed in a cuvette of optical quartz and illuminated with light of a 500-W mercury lamp mounted at a distance of 0.4 m. Light with 365-nm wavelength was cut out from the mercury lamp spectrum with color filters. The measurements were performed at room temperature, 293-294 K. The solution temperature was monitored with a thermometer in the cuvette to within 0.5°C. All samples were illuminated for 85 min. During this time the solution warmed by not more than 1°C. The optical spectra were measured with a Specord UV-VIS instrument.

As seen from Figs. 2 and 3, the absorption edge of all starting solutions was in the region of 380 nm. Our optical measurements revealed two types of solutions. In solutions of the first type, illumination with 365-nm light creates an absorption band in the region of 750 nm (Fig. 2). Illumination of the solutions of the second type initiated changes at shorter wavelengths, 380–420 nm; after the illumination, they had no longer the absorption peak at 750 nm, and the absorption-edge tail shifted toward longer wavelengths (Fig. 3). The solutions of type 1 are those with $(NH_4)_6Mo_7O_{24}$ concentration of 0.2M, and $C_6H_8O_7$ concentrations of 4M, 3M, 1M, as well as the solution 0.027M $(NH_4)_6Mo_7O_{24}$ + 0.071M $C_6H_8O_7$, and solutions of type 2, those with $(NH_4)_6Mo_7O_{24}$ concentration of 0.2M, and $C_6H_8O_7$ concentrations of 2M and 1.5M, as well as the solution 0.018M $(NH_4)_6Mo_7O_{24}$ + 0.071M $C_6H_8O_7$.
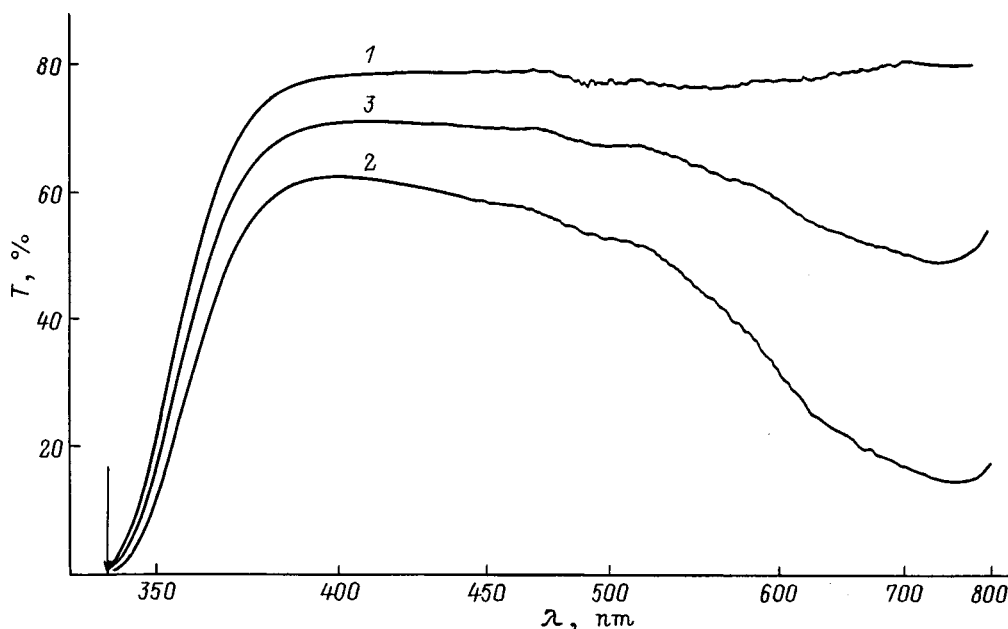
FIG. 2. Transmission spectra of solutions of type 1 {0.027M $(NH_4)_6$ $[Mo_7O_{24}]$ + 0.071M $C_6H_8O_7$}: *1* — starting spectrum, *2* — spectrum of the solution 85 min after the illumination, *3* — spectrum of the solution 30 h after completion of illumination. The arrow identifies the absorption edge.
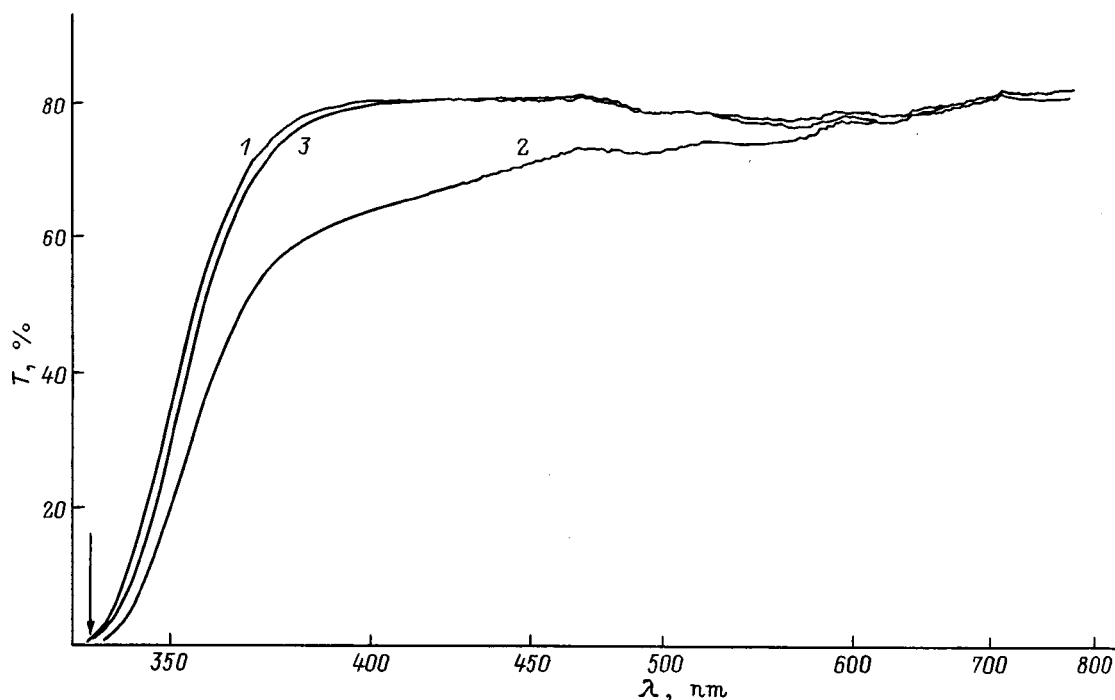
FIG. 3. Transmission spectra of solutions of type 2 {0.018M $(NH_4)_6$ $[Mo_7O_{24}]$ + 0.071M $C_6H_8O_7$}: *1* — starting spectrum, *2* — spectrum of the solution 85 min after the illumination, *3* — spectrum of the solution 30 h after completion of illumination. The arrow identifies the absorption edge.

No changes in the optical spectra of the solutions containing the inorganic acids HCl and NHO_3 were observed to occur under UV illumination. Prolonged exposure of the solutions caused color saturation, and after the illumination was turned off, the color gradually faded (Figs. 2 and 3). The time taken by the spectra to recover their initial state was 20–50 h.

3. PHYSICOCHEMICAL MEASUREMENTS

We carried out experiments to reveal the relation between the UV-induced change in the optical properties of the solutions and the proton concentration in the solution. With this purpose in mind, we measured the pH of the solutions under illumination and the UV-induced emf. The solutions used in the pH and photogalvanic-emf measurements were: 1 — 0.027M $(NH_4)_6Mo_7O_{24}$ + 0.071M $C_6H_8O_7$ and 2 — 0.018M $(NH_4)_6Mo_7O_{24}$ + 0.071M $C_6H_8O_7$. The solution under study was placed in a quartz cuvette which contained also the electrodes of the pH meter and a thermometer. To check the temperature dependence of pH, the initial solution was warmed to 305 K. The pH value essentially did not change during the procedure.

Figure 4 displays the dependence of pH on illumination time for compositions 1 and 2. Note that this dependence for solution 1 shows a tendency to saturation, whereas for solution 2 the pH variations lie within experimental error, i.e. pH practically does not change.

To measure the photogalvanic emf induced by illumination, the solutions of compositions 1 and 2 were placed in an opaque plastic container separated by a porous partition. One half of the solution was exposed to illumination, while the other half was screened from the light. The emf thus generated was measured by the compensation method using two platinum electrodes immersed in the solution. The illuminated electrode was charged negatively in both solution 1 and solution 2. The dependences of the photogalvanic emf on exposure time for solutions 1 and 2 are presented in Fig. 5. These dependences likewise exhibit a trend to saturation. Note that the photogalvanic emf for solution–1 is 100 mV, which is more than twice that for solution 2 (35–40 mV). After completion of illumination, both solutions undergo relaxation of the spectral characteristics, pH, and photogalvanic emf toward their initial levels. Unlike Ref. 1, where one observed decarboxylation of acetic acid, no evolution of a gas was observed in our case. The samples studied were capable of sustaining many coloring cycles.
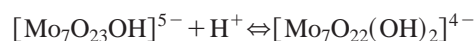
4. DISCUSSION OF RESULTS

As already mentioned, clusters possess a high reactivity, as a result of which a number of reactions giving rise to formation of complexes of molybdenum oxide clusters with associated chemical particles take place in the system under study. One has investigated to date protonation reactions (1)–(3) of the $[Mo_7O_{24}]^{6-}$ cluster in a solution of a sufficiently high acidity and determined their enthalpies ΔH and entropies ΔS:[8]

$$[Mo_7O_{24}]^{6-} + H^+ \Leftrightarrow [Mo_7O_{23}OH]^{5-}$$

$$\Delta H = 2.6 \pm 0.3 \text{ Kcal/mol},$$

$$\Delta S = 29 \pm 1 \text{ cal/mol K}. \tag{1}$$

$$[Mo_7O_{23}OH]^{5-} + H^+ \Leftrightarrow [Mo_7O_{22}(OH)_2]^{4-}$$

$$\Delta H = 0.8 \pm 0.5 \text{ Kcal/mol},$$

$$\Delta S = 19 \pm 2 \ \text{cal/mol K}. \tag{2}$$

$$[\text{Mo}_7\text{O}_{22}(\text{OH})_2]^{4-} + \text{H}^+ \Leftrightarrow [\text{Mo}_7\text{O}_{21}(\text{OH})_3]^{3-}$$
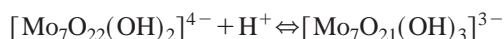
$$\Delta H = -0.6 \pm 1.3 \ \text{Kcal/mol},$$

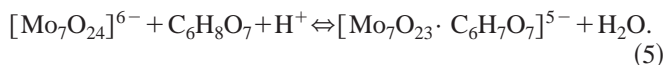$$\Delta S = 10 \pm 4 \ \text{cal/mol K}. \tag{3}$$

In these reactions, some of the end oxygen atoms in a cluster attach a proton to become OH groups. The above values of the enthalpies and entropies indicate that reactions (1)–(3) are reversible at room temperature. It is known also that protonation may cause formation of a cluster containing a water molecule as a ligand

$$[\text{Mo}_7\text{O}_{24}]^{6-} + 2\text{H}^+ \Leftrightarrow [\text{Mo}_7\text{O}_{23}\cdot\text{H}_2\text{O}]^{4-}. \tag{4}$$
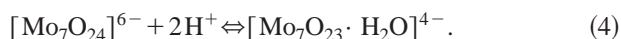
These processes cannot, however, account alone for the observed photochromic properties of the system studied. First, one does not observe any effect of UV illumination on the aqueous solutions which do not contain an organic acid. Second, if photogalvanic emf had been generated only by the difference in the proton chemical potential in different parts of the cuvette as a result of reactions (1)–(4) and of the reverse ones, it would have been of the order of 14–15 mV, which is substantially less than the experimental values (Fig. 5). This brings one to the conclusion that the main contribution to photogalvanic emf is due to the modified molybdenum clusters.

One has to conjecture that the system under study becomes photosensitive as a result of protonation which occurs simultaneously with the substitution reactions modifying the

cluster. In these reactions, the molecules of the organic acid replace the oxygen atom to become ligands in the complex, for instance,

$$[\text{Mo}_7\text{O}_{24}]^{6-} + \text{C}_6\text{H}_8\text{O}_7 + \text{H}^+ \Leftrightarrow [\text{Mo}_7\text{O}_{23}\cdot\text{C}_6\text{H}_7\text{O}_7]^{5-} + \text{H}_2\text{O}. \tag{5}$$

Citric acid is tribasic and is capable of dissociating in all three carboxyl groups to form five kinds of anions. Because each of the acid forms can join the cluster through different functional groups, reaction (5) can produce many different complexes in which the molybdenum oxide cluster $[\text{Mo}_7\text{O}_{24}]^{6-}$ is bound to a citric acid molecule; apart from this, more than one acid molecule can become attached. One of possible structural versions of the $[\text{Mo}_7\text{O}_{23}\cdot\text{C}_6\text{H}_7\text{O}_7]^{5-}$ complex was constructed with a standard quantummechanical program package and visualized by means of the RasMol code (Fig. 1b). The linear size of the complex is approximately 2 nm.

UV illumination of this complex gives rise to metal reduction simultaneously with elimination of the proton, which enters the medium (Fig. 6):
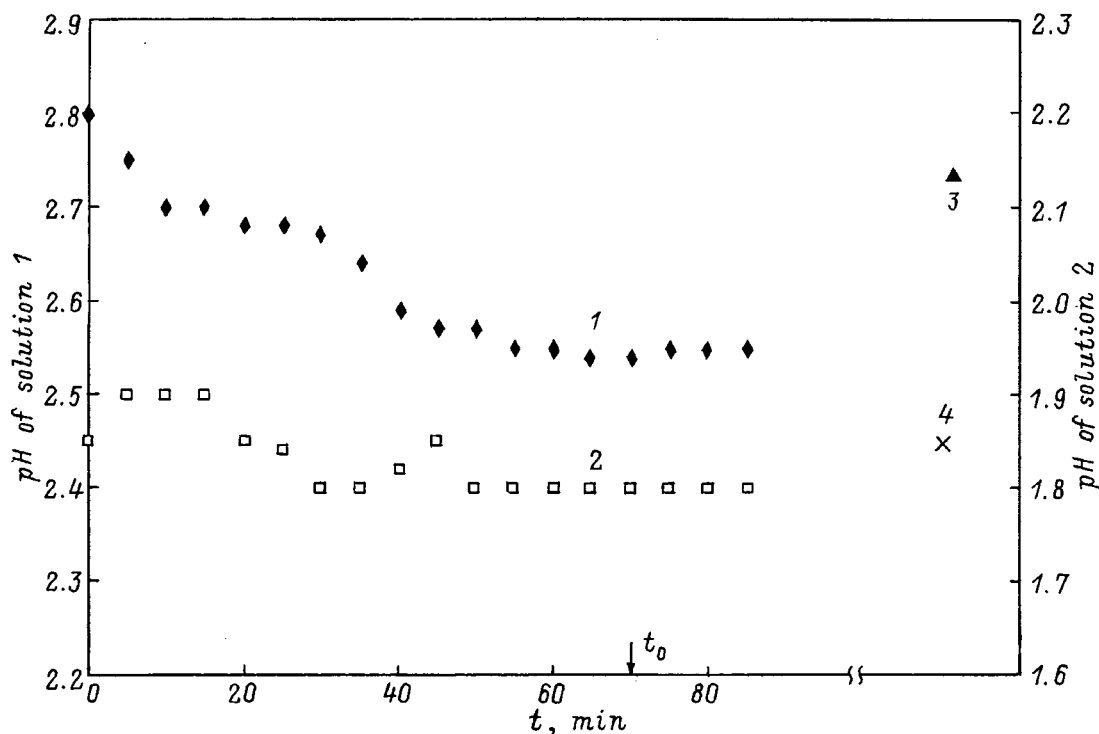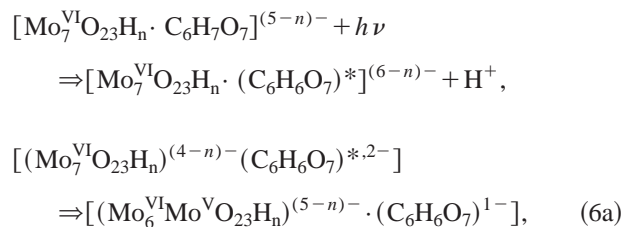
$$[\text{Mo}_7^{\text{VI}}\text{O}_{23}\text{H}_n\cdot\text{C}_6\text{H}_7\text{O}_7]^{(5-n)-} + h\nu$$

$$\Rightarrow [\text{Mo}_7^{\text{VI}}\text{O}_{23}\text{H}_n\cdot(\text{C}_6\text{H}_6\text{O}_7)^*]^{(6-n)-} + \text{H}^+,$$

$$[(\text{Mo}_7^{\text{VI}}\text{O}_{23}\text{H}_n)^{(4-n)-}(\text{C}_6\text{H}_6\text{O}_7)^{*,2-}]$$

$$\Rightarrow [(\text{Mo}_6^{\text{VI}}\text{Mo}^{\text{V}}\text{O}_{23}\text{H}_n)^{(5-n)-}\cdot(\text{C}_6\text{H}_6\text{O}_7)^{1-}], \tag{6a}$$

FIG. 4. Dependence of the proton concentration in the solutions on illumination time. *1* — type-1 solution, *2* — type-2 solution, *3* — type-1 solution 30 h after the illumination, *4* — type-2 solution 30 h after the illumination, t_0 — end of illumination.
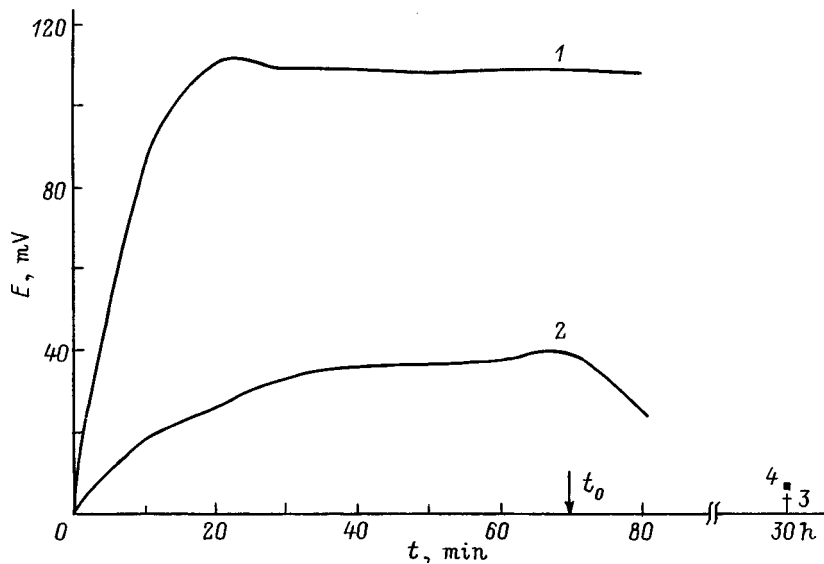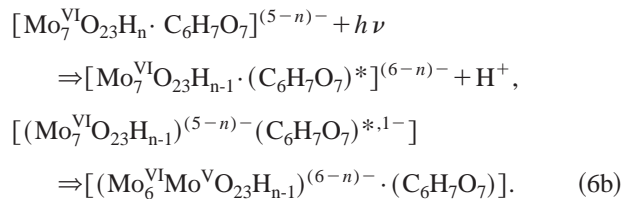
FIG. 5. Dependence of photogalvanic emf of the solutions on illumination time. *1* — type-1 solution, *2* — type-2 solution, *3* — residual emf of type-1 solution 30 h after the illumination, *4* — residual emf of type-2 solution 30 h after the illumination, t_0 — end of illumination.

$$[Mo_7^{VI}O_{23}H_n \cdot C_6H_7O_7]^{(5-n)-} + h\nu$$
$$\Rightarrow [Mo_7^{VI}O_{23}H_{n-1} \cdot (C_6H_7O_7)^*]^{(6-n)-} + H^+,$$

$$[(Mo_7^{VI}O_{23}H_{n-1})^{(5-n)-}(C_6H_7O_7)^{*,1-}]$$
$$\Rightarrow [(Mo_6^{VI}Mo^V O_{23}H_{n-1})^{(6-n)-} \cdot (C_6H_7O_7)]. \quad (6b)$$

The asterisk denotes here an excited state, in reaction (6a) the proton is detached from the acid molecule, and in reaction (6b), from the protonated cluster.

The final products of these reactions are metastable, and the complex returns to the ground state, as a result of which after the completion of illumination the solution undergoes bleaching, for instance, by the reaction

$$[(Mo_6^{VI}Mo^V O_{23}H_n)^{5-} \cdot (C_6H_6O_7)^{1-}] + H^+$$
$$\Rightarrow [Mo_7^{VI}O_{23}H_n \cdot (C_6H_7O_7)]^{5-}. \quad (7)$$
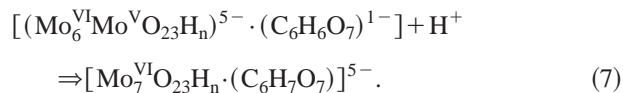
The reaction cycle (6)–(7) can repeat over and over again, which accounts for the observed reversibility of the processes.

The mechanism of the photochromic effect in aqueous solutions of an organic acid containing transition-metal oxide clusters proposed by us can be summed up as follows. A complex of molybdenum oxide cluster having citric acid as a ligand forms in reactions (1)–(5) in the system under study. UV illumination transfers the organic acid in such a complex to an excited state [the first parts of reactions (6a) and (6b)]. After this, the electron is transferred from the organic compound to the metal atom, with the corresponding change in the oxidation state of the Mo atom in the cluster from 6+ to 5+ [the completion of reactions (6a) and (6b)], and this gives rise to the formation of an absorption band associated with the *d-d* transitions appearing in the electronic spectrum around 750 nm. At the same time the proton is eliminated
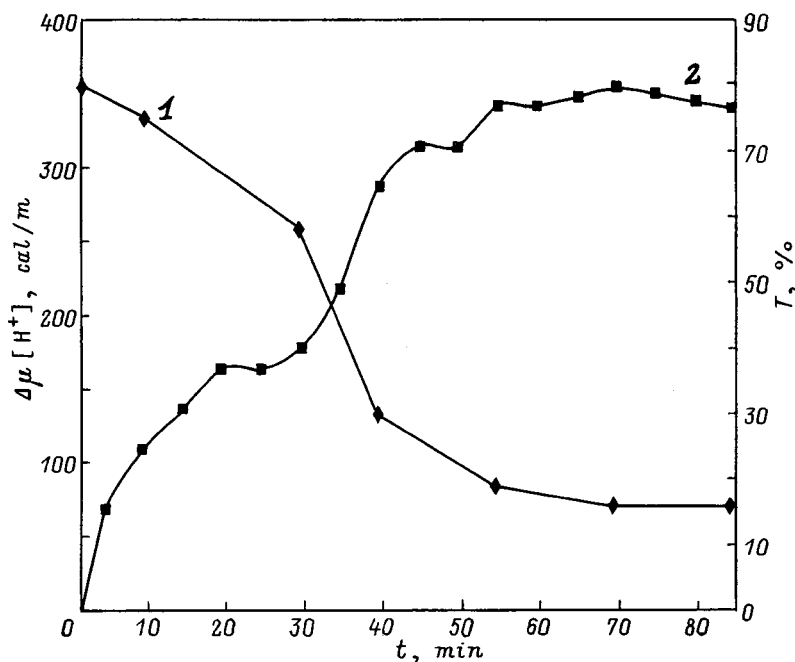

FIG. 6. Correlation between the optical properties of type-1 solution and the change in the proton chemical potential $\Delta\mu\,[H^+]$ in the solution. *1* — variation of the proton chemical potential in the solution vs illumination time, *2* — variation of the transmission of the solution at the wavelength of 750 nm vs illumination time; $\Delta\mu\,[H^+] = RT \ln [H^+]$.

from the cluster or from the acid attached to it. The electron transfer process is characteristic of solutions of type 1. In solutions of type 2, photoexcitation changes the cluster conformation and shifts the absorption edge caused by excitations from the oxygen orbitals. In both cases, the complex thus formed is energetically unstable and transfers spontaneously to the ground state [for example, by reaction (7)], which brings about gradual bleaching of the solution and recovery of the initial proton concentration (Fig. 4).

This mechanism demonstrates the unique feature of clusters in that they occupy an intermediate position between the crystals and molecules. On the one hand, the $[Mo_7O_{24}]^{6-}$ cluster is small enough to feel the changes occurring on its surface when an organic acid or any other ligand becomes attached to it. On the other hand, the number of atoms comprising it is large enough to create a potential barrier which inhibits cluster transfer back to the ground state. This barrier appears in the atomic rearrangement as the transfer of the photoexcited electron changes the electronic structure of the complex.

Thus an explanation is proposed for the observed existence of two kinds of photoinduced coloring (solutions of types 1 and 2). They differ in the behavior of the clusters after photoexcitation. The reason for this lies in that the electron transfer responsible for the photochromic effect is a process sensitive to the differences in the complex structure initiated by a relatively small change in the concentration of the starting chemical components.

[1] T. Yamase and T. Kurozumi, J. Chem. Soc., Dalton Trans. 2205 (1983).
[2] C. Bechinger, G. Oefinger, S. Herminghaus, and P. Leiderer, J. Appl. Phys. **74**, 4527 (1993).
[3] T. Yamase, J. Chem. Soc., Dalton Trans., 1987 (1982).
[4] T. Yamase and T. Ikawa, Inorg. Chim. Acta **37**, L529 (1979).
[5] T. Yamase, Inorg. Chim. Acta **64**, L155 (1982).
[6] T. Yamase and T. Kurozumi, Inorg. Chim. Acta **83**, L25 (1984).
[7] R. I. Buckley and R. J. H. Clark, Crit. Rev. Solid State Mater. Sci. **65**, 167 (1985).
[8] M. T. Pope, *Heteropoly and Isopoly Oxometalates* (Springer, Berlin, 1983).
[9] H. R. Zeller and H. U. Beyler, Appl. Phys. **13**, 231 (1977).
[10] K. G. Burtseva, L. A. Voropanova, and L. A. Kochubeǐ, Zh. Neorg. Khim. **29**, 1463 (1984).
[11] R. I. Maksimovskaya, S. M. Maksimov, A. A. Blokhin, and V. P. Taushkanov, Zh. Neorg. Khim. **35**, 1011 (1991).
[12] A. Michalak, K. Hermann, and M. Witko, Surf. Sci. **366**, 323 (1996).
[13] J. Niu, X. You, and C. Duan, Inorg. Chem. **35**, 4211 (1996).
[14] V. N. Andreev, F. A. Chudnovskii, S. E. Nikitin, and S. V. Kozyrev, *Abstracts of the 3rd International Workshop on Fullerenes and Atomic Clusters* (St. Peterburg, Russia, 1997), p. 282.
[15] V. N. Andreev, F. A. Chudnovskii, S. E. Nikitin, and S. V. Kozyrev, Mol. Mater. **10**, 409 (1998).

Translated by G. Skrebtsov

Structure and stability of clusters on metal surfaces

N. A. Levanov, A. A. Katsnel'son, and A. É. Moroz

M. V. Lomonosov Moscow State University 119899 Moscow, Russia

V. S. Stepanyuk

M. V. Lomonosov Moscow State University 119899 Moscow, Russia;
Martin Luther University, Halle-Wittenburg, D-06108 Halle, Germany

W. Hergert

Martin Luther University, Halle-Wittenburg, D-06108 Halle, Germany

K. Kokko

Turku University, FIN-20014 Turku, Finland

Small clusters of $3d$ metals Ni/Ni(001), Cu/Cu(001), $4d$-Pd/Pd(001), Ag/Ag(001), $5d$-Pt/Pt(001), and Au/Au(001) are investigated by semiempirical methods using multiparticle interatomic interaction potentials. It is shown that the same magic numbers (4, 6, and 9) are characteristic for all metals indicated; these numbers are determined by the symmetry characteristics of the clusters, related to the morphology of the fcc (001) substrate. It is shown for Pt/Pt(111) that small clusters of seven, ten, and more atoms are stable for the fcc (111) surface. This confirms that the magic numbers are associated with the symmetry of the clusters. © *1999 American Institute of Physics.* [S1063-7834(99)04307-5]

The current level of scanning tunneling microscopy (STM) investigations makes it possible to grow the most diverse clusters on metal substrates.[1,2] The intensive work in this field is largely associated with the fact that clusters on substrates possess unique magnetic properties[3–5] and could be used in the future to produce fundamentally new magnetic materials. The stability of small clusters arising at the initial stage of growth of thin films makes it possible to judge the growth mechanism occurring in practice. The observation of sharp peaks at 2, 8, 20, and 40 in the mass spectrum of Na clusters[6] and the direct analogy with magic numbers of stable atomic nuclei have provided the basis for experimental and theoretical works in cluster physics. The study of free clusters has shown that the spectrum of the most stable configurations, called magic configurations, could be due, in the first place, to filling of electronic shells[6] and, in the second place, the symmetry of interatomic bonds.[7] For example, for Na, the most stable $3D$ clusters contained 2, 8, 20, ... atoms, whereas, for free clusters of inert gases and certain transition metals, icosahedral configurations with 13, 55, ... atoms are characteristic. Even the first studies of clusters on substrates have demonstrated[8] that the spectrum of magic numbers is different from the case of free clusters. The substrate plays an important role in the formation of the structure and properties of clusters on a substrate.[9] Thus it was shown in Ref. 8, where Al/Al(001) and Al/Al(111) clusters were investigated, that stable clusters contain 4, 6, 8, 10 and 4, 7, 10 atoms, respectively. The behavior of Li/Li(111) and Al/Al(111) was found to be different. For Al the configurations 4, 6, and 9 were stable; as explained by the presence of strong s–p hy-

bridization in Al. Small Li/Li(111) clusters with an even number of atoms are most stable; this tendency disappears as the number of atoms in a cluster increases. Thus a nine-atom cluster is more stable than a ten-atom cluster. Therefore, just as for free clusters, the electronic properties of atoms and the symmetry of atomic bonds, which is associated with the type of substrate, influence the stability of clusters on substrates. In Ref. 7 Ag/Ag(001) clusters were investigated ''from first principles'' (the Green's function method) as well as by semiempirical methods with multiparticle potentials. It was shown that in both approaches the magic clusters contain 4, 6, and 9 atoms. The authors of Ref. 10 investigated the behavior of Pt/Pt(001). An experiment using field-ion microscopy shows that chains consisting of three and five Pt atoms are stable configurations, while the corresponding compact islands are metastable. Calculations performed by the embedded atom method (EAM) explain the stability of chains. Ni/Ni(001) and Pt/Pt(001) clusters have been calculated in Ref. 11. It was shown that configurations of three-, five-, and eight-atom clusters for Ni and Pt are different. Linear chains are formed by Pt, while compact islands are more stable for Ni.

Small clusters on substrates correspond to the onset of thin-film growth. Experiments by G. Comsa[12] on the scattering of He molecular beams by Pt(111) surface have shown that the scattering intensity during the deposition of Pt atoms depends on the temperature. To explain this result the authors considered the binding energy of clusters in terms of the number of bonds. If deposition is conducted at low temperature and the probability of two bonds between atoms of

a cluster rupturing simultaneously is small, then the conditions for growth of large clusters are realized. However, if the temperature increases to 600 K, then two bonds can easily rupture, while the probability that three bonds rupture simultaneously remains small. In this case the smallest stable Pt/Pt(111) cluster contains seven atoms, since three bonds must be ruptured in order to detach one atom from a compact heptamer. The next stable configuration is obtained by adding three atoms and is a compact decamer. This same system has been investigated experimentally in Ref. 13. It was found that adatoms can occupy fcc as well as hcp positions at 20 K. Adatoms in hcp positions are less strongly bound, and they switch to fcc position at temperatures of the order of 45 K.

In the present work the embedded atom method (EAM) and the Rossato–Guillope–Legrand potential, obtained in the tight-binding model, are used to investigate systematically Cu/Cu(001), Ni/Ni(001), Pd/Pd(001), Ag/Ag(001), Pt/Pt(001), and Au/Au(001) clusters. The binding energy of the atoms in clusters and its second derivative are calculated taking account of the relaxation at zero temperature. The reasons why linear chains are stable for Pt and Au are analyzed. The system Pt/Pt(111) is studied to assess the effect of substrate orientation on cluster stability.

A brief discussion of the multiparticle potentials used is presented in Sec. 1. The computational method is developed in Sec. 2. The results are discussed in Sec. 3.

1. THEORY

1.1. Multiparticle interatomic interaction potentials

The cohesion energy can be written in the form[14–19]

$$E_{coh} = E_{rep} + E_{bond}. \tag{1}$$

The repulsive energy E_{rep} is represented as a sum of pair repulsive potentials, and the binding energy is expressed in terms of the total density of states $D(E)$

$$E_{bond} = 2\sum_i \int^{E_F} (E - \varepsilon_i) d_i(E) dE. \tag{2}$$

In the second-moment approximation the binding energy is proportional to the square root of the second moment

$$E_{bond}^{(i)} = \text{const}^{1/2}. \tag{3}$$

Since $\mu_i^{(2)}$ is the sum of overlap integrals between the *i*-th atom and its neighbors, the binding energy per atom can be represented as the square root of the sum of the pair interactions between the atom *i*-th and its nearest neighbors.

1.2. Rossato–Guillope–Legrand (RGL) multiparticle potential

In the tight-binding model the contribution of a pair of atoms to the binding energy depends on the distance between the atoms and the character of the neighbors. For this reason, for the RGL potential[17,18] the binding energy is of a multiparticle character and can be represented as

$$E'_{bond} = -\left\{ \sum_{j\neq i} \xi_{\alpha\beta}^2 e^{-2q_{\alpha\beta}(r_{ij}/r_0^{\alpha\beta}-1)} \right\}^{1/2}, \tag{4}$$

where r_{ij} is the distance between the atoms *i* and *j*, $r_0^{\alpha\beta}$ is the distance between the nearest neighbors in the $\alpha\beta$ lattice, ξ is the effective exchange overlap integral, and q determines the dependence of the latter on distance. To ensure stability of the system a Born–Mayer pair repulsion

$$E_{rep}^i = \sum_j A_{\alpha\beta} e^{-p_{\alpha\beta}(r_{ij}-1)} \tag{5}$$

is added to the binding energy.

This term corresponds to electrostatic repulsion. The total cohesion energy is

$$E_{coh} = \sum_i (E_{rep}^i + E_{bond}^i). \tag{6}$$

The free parameters A, ξ, p, q, and r_0 are fit to the experimental values of the cohesion energy, the lattice constant, and the elastic moduli at zero temperature. The summation in Eqs. (4) and (5) extends to five neighbors in a cubic structure and nine neighbors in a hexagonal structure.

1.3. Embedded atom method (EAM)

In the EAM[19,20] the negative contribution to the cohesion energy is

$$\sum_i F_i(\rho_{h,i}), \quad \rho_{h,i} = \sum_{j\neq i} \rho_j^a(R_{ij}),$$

where F_i is the embedding function and $\rho_{h.i}$ is the total electron density produced by the atomic environment at the location of atom *i*. The repulsion can be written as a sum of pair potentials

$$\frac{1}{2} \sum_i \sum_{j\neq i} \phi_{ij}(R_{ij}), \quad \phi_{ij} = Z_i(R)Z_j(R)/R,$$

$$Z(R) = Z_0(1 + \beta R^\nu)e^{-\alpha R}. \tag{7}$$

The binding energy in the RGL and EAM potentials has the general form $A\sum_i F(\rho_i)$. For RGL ρ_i is the width of the density of states function, whereas for EAM ρ_i is the total electron density at the location of the *i*-th atom. The electron density can be calculated using the Clementi–Roetti[21] results for the electron densities of free atoms in the Hartree–Fock theory. The cohesion energy is

$$E_{coh} = \sum_i F_i(\rho_{h,i}) + \frac{1}{2} \sum_i \sum_{j\neq i} \phi_{ij}(Rij). \tag{8}$$

The following data were used in Ref. 19 to obtain a fit: the sublimation energy, the lattice constant, the elastic moduli, the vacancy formation energy, and the energy of the bcc phase.

2. METHOD

The surface of the metals investigated was modeled by a computational cell consisting of eight atomic layers, each layer containing 128 atoms. Periodic boundary conditions are imposed on the system in two directions perpendicular to the vertical axis; the two bottom layers are static. The equations of motion are integrated using a leap-frog algorithm[22]
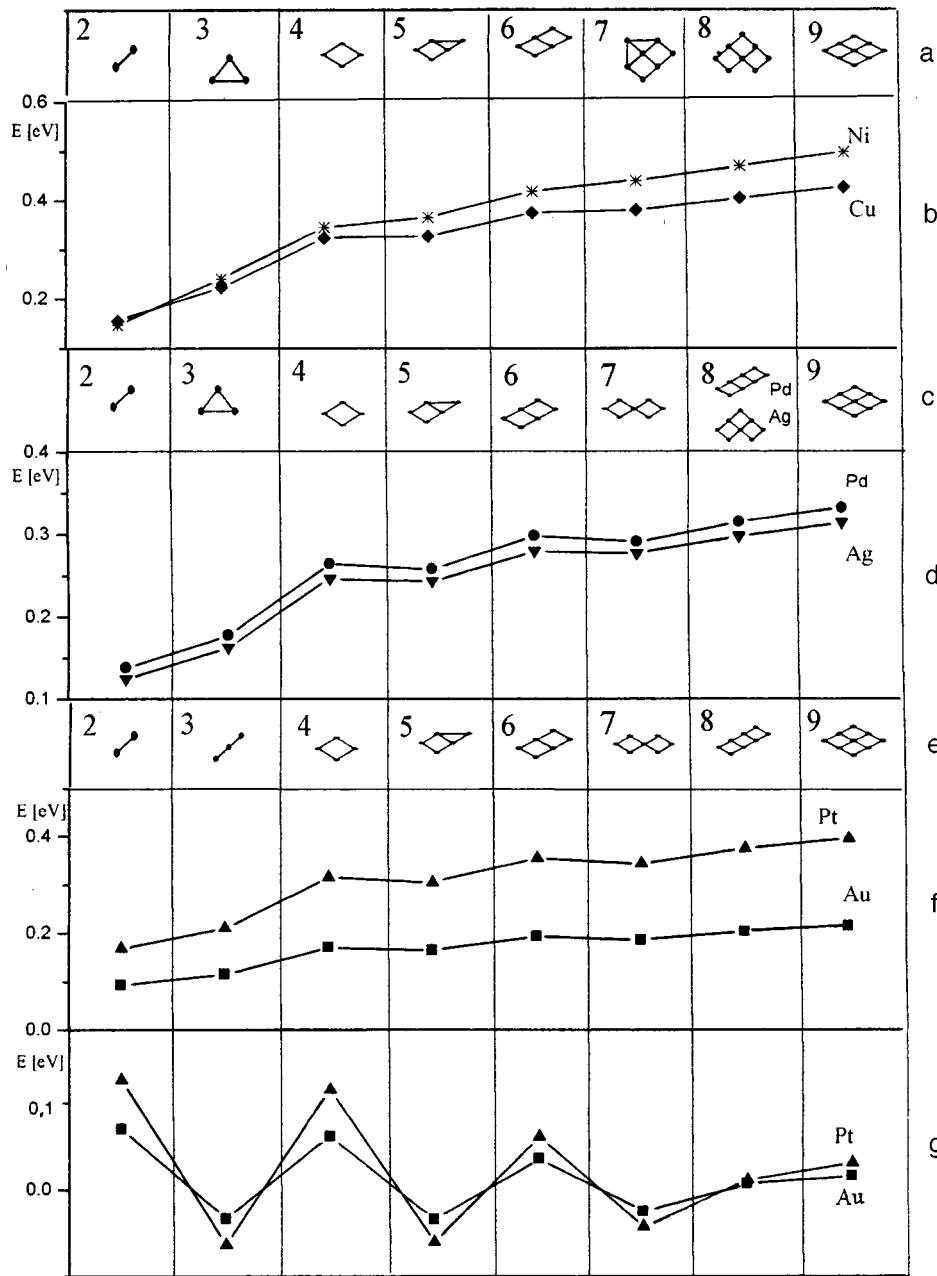
FIG. 1. Form of stable ultrasmall clusters on (001) substrates, the binding energy of such clusters (in eV/atom), and the second derivative of the binding energy as a function of cluster size for a number of transition metals: a — form of stable clusters for Cu and Ni; b — energy of stable clusters for the same metals; c — form of stable clusters for Ag and Pd; d — energy of stable clusters for the same metals; e — form of stable clusters for Au and Pt; f — energy of stable clusters for the same metals; g — second derivative of the binding energy for Au and Pt.

with time step 10^{-15} s. The following procedure is used to cool the system: During the simulation process the particle velocities directed opposite to the forces exerted by the surrounding atoms are set equal to zero. This cooling procedure is ordinarily much faster than the conventional velocity scaling. The method of steepest descent is used to search for a global minimum of the potential energy of the system.[23] The system is heated to a temperature above the melting point, after which, for example, 100 configurations of the system in the heated state are recorded with a definite time interval. Next, all recorded configurations are cooled. In this manner the system can fall into different minima. We choose the lowest minimum. This approach is optimal, though it cannot, generally speaking, guarantee that a global minimum will be found.[24–26]

At the start of the simulation process the atoms occupy the sites of an ideal fcc lattice. The binding energy and its second derivative[7]

$$E_{bind}^n = \frac{(E_{cluster} - E_{sub}) - n(E_1 - E_{sub})}{n}, \qquad (9)$$

$$E_{diff}^n = 2E_{bind}^n - E_{bind}^{n+1} - E_{bind}^{n-1} \qquad (10)$$

serve to characterize the stability of an *n*-atom cluster on a substrate.

In Eq. (9) $E_{cluster}$ is the energy of a system with a cluster on a substrate, E_1 is the energy of the system with one adatom, and E_{sub} is the energy of the substrate. All energies refer to relaxed configurations. Clusters with the minimum energy are stable.

3. RESULTS AND DISCUSSION

The stable configurations of $3d$, $4d$, and $5d$ metals calculated with the RGL potential are presented in Fig. 1. For the $3d$ metals Ni and Cu, compact islands (their shape is shown in Fig. 1a) are energetically more stable. As the number of atoms in a cluster increases, the binding energy per atom (Fig. 1b) increases (in discussing the results it is convenient to use the absolute value of the binding energy; then the minima and maxima must be interchanged). The most stable configurations of clusters are determined according to the maxima of the second derivative of the binding energy and correspond to compact structures consisting of 4, 6, and 9 atoms. The form of these curves is virtually identical for all six metals, so that we shall confine ourselves to illustrating these curves for Pt and Au (Fig. 1g). A stable cluster of eight atoms is obtained from a nine-atom (3×4) cluster by removing one corner atom. The same magic configurations are observed for Pd and Ag (Fig. 1c), but the configuration of a seven-atom cluster is different from $3d$ metals. Moreover, for Ag the configuration of an eight-atom cluster is the same as for Ni and Cu, whereas for Pd the 4×2 structure, which differs from the preceding structure by a smaller number of second neighbors (six instead of seven), is stable. The size-dependence of the energy of Pd and Ag clusters is given in Fig. 1d.

Next we shall consider stable configurations of $5d$ metals. Their form is given in Fig. 1e, the energy of the stable clusters is given in Fig. 1f, and the second derivative is given in Fig. 1g. Once again the magic numbers are largely determined by the substrate geometry and correspond to close-packed compact islands (4, 6, 9). For three-atom clusters the linear chain is more stable for Pt and Au than a compact island. Stable seven- and eight-atom clusters are the same for Pd. However, a compact island consisting of five atoms for Pt is more stable than a linear chain. This contradicts Ref. 10, where it is shown that linear chains of three and five atoms are more stable than the corresponding islands. This discrepancy is probably due to the fact that fitting the inter-

TABLE I. Binding energy for the first, second, and third neighbors (eV/atom).

Atom	I	II	III
Cu	-0.16	-0.02	0.01
Ni	-0.15	-0.07	-0.02
Ag	-0.12	-0.01	0.001
Pd	-0.14	0.005	0.002
Pt	-0.17	0.02	0.003
Au	-0.09	0.01	0.004

particle interaction potential to the bulk properties does not fully take account of the properties of the surface and of nanostructures.

The binding energies of dimers in the position of the first, second, and third neighbors on a surface calculated by the RGL potential are presented in Table I. The data presented undeniably characterize the dependence of the binding energy of a dimer on the interatomic distance though, strictly speaking, the binding energy of a pair of atoms in a cluster can differ from the binding energy of a dimer. The contribution of the second neighbors to the energy is maximum for Ni. This is because, for the metals considered, the d shell is unfilled only in Ni, and in consequence the d–d interaction is stronger for Ni. For Ni, Cu, and Ag the binding energy of the second neighbors is negative, i.e. the second neighbors are attracted, whereas for Pd, Pt, and Au the binding energy of two atoms in the positions of the second neighbors is positive and the atoms repel one another. The surroundings of atoms in chain- and island-type clusters differ by the number of second and subsequent neighbors. Thus, atoms in three-atom chains have only first and third neighbors, while three-atom islands possess, correspondingly, have only first and second neighbors. Therefore three-atom Pt and Au chains are more stable than three-atom islands. The stability of different clusters can also be considered on this basis. For example, stable clusters of eight Ni, Cu, and

TABLE II. Absolute values of binding energy for different configurations having the same number of atoms (RGL potentials, eV/atom).

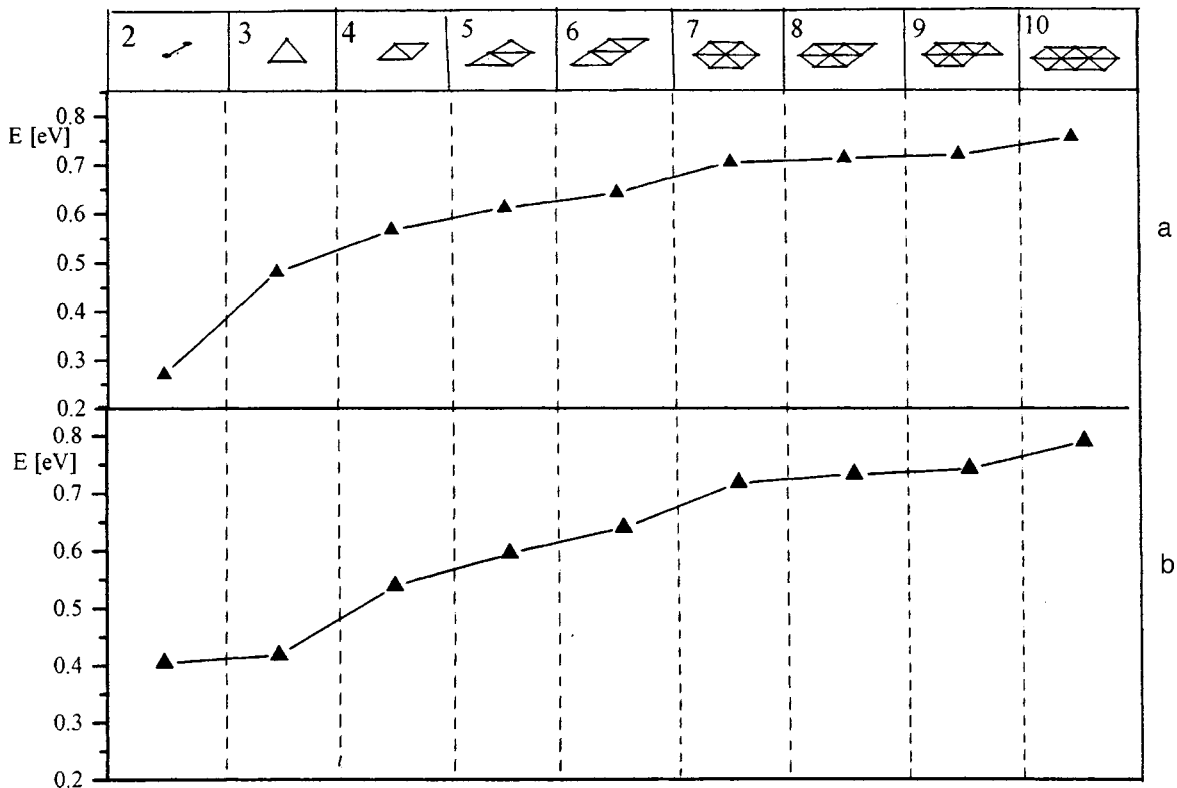|	3 △	3 ╱	5 ◇	5 ╱	7 ◈	7 ∿	7 ◇	7 ◇	8 ◇	8 ◈
Ni	0.2404	0.2028	0.3646	0.246	0.4396	0.4356	0.4195	0.4253	0.454	0.4706
Cu	0.2234	0.211	0.3271	0.2445	0.3806	0.3777	0.3736	0.3733	0.3936	0.4053
Pd	0.1775	0.174	0.2574	0.2023	0.2868	0.2906	0.2883	0.2887	0.3148	0.3137
Ag	0.1676	0.1597	0.2431	0.1861	0.2742	0.2766	0.2736	0.2728	0.2965	0.2974
Pt	0.2093	0.2103	0.3054	0.2435	0.3383	0.3441	0.3422	0.3431	0.3752	0.3727
Au	0.1117	0.1146	0.1646	0.1325	0.182	0.1827	0.185	0.1856	0.2035	0.2018

FIG. 2. Binding energy calculated for stable Pt clusters on a Pt(111) substrate by the RGL method (a) and the EAM method (b). The number of atoms per cluster and the cluster shapes are shown at the top.

Ag atoms should be different from eight-atom Pd, Pt, and Au clusters (Table II).

The simulation of Pt/Pt(001) by RGL and EAM potentials shows that the binding energy of linear chains for both metals is essentially identical, but the energy of compact islands is much lower for EAM. This is because the interaction energy of the first neighbors for RGL and EAM is virtually identical, and the positive energy corresponding to the repulsion of second neighbors is larger for EAM. Since the positive contribution of the second neighbors to the energy is larger for EAM, linear chains consisting of three and five atoms are more stable than the corresponding compact islands.

In summary, for metals with long tails of the electron density the binding energy of the second neighbors can be positive. For small clusters, therefore, linear cluster structures on substrates become most stable. The magic numbers of all six metals are determined by the structure of the substrate and correspond to compact structures consisting of 4, 6, and 9 atoms. It is evident from Table I that the binding energy between atoms is high for nearest neighbors and decreases, oscillating with increasing distance between the atoms considered. For this reason, if the system contains more than four or five atoms, the nearest neighbors of some atoms are not nearest neighbors for other atoms. As a result, the contribution due to the interaction between distant neighbors to the energy is found to be very small and the interaction between nearest neighbors, multiplied by the number of such neighbors, is the dominant contribution. The relative number of interior atoms in a cluster is greater for clusters with a

compact symmetric shape. Therefore such clusters are most stable. It is impossible to apply this rule directly to the very small clusters considered in the present work, but it can be transformed into a different rule: The energy of a system is all the larger in absolute magnitude, the larger the number of nearest neighbors in it. This number is obviously higher for compact symmetric clusters (for the same number of atoms in the system).

In conclusion, we shall present the results of a simulation of homogeneous Pt clusters on a close-packed Pt/Pt(111) surface. The results are compared with the experiment of Ref. 12. The stable structures of clusters of up to 10 atoms calculated with RGL and EAM potentials are presented in Fig. 2. In contrast to an fcc (001) surface the clusters do not contain any atoms located at distance a from one another. The second neighbors on the fcc (111) surface are located at a distance $a\sqrt{3/2}$ and correspond to the third coordination sphere in the bulk. Such neighbors first appear in four-atom clusters. Their contribution to the binding energy will be much smaller than for the fcc (001) surface. Therefore the stability of small clusters is due to the maximum number of bonds per atom, in agreement with the rule stated above. For the two potentials used, seven- and ten-atom clusters are magic. The number of bonds per atom is maximum for these clusters. The binding energy of a dimer is much lower for the RGL potential than for the EAM potential (0.27 and 0.40 eV). For this reason, for the RGL potential a maximum of the second derivative (10) corresponds to a trimer. For EAM the binding energy per atom of a cluster in a dimer

is essentially equal to the energy of a trimer, 0.40 and 0.42 eV, respectively. As a result, the maximum of the second derivative occurs for a four-atom cluster and the magic numbers for Pt/Pt(111) are 4, 7, and 10. This difference in the binding energies is due to the fact that the relaxation of the surface is very different for the RGL and EAM potentials.[17,20] For example, for Pt/Pt(001) the relaxation of the first layer Δz_{12} with RGL and EAM potentials is -4.1% and -6.9%, respectively, while for Ag the relaxation of the second layer Δz_{23} is very small for RGL and EAM, but has a different sign ($+0.6\%$ and -0.05%). In accordance with Ref. 13 the binding energy of the same clusters in fcc and hcp positions are essentially identical in our calculations. This is because the upper layer of the substrate determines the binding energy of atoms in a cluster.

In summary, the topology of the fcc (001) surface is reponsible for the fact that the magic numbers are the same for all six metals investigated (4, 6, and 9). The relation between the magic numbers and cluster symmetry is obvious; it ensures that the boundary atoms make the smallest contribution. However, as the tails of the electron density increase, the contribution of the second and subsequent neighbors increases. For this reason, on switching from $3d$ to $4d$ and $5d$ metals, as the electron density increases, the stable configurations of clusters on substrates also change. For Pt and Au, even certain linear clusters become stable. The relation between magic numbers and cluster symmetry is also confirmed for the fcc (111) surface. In this case symmetric seven- and ten-atom clusters become energetically stable. Since fitting the RGL and EAM parameters is done for bulk characteristics, the relaxation is different for different potentials. For this reason, to describe the energetics of nanostructures correctly not only bulk but also surface properties must be taken into account when determining the parameters of the potential. Our group is conducting work in this direction. One possible method is to use first-principles calculations (the Korringa–Kohn–Rostoker method) for clusters on surfaces.[3]

[1] M. F. Crommie, C. P. Lutz, and D. M. Eigler, Science **262**, 218 (1993).
[2] G. Meyer, B. Neu, and K.-H. Rieder, J. Appl. Phys. **A60**, 345 (1995).
[3] K. Wildberger, V. S. Stepanyuk, P. Lang, R. Zeller, and P. H. Dederichs, Phys. Rev. Lett. **74**, 2551 (1995).
[4] V. S. Stepanyuk, W. Hergert, K. Wildberger, R. Zeller, and P. H. Dederichs, Phys. Rev. B **53**, 2121 (1996).
[5] V. S. Stepanyuk, W. Hergert, P. Rennert, K. Wildberger, R. Zeller, and P. H. Dederichs, Phys. Rev. B **54**, 14 121 (1996).
[6] W. D. Knight, K. Clemenger, W. A. de Heer, W. A. Saunders, M. Y. Chou, and M. L. Cohen, Phys. Rev. Lett. **52**, 2141 (1984).
[7] S. K. Nayak, P. Jena, V. S. Stepanyuk, W. Hergert, and K. Wildberger, Phys. Rev. B **56**, 6952 (1997).
[8] H. Hakkinen and M. Manninen, Phys. Rev. Lett. **76**, 1599 (1996).
[9] A. K. Ray, B. K. Rao, and P. Jena, Phys. Rev. B **48**, 14 702 (1993).
[10] P. R. Schwoebel, S. M. Foiles, C. L. Bisson, and G. L. Kellogg, Phys. Rev. B **40**, 10 639 (1989).
[11] C. Liu and J. Adams, Surf. Sci. **268**, 73 (1992).
[12] G. Rosenfeld, A. F. Becker, B. Poelsema, L. X. Verheij, and George Comsa, Phys. Rev. Lett. **69**, 917 (1992).
[13] A. Golzhauser and G. Ehrlich, Phys. Rev. Lett. **77**, 133 (1996).
[14] A. P. Sutton and J. Chen, Philos. Mag. Lett. **61**, 139 (1990).
[15] S. P. Chen, A. F. Voter, and D. J. Srolovith, J. Mater. Res. **4**, 62 (1989).
[16] A. P. Sutton, M. W. Finnis, D. G. Pettifor, and Y. Ohta, J. Phys. C **21**, 35 (1988).
[17] M. W. Finnis and J. E. Sinclair, Philos. Mag. A **50**, 45 (1984).
[18] F. Rafii-Tabar and A. P. Sutton, Philos. Mag. Lett. **63**, 217 (1991).
[19] V. Rossato, M. Guillope, and B. Legrand, Philos. Mag. A **59**, 321 (1989).
[20] F. Cleri and V. Rossato, Phys. Rev. B **48**, 22 (1993).
[21] M. S. Daw and M. I. Baskes, Phys. Rev. B **29**, 6443 (1984).
[22] S. M. Foiles, M. I. Baskes, and M. S. Daw, Phys. Rev. B **33**, 7983 (1986).
[23] E. Clementi and C. Roetti, At. Data Nucl. Data Tables **14**, 177 (1974).
[24] R. W. Hockni and I. W. Istwood, *Computer Simulation Using Particles* (McGraw-Hill, New York, 1981).
[25] F. Stillinger and T. Weber, Phys. Rev. A **25**, 978 (1982).
[26] S. K. Nayak, B. Reddy, B. K. Rao, S. N. Khanna, and P. Jena, Chem. Phys. Lett. **253**, 390 (1996).

Translated by M. E. Alferieff